remote sensing

Special Issue Reprint

BDS/GNSS for Earth Observation

Edited by
Shuanggen Jin and Gino Dardanelli

mdpi.com/journal/remotesensing

MDPI

BDS/GNSS for Earth Observation

BDS/GNSS for Earth Observation

Editors

Shuanggen Jin
Gino Dardanelli

MDPI

Basel • Beijing • Wuhan • Barcelona • Belgrade • Novi Sad • Cluj • Manchester

Editors

Shuanggen Jin
Chinese Academy of Sciences
Shanghai, China

Gino Dardanelli
Università degli Studi di Palermo
Palermo, Italy

Editorial Office
MDPI
St. Alban-Anlage 66
4052 Basel, Switzerland

This is a reprint of articles from the Special Issue published online in the open access journal *Remote Sensing* (ISSN 2072-4292) (available at: https://www.mdpi.com/journal/remotesensing/special_issues/BDS_GNSS).

For citation purposes, cite each article independently as indicated on the article page online and as indicated below:

Lastname, A.A.; Lastname, B.B. Article Title. *Journal Name* **Year**, *Volume Number*, Page Range.

ISBN 978-3-0365-8996-1 (Hbk)
ISBN 978-3-0365-8997-8 (PDF)
doi.org/10.3390/books978-3-0365-8997-8

Contents

About the Editors

Shuanggen Jin

Shuanggen Jin is the Vice-President and a Professor at Henan Polytechnic University, China, and a Professor at the Shanghai Astronomical Observatory, CAS, China. He is a Member of Academia Europaea, the European Academy of Science, the Russian Academy of Natural Sciences, and the Turkish Academy of Sciences, and is also a Fellow of the African Academy of Sciences, the Electromagnetics Academy, IUGG, and IAG. He received a B.Sc. in Geodesy from Wuhan University in 1999 and a Ph.D. in Geodesy from the University of Chinese Academy of Sciences in 2003. His main research interests are Satellite Navigation, Space Geodesy, Remote Sensing, and Space/Planetary Exploration. He has published over 500 papers in ESR, JGR, IEEE TGRS, EPSL, RSE, JG, etc., and 12 books/monographs with over 12,000 citations and an H-index 58; he has also published more than 20 patents/software copyrights, and has been invited to speak at over 100 talks. He has led over 30 projects from Europe's ESA, China–Germany (NSFC-DFG), China's National Key R&D Program, and NSFC. He teaches Geodesy and Geophysics at the undergraduate and postgraduate levels and has supervised over 30 Ph.D. and 50 M.Sc. candidates, as well as 20 Post-Docs.

Gino Dardanelli

Gino Dardanelli (BSc in Civ. Eng., Ph.D. in Geodesy and Topography) was an Associate Professor (full position) at the University of Palermo (Italy) with experience in navigation positioning systems (GNSS). He participated in the surveying of two archaeological missions in partnership with La Sapienza University of Rome, Elaiussa Sebaste, Turkey (2012, 2013).

He has experience with more than 50 projects at the department involved in the acquisition, processing, and interpretation of survey data since 2002. With reference to research work, he has produced more than 100 publications, many of which have been presented at national and international seminars and congresses.

He serves on numerous Editorial Boards of scientific journals, including *Geographia Technica*, *Survey Review, ISPRS International Journal of Geo-Information* MDPI, *Civil Engineering Journal* (C.E.J), *Journal of Environmental and Earth Sciences*. .

Preface

For millennia, human communities have wondered about the possibility of observing phenomena in their surroundings, and in particular those affecting the Earth on which they live.

More generally, it can be conceptually defined as Earth observation (EO) and is the collection of information about the biological, chemical and physical systems of planet Earth. It can be undertaken through sensors in direct contact with the ground or airborne platforms (such as weather balloons and stations) or remote-sensing technologies. However, the definition of EO has only become significant in the last 50 years, since it has been possible to send artificial satellites out of Earth's orbit.

Referring strictly to civil applications, satellites of this type were initially designed to provide satellite images; later, their purpose expanded to include the study of information on land characteristics, growing vegetation, crops, and environmental pollution. The data collected are used for several purposes, including the identification of natural resources and the production of accurate cartography. Satellite observations can cover the land, the atmosphere, and the oceans.

Remote-sensing satellites may be equipped with passive instrumentation such as infrared or cameras for imaging the visible or active instrumentation such as radar. Generally, such satellites are non-geostationary satellites, i.e., they move at a certain speed along orbits inclined with respect to the Earth's equatorial plane, often in polar orbit, at low or medium altitude, Low Earth Orbit (LEO) and Medium Earth Orbit (MEO), thus covering the entire Earth's surface in a certain scan time (properly called 'temporal resolution'), i.e., in a certain number of orbits around the Earth.

The first remote-sensing satellites were the American NASA/USGS Landsat Program; subsequently, the European: ENVISAT (ENVironmental SATellite), ERS (European Remote-Sensing satellite), RapidEye, the French SPOT (Satellite Pour l'Observation de laTerre), and the Canadian RADARSAT satellites were launched. The IKONOS, QuickBird, and GeoEye-1 satellites were dedicated to cartography. The WorldView-1 and WorldView-2 satellites and the COSMO-SkyMed system are more recent. The latest generation are the low payloads called Small Satellites, e.g., the Chinese BuFeng-1 and Fengyun-3 series.

Also, Global Navigation Satellite Systems (GNSSs) have captured the attention of researchers worldwide for a multitude of Earth monitoring and exploration applications. On the other hand, over the past 40 years, GNSSs have become an essential part of many human activities. As is widely noted, there are currently four fully operational GNSSs; two of these were developed for military purposes (American NAVstar GPS and Russian GLONASS), whilst two others were developed for civil purposes such as the Chinese BeiDou satellite navigation system (BDS) and the European Galileo. In addition, many other regional GNSSs, such as the South Korean Regional Positioning System (KPS), the Japanese quasi-zenital satellite system (QZSS), and the Indian Regional Navigation Satellite System (IRNSS/NavIC), will become available in the next few years, which will have enormous potential for scientific applications and geomatics professionals.

In addition to their traditional role of providing global positioning, navigation, and timing (PNT) information, GNSS navigation signals are now being used in new and innovative ways. Across the globe, new fields of scientific study are opening up to examine how signals can provide information about the characteristics of the atmosphere and even the surfaces from which they are reflected before being collected by a receiver.

EO researchers monitor global environmental systems using in situ and remote monitoring tools. Their findings provide tools to support decision makers in various areas of interest, from security to the natural environment. GNSS signals are considered an important new source of information because they are a free, real-time, and globally available resource for the EO community.

Shuanggen Jin and Gino Dardanelli
Editors

remote sensing

MDPI

Article

Long-Term Variations of Plasmaspheric Total Electron Content from Topside GPS Observations on LEO Satellites

Shuanggen Jin [1,2,*], Chao Gao [1,3], Liangliang Yuan [1], Peng Guo [1], Andres Calabia [2], Haibing Ruan [2] and Peng Luo [1,4]

[1] Shanghai Astronomical Observatory, Chinese Academy of Sciences, Shanghai 200030, China; cgao@shao.ac.cn (C.G.); llyuan@shao.ac.cn (L.Y.); gp@shao.ac.cn (P.G.); luopeng@shao.ac.cn (P.L.)
[2] School of Remote Sensing and Geomatics Engineering, Nanjing University of Information Science and Technology, Nanjing 210044, China; andres@calabia.com (A.C.); rhb@nuist.edu.cn (H.R.)
[3] School of Astronomy and Space Science, University of Chinese Academy of Sciences, Beijing 100049, China
[4] School of Communication and Information Engineering, Shanghai University, Shanghai 200444, China
* Correspondence: sgjin@shao.ac.cn or sg.jin@yahoo.com; Tel.: +86-021-34775292

Abstract: The plasmasphere is located above the ionosphere with low-energy plasma, which is an important component of the solar-terrestrial space environment. As the link between the ionosphere and the magnetosphere, the plasmasphere plays an important role in the coupling process. Therefore, it is of great significance to study the electron content variation of the plasmasphere for the solar-terrestrial space environment. Nowadays, the topside global positioning system (GPS) observations on Low Earth Orbit (LEO) satellites provide a unique opportunity to estimate and study variations in the plasmasphere. In this paper, the plasmaspheric total electron content (PTEC) is estimated, and its long-term variations are studied from topside GPS observations onboard the Constellation Observing System for Meteorology, Ionosphere, and Climate (COSMIC). The PTEC in the daytime is higher than that in the nighttime, with the peak between 14:00 and 17:00 in the magnetic local time, while the minimum value of PTEC in the belt appears between 3:00 and 6:00 in the magnetic local time before sunrise. For seasonal variations, the PTEC is the highest in spring of the northern hemisphere and the lowest in summer of the northern hemisphere regardless of the state of the solar activity. The long-term variation in PTEC is further analyzed using 11-year COSMIC GPS observation data from 2007 to 2017. A high correlation between PTEC and the F10.7 indices is found. Particularly in the geomagnetic high-latitude region during the daytime, the correlation coefficient reaches 0.93. The worst case occurs during the nighttime in the geomagnetic middle-latitude region, but the correlation coefficient is still higher than 0.88. The long-term variations of plasmaspheric TEC are mainly related to the solar activity.

Keywords: plasmasphere; PTEC; GPS; GCPM; F10.7 index

Citation: Jin, S.; Gao, C.; Yuan, L.; Guo, P.; Calabia, A.; Ruan, H.; Luo, P. Long-Term Variations of Plasmaspheric Total Electron Content from Topside GPS Observations on LEO Satellites. *Remote Sens.* **2021**, *13*, 545. https://doi.org/10.3390/rs13040545

Academic Editor: Roberta Giuliani
Received: 7 January 2021
Accepted: 29 January 2021
Published: 3 February 2021

1. Introduction

With the continuous exploration into deep space and the increasing variety of electromagnetic applications, such as communication and navigation, monitoring and understanding of the solar-terrestrial space environment have become a hot field, including the Earth's neutral atmosphere, ionosphere, plasmasphere, magnetosphere, and so on [1]. The plasmasphere is a part of magnetosphere, also called the inner magnetosphere [2], which starts from the top of the ionosphere and ends at the plasmapause. The plasmasphere is a donut-shaped region surrounding the Earth, containing the coldest plasma of the magnetosphere [3]. It is currently believed that the charged particles in the plasmasphere mainly come from escape of the ionosphere and capture from the solar wind [4,5]. Richards et al. [6] examined the relative importance of ionospheric and thermospheric densities and temperatures in producing the annual variation of the plasmaspheric electron density. Lee et al. [7] compared the global plasmaspheric total electron content (TEC) with

the ionospheric TEC simultaneously measured by Jason-1 satellite during the declining phase of solar cycle 23, and the results showed that the plasmaspheric density structures fundamentally followed the ionosphere, but there were still significant differences.

Radio signals are refracted by the charged particles, which affects satellite navigation, positioning and microwave remote sensing. When the navigation signals of Global Navigation Satellite System (GNSS) pass through the Earth's ionosphere and plasmasphere, they are delayed due to the refraction. The magnitude of the impact is related to the total electron content (TEC) of the signal path [8]. Although the electron density of the plasmasphere is much lower than that of the ionosphere, the region covered by the plasmasphere is dozens of times larger than that covered by the ionosphere. Therefore, the electron content of the plasmasphere accounts for a considerable proportion of the total electron content, which is usually about 10% in the daytime, but can reach 60% in the nighttime [9,10].

In some practical applications, for example, when using a single frequency GPS receiver for navigation and positioning, it is impossible to eliminate the effects of charged particles by ionosphere-free combined observations, while ionospheric empirical models are not precise enough to eliminate the error caused by such delay. Current main ionospheric models, such as the International Reference Ionosphere (IRI) model and the NeQuick model, can only estimate the electron content of the ionosphere, but ignore the plasmaspheric TEC (PTEC). Therefore, the corresponding delay effect cannot be estimated or corrected precisely, which has an impact on the final positioning results [11,12]. Therefore, it is important to estimate the PTEC for the delay correction. Furthermore, the coupling processes between the plasmasphere and the ionosphere are very complex. The studies on the plasmaspheric electron content variations and dynamic coupling processes between the plasmasphere and the ionosphere are crucial for understanding the plasmasphere [13].

Before the advent of GNSS radio occultation technology, the PTEC was generally difficult to measure directly. The TEC acquired by ground GNSS receivers is the total electron content of the ionosphere and the plasmasphere. The ionospheric TEC (ITEC) can be obtained from the ionosonde or incoherent scattering radar (ISR), and then PTEC is indirectly calculated by subtracting ITEC from the total TEC [14,15]. However, there are a series of problems with these methods. Firstly, normally the electron density profile below the peak value of F2 layer can be obtained by the ionosonde, and the electron density profile above the peak value is extrapolated by the Chapman function [16]. Secondly, the number of observation stations of ionosonde and ISR is relatively small, and the distribution is very sparse. In addition, the cost is a little high, which leads to limited coverages in the global ionospheric observations. Furthermore, there are likely systematic deviations between different observation techniques and methods, which will be involved into the PTEC estimation. Therefore, it is challenging to accurately estimate PTEC and establish the plasmaspheric model.

Nowadays, with the increasing number of GNSS Radio Occultation observations on Low Earth Orbit (LEO) satellites, the topside GNSS observations on LEO satellites provide a unique opportunity to directly estimate PTEC and study its variations in the plasmasphere, particularly Constellation Observing System for Meteorology, Ionosphere, and Climate (COSMIC) with six LEO satellites. The COSMIC can provide more than 2500 occultation events per day during the normal operation period of six LEO satellites [17,18]. In this paper, the PTEC is estimated, and its long-term variations are studied based on topside GPS observations on COSMIC with providing the slant TEC (sTEC) of the signal path. The sTEC is transformed into vertical TEC (vTEC) by a mapping function, and then the grid model of PTEC is established. The spatial and temporal distribution characteristics of PTEC are analyzed as well as its long-time variation characteristics from January 2007 to December 2017. In Section 2, the data and method are introduced, the results and analysis are presented in Section 3, and finally, conclusions are given in Section 4.

2. Data and Method

The data used in this paper are the precise podTec provided by COSMIC from January 2007 to December 2017, which can be obtained from the COSMIC data analysis and archiving center (https://www.cosmoc.ucar.edu/cdaac/). The PodTec files provide UTC time, three-dimensional coordinates of LEO and GPS satellites, observation elevation of the GPS-LEO observation link at LEO satellite, and the slant TEC on the signal path. It is worth noting that the hardware delays of the transmitters on GPS satellites and the receivers on COSMIC satellites have been deducted from the TEC, and the sampling rate of the observations is 1 s [19]. Since the volume of observation data after 2017 is too small, we only use the observation data from 2007 to 2017 in this paper. In addition, to ensure the consistency of the altitude region covered by the observations, the observation data before LEO satellites lifting their orbits are also eliminated.

To estimate the plasmaspheric TEC, it is necessary to set a thin shell, and the electron content is assumed to be concentrated on the shell. The method of the gridded plasmaspheric TEC model is basically the same as that of the Global Ionosphere Model (GIM) [20,21]. We tested the effects of the thin shell heights on PTEC results, and found a small difference and little effect on the temporal and spatial distribution of PTEC. Therefore, we set the altitude of the thin shell at 1400 km. Detailed plasmaspheric TEC modeling is shown in Figure 1.

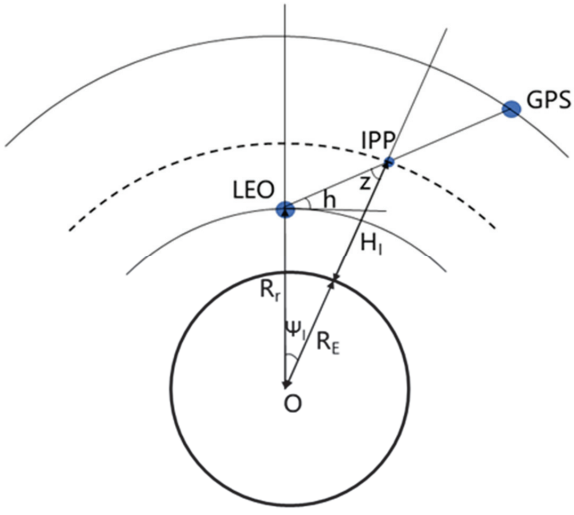

Figure 1. Diagram of topside GPS observations of LEO satellite and the single layer plasmasphere hypothesis.

Firstly, the baseline between the LEO and GPS satellites is transformed to the station-centered coordinate system, and then the azimuth angle A and the elevation angle h are calculated as:

$$X_{NEU} = \begin{bmatrix} -\sin B\cos L & -\sin B\sin L & \cos B \\ -\sin L & \cos L & 0 \\ \cos B\cos L & \cos B\sin L & \sin B \end{bmatrix} X_{XYZ} \quad (1)$$

$$A = \arctan\left(\frac{X_E}{X_N}\right) \quad (2)$$

$$h = \arctan\left(\frac{X_U}{\sqrt{X_N^2 + X_E^2}}\right) \quad (3)$$

where B and L are the geographic latitude and longitude of the LEO satellite, respectively, and X_{XYZ} and X_{NEU} are the coordinates of the LEO-GPS baseline in Earth-centered Earth-fixed (ECEF) coordinate system and the station-centered coordinate system, respectively.

To reduce the mapping errors and multipath effects, only the observations with an elevation angle greater than 40° are used to establish the plasmaspheric TEC grid model. The sTEC observations with negative values or over 100 TECU, which can be considered to be unreasonable observations, are also removed. Then, we calculate the obliquity factor z between LEO and GPS satellites and the vertical TEC:

$$z = \arcsin[(R_r cosh)/(R_E + H_I)] \tag{4}$$

$$vTEC = sTEC \cdot \cos(z) \tag{5}$$

where R_r is the distance between the receiver on the LEO satellite and the Earth's center, R_E is the radius of the Earth, H_I is the altitude of the single layer plasmasphere (here we set it as 1400 km). Then, the geographic longitude and latitude of the plasmaspheric piercing point can be calculated as follows:

$$\Psi_I = \pi/2 - h - z \tag{6}$$

$$\varphi_I = \arcsin(\sin B \cos \Psi_I + \cos B \sin \Psi_I \cos A) \tag{7}$$

$$\lambda_I = L + \arcsin(\sin \Psi_I \sin A / \cos \varphi_I) \tag{8}$$

where Ψ_I is the geocentric angle between LEO satellite and the piercing point, and φ_I and λ_I are the geographic latitude and longitude of the piercing point, respectively.

The geographic longitude and latitude are converted to geomagnetic longitude and latitude, and the magnetic local time is calculated as follows:

$$m\varphi_I = \arcsin(\sin(\varphi_I)\sin(b_0) + \cos(\varphi_I)\cos(b_0)\cos(l_0 - 1)) \tag{9}$$

$$m\lambda_I = \arctan\left(\frac{\cos(\varphi_I)\sin(l_0 - 1)/\cos(m\varphi_I)}{(\sin(b_0)\sin(m\varphi_I) - \sin(\varphi_I))/(\cos(b_0)\cos(m\varphi_I))}\right) \tag{10}$$

$$mLT_I = UT_I + (m\lambda_I - l_0)/\left(15^\circ \times \pi/180^\circ\right) \tag{11}$$

where $m\varphi_I$ and $m\lambda_I$ are the geomagnetic latitude and longitude of the piercing point, respectively, b_0 and l_0 are the geographic latitude and longitude of the geomagnetic north pole, respectively, and $b_0 = 80.0^\circ$, and $l_0 = -72.2^\circ$, UT_I and mLT_I are the universal time and magnetic local time of the observation, respectively.

Finally, we divide all the observations in a month or a season into groups with a latitudinal resolution of 2.5° and a temporal resolution of 20 min, and the observations in each group are weighted and averaged according to the value of $\left(1 + cos^2 h\right)^{-1}$ as the PTEC of the corresponding grid point. In all the formulas above, angles are in radians and distances are in kilometers.

3. Results and Analysis

The COSMIC constellation consists of six LEO satellites, which provide dense global coverage plamaspheric observations. Figure 2 shows the geographical distribution of the piercing points on the 1400 km thin shell on 2 January 2008. Due to the inclination of the satellite orbits and the lowest observation elevation angle of 40°, the distribution of the piercing points has gaps at the north and south poles. However, in the region between 72°S and 72°N, the topside observations of LEO satellites are well-distributed, and all observations can be regarded as observations from GPS satellite altitude (about 20,200 km) to COSMIC satellite altitude (about 800 km). Although this altitude range is not exactly consistent with the real plasmasphere, the observations are homogeneous in the detection altitude, and basically contain most of the charged particles of the plasmasphere, so they

can be regarded as the observations for the plasmasphere. These conditions are quite favorable for plasmaspheric modeling.

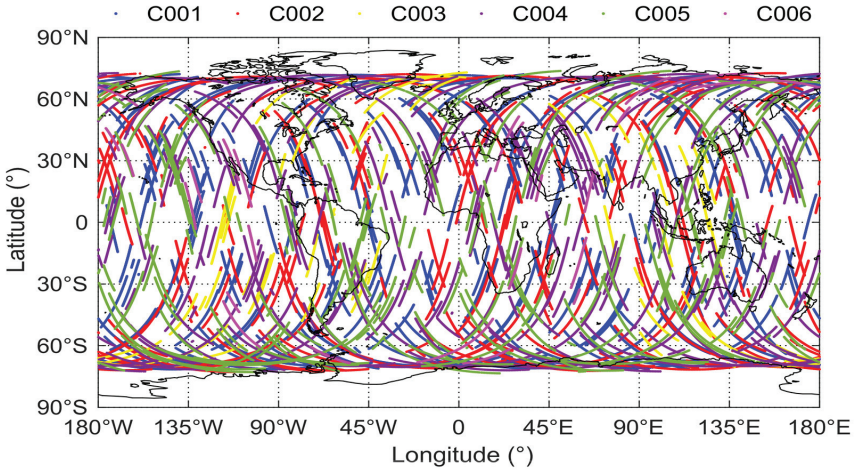

Figure 2. The distribution of COSMIC piercing points at the 1400 km thin shell on 2 January 2008

3.1. PTEC Estimation from COSMIC

According to the definition of plasmasphere, the distribution of charged particles is dominated by the Earth's magnetic field. Therefore, the geomagnetic coordinate system is used in modeling. The magnitude of PTEC is closely related to the position of the sun, so the geomagnetic longitude is converted to the magnetic local time. On the basis of topside GPS observations of COSMIC, the plasmaspheric TEC grid model is estimated. This paper mainly analyzes the temporal and spatial distribution and long-term variation of PTEC, considering the volume of data and the convenience of analysis, so we divide the observations separately by month and model. In this way, the effects of long-period variations like solar activity on PTEC are preserved, while the influence of geomagnetic activities, such as magnetic storms and sub-magnetic storms, which are relatively short-lived (from a few hours to one or two days), is averaged over one month's observations, with a minimal impact on modeling. When analyzing the seasonal variation of PTEC, we combine the observations of three months together and re-weight the observations to calculate the PTEC.

The Global Core Plasma Model (GCPM) is the first real global plasmaspheric model, and was established by Gallagher et al. [22] by integrating density distribution models of different regions. It covers the ionosphere, plasmasphere, plasmapause, plasmaspheric poles, and so on. In the ionosphere, GCPM adopts the international reference ionosphere model IRI. The plasmaspheric region is based on the density distribution model of H+ established according to the observations of DE-1 satellite by Gallagher et al. [22]. The Persoon model is adopted in the polar regions [23]. These regional models are integrated by mathematical fitting to create a static three-dimensional plasmaspheric model GCPM, which can extend from the ionosphere to 8 to 9 radii of the Earth.

Figure 3 shows the comparison of PTEC from the topside GPS observations of COSMIC in January 2008 with the GCPM and the differences in the bottom panel. The blank regions in the top and bottom panels are caused by the fact that the observations of COSMIC cannot completely cover the polar region. In January 2008, the state of solar activity was quiet, and the F10.7 indices exhibit little change, at less than 80 sfu. This that the observations of PTEC from COSMIC and GCPM are almost consistent with respect to the overall characteristics. There is a significant belt with higher values of PTEC at geomagnetic latitudes between -45° and 45°, and PTEC values in the daytime are higher than those in the nighttime. In addition, the PTEC values in the top panel decrease slowly from the

geomagnetic equatorial region to the geomagnetic polar regions, while in the middle panel, the PTEC values decrease rapidly in the geomagnetic middle-latitude regions. As a result, the differences show significant zonal belt distribution in the bottom panel, and in the middle and high geomagnetic latitudinal regions.

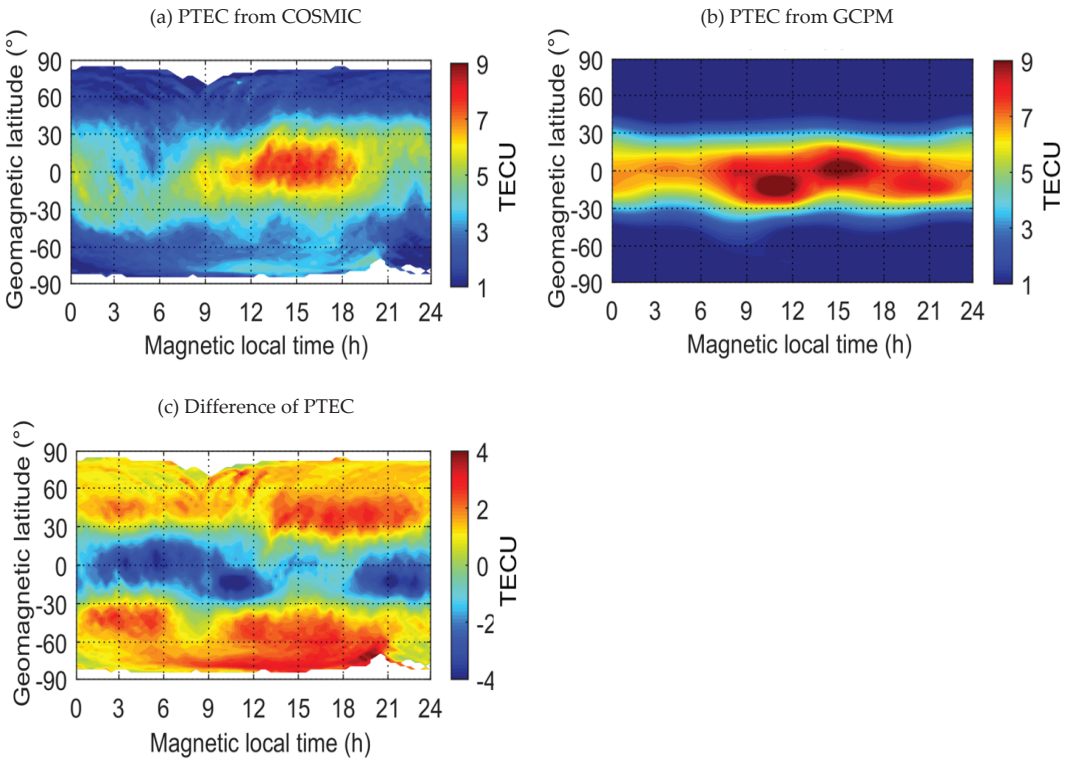

Figure 3. Comparison of PTEC from topside GPS observations of COSMIC and GCPM in January 2008 (The altitude range is from about 800 km to 20,200 km): (**a**) PTEC from COSMIC, (**b**) PTEC from GCPM, and (**c**) difference of PTEC.

The left panel in Figure 4 shows the comparison of the PTEC values from topside GPS observations of COSMIC and GCPM in January 2008 at corresponding positions. The correlation coefficient of PTEC values is 0.85, which indicates a good consistency between the PTEC from COSMIC observations and GCPM. The right panel shows the distribution histogram of PTEC differences. Almost all the differences are within ± 4 TECU, and the numbers of differences over ± 3 TECU are less than 5% of the total statistics, which also shows that the two PTEC results are in good agreement with each other.

In general, it has a relatively high correlation of PTEC between GCPM and the COSMIC observations, and the correlation is higher in quiet period of solar activity. However, since GCPM is a model fitted by mathematical formulas, the result is very smooth in numerical value and therefore the details cannot be seen from the model. The PTEC estimation from topside GPS observations of COSMIC is based on the actual observations, which contains more rich details.

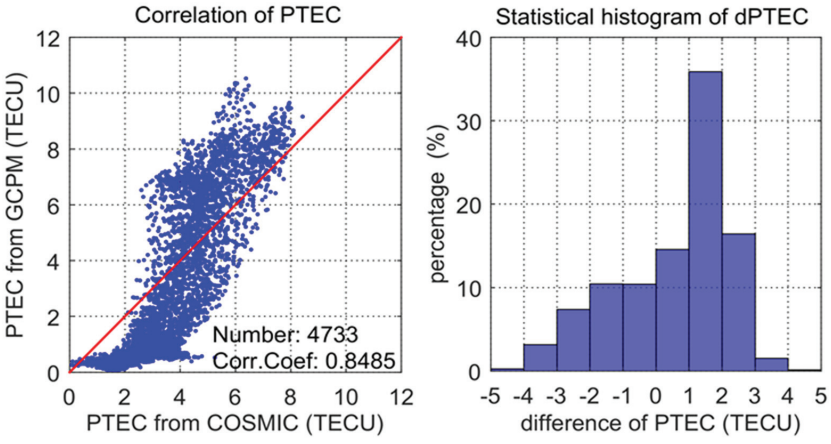

Figure 4. Comparison and difference distribution of PTEC from topside GPS observations of COSMIC and GCPM in January 2008.

3.2. Temporal-Spatial Distribution Characteristics of PTEC

The long-term variations of plasmaspheric TEC and its temporal-spatial distribution characteristics are analyzed using COSMIC-derived PTEC. According to the solar activity, we selected 2008 and 2014 as the representatives of low and high solar activity years, respectively, and established the PTEC gridded model using COSMIC observations by month and season, and the monthly and seasonal variations characteristics of PTEC under different states of solar activity are analyzed.

Figures 5 and 6 show monthly and seasonal variations of plasmaspheric TEC in 2008, respectively. Observations of January and February 2009 were also used in the subgraph in the bottom right panel of Figure 6. The PTEC values in different months or seasons have the same following basic characteristics: PTEC values at daytime are higher than those at nighttime; PTEC values in lower geomagnetic latitudinal regions are higher than those in higher geomagnetic latitudinal regions; and there are obvious zonal belts with higher PTEC values within the $\pm 45^{\circ}$ geomagnetic latitudinal region. This is because the solar incidence angle in the geomagnetic low-latitude region is the greatest in the daytime, where the plasmasphere captures the most energy, and thus generates more charged particles through ionization. These phenomena can also prove a close relationship between the plasmaspheric TEC and solar activity, which will be analyzed in the next section.

In the high PTEC value belts within $\pm 45^{\circ}$ geomagnetic latitude, the peak values of PTEC in monthly and seasonal models all appear in the geomagnetic equatorial region between 14:00 to 17:00 o'clock in the magnetic local time, while the minimum values of PTEC appear between 3:00 and 6:00 o'clock in the magnetic local time. This can be explained by the coupling process between the plasmasphere and the ionosphere. The charged particles in the ionosphere drift upward along the Earth's magnetic field lines to the plasmasphere in the daytime, while the charged particles in the plasmasphere will return to the ionosphere to maintain the electron density of the F layer in the nighttime, so the electron content of plasmasphere will reach the minimum value before sunrise [24]. In Figure 5, we can see that values of plasmaspheric TEC in June, July and August 2008 are significantly lower than those in other months, and values of plasmaspheric TEC in March and November are the highest. At the seasonal scale, the plasmaspheric TEC is the highest in the northern hemisphere spring and the lowest in northern summer, which are related to the variation of the vertical radiation region of the sun. The seasonal variation of the plasmaspheric TEC is consistent with the variation of the ionospheric TEC due to the strong coupling interaction [25].

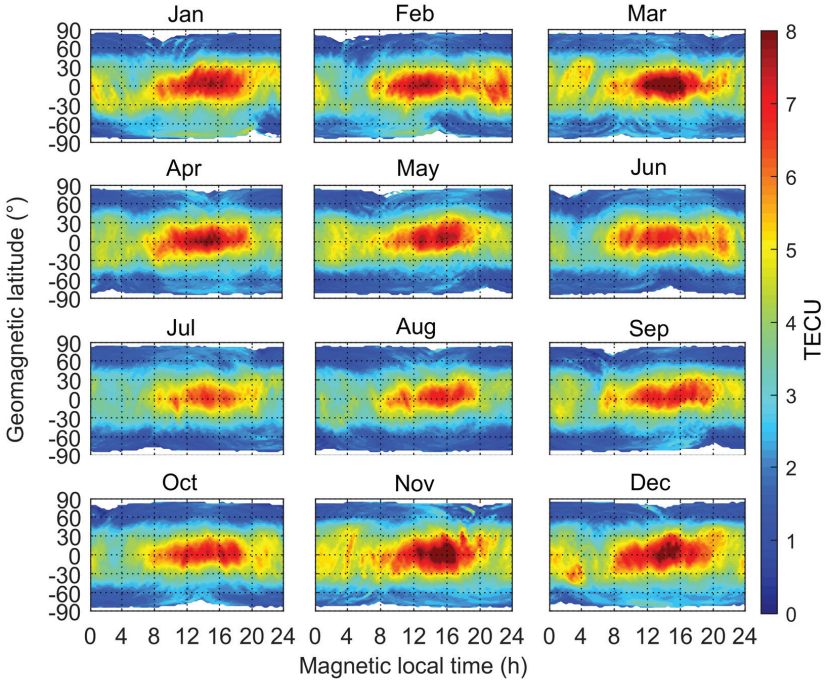

Figure 5. Monthly variation of plasmaspheric TEC in 2008.

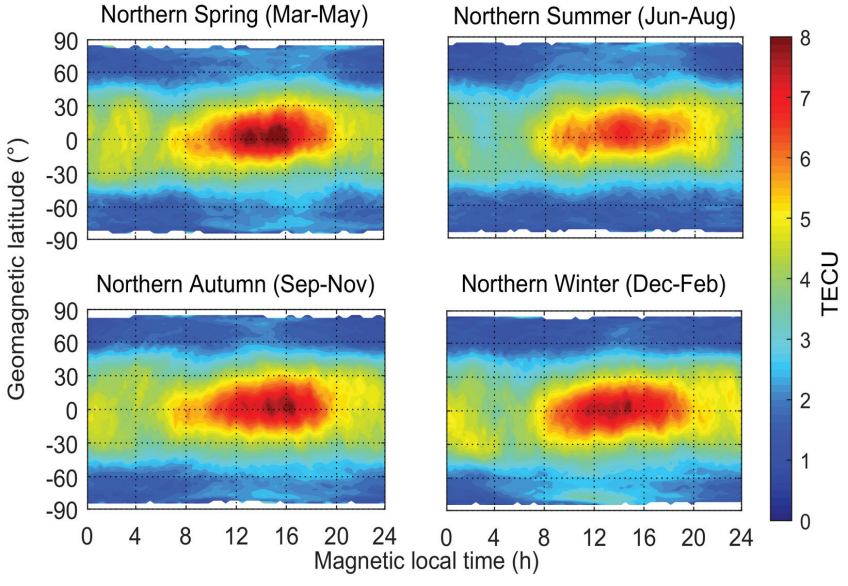

Figure 6. Seasonal variation of plasmaspheric TEC in 2008.

To analyze the influence of magnetic local time and geomagnetic latitude on plasmaspheric TEC, we divided the monthly PTEC into six parts. There are daytime and nighttime regions: the magnetic local time from 6:00 to 18:00 o'clock is the daytime, and the nighttime is from 18:00 to the second day's 6:00 o'clock. As for geomagnetic latitude, it

is divided into low-latitude, mid-latitude and high-latitude, with boundaries of ±30° and ±60°. The average PTEC of each region was calculated, and is shown in Figure 7. Since the solar and geomagnetic activities were quite calm in 2008, the variations of plasmaspheric TEC in different regions were also small and gentle, with a maximum variation range of about 1.2 TECU. Apparently, the maximum values of plasmaspheric TEC always appeared in the low-latitude region in the daytime, and the maximum value was in November 2008, reaching 6.2 TECU. The sub-maximum values were in the nighttime low-latitude region, with a maximum value of 5 TECU in November. The differences between daytime and nighttime PTEC in the low-latitude region are about 1 TECU. In mid-latitude region, the plasmaspheric TEC is around 3 TECU, and there is a small difference between daytime and nighttime. However, the relative differences of plasmaspheric TEC between daytime and nighttime are quite large for the small value of PTEC in high-latitude region. In general, the effect of geomagnetic latitude on plasmaspheric TEC is more obvious.

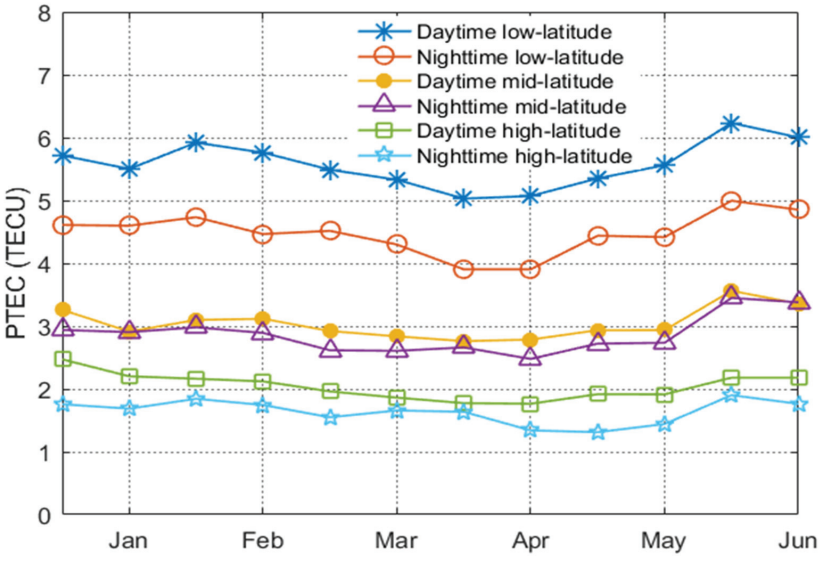

Figure 7. Monthly mean daytime and nighttime PTEC in different geomagnetic latitudes in 2008.

Figures 8 and 9 show the monthly and seasonal variations of plasmaspheric TEC in 2014, respectively. Observations of January and February 2015 are also used in in the subgraph at bottom right of Figure 9. The basic distribution characteristics of plasmaspheric TEC mentioned above still exist. The most obvious difference is that the belts with higher PTEC values are wider during the solar active period, especially in the daytime, which indicates that during the solar active period, a larger region of the plasmasphere can receive strong solar radiation, thus ionizing to generate more charged particles. In terms of numerical value, the peak values of PTEC are significantly higher than those in 2008, which are almost double in some months. In June, July and August 2014, the values of plasmaspheric TEC are smaller than those in other months, which is the same as 2008. This phenomenon is also reflected on the seasonal scale, whereby the values of plasmaspheric TEC in northern summer are much lower than those in other seasons. An interesting phenomenon is that the local maximum values of PTEC appear around 12:00 o'clock in the region of geomagnetic latitude -80° in spring, autumn and winter of the northern hemisphere, which indicates that the charged particles of the plasmasphere will accumulate in this region at noon, and its physical mechanism needs to be further studied.

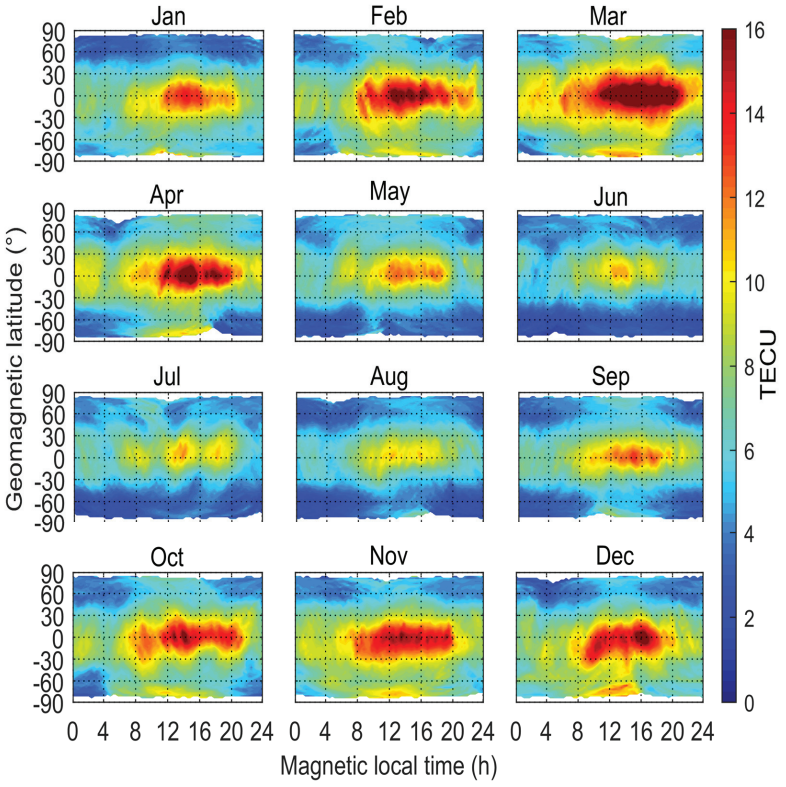

Figure 8. Monthly variation of plasmaspheric TEC in 2014.

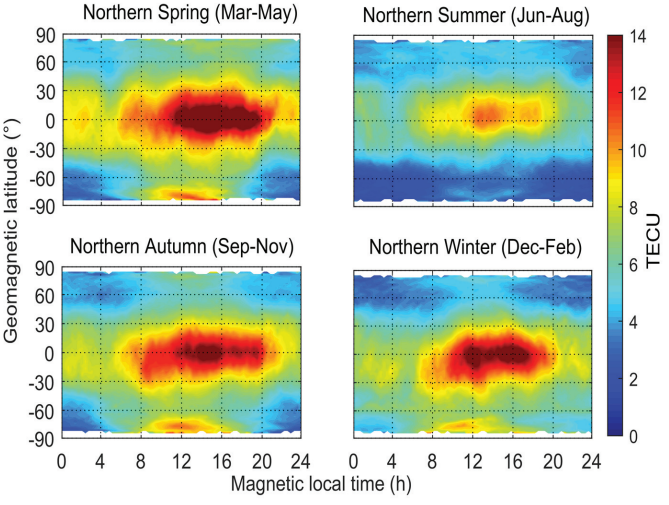

Figure 9. Seasonal variation of plasmaspheric TEC in 2014.

In the same way, we also analyzed the influence of magnetic local time and geomagnetic latitude on plasmaspheric TEC in 2014, during which year the solar activity was very active. An obvious feature is that the maximum values of plasmaspheric TEC in different regions all appeared in March, and the maximum reached 13.7 TECU in the

daytime low-latitude region (Figure 10). The variations of plasmaspheric TEC in different regions were relatively large, with a maximum variation range of about 5.6 TECU, and the relative variations were also greater than those in 2008. The same characteristics as 2008 were not repeated here. An obvious distinction is that values of plasmaspheric TEC in the daytime high-latitude region were higher than those in the nighttime mid-latitude region, except for January, June and July, which shows that the high-latitude region was more affected in intense periods of solar activity.

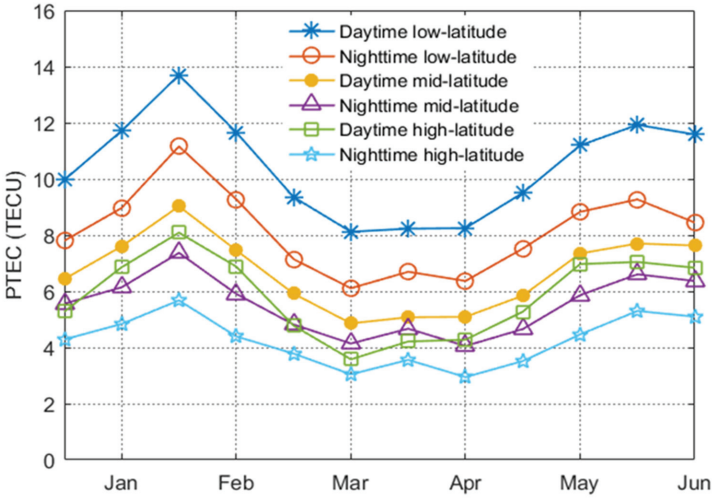

Figure 10. Monthly mean daytime and nighttime PTEC in different geomagnetic latitudes in 2014.

3.3. Correlation with Solar Activity

The plasmasphere is located above the Earth's ionosphere with much lower particle density, but it is greatly affected by the solar radiation, which leads to the complex characteristics of plasmaspheric electron density variation. To study the relationship between plasmaspheric TEC and solar activity, we chose the F10.7 index as the reference indicator. There is a strong correlation between the 10.7 cm radio flux and the number or area of sunspots. At present, as one of the most important indices of solar activity, the F10.7 index has been widely used in space weather research and related studies of ionosphere and magnetosphere [26].

Figure 11 shows the monthly mean F10.7 indices and monthly mean PTEC from 2007 to 2017, where the red line represents the monthly mean F10.7 indices, corresponding to the left ordinate, and the blue line represents the plasmaspheric TEC, corresponding to the right ordinate. Before 2011, the monthly mean F10.7 indices were relatively small, and the variation was relatively gentle. During this period, the solar activity was relatively calm. After January 2011, the monthly mean F10.7 index rose sharply, and the variation was very intense, indicating that the solar activity was in an active period. Then, after 2015, the F10.7 index began to decline, and the solar activity decreased accordingly. The variation of monthly mean PTEC (the arithmetic average of PTEC at each grid point of the monthly plasmaspheric model) from 2007 to 2017 is shown in Figure 11, and the standard deviation of each monthly mean PTEC is also calculated and shown with an error bar. Most of the standard deviations are less than 2.5 TECU, which indicates that the monthly mean PTEC is of significance. The values of monthly mean PTEC were also low before 2011, basically no more than 5 TECU, and the variation was relatively gentle. After 2011, the monthly mean PTEC also began to rise, and then began to decline after 2015, which was basically consistent with the variation of the monthly mean F10.7 indices.

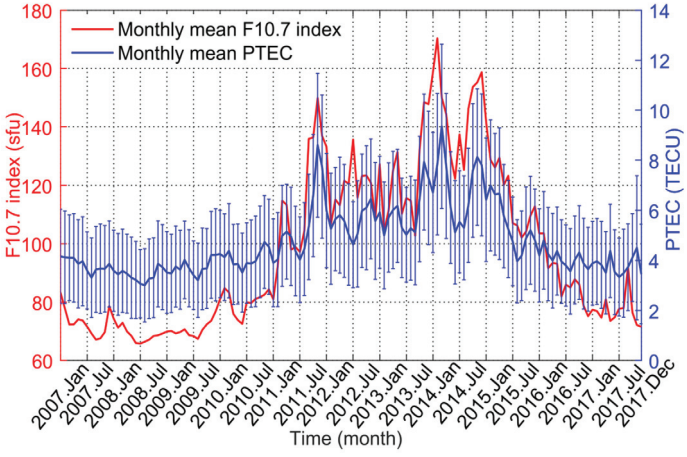

Figure 11. Monthly mean F10.7 index and monthly mean PTEC from January 2007 to December 2017.

To determine the correlation between PTEC and solar activity in the daytime and nighttime, we divided the plasmaspheric TEC into the daytime region and nighttime region, and the division standard was the same as in the previous section. Similarly, the values of PTEC in the daytime and nighttime were averaged by month, respectively. The mean values and the standard deviations are shown in Figure 12. The variations of PTEC in the daytime and nighttime are basically synchronous with differences less than 2 TECU, and both show consistency with the variation of the monthly mean F10.7 indices.

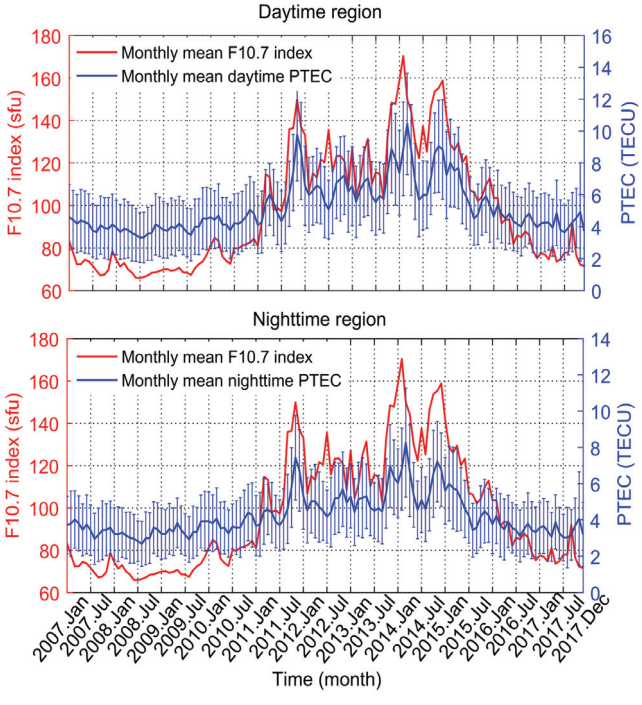

Figure 12. Monthly mean F10.7 index and monthly mean daytime and nighttime PTEC from January 2007 to December 2017.

To further estimate the correlation between PTEC and the F10.7 index, we divided the monthly plasmaspheric TEC into latitudinal regions according to the geomagnetic latitude and the magnetic local time, and the criteria of division are the same as mentioned before. The monthly mean PTEC for each geomagnetic latitudinal region was calculated for daytime and nighttime. Then, they were counted with the corresponding monthly mean F10.7 indices in different subgraphs in Figure 13. There are strong correlations between the monthly mean F10.7 indices and the monthly mean daytime and nighttime PTEC in each latitudinal region. In the same geomagnetic latitudinal region, the correlation between the monthly mean PTEC and the monthly mean F10.7 indices in the daytime is higher than that in the nighttime. This is because the plasmasphere in the daytime is directly exposed to the sun and can receive solar radiation and the energy directly, while in the nighttime, the plasmasphere is more affected by the ionosphere, which reduces the correlation with the solar activity. In the term of geomagnetic latitudinal region, the correlation in the geomagnetic high-latitude region is also the highest, while the geomagnetic middle-latitude region has the lowest correlation. However, among these correlation coefficients, the lowest one is still more than 0.88, indicating a very strong relationship between plasmaspheric TEC and the solar activity.

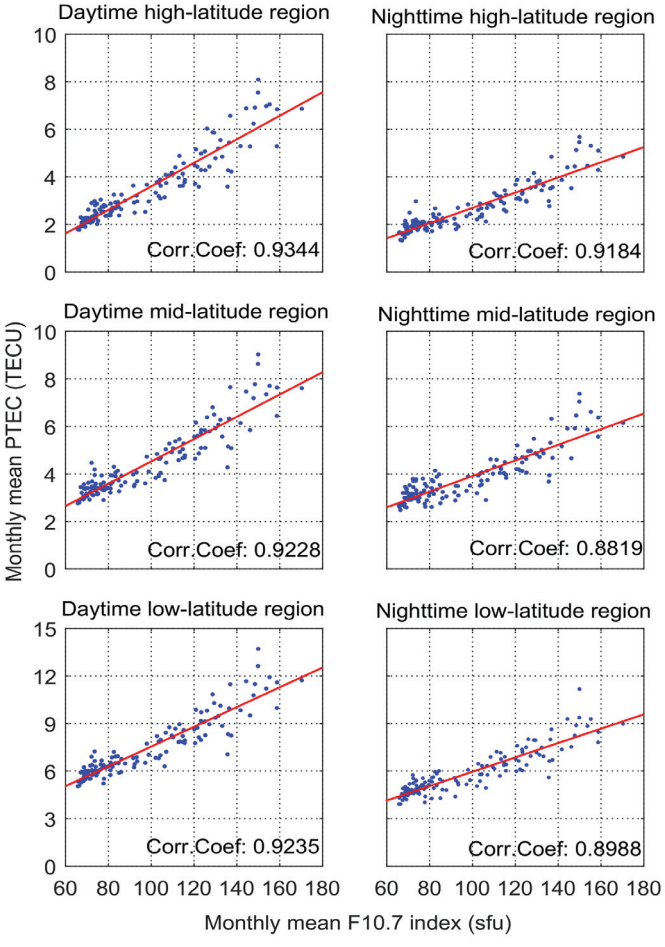

Figure 13. Correlations between monthly mean F10.7 index and monthly mean daytime and nighttime PTEC in different geomagnetic latitude regions

4. Conclusions

Using the topside GPS observations on COSMIC, the long-term plasmaspheric total electron content was obtained. By comparison with the GCPM, the plasmaspheric TEC from the topside observations of COSMIC was verified. Using the observation data in the solar minimum year 2008 and the solar maximum year 2014, PTEC was estimated at the monthly and seasonal scales, respectively, and its temporal-spatial distribution characteristics under different states of the solar activity were analyzed. The PTEC was mainly distributed in a belt region around the Earth within $\pm 45^{\circ}$ of the geomagnetic latitude. The plasmaspheric TEC in the daytime is higher than that in the nighttime, which reaches a peak between 14:00 and 17:00 in magnetic local time, while the minimum value of PTEC in the belt appears between 3:00 and 6:00 in magnetic local time before sunrise. For seasonal variations, the plasmaspheric TEC is the highest in the spring of the northern hemisphere and the lowest in the summer of the northern hemisphere, regardless of the state of solar activity. The variations of monthly mean PTEC in different regions were quite gentle during the solar minimum year 2008, while dramatical changes were found during the solar maximum year 2014. Furthermore, the long-term variations of the 11-year plasmaspheric TEC were analyzed with the F10.7 index as the reference indicator. The results showed a strong correlation between plasmaspheric TEC and solar activity.

Author Contributions: Conceptualization, S.J., C.G. and L.Y.; methodology, S.J., and C.G; software, C.G.; validation, S.J., C.G. and L.Y.; formal analysis, C.G.; investigation, C.G., and L.Y.; data curation, C.G., and P.L.; writing—original draft preparation, S.J., C.G., and P.L.; writing—review and editing, A.C., H.R., and P.G.; visualization, S.J.; supervision, S.J.; project administration, S.J.; funding acquisition, S.J. All authors have read and agreed to the published version of the manuscript.

Funding: This research was funded by the National Natural Science Foundation of China (No. 12073012 and No. 41761134092), Shanghai Leading Talent Project (Grant No. E056061), Jiangsu Province Distinguished Professor Project (Grant No. R2018T20), and Startup Foundation for Introducing Talent of NUIST (Grant No.2243141801036).

Data Availability Statement: The data presented in this study are available from the corresponding website.

Acknowledgments: We thank the CDAAC (COSMIC Data Analysis and Archive Center) for providing the podTec observation data and SEPC (Space Environment Prediction Center) for providing the F10.7 indices.

Conflicts of Interest: The authors declare no conflict of interest.

References

1. Gopalswamy, N.; Mewaldt, R.; Torsti, J. Solar Eruptions and Energetic Particles: An Introduction. *Geophys. Monogr. Ser.* **2006**, *165*, 1–5.
2. Carpenter, D.L.; Lemaire, J. The Plasmasphere Boundary Layer. *Ann. Geophys.* **2004**, *22*, 4291–4298. [CrossRef]
3. Nishida, A. Formation of plasmapause, or magnetospheric plasma knee, by the combined action of magnetospheric convection and plasma escape from the tail. *J. Geophys. Res.* **1966**, *71*, 5669–5679. [CrossRef]
4. Lemaire, J. Plasma distribution models in a rotating magnetic dipole and refilling of plasmaspheric flux tubes. *Phys. Fluids B Plasma Phys.* **1989**, *1*, 1519–1525. [CrossRef]
5. Wolfgang, B.; Götz, P.; Hermann, L. Characteristics of high-speed ion flows in the plasma sheet. *J. Geophys. Res. Atmos.* **1990**, *95*, 3801–3809.
6. Richards, P.G.; Chang, T.; Comfort, R.H. On the causes of theannual variation in the plasmaspheric electron density. *J. Atmos. Sol. Terr. Phys.* **2000**, *62*, 935–946. [CrossRef]
7. Lee, H.B.; Jee, G.; Kim, Y.H.; Shim, J.S. Characteristics of global plasmaspheric TEC in comparison with the ionosphere simultaneously observed by Jason-1 satellite. *J. Geophys. Res. Space Phys.* **2013**, *118*, 935–946. [CrossRef]
8. Jin, S.G.; Su, K. PPP models and performances from single- to quad-frequency BDS observations. *Satell. Navig.* **2020**, *1*, 16. [CrossRef]
9. Cherniak, I.V.; Zakharenkova, I.E.; Krankowski, A.; Shagimuratov, I.I. Plasmaspheric electron content derived from GPS TEC and FORMOSAT-3/COSMIC measurements: Solar minimum condition. *Adv. Space Res.* **2012**, *50*, 427–440. [CrossRef]
10. Yizengaw, E.; Moldwin, M.B.; Galvan, D.; Iijima, B.A.; Komjathy, A.; Mannucci, A.J. Global plasmaspheric TEC and its relative contribution to GPS TEC. *J. Atmos. Sol-Terr. Phys.* **2008**, *70*, 1541–1548. [CrossRef]

11. Bilitza, D.; Reinisch, B.W. International Reference Ionosphere 2007: Improvements and new parameters. *Adv. Space Res.* **2008**, *42*, 599–609. [CrossRef]
12. Leitinger, R.; Zhang, M.L.; Radicella, S.M. An improved bottomside for the ionospheric electron density, model NeQuick. *Ann. Geophys.* **2005**, *48*, 525–534.
13. Zhang, M.L.; Liu, L.B.; Wan, W.X.; Ning, B.Q. Variation of the plasmaspheric electron content derived from the podTEC observations of COSMIC LEO satellites to GPS signals. *Chin. J. Geophys.* **2016**, *59*, 1–7.
14. Belehaki, A.; Jakowski, N.; Reinisch, B.W. Plasmaspheric electron content derived from GPS TEC and digisonde ionograms. *Adv. Space Res.* **2004**, *33*, 833–837. [CrossRef]
15. Chong, X.Y.; Zhang, M.L.; Zhang, S.R.; Wen, J. An investigation on plasmaspheric electron content derived from ISR and GPS observations at Millstone Hill. *Chin. J. Geophys.* **2013**, *56*, 738–745.
16. Reinisch, B.W.; Huang, X. Deducing topside profiles and total electron content from bottomside ionograms. *Adv. Space Res.* **2001**, *27*, 23–30. [CrossRef]
17. Hajj, G.A.; Lee, L.C.; Pi, X.; Romans, L.; Schreiner, W.; Straus, P.; Wang, C. COSMIC GPS Ionospheric Sensing and Space Weather. *Terr. Atmos. Ocean Sci.* **2000**, *11*, 235–272. [CrossRef]
18. Hu, X.; Liou, Y.A.; Gong, X.Y.; Chiu, T.C.; Yeh, W.H.; Wang, X.; Wu, X.; Xiao, C.; Xu, L. Inversion of COSMIC atmospheric open-loop radio occultation data. *Chin. J. Geophys.* **2009**, *52*, 2195–2200.
19. Yue, X.; Schreiner, W.S.; Hunt, D.C.; Rocken, C.; Kuo, Y.H. Quantitative evaluation of the low Earth orbit satellite based slant total electron content determination. *Space Weather* **2011**, 9. [CrossRef]
20. Klobuchar, J.A. Ionospheric Time-Delay Algorithm for Single-Frequency GPS Users. *IEEE Trans. Aerosp. Electron. Syst.* **1987**, *23*, 325–331. [CrossRef]
21. Cai, C.S.; Liu, Z.Z.; Xia, P.F.; Dai, W. Cycle slip detection and repair for undifferenced GPS observations under high ionospheric activity. *GPS Solut.* **2013**, *17*, 247–260. [CrossRef]
22. Gallagher, D.L.; Craven, P.D.; Comfort, R.H. Global core plasma model. *J. Geophys. Res.* **2000**, *105*, 18819–18833. [CrossRef]
23. Craven, P.D.; Gallagher, D.L.; Comfort, R.H. Relative concentration of He+ in the inner magnetosphere as observed by the DE 1 retarding ion mass spectrometer. *J. Geophys. Res. Space* **1997**, *102*, 2279–2289. [CrossRef]
24. Singh, A.K.; Singh, R.P.; Siingh, D. State studies of Earth's plasmasphere: A review. *Planet. Space Sci.* **2011**, *59*, 810–834. [CrossRef]
25. Huo, X.L.; Yuan, Y.B.; Ou, J.K.; Wen, D.B.; Luo, X.W. The diurnal variations, semiannual and winter anomalies of the ionospheric TEC based on GPS data in China. *Prog. Nat. Sci.* **2005**, *15*, 56–60.
26. Covington, A.E. Solar Noise Observations on 10.7 Centimeters. *Proc. IRE* **1948**, *36*, 454–457. [CrossRef]

remote sensing

MDPI

Article

High-Precision GNSS PWV and Its Variation Characteristics in China Based on Individual Station Meteorological Data

Mingliang Wu [1,2], Shuanggen Jin [2,3], Zhicai Li [4,*], Yunchang Cao [5], Fan Ping [6] and Xu Tang [3]

[1] College of Civil Engineering and Mechanics, Xiangtan University, Xiangtan 411105, China; wumingliang@shao.ac.cn
[2] Shanghai Astronomical Observatory, Chinese Academy of Sciences, Shanghai 200030, China; sgjin@shao.ac.cn
[3] School of Remote Sensing and Geomatics Engineering, Nanjing University of Information Science and Technology, Nanjing 210044, China; xu.tang@nuist.edu.cn
[4] Department of Geodesy, National Geomatics Center of China, Beijing 100830, China
[5] Center for Meteorological Exploration, China Meteorological Administration, Beijing 100081, China; caoyc@nsmc.cma.gov.cn
[6] Institute of Atmospheric Physics, Chinese Academy of Sciences, Beijing 100029, China; pingf@mail.iap.ac.cn
* Correspondence: zcli@ngcc.cn; Tel.: +86-10-63881436

Abstract: The Global Navigation Satellite System (GNSS) plays an important role in retrieving high temporal–spatial resolution precipitable water vapor (PWV) and its applications. The weighted mean temperature (T_m) is a key parameter for the GNSS PWV estimation, which acts as the conversion factor from the zenith wet delay (ZWD) to the PWV. The T_m is determined by the air pressure and water vapor pressure, while it is not available nearby most GNSS stations. The empirical formular is often applied for the GNSS station surface temperature (T_s) but has a lower accuracy. In this paper, the temporal and spatial distribution characteristics of the coefficients of the linear T_m-T_s model are analyzed, and then a piecewise-linear T_m-T_s relationship is established for each GPS station using radiosonde data collected from 2011 to 2019. The T_m accuracy was increased by more than 10% and 20% for 86 and 52 radiosonde stations, respectively. The PWV time series at 377 GNSS stations from the infrastructure construction of national geodetic datum modernization and Crustal Movement Observation Network of China (CMONC) were further obtained from the GPS observations and meteorological data from 2011 to 2019. The PWV accuracy was improved when compared with the Bevis model. Furthermore, the daily and monthly average values, long-term trend, and its change characteristics of the PWV were analyzed using the high-precision inversion model. The results showed that the averaged PWV was higher in Central-Eastern China and Southern China and lower in Northwest China, Northeast China, and North China. The PWV is increasing in most parts of China, while the some PWVs in North China show a downward trend.

Keywords: GPS meteorology; weighted mean temperature; precipitable water vapor; radiosonde

Citation: Wu, M.; Jin, S.; Li, Z.; Cao, Y.; Ping, F.; Tang, X. High-Precision GNSS PWV and Its Variation Characteristics in China Based on Individual Station Meteorological Data. *Remote Sens.* **2021**, *13*, 1296. https://doi.org/10.3390/rs13071296

Academic Editor: Stefania Bonafoni

Received: 24 February 2021
Accepted: 25 March 2021
Published: 29 March 2021

1. Introduction

Water vapor is an important part of the Earth's hydrosphere and plays a key role in the energy exchange and water cycle in nature. The atmospheric water vapor content is limited by local temperature and pressure and is closely related to the formation of various precipitation, such as clouds, rain, and snow [1]. Accurate measurements of water vapor and its distribution changes have become one of the basic problems in synoptics, weather forecasting, and climate research [2–5]. One of the indicators to measure the amount of atmospheric water vapor is the precipitable water vapor (PWV), which represents a certain height of the water column produced by the condensation of all tropospheric atmospheric water vapor in the column per unit bottom area at any time into liquid water. Since the demand for real-time and accurate weather services is becoming more and more urgent, the traditional detection technologies such as radiosondes, water vapor radiometers, and

solar photometers cannot meet the application requirements for continuous high-precision, high-temporal resolution monitoring of water vapor.

Nowadays, Global Navigation Satellite System (GNSS) technology has become an important means to obtain precipitable water vapor with high temporal and spatial resolution, and many scholars have used GNSS technology to study global or regional climate change and characteristics [6–12]. Bevis et al. first proposed the concept of GPS meteorology and obtained the global surface temperature and weighted mean temperature from 8718 radiosonde stations in North America and explained the linear relationship coefficient and specific process of ground-based GPS inversion of water vapor [13]. Ross and Rosenfeld used 23 years of profile data from 53 radiosonde stations from the National Center for Atmospheric Research to calculate the global T_m-T_s linear coefficient and demonstrated that it was related to the station and the season except the equatorial region [14]. Several T_m-T_s conversion models were established for different regions and different seasons using limited meteorological observation data [15–18]. Yao et al. established the nonlinear transformation relationship by combining mathematical statistics and derivation, which can improve the accuracy of fitting in China [19]. However, many GPS stations are not equipped with temperature and pressure sensors due to cost and other reasons. Hence, it is impossible to use transformation coefficient from real observations to calculate T_m.

Many researchers used the National Centers for Environmental Prediction (NCEP), and the European Center for Medium-term Weather Prediction (ECMWF) reanalyzed data and interpolated data from the ground meteorological observation station to obtain ground temperature and air pressure for ground-based GNSS PWV inversion [20–25]. Yao et al. established a global T_m model and a tropospheric delay model using spherical harmonic functions with considering annual, semi-annual, and diurnal changes, which greatly improved the accuracy of the PWV estimation [26,27]. However, the empirical models have relatively low accuracy. The research on T_m-T_s models in the region of China was mostly focused on climate zones and seasonal divisions. Since many GPS stations in China lacked meteorological data in the past, they cannot obtain precise PWV, as well as investigate their long-term variation characteristics of GPS PWV.

In this study, we collected more radiosonde stations observations at co-located GNSS stations from the infrastructure construction of national geodetic datum modernization and Crustal Movement Observation Network of China (CMONC). The temporal and spatial distribution characteristics of the T_m-T_s model were analyzed from radiosonde data, and a piecewise-linear model was established at each radiosonde station in China. With this model, the nine-year GPS PWV time series at GNSS stations was obtained from CMONC GNSS observations and meteorological data. The precision of the PWV was evaluated, and the distribution characteristics and their changes were investigated. Section 2 shows the data and methods, evaluation and comparison are presented in Section 3, variations in the characteristics of GNSS PWV are presented in Section 4, and finally, the conclusions are given in Section 5.

2. Data and Methods

2.1. Observation Data

The infrastructure construction of national geodetic datum modernization in China was launched in 2012 and completed in 2017, which contained 210 GPS stations. A high-precision, dynamic, and unified modern surveying and mapping datum system was established to provide coordinate frame services, including data products, real-time positioning, processing and analysis, and other services [28]. Crustal Movement Observation Network of China (CMONC) was established in 2006 and completed in 2012, which contained 360 GPS stations [29,30]. The National Geomatics Center of China (NGCC) provided the hourly ZTD data and 1-h measured temperature and atmospheric pressure data at these GPS stations from 2011 to 2019. We used BERNESE 5.2 software [31] to process the raw data, including the implementation of daily solutions and adjustments [32].

The Integrated Global Radiosonde Archive (IGRA) has released radiosonde and pilot balloon observations with more than 2700 stations around the world since 1905, including air pressure, temperature, geopotential height, and relative humidity (ftp://ftp.ncdc.noaa.gov/pub/data/igra, accessed on 24 January 2021), whose temporal resolution is 12 h. We used IGRA-released radiosonde profiles in China from 2011 to 2019 to calculate the T_m at each radiosonde station. Figure 1 shows all the used GPS stations and radiosonde stations.

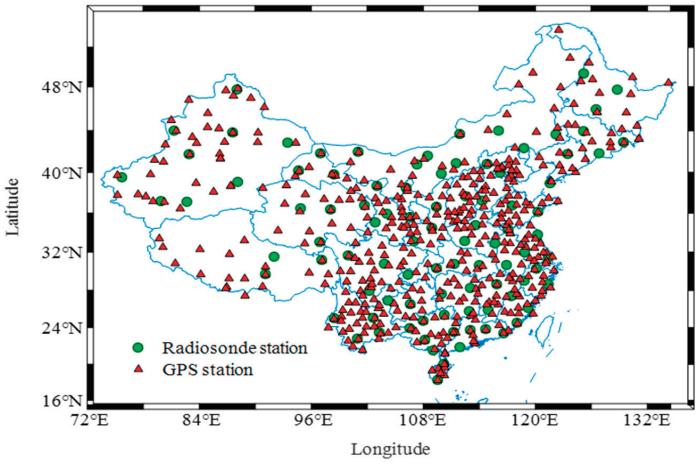

Figure 1. Distribution of GPS stations from the infrastructure construction of national geodetic datum modernization and Crustal Movement Observation Network of China (CMONC) in mainland China. The green circle is the radiosonde station, and the red triangle is the GPS station.

2.2. Establishment of Site-Specific Piecewise-Linear T_m-T_s Relationship

T_m is related to the temperature and vapor pressure at different altitudes in the atmosphere, which can be obtained from the IGRA. The method to calculating the 12-h T_m can be expressed as [13]:

$$T_m = \frac{\int_{z_0}^{+\infty}\left(\frac{e}{T}\right)dz}{\int_{z_0}^{+\infty}\left(\frac{e}{T^2}\right)dz} \approx \frac{\sum_{i=1}^{N}\left(\frac{e_i}{T_i}\right)\Delta z_i}{\sum_{i=1}^{N}\left(\frac{e_i}{T_i^2}\right)\Delta z_i} \quad (1)$$

where e (hPa) refers to the water vapor pressure, T (K) is the corresponding temperature, and Z (m) denotes the starting height of integration. Δz_i (m) denotes the altitude of the ith atmospheric layer, N denotes the number of the atmospheric layer, e_i (hPa) denotes the water vapor pressure of ith atmospheric layer, and T_i (K) denotes the temperature of ith atmospheric layer. We converted the geopotential height into the geoid height in the calculation process.

The empirical formula based on the long-term radiosonde data in the study area and the linear relationship between surface temperature T_s and T_m can be established by a regression analysis as:

$$T_m = a \cdot T_s + b \quad (2)$$

where a and b are the linear regression equation parameters.

The T_m variation has a significant annual variation. In some studies, the half-year variations and the daily variations are also considered when building the model. In order to get the time-varying characteristics of the T_m-T_s coefficient, a piecewise-linear least squares fitting is performed for each radiosonde station for one month.

2.3. PWV from Site-Specific Piecewise-Linear T_m-T_s Relationship

Three hundred and seventy-seven GPS stations were selected for estimating the PWV time series. Since the cubic spline method has a higher accuracy than the nearest-neighbor interpolation method and linear interpolation method, we used the cubic spline method to obtain the T_m-T_s model coefficients a and b at the GPS stations in the corresponding time period.

ZTD is the sum of Zenith Hydrostatic Delay (ZHD) and Zenith Wet Delay (ZWD), as

$$\mathrm{ZTD} = \mathrm{ZHD} + \mathrm{ZWD} \tag{3}$$

The Saastamoinent model has been widely used for ZHD computation [33], as

$$\mathrm{ZHD} = 0.002277 \cdot \frac{P}{1 - 0.0026 \cdot cos\,(2\phi) - 0.00028 \cdot h_0} \tag{4}$$

where P (hPa) denotes the ground pressure of the GPS station, ϕ denotes the latitude of the GPS station, and h_0 (m) denotes the elevation of the GPS station.

The ZWD is caused by water vapor in the atmosphere under nonstatic equilibrium. Generally, empirical models and meteorological parameters at GPS station are used to obtain the ZHD, and then, the ZHD is deducted from the ZTD to obtain the ZWD.

$$\mathrm{ZWD} = \mathrm{ZTD} - \mathrm{ZHD} \tag{5}$$

The linear relationship between the ZWD and PWV can be expressed as [13]

$$\mathrm{PWV} = \Pi \cdot \mathrm{ZWD} \tag{6}$$

$$\Pi = \frac{10^6}{\rho_w \cdot \frac{R}{m_w} \cdot \left[\frac{k_3}{T_m} + k_2 - \frac{m_w}{m_d} \cdot k_1\right]} \tag{7}$$

where Π is the conversion factors between the ZWD and PWV; Π is a function of T_m; ρ_w represents the density of the liquid water; R is the universal gas constant and R = 8314 $\mathrm{Pa \cdot m^3 \cdot K^{-1} \cdot kmol^{-1}}$; m_w represents the molar mass of water vapor and m_w = 18.02 $\mathrm{kg \cdot kmol^{-1}}$; m_d represents the molar mass of the dry atmosphere and m_d = 28.96 $\mathrm{kg \cdot kmol^{-1}}$; and k_1, k_2, and k_3 are constants (k_1 = 77.604 ± 0.014 K/hPa, k_2 = 70. 4 K/hPa, and k_3 = (3.776 ± 0.014) × 10^5 $\mathrm{K^2/hPa}$) [13].

In general, approximately 6.7 mm of ZTD error will cause a PWV error of 1 mm. Hence, the ZTD with a Root Mean Square Error (RMSE) of greater than 6.7 mm are eliminated. In addition, ZTD data and meteorological parameters are missing at some stations in a few time periods. For sites with missing data for more than one year, they will not be used when analyzing the long-term changes. Then, Equations (3)–(6) were used for high-precision PWV estimations based on the site-specific piecewise-linear T_m-T_s relationship in China. Finally, the PWV time series derived from 377 GPS stations in China from 2011 to 2019 were obtained.

2.4. PWV from Radiosonde

The PWV at the radiosonde station is calculated as follows:

$$\mathrm{PWV} = \int_0^{p_0} \frac{q}{\rho_w g} d_p \tag{8}$$

where p (hPa) denotes the atmospheric pressure, p_0 (hPa) is the ground pressure at the GPS station, q ($\mathrm{g \cdot kg^{-1}}$) denotes the specific humidity, g ($\mathrm{m \cdot s^{-2}}$) is the acceleration of gravity, and ρ_w ($\mathrm{g \cdot cm^{-3}}$) refers to the density of the liquid water. By discretizing Equation (8),

the integral equation of PWV from the ground to the top of the atmosphere is obtained as follows:

$$\mathrm{PWV} = -\frac{1}{g}\sum_{p_0}^{p} q \times p \tag{9}$$

2.5. Fitting Function of the PWV Time Series

Jin and Luo [34] analyzed the PWV series derived from 155 globally distributed GPS sites observations and found that most of the periods of the PWV series were 1 year, 0.5 years, 1 day, and 0.5 days. To fit the PWV time series of 377 GPS stations in China, we established the following equation:

$$\begin{aligned}\mathrm{PWV} = k_0 + k_1 \cdot \cos\left(\frac{DOY - c_1}{365.25}\cdot 2\pi\right) + k_2 \cdot \cos\left(\frac{DOY - c_2}{365.25}\cdot 4\pi\right) + k_3 \cdot \cos\left(\frac{HOD - c_3}{24}\cdot 2\pi\right) \\ + k_4 \cdot \cos\left(\frac{HOD - c_4}{24}\cdot 4\pi\right) + \varepsilon\end{aligned} \tag{10}$$

where k_0 is a constant term; k_1, k_2, k_3, k_4, c_1, c_2, c_3, and c_4 are the amplitude and phase at the period (1 year, 0.5 years, 1 day, and 0.5 days); DOY is the day of year; HOD is the hour of day; and ε is the residual. The least square method was used to determine the unknown parameters in Equation (10) with the PWV time series.

3. Evaluation and Comparison

3.1. Spatial Distribution and Time-Varying Characteristics of the T_m-T_s Coefficient

Figure 2 shows the spatial distribution of the T_m-T_s relationship coefficients. The slope coefficient ranges from 0.5 to 0.7 in South China, around 0.7 in Northwest China, and about 0.8 in Central and Northeast China. As shown in the right panel, the intercept coefficient is from 80 to 140 in Southern China, about 60 in Central and Northwestern China, and approximately 20 in Northeastern China.

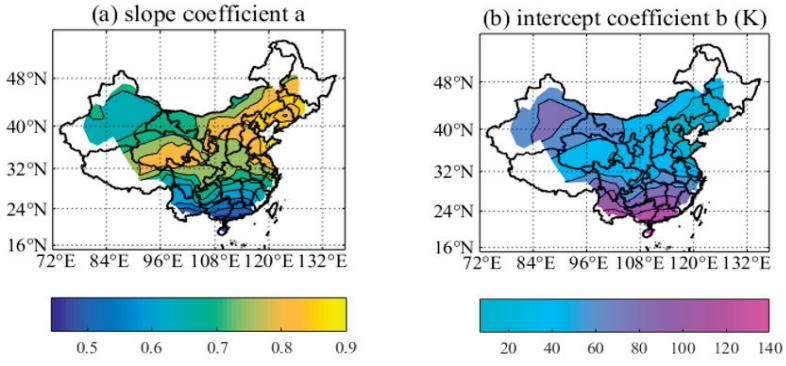

Figure 2. Distribution of the T_m-T_s fitting coefficients a and b at each station by $T_m = a * T_s + b$. (**a**) The slope coefficient a and (**b**) the intercept coefficient b.

Figure 3 shows the distribution diagram of the slope coefficient with the elevation, latitude, and longitude. No evident correlation is found with the elevation and longitude, whereas there is strong positive correlation with the latitude, especially in low-latitude areas. Some studies have shown that when the same T_m-T_s coefficient is used at a global scale, it will cause different errors in the T_m of different latitudes [35,36]. Wang et al. found that the T_m derived from the Bevis T_m-T_s relationship has a cold bias in the tropics and subtropics and a warm bias in middle and high latitudes, and furthermore, the RMS was dominated by the mean bias rather than the random error. Therefore, the distribution of the T_m-T_s coefficients is mostly related to the latitude. The slope coefficient a is generally

less than 0.6 in low-latitude areas, which is consistent with the previous results of some global T_m-T_s models.

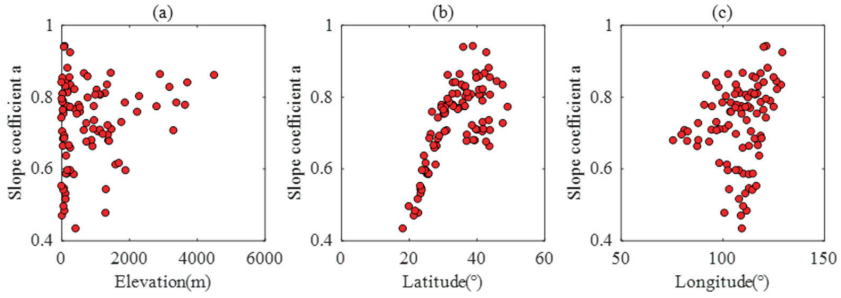

Figure 3. Distribution of the T_m-T_s model slope coefficient with the elevation (**a**), latitude (**b**), and longitude (**c**).

The monthly coefficients of the T_m-T_s model are obtained. The slope coefficients have obvious annual cycle at most stations. The time series of slope coefficients at four radiosonde stations are randomly selected and shown in Figure 4. The information of the four stations is shown in Table 1. The slope coefficients of the T_m-T_s model vary greatly with the time, from about 0.5–1. The regression slope and its changing tendency are smaller at the SIMAO station, which is due to the lower latitude.

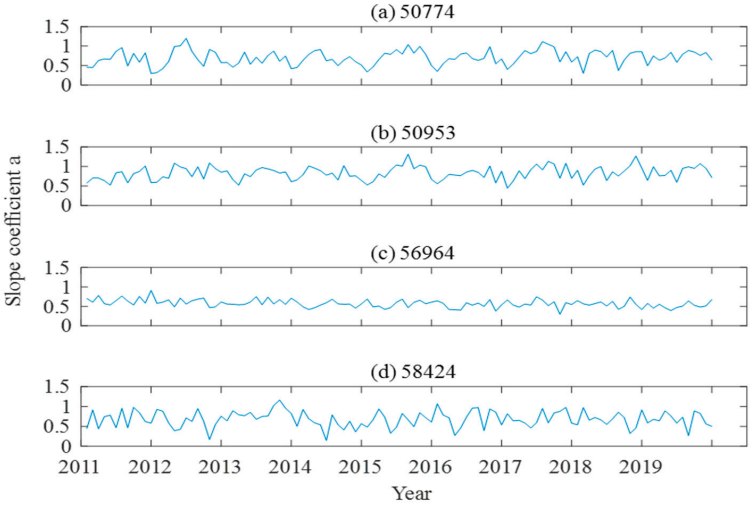

Figure 4. Monthly slope coefficient of the T_m-T_s model from 2011 to 2019.

Table 1. Information about the 4 stations used in Figure 4.

Name	Number	Latitude (°)	Longitude (°)	Height (m)
YICHUN	50,774	47.72	128.83	264.8
HARBIN	50,953	45.93	126.57	118.3
SIMAO	56,964	22.77	100.98	1303.0
ANQING	58,424	30.62	116.97	62.0

3.2. Comparison with Bevis T_m-T_s Relationship

We calculated the root mean square error (RMSE) (in unit of K) and accuracy improvement (%) of T_m for 94 radiosonde station, which are shown in Figure 5. Compared with the Bevis model, the site-specific piecewise-linear model has a significant improvement in the regression accuracy at most stations due to the consideration of the temporal and spatial distributions of the T_m-T_s conversion coefficient. According to the statistics, the T_m accuracy with 86 radiosonde stations is increased by more than 10% and by more than 20% with 52 radiosonde stations, and the lowest is increased by 6% (station 58457, 30.23° N, 120.17° E), and the highest is increased by 69% (station 56691, 26.87° N, 104.28° E).

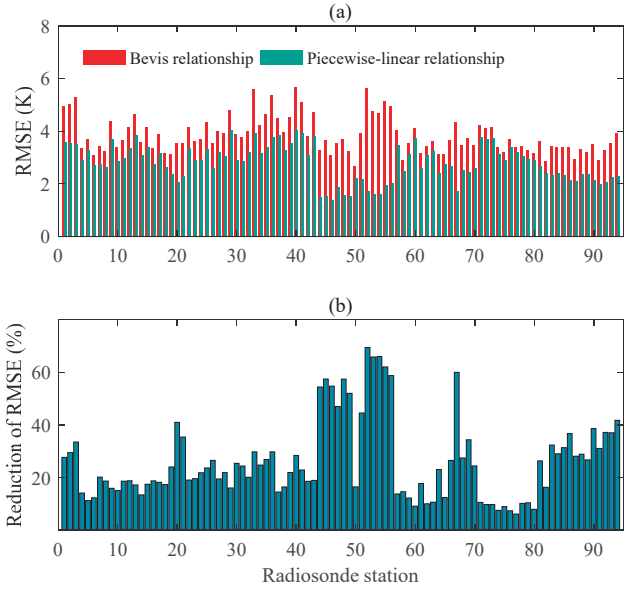

Figure 5. RMSE (K) (**a**) and accuracy improvement of the T_m (**b**) calculated by the site-specific piecewise-linear and Bevis T_m-T_s relationship.

Figure 6 shows the RMSE distribution of the Bevis model and the site-specific piecewise-linear model. As we can see, compared with the Bevis model, the single-station piecewise-linear model has a greater accuracy improvement in the southern, southwest, and northeastern regions by more than 30%. The increase in the central and northwestern regions is relatively small and approximately 15%.

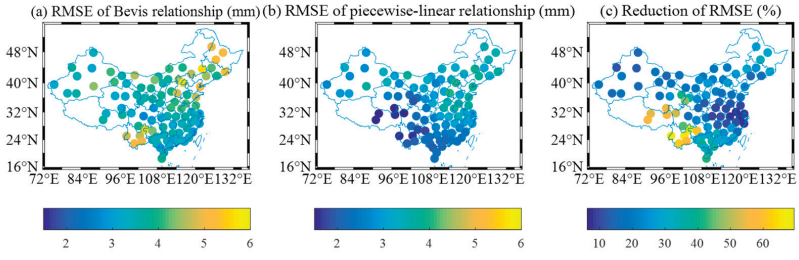

Figure 6. RMSE (K) distribution of the T_m calculated by the site-specific piecewise-linear relationship (**a**), Bevis T_m-T_s relationship (**b**), and reduction of the RMSE (%) by the site-specific piecewise-linear T_m-T_s relationship (**c**).

3.3. Comparison with GPS-Derived PWV and Radiosonde PWV

The selected GPS stations are closer to the radiosonde, in which the horizontal distance is less than 10 km and the elevation difference is less than 100 m. The water vapor obtained by the integral of the radiosonde profile data was used to evaluate the ground-based GPS PWV based on the Bevis model and the site-specific piecewise-linear T_m-T_s model. We calculated the deviation bias (in unit of mm) and relative errors. For example, Figure 7 shows the results at GXHC station in 2018. The accuracy of the PWV is better based on the site-specific piecewise-linear T_m-T_s relationship when compared to the Bevis's model.

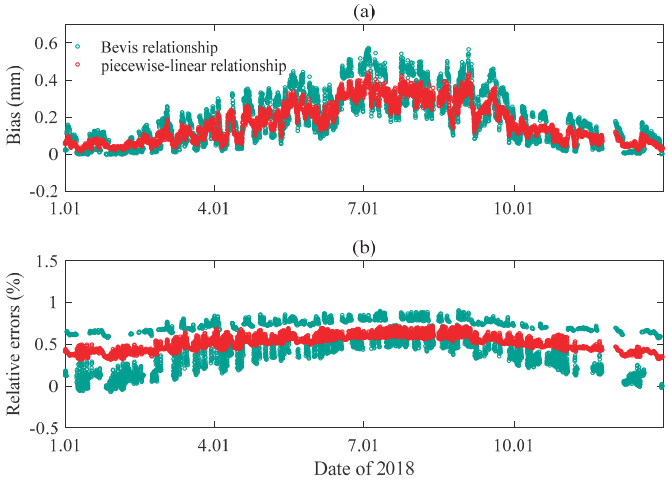

Figure 7. Bias (mm) (**a**) and relative error (%) (**b**) of the precipitable water vapor (PWV) calculated based on different T_m-T_s models at GXHC station in 2018. The blue dots are the PWV based on the Bevis model, and the red dots are the PWV based on the site-specific piecewise-linear model.

The distribution of water vapor in the atmosphere is not uniform. Thus, the ground-based GPS water vapor can get the average distribution of water vapor in each satellite signal direction. In addition, the layered meteorological parameter data of the radiosonde is not strictly vertical. These factors will bring errors into the PWV results. However, it still can be seen that the accuracy of the PWV is significantly improved based on site-specific piecewise-linear T_m-T_s relationship, especially when there are more atmospheric water vapors in the summer.

4. Variations Characteristics of GNSS PWV

4.1. Spatial Distribution of PWV in China

The annual averaged PWV at all GPS stations from 2011 to 2019 in China range from 0 to 48 mm. As shown in Figure 8, the annual averaged PWV in Central-Eastern China and Southern China are relatively high, reaching above 25 mm, while the annual averaged PWV in Northwest, Northeast, and Northern China regions are lower, below 15 mm. Southeast China has a low latitude and is close to the East China Sea and the South China Sea, which are subject to subtropical monsoons. Monsoons transport water vapor from the sea to these areas, resulting in the higher annual averaged PWV [37]. Northwest China has a relatively high latitude and is an inland region with a temperate continental climate, so the annual averaged PWV is lower.

The GPS stations are divided into four regions: the eastern central region (24.5°–37° N, 105°–123° E), the southern region (19°–24. 5° N, 105°–120° E), the northwestern region (42°–49° N, 80°–90° E), and the northeastern region (37°–50° N, 110°–130° E). Figure 9 shows the nine-year daily averaged PWV of these four regions. The variation characteristics of the PWV in each region are consistent throughout the year, with the peaks in June and

July and the droughts in January and December. Among them, the peak in Southern China appeared the earliest, which was affected by the south-to-north monsoon. Atmospheric circulation transported the water vapor to the Yangtze River Basin and then continued to transport it to other regions [38].

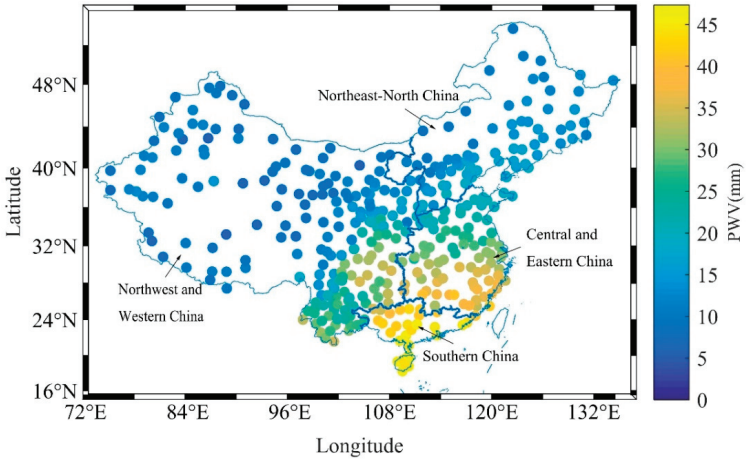

Figure 8. Annual averaged PWV (mm) in China from 2011 to 2019.

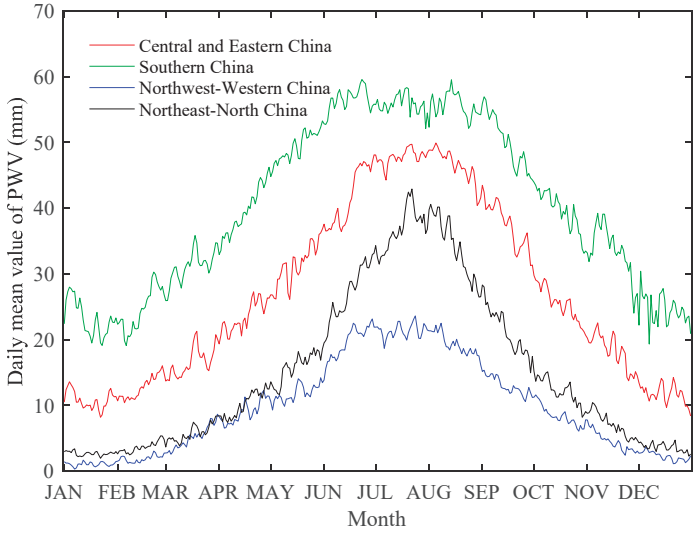

Figure 9. Nine-year averaged daily PWV (mm) in four regions of China from 2011 to 2019.

4.2. Seasonal Variations of PWV in China

Figures 10 and 11 show the annual and semiannual PWV variation amplitudes at 377 GPS sites. The spatial distribution of the annual PWV variations is similar to the annual average distribution of the PWV. Central China, Southern China, and the southeast coastal areas have higher annual PWV variation amplitudes, reaching about 15 mm, while the annual cycle amplitude in Northwest China is lower, below 10 mm. The semiannual PWV variation amplitudes are relatively small, about 3–9 mm. Among them, the semiannual PWV variation amplitudes are the highest in Central China and Southwest China, reaching

above 6 mm, while the semiannual PWV variation amplitudes in Southern China and Northwestern China are lower, below 5 mm.

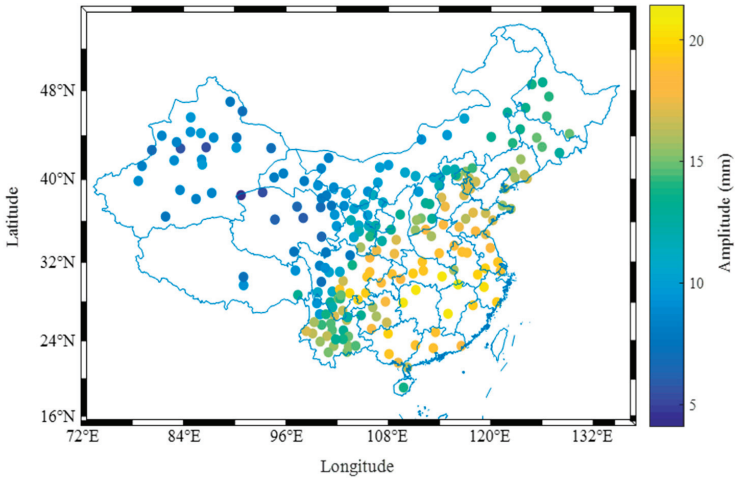

Figure 10. Annual PWV variation amplitudes (mm) at 377 GPS sites.

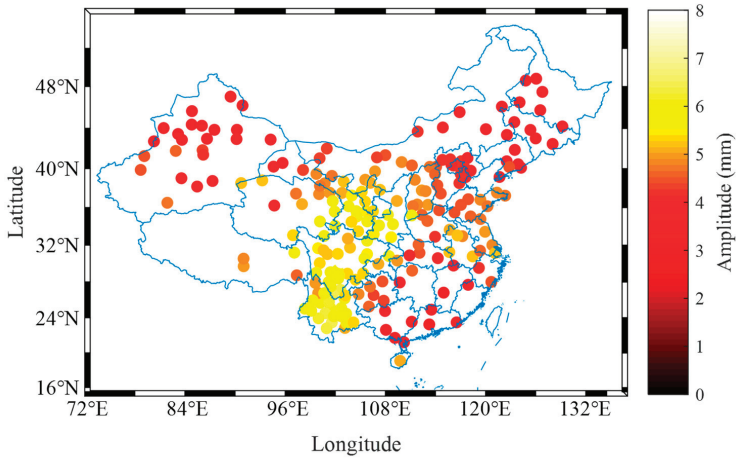

Figure 11. Semiannual PWV variation amplitudes (mm) at 377 GPS sites.

4.3. Long-Term Variation Trend of PWV in China

Figure 12 shows the long-term variation trends of the PWV (mm/year) of all GPS stations from 2011 to 2019. It can be seen that the PWV has been increasing in most parts of China, while the PWV in Northeast China shows a downward trend. To understand the variations of the PWV in more detail, a monthly anomaly of the PWV is obtained by subtracting the monthly averaged PWV of every month from the mean value of the monthly averaged nine-year PWV in each region, which can be seen in Figure 13. The monthly anomaly of the PWV was mainly negative before 2015 and then turned negative. The PWV in Northwest China, Northeast China, and Northern China were relatively stable, and the monthly mean value changed little, which was related to the dry inland climate.

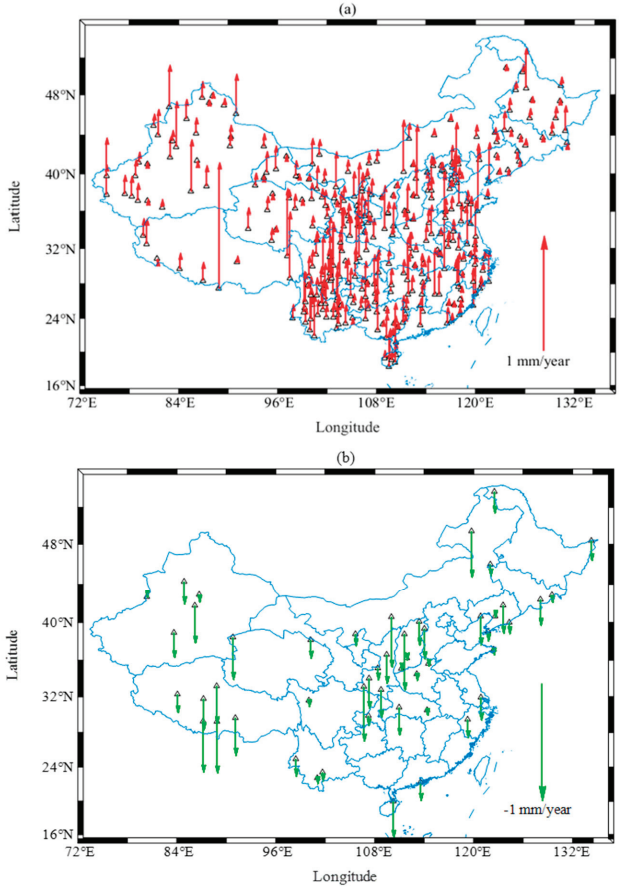

Figure 12. Long-term variation trend of the PWV. The red upward arrows (**a**) stand for the increase of the PWV variation trend (mm/year), and the green downward arrows (**b**) represent the decrease of the PWV variation trend (mm/year).

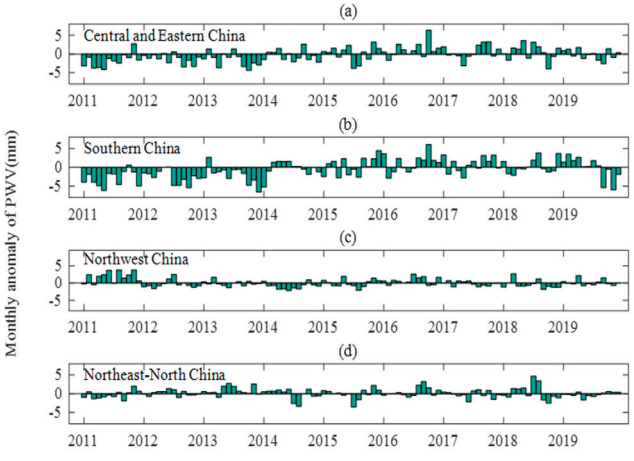

Figure 13. Monthly anomaly (mm) of the PWV in four regions of China.

5. Discussion

Most of the published T_m models that considered the temporal and spatial distributions of the relationship between the T_m and meteorological measurements have been empirical models on a global scale. Their accuracy remains to be verified in a specific area and a period of time. Here, we estimated the monthly coefficients at each station, and Table 2 shows the comparison between the piecewise-linear model and two recently published representative models: the time-varying global-gridded T_s–T_m model (TVGG) and neural network-based T_m model (NN). We tested our model with radiosonde data from 2011 to 2019, and the results showed that our model has the best accuracy.

Table 2. Statistics of the T_m estimates for different models.

Statistics	Bevis	TVGG	NN-I	Piecewise Linear
Bias (K)	−0.74	−1.25	0.03	0.00
RMS (K)	4.58	3.84	3.62	3.38

The spatial distribution characteristics of the PWV are consistent with other studies in different years [39,40]. There are bimodal characteristics of the PWV in Southern China, and the formation mechanism of the bimodal characteristics remains to be further studied. The past results of some studies in China indicated that the PWV showed a downward trend from 1995 to 2012 [41–43], while the trends of this article are upward from 2011 to 2019. Most PWV in Central and Eastern China and Southern China show an upward trend and some PWV in North China is downward from 2011 to 2019. The monthly averaged PWV increased significantly in 2015, which was affected by the El Niño.

6. Conclusions

In this study, we analyzed the temporal and spatial distribution characteristics of the coefficients of the linear T_m-T_s model and showed that the distribution of T_m-T_s coefficients is mainly related to the latitude. The T_m-T_s conversion coefficient changes with the time and has an obvious annual cycle. Based on the spatial distribution and time-varying characteristics of the T_m-T_s coefficients, a site-specific piecewise-linear model was established. Compared with the Bevis model, this model reduced the T_m RMS by more than 20% for the most of the tested radiosondes. The accuracy of GPS PWV is better based on the site-specific piecewise-linear T_m-T_s relationship when compared to the Bevis model. Furthermore, the PWV time series at 377 GNSS stations were further obtained and analyzed from the GPS observations and meteorological data from 2011 to 2019. The results showed that the average PWV in Central and Eastern China and Southern China is higher, reaching more than 25 mm, while the average value is lower and below 15 mm in Northwest China, Northeast China, and North China. The PWV is increasing in most parts of China, while some PWV in North China show a downward trend.

Author Contributions: Conceptualization, S.J. and Z.L.; methodology, S.J. and M.W.; software, M.W.; validation, S.J., Z.L. and F.P.; formal analysis, M.W.; investigation, M.W. and S.J.; data curation, Z.L. and S.J.; writing—original draft preparation, M.W. and S.J.; writing—review and editing, F.P., Y.C. and X.T.; visualization, M.W.; supervision, S.J.; project administration, S.J.; and funding acquisition, S.J. and Z.L. All authors have read and agreed to the published version of the manuscript.

Funding: This work was supported by the Strategic Priority Research Program Project of the Chinese Academy of Sciences (Grant No. XDA23040100), National Natural Science Foundation of China (NSFC) Project (Grant No. 12073012), and National Key Research and Development Program of China (No. 2016YFB0501405).

Institutional Review Board Statement: Not applicable.

Informed Consent Statement: Not applicable.

Data Availability Statement: Radiosonde data are available from the Integrated Global Radiosonde Archive (IGRA) (ftp://ftp.ncdc.noaa.gov/pub/data/igra, accessed on 24 January 2021).

Acknowledgments: The authors are grateful to the infrastructure construction of the national geodetic datum modernization in China and Crustal Movement Observation Network of China (CMONC) for providing the GPS observation data.

Conflicts of Interest: The authors declare no conflict of interest.

References

1. Philipona, R.; Dürr, B.; Ohmura, A.; Ruckstuhl, C. Anthropogenic greenhouse forcing and strong water vapor feedback increase temperature in Europe. *Geophys. Res. Lett.* **2005**, *32*. [CrossRef]
2. Gendt, G.; Dick, G.; Reigber, C.; Tomassini, M.; Liu, Y.; Ramatschi, M. Near real time GPS water vapor monitoring for numerical weather prediction in Germany. *J. Meteorol. Soc. Jpn. Ser. II* **2004**, *82*, 361–370. [CrossRef]
3. Boutiouta, S.; Lahcene, A. Preliminary study of GNSS meteorology techniques in Algeria. *Int. J. Remote Sens.* **2013**, *34*, 5105–5118. [CrossRef]
4. Sapucci, L.F. Evaluation of modeling water-vapor-weighted mean tropospheric temperature for GNSS-integrated water vapor estimates in Brazil. *J. Appl. Meteorol. Climatol.* **2014**, *53*, 715–730. [CrossRef]
5. Ning, T.; Wickert, J.; Deng, Z.; Heise, S.; Dick, G.; Vey, S.; Schöne, T. Homogenized time series of the atmospheric water vapor content obtained from the GNSS reprocessed data. *J. Clim.* **2016**, *29*, 2443–2456. [CrossRef]
6. Jin, S.; Su, K. PPP models and performances from single-to quad-frequency BDS observations. *Satell. Navig.* **2020**, *1*, 1–13. [CrossRef]
7. Jin, S.; Gao, C.; Li, J. Atmospheric sounding from Fengyun-3C GPS radio occultation observations: First results and validation. *Adv. Meteorol.* **2019**, *1*, 1–13. [CrossRef]
8. Jin, S.; Li, Z.; Cho, J. Integrated water vapor field and multiscale variations over China from GPS measurements. *J. Appl. Meteorol. Climatol.* **2008**, *47*, 3008–3015. [CrossRef]
9. Jones, J.; Guerova, G.; Douša, J.; Dick, G.; de Haan, S.; Pottiaux, E.; van Malderen, R. *Advanced GNSS Tropospheric Products for Monitoring Severe Weather Events and Climate*; COST Action ES1206 Final Action Dissemination Report; Springer: Berlin/Heidelberg, Germany, 2019; p. 563.
10. Steiner, A.; Kirchengast, G.; Foelsche, U.; Kornblueh, L.; Manzini, E.; Bengtsson, L. GNSS occultation sounding for climate monitoring. *Phys. Chem. Earth Part A Solid Earth Geod.* **2001**, *26*, 113–124. [CrossRef]
11. Smith, T.L.; Benjamin, S.G.; Gutman, S.I.; Sahm, S. Short-range forecast impact from assimilation of GPS-IPW observations into the Rapid Update Cycle. *Mon. Weather Rev.* **2007**, *135*, 2914–2930. [CrossRef]
12. Kourtidis, K.; Stathopoulos, S.; Georgoulias, A.; Alexandri, G.; Rapsomanikis, S. A study of the impact of synoptic weather conditions and water vapor on aerosol–cloud relationships over major urban clusters of China. *Atmos. Chem. Phys.* **2015**, *15*, 10955–10964. [CrossRef]
13. Bevis, M.; Businger, S.; Herring, T.A.; Rocken, C.; Anthes, R.A.; Ware, R.H. GPS meteorology: Remote sensing of atmospheric water vapor using the Global Positioning System. *J. Geophys. Res. Atmos.* **1992**, *97*, 15787–15801. [CrossRef]
14. Ross, R.J.; Rosenfeld, S. Estimating mean weighted temperature of the atmosphere for Global Positioning System applications. *J. Geophys. Res. Atmos.* **1997**, *102*, 21719–21730. [CrossRef]
15. Bokoye, A.I. Multisensor analysis of integrated atmospheric water vapor over Canada and Alaska. *J. Geophys. Res. Atmos.* **2003**, *108*, 4480. [CrossRef]
16. Emardson, T.R.; Derks, H.J. On the relation between the wet delay and the integrated precipitable water vapour in the European atmosphere. *Meteorol. Appl. A J. Forecast. Pract. Appl. Train. Tech. Model.* **2000**, *7*, 61–68. [CrossRef]
17. Wang, J.; Zhang, L.; Dai, A.; Hove, T.V.; Baelen, J.V. A near-global, 2-hourly data set of atmospheric precipitable water from ground-based GPS measurements. *J. Geophys. Res. Atmos.* **2007**, *112*, 112. [CrossRef]
18. Zhang, H.P.; Liu, J.N.; Zhu, W.Y.; Huang, C. Remote sensing of PWV using ground-based GPS data in Wuhan region. *Prog. Astron.* **2005**, *23*, 169–179.
19. Yao, Y.; Liu, J.; Zhang, B.; He, C. Nonlinear relationships between the surface temperature and the weighted mean temperature. *Geomat. Inf. Sci. Wuhan Univ.* **2015**, *40*, 112–116.
20. Jade, S.; Vijayan, M. GPS-based atmospheric precipitable water vapor estimation using meteorological parameters interpolated from NCEP global reanalysis data. *J. Geophys. Res. Atmos.* **2008**, *113*. [CrossRef]
21. Means, J.D.; Cayan, D. Precipitable water from GPS Zenith delays using North American regional reanalysis meteorology. *J. Atmos. Ocean. Technol.* **2013**, *30*, 485–495. [CrossRef]
22. Zhao, Q.; Yao, Y.; Yao, W.; Zhang, S. GNSS-derived PWV and comparison with radiosonde and ECMWF ERA-Interim data over mainland China. *J. Atmos. Sol. Terr. Phys.* **2019**, *182*, 85–92. [CrossRef]
23. Lu, C.; Li, X.; Cheng, J.; Dick, G.; Ge, M.; Wickert, J.; Schuh, H. Real-time tropospheric delay retrieval from multi-GNSS PPP ambiguity resolution: Validation with final troposphere products and a numerical weather model. *Remote Sens.* **2018**, *10*, 481. [CrossRef]

24. Abimbola, O.J.; Falaiye, O.A.; Omojola, J. Estimation of Precipitable Water Vapour in Nigeria Using NIGNET GNSS/GPS, NCEP-DOE Reanalysis II and Surface Meteorological Data. *J. Phys. Sci.* **2017**, *28*, 19. [CrossRef]
25. Zhang, H.; Yuan, Y.; Li, W.; Zhang, B.; Sensing, R. A real-time precipitable water vapor monitoring system using the national GNSS network of China: Method and preliminary results. *IEEE J. Sel. Top. Appl. Earth Obs.* **2019**, *12*, 1587–1598. [CrossRef]
26. Yao, Y.; Zhu, S.; Yue, S. A globally applicable, season-specific model for estimating the weighted mean temperature of the atmosphere. *J. Geod.* **2012**, *86*, 1125–1135. [CrossRef]
27. Yao, Y.; Hu, Y.; Yu, C.; Zhang, B.; Guo, J. An improved global zenith tropospheric delay model GZTD2 considering diurnal variations. *Nonlinear Process. Geophys.* **2016**, *23*, 127–136. [CrossRef]
28. Zhang, P.; Wu, J.; Sun, Z. Construction and Service of the National Geodetic Datum. *Geomat. World* **2018**, *25*, 39–41, 46.
29. Gan, W.; Li, Q.; Zhang, R.; Shi, H. Construction and Application of Tectonic and Environmental Observation Network of Mainland China. *J. Eng. Stud.* **2012**, *4*, 16–23.
30. Jin, S.; Park, P.-H.; Zhu, W. Micro-plate tectonics and kinematics in Northeast Asia inferred from a dense set of GPS observations. *Earth Planet. Sci. Lett.* **2007**, *257*, 486–496. [CrossRef]
31. Dach, R.; Lutz, S.; Walser, P.; Fridez, P. *Bernese GNSS Software*, version 5.2; Astronomical Institute, University of Bern: Bern, Switzerland, 2015.
32. Li, Z.; Wen, Y.; Zhang, P.; Liu, Y.; Zhang, Y. Joint Inversion of GPS, Leveling, and InSAR Data for The 2013 Lushan (China) Earthquake and Its Seismic Hazard Implications. *Remote Sens.* **2020**, *12*, 715. [CrossRef]
33. Saastamoinen, J. Contributions to the theory of atmospheric refraction. *Bull. Géodésique* **1973**, *107*, 13–34. [CrossRef]
34. Jin, S.; Luo, O. Variability and climatology of PWV from global 13-year GPS observations. *IEEE Trans. Geosci. Remote Sens.* **2009**, *47*, 1918–1924.
35. Liou, Y.-A.; Teng, Y.-T.; Van Hove, T.; Liljegren, J.C. Comparison of Precipitable Water Observations in the Near Tropics by GPS, Microwave Radiometer, and Radiosondes. *J. Appl. Meteorol.* **2001**, *40*, 5–15. [CrossRef]
36. Wang, J.; Zhang, L.; Dai, A. Global estimates of water-vapor-weighted mean temperature of the atmosphere for GPS applications. *J. Geophys. Res. Atmos.* **2005**, *110*. [CrossRef]
37. Guan, X.; Yang, L.; Zhang, Y.; Li, J. Spatial distribution, temporal variation, and transport characteristics of atmospheric water vapor over Central Asia and the arid region of China. *Glob. Planet. Chang.* **2019**, *172*, 159–178. [CrossRef]
38. Liu, Y.; Ding, Y. Analysis of the basic features of the onset of Asian summer monsoon. *Acta Meteorol. Sin.* **2007**, *21*, 511–526.
39. Zhao, Q.; Yang, P.; Yao, W.; Yao, Y. Hourly PWV Dataset Derived from GNSS Observations in China. *Sensors* **2020**, *20*, 231. [CrossRef] [PubMed]
40. Gui, K.; Che, H.; Chen, Q.; Zeng, Z.; Zheng, Y.; Long, Q.; Sun, T.; Liu, X.; Wang, Y.; Liao, T.; et al. Water vapor variation and the effect of aerosols in China. *Atmos. Environ.* **2017**, *165*, 322–335. [CrossRef]
41. Durre, I.; Williams, C.N.; And, X.Y.; Vose, R.S. Radiosonde-based trends in precipitable water over the Northern Hemisphere: An update. *J. Geophys. Res. Atmos.* **2009**, *114*. [CrossRef]
42. Wang, R. Characteristics of Water Vapor, Precipitation, Temperature and Humidity in Mainland China Based on IGRA and TRMM PR. Ph.D. Thesis, University of Science and Technology of China, Hefei, China, 2019.
43. Wong, M.S.; Jin, X.; Liu, Z.; Nichol, J.; Chan, P. Multi-sensors study of precipitable water vapour over mainland China. *Int. J. Climatol.* **2015**, *35*, 3146–3159. [CrossRef]

remote sensing

MDPI

Article

NRTK, PPP or Static, That Is the Question. Testing Different Positioning Solutions for GNSS Survey

Gino Dardanelli *, Antonino Maltese, Claudia Pipitone, Alessandro Pisciotta and Mauro Lo Brutto

Department of Engineering, University of Palermo, 90128 Palermo, Italy; antonino.maltese@unipa.it (A.M.); Claudia.pipitone02@unipa.it (C.P.); alessandro.pisciotta@community.unipa.it (A.P.); mauro.lobrutto@unipa.it (M.L.B.)

* Correspondence: gino.dardanelli@unipa.it; Tel.: +39-09123896228

Abstract: Worldwide, the determination of the coordinates from a Global Navigation Satellite System (GNSS) survey (in Network Real Time Kinematic, Precise Point Positioning, or static mode) has been analysed in several scientific and technical applications. Many of those have been carried out to compare Precise Point Positioning (PPP), Network Real Time Kinematic (NRTK), and static modes' solutions, usually, using the latter as the true or the most plausible solution. This approach is not always possible as the static mode solution depends on several parameters (baseline length, acquisition time, ionospheric, and tropospheric models, etc.) that must be considered to evaluate the accuracy of the method. This work aims to show the comparison among the GNSS survey methods mentioned above, using some benchmark points. The tests were carried out by comparing the survey methods in pairs to check their solutions congruence. The NRTK and the static solutions refer to a local GNSS CORS network's analysis. The NRTK positioning has been obtained with different methods (VRS, FKP, NEA) and the PPP solution has been calculated with two different software (RTKLIB and CSRS-PPP). A statistical approach has been performed to check if the distribution frequencies of the coordinate's residual belong to the normal distribution, for all pairs analysed. The results show that the hypothesis of a normal distribution is confirmed in most of the pairs and, specifically, the Static vs. NRTK pair seems to achieve the best congruence, while involving the PPP approach, pairs obtained with CSRS software achieve better congruence than those involving RTKLIB software.

Keywords: NRTK; PPP; static; congruence; GNSS; CORS

Citation: Dardanelli, G.; Maltese, A.; Pipitone, C.; Pisciotta, A.; Lo Brutto, M. NRTK, PPP or Static, That Is the Question. Testing Different Positioning Solutions for GNSS Survey. *Remote Sens.* **2021**, *13*, 1406. https://doi.org/10.3390/rs13071406

Academic Editor: Stefania Bonafoni

Received: 18 February 2021
Accepted: 3 April 2021
Published: 6 April 2021

1. Introduction

The coordinates from a Global Navigation Satellite Systems (GNSS) survey, as it is known throughout literature, can be computed with different approaches (relative and differential techniques, or absolute precise point positioning method). Traditionally, according to the relative survey, there are many differences distinguishing the static and the kinematic modes (RTK, real time kinematic or NRTK, network-based RTK). Specifically, the static mode allows reaching the highest precisions, despite the time involved for the survey and the data post-processing could limit its application [1–4]. Using the kinematic mode, the distance between the master and the rover receivers needs to be low, generally less than 20 km to solve the ambiguity phase fixing with "on the fly" procedure in order to retrieve the centimetre accuracy of the static positioning [5]. To overcome the above mentioned constrain, in the last few years, the GNSS Continuously Operating Reference Stations (CORS) networks have been widely used for real time positioning with high-precision. The presence of widely spread GNSS CORS networks encouraged the use of the NRTK technique that allows overcoming the limits of the distances among the stations. The use of GNSS CORS network, also, allows applying differential corrections more reliable on wide areas, such as the Virtual Reference Station (VRS) approach [6], the Multi Reference Station (MRS) approach [7], the Flächen Korrektur Parameter (FKP) approach or other

surface correction approaches [8,9]. Several authors [10–12] demonstrated that the NRTK technique allows reaching centimeter accuracy, comparable with the accuracy of the static measurements.

The fundamentals of the PPP method were presented in [13] and in [14]. Many other research have discussed this methodology, to establish a geodetic survey control network [15] and to verify the possibilities of multi-constellation measurements for both static and kinematic acquisitions, to improve the convergence of PPP solutions [16–19]. The accuracy of PPP method has also been studied comparing the outcomes from online web services using different software and satellite ephemerides products [20], evaluating the performances of online free available PPP services for static positioning and tropospheric delay estimation [21,22]. Other works have also analyzed the possibility to achieve high positioning accuracy with PPP using a short period of observations [17,23–25].

A very prominent segment of PPP applications, known to the scientific community as GNSS-Ionosphere, has been developed to measure the ionospheric total electron content (TEC) aiming monitoring the global ionospheric climate. The TEC observations record regional ionospheric perturbations due to earthquakes/tsunamis, or geomagnetic storms, typhoon, and eclipses.

Moreno et al. [26] examined the relation between large changes in the rate of TEC with positioning errors in single PPP epochs, at equatorial latitudes during post-sunset hours, establishing that estimated altitudes have errors up to several meters for a single-epoch positioning. Results have been validated via the online CSRS-PPP software using three International GNSS Services (IGS) stations. Afraimovich et al. [27] report that the total GPS L2 phase slipped during the recovery phase of a geomagnetic storm due to GPS signal scattering on field aligned irregularities, both for the lines-of-sight aligned to the magnetic field line (the field of aligned scattering) and across the magnetic field line (the field of across scattering). Demyanov et al. [28] observed that the signal carrier phase scintillations can be caused by the ionospheric irregularities and also by a satellite oscillator anomalies and troposphere. The authors also reports that the parameter sensitivity crucially depends on the GPS receiver hardware and the carrier phase data sampling rate. A second-order derivative of the GPS signal phase is suggested as a mean to detect small-scale ionospheric irregularities. It was found that a 50 Hz data sampling rate is an adequate time resolution to reveal small-scale irregularities responsible for the ionospheric scintillations. More recently, Jin et al. [29], by analyzing a decade long observations of Constellation Observing System for Meteorology, Ionosphere, and Climate (COSMIC), estimated the long-term variations of the plasmaspheric total electron content (PTEC).

The above-mentioned studies propose methodologies and mathematical approaches to analyze peculiar environmental conditions (magnetic storms, solar flares, atmospheric storms, and ionospheric scintillations) inducing positioning inaccuracies as highlighted in the suggested references, which may be referred to for further details, without claiming to be exhaustive.

In this work, we aim to compare NRTK, PPP and static methodologies to retrieve the coordinates of several benchmarks. The NRTK and static solutions have been performed using the GNSS CORS network of University of Palermo (UNIPA) located in the western-part of Sicily (Italy) included in the national Topcon Italy GNSS CORS network (TopNET live, [30]). The PPP solutions were carried out using two different software: the Canadian Spatial Reference System Precise Point Positioning (CSRS-PPP) online Web service and the open source program package RTKLIB. To compare Static and PPP solutions, only an hour of observations was considered.

In the assessment of NRTK or PPP positioning, most scientific studies use as reference the results obtained by the comparison with static mode positioning, especially if the processing is performed with scientific software (Bernese, GAMIT (GNSS at MIT, Massachusetts Institute of Technology), GBLOCK (Global Kalman filter), GIPSY-OASIS (GNSS-Inferred Positioning System and Orbit Analysis Simulation Software)) in which it is possible the errors' components modelling (final ephemeris, tropospheric, ionospheric).

Based on results from similar tests (short baselines, 10–30 kilometres in length, observed for a hour), it has been demonstrated that the commercial software packages performs better than a scientific one (e.g., Bernese) [31,32].

However, in this study, the static observations are relatively short (about an hour) and the static processing was processed with a commercial software; these conditions are not able to guarantee the best performance of static positioning, since, as reported by [20,31], the results of the processing can be different from each other (difference of a few centimetres), in the three geodetic components, depending on the software used.

For these reasons, the best strategy, used by the authors of this work, established the comparison between all different modes (NRTK, PPP, static) in order to provide a congruence analysis of the results obtained with different approaches.

The paper is organized as follows. A description of the UNIPA GNSS CORS network, the benchmark tests and a short introduction to the software involved for the analyses are discussed in Section 2. A synopsis of the results is presented and discussed in Section 3, and finally, concluding remarks and future applications are reported in Section 4.

2. Materials and Methods

2.1. UNIPA GNSS CORS Network

The UNIPA GNSS CORS network has been materialized in 2006 for scientific purposes by University of Palermo [33]. It is made up of eight CORSs located in western Sicily with inter-distances ranging between 22 and 80 km, equipped with Topcon NET G-3 GPS and GLONASS enabled receivers.

Up to 2012, the Control Centre (CC) was at the Department of Engineering of University of Palermo and the GNSS − State Monitoring and Representation Technique (GNSMART) software by Geo++ was used to manage the CORS network and to produce the NRTK corrections. From 2013, all reference stations were included in the NetGEO GNSS CORS network, managed by Topcon Italy. The network provides daily RINEX data (30″), hourly raw data (1″) and real-time GNSS data streams code, Nearest Station (hereinafter NEA), VRS and FKP.

Preliminary, the coordinates of the reference stations were established in ITRF05 and ETRF89 (epoch 1989.0) frames. Recently, six CORSs have been included in the Italian GNSS dynamic network denominated Rete Dinamica Nazionale (RDN), that is a Regional Reference Frame sub-commission for Europe (EUREF) European sub-network, aiming to monitor the reference system variations [34]. The RDN network is computed in the ETRF2000 reference frame (epoch 2008.0) using the Bernese 5.0 software; thus, the coordinates of the UNIPA GNSS CORS network have been also calculated in this frame. Data from UNIPA GNSS CORS network have been also included within a European regional integration of long-term national dense network solutions [35] for the positions and velocities of more than 3000 stations.

In the last few years, the UNIPA GNSS CORS network has been involved for scientific applications in different fields, including the electromagnetic pollution monitoring via a GPS-GIS integrated system [36], the trajectories calculation of Mobile Mapping System (MMS) [37,38], the dams monitoring with integrated InSAR and GNSS techniques [39,40], the geodetic measurements of the stalactite elevation in geological analyses [41], the use of unmanned aerial vehicles for soil moisture characterization [42], the positioning and guidance of agricultural machines via GNSS [43], the monitoring of active faulting, with integrated geodetic and InSAR techniques [44,45].

2.2. Static, NRTK Survey and Software Processing

In the last years, several projects were carried out to evaluate the performance of the UNIPA GNSS CORS network using several GPS reference benchmarks. These reference benchmarks have been also used for our tests since they have good-excellent sky visibility and therefore were suitable for GPS-GLONASS observations. In order to use permanently materialized points, easily reachable and detectable without specific arrangements, the

GNSS reference benchmarks have been chosen among the points belonging to the national and local static GNSS networks in Sicily. Fourteen of those belong to the national static GNSS network (IGM95 network), and fifty-seven to the local GNSS network. The IGM95 network was developed by Italian Military Geographic Institute (IGM) in the nineties using differential techniques and it was calculated in the European ETRS89 system, using the EUREF points available in the country [46]. The network is connected with the levelling geodetic networks and it is made up of 3000 distributed points (177 are located in Sicily), approximately distant 20 km with a Root-Mean-Square Error (RMSE) of ±5 cm. The local static GNSS regional network in Sicily was mainly developed for technical applications and it is made up of 523 points, spaced 7–9 km from each other. Benchmarks have been stabilized in various modes, including concrete pier with aluminum plate, stainless steel, stainless steel mast, and roof mounted on buildings, according to national regulations.

The coordinates of the local static GNSS network have been computed with observations of three independent bases in relation to the points of the IGM95 network. All these points are distributed on the area covered by the UNIPA GNSS CORS network and they have been used for the tests of this work (Figure 1); in addition, some new reference points (fifteen points) were also materialized (mostly around the city of Palermo) and used for the tests.

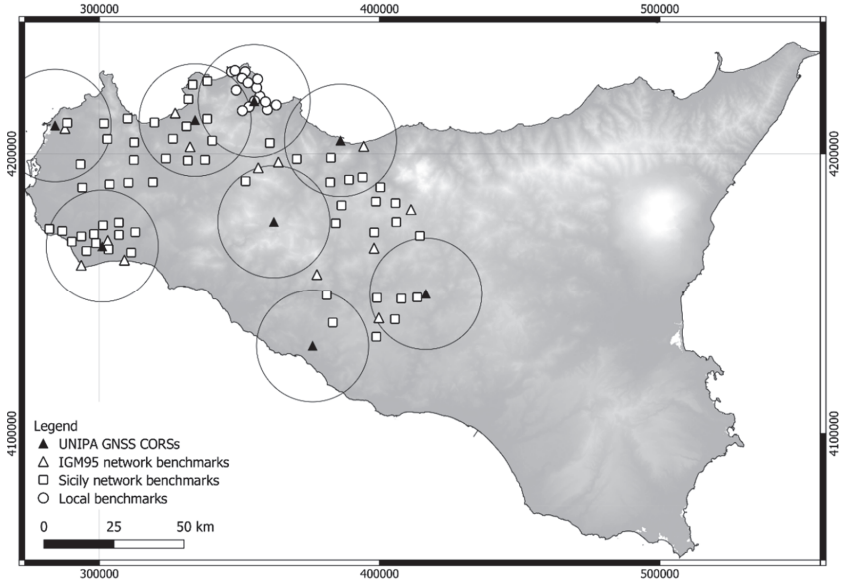

Figure 1. UNIPA GNSS CORSs (black triangles) and GNSS reference benchmarks (IGM95 network benchmarks, white triangles; Sicily network benchmarks, white squares; local benchmarks, white circles); 20 km buffer circles from the GNSS CORS are shown. Reference system UTM-WGS84 33N (ETRF2000-RDN2008)-EPSG6708.

Preliminarily, the coordinates of all GNSS reference benchmarks were computed in ITRF05 frame performing the static survey with dual-frequency GNSS receivers Topcon HiPer-Pro and Topcon GR3, equipped with controller FC-100 and FC-200. The occupation time was about 60 min. We chose a one hour observations since distances from CORSs to benchmarks were about 15–20 km at most (≈80% of the benchmarks), and according to literature [31,32] this occupation time is sufficient at these distances. A maximum distance of ≈30 Km characterizes an IGM95 benchmark. The elevation mask was set to 10 degrees, the epoch/logging rate to 15 s, and the maximum PDOP was fixed to 6.

The Topcon Tools package ver. 8.2.3 by Topcon Corporation was used for the static measurements. The software allows the data processing from different devices such as total stations, digital levels and GNSS receivers, and it is used in several technical-scientific applications [47,48]. Topcon Tools uses the Modified Hopfield Model for the tropospheric corrections [49]. The employed positioning mode was Code-based differential ("CODE DIFF"), the time range and the cut-off angle were set to 15 s and 10 degrees, respectively. Each GPS reference benchmark was measured with three independent baselines from the nearest permanent stations. The precision of all GNSS reference benchmark coordinates in ITRF05 frame is approximately few millimeters.

The survey was verified by recalculating the coordinates of the benchmark, belonging to the IGM95 and local network in Sicily, in the ETRF89 frame (epoch 1989.0) and then the results were compared with the official coordinates; the differences between the results were in the same order of magnitude of the intrinsic accuracy of the geodetic networks. For the NRTK processing was used GNSMART (GNSS − State Monitoring and Representation Technique), developed by Geo++ GmbH (Garbsen, Germany). It is one of the earliest systems guaranteeing an uniform coverage for the absolute positioning in real time with centimeter precision [50]. The GNSS observations (GPS and GLONASS, in this study) are stored in RTCM 2.3 (Radio Technical Commission for Maritime Services) format, able to send the differential corrections (VRS, FKP, NEA). GNSMART uses the same tropospheric delay model of Topcon Tools (the modified Hopfield model) [51], with two scaling parameter/station, while regarding the ionospheric delay a single layer model with polynomial, one bias per satellite (vertical delay), with 3D Gauss–Markov process (one bias per receiver−satellite combination) [50]. Also used Meridiana ver. 2011, developed by GEOPRO s.r.l. (Ancona, Italy), only for recording data from the different NRTK corrections (VRS, FKP, NEA).

The NRTK positioning was carried out using a scientific protocol given by [52]. Specifically, it is based on taking measurements during the weekdays from 8:00 am to 6:00 pm, without a preliminary check about the geometric configuration of the satellites or the stations efficiency and using dual-frequency geodetic GNSS receivers Topcon Hiper-Pro (by Topcon Corporation, Japan) with controller FC-100. Two separate sessions are recorded for each benchmark to obtain independent satellite configurations; for each session, four independent tests (from the startup to the turning off of the instruments) for each network solution, were analyzed (VRS, FKP, NEA). The results, recorded at the fifth epoch, were accepted with both phase solution and ambiguity phase fixed, while the solution is considered rejected when the ambiguity phase fixing did not occur within five minutes since the connection with the software (float or stand-alone solution).

Overall, 86 GNSS reference benchmarks have been measured in NRTK survey (out over 100 benchmarks); indeed, some benchmarks during the investigation were damaged and not detectable. Also, the computation of the VRS, FKP, and NEA solutions was not possible for all points. The NEA solution has been only used for GNSS reference benchmarks distant less than about 20 km from the nearest reference station. An evaluation between valid tests, in which the NRTK corrections were obtained, and failed tests, in which the receiver has not received the network corrections, showed that the VRS correction was achieved for 72% of GNSS benchmarks, the FKP for 61% and the NEA for 59%. Totally, the benchmarks used to detect the differential corrections were 61, 52, and 50 in VRS, FKP, and NEA modes, respectively.

2.3. PPP Software Processing

The PPP processing was carried out using one-hour of static acquisitions and two different packages, CSRS-PPP and RTKLib.

CSRS-PPP is an on-line service developed by Geodetic Survey Division of Natural Resources Canada that allows an easy access to the Canadian Spatial Reference System (CSRS). The CSRS-PPP allows GPS users in Canada (and abroad) to achieve accurate positioning by submitting GPS observations from a single receiver over the Internet. It

can process GNSS observations from single or dual-frequency GPS receivers operating in static or kinematic mode. The aim to this software is the use of precise GNSS orbit and clock products generated through international collaborations [53–55]. CSRS-PPP uses the Estimate ZTD (Zenith Total Delay) model for tropospheric corrections, with the IGS final (Repro1) orbits and Observations Frequency Mode Phase and Code Double Static in which the elevation cut-off is 15°.

Within this research, the raw data of all 86 benchmarks were sent by email; the computation reports, by the software online, included the coordinates in the ITRF05 frame and the associated plots.

RTKLib (version 2.4.2 p13) is an open source program package used for standard and precise positioning with GNSS (Takasu and Yasuda 2009) [56]. This software is widely used in scientific research for smartphone in static and kinematic modes [57], although the performance of GPS-only, BeiDou Navigation Satellite System (BDS)-only, and combination of BDS/GPS have been analyzed recently [58]. The NRTK corrections to the raw data have been also applied to a GNSS CORS of the mass market receivers [59,60]. However, the Pseudo-VRS technique incorporates high-precision GNSS positioning methods, for instance in the developments of vehicle-to-vehicle communication [61]. The software was used for static and kinematic surveys using GNSS multi-constellation receivers acquiring GPS, GLONASS and Galileo Open Service (OS) [62]; more recently, its performance using the GNSS multi-constellation PPP technique in static mode has been also analyzed [19].

The processing with RTKLib was performed by selecting the Ionospheric Iono-Free LC model and the Estimate ZTD to correct the ionospheric and the tropospheric influence, respectively; and the IGS (International GNSS Service) ephemerids to correct orbit and clock, in accordance with a similar studies conduct recently by Angrisano et al. [19]. In particular:

- GDOP threshold is set to reject solutions with GDOP values higher than 30°, and a mask-angle equal to 10° is applied.
- No ambiguity resolution strategy is used, since the PPP-AR (Ambiguity Resolution) function selectable in RTKLib software, was experimental at experimental at the time of data processing, providing unstable and inaccurate solution with respect to standard PPP according to the RTKLib manual. A detailed description of Ambiguity Resolution, in particular using GLONASS, is reported in [63].
- The Phwindup (phase wind-up) option is set to correct the delay caused by the relative rotation between the satellite and receiver antennas.
- Reject Ecl, is set to exclude the GPS Block IIA eclipsed satellites, that degrade the PPP solutions due to unpredicted behavior of yaw-attitude.
- RAIM (Receiver Autonomous Integrity Monitoring Receiver Autonomous Integrity Monitoring) FDE (Fault Detection Fault Detection and Exclusion) detect and exclude possible outliers from the measurements set used for the solution computation.
- Sat PCV (phase center variations) and Rec PVC, were set to consider the phase center variations of the satellite and the receiver, respectively. It requires the so-called "igs14.atx" file, provided by the IGS (International GNSS Service), containing the correction parameters of several types of antenna.

The Ionospheric Iono-Free model and the estimated zenith total delay (ZTD) option were selected to correct the ionospheric and the tropospheric influence, respectively, while through the IGS ephemerids we accounts for the orbit and clock corrections [19].

The Saastamoinen model [64] computes the tropospheric delay T_r using the following expression (1):

$$T_r = \frac{0.002277}{\cos(z)}\left[p + \left(\frac{1255}{T} + 0.05\right)e - tan^2(z)\right] \quad (1)$$

where: p, is the total pressure; T, is the absolute temperature of the air; e, is the partial pressure of water vapor; z, is the zenith angle.

In the Saastamoinen model [64], a standard atmosphere is considered as a reference, the geodetic height is approximated to the ellipsoidal height, and a humidity percentage is fixed to 70%.

The model considers the troposphere as divided into two layers. The first layer, from the earth surface to 10 km on it, has a constant descent rate of temperature of 6.5 °C km^{-1}. The second layer, from 10 to 70 km on the earth surface, has assumed having a constant temperature value. Therefore, for atmospheric refraction integral, the function of refractive index can be computed based on the zenith distance trigonometric functions and term wise integration. In this way, the ZTD is expressed as (2)–(4):

$$ZTD = 0.002277 \frac{(P_0 + \left(0.05 + \frac{1255}{P_0 + 273.15}\right) e_0}{f(\varphi,\ h)} \tag{2}$$

$$e_0 = r_h \cdot r_h \cdot 6.11 \cdot 10^{\frac{7.5T_0}{T_0 + 273.3}} \tag{3}$$

$$f(\varphi,\ Z) = 1 - 0.00266 \cos 2\varphi - 0.00028Z \tag{4}$$

where P_0, T_0, and e_0 are, respectively, the surface pressure, the surface temperature, and the water vapor pressure at the surface level, r_h is the relative humidity, $f(\varphi, Z)$ is the correction of gravity acceleration caused by the rotation of the earth, and φ and Z are the point latitude and altitude, respectively.

The Estimate ZTD model computes the tropospheric delay starting from the expression of the Saastamoinen model with the zenith angle and relative humidity equal to zero and employing the NMF (Niell Mapping Function), based on receiver geographical coordinates and measurement time [65]. The mapping function in terms of the elevation (El) and the azimuth (Az) angles between the satellite and the receiver is expressed as:

$$M(El) = M_w(E)\{1 + \cot(El) \cdot (G_N \cos(El) \cdot (G_N \cos(\mathrm{Az}) + G_E \sin(Az))\} \tag{5}$$

$$T_{r,z} = M_h(El) \cdot Z_H + M(El)(Z_T - Z_H) \tag{6}$$

where, Z_T accounts for the tropospheric zenith total delay that is estimated from the extended Kalman filter together with the north (G_N) and the east (G_E) components of the tropospheric gradient. Z_H accounts for the tropospheric zenith hydro-static delay computed using a tropospheric model, such as Saastamoinen, Hopfield [51], or modified Hopfield models with the zenith angle and relative humidity equal to zero. M_h (El) and M_w (El) are, respectively, the hydro-static and wet mapping-functions.

Niell [65] kept the basic form of the Herring (MTT model, [66]) mapping function adding a height correction term and assuming that the elevation dependence is a function of only geographical parameters (if we accept that, in a way, the day of the year is also a constant and independent parameter) and proposed the function (7):

$$m(v) = \frac{1 + \frac{a}{1 + \frac{b}{1+c}}}{\sin(v) + \frac{a}{\sin(v) + \frac{b}{\sin(v)+c}}} + \Delta m(v) \tag{7}$$

The wet delay parameters $a, b,\ c$ are given at tabular latitude φ_i 15°, 30°, 45°, 60° and 75°. The hydrostatic parameters $a_h,\ b_h,\ and\ c_h$ at time in UT days is calculated as (8):

$$a_h(\phi_i, t) = a_{avg}(\phi_i) - a_{amp}\ (\phi_i) \cos\left(2\pi \frac{t - T_0}{365.25}\right) \tag{8}$$

where a_{avg} and a_{amp} are given at tabular latitude φ_i 15°, 30°, 45°, 60° and 75°, and T_0 is the adopted phase, DOY 28 as described in [66]

The height correction is given by (9) as a function of the coefficients a_h, b_h, and c_h and the orthometric height:

$$\Delta m(v) = \frac{1}{\sin(v)} - \frac{1 + \frac{a_h}{1+\frac{b_h}{1+c_h}}}{\sin(v) + \frac{a_h}{\sin(v)+\frac{b_h}{\sin(v)+c_h}}} \times H \quad (9)$$

2.4. Data Analysis

The aim of this work is to evaluate the congruence of different positioning solutions obtained with alternative GNSS methodologies. The solutions' congruence was assessed by statistically analyzing the coordinate's differences on selected benchmarks. The analysis was performed by considering separately each coordinate component, North (N), East (E) and Ellipsoidal Height (Z). The static results were compared to NRTK solutions, namely VRS, FKP and NEA, and PPP solutions by CSRS and RTKLIB. The NRTK solutions were compared to the two PPP solutions; in additional, the two PPP solutions (CSRS and RTKLIB) were compared with each other. Totally, twelve different comparisons have been carried out (Figure 2): Static vs. CSRS, Static vs. RTKLIB, CSRS vs. RTKLIB, CSRS vs. VRS, CSRS vs. FKP, CSRS vs. NEA, RTKLIB vs. VRS, RTKLIB vs. FKP, RTKLIB vs. NEA, Static vs. VRS; Static vs. FKP and finally Static vs. NEA.

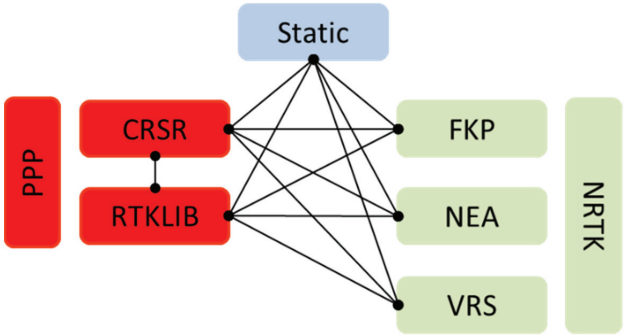

Figure 2. Conceptual scheme of comparisons. In light blue, green and red the 3 GNSS processing families: Static, NRTK and PPP, respectively.

The procedure used for statistical analysis aimed to remove the extreme values (considered as possible outliers), if occurring. Indeed, some authors analyzed the statistical distribution of GNSS errors [67] using a normal distribution as discussed and justified by [68]. A normal distribution was fitted to the empirical frequency under the hypotheses of equal mean and standard deviation. According to Specht [67], values exceeding 95.4% in the cumulative frequency, corresponding to a span of ± 2 standard deviations from the mean, were considered possible outliers and removed from the comparison. Although it can be considered a poorly conservative threshold [69], it allows dealing with relatively small sets of observations. The normal distribution is considered separately from each of the measured coordinates [67]. The correlation between coordinate components is neglected in the univariate analysis, moreover multivariate analyses of outliers tend to reject less data samples than univariate under the same confidence level [70]. Despite these approximations, univariate analysis occurs in a relatively straightforward examination with the identification of possible outliers [70].

Several statistical tests can be applied to examine the consistency of empirical distribution with the theoretical normal distribution, including the Anderson–Darling [71], Cramér-von Mises [72], Kolmogorov–Smirnov [73], and Lilliefors [74] tests.

Two tests were selected being the most frequently applied to verify if the empirical distribution of the solutions differences, once removed the possible outliers, follows a

normal distribution, namely the Kolmogorov–Smirnov (KS) and the Anderson–Darling (AD) tests. The KS test is a non-parametric method and it was used to assess whether the empirical distribution frequency of the coordinates differences belongs to a reference normal distribution (the null hypothesis, H_0) against the alternative hypothesis (H_1) that the empirical distribution does not fit the theoretical distribution [75]. The null hypothesis was evaluated for rejection at a significance level α, by comparing the KS value, resulting from the test, with the critical value, KSC. As well as the two-sample KS test, the two-sample AD test is used to test whether the two samples originate from the same distribution [76]. The AD test can be considered a modification of the KS test and it weighs more the tails than the KS test does.

The mean values, μ, and the standard deviations, σ, of the coordinates differences, ΔN, ΔE and Δh, were compared, as well, to the corresponding value prior removing extreme values. Another two statistical indices, the sample skewness, S, and the kurtosis index, K, [77], evaluated before and after extreme values removal, allowed assessing whether and how much the empirical frequency distribution gets more symmetricity and mesokurticity.

After removing extreme values, the determination coefficient, r^2, between the empirical frequency and the corresponding values of the fitted normal distribution, was used to measure the strength of a linear relation between the corresponding values. All correlations are classified according to Evans [78].

3. Results and Discussion

The first analysis aimed to check the range of variability of coordinates differences for all pairs involved (Table 1). This analysis shows that the variability of the pairs involving RTKLIB is always much higher than the other, as confirmed by the range always higher than 500 mm, 1000 mm and 500 mm for N, E and h components. In the other cases the range of variability is less than 400 mm, excluding the differences for h component in the comparisons Static vs. CSRS and Static vs. RTKLIB, where the values are 531 mm and 594 mm, respectively. A suitable comparison of the results should require the removal of any outliers, if occurring. So, as discussed in the previous section, assuming that the coordinates' differences belong to a normal distribution, the extreme values can be considered possible outliers and then removed. Some statistics descriptors of the ΔN, ΔE and Δh algebraic differences among different pairs of solutions were applied to discuss if and to what extent different solutions lead to comparable results.

Table 1. Range of variability of the coordinate differences (min – max in mm).

Min Max (mm)	Static CSRS	Static RTKLIB	RTKLIB CSRS	Static VRS	Static FKP	Static NEA	CSRS VRS	CSRS FKP	CSRS NEA	RTKLIB VRS	RTKLIB FKP	RTKLIB NEA
ΔN	−50	−409	−107	−47	−60	−32	−78	−70	−75	−85	−209	−82
	100	133	116	110	36	41	105	56	54	433	585	652
ΔE	−184	−606	−603	−148	−121	−149	−131	−106	−169	−492	−782	−697
	141	462	745	190	118	78	170	122	101	580	583	653
Δh	−185	−375	−402	−206	−137	−135	−130	−170	−120	−318	−166	−245
	346	219	298	187	173	174	203	208	210	504	1328	480

The mean values μ of the coordinates differences, calculated before and after outliers removal, were compared for the different cases (Figure 3). Once extreme values were removed, it was observed that μ of ΔN, ΔE and Δh increases while oppositely decreases in other cases, depending on the values and the number of extreme values removed. As already highlighted, in the analysis of the range of variability, the pairs involving RTKLIB behave differently than the remaining pairs except for the comparison RTKLIB vs. CSRS which shows similar values to the other cases. Specifically, μ for the RTKLIB vs. NRTK (VRS, FPK and NEA) comparison was on average 85, 65 and 144 mm in the pre outliers removal and 81, 93, and 146 in the post outliers removal, respectively, for of ΔN, ΔE, and Δh, while in the Static vs. RTKLIB comparison was −53, −52, and −83 mm in the pre outliers

removal and −47, −40, and −68 in the post outliers removal. For the other observations the mean values on average was 3, 8 and 51 mm in the pre outliers' removal and 5, 11, and 59 mm in the post outliers removal respectively for ΔN, ΔE, and Δh.

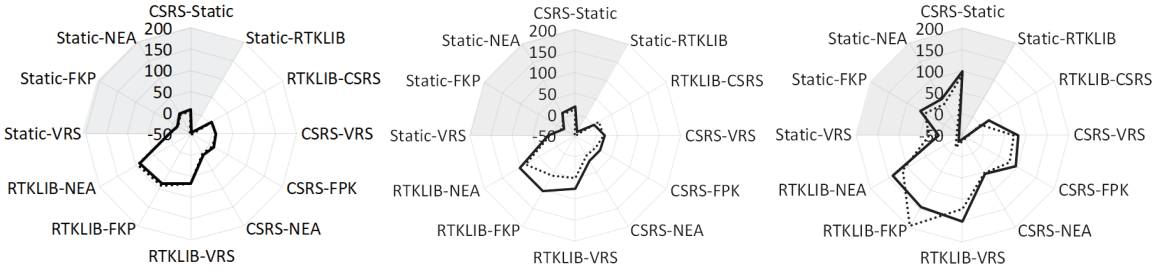

Figure 3. Mean values, μ (mm), of: (**a**) ΔN; (**b**) ΔE; (**c**) Δh differences, pre and post outliers' removal (dashed and continuous lines, respectively). Pairs involving static are here highlighted in grey and in figures hereinafter.

Also, for the standard deviation σ, a similar behavior can be observed. Generally, σ are higher for the pairs involving RTKLIB (RTKLIB vs. NRTK and Static vs. RTKLIB) compared to the remaining pairs, 119, 212, and 164 mm on average for ΔN, ΔE, and Δh, respectively, compared to the remaining pairs (25, 50, and 26 mm for ΔN, ΔE, and Δh, respectively) (Figure 4). The lowest σ were always obtained for Static vs. NRTK pairs (σ of 22, 44 and 73 mm, on the average in the pre outliers removal and of 18, 33, and 54 mm in post outliers removal). As expected, σ is often reduced after removing the extreme values; the reduction is more evident for ΔN and Δh than for ΔE.

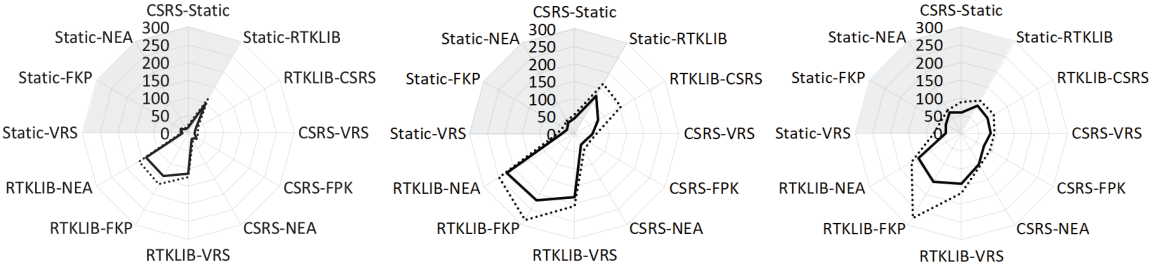

Figure 4. Standard deviation, σ (mm), of: (**a**) ΔN; (**b**) ΔE; (**c**) Δh differences, pre and post outliers' removal (dashed and continuous lines, respectively).

The highest skewness characterizes the ΔN component of the Static vs. VRS and Static vs. CSRS differences (S ≈ 1.54 and 0.78, Figure 5, panel a, continuous line) and the ΔE component of the Static vs. VRS and Static vs. FKP differences (S ≈ 0.51 and 0.55). The extreme values removal generally reduces the asymmetry of the differences frequency distribution (Figure 5), except for the ΔN component of Static vs. NEA and the Δh component of CSRS vs. VRS, CSRS vs. FKP and Static vs. VRS. The reductions for CSRS vs. Static, CSRS vs. NEA and Static vs. FKP were 57, 58 and 50%, respectively. Static vs. NEA and Static vs. PPP (CSRS and RTKLIB) exhibited the lowest average skewness (S ≈ 0.07 and 0.06, respectively) after the extreme values removal, while CSRS vs. FKP showed the highest average skewness (S ≈ 0.58).

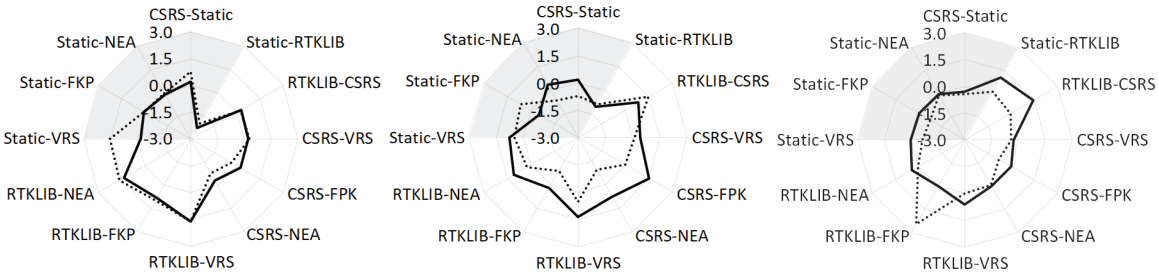

Figure 5. Skewness, S: (**a**) ΔN; (**b**) ΔE; (**c**) Δh differences, pre and post outliers' removal (dashed and continuous lines, respectively).

The highest leptokurticity characterizes the Static vs. VRS for the ΔN component (K ≈ 8.6), RTKLIB vs. CSRS for the ΔE component (K ≈ 10.9) and RTKLIB vs. FKP for the Δh component (K ≈ 7.8) before extremes removal (Figure 6, continuous lines). Once extreme values were removed (dashed lines), the abovementioned pairs loose leptokurticity (K ≈ 0.3, 4.7, and –0.1 for ΔN, ΔE and Δh, respectively).

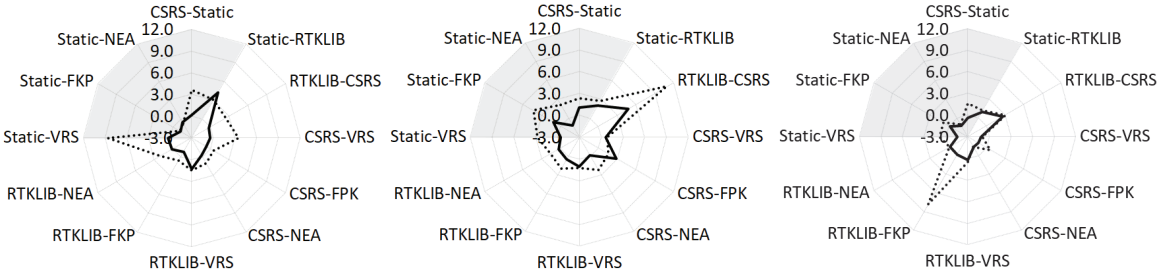

Figure 6. Kurtosis, K: (**a**) ΔN; (**b**) ΔE; (**c**) Δh differences, pre and post outliers' removal (dashed and continuous lines, respectively).

According to the KS test, the differences belong to a normal distribution at a significance level α (Figure 7 panel a, α = 0.05) except for ΔE for the Static vs. FKP pair, and ΔN for the Static vs. RTKLIB and RTKLIB vs. VRS pairs, where the null hypothesis is rejected and the ratio KS/KSC is greater than unity (1.16, 1.31, and 1.14). The lowest values of KS/KSC characterize the RTKLIB vs. CSRS pair (0.27, on the average). According to these results, the AD test shows that the differences belong to a normal distribution (Figure 7 panel b, α = 0.05) excluding one more time ΔE in the Static vs. FKP pair, ΔN in the RTKLIB vs. VRS and RTKLIB vs. NEA differences, and ΔZ in the Static vs. RTKLIB pair (AD/ADC = 1.07, 2.28, 1.17, and 1.15, respectively). The lowest value of AD/ADC was achieved for the CSRS vs. NEA differences (0.16 on the average). If the variables (e.g., ΔN, ΔE and Δh) are normally distributed and independent, this implies they are "jointly normally distributed", i.e., their pairs must have multivariate normal distribution [79].

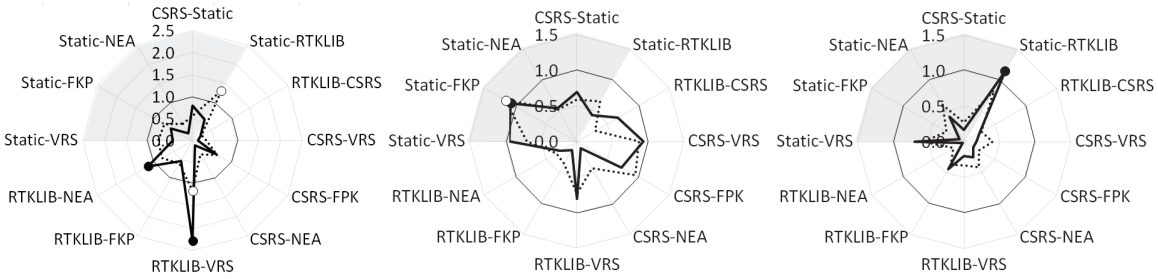

Figure 7. Normality tests applied on the frequencies of: (**a**) ΔN; (**b**) ΔE and (**c**) Δh. The ratio between KS and KSC based on the Two-Sample Kolmogorov-Smirnov Test are represented with dashed lines. The critical value KSC was calculated at a significance level $\alpha = 0.05$. Values exceeding the critical thresholds are represented with white circles. The ratio between AD and ADC based on the Two-Sample Anderson-Darling Test are represented with continuous lines. The critical value ADC was calculated at a significance level $\alpha = 0.05$. Values exceeding the critical thresholds are represented with black circles. ΔN axis ranges between 0 and 2.5, while ΔE and Δh axes range between 0 and 1.5.

The determination coefficients are used to corroborate the assumption that after removing the extreme values, the normal distribution well describes the empirical distribution. At least, only the pairs Static vs. CSRS, RTKLIB vs. CSRS and CSRS vs. NEA exhibit moderate correlation for all components. Analyzing the ΔN differences, results shown that, CSRS vs. Static, RTKLIB vs. CSRS, CSRS vs. VRS and Static vs. VRS pairs exhibit very strong correlations ($r^2 = 0.81$, 0.93, 0.74 and 0.67, respectively) (Table 2). Considering the ΔE differences, only, RTKLIB vs. CSRS exhibits the maximum value of r^2 ($r^2 = 1.00$), while the Δh differences exhibit very strong correlation for the pairs RTKLIB vs. FKP, RTKLIB vs. NEA, Static vs. VRS and Static vs. FKP ($r^2 = 0.64$, 0.77, 0.69 and 0.85, respectively). Very weak and weak correlations were removed from Table 2.

Table 2. Determination coefficient, r^2, between empirical and normal frequencies of ΔN, ΔE and Δh differences among pairs of processing techniques (after extreme values removal): very strong correlations ($r^2 > 0.62$) are highlighted in bold, correlations assumed as strong are in the following range ($0.35 < r^2 \leq 0.62$), moderate correlations ($0.16 \leq r^2 < 0.35$) are reported in grey, very weak and weak correlations ($r^2 < 0.15$) were removed.

R^2	Static CSRS	Static RTKLIB	RTKLI CSRS	Static VRS	Static FKP	Static NEA	CSRS VRS	CSRS FKP	CSRS NEA	RTKLIB VRS	RTKLIB FKP	RTKLIB NEA
ΔN	0.81		0.93	0.67		0.30	0.74		0.45			
ΔE	0.57	0.30	1.00	0.39	0.20		0.29	0.23	0.58		0.34	0.21
Δh	0.43	0.21	0.59	0.69	0.84				0.23	0.54	0.64	0.77

Finally, once removing extreme values, a comparison between the best fitting normal distribution and the empirical distribution frequencies has been performed for the Static vs. VRS, CSRS vs. VRS and CSRS vs. Static coordinates differences (Figure 8). The minima and maxima *x*-axis values change for different pairs according to the corresponding range of variability. From the comparison, the best fitting seems to characterize the ΔN differences. The maximum range of variability is ~ ± 80 mm (CSRS vs. VRS, panel b). The distributions of the empirical frequencies of ΔE CSRS vs. Static and Δh CSRS vs. VRS show many gaps, while those of ΔE Static vs. VRS and Δh CSRS vs. Static highlight a secondary peak. By visually interpreting the empirical frequency distributions of the ΔN and ΔE differences: the ΔN Static vs. VRS, CSRS vs. VRS and CSRS vs. Static well represent the bell shape. Meanwhile, ΔE Static vs. VRS, Static vs. CSRS relatively well represent the bell shape. Considering the altimetric component Δh, only the Static vs. VRS rather well represents the bell shape.

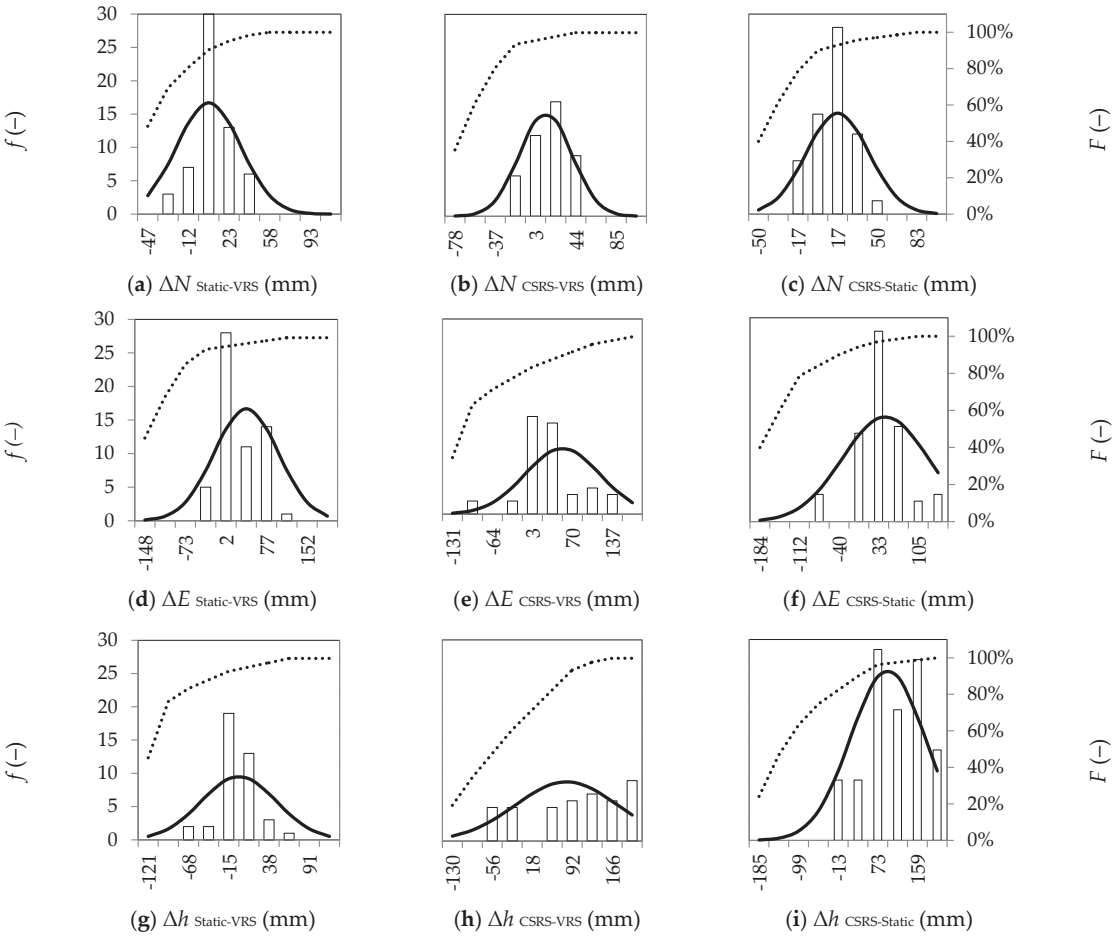

Figure 8. Empirical distribution frequency after extreme values removal (empty bars), best fitting normal distribution (black lines) and cumulative frequency of the empirical frequency before removing the extreme values (dashed line). ΔN, ΔE and Δh differences (mm) are represented in the upper, central and lower graphs, respectively. Static vs. VRS, CSRS vs. VRS and CSRS vs. Static differences are represented in the left, central and right graphs, respectively, the minimum and maximum *x*-axis values change for the different pairs according to the corresponding range of variability: (**a**) $\Delta N_{\text{Static-VRS}}$ (mm), (**b**) $\Delta N_{\text{CSRS-VRS}}$ (mm), (**c**) $\Delta N_{\text{CSRS-Static}}$ (mm), (**d**) ΔE Static-VRS (mm), (**e**) ΔE CSRS-VRS (mm), (**f**) ΔE CSRS-Static (mm), (**g**) Δh Static-VRS (mm), (**h**) Δh CSRS-VRS (mm), (**i**) Δh CSRS-Static (mm)

The range of variability of the 5 pairs involving RTKLIB remains higher than that of the remaining 7 pairs (Table 3), even after removing the extreme values for all computation schemes. The average ΔN, ΔE and Δh indeed were 374, 791, and 540 mm being reduced of ~102 mm, while they were slightly reduced for the latter seven being 76, 170, and 232 mm. The lowest range of variability min–max pre extremes value removal were obtained for Static vs. NRTK pairs (109, 268, and 337 mm for ΔN, ΔE, and Δh, on the average), and it remains the lowest also after removal (70, 135, and 190 mm).

Table 3. Range of variability minima – maxima values, min – max (mm), for ΔN, ΔE and Δh differences, post removal of the extreme values.

Min Max (mm)	Static CSRS	Static RTKLIB	RTKLIB CSRS	Static VRS	Static FKP	Static NEA	CSRS VRS	CSRS FKP	CSRS NEA	RTKLIB VRS	RTKLIB FKP	RTKLIB NEA
ΔN	−24	−353	−42	−38	−52	−20	−23	−33	−37	−42	−124	−36
	54	46	67	40	29	31	52	56	43	355	374	431
ΔE	−92	−418	−201	−43	−82	−51	−106	−32	−42	−173	−481	−269
	141	258	341	118	34	78	151	122	101	580	583	653
Δh	−33	−204	−120	−61	−44	−49	−69	−23	−96	−76	−166	−120
	212	219	298	69	173	174	203	208	210	504	511	480

4. Conclusions

As a result of this work, the coordinates retrieved with different GNSS approaches (static, NRTK, and PPP) were compared. It is commonly accepted that the static survey guarantees the best results in terms of precision, increasing the occupation time, but it needs a long time to post-process data. The NRTK technique allows the measurements of coordinates in real-time, but strictly depends on the network configuration and the active reference stations during the processing. Finally, the PPP approach is automatized with online software, but needs the implementation of ultra-precise ephemerides and post-processing elaboration.

Some statistics descriptors of the north, east, and ellipsoidal height differences among different pairs of solutions were analyzed, among the Static, NRTK, and PPP methodologies.

Among the twelve pairs of evaluated solutions, those five involving RTKLIB exhibited a different behavior compared to the others and they often did not belong to a normal distribution.

Once extreme values were removed, the Static vs. NRTK pair showed the lowest range of variability and the lowest standard deviation (≈−70, 135, 190 mm and 18, 33, and 54 mm on average, respectively, for the ΔN, ΔE and Δh).

The analysis of Kurtosis highlighted that, on the average, the frequency distribution loses leptokurticity tending to the normal distribution (particularly the CSRS vs. Static, CSRS vs. VRS, RTKLIB vs. NEA and Static vs. FKP pairs). The standard deviation of the differences for the N, E and h components of pairs which did not involve RTKLIB was ~20, ~40, and ~70 mm, respectively, while the standard deviation of the differences for the ΔN, ΔE, and Δh components of pairs involving RTKLIB was ~100, ~170, and ~120 mm, respectively.

Two statistic tests, the Kolmogorov–Smirnov and the Anderson–Darling, were implemented to verify if the frequency distribution of the differences belonged to a normal distribution. Both showed that excluding the ΔE in the Static vs. FKP comparison, and some pairs including RTKLIB (Static vs. RTKLIB for ΔN and Δh, Static vs. VRS and Static vs. NEA for N), for which the null hypothesis is rejected, mostly the distribution frequency of the differences among pairs belonged to a normal distribution, at a significance threshold of 0.05. In particular, according to the Kolmogorov–Smirnov test, the best values were found for the differences CSRS vs. Static and CSRS vs. NEA, while in agreement with the Anderson–Darling test, the best values were found for Static vs. NEA and once again for PPP vs. NEA differences.

The coefficient of determination between the empirical and the theoretical frequency distributions provided a measure of how well observed frequencies were replicated by the theoretical frequencies. The analysis highlighted that CSRS vs. Static, RTKLIB vs. CSRS and Static vs. VRS exhibited the highest correlations (~0.6 – 0.9) while Static vs. FKP, Static vs. NEA, CSRS vs. VRS, and CSRS vs. FKP exhibited weak correlations.

Need to be remarked that the aim of this work was to analyze the congruence of the solutions obtained with different methodologies (Static, PPP and NRTK), nor to judge software packages. Although the lowest congruencies seem characterizing the pairs involving RTKLIB, this result should not be considered a criticism on the performance of this

well-known open access program, which undoubtedly is one among of the most useful PPP processing software available, given its very straightforward applicability, considering also that our analysis is limited to one hour of data.

With extended observation times, the congruence among different solutions could be enhanced. Moreover, enlarging the number of benchmarks, the accuracy of the NRTK positioning compared to PPP and Static should be improved, in turn affecting related congruencies.

Other analyses are required to further investigate the performances of different solutions and to test other methods for GNSS network solutions (such as the Master Auxiliary Concepts, MAC). In addition, the recent development of Galileo and Beidou-3 constellations could give more indications than those obtained in this study with only GPS and GLONASS constellations.

In the last few years, several applications have been developed employing the IGS stations in static mode. Specifically, the available online services and packages include the Automatic Precise Positioning Service (APPS), GPS Analysis and Positioning Software, the Canadian Spatial Reference System precise point positioning service, and the MagicPPP [17,23–25], or the comparative analysis of ZTD-estimates obtained with six different software packages (JPL's APPS [80], CSRS-PPP, MagicGNSS [81], European Space Agency and Barcelona's tech GNSSLab Tool (gLAB) [82], RTKLIB, the University of Nottingham's POINT) respect the ZTD-estimates obtained from the IGS tropospheric product [17,23–25]. Moreover, these applications and services could be engaged to analyze the PPP positioning compared to other solutions.NRTK, PPP, or Static, that is the question!

Author Contributions: Conceptualization, G.D.; methodology, G.D., A.M., C.P., and G.D.; validation, A.M., C.P., and G.D.; data curation, A.P. and G.D.; writing—review and editing, A.M., C.P., G.D., and M.L.B.; supervision, M.L.B. All authors have read and agreed to the published version of the manuscript.

Funding: This research received no external funding.

Institutional Review Board Statement: Not Applicable.

Informed Consent Statement: Not Applicable.

Data Availability Statement: GNSS data support the findings of this study are available from the corresponding author upon reasonable request.

Conflicts of Interest: The authors declare no conflict of interest.

Abbreviations

Acronym	Meaning
AD	Anderson-Darling Test
APS	Automatic Precise Positioning Service
AR	Ambiguity Resolution
CC	Control Centre
CODE DIFF	Code-based differential
CORS	Continuously Operating Reference Station
COSMIC	Constellation Observing System for Meteorology, Ionosphere, and Climate
CSRS	Canadian Spatial Reference System
DEM	Digital Elevation Model
DInSAR	Differential InSAR
DOY	Day of Year
ETRF	European Terrestrial Reference System
EUREF	Regional Reference Frame sub-commission for Europe
FKP	Flächen-Korrektur-Parameter
FTP	File Transfer Protocol

GAMIT	GNSS at MIT, Massachusetts Institute of Technology
GBLOCK	Global Kalman filter
GIPSY-OASIS	GNSS-Inferred Positioning System and Orbit Analysis Simulation Software
GLONASS	GLObal NAvigation Satellite System
GNSMART	GNSS − State Monitoring And Representation Technique
GNSS	Global Navigation Satellite System
GPS	Global Positioning System
InSAR	Interferometric SAR
IGM	Istituto Geografico Militare
IGS	International GNSS Service
ITRF	International Terrestrial Reference System
KS	Kolmogorov-Smirnov Test
MAC	Master Auxiliary Concepts
MRS	Multi Reference Station
MMS	Mobile Mapping System
NEA	Nearest
NMF	Niell Mapping Function
NRTK	Network-based Real Time Kinematic
PCV	Phase Center Variations
PTEC	Plasmaspheric Total Electron Content
PPP	Precise Point Positioning
RAIM FDE	Receiver Autonomous Integrity Monitoring Fault Detection and Exclusion
RDN	Rete Dinamica Nazionale
RTCM	Radio Technical Commission for Maritime Services
VRS	Virtual Reference Station
WGS84	World Geodetic System 1984

References

1. Leick, A. *GPS Satellite Surveying*; Wiley: Hoboken, NJ, USA, 1990.
2. Mader, G.L. Rapid Static and Kinematic Global Positioning System Solutions Using the Ambiguity Function Technique. *J. Geophys. Res.* **1992**, *97*, 3271–3283. [CrossRef]
3. Hofmann-Wellenhof, B.; Lichtenegger, H.; Collins, J. *Global Positioning System: Theory and Practice*, 4th ed.; Springer: Wien, Austria, 1997; ISBN 978-3-211-82839-7.
4. Xu, G. *GPS: Theory, Algorithms and Applications*, 2nd ed.; Springer: Berlin/Heidelberg, Germany, 2007; ISBN 978-3-642-09181-0.
5. Zhang, K.; Wu, F.; Wu, S.; Rizos, C.; Roberts, C.; Ge, L.; Yan, T.; Gordini, C.; Kealy, A.; Hale, M. Sparse or Dense: Challenges of Australian Network RTK. In Proceedings of the IGNSS, Surfers Paradise, Australia, 17–21 July 2006.
6. Wanninger, L. Virtual Reference Stations (VRS). *Gps Solut.* **2003**, *7*, 143–144. [CrossRef]
7. Fotopoulos, G.; Cannon, M.E. An Overview of Multi-Reference Station Methods for Cm-Level Positioning. *GPS Solut.* **2001**, *4*. [CrossRef]
8. Keenan, C.R.; Zebhauser, B.E.; Euler, H.-J.; Wübbena, G. Using the Information from Reference Station Networks: A Novel Approach Conforming to RTCM V2.3 and Future V3.0. In Proceedings of the 2002 IEEE Position Location and Navigation Symposium (IEEE Cat. No.02CH37284), Palm Springs, CA, USA, 15–18 April 2002; pp. 320–327.
9. Kim, J.; Song, J.; No, H.; Han, D.; Kim, D.; Park, B.; Kee, C. Accuracy Improvement of DGPS for Low-Cost Single-Frequency Receiver Using Modified Flächen Korrektur Parameter Correction. *ISPRS Int. J. Geo-Inf.* **2017**, *6*, 222. [CrossRef]
10. Garrido, M.S.; Giménez, E.; de Lacy, M.C.; Gil, A.J. Testing Precise Positioning Using RTK and NRTK Corrections Provided by MAC and VRS Approaches in SE Spain. *J. Spat. Sci.* **2011**, *56*, 169–184. [CrossRef]
11. Tusat, E. A Comparison of the Accuracy of VRS and Static GPS Measurement Results for Production of Topographic Map and Spatial Data: A Case Study on CORS-TR. *Teh. Vjesn.* **2018**, *25*, 158–163. [CrossRef]
12. Prochniewicz, D.; Szpunar, R.; Kozuchowska, J.; Szabo, V.; Staniszewska, D.; Walo, J. Performance of Network-Based GNSS Positioning Services in Poland: A Case Study. *J. Surv. Eng.* **2020**, *146*, 05020006. [CrossRef]
13. Zumberge, J.F.; Heflin, M.B.; Jefferson, D.C.; Watkins, M.M.; Webb, F.H. Precise Point Positioning for the Efficient and Robust Analysis of GPS Data from Large Networks. *J. Geophys. Res. B Solid Earth* **1997**, *102*, 5005–5017. [CrossRef]
14. Kouba, J.; Héroux, P. Precise Point Positioning Using IGS Orbit and Clock Products. *Gps Solut.* **2001**, *5*, 12–28. [CrossRef]
15. Ebner, R.; Featherstone, W.E. How Well Can Online GPS PPP Post-Processing Services Be Used to Establish Geodetic Survey Control Networks. *J. Appl. Geod.* **2008**, *2*, 149–157. [CrossRef]
16. Anquela, A.B.; Martín, A.; Berné, J.L.; Padín, J. Gps and Glonass Static and Kinematic PPP Results. *J. Surv. Eng.* **2013**, *139*, 47–58. [CrossRef]
17. Yigit, C.O.; Gikas, V.; Alcay, S.; Ceylan, A. Performance Evaluation of Short to Long Term GPS, GLONASS and GPS/GLONASS Postprocessed PPP. *Surv. Rev.* **2014**, *46*, 155–166. [CrossRef]

18. Abd Rabbou, M.; El-Rabbany, A. Performance Analysis of Precise Point Positioning Using Multi-Constellation GNSS: GPS, GLONASS, Galileo and BeiDou. *Surv. Rev.* **2017**, *49*, 39–50. [CrossRef]
19. Angrisano, A.; Dardanelli, G.; Innac, A.; Pisciotta, A.; Pipitone, C.; Gaglione, S. Performance Assessment of PPP Surveys with Open Source Software Using the GNSS GPS-GLONASS-Galileo Constellations. *Appl. Sci.* **2020**, *10*, 5420. [CrossRef]
20. Ocalan, T.; Erdogan, B.; Tunalioglu, N.; Durdag, U.M. Accuracy Investigation of PPP Method versus Relative Positioning Using Different Satellite Ephemerides Products near/under Forest Environment. *Earth Sci. Res. J.* **2017**, *20*, D1–D9. [CrossRef]
21. Guo, Q. Precision Comparison and Analysis of Four Online Free PPP Services in Static Positioning and Tropospheric Delay Estimation. *Gps Solut.* **2015**, *19*, 537–544. [CrossRef]
22. Astudillo, J.M.; Lau, L.; Tang, Y.-T.; Moore, T. Analysing the Zenith Tropospheric Delay Estimates in On-Line Precise Point Positioning (PPP) Services and PPP Software Packages. *Sensors* **2018**, *18*, 580. [CrossRef]
23. Geng, J.; Meng, X.; Teferle, F.N.; Dodson, A.H. Performance of Precise Point Positioning with Ambiguity Resolution for 1- to 4-Hour Observation Periods. *Surv. Rev.* **2010**, *42*, 155–165. [CrossRef]
24. El-Mowafy, A. Analysis of Web-Based GNSS Post-Processing Services for Static and Kinematic Positioning Using Short Data Spans. *Surv. Rev.* **2011**, *43*, 535–549. [CrossRef]
25. Gandolfi, S.; Tavasci, L.; Poluzzi, L. Study on GPS–PPP Precision for Short Observation Sessions. *GPS Solut.* **2017**, *21*, 887–896. [CrossRef]
26. Moreno, B.; Radicella, S.; de Lacy, M.C.; Herraiz, M.; Rodriguez-Caderot, G. On the Effects of the Ionospheric Disturbances on Precise Point Positioning at Equatorial Latitudes. *GPS Solut* **2011**, *15*, 381–390. [CrossRef]
27. Afraimovich, E.L.; Ishin, A.B.; Tinin, M.V.; Yasyukevich, Y.V.; Jin, S.G. First Evidence of Anisotropy of GPS Phase Slips Caused by the Mid-Latitude Field-Aligned Ionospheric Irregularities. *Adv. Space Res.* **2011**, *47*, 1674–1680. [CrossRef]
28. Demyanov, V.V.; Yasyukevich, Y.V.; Jin, S.; Sergeeva, M.A. The Second-Order Derivative of GPS Carrier Phase as a Promising Means for Ionospheric Scintillation Research. *Pure Appl. Geophys.* **2019**, *176*, 4555–4573. [CrossRef]
29. Jin, S.; Gao, C.; Yuan, L.; Guo, P.; Calabia, A.; Ruan, H.; Luo, P. Long-Term Variations of Plasmaspheric Total Electron Content from Topside GPS Observations on LEO Satellites. *Remote Sens.* **2021**, *13*, 545. [CrossRef]
30. TopNET live. Available online: https://www.topconpositioning.com/it/enterprise-services-and-subscriptions/gnss-correction-services/topnet-live (accessed on 31 March 2021).
31. Mageed, K.M.A. Comparison of GPS Commercial Software Packages to Processing Static Baselines up to 30 Km. *Arpn J. Eng. Appl. Sci.* **2015**, *10*, 10640–10650.
32. Andritsanos, V.D.; Arabatzi, O.; Gianniou, M.; Pagounis, V.; Tziavos, I.N.; Vergos, G.S.; Zacharis, E. Comparison of Various GPS Processing Solutions toward an Efficient Validation of the Hellenic Vertical Network: The Elevation Project. *J. Surv. Eng.* **2016**, *142*. [CrossRef]
33. Dardanelli, G.; Lo Brutto, M.; Pipitone, C. GNSS Cors Network of the University of Palermo: Design and First Analysis of Data. *Geogr. Tech.* **2020**, *15*, 43–69. [CrossRef]
34. Baroni, L.; Cauli, F.; Farolfi, G.; Maseroli, R. Final Results of the Italian «Rete Dinamica Nazionale» (RDN) of Istituto Geografico Militare Italiano (IGMI) and Its Alignment to ETRF2000. *Boll. Di Geod. E Sci. Affin.* **2009**, *68*, 287–317.
35. Kenyeres, A.; Bellet, J.G.; Bruyninx, C.; Caporali, A.; de Doncker, F.; Droscak, B.; Duret, A.; Franke, P.; Georgiev, I.; Bingley, R.; et al. Regional Integration of Long-Term National Dense GNSS Network Solutions. *GPS Solut.* **2019**, *23*. [CrossRef]
36. Ammoscato, A.; Corsale, R.; Dardanelli, G.; Scianna, A.; Villa, B. GPS-GIS Integrated System for Electromagnetic Pollution. *Int. Arch. Photogramm.* **2008**, *37*, 491–498.
37. Dardanelli, G.; Carella, M. Integrated surveyng with mobile mapping system, egnos, ntrk and laser technologies in the Park "Ninni Cassara" in Palermo. *ISPRS J. Photogramm. Remote Sens.* **2013**, *2*, 95–100. [CrossRef]
38. Dardanelli, G.; Paliaga, S.; Allegra, M.; Carella, M.; Giammarresi, V. Geomatic Applications Tourban Park in Palermo. *Geogr. Tech.* **2015**, *10*, 28–43.
39. Dardanelli, G.; La Loggia, G.; Perfetti, N.; Capodici, F.; Puccio, L.; Maltese, A. Monitoring Displacements of an Earthen Dam Using GNSS and Remote Sensing. In *Remote Sensing for Agriculture, Ecosystems, and Hydrology XVI*; International Society for Optics and Photonics: Bellingham, WA, USA, 2014; Volume 9239.
40. Pipitone, C.; Maltese, A.; Dardanelli, G.; Brutto, M.L.; Loggia, G.L. Monitoring Water Surface and Level of a Reservoir Using Different Remote Sensing Approaches and Comparison with Dam Displacements Evaluated via GNSS. *Remote Sens.* **2018**, *10*, 71. [CrossRef]
41. Stocchi, P.; Antonioli, F.; Montagna, P.; Pepe, F.; Lo Presti, V.; Caruso, A.; Corradino, M.; Dardanelli, G.; Renda, P.; Frank, N.; et al. A Stalactite Record of Four Relative Sea-Level Highstands during the Middle Pleistocene Transition. *Quat. Sci. Rev.* **2017**, *173*, 92–100. [CrossRef]
42. Petropoulos, G.P.; Maltese, A.; Carlson, T.N.; Provenzano, G.; Pavlides, A.; Ciraolo, G.; Hristopulos, D.; Capodici, F.; Chalkias, C.; Dardanelli, G.; et al. Exploring the Use of Unmanned Aerial Vehicles (UAVs) with the Simplified 'Triangle' Technique for Soil Water Content and Evaporative Fraction Retrievals in a Mediterranean Setting. *Int. J. Remote Sens.* **2020**, *42*, 1–20. [CrossRef]
43. Catania, P.; Comparetti, A.; Febo, P.; Morello, G.; Orlando, S.; Roma, E.; Vallone, M. Positioning Accuracy Comparison of GNSS Receivers Used for Mapping and Guidance of Agricultural Machines. *Agronomy* **2020**, *10*, 924. [CrossRef]

44. Barreca, G.; Bruno, V.; Dardanelli, G.; Guglielmino, F.; Lo Brutto, M.; Mattia, M.; Pipitone, C.; Rossi, M. An Integrated Geodetic and InSAR Technique for the Monitoring and Detection of Active Faulting in Southwestern Sicily. *Ann. Geophys.* **2020**, *63*. [CrossRef]
45. Pipitone, C.; Dardanelli, G.; Lo Brutto, M.; Bruno, V.; Mattia, M.; Guglielmino, F.; Rossi, M.; Barreca, G. Use of CORS Time Series for Geodynamics Applications in Western Sicily (Italy). In *Proceedings of the R3 in Geomatics: Research, Results and Review, October 2020, Naples Italy*; Parente, C., Troisi, S., Vettore, A., Eds.; Springer International Publishing: Cham, Switzerland, 2020; pp. 61–76.
46. Surace, L. The New National Geodetic Network IGM95: Analysis of the Results. *Boll. Di Geod. E Sci. Affin.* **1997**, *56*, 357–378.
47. Dawidowicz, K.; Krzan, G.; Świątek, K. Relative Gps/Glonass Coordinates Determination in Urban Areas–Accuracy Anaysis. In Proceedings of the15th International Multidisciplinary Scientific GeoConference SGEM 2015, Albena, Bulgaria, 18–24 June 2015; Volume 2, pp. 423–430.
48. Uradziński, M.; Bakuła, M. Assessment of Static Positioning Accuracy Using Low-Cost Smartphone GPS Devices for Geodetic Survey Points' Determination and Monitoring. *Appl. Sci.* **2020**, *10*, 5308. [CrossRef]
49. GOAD, C.C. A Modified Hopfield Tropospheric Refraction Correction Model. In Proceedings of the Fall Annual Meeting American Geophysical Union, San Francisco, CA, USA, 12–17 December 1974.
50. Wübbena, G.; Schmitz, M.; Bagge, A. PPP-RTK: Precise Point Positioning Using State-Space Representation in RTK Networks. In Proceedings of the 18th International Technical Meeting of the Satellite Division of The Institute of Navigation (ION-GNSS 2005), Long Beach, CA, USA, 13–16 September 2005; Volume 2005, pp. 2584–2594.
51. Hopfield, H.S. Two-Quartic Tropospheric Refractivity Profile for Correcting Satellite Data. *J. Geophys. Res.* **1969**, *74*, 4487–4499. [CrossRef]
52. Benciolini, B.; Biagi, L.; Crespi, M.; Manzino, A.; Roggero, M. Linee Guida per La Realizzazione Di Reti Di Stazioni Permanenti Di Servizio. *Boll. Di Geod. E Sci. Affin.* **2006**, *65*, 90–121.
53. Johnson, P.M.; Tjahjono, D. Assessing Software Review Meetings: A Controlled Experimental Study Using CSRS. In Proceedings of the 19th International Conference on Software Engineering, Boston, MA, USA, 17 May 1997; Association for Computing Machinery: New York, NY, USA, 1997; pp. 118–127.
54. Tétreault, P.; Kouba, J.; Héroux, P.; Legree, P. CSRS-PPP: An Internet Service for GPS User Access to the Canadian Spatial Reference Frame. *Geomatica* **2005**, *59*, 17–28.
55. Dawidowicz, K.; Krzan, G. Coordinate Estimation Accuracy of Static Precise Point Positioning Using On-Line PPP Service, a Case Study. *Acta Geod. Et Geophys.* **2014**, *49*, 37–55. [CrossRef]
56. Takasu, T.; Kubo, N.; Yasuda, A. Development, Evaluation and Application of RTKLIB: A Program Library for RTK-GPS. In Proceedings of the GPS/GNSS Symposium, Tokyo, Japan, 20–22 November 2007; pp. 213–218.
57. Wu, Q.; Sun, M.; Zhou, C.; Zhang, P. Precise Point Positioning Using Dual-Frequency GNSS Observations on Smartphone. *Sensors* **2019**, *19*, 2189. [CrossRef]
58. Liu, T.; Li, B. Single-Frequency BDS/GPS RTK with Low-Cost U-Blox Receivers. In Proceedings of the 2017 Forum on Cooperative Positioning and Service (CPGPS 2017), Harbin, China, 19–21 May 2017; pp. 232–238.
59. Cina, A.; Dabove, P.; Manzino, A.M.; Piras, M. Augmented Positioning with CORSs Network Services Using GNSS Mass-Market Receivers. In Proceedings of the 2014 IEEE/ION Position, Location and Navigation Symposium-PLANS 2014, Monterey, CA, USA, 5–8 May 2014; pp. 359–366.
60. Mahato, S.; Santra, A.; Dan, S.; Rakshit, P.; Banerjee, P.; Bose, A. Preliminary Results on the Performance of Cost-Effective GNSS Receivers for RTK. In Proceedings of the 2019 URSI Asia-Pacific Radio Science Conference (AP-RASC), New Delhi, India, 9–15 March 2019.
61. Stephenson, S.; Meng, X.; Moore, T.; Baxendale, A.; Edwards, T. A Fairy Tale Approach to Cooperative Vehicle Positioning. In Proceedings of the 2014 International Technical Meeting of The Institute of Navigation, San Diego, CA, USA, 27–29 January 2014; pp. 431–440.
62. Cefalo, R.; Novelli, A.; Sluga, T.; Snider, P.; Tarantino, E.; Tommasi, A. Static and Kinematic Surveys Using GNSS Multi-Constellation Receivers and GPS, GLONASS and Galileo Data. In *Proceedings of the Computational Science and Its Applications–ICCSA, Melbourne, Australia, 2–5 July 2018*; Lecture Notes in Computer Science; Springer: Cham, Switzerland, 2018; pp. 349–363. [CrossRef]
63. GLONASS Ambiguity Resolution: Identical Receivers. Available online: https://rtklibexplorer.wordpress.com/2016/04/30/glonass-ambiguity-resolution-identical-receivers/ (accessed on 31 March 2021).
64. Saastamoinen, J. Atmospheric Correction for the Troposphere and Stratosphere in Radio Ranging Satellites. In *The Use of Artificial Satellites for Geodesy*; American Geophysical Union (AGU): Washington, WA, USA, 1972; pp. 247–251. ISBN 978-1-118-66364-6.
65. Niell, A.E. Global Mapping Functions for the Atmosphere Delay at Radio Wavelengths. *J. Geophys. Res. Solid Earth* **1996**, *101*, 3227–3246. [CrossRef]
66. Herring, T.A. Modeling Atmospheric Delays in the Analysis of Space Geodetic Data. In *Procedures of Refraction of Transatmospheric Simals in Geodesy*; De Munck, J.C., Spoelstra, T.A., Eds.; Netherlands Geodetic Commission Publications on Geodesy: Delft, The Netherlands, 1992; Volume 36.
67. Specht, M. Statistical Distribution Analysis of Navigation Positioning System Errors—Issue of the Empirical Sample Size. *Sensors* **2020**, *20*, 7144. [CrossRef]

68. Mertikas, S.; Wells, D.; Leenhouts, P. Treatment of Navigational Accuracies: Proposals for the Future. *Navigation* **1985**, *32*, 68–84. [CrossRef]
69. Miller, J. Short Report: Reaction Time Analysis with Outlier Exclusion: Bias Varies with Sample Size. *Q. J. Exp. Psychol. Sect. A* **1991**, *43*, 907–912. [CrossRef]
70. Feng, Y. Regression and Hypothesis Tests for Multivariate GNSS State Time Series. *JGPS* **2012**, *11*, 33–45. [CrossRef]
71. Anderson, T.W.; Darling, D.A. A Test of Goodness of Fit. *J. Am. Stat. Assoc.* **1954**, *49*, 765–769. [CrossRef]
72. Cramér, H. On the composition of elementary errors: First paper: Mathematical deductions. *Scand. Actuar. J.* **1928**, *1928*, 13–74. [CrossRef]
73. Smirnov, N. Table for Estimating the Goodness of Fit of Empirical Distributions. *Ann. Math. Stat.* **1948**, *19*, 279–281. [CrossRef]
74. Lilliefors, H.W. On the Kolmogorov-Smirnov Test for Normality with Mean and Variance Unknown. *J. Am. Stat. Assoc.* **1967**, *62*, 399–402. [CrossRef]
75. Karson, M. Handbook of Methods of Applied Statistics. Volume I: Techniques of Computation Descriptive Methods, and Statistical Inference. Volume II: Planning of Surveys and Experiments. I. M.; Chakravarti, R.G. Laha, and J.; Roy, New York, John Wiley; 1967, $9.00. *J. Am. Stat. Assoc.* **1968**, *63*, 1047–1049. [CrossRef]
76. Stephens, M.A. EDF Statistics for Goodness of Fit and Some Comparisons. *J. Am. Stat. Assoc.* **1974**, *69*, 730–737. [CrossRef]
77. Joanes, D.N.; Gill, C.A. Comparing Measures of Sample Skewness and Kurtosis. *J. R. Stat. Soc. Series D (Stat.)* **1998**, *47*, 183–189. [CrossRef]
78. Evans, J.D. *Straightforward Statistics for the Behavioral Sciences*; Brooks/Cole Pub. Co.: Pacific Grove, CA, USA, 1996; ISBN 978-0-534-23100-2.
79. Gut, A. An Intermediate Course in Probability. In *Springer Texts in Statistics*, 2nd ed.; Springer: New York, NY, USA, 2009; ISBN 978-1-4419-0161-3.
80. The Precise Point Positioning Software Centre—Online PPP Services. Available online: http://www2.unb.ca/gge/Resources/PPP/OnlinePPPs.html (accessed on 31 March 2021).
81. MagicGNSS. Available online: https://magicgnss.gmv.com/ (accessed on 31 March 2021).
82. Ibanez, D.; Rovira-Garcia, A.; Sanz, J.; Juan, J.M.; Gonzalez-Casado, G.; Jimenez-Banos, D.; Lopez-Echazarreta, C.; Lapin, I. The GNSS Laboratory Tool Suite (GLAB) Updates: SBAS, DGNSS and Global Monitoring System. In Proceedings of the 2018 9th ESA Workshop on Satellite NavigationTechnologies and European Workshop on GNSS Signals and Signal Processing (NAVITEC), Noordwijk, The Netherlands, 5–7 December 2018; pp. 1–11.

remote sensing

MDPI

Article

A New Method to Determine the Optimal Thin Layer Ionospheric Height and Its Application in the Polar Regions

Hu Jiang [1,2,3], Shuanggen Jin [1], Manuel Hernández-Pajares [4], Hui Xi [5,6], Jiachun An [2,*], Zemin Wang [2], Xueyong Xu [3] and Houxuan Yan [3]

[1] School of Remote Sensing and Geomatics Engineering, Nanjing University of Information Science and Technology, Nanjing 210044, China; jianghu@whu.edu.cn (H.J.); sgjin@nuist.edu.cn (S.J.)
[2] Chinese Antarctic Center of Surveying and Mapping, Wuhan University, Wuhan 430079, China; zmwang@whu.edu.cn
[3] North Information Control Research Academy Group Co., Ltd., Nanjing 211153, China; xxyyeah@mail.ustc.edu.cn (X.X.); yhx412@126.com (H.Y.)
[4] IonSAT, Universitat Politècnica de Catalunya (UPC-IonSAT, SSTRG-IEEC), 08034 Barcelona, Spain; manuel.hernandez@upc.edu
[5] College of Geography and Environment, Shandong Normal University, Jinan 250358, China; xihui@asch.whigg.ac.cn
[6] State Key Laboratory of Geodesy and Earth's Dynamics, Innovation Academy for Precision Measurement Science and Technology, CAS, Wuhan 430077, China
* Correspondence: jcan@whu.edu.cn

Abstract: The conversion between the line-of-sight slant total electron content (STEC) and the vertical total electron content (VTEC) depends on the mapping function (MF) under the widely used thin layer ionospheric model. The thin layer ionospheric height (TLIH) is an essential parameter of the MF, which affects the accuracy of the conversion between the STEC and VTEC. Due to the influence of temporal and spatial variations of the ionosphere, the optimal TLIH is not constant over the globe, particularly in the polar regions. In this paper, a new method for determining the optimal TLIH is proposed, which compares the mapping function values (MFVs) from the MF at different given TLIHs with the "truth" mapping values from the UQRG global ionospheric maps (GIMs) and the differential TEC (dSTEC) method, namely the dSTEC- and GIM-based thin layer ionospheric height (dG-TLIH) techniques. The optimal TLIH is determined using the dG-TLIH method based on GNSS data over the Antarctic and Arctic. Furthermore, we analyze the relationship between the optimal TLIH derived from the dG-TLIH method and the height of maximum density of the F2 layer (hmF2) based on COSMIC data in the polar regions. According to the dG-TLIH method, the optimal TLIH is mainly distributed between 370 and 500 km over the Arctic and between 400 and 500 km over the Antarctic in a solar cycle. In the Arctic, the correlation coefficient between the hmF2 and optimal TLIH is 0.7, and the deviation between them is 162 km. Meanwhile, in the Antarctic, the correlation coefficient is 0.60, with a phase lag of ~3 months, with the hmF2 leading the optimal TLIH, and the deviation between them is 177 km.

Keywords: thin layer ionospheric height (TLIH); mapping function; dG-TLIH technique; global navigation satellite system (GNSS); height of maximum density of the F2 layer (hmF2)

Citation: Jiang, H.; Jin, S.; Hernández-Pajares, M.; Xi, H.; An, J.; Wang, Z.; Xu, X.; Yan, H. A New Method to Determine the Optimal Thin Layer Ionospheric Height and Its Application in the Polar Regions. *Remote Sens.* **2021**, *13*, 2458. https://doi.org/10.3390/rs13132458

Academic Editor: Stefania Bonafoni

Received: 10 May 2021
Accepted: 21 June 2021
Published: 23 June 2021

1. Introduction

The ionosphere is an important part of the solar-terrestrial space environment, and it is closely related to human production and life. Due to the influence of free electrons in the ionosphere, global navigation satellite system (GNSS) signals are affected by the reflection, refraction, and delay of the ionosphere [1–3]. In order to improve the correction accuracy of ionospheric error for single-frequency users, it is necessary to obtain the temporal and spatial distribution of the ionospheric total electron content (TEC) [4].

Most of the ionospheric correction information broadcasted by GNSS and their augmentation systems (such as WAAS and EGNOS) provides users with the vertical TEC (VTEC) based on two-dimensional ionospheric models [5–7]. GNSS users need to convert the VTEC to slant TEC (STEC) on the satellite-to-receiver line-of-sight (LOS) path, under the thin layer ionospheric model (TLIM) [7]. The conversion between VTEC and STEC is performed through a mapping function (MF) related to satellite elevation and thin layer ionospheric height (TLIH).

In order to realize the conversion between STEC and VTEC, the ionosphere is assumed to be an infinitely thin fixed-height layer. The intersection of the straight line from the satellite to the receiver and the thin layer is called the ionosphere piercing point (IPP) [7]. The STEC at the IPP represents the ionospheric TEC in the LOS path from the satellite to the receiver. Two-dimensional ionospheric models can be used to calculate the VTEC at the IPP. Then, the thin layer ionospheric model (TLIM) assumes a sample vertical gradient of ionospheric electron density, typically for ground-based receivers [8–10]. Nava et al. [11] detected the influence of electron density gradients for the thin layer model in the American sector using the coinciding pierce point (CPP) technique. In the calm period of the ionosphere, the TLIM can successfully simulate VTEC in the middle latitudes. However, in low-latitude regions or in the case of ionospheric storms, the TLIM can produce ionospheric mapping errors (IMEs) of up to dozens of TEC units (TECU) [12–14]. In order to reduce the impact of IMEs, many scholars have detected the optimal TLIH under different temporal and spatial conditions [11,15–17].

The TLIH is an important parameter of the mapping function, and it directly affects the conversion accuracy between STEC and VTEC [11]. It is usually selected at a ground height of between 350 km and 450 km [4,18]. Klobuchar [4] suggested that the global positioning system (GPS) broadcast ionospheric model uses a TLIH of 350 km. Wide-area augmentation systems also establish ionospheric TEC grid models with a TLIH of 350 km [19]. The global ionosphere map (GIM) products provided by the International GNSS Service (IGS) Ionospheric Analysis Center use a TLIH of 450 km [18,20,21]. However, in comparison with the Chapman profile mapping function, the mapping function value based on a TLIH of 428.8 km is the closest to the true value on the global scale [7]. Li et al. [17] determined the optimized TLIH using combined IGS global ionospheric maps over China. Birch et al. [15] determined the TLIH by comparing the TEC from a pair of satellites observed simultaneously along slant and vertical paths over a ground station. However, due to the limitations of satellite orbit inclination and the accuracy of the GIM model [22], the aforementioned methods are not applicable in the polar regions. In addition, the height of maximum density of the F2 layer (hmF2) has also been used to model the ionospheric TEC, and it is superior to the constant TLIH [23,24].

The polar regions, namely the Arctic and the Antarctic, are the locations of the geographical and geomagnetic poles. The magnetic field lines over the polar caps penetrate the Earth or extend outward to connect with the interplanetary magnetic field, and the high-energy particles are mapped into the high-latitude ionosphere along magnetic field lines [25]. The polar ionosphere is controlled by the solar wind and the interplanetary magnetic field; meanwhile, it is coupled with the magnetosphere and thermosphere [26,27]. Many factors cause the complex characteristics of the ionosphere in the polar regions [28]. Moreover, the large-scale convection of the ionosphere in the polar regions also affects the ionospheric electron density [29]. The temporal and spatial variations of the ionosphere in the polar regions is obviously different from those at middle and low latitudes. However, there are still some problems that have not been systematically investigated over the Antarctic and Arctic, for example, whether the most widely used TLIH of 350–450 km is valid, and how to choose the range of optimal TLIH values for TEC conversion.

This paper presents a new method for detecting the optimal TLIH based on the dSTEC (differential STEC) measurements and UQRG (UPC quarter-of-an-hour rapid GIM) GIMs [6,30]. Meanwhile, we analyzed the reference range of the optimal TLIH values during almost one and a half solar cycles from 2003 to 2018 over the Antarctic and Arctic

to mitigate ionospheric delay errors, using ionospheric modeling under the TLIM based on the new method, and the relationships between the optimal TLIH and the hmF2 were analyzed. To provide a detailed analysis of the variations of the optimal TLIH during a solar cycle, Constellation Observing System for Meteorology, ionosphere, climate (COSMIC), and GNSS data are used in this paper.

2. Methods and Data

2.1. The CPP Method

The conversion between VTEC and STEC is given by a mapping function related to satellite elevation and the TLIH, as shown in Equation (1).

$$mf(E) = \frac{STEC}{VTEC} \cong \frac{1}{\cos z} = \frac{1}{\sqrt{1 - (R\cos(E)/(R+H))^2}} \quad (1)$$

where $mf(\bullet)$ denotes the mapping function, R is the geocentric distance of the receiver antenna, H is the thin layer ionospheric height, z is the satellite zenith distances at the IPP, and E is the satellite elevation at the observation point receiver antenna phase center (see Figure 1).

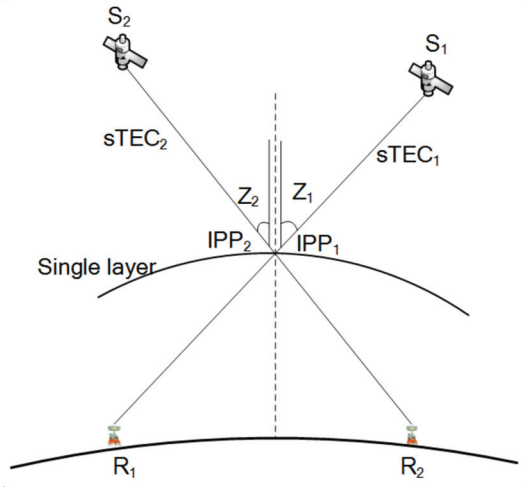

Figure 1. Geometry for estimating the ionospheric mapping errors (IMEs) [16].

The CPP method determines the optimal TLIH by analyzing the IMEs based on all pairs of CPP for a given epoch [11]. As illustrated in Figure 1, for practical purposes, if two pierce points, IPP_1 and IPP_2, satisfy Equation (2), they are considered to be a "coinciding" pierce point:

$$\begin{cases} |\varphi_1 - \varphi_2| < 0.2^\circ \\ |\lambda_1/\cos(\varphi_1) - \lambda_2/\cos(\varphi_2)| < 0.2^\circ \end{cases} \quad (2)$$

where (φ_1, λ_1) and (φ_2, λ_2) are the geomagnetic latitude and longitude of ionospheric IPP_1 and IPP_2, and the unit is degrees.

According to the thin layer approximation for the ionosphere, the converted VTEC values at IPP_1 and IPP_2 should be equivalent. However, due to the strong gradients of ionospheric electron density, conversion between the STEC and VTEC using the mapping function could result in TEC conversion errors related to the TLIH. The difference between the two converted VTEC values at IPP_1 and IPP_2 is defined as the IMEs, as shown in Equation (3). The optimalTLIH is defined as the one that minimizes the slant-to-vertical

TEC conversion errors. In order to obtain enough CPP ionospheric TEC, dense GNSS monitoring stations are required to use this method.

$$\Delta VTEC = |VTEC_1 - VTEC_2| = \left| \frac{STEC_1}{mf(Z_1)} - \frac{STEC_2}{mf(Z_2)} \right| \quad (3)$$

The STEC is derived from the GPS dual-frequency pseudo-range and carrier–phase measurements based on carrier-to-code leveling methods [7]. In addition, the differential code biases (DCB) products provided by the Center for Orbit Determination in Europe [31] were adopted to eliminate the GPS satellite DCBs. The receiver DCBs are estimated in conjunction with ionospheric model parameters using the generalized triangular series function [32].

2.2. The dG-TLIH Method

To overcome the limitations of the existing methods used in the polar regions, a new approach, based on the UQRG GIMs and dSTEC method [6], is proposed for optimal TLIH determination.

The GNSS dual-frequency carrier–phase observation equation can be expressed as follows:

$$\phi^s_{r,k}(t) = \rho^s_r(t) + c(\delta t_r(t) - \delta t^s(t)) - \kappa_k \delta I^s_{r,1}(t) + \delta T^s_r(t) + c(\gamma^s_k + \gamma_{r,k}) + \vartheta_k(t) + \lambda_k N^s_{r,k}(t) + \varepsilon_\phi \quad (4)$$

where s, r, k denote the satellite PRN, receiver, and frequency, respectively; $\phi^s_{r,k}$ represents the carrier–phase measurement at frequency f_k; ρ^s_r is the geometric range from satellite s to receiver r; c is the speed of light in a vacuum; δt_r and δt^s are the receiver and satellite clock errors; $\kappa_k = \frac{f_1^2}{f_k^2}$ is a constant factor; $\delta I^s_{r,1} = \frac{40.3 STEC^s_r}{f_1^2}$ denotes the ionospheric delays at frequency f_1; δT^s_r denotes the tropospheric delays; γ^s_k and $\gamma_{r,k}$ are the satellite and receiver–phase instrumental delays; ϑ_k is the carrier–phase windup and is considered corrected; λ_k denotes the wavelength at frequency f_k; $N^s_{r,k}$ is the carrier–phase ambiguity; and ε_ϕ is the noise and multipath effect of carrier–phase measurements.

According to Equation (4), the geometry-free combination of the carrier phase can be calculated as follows:

$$\begin{cases} \phi^s_{r,GF}(t) = \phi^s_{r,1}(t) - \phi^s_{r,2}(t) = \upsilon \cdot STEC^s_r(t) + \widetilde{N}^s_r + \varepsilon_{\phi_{GF}} \\ \widetilde{N}^s_r = (\lambda_1 \widetilde{N}^s_{r,1} - \lambda_2 \widetilde{N}^s_{r,2}) + c(\gamma_{r,1} - \gamma_{r,2}) + c(\gamma^s_1 - \gamma^s_2) \end{cases} \quad (5)$$

where $\upsilon = 40.3 \times 10^{16} \times (f_2^{-2} - f_1^{-2})$ is the conversion factor between the ionospheric delay ($\delta I^s_{r,1}$) and the ionospheric TEC ($STEC^s_r$). Along a phase-continuous satellite-receiver arc, as shown in Figure 2, there is an observation time ($t_{E_{\max}}$) with the maximum elevation. In theory, an observation value with higher elevation has lower errors, due to the much lower relevance of the mapping function. Based on Equation (5), in a continuous satellite–receiver arc of measurements, the difference in the given $\phi^s_{r,GF}(t)$ and the $\phi^s_{r,GF}(t_{E_{\max}})$ can be expressed as:

$$\Delta S(t) = \phi^s_{r,GF}(t) - \phi^s_{r,GF}(t_{E_{\max}}) = \upsilon(STEC^s_r(t) - STEC^s_r(t_{E_{\max}})) \quad (6)$$

where the definitions of the variables in Equation (6) are the same as in Equation (5).

According to Equation (6), the amount of STEC change between the given time t and the time $t_{E_{\max}}$ can be expressed as:

$$dSTEC(t) = \frac{1}{\upsilon}\Delta S(t) = STEC(t) - STEC(t_{E_{\max}}) \quad (7)$$

where the definitions of the variables in Equation (7) are the same as that in Equation (6). Since the dSTEC is calculated from carrier–phase observations, its accuracy is less than 0.1 TECU.

According to Equation (7), the STEC at the given time t can be expressed as Equation (8) for each given pair of satellites and receivers, and for a common arc of measurements.

$$STEC(t) = STEC(t_{E_{max}}) + dSTEC(t) \tag{8}$$

Indeed, the "true" mapping value at the given time t can be expressed as:

$$MF_T(t) = \frac{STEC(t)}{VTEC(t)} = \frac{VTEC(t_{E_{max}}) \cdot mf(E_{max}) + dSTEC(t)}{VTEC(t)} \tag{9}$$

where $VTEC(t_{E_{max}})$ and $VTEC(t)$ are the vertical TEC at the maximum elevation and time t, respectively, calculated using UQRG–GIM; and $mf(E_{max})$ is the mapping function value, calculated by Equation (1) at the maximum elevation. As can be seen from the equation, the "true" mapping value is independent of the TLIH.

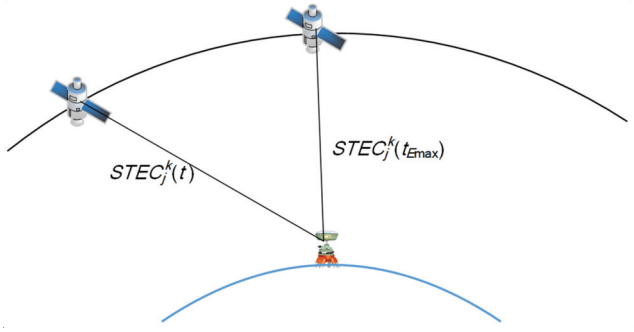

Figure 2. Schematic diagram of dSTEC method.

The mapping function error indicator (σ_H) at a given TLIH can be expressed as

$$\sigma_H = \sqrt{\frac{1}{n}\sum_{i=1}^{n}\left(MF_T(t_i) - mf_H(E_{t_i})\right)^2} \tag{10}$$

where n is the total number of samples; $MF_T(t_i)$ denotes the mapping value calculated by Equation (9) at time t_i; E_{t_i} is the satellite elevation; and $mf_H(\cdot)$ denotes the mapping function with the TLIH of H.

According to Equation (10), the indicator σ_H at different TLIHs can be calculated, and then the TLIH corresponding to the minimum σ_H can be selected as the optimal TLIH. According to previous studies, it has been found that when the elevation angle is increased to approximately 40°, the mapping errors caused by ionospheric gradients can be ignored. Then, the STEC calculated by Equation (8) is not affected by the ionospheric gradient. Therefore, for the present study, only a continuous satellite–receiver arc with a time length of more than 2 h and a maximum elevation angle greater than 50° were used.

In this paper, only the STEC at the maximum elevation angle in the continuous arc segment is calculated using the GIM model and the mapping function, to reduce the influence of the ionospheric gradients. Therefore, the reliability of this method depends on the accuracy of the GIM model used. In this study, the VTEC value was calculated by the UQRG–GIM model, which is provided by UPC, one of the IGS Ionosphere Working Group members. According to the comparison with the VTEC altimeter and globally distributed dSTEC GPS data, the RMS errors of the UQRG–GIM model are 2.0 TECU and 0.5 TECU, respectively [6]. In comparison with other GIM models, UQRG is the most accurate, and it has been used to detect ionospheric events in the polar regions [30].

2.3. Observation Data

In order to investigate the variation of optimal TLIH at high latitudes, datasets under different spatio-temporal conditions were used, including GPS data for the 2003–2018 period and COSMIC data for the 2007–2016 period. The time series of solar activity index F10.7 is shown in Figure 3.

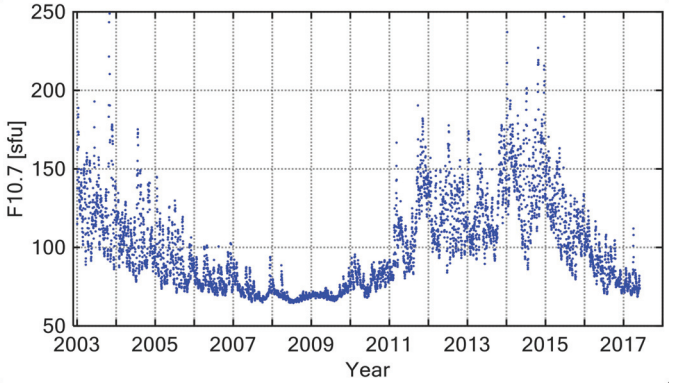

Figure 3. Time series of the solar activity index F10.7 from 2003 to 2017.

GPS observations provided by the IGS and the Polar Earth Observing Network (POLENET) were used in this study. Figure 4 shows the geographical locations of the GPS ground stations over the Arctic and Antarctic, where the blue points are used for mapping ionospheric total electron content (TEC), the red circles are used for detecting the optimal thin layer ionospheric height (TLIH), and the green points are used for evaluating the ionospheric TEC model. For the present study, the sampling rate of the GPS measurements was set to 30 s. The maximum elevation of the GPS measurements was greater than 60° at latitude 75°. Before 2010, only a few stations with non-uniform distribution were available in the Antarctic [28]. In addition, in order to show the relationship between the IMEs and the TLIH, global GPS ground observation data from the IGS (www.igs.org/station-resources/#site-guidelines, accessed date: 1 December 2019) were used.

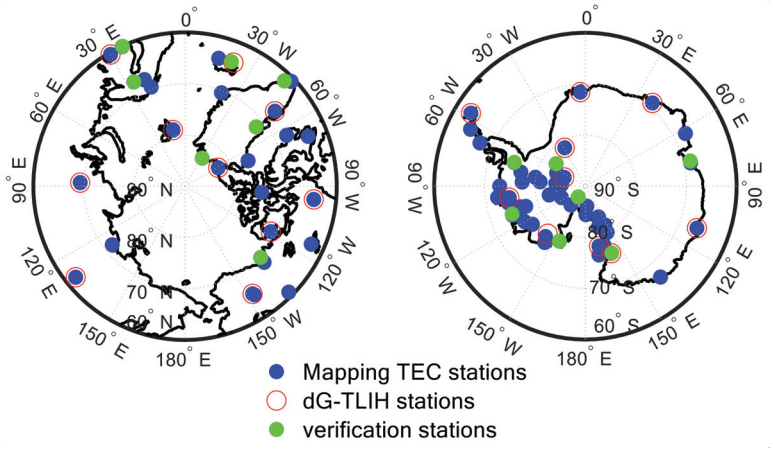

Figure 4. Locations of GPS ground stations over the Arctic (left) and Antarctic (right), with the blue points mapping ionospheric total electron content (TEC), the green points detecting the optimal thin layer ionospheric height (TLIH), and the red circles evaluating the ionospheric TEC model.

To better understand how the hmF2 varies depending on solar activity and season in the polar regions, COSMIC data for the years 2007–2016, which were obtained from the COSMIC Data Analysis and Archive Center (CDAAC, http://cosmic-io.cosmic.ucar.edu/cdaac/index.html, accessed date: 1 January 2018), are also considered.

3. Results and Discussion

3.1. Optimal TLIH Determination Using CPP Method

The CPP technique requires a dense GNSS monitoring network; otherwise, it is difficult to obtain GPS-derived TEC observations for the "coinciding" pierce points for a given epoch. To investigate the effects of the electron density gradients on the global ionosphere, GPS-derived STEC data for DOY 203, 300, and 355 in the year 2014 were used. The STEC data were obtained using a GPS satellite tracked globally by 460 IGS ground stations. The experiment was repeated for three different levels of solar activity: low (F10.7 = 92.6 sfu), medium (F10.7 = 187.8 sfu), and high (F10.7 = 205.8 sfu), corresponding to DOY 203, 300, and 355 in the year 2014, respectively. For the present study, the sampling interval of the data was set to 30 s, and only the STEC data corresponding to the line-of-sight of the receiver to the satellite with elevation angles between 15° and 40° at the observation points were used.

Values were computed for all epochs available during the analysis period. Examples of IMEs as a function of local time for different thin layer heights are illustrated in Figure 5. It can be seen that the solar activity had a significant impact on the IMEs: during low solar activity (DOY 203), most of the IMEs were between 0 and 8.0 TECU and there was no significant fluctuation; during medium solar activity (DOY 300), most of the IMEs were between 0 and 10 TECU, but the IMEs in the daytime were obviously greater than those in the nighttime, and some error values were higher than 20 TECU; during high solar activity (DOY 355), the IMEs increased significantly and large fluctuations appeared. In particular, during local times 00:00–04:00 and 13:00–16:00, the maximum IME reached up to 80 TECU, which was larger than at other times. Therefore, ignoring the ionospheric gradient when using TLIM will introduce significant errors caused by the conversion between STEC and VTEC. In addition, the standard deviations of the IMEs were smallest at the thin layer height of 400 km, during the selected days.

According to previous studies [15,16,33], it has been found that IMEs are related to latitude and TLIH. In the Northern Hemisphere, IMEs at high latitudes are greater than those at middle latitudes [16]. Although the TEC at high latitudes is lower than that at middle latitudes, due to the complex ionospheric variations in the polar regions, both the ionospheric gradient and the IMEs are larger than those at middle latitudes. In order to improve the conversion accuracy between the STEC and VTEC, it is necessary to deeply study the variation of the thin layer ionospheric height in the polar regions. All IGS tracking stations north of 55°N were used in 30 s intervals. The mapping errors at the thin layer ionospheric height ranging from 300 to 700 km in steps of 50 km were calculated, and the thin layer height corresponding to the minimum error was selected as the optimal TLIH. Figure 6 presents the time series and histograms of the optimal TLIH for the Arctic region from 2003 to 2014, based on the CPP method. The optimal TLIH increased with the increase in solar activity. As illustrated in Figure 6, the highest proportion of the optimal TLIH was 400 km. The TLIH had a relatively low resolution of 50 km, mainly because this method was too computationally intensive and time-consuming. Meanwhile, the low resolution could introduce some errors, which could decrease the accuracy and reliability of the results.

Although the use of the CPP method to determine the TLIH has been investigated by many researchers in recent years, there are still some limitations with this method when it is used in the polar regions. First, this method depends on the dense GNSS monitoring network, but the available stations are few in the polar regions and their distributions are uneven. Therefore, it is difficult to get enough evenly distributed GNSS-derived TEC observations for the "coinciding" pierce points for a given epoch. Second, ionosphere

activity is intense, as ionospheric scintillation and patches often occur in the polar regions, both of which have greater effects on the statistical results of the CPP method.

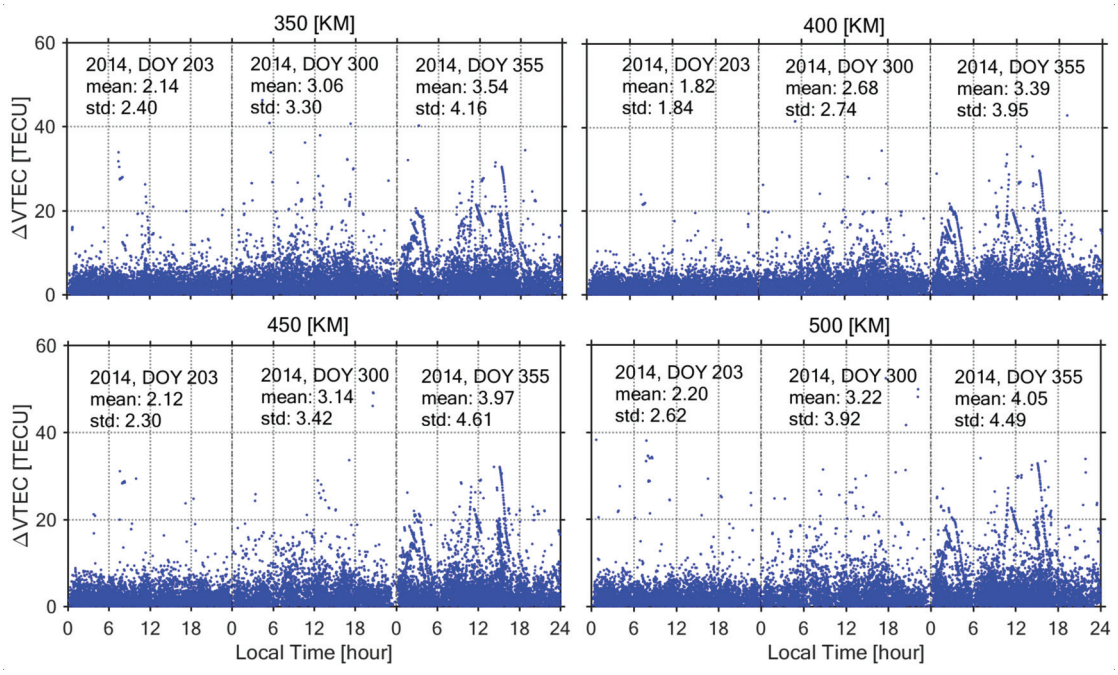

Figure 5. IMEs as a function of local time for different layer heights. The data are related to the periods DOY 203, 300, and 355 in the year 2014.

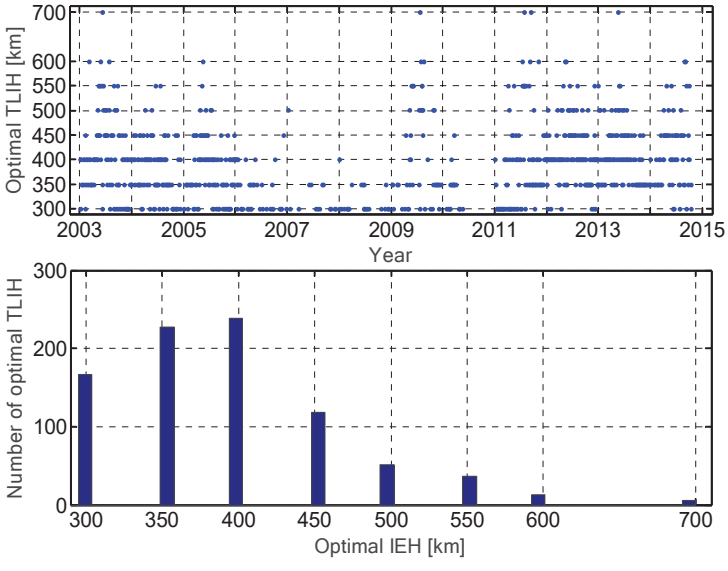

Figure 6. Time series (top) and histograms (bottom) of daily optimal TLIH for the Arctic region from 2003 to 2014 based on the CPP method.

3.2. Optimal TLIH Determination Using dG-TLIH Method

Considering the limitations of the CPP method, a new approach for detecting the optimal TLIH is proposed. Figure 7 shows the time series and histograms of the daily optimal TLIH based on the dSTEC method and UQRG–GIM during a whole solar cycle: days 001, 2002 to 223, 2018 in the polar regions. In this experiment, the resolution of the TLIH was set to 1.0 km. As illustrated in Figure 7, the optimal TLIH typically varies from 300 to 600 km, and the difference between the maximum and the minimum is about 100 km in one year in the polar regions. In addition, solar activity has a considerable influence on the optimal TLIH, which is manifested as an upward optimal TLIH with the increase in solar activity, and which is similar to the optimal TLIH from the CPP method variation against solar activity shown in Figure 6. In the Arctic region, the optimal TLIH is mainly distributed between 370 and 500 km. During high solar activity years (2011–2014), the optimal TLIH mainly varies from 400 to 500 km, and during low solar activity years (2007–2009), the optimal TLIH mainly ranges from 300 to 500 km. In the Antarctic region, the distribution of the optimal TLIH has been more dispersed than that in the Arctic, especially before 2010. This can be attributed to the fact that the GNSS observation stations in the Antarctic are few and unevenly distributed, resulting in the low accuracy of the GIM model in this region, which affects the reliability of the mapping value. The time series of optimal TLIH can reflect its overall trend of change over the Antarctic. In addition, the optimal TLIHs show different seasonal characteristics: in the Arctic, the peak of optimal TLIH occurs from February to March and the valley appears from September to October, while in the Antarctic, the peaks appear from April to May and the valley appears from November to December. The seasonal variations of optimal TLIH are caused by many factors. In the summer, with the increase of local solar activity, the ionization of the middle and lower atmosphere increases, which leads to the downward movement of the optimal TLIH. In the winter, with the weakening of the local solar activity, the ionization of the middle and lower atmosphere weakens, resulting in the upward movement of the optimal TLIH. In addition, the polar ionosphere is affected by the magnetosphere and the interplanetary magnetic field, and the electron density also fluctuates.

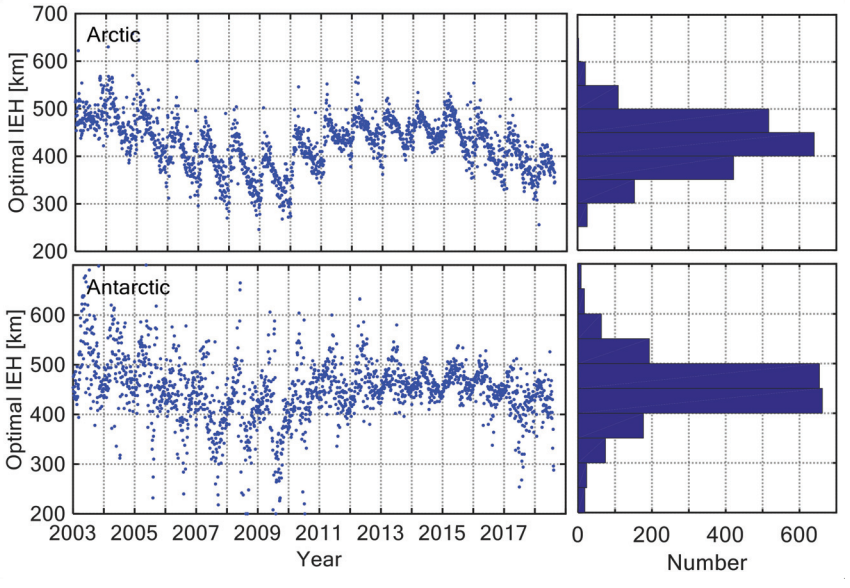

Figure 7. Time series (left) and histograms (right) of daily optimal TLIH during a whole solar cycle: days 001, 2002 to 223, 2018 over the Arctic (top) and Antarctic (bottom).

To further analyze the variations of the optimal TLIH across different seasons and solar activity conditions, we computed the "true" mapping values based on Equation (9) and the mapping function values based on Equation (1) corresponding to the different TLIHs. Figures 8 and 9 show the variation in the mapping values computed by Equations (1) and (9) as a function of elevation angle for different TLIH under three different solar activity conditions: low (2009), medium (2016), and high (2014), for the months of March, June, September, and December over the Antarctic and Arctic, respectively. The "true" mapping values vary considerably across different seasons and years. During a low solar activity year (2009), there were significant differences in the mapping values in the different seasons, which is consistent with the characteristic of the optimal TLIH shown in Figure 7. When the elevation angles were greater than 50°, the mapping values tended to be uniform. When the elevation angles are the same, the largest mapping value occurs in the spring and the smallest in the autumn in the Antarctic, as contrasted to the Arctic region. In addition, we also find that the mapping function values corresponding to different TLIHs were very different when the elevation angle was less than 15°.

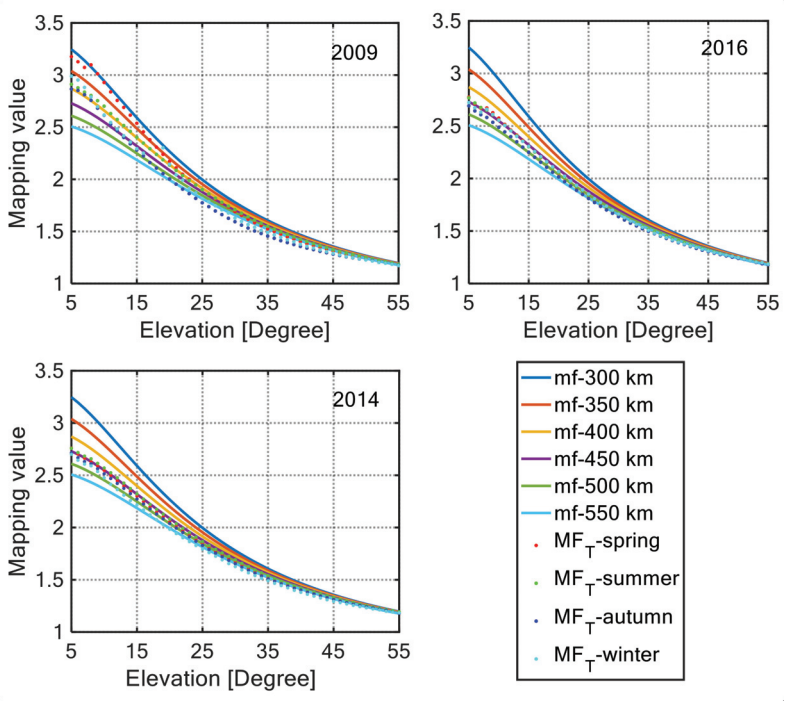

Figure 8. Variation of the mapping values computed by Equation (1) for different TLIHs and Equation (9) against elevation angles for three different solar activity conditions: low (2009), medium (2016), and high (2014), for the seasons of spring (September), summer (December), autumn (March), and winter (June) over the Antarctic.

Table 1 shows the optimal TLIH and the corresponding mapping function error indicator (σ_H) estimated by Equation (10) in March, June, September, and December during low (2009), medium (2016), and high (2014) solar activity years in the polar regions. The standard deviations at low solar activity are relatively larger than those at high solar activity, which indicates that the mapping values fluctuate greatly during low solar activity years. The difference between the maximum optimal TLIH in March and the minimum in September is more than 120 km. There are two main causes for the large fluctuations of the mapping values during low solar activity. First, the ionospheric TEC is smaller during

low solar activity, and a slight change in the TEC will cause a great change in the mapping value. Second, there are few available GNSS tracking stations in Antarctica (especially before 2010) and the stations are unevenly distributed, resulting in low accuracy of the GIM model, which affects the reliability of the mapping value. At both medium and high solar activities, the variation of optimal TLIH in one year was only about 50 km. On the same date, the optimal TLIH in the Antarctic was higher than in the Arctic.

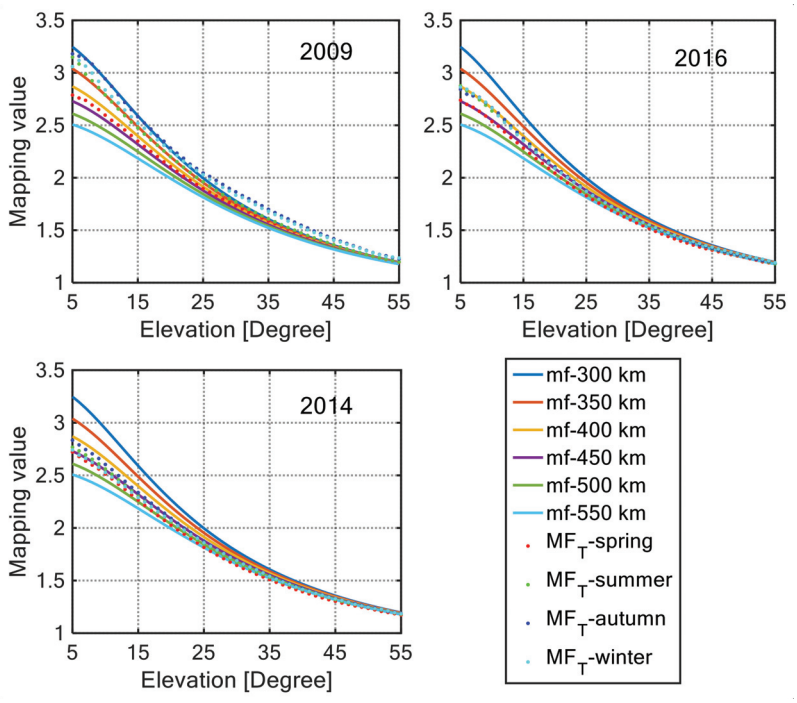

Figure 9. Variation of the mapping values computed by Equation (1) for different TLIHs and Equation (9) against elevation angles for three different solar activity conditions: low (2009), medium (2016), and high (2014), for the months of spring (March), summer (June), autumn (September), and winter (December) over the Arctic.

Table 1. The optimal TLIHs (km) and the corresponding standard deviations in March, June, September, and December of 2009, 2014, and 2016, respectively, over the Antarctic and Arctic.

Region	Year	Month			
		March	June	September	December
Antarctic	2009	(448, 0.08)	(386, 0.16)	(322, 0.06)	(392, 0.02)
	2016	(492, 0.03)	(460, 0.02)	(454, 0.03)	(456, 0.03)
	2014	(476, 0.02)	(506, 0.04)	(460, 0.02)	(446, 0.01)
Arctic	2009	(424, 0.02)	(342, 0.02)	(300, 0.06)	(322, 0.05)
	2016	(466, 0.03)	(414, 0.02)	(410, 0.02)	(412, 0.02)
	2014	(480, 0.03)	(452, 0.02)	(428, 0.02)	(460, 0.01)

The ionospheric gradient does not have a significant influence on the thin layer model with an elevation angle above 50°. Therefore, only cases with an elevation angle lower than 56° were considered in the experiment. Figure 10 shows the variations of optimal TLIH against the day of year (DOY) and elevation angle in low (2009), medium (2016), and high (2014) solar activity years in the polar regions. It can be seen that the optimal TLIH

increases with the increase in elevation angle. At low solar activity, the optimal TLIH with elevation between 25° and 55° in the Antarctic was significantly higher than that in the Arctic. The maximum value of the optimal TLIH in one year occurs in local winter, and the minimum occurs in local summer.

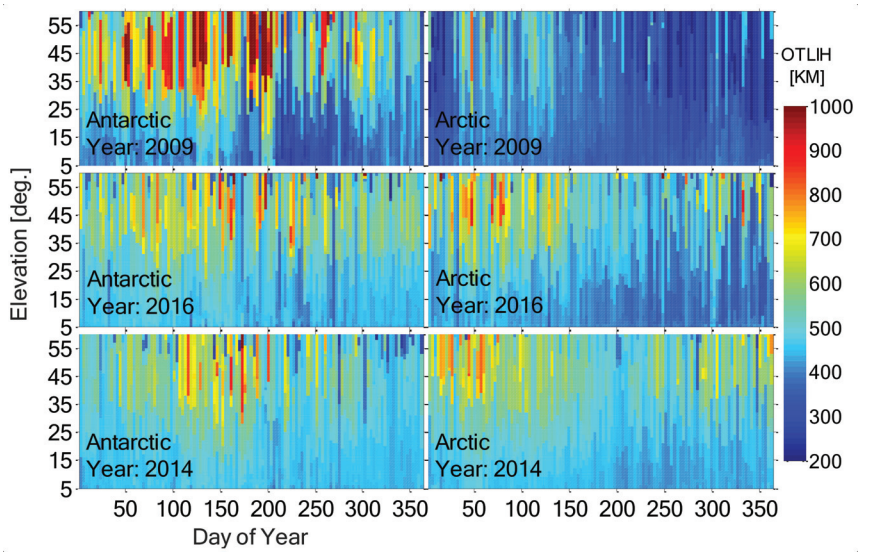

Figure 10. Variations of the optimal thin layer ionospheric height (TLIH) for three different solar activity conditions: low (2009), medium (2016), and high (2014), over the Antarctic (left) and Arctic (right), and as a function of the day of year (DOY) and elevation angle.

In order to verify the reliability of the dG-TLIH method, we used three kinds of TLIH (350 km, 450 km, and optimal TLIH from the dG-TLIH method) to build the ionosphere TEC model in the polar regions. The spherical cap harmonic (SCH) model was used to construct the ionospheric TEC model. The specific parameters of the SCH model are shown in previous research [28]. The numerical experiment was repeated for three different levels of solar activity: low (DOY 136, 2017), medium (DOY 127, 2014), and high (DOY 46, 2014), as detailed in Table 2.

Table 2. The information of solar activity and optimal TLIH for the 3 days selected to verify the reliability of the optimal TLIH over the Antarctic and Arctic.

Time	F10.7 (sfu)	Optimal TLIH (km)	
		Antarctic	Arctic
DOY 046, 2014	162.1	464	508
DOY 127, 2014	145.9	504	466
DOY 136, 2017	71.9	328	376

In addition, we compared the performances of the three models based on different TLIHs for mapping the polar ionospheric TEC using dSTEC method [6]. Table 3 presents the mapping bias and RMS errors of the three models for the Arctic and Antarctic regions, respectively. The statistical results were based on the dSTEC measurements provided by the verification stations shown in Figure 3. When the elevation angle of the satellite was greater than 40°, the influence of ionospheric gradient on the thin layer ionospheric model was weak. Therefore, statistical results only considered the data in the range of 10° to 40° for the elevation angle. It can be seen from the table that the performance of the model based on the optimal TLIH was better than the model based on 350 and 450 km, especially

in the case of high solar activity. By statistical analysis of the average of bias and RMS error on these three days, it can be found that in the Antarctic, the model bias error from the optimal TLIH was better than 1.21 and 0.20 TECU for 350 and 450 km, respectively, and the RMS error was better than 0.79 and 0.06 TECU, respectively; meanwhile in the Arctic, the bias error was better than 1.22 and 0.25 TECU for 350 and 450 km, respectively, and the RMS error was better than 0.90 and 0.20 TECU, respectively.

Table 3. Statistical results of ionospheric TEC models for different TLIHs using dSTEC measurements in the Antarctic and Arctic.

Region	Time	TLIH (km)	Bias (TECU)	RMS (TECU)
Antarctic	DOY 046, 2014	350	5.14	7.91
		450	2.48	5.94
		464	2.14	5.80
	DOY 127, 2014	350	1.52	3.98
		450	1.09	3.75
		504	0.91	3.73
	DOY 136, 2017	350	0.36	1.64
		450	0.41	1.66
		328	0.35	1.64
Arctic	DOY 046, 2014	350	2.90	5.51
		450	1.81	4.96
		508	1.35	4.50
	DOY 127, 2014	350	3.41	4.66
		450	1.59	3.22
		466	1.36	3.12
	DOY 136, 2017	350	0.54	1.96
		450	0.53	1.82
		376	0.49	1.80

3.3. Relationship between hmF2 and Optimal TLIH

According to previous research [17,23,24], hmF2 is related to the TLIH, but it is typically lower due to the asymmetry in the electron density profiles at GNSS transmitter heights, and it can reflect the characteristics of the TLIH to a certain extent. In general, the centroid height of the ionospheric electron density was used as the TLIH. In practical applications, the centroid height of the ionospheric electron density is equal to the hmF2 plus 80 km [23]. Therefore, as an indicator of the TLIH, we analyzed the relationship of the hmF2 from COSMIC data and the optimal TLIH from the dG-TLIH method in the Arctic and Antarctic.

Figure 11 shows the time series of the daily optimal TLIH from the dG-TLIH method, the hmF2 from the COSMIC data, and the solar activity index F10.7, from 2007 to 2016 in the Arctic. In nearly one solar cycle, the daily mean hmF2 ranges from 200 to 330 km. It can be seen that the hmF2 is highly correlated with optimal TLIH, and increases with the increase in the solar activity. The correlation coefficient between these two variables is up to 0.70 in the Arctic.

Figure 12 shows the time series of the daily optimal TLIH from the dG-TLIH method, the hmF2 from the COSMIC data, and the solar activity index F10.7, from 2007 to 2016 in the Antarctic. It can be seen that the time series of the optimal TLIHs are relatively dispersed. In order to better analyze the change characteristics of the optimal TLIH, we use a Fourier series to fit it, as shown by the green line in Figure 12. Although both the optimal TLIH and the hmF2 have an upward trend with the increase in solar activity, the change trend of the two variables in one year is opposite, especially in the high solar activity year. Therefore, we measured the relationship between the optimal TLIH and the hmF2 by

the maximum correlation coefficient and corresponding phase discrepancy, as shown in Figure 13. The optimal TLIH positively relates to the hmF2, with a correlation coefficient of 0.60 and a phase lag of ~3 months, with the hmF2 leading optimal TLIH.

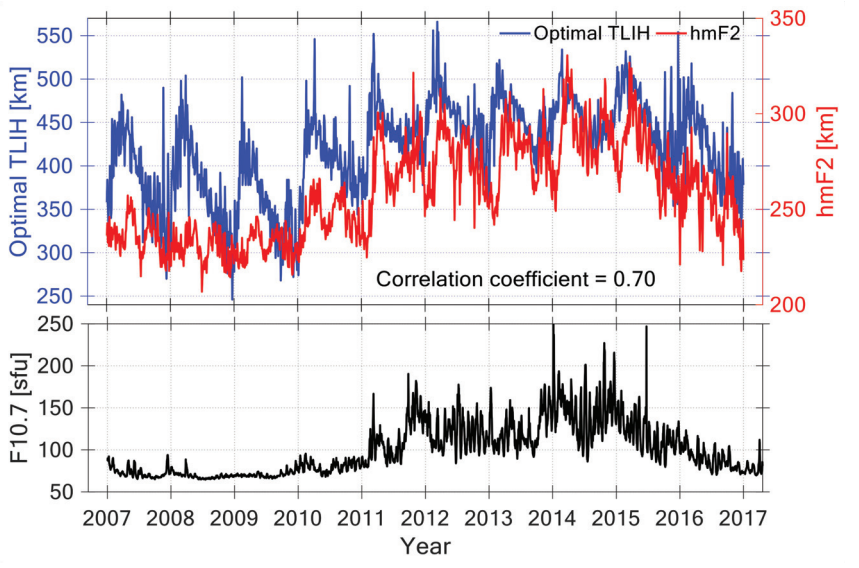

Figure 11. Time series of optimal TLIH (blue line), hmF2 (red line), and the levels of solar activity, F10.7 (bottom), from 2007 to 2016 over the Arctic.

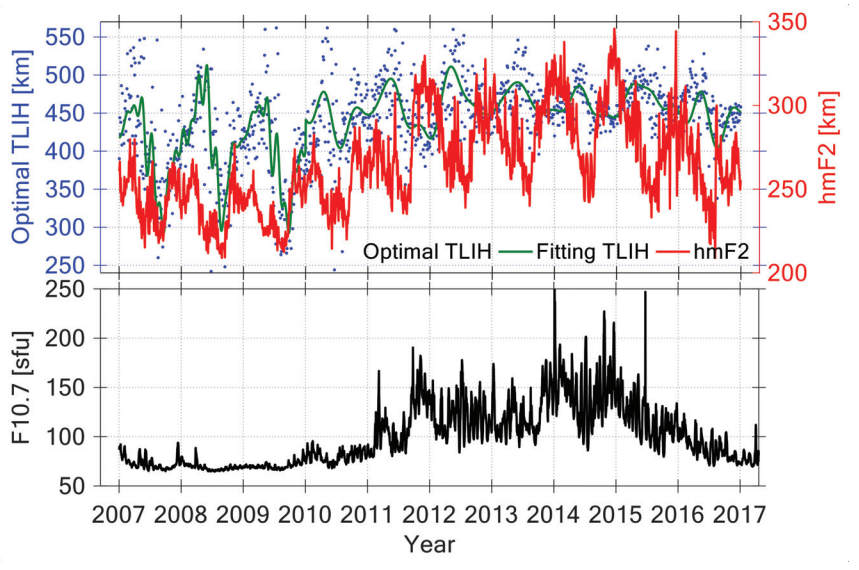

Figure 12. Time series of optimal TLIH (blue dots), fitting TLIH (green line), hmF2 (red line), and levels of solar activity, F10.7 (bottom), from 2007 to 2016 over the Antarctic.

In the Arctic, the average values of optimal TLIH and hmF2 were 420.43 and 258.43 km during 2007–2016, respectively; meanwhile in the Antarctic, they were 441.87 and 264.60 km, respectively. The differences between the optimal TLIH and the hmF2 were 162 and 177.27 km over the Arctic and Antarctic, respectively, which is greater than the empirical

value of 80 km. The main reason for this lies in the existence of the plasmasphere outside the ionosphere, and the TEC observed by GNSS will inevitably reflect the contribution of the plasmasphere [23]. The contribution of the plasmasphere to the vertical TEC is about 10~20% during the day and up to 50% at night [34].

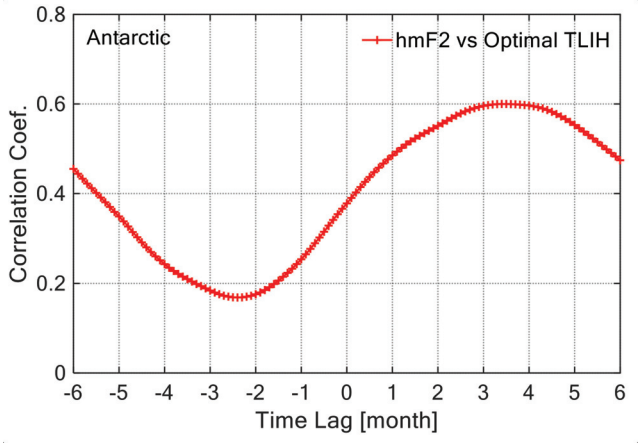

Figure 13. The correlation between the optimal TLIH and the hmF2; positive lag means hmF2 leads, and vice versa.

4. Conclusions

In this paper, a new method (dG-TLIH) to determine optimal TLIH was proposed, and the optimal TLIH was determined using the dG-TLIH method and the CPP technique over the Antarctic and Arctic based on GNSS data during a period of about one solar cycle. Relationships between the optimal TLIH from the dG-TLIH method and the hmF2 from the COSMIC data in the polar regions were analyzed.

According to the tests of the CPP technique, the results indicate that the optimal TLIH ranges from 300 to 600 km, and the height of 400 km ws the most frequent TLIH during 2003–2014 in the Arctic. Because the method requires dense and uniform ground tracking stations, it is not suitable for use in the Antarctic. When compared to the CPP method, the dG-TLIH method used in this study overcomes the limitation of requiring dense observation stations. According to the test of the dG-TLIH method, it is also confirmed that the optimal TLIH is related to solar activity, which mostly ranges from 320 to 500 km during one solar cycle. The optimal TLIH values present obviously seasonal variation characteristics, and most of the maximum and minimum values occurred in local winter and summer, respectively. Compared with the fixed TLIH (350 and 450 km), the bias errors of the ionospheric TEC model based on the optimal TLIH are decreased by 0.05 to 3.0 TECU, and the RMS errors are decreased by 0.02 to 2.11 TECU under different solar activity. According to the analysis of the relationship between the optimal TLIH and the hmF2, it was found that in the Arctic, the correlation coefficient between the hmF2 and optimal TLIH was 0.7, and the deviation between them was 162 km. In the Antarctic, they had a correlation coefficient of 0.60 with a phase lag of ~3 months, with the hmF2 leading the optimal TLIH, and the deviation between them was 177 km.

In order to facilitate ionospheric TEC modeling, we give an optimal TLIH each day over the Antarctic or Arctic. However, because the variation of ionospheric electron density is affected by solar activity, latitude, season, time, and other factors, it leads to the complex spatiotemporal variation of the optimal TLIH. In addition, the shape of the earth also needs to be taken into account when determining the optimal TLIH at the global scale. These problems will be the focus of future study.

Author Contributions: Conceptualization, H.J. and J.A.; methodology, M.H.-P.; data curation, H.J. and H.X.; validation, H.X. and H.J.; formal analysis, S.J. and M.H.-P.; writing—original draft, H.J. and H.X.; writing—review and editing, H.J., S.J., M.H.-P., J.A., Z.W., X.X. and H.Y. All authors have read and agreed to the published version of the manuscript.

Funding: This research was funded by the National Natural Science Foundation of China, grant number 41776195, 41941010, 41531069; and the State Key Laboratory of Geodesy and Earth's Dynamics, Innovation Academy for Precision Measurement Science and Technology, CAS, grant number SKLGED2021-2-3.

Institutional Review Board Statement: Not applicable.

Informed Consent Statement: Not applicable.

Data Availability Statement: Not applicable.

Acknowledgments: We thank the following organizations and projects for providing the data used in this work: International GNSS Services (IGS, accessed date: 1 December 2019), the Polar Earth Observing Network (POLENET, accessed date: 1 December 2019), and the COSMIC Data Analysis and Archive Center (CDAAC, accessed date: 1 January 2018).

Conflicts of Interest: The authors declare no conflict of interest.

References

1. Hernández-Pajares, M.; Juan, J.M.; Sanz, J.; Aragón-Àngel, À.; García-Rigo, A.; Salazar, D.; Escudero, M. The ionosphere: Effects, GPS modeling and the benefits for space geodetic techniques. *J. Geod.* **2011**, *85*, 887–907. [CrossRef]
2. Su, K.; Jin, S.; Hoque, M.M. Evaluation of Ionospheric Delay Effects on Multi-GNSS Positioning Performance. *Remote Sens.* **2019**, *11*, 171. [CrossRef]
3. Yuan, Y.; Ou, J. An improvement to ionospheric delay correction for single-frequency GPS users–the APR-I scheme. *J. Geod.* **2001**, *75*, 331–336. [CrossRef]
4. Klobuchar, J.A. Ionospheric time-delay algorithm for single-frequency GPS users. *IEEE Trans. Aerosp. Electron. Syst.* **1987**, *23*, 325–331. [CrossRef]
5. Blanch, J. *Using Kriging to Bound Satellite Ranging Errors due to the Ionosphere*; Stanford University: Stanford, CA, USA, 2003.
6. Hernández-Pajares, M.; Roma-Dollase, D.; Krankowski, A.; García-Rigo, A.; Orús-Pérez, R. Methodology and consistency of slant and vertical assessments for ionospheric electron content models. *J. Geod.* **2017**, *91*, 1405–1414. [CrossRef]
7. Schaer, S. *Mapping and Predicting the Earth's Ionosphere Using the Global Positioning System*; University of Berne: Berne, Switzerland, 1999.
8. Brunini, C.; Camilion, E.; Azpilicueta, F. Simulation study of the influence of the ionospheric layer height in the thin layer ionospheric model. *J. Geod.* **2011**, *85*, 637–645. [CrossRef]
9. Hoque, M.M.; Jakowski, N.; Berdermann, J. A new approach for mitigating ionospheric mapping function errors. In Proceedings of the 27th International Technical Meeting of the Satellite Division of the Institute of Navigation (ION GNSS+), Tampa, FL, USA, 8–12 September 2014; pp. 1183–1189.
10. Zhao, J.; Zhou, C. On the optimal height of ionospheric shell for single-site TEC estimation. *GPS Solut.* **2018**, *22*, 48. [CrossRef]
11. Nava, B.; Radicella, S.; Leitinger, R.; Coïsson, P. Use of total electron content data to analyze ionosphere electron density gradients. *Adv. Space Res.* **2007**, *39*, 1292–1297. [CrossRef]
12. Durmaz, M.; Karslioğlu, M.O. Non-parametric regional VTEC modeling with Multivariate Adaptive Regression B-Splines. *Adv. Space Res.* **2011**, *48*, 1523–1530. [CrossRef]
13. Pullen, S.; Park, Y.S.; Enge, P. Impact and Mitigation of Ionospheric Anomalies on Ground-Based Augmentation of GNSS. *Radio Sci.* **2009**, *44*, RS0A21. [CrossRef]
14. Hernández-Pajares, M.; Juan, J.; Sanz, J. New approaches in global ionospheric determination using ground GPS data. *J. Atmos. Solar-Terr. Phys.* **1999**, *61*, 1237–1247. [CrossRef]
15. Birch, M.J.; Hargreaves, J.K.; Bailey, G.J. On the use of an effective ionospheric height in electron content measurement by GPS reception. *Radio Sci.* **2002**, *37*, 1015. [CrossRef]
16. Jiang, H.; Wang, Z.; An, J.; Liu, J.; Wang, N.; Li, H. Influence of spatial gradients on ionospheric mapping using thin layer models. *GPS Solut.* **2018**, *22*, 2. [CrossRef]
17. Li, M.; Yuan, Y.; Zhang, B.; Wang, N.; Li, Z.; Liu, X.; Zhang, X. Determination of the optimized single-layer ionospheric height for electron content measurements over China. *J. Geod.* **2018**, *92*, 169–183. [CrossRef]
18. Li, Z.; Yuan, Y.; Wang, N.; Hernandez-Pajares, M.; Huo, X. SHPTS: Towards a new method for generating precise global ionospheric TEC map based on spherical harmonic and generalized trigonometric series functions. *J. Geod.* **2015**, *89*, 331–345. [CrossRef]
19. Krankowski, A.; Shagimuratov, I.I.; Ephishov, I.I.; Krypiak-Gregorczyk, A.; Yakimova, G. The occurrence of the mid-latitude ionospheric trough in GPS-TEC measurements. *Adv. Space Res.* **2009**, *43*, 1721–1731. [CrossRef]

20. Hernández-Pajares, M.; Juan, J.M.; Sanz, J.; Orus, R.; Garcia-Rigo, A.; Feltens, J.; Komjathy, A.; Schaer, S.C.; Krankowski, A. The IGS VTEC maps: A reliable source of ionospheric information since 1998. *J. Geod.* **2009**, *83*, 263–275. [CrossRef]
21. Mannucci, A.J.; Wilson, B.D.; Yuan, D.N.; Ho, C.H.; Lindqwister, U.J.; Runge, T.F. A global mapping technique for GPS-derived ionospheric total electron content measurements. *Radio Sci.* **1998**, *33*, 565–582. [CrossRef]
22. Jiang, H.; Liu, J.; Wang, Z.; An, J.; Ou, J.; Liu, S.; Wang, N. Assessment of spatial and temporal TEC variations derived from ionospheric models over the polar regions. *J. Geod.* **2019**, *93*, 455–471. [CrossRef]
23. Wen, J.; Wan, W.; Ding, F.; Le, X.; Yu, C.; Liu, L. Experimental observation and statistical analysis of the vertical TEC mapping function. *Chin. J. Geophys.* **2010**, *53*, 22–29.
24. Xiang, Y.; Gao, Y. An Enhanced Mapping Function with Ionospheric Varying Height. *Remote Sens.* **2019**, *11*, 1497. [CrossRef]
25. Kamide, Y.; Baumjohann, W. Magnetosphere-Ionosphere Coupling. *J. Geophys. Res. Space Phys.* **1979**, *84*, 7239–7246.
26. Liu, J.; Chen, R.; An, J.; Wang, Z.; Hyyppa, J. Spherical cap harmonic analysis of the Arctic ionospheric TEC for one solar cycle. *J. Geophys. Res. Space Phys.* **2014**, *119*, 601–619. [CrossRef]
27. Skone, S.H. *Wide Area Ionosphere Grid Modelling in the Auroral Region*; University of Calgary: Calgary, AB, Canada, 1998.
28. Xi, H.; Jiang, H.; An, J.; Wang, Z.; Xu, X.; Yan, H.; Feng, C. Spatial and Temporal Variations of Polar Ionospheric Total Electron Content over Nearly Thirteen Years. *Sensors* **2020**, *20*, 540. [CrossRef]
29. Coley, W.R.; Heelis, R.A. Seasonal and universal time distribution of patches in the northern and southern polar caps. *J. Geophys. Res.* **1998**, *103*, 29229–29237. [CrossRef]
30. Hernández-Pajares, M.; Lyu, H.; Aragón-Ngel, N.; Monte-Moreno, E.; Liu, J.; An, J.; Jiang, H. Polar Electron Content from GPS Data-Based Global Ionospheric Maps: Assessment, Case Studies, and Climatology. *J. Geophys. Res. Space Phys.* **2020**, *125*, e2019JA027677. [CrossRef]
31. Dach, R.; Brockmann, E.; Schaer, S.; Beutler, G.; Meindl, M.; Prange, L.; Bock, H.; Jäggi, A.; Ostini, L. GNSS processing at CODE: Status report. *J. Geod.* **2009**, *83*, 353–365. [CrossRef]
32. Yuan, Y.; Ou, J. A generalized trigonometric series function model for determining ionospheric delay. *Prog. Nat. Sci.* **2004**, *14*, 1010–1014. [CrossRef]
33. Arikan, F.; Erol, C.; Arikan, O. Regularized estimation of vertical total electron content from Global Positioning System data. *J. Geophys. Res.* **2003**, *108*, 1469. [CrossRef]
34. Lunt, N.; Kersley, L.; Bishop, G.J.; Mazzella, A.J.; Bailey, G.J. The effect of the protonosphere on the estimation of GPS total electron content: Validation using model simulations. *Radio Sci.* **1999**, *34*, 1261–1271. [CrossRef]

remote sensing

MDPI

Article

Modified Interpolation Method of Multi-Reference Station Tropospheric Delay Considering the Influence of Height Difference

Yakun Pu [1,2], Min Song [1,*] and Yunbin Yuan [1]

[1] State Key Laboratory of Geodesy and Earth's Dynamics, Innovation Academy for Precision Measurement Science and Technology, Chinese Academy of Sciences, Wuhan 430077, China; yakunpu@apm.ac.cn (Y.P.); yybgps@whigg.ac.cn (Y.Y.)
[2] University of Chinese Academy of Sciences, Beijing 100049, China
* Correspondence: msong@apm.ac.cn

Abstract: In network real-time kinematic (NRTK) positioning, atmospheric delay information is critical for generating virtual observations at a virtual reference station (VRS). The traditional linear interpolation method (LIM) is widely used to obtain the atmospheric delay correction. However, even though the conventional LIM is robust in the horizontal direction of the atmospheric error, it ignores the influence of the vertical direction, especially for the tropospheric error. If the height difference between the reference stations and the rover is large and, subsequently, tropospheric error and height are strongly correlated, the performance of the traditional method is degraded for tropospheric delay interpolation at the VRS. Therefore, considering the height difference between the reference stations and the rover, a modified linear interpolation method (MLIM) is proposed to be applied to a conventional single Delaunay triangulated network (DTN). The systematic error of the double-differenced (DD) tropospheric delay in the vertical direction is corrected first. The LIM method is then applied to interpolate the DD tropospheric delay at the VRS. In order to verify the performance of the proposed method, we used two datasets from the American NOAA continuously operating reference stations (CORS) network with significant height differences for experiments and analysis. Results show that the DD tropospheric delay interpolation accuracy obtained by the modified method is improved by 84.1% and 69.6% on average in the two experiments compared to the conventional method. This improvement is significant, especially for low elevation satellites. In rover positioning analysis, the traditional LIM has a noticeable systematic deviation in the up component. Compared to the conventional method, the positioning accuracy of the MLIM method is improved in the horizontal and vertical directions, especially in the up component. The accuracy of the up component is reduced from tens of centimeters to a few centimeters and demonstrates better positioning stability.

Keywords: GPS; NRTK; VRS; tropospheric delay; interpolation

Citation: Pu, Y.; Song, M.; Yuan, Y. Modified Interpolation Method of Multi-Reference Station Tropospheric Delay Considering the Influence of Height Difference. *Remote Sens.* **2021**, *13*, 2994. https://doi.org/10.3390/rs13152994

Academic Editor: Stefania Bonafoni

Received: 9 June 2021
Accepted: 26 July 2021
Published: 29 July 2021

1. Introduction

The traditional single-baseline real-time kinematic (RTK) positioning technology has been developed over the last several decades. However, due to the influence of atmospheric errors, orbital errors, and other distance-related errors, the distance between the rover and the reference station can only be about 10 km for centimeter-level positioning. The emergence of network real-time kinematic (NRTK), which is based on multiple reference stations, has expanded the scope of services for precise real-time positioning [1–3]. Virtual reference station (VRS) technology has been widely applied in NRTK data processing. When the ambiguities between reference stations are fixed in the network, distance-dependent errors, such as the double-differenced (DD) ionospheric and tropospheric delay of baselines, can easily be calculated. Using the estimated error among the reference stations, we can obtain

the corresponding error between the reference stations and the VRS near the rover through the interpolation method. Finally, the generated virtual observations and the rover's actual observations can be used for short baseline relative positioning, and the centimeter-level coordinates of the rover can be quickly obtained [4,5].

After extracting the atmospheric error from the baseline of the reference stations correctly, selecting the appropriate algorithm to generate the virtual observations at the VRS becomes a crucial issue. Therefore, researchers have proposed several interpolation models. Wanninger originally proposed a linear interpolation method (LIM) that requires at least three reference stations around the rover. The dual-frequency phase observations and the known coordinates of the reference station are applied to derive the regional DD ionospheric model [6]. The LIM can also build the model of other distance-dependent errors, such as tropospheric delay [7]. Han and Rizos introduced a linear combination model (LCM) of single-differenced (SD) observations, mainly used to eliminate orbital errors and that can be applied to model atmospheric errors [8]. The distance-based linear interpolation method (DIM), proposed by Gao et al., interpolates the rover's ionospheric delay based on the distance between the reference stations and the rover [9]. Wübbena applied a suitable trend surface, called the low-order surface model (LSM), to simulate the distance-dependent error trend in the network. The coefficients of the LSM model can be obtained from the observation data of the reference stations by the least-squares adjustment [10]. The least-squares collocation method can also be applied to interpolate the atmospheric delay [11–13]. A comprehensive comparison of the advantages and disadvantages of these interpolation methods was undertaken by Dai et al. [14], Fotopoulos et al. [15], Wu et al. [16], and Al-Shaery et al. [17]. All results showed that the effects of these interpolation methods are similar. It is difficult to say which one performs the best. However, The LSM requires at least four stations to resolve the model coefficients. If the network is formed by Delaunay triangulation in VRS mode, it is difficult to use LSM in the smallest triangular unit. The rover station is generally surrounded by three reference stations in the traditional Delaunay triangulated network (DTN), so the LIM method is easier to implement for a triangulation model.

With the increase of the baseline length, the correlation of tropospheric errors among the stations decreases, which leads to large residual errors in DD observations. Significant residual errors will affect the ambiguity resolution (AR) and positioning quality. Since the tropospheric delay is highly correlated with elevation, its correlation coefficient exceeds 0.9, which will seriously affect the estimation of the station positions [18–20]. Landau used the experimental data of the German SAPOS network and found that when an obvious height difference exists between the rover and reference stations, the tropospheric delay systematic error caused by the height deviation can reach 6.8 cm [21]. If the interpolation algorithms mentioned above are applied in the smallest triangular unit directly, they only consider the horizontal distribution of the tropospheric errors. The tropospheric delay interpolated at the VRS is strongly constrained in the horizontal plane that is formed by the reference stations. The tropospheric delay in the vertical direction may be significantly inaccurate. Wu et al. proposed that the multi-baseline tropospheric delay interpolation method has better accuracy than the traditional LIM in the star network [22]. In addition, based on the BP artificial neural network method, Qiu et al. used a neural network to better correct the tropospheric delay and build the spatial tropospheric delay error model [23].

The above-mentioned interpolation methods either did not consider the systematic error of the tropospheric delay caused by the height difference between the user station and the reference station or required using multiple baselines and complex modeling methods, which are not convenient in practice. In our study, we proposed an improved linear interpolation method that was simple to implement and that was effective. Taking the height difference between the reference stations and the rover into account, the prior model of the troposphere was used to correct the estimated DD tropospheric delay on the network baseline first. After that, the LIM was used to interpolate the tropospheric

delay between the VRS and the master reference station. Finally, the interpolated value was applied to generate virtual observations and positioning.

The main objective of this research is to improve the accuracy of the tropospheric delay correction using the interpolation algorithm in the NRTK of the Delaunay triangulated network (DTN) model in order to obtain more stable and more accurate positioning results through the modified method, especially in the vertical direction. The structure of this paper is as follows: In Section 2, the calculation method of the DD tropospheric delay of the network baseline is introduced, and the traditional LIM and MLIM methods are presented in detail. In Section 3, using the experimental data from the triangular units, the accuracy of the tropospheric delay correction when applying both the conventional and modified methods is analyzed with different satellite elevation angles. The difference in the positioning results from the two methods is compared. The results of the analyses are then discussed in Section 4. Finally, the conclusions are drawn, and further research directions are suggested in Section 4.

2. Materials and Methods

Here, we first describe the VRS's tropospheric delay acquisition process, which includes the calculation of the DD tropospheric delay among the reference stations and the traditional modeling method of the tropospheric delay at the VRS. The modified method is then developed in Section 2.2, using the prior tropospheric model to correct the tropospheric elevation system error due to the height difference between the reference and the rover stations and combining the LIM interpolation algorithm with the calculated DD tropospheric delay to obtain the DD tropospheric delay between the VRS and the master station.

2.1. Calculation and Modeling Process of the Tropospheric Delay

In order to accurately obtain the tropospheric delay of the network baselines, we established the DD observation equations to obtain the wide-lane (WL) ambiguities, which can be expressed as follows:

$$\begin{cases} L^{ij}_{rb,WL} = \rho^{ij}_{rb} + T^{ij}_{rb} + \frac{f_1}{f_2}(I^j_{rb,1} - I^i_{rb,1}) + \lambda_{WL}(N^j_{rb,WL} - N^i_{rb,WL}) + \varepsilon^{ij}_{rb,WL} \\ L^{ij}_{rb,1} = \rho^{ij}_{rb} + T^{ij}_{rb} - (I^j_{rb,1} - I^i_{rb,1}) + \lambda_1(N^j_{rb,1} - N^i_{rb,1}) + \varepsilon^{ij}_{rb,1} \\ P^{ij}_{rb,1} = \rho^{ij}_{rb} + T^{ij}_{rb} + (I^j_{rb,1} - I^i_{rb,1}) + e^{ij}_{rb,1} \\ P^{ij}_{rb,2} = \rho^{ij}_{rb} + T^{ij}_{rb} + \frac{f_1^2}{f_2^2}(I^j_{rb,1} - I^i_{rb,1}) + e^{ij}_{rb,2} \\ \widetilde{I^{ij}_{rb,1}} = I^j_{rb,1} - I^i_{rb,1} \end{cases} \quad (1)$$

where the subscripts r and b identify the reference stations, and the superscripts i and j denote the reference and rover satellites, respectively. $L^{ij}_{rb,WL}$, $L^{ij}_{rb,1}$, $P^{ij}_{rb,1}$, and $P^{ij}_{rb,2}$ represent the DD carrier and the pseudorange observations of the WL, and $L1$, $P1$, and $P2$ are in meters. ρ^{ij}_{rb} is the DD geometric distance from the satellite to receiver. T^{ij}_{rb} is the DD slant tropospheric delay of each satellite pair. $I^i_{rb,1}$ and $I^j_{rb,1}$ are the SD ionospheric delays on $L1$. $N^i_{rb,WL}$, $N^j_{rb,WL}$, $N^i_{rb,1}$, and $N^j_{rb,1}$ are the SD WL and $L1$ ambiguities. f_1 and f_2 are the frequencies of $L1$ and $L2$, and λ_{WL} and λ_1 are the wavelengths of WL and $L1$. $\varepsilon^{ij}_{rb,WL}$, $\varepsilon^{ij}_{rb,1}$, $e^{ij}_{rb,1}$, and $e^{ij}_{rb,2}$ denote all other errors, including the noise of the DD carrier and the pseudorange. $\widetilde{I^{ij}_{rb,1}}$ is DD ionospheric pseudo-observation.

Using WL ambiguity obtained by Equation (1), the $L1$ ambiguity was then estimated using the following observation equation:

$$\begin{cases} L^{ij}_{rb,IF} = \rho^{ij}_{rb} + T^{ij}_{rb} + \frac{C}{f_1+f_2}(N^j_{rb,1} - N^i_{rb,1}) + \frac{Cf_2}{f_1^2+f_2^2}N^{ij}_{rb,WL} + \varepsilon^{ij}_{rb,IF} \\ P^{ij}_{rb,IF} = \rho^{ij}_{rb} + T^{ij}_{rb} + e^{ij}_{rb,IF} \end{cases} \quad (2)$$

where *IF* denotes the ionosphere-free combination. $N_{rb,WL}^{ij}$ is DD WL ambiguities. The other symbols are the same as in Equation (1).

The prerequisite for obtaining the DD tropospheric delay is to resolve the ambiguity correctly. Generally, the baseline difference of the reference stations is tens of kilometers or even more than 100 km, and the AR is difficult. Therefore, we used Equation (1) to estimate the SD *WL* ambiguity, and the SD *L*1 ambiguity was then estimated by applying Equation (2). The ionospheric delay is one of the major factors restricting the AR among the reference stations. This effect is handled with a temporal and spatial correlation weighting scheme for the ionospheric pseudo-observations in Equation (1) [13,24]. The DD ionospheric pseudo-observations can be obtained from the broadcast Klobuchar ionospheric model [25] or the IGS global ionosphere models (GIM). We selected the GIM model because it has better accuracy than the broadcast Klobuchar model [26]. On the other hand, the UNB3m model combined with Niell mapping functions (NMF) was used to compute the hydrostatic tropospheric corrections [27,28]. The wet tropospheric delay was estimated as the relative tropospheric zenith delay (RZTD) parameter [29].

The Kalman filter was adopted to estimate the float SD *WL*, *L*1 ambiguity, the SD ionospheric delay, and the RZTD. The DD ambiguity was obtained from the SD ambiguity through the transition matrix, and the LAMBDA method was applied to obtain the integer of the DD *WL* and *L*1 ambiguities [30]. The *L*2 DD ambiguity could then be directly derived from the linear relationship between the *WL* and *L*1 DD ambiguities.

After we obtained the *L*1 and *L*2 DD integer ambiguities, the tropospheric slant delay corresponding to each satellite pair between *r* and *b* was calculated as follows:

$$\hat{T}_{rb}^{ij} = \frac{f_1^2}{f_1^2 - f_2^2}(L_{rb,2}^{ij} - \lambda_1 \widetilde{N}_{rb,1}^{ij}) - \frac{f_2^2}{f_1^2 - f_2^2}(L_{rb,2}^{ij} - \lambda_2 \widetilde{N}_{rb,2}^{ij}) - \rho_{rb}^{ij} \tag{3}$$

where $\hat{T}_{rb}^{ij}$ represents the calculated DD tropospheric delay. $\widetilde{N}_{rb,1}^{ij}$ and $\widetilde{N}_{rb,2}^{ij}$ denote fixed DD ambiguities on *L*1 and *L*2 in units of cycles. Observation noise, multipath effects, and other errors are ignored here.

Generally, at least three reference stations around the rover are used to build a DD tropospheric interpolation model, and the reference station closest to the rover is selected as the master reference station, while the other two are auxiliary reference stations. The interpolation model for applying the LIM can be expressed as

$$\hat{T} = B\mathrm{X}_{\mathrm{ab}} \tag{4}$$

$$\hat{T} = \begin{bmatrix} \hat{T}_{M,1}^{ij} \\ \hat{T}_{M,2}^{ij} \\ \vdots \\ \hat{T}_{M,n-1}^{ij} \end{bmatrix} B = \begin{bmatrix} \Delta X_{M,1} & \Delta Y_{M,1} \\ \Delta X_{M,2} & \Delta Y_{M,2} \\ \vdots & \vdots \\ \Delta X_{M,n-1} & \Delta Y_{M,\mathrm{n}-1} \end{bmatrix} \mathrm{X}_{ab} = \begin{bmatrix} a \\ b \end{bmatrix} \tag{5}$$

where *i*, *j* denote the reference and rover satellite, subscript *M* is the master reference station, and $1, 2, \ldots, n-1$ represent the auxiliary reference stations. ΔX and ΔY are the difference of the horizontal coordinates between the master and auxiliary reference stations. $\hat{T}$ is the calculated DD tropospheric delay, and *B* is the coefficient matrix. When the DD tropospheric delay is determined by (3), the coefficients *a* and *b* in (5) can be estimated by least-squares adjustment:

$$\mathrm{X}_{ab} = \left(B^T B\right)^{-1} B^T \hat{T} \tag{6}$$

The DD tropospheric delay between the VRS and the master reference station can then be obtained as follows:

$$T_{M,V}^{\mathrm{ij}} = \begin{bmatrix} \Delta X_{M,V} & \Delta Y_{M,V} \end{bmatrix} \cdot \mathrm{X}_{\mathrm{ab}} = \begin{bmatrix} \Delta X_{M,V} & \Delta Y_{M,V} \end{bmatrix} \cdot \left(B^T B\right)^{-1} B^T \hat{T} \tag{7}$$

where $T^{ij}_{M,V}$ is the interpolated DD tropospheric delay between the master reference station and the VRS for the satellite pair i, j. $\Delta X_{M,V}$ and $\Delta Y_{M,V}$ are the difference in the horizontal coordinates between the VRS and the master reference station.

2.2. The Modified Tropospheric Interpolation Algorithm

In GNSS data processing, the ionosphere is assumed to be a single-layer model above the earth, and its height is generally 350 km. For a small area, the point where the satellite signal passes through the single layer will form an approximate plane. Therefore, when ionospheric changes are not active, using conventional LIM to interpolate the ionospheric delay will achieve a sufficient accuracy in the NRTK. Compared to the ionospheric delay, the tropospheric temporal and spatial distribution characteristics are significantly different. The tropospheric delay is affected by both horizontal and height factors. It can be seen from Section 2.1 that the traditional interpolation method only uses horizontal coordinates to interpolate tropospheric errors, but ignores the vertical element. This method constrains the interpolation of the tropospheric delay to the height level constituted by reference stations. When the height of the rover is much higher or lower than the selected reference stations, it causes the positioning performance to decrease, especially in the up component. Therefore, we proposed that the tropospheric system error caused by the height difference between the reference stations and rovers should be corrected first. The LIM was then used for the DD tropospheric delay modeling.

Assuming that the reference stations M, A, and B form a triangular unit and assuming that station M is selected as the master reference station, A and B are the two auxiliary reference stations. The coordinates of the VRS are the result of the standard point positioning (SPP) of the rover. Suppose the height of the VRS is much higher or lower than the reference stations. In that case, the tropospheric delay between the master station and the auxiliary reference stations calculated by Equation (3) needs to be corrected in advance before applying the LIM. Take the baseline between A and M as an example. The calculated DD tropospheric delay is

$$T^{ij}_{MA}(\Delta h_{MA}) = T^{ij}_{A}(h_A) - T^{ij}_{M}(h_M) \tag{8}$$

where $T^{ij}_{MA}(\Delta h_{MA})$ is the calculated DD tropospheric delay of the reference and rover satellite, i and j are on the baseline MA with the height difference Δh_{MA}. $T^{ij}_{A}(h_A)$, and $T^{ij}_{M}(h_M)$ are the SD tropospheric delays of the reference and rover satellites i, j at stations A and M, with heights of h_A and h_M, respectively.

The SD tropospheric delay correction equations for station A and M are as follows:

$$\overline{T}^{ij}_{A}(h_A) = T^{ij}_{A}(h_A) + T_{CorA} \tag{9}$$

$$\overline{T}^{ij}_{M}(h_M) = T^{ij}_{M}(h_M) + T_{CorM} \tag{10}$$

where $\overline{T}^{ij}_{A}(h_A)$ and $\overline{T}^{ij}_{M}(h_M)$ are the corrected SD tropospheric delays for stations A and M. The specific derivations of the correction terms T_{CorA} and T_{CorM} are as follows:

$$\begin{aligned} T_{CorA} &= T^{ij}_{A}(h_V) - T^{ij}_{A}(h_A) \\ &= ZTD_A(\mathrm{h}_V) \times (MF^{j}_{A}(\mathrm{h}_V) - MF^{i}_{A}(\mathrm{h}_V)) - ZTD_A(\mathrm{h}_A) \times (MF^{j}_{A}(\mathrm{h}_A) - MF^{i}_{A}(\mathrm{h}_A)) \end{aligned} \tag{11}$$

$$\begin{aligned} T_{CorM} &= T^{ij}_{M}(h_V) - T^{ij}_{M}(h_M) \\ &= ZTD_M(\mathrm{h}_V) \times (MF^{j}_{M}(\mathrm{h}_V) - MF^{i}_{M}(\mathrm{h}_V)) - ZTD_M(\mathrm{h}_M) \times (MF^{j}_{M}(\mathrm{h}_M) - MF^{i}_{M}(\mathrm{h}_M)) \end{aligned} \tag{12}$$

where T_{CorA} and T_{CorM} are the correction items, and h_A and h_V are the height of station A and the VRS, respectively. $ZTD_A(h_A)$ and $ZTD_A(h_V)$ represent the ZTD at station A with height h_A and h_V, respectively, which can be calculated using the prior model.

$MF_A^j(h_A)$, $MF_A^i(h_A)$, $MF_A^j(h_V)$ and $MF_A^j(h_V)$ denote the tropospheric mapping functions corresponding to the satellites i, j at station A with the height h_A and h_V, respectively.

Although the ZTD calculated by the prior model has model errors, the difference of the ZTD obtained by the prior model at the same horizontal position but at different heights can effectively eliminate the tropospheric system error caused by the height difference. Therefore, the T_{CorA} and T_{CorM} obtained by the prior model still have a high correction accuracy. We substituted Equations (11) and (12) into Equations (9) and (10), respectively, and replaced $T_A^{ij}(h_A)$ and $T_M^{ij}(h_M)$ in Equation (8) with $\overline{T}_A^{ij}(h_A)$ and $\overline{T}_M^{ij}(h_M)$ in Equations (9) and (10). Equation (8) then became

$$\overline{T}_{MA}^{ij}(\Delta h_{VV}) = \overline{T}_A^{ij}(h_A) - \overline{T}_M^{ij}(h_M) = T_A^{ij}(h_V) - T_M^{ij}(h_V) \tag{13}$$

where $\overline{T}_{MA}^{ij}(\Delta h_{VV})$ is the corrected DD tropospheric delay of the reference and rover satellites i, j on the baseline MA.

The mean error of the ZTD calculated by the UNB series model in North America is about 2 cm [31], which represents good accuracy. The NMF and other mapping functions have similar accuracy. Taking the experimental data from North America into account, the tropospheric systematic deviation correction was calculated using the UNB3m model with the NMF in this paper. After correcting the systematic error of the DD tropospheric delay in advance, and then using the LIM for interpolation, a DD tropospheric delay with no height difference deviation on the VRS baseline and the master station could be obtained.

3. Results

In this chapter, we first describe the two experimental datasets used to verify the modified interpolation algorithm. After that, in the first experiment, we chose different periods and satellites in various triangular units in Dataset One to analyze the tropospheric delay interpolation effect of the traditional and modified methods. In the second experiment, several satellites in the same period in the same triangle unit in Dataset Two were selected to analyze the interpolation effects. Finally, the positioning performance after adopting the traditional and proposed methods was analyzed.

3.1. Experimental Data

The experimental data were from the US CORS network. We chose 21 stations as reference stations and another ten stations as simulated rovers for experimental analysis. These data were divided into two experimental datasets.

Dataset One consisted of six independent triangular units, and each unit contained a simulated rover. Dataset Two only had one triangle unit, but it included four simulated rover stations. The plane distribution and baseline length of Dataset One and Dataset Two are shown in Figures 1 and 2. The reference station closest to each rover was selected as the master reference station; they are connected by the green dashed line in the figure. Figures 3 and 4 show the station height distribution of the two datasets. The observation data on day of year (DOY) 180 in 2020 were selected. The sampling interval was set to 30 s, and the cut-off angle was set to 15°.

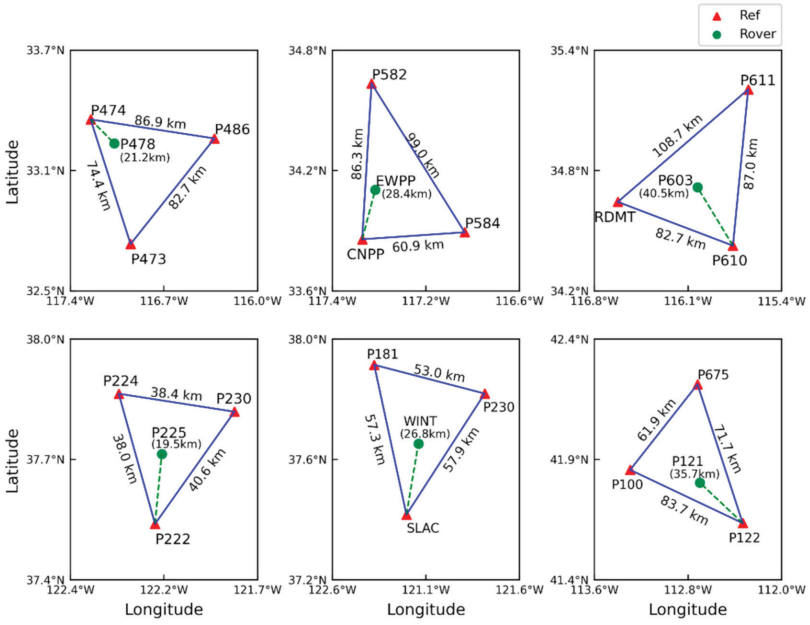

Figure 1. Geographical distribution of the selected stations in Dataset One.

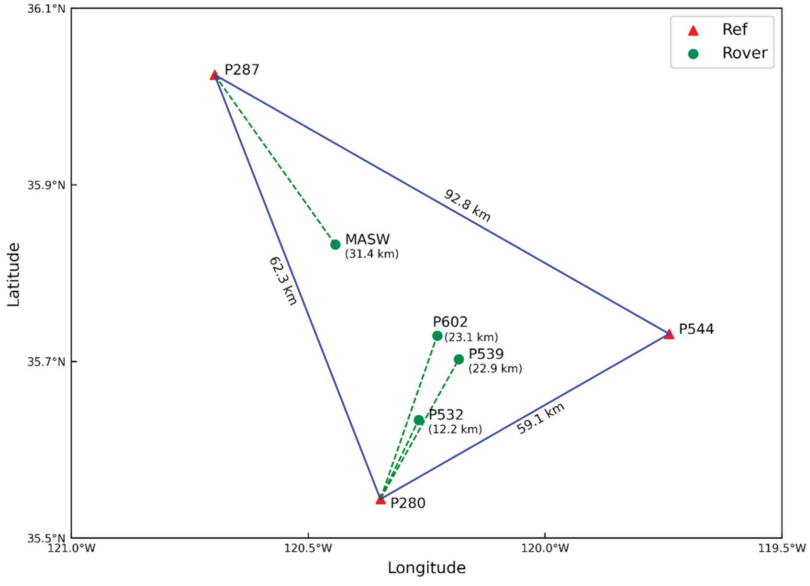

Figure 2. Geographical distribution of the selected stations in Dataset Two.

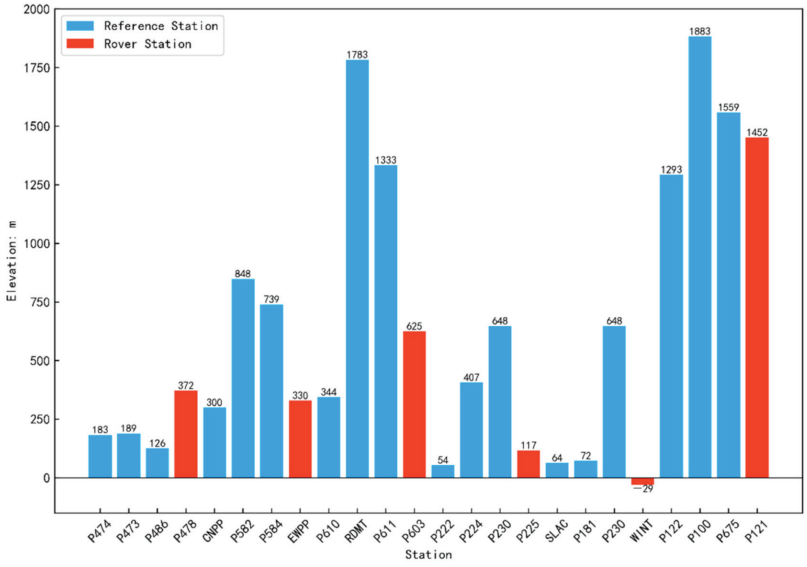

Figure 3. The elevation distribution of the stations in Dataset One.

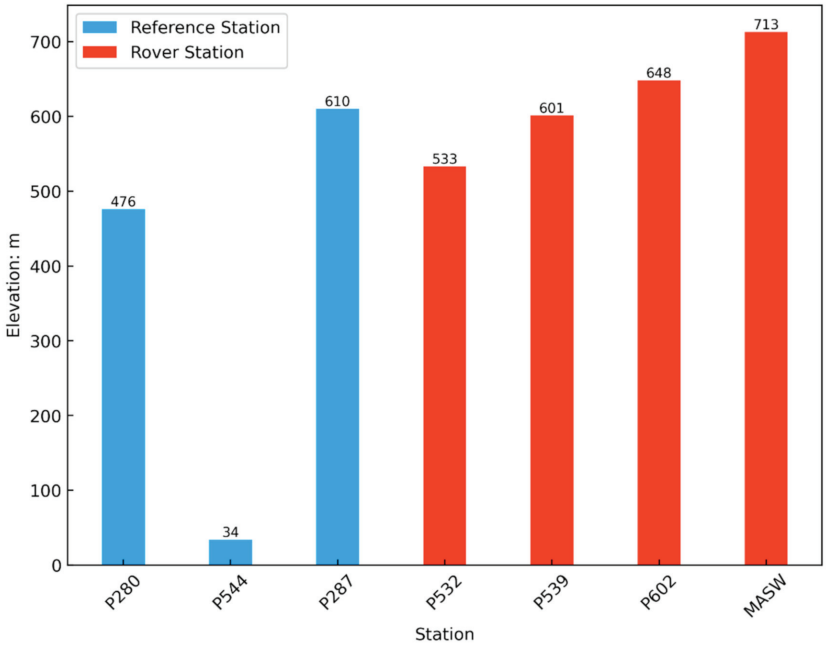

Figure 4. The elevation distribution of the stations in Dataset Two.

The coordinates of the reference stations and the simulated rovers were obtained from the US CORS website and were used as known coordinates in the experiments. The Kp index, proposed by Bartels, is an indicator of geomagnetic activity and is updated every three hours [32]. We checked the Kp value of DOY 180 in 2020; the maximum was 2 and the minimum was 0, which meant that the ionosphere was quiet on that day. Therefore, the DD ionospheric delay obtained by the LIM had high accuracy, and it did not affect the

tropospheric delay interpolation. Multipath effects, antenna phase center correction, and other errors were ignored.

The slant DD tropospheric delay between the auxiliary and master stations is calculated using Equation (3). The traditional LIM and modified LIM are then applied to obtain the slant DD tropospheric delay between the rover and master stations. The true value of *ZTD* between the rover and the master reference stations could be obtained using the latest Canadian Spatial Reference System precise point positioning (CSRS-PPP) service, provided by Natural Resources Canada [33]. Since the estimation accuracy could reach 0–2 cm [34,35], the slant DD tropospheric delay of each satellite pair calculated in combination with the mapping function could be used as the reference true value. The whole experiment was conducted in post-processing mode.

3.2. Analysis of Tropospheric Delay Interpolation Results with Dataset One

The triangular units of Dataset One were distributed in different areas, and the height distribution of the reference stations and rovers also had apparent differences. They were used to verify the effectiveness of the proposed method compared to the traditional LIM. The DD tropospheric delay was obtained using the CSRS-PPP as the true value. The values of the root mean square (RMS) of the tropospheric delay obtained by the two methods were analyzed and compared.

In each triangle unit, we selected different periods, different elevation angle changes, and three continuously observed satellites to analyze the effect of tropospheric interpolation. The results were obtained using both the traditional LIM and the modified LIM, which are denoted here as TLIM and MLIM. A comparison with the true value is shown in Figures 5–10.

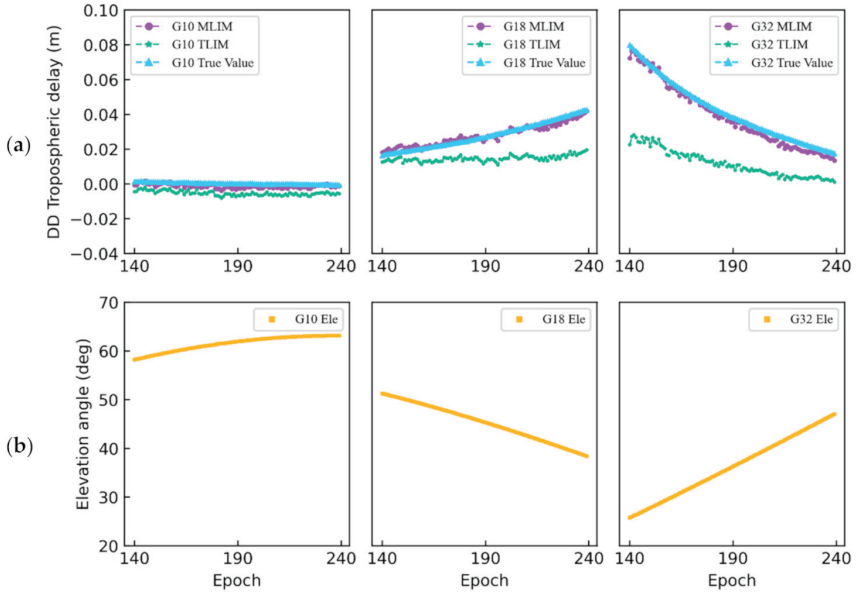

Figure 5. The DD tropospheric delay obtained by different methods (**a**) and elevation angles (**b**) for satellites G10, G18, and G32 at the rover station P478.

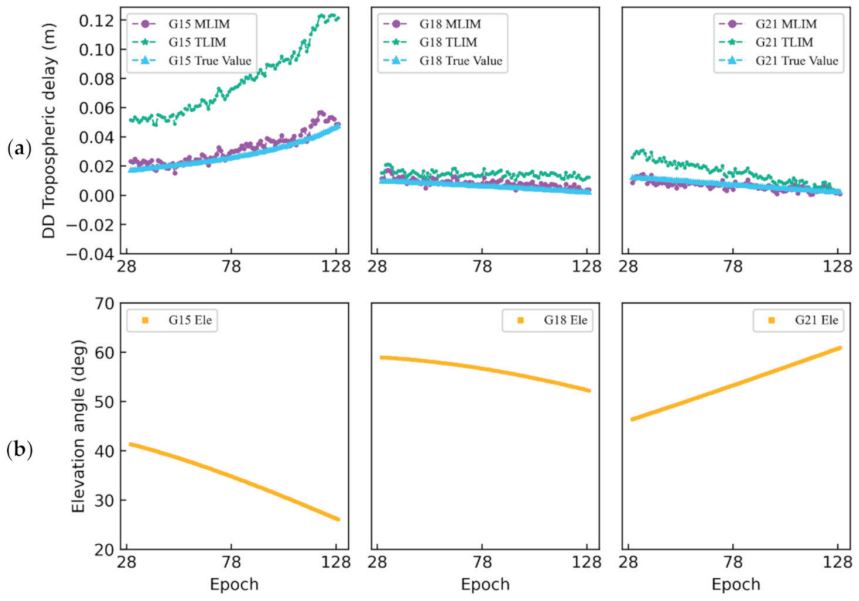

Figure 6. The DD tropospheric delay obtained by different methods (**a**) and elevation angles (**b**) for satellites G15, G18, and G21 at the rover station EWPP.

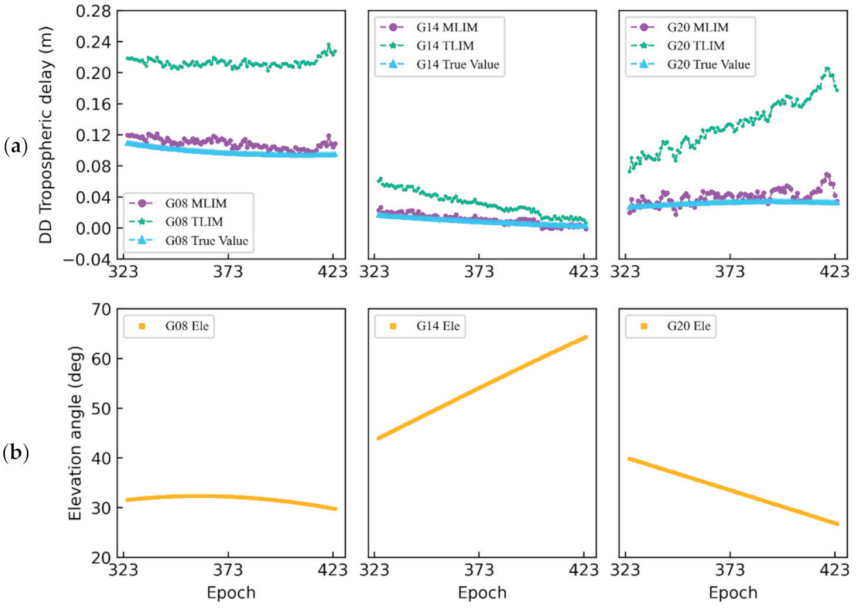

Figure 7. The DD tropospheric delay obtained by different methods (**a**) and elevation angles (**b**) for satellites G08, G14, and G20 at the rover station P603.

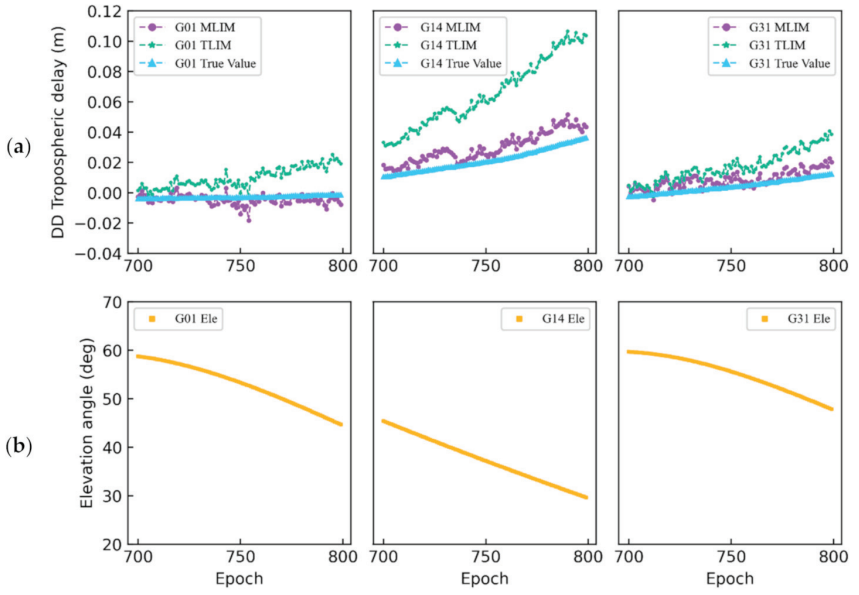

Figure 8. The DD tropospheric delay obtained by different methods (**a**) and elevation angles (**b**) for satellites G01, G14, and G31 at the rover station P225.

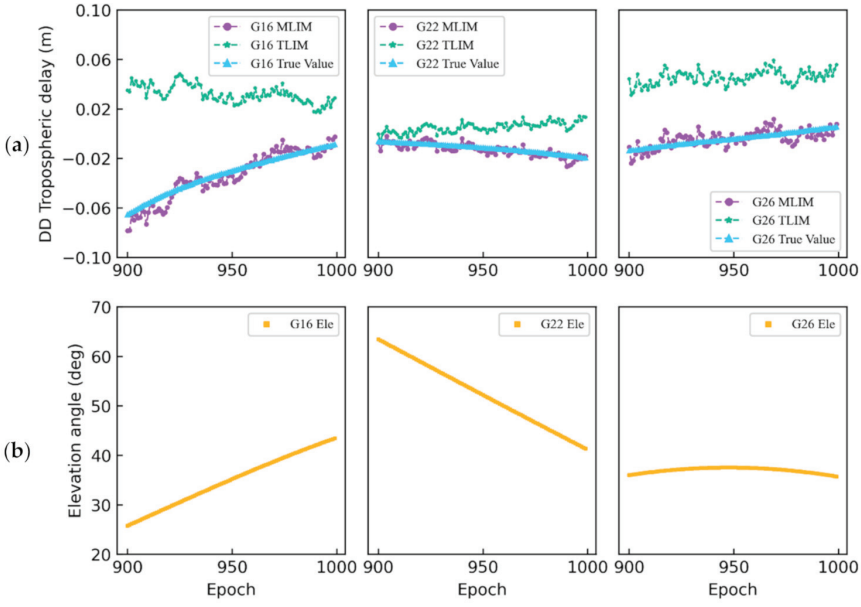

Figure 9. The DD tropospheric delay obtained by different methods (**a**) and elevation angles (**b**) for satellites G16, G22, and G26 at the rover station WINT.

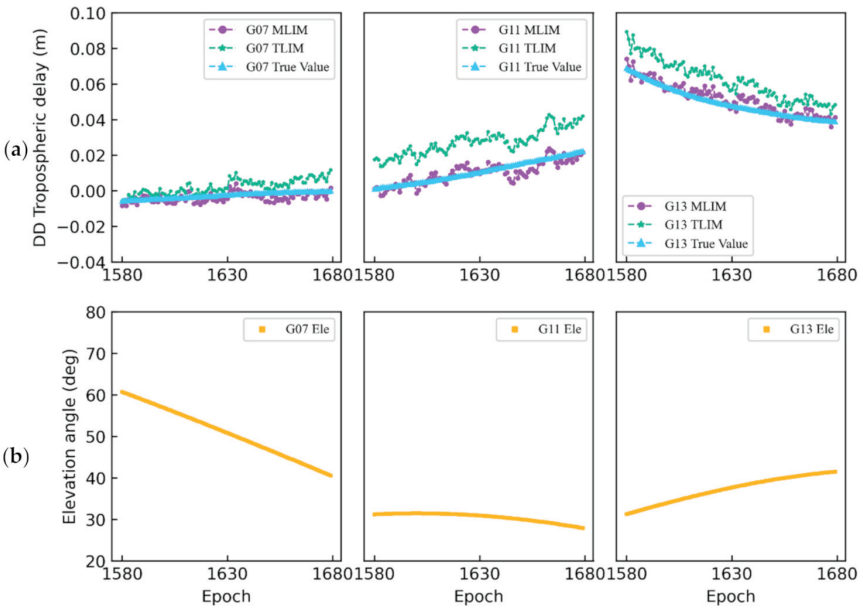

Figure 10. The DD tropospheric delay obtained by different methods (**a**) and elevation angles (**b**) for satellites G07, G11, and G13 at the rover station P121.

We selected three satellites with different elevation angle range changes on each rover for the analysis. The trend of elevation angle changes for these selected satellites was also different. Overall, from Figures 5–10, we can see that as the elevation angles of each satellite increased, the DD tropospheric delay became smaller, and vice versa. These selected satellites can be divided into three types: low-elevation, medium-elevation, and high-elevation angle satellites.

For high elevation angle satellites, we took G10, G18, and G14 in Figures 5–7 as examples. The DD tropospheric delay obtained using TLIM at the VRS had a slight offset from the true value. However, the DD tropospheric delay corrected using MLIM almost coincided with the true value. For G14, which had the largest elevation angle increase, the results of the proposed method were the most consistent with the true value.

Similarly, we took G18, G20, and G14 in Figures 5, 7 and 8 as medium elevation angle satellites for analysis. These three satellites showed a downward trend in the range of medium elevation angles. The offset between the DD tropospheric delay obtained by the TLIM and true value was obvious. As the elevation angles of these satellites decreased, these offsets became larger. The changing trend of the TLIM value and the true value was not the same. When MLIM was adopted, the offsets between the interpolation results of the MLIM and true value were mostly eliminated, and a better correction effect was obtained.

From Figures 7, 9 and 10, the low elevation angle satellites G08, G16, and G11 were analyzed. Their elevation angles were relatively low, and they showed almost no change trend. Therefore, their tropospheric delay change trends according to the TLIM, MLIM, and true values were not noticeable. However, their tropospheric delay values were considerable. This is because the lower the elevation, the longer the satellite signal propagation path becomes, and the delay of signal propagation will increase the range of the troposphere. The most significant offsets between TLIM and the true value occurred with this type of elevation satellite. Although the DD tropospheric delay obtained by the MLIM still had a small difference from the true value, it effectively eliminated this offset compared to the TLIM.

It can be seen that whether the DD tropospheric delay interpolated by the proposed method is from high elevation or low elevation satellites, the offset with the true value is smaller. For all of the satellites, the trend of the MLIM results was consistent with the true value.

The statistical analysis of the results of the TLIM and MLIM for each rover is shown in Figure 11. Overall, the RMS errors of the MLIM are smaller than those of the TLIM. This indicates that the accuracy of the interpolated tropospheric delay improved after applying the proposed method. The RMS errors of the MLIM on each continuously observed satellite showed a significant improvement. The maximum increases were achieved on the G32, G29, G08, G11, G16, and G11 satellites at stations P478, EWPP, P603, P225, WINT, and P121, respectively, with an improvement of 90.1%, 92.5%, 90.0%, 93.2%, 90.6%, and 78.5%.

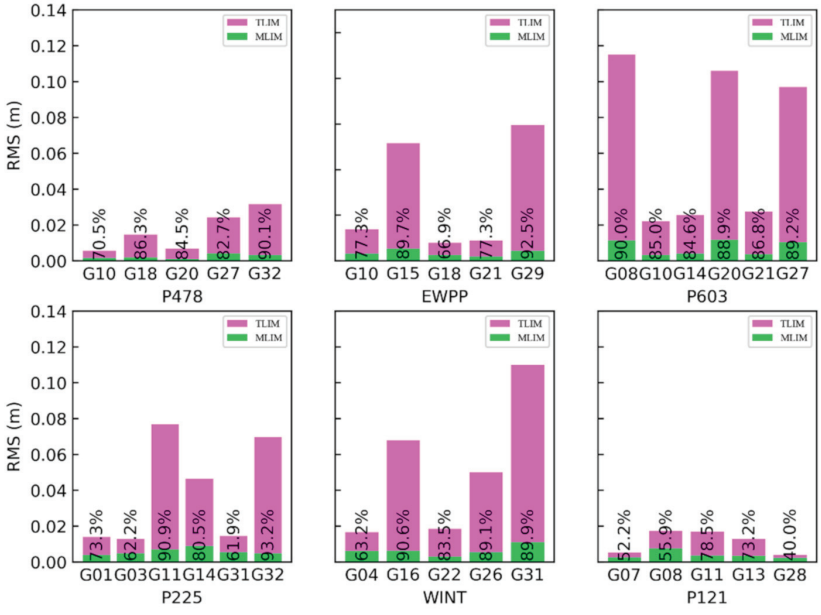

Figure 11. RMS errors of the DD tropospheric delay using modified and traditional methods for all non-reference satellites at all rover stations. The percentages on each bar are the improvements of the MILM with respect to the TLIM.

To analyze all tropospheric interpolation accuracies for all of the satellites with different elevation angles during the selected period for each rover, Figure 12 shows the TLIM and MLIM modeling error curves for all of the satellites with different elevation angles. Overall, from Figure 12, we can see the accuracy of the tropospheric modeling using TLIM increased with increasing satellite elevation. However, the accuracy of the MLIM was always better than that of the TLIM at any elevation interval. For low elevation satellites, the error of the TLIM was obvious. For example, the error forP603 reached 0.2 m, but the error from the MLIM was still minimal. The mean error values of the TLIM were 0.017 m, −0.027 m, 0.068 m, 0.029 m, 0.045 m, and 0.010 m, and the corresponding standard deviations (STD) were 0.014 m, 0.023 m, 0.048 m, 0.023 m, 0.031 m, and 0.006 m, respectively. The accuracy of the MLIM was significantly improved, especially for low elevation satellites. The mean errors of each rover were 0.002 m, 1.65×10^{-5} m, 0.007 m, 0.005 m, 0.005 m, and 0.003 m, and the corresponding STDs were 0.002 m, 0.004 m, 0.006 m, 0.004 m, 0.004 m, and 0.002 m, respectively. The discontinuous part in Figure 12 indicates that there were no visible or ambiguity fixed satellites within that elevation angle range.

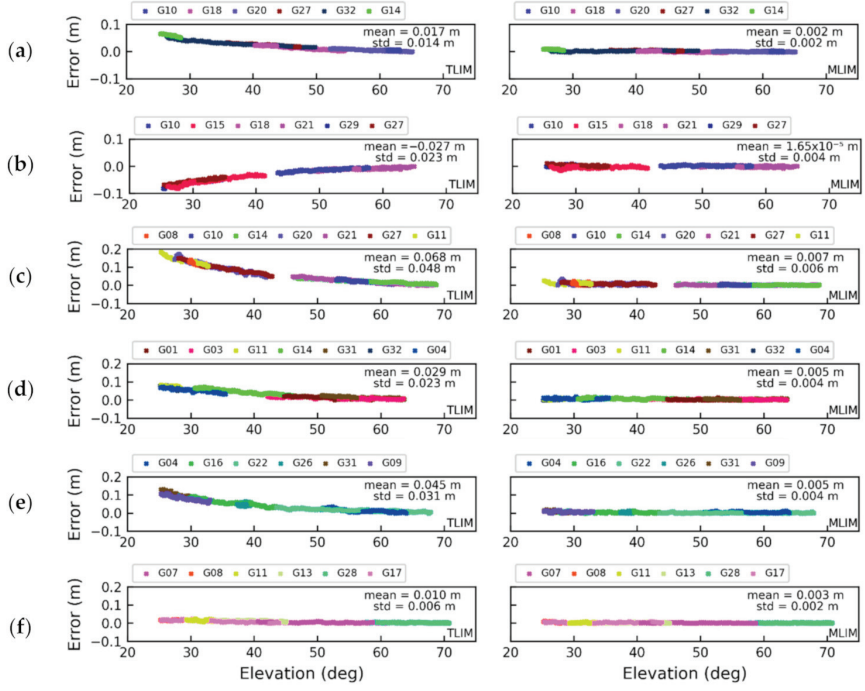

Figure 12. The DD tropospheric delay interpolation errors obtained by the TLIM and MLIM (left and right) with different satellite elevation angles at different rover stations: (**a**) P478, (**b**) EWPP, (**c**) P603, (**d**) P225, (**e**) WINT, and (**f**) P121.

The mean RMS errors of the DD tropospheric delay obtained by the two methods for all satellites are listed in Table 1. The statistical analysis showed that the RMS of the TLIM reached tens of centimeters, while the RMS of the interpolation using the proposed method was only several millimeters. The improvement reached 87.5%, 87.9%, 89.5%, 85.4%, 87.9%, and 66.7%, respectively. This indicated that the modified algorithm performed better than the traditional algorithm, especially for satellites with lower elevation angles.

Table 1. The mean RMS and improvement percentage of the interpolated DD tropospheric delay using the TLIM and MLIM at each rover station in Dataset One.

Station ID	P478	EWPP	P603	P225	WINT	P121
TLIM RMS (m)	0.024	0.033	0.076	0.041	0.058	0.012
MLIM RMS (m)	0.003	0.004	0.008	0.006	0.007	0.004
Improvement (%)	87.5	87.9	89.5	85.4	87.9	66.7

3.3. Analysis of the Tropospheric Delay Interpolation Results with Dataset Two

Dataset Two only had one triangle unit, but it contained four rovers with different elevations. We also compared and analyzed the performance of the TLIM and MLIM at these stations.

We selected three identical satellites, G10, G18, and G27, at these four rovers to analyze the effect tropospheric interpolation during the same period. The results are illustrated in Figure 13.

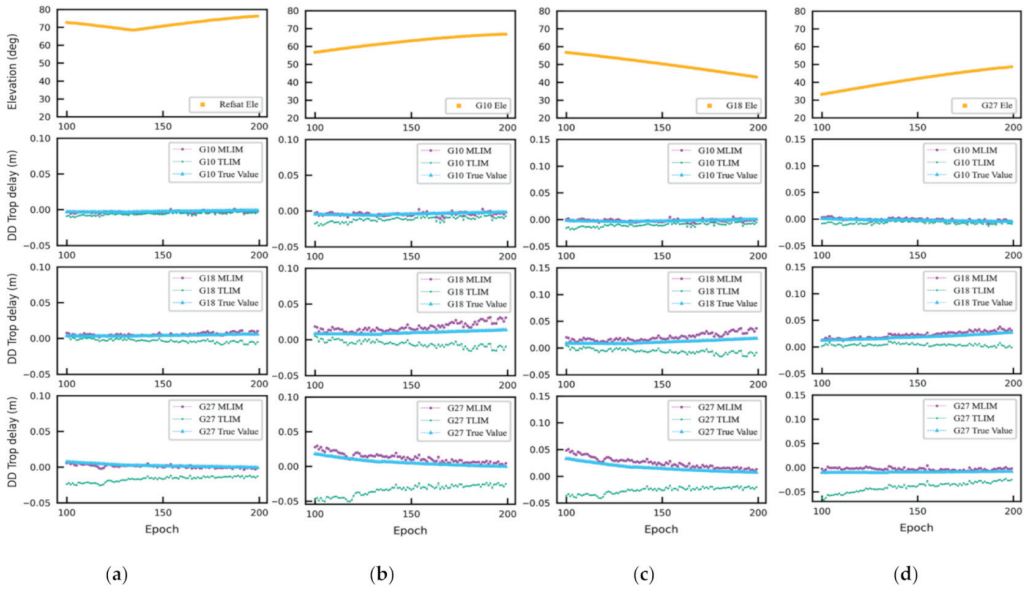

Figure 13. Elevation angles (upper row) for the reference satellites G10, G18, and G27. The DD tropospheric delay obtained using the TLIM and the PPP method (three lower rows) at different rover stations: (**a**) P532, (**b**) P539, (**c**) P602, and (**d**) MASW.

As shown in Figure 13, the interpolated DD tropospheric delay by the MLIM was highly consistent with the true value for G10 at the highest elevation. For G18, which had an elevation angle on a downward trend, although there were still some deviations compared to the true value, the MLIM results were also closer to the true value. Analyzing the satellite G27, although its elevation angle was increasing, it had the lowest elevation angle among the three satellites. Its TLIM results showed that the effect of directly interpolating the tropospheric delay was not satisfactory. However, after adopting the MLIM, the value of the DD tropospheric delay interpolation was consistent with the true value. Therefore, the modified interpolation method had a better correction effect, even for low-elevation satellites.

The RMS of the DD tropospheric delays obtained using the TLIM and MLIM for each rover during the selected period are shown in Figure 14. The maximum improvement values of the MLIM at the four rovers compared to the TLIM were 93.0%, 83.4%, 78.3%, and 79.3%, respectively.

Further, troposphere modeling errors for all of the satellites over the selected observation period are shown in Figure 15. The mean errors of the TLIM were 0.011 m, 0.027 m, 0.029 m, and 0.021 m, and the corresponding STDs were 0.010 m, 0.027 m, 0.029 m, and 0.020 m, respectively. The accuracy of the MLIM was dramatically improved, with mean errors of −0.002 m, −0.006 m, 0.009 m, and 0.006 m, and the corresponding STDs were 0.007 m, 0.007 m, 0.008 m, and 0.006 m, respectively.

The mean RMS of the DD tropospheric delay using the traditional and the modified methods for all of satellites in Dataset Two is shown in Table 2. It can be seen that the mean RMS error of the TLIM of each station, P532, P539, P602, and MASW, were 0.012 m, 0.033 m, 0.035 m, and 0.026 m, respectively. However, the mean RMS error of the MLIM were 0.005 m, 0.008 m, 0.010 m, and 0.007 m. These values represent improvements of 58.3%, 75.6%, 71.4%, and 73.1%, respectively, which are consistent with the requirements of the accuracy of DD tropospheric delay interpolation that need to be met in order to generate VRS observations in the NRTK.

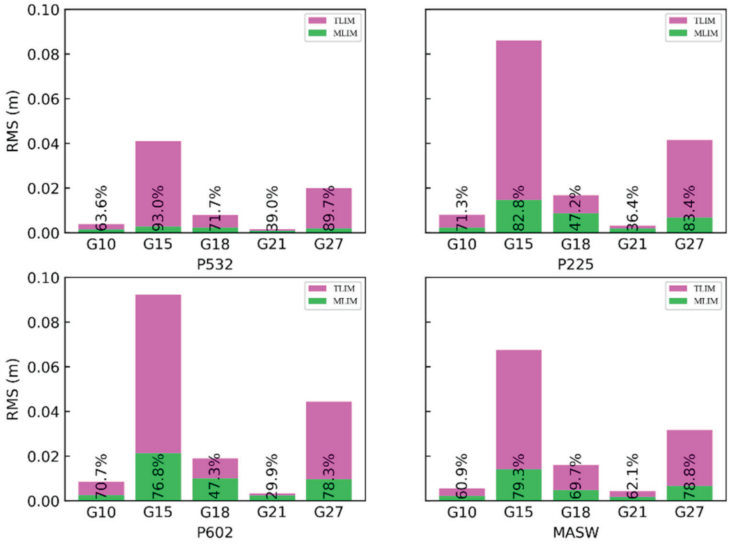

Figure 14. RMS errors of the DD tropospheric delay using modified and traditional methods for all non-reference satellites at all rover stations. The percentages on each bar are the improvements of the MILM with respect to the TLIM.

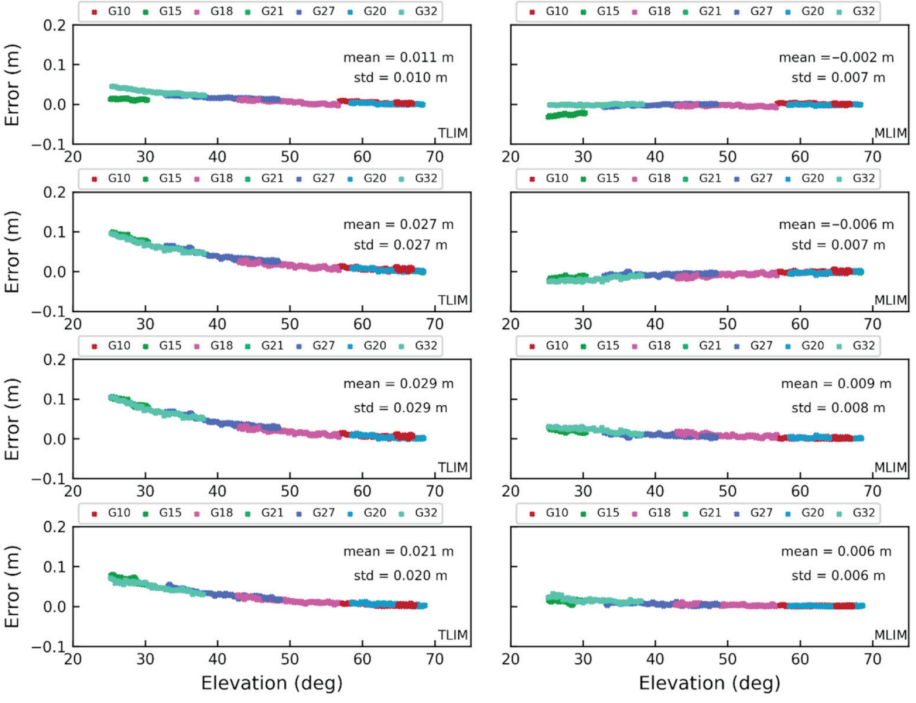

Figure 15. DD tropospheric delay interpolation errors obtained by the TLIM and MLIM (left and right) with different satellite elevation angles at different rover stations (from top to bottom): P532, P539, P602, and MASW.

Table 2. The mean RMS errors and improvement percentage of the interpolated DD tropospheric delay using the TLIM and MLIM at each rover station in Dataset Two.

Station ID		P532	P539	P602	MASW
	TLIM RMS (m)	0.012	0.033	0.035	0.026
	MLIM RMS (m)	0.005	0.008	0.010	0.007
	Improvement (%)	58.3	75.6	71.4	73.1

3.4. Comparison of the Positioning Results of Dataset One and Dataset Two

According to the proposed and traditional tropospheric interpolation delay results, the positioning performance of these rovers using the VRS was investigated in this section. The DD tropospheric delay was obtained through both the TLIM and MLIM. We then used these interpolated atmospheric delays to generate virtual carrier phase and pseudorange observations, which were applied to the final rover positioning. The RMS errors of the positioning results were analyzed in this paper. We expected that the proposed method would show a better positioning performance, especially in the up component and under significant height differences.

3.4.1. Dataset One

The positioning error of the TLIM and MLIM is shown in Figure 16, using station P225 as an example. It can be seen that the positioning error of the MLIM showed a significant improvement in the up component. However, there was little difference between the TLIM and MLIM in the horizontal direction. Only the results of the fixed solutions were counted here, and the MLIM had more fixed solutions than the TLIM. The positioning results of each rover in Dataset One are given in Table 3. In terms of the RMS, the accuracy in the three directions for all of the rovers was improved after using the MLIM. There were slight improvements in the horizontal direction, but remarkable improvements were achieved in the up component. All the RMS errors of the up component obtained using the MLIM were within 5 cm. The most obvious improvement occurred at P603, in which the accuracy of the RMS, changing from 24.95 cm to 4.24 cm, improved by 83%. It can be seen from Figure 16 that the positioning result became more stable after the proposed method was applied.

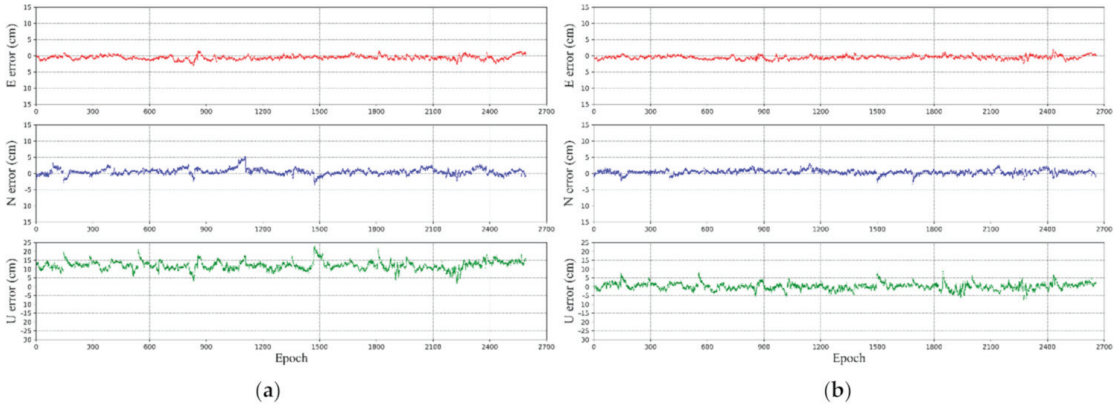

Figure 16. The TLIM (**a**) and MLIM (**b**) positioning errors with respect to the epoch during the selected data period at rover P225.

Table 3. Positioning RMS statistical results of each rover station in Dataset One.

Station ID			Accuracy (cm) E	N	U
P478	RMS	TLIM	0.74	0.93	11.59
		MLIM	0.63	0.76	3.42
EWPP	RMS	TLIM	0.91	1.05	12.91
		MLIM	0.79	0.89	2.67
P603	RMS	TLIM	1.35	1.76	24.95
		MLIM	0.94	1.05	4.24
P225	RMS	TLIM	0.85	1.08	12.34
		MLIM	0.75	0.79	1.96
WINT	RMS	TLIM	0.96	1.21	13.36
		MLIM	0.87	0.72	4.32
P121	RMS	TLIM	0.76	1.07	4.42
		MLIM	0.78	1.07	2.65

3.4.2. Dataset Two

Similarly, taking MASW as an example, it can be seen from Figure 17 that the accuracy improvement in the up direction was obvious. Table 4 shows the statistical positioning results of all of the rovers in Dataset Two. Analyzing the RMS results of the four rover stations, the accuracy of the TLIM was within 2 cm in the east and north directions. The accuracy of the up component was about 17 cm. After applying the MLIM, the positioning accuracy of all rovers was within 1 cm in the east and north directions. The accuracy in the up direction was within 5 cm, reaching the general accuracy level of the NRTK positioning. Figure 17 and Table 4 showed that in the case of the height distribution of Dataset Two, the positioning results using the modified interpolation methods were reliable and stable. %clearpage

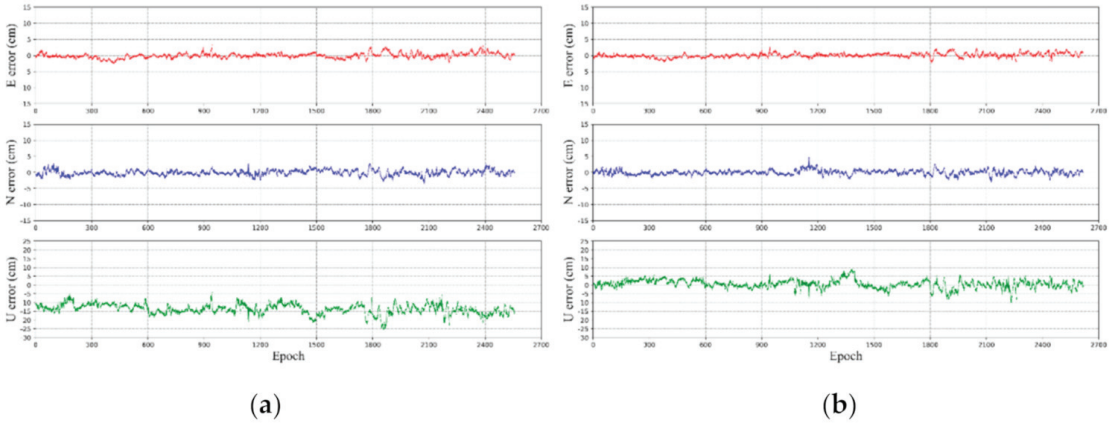

Figure 17. TLIM (**a**) and MLIM (**b**) positioning errors with respect to the epoch during the selected data period at rover MASW.

Table 4. Positioning RMS statistical results of each rover station in Dataset Two.

Station ID			Accuracy (cm) E	N	U
P532	RMS	TLIM	0.74	0.74	6.91
		MLIM	0.77	0.64	1.44
P539	RMS	TLIM	0.93	1.13	16.05
		MLIM	0.83	0.84	3.28
P602	RMS	TLIM	0.77	1.03	17.22
		MLIM	0.67	0.77	4.01
MASW	RMS	TLIM	0.80	0.85	14.04
		MLIM	0.67	0.76	2.48

The results of these experiments demonstrate that the accuracy of the traditional LIM DD tropospheric delay at the VRS deteriorates when a relatively significant height difference exists between the rover and the reference stations. The results also confirm that as the satellite elevation angle drops, the delay of the satellite signal passing through the troposphere increases, and the effect of interpolating the tropospheric delay will worsen.

It can be seen from these results that the more significant the height difference between the rover and the reference station, the worse the tropospheric accuracy obtained by using TLIM is, and the better the correction effect by using MLIM is. The average RMS error of the conventional method was 0.035 m. The MLIM's average RMS was only 0.006 m.

According to the results when using VRS observations for rover positioning, the modified method showed a slight improvement in the horizontal direction compared to the traditional method. However, the accuracy of the proposed method was significantly improved in the vertical direction. Therefore, when building or selecting reference station sites, one should thoroughly consider whether the height distribution of the reference station is approximately consistent. In addition, the height difference between the potential users and the reference stations should be as small as possible. Otherwise, a method similar to the MLIM should be used to solve the impact of the height difference in the NRTK.

It should be noted that this experiment only verified that a considerable height difference between the reference station and the rover would cause systematic errors when modeling the DD tropospheric delay in the NRTK. The heights of the reference stations and the rovers were quite different: Dataset One was from −29 m to about 1900 m, and Dataset Two was from 34 m to 713 m. The maximum height difference between the rover and reference stations of each triangle unit is from 245 m to 1158 m in Dataset One, and the maximum height difference is from 499 m to 679 m in Dataset Two. In addition, when the LIM is used to interpolate the atmospheric delay, the spatial distance and height difference between the rover and each reference station should be treated as the weighting factor for interpolating the DD tropospheric delay in each triangle unit. This perspective should be studied through further experiments in the future.

4. Conclusions

This study confirmed that a height difference between reference stations and rovers leads to a decrease of interpolation DD tropospheric delay accuracy. Therefore, based on the tropospheric delay correction model and traditional LIM, we proposed the MLIM correction method for the triangular VRS mode. This method corrects the systematic error of the tropospheric delay caused by height differences in advance. It then applies the LIM to interpolate the corrected value to obtain the DD tropospheric delay between the rover and the master stations. We compared the accuracy of TLIM and MLIM by modeling the DD tropospheric delay by using two datasets of triangular units in VRS mode. Finally, the positioning performance of the two methods was evaluated.

In the first experiment, we selected six independent triangular units in different areas. The accuracy of the DD tropospheric delay modeling, which used traditional LIM, was

inferior. This phenomenon is evident for satellites with low elevation angles. Compared to traditional LIM, the accuracy of interpolated DD tropospheric delay was significantly improved after using the modified method, especially for the satellites with lower elevation angles. The second experiment considered only one triangular unit, but it included rover stations with different elevation distributions. From the perspective of the tropospheric interpolation results, as the height of each rover increased, the accuracy of the tropospheric interpolation using the conventional method deteriorated. After adopting the MLIM, the RMS error was significantly improved.

In terms of positioning performance, the up component accuracy obtained by the TLIM showed a noticeable systematic deviation, and the worst results in the two datasets could still reach the decimeter level. However, this situation improved significantly after using the MLIM, and the positioning results of all of stations in the up direction reached just a few centimeters. In the horizontal direction, although the accuracy of the proposed algorithm was similar to that of the traditional algorithm, there was still a slight improvement. In addition, the positioning result of the proposed method is more stable than that of the conventional method.

In summary, the proposed method significantly improved the tropospheric delay interpolation and the positioning performance in the NRTK triangulation network. It should be noted that this paper only analyzed the influence of the DD tropospheric delay interpolation in the NRTK where the height distribution of the reference stations and the rover stations were quite different, and further research should be devoted to investigating how the height difference of the reference stations and the spatial distance between the rover and reference stations can affect the DD tropospheric interpolation accuracy in the NRTK.

Author Contributions: Y.P. provided the initial idea and wrote the manuscript; Y.P. and M.S. designed and performed the research; M.S. helped with the writing and revising, and Y.Y. and M.S. partially financed the research. All authors have read and agreed to the published version of the manuscript.

Funding: This work was supported by the National Key Research Program (No. 2016YFB0501900) and China Natural Science Funds (No. 41604033 and 41874093). The third author is supported by the Wang Kuancheng Pioneer Talents Project Lu Jiaxi International Team Program.

Institutional Review Board Statement: Not applicable.

Informed Consent Statement: Not applicable.

Data Availability Statement: Publicly available datasets were analyzed in this study. The GPS observation data from the NOAA CORS network are available at https://www.ngs.noaa.gov/UFCORS/ (accessed on 26 April 2021). The GPS broadcast ephemeris data are available at https://cddis.nasa.gov/archive/gnss/data/daily/ (accessed on 26 April 2021). The GIM products from IGS can be obtained at https://cddis.nasa.gov/archive/gnss/products/ionex/ (accessed on 26 April 2021).

Acknowledgments: The authors gratefully acknowledged the Canadian Spatial Reference System Precise Point Positioning (CSRS-PPP) service, the NOAA CORS network for providing the GNSS data, and the IGS for providing the GIM products.

Conflicts of Interest: The authors declare no conflict of interest.

References

1. Wanninger, L. Virtual reference stations (VRS). *GPS Solut.* **2003**, *7*, 143–144. [CrossRef]
2. Bakuła, M.; Przestrzelski, P.; Kaźmierczak, R. Reliable technology of centimeter GPS/GLONASS surveying in forest environments. *IEEE Trans. Geosci. Remote Sens.* **2014**, *53*, 1029–1038. [CrossRef]
3. Paziewski, J.; Sieradzki, R.; Baryla, R. Multi-GNSS high-rate RTK, PPP and novel direct phase observation processing method: Application to precise dynamic displacement detection. *Meas. Sci. Technol.* **2018**, *29*, 035002. [CrossRef]
4. Hu, G.R.; Khoo, H.S.; Goh, P.C.; Law, C.L. Development and assessment of GPS virtual reference stations for RTK positioning. *J. Geod.* **2003**, *77*, 292–302. [CrossRef]

5. Chen, X.; Han, S.; Rizos, C.; Goh, P.C. Improving real time positioning efficiency using the Singapore integrated multiple reference station network (SIMRSN). In Proceedings of the 13th International Technical Meeting of the Satellite Division of the Institute of Navigation (ION GPS 2000), Salt Lake City, UT, USA, 19–22 September 2000.
6. Wanninger, L. Improved ambiguity resolution by regional differential modelling of the ionosphere. In Proceedings of the 8th International Technical Meeting of the Satellite Division of The Institute of Navigation (ION GPS 1995), Palm Springs, CA, USA, 12–15 September 1995.
7. Wanninger, L. The performance of virtual reference stations in active geodetic GPS-networks under solar maximum conditions. In Proceedings of the 12th International Technical Meeting of the Satellite Division of The Institute of Navigation (ION GPS 1999), Nashville, TN, USA, 14–17 September 1999.
8. Han, S.; Rizos, C. GPS network design and error mitigation for real-time continuous array monitoring systems. In Proceedings of the 9th International Technical Meeting of the Satellite Division of The Institute of Navigation (ION GPS 1996), Kansas City, MO, USA, 17–20 September 1996.
9. Gao, Y.; Li, Z.; McLellan, J. Carrier phase based regional area differential GPS for decimeter-level positioning and navigation. In Proceedings of the 10th International Technical Meeting of the Satellite Division of The Institute of Navigation (ION GPS 1997), Kansas City, MO, USA, 16–19 September 1997.
10. Wübbena, G.; Bagge, A.; Seeber, G.; Böder, V.; Hankemeier, P. Reducing distance dependent errors for real-time precise DGPS applications by establishing reference station networks. In Proceedings of the 9th International Technical Meeting of the Satellite Division of The Institute of Navigation (ION GPS 1996), Kansas City, MO, USA, 17–20 September 1996.
11. Odijk, D.; Marel, H.V.D.; Song, I. Precise GPS Positioning by Applying Ionospheric Corrections from an Active Control Network. *GPS Solut.* **2000**, *3*, 49–57. [CrossRef]
12. Marel, H.V. Virtual GPS reference stations in the Netherlands. In Proceedings of the 11th International Technical Meeting of the Satellite Division of The Institute of Navigation (ION GPS 1998), Nashville, TN, USA, 15–18 September 1998.
13. Odijk, D. Fast precise GPS positioning in the presence of ionospheric delays. *Publ. Geod.* **2002**, *52*.
14. Dai, L.; Han, S.; Wang, J.; Rizos, C. Comparison of interpolation algorithms in network-based GPS techniques. *NAVIGATION J. Inst. Navig.* **2003**, *50*, 277–293. [CrossRef]
15. Fotopoulos, G.; Cannon, M. An overview of multi-reference station methods for cm-level positioning. *GPS Solut.* **2001**, *4*, 1–10. [CrossRef]
16. Wu, S. Performance of regional atmospheric error models for NRTK in GPSnet and the implementation of a NRTK system. *RMIT Univ. Aust.* **2009**.
17. Al-Shaery, A.; Lim, S.; Rizos, C. Investigation of different interpolation models used in Network-RTK for the virtual reference station technique. *J. Glob. Position. Syst.* **2011**, *10*, 136–148. [CrossRef]
18. Huang, L.; Liu, L.; Yao, C. A zenith tropospheric delay correction model based on the regional CORS network. *Geod. Geodyn.* **2012**, *3*, 53–62.
19. Wielgosz, P.; Cellmer, S.; Rzepecka, Z.; Paziewski, J.; Grejner-Brzezinska, D.A. Troposphere modeling for precise GPS rapid static positioning in mountainous areas. *Meas. Sci. Technol.* **2011**, *22*, 045101. [CrossRef]
20. Yin, H.; Huang, D.; Xiong, Y. Regional tropospheric delay modeling based on GPS reference station network. In *VI Hotine-Marussi Symposium on Theoretical and Computational Geodesy*; Springer: Berlin/Heidelberg, Germany, 2008.
21. Landau, H.; Vollath, U.; Chen, X. Virtual reference stations versus broadcast solutions in network RTK–advantages and limitations. In Proceedings of the GNSS, Graz, Austria, 22–24 April 2003.
22. Wu, B.; Gao, C.; Pan, S.; Deng, J.; Gao, W. Regional modeling of atmosphere delay in network rtk based on multiple reference station and precision analysis. In Proceedings of the China Satellite Navigation Conference (CSNC) 2015 Proceedings, Xi'an, China, 13–15 May 2015; Springer: Berlin/Heidelberg, Germany, 2015; Volume II.
23. Lei, Q.; Lei, L.; Zemin, W. An tropospheric delay model for GPS NET RTK. In Proceedings of the 2010 Second International Conference on Information Technology and Computer Science, Kiev, Ukraine, 24–25 July 2010.
24. Hu, G.; Abbey, D.A.; Castleden, N.; Featherstone, W.E.; Earls, C.; Ovstedal, O.; Weihing, D. An approach for instantaneous ambiguity resolution for medium-to long-range multiple reference station networks. *GPS Solut.* **2005**, *9*, 1–11. [CrossRef]
25. Klobuchar, J.A. Ionospheric effects on GPS. *Glob. Position. Syst. Theory Appl.* **1991**, *1*, 517–546.
26. Vstedal, O. Absolute Positioning with Single-Frequency GPS Receivers. *GPS Solut.* **2002**, *5*, 33–44. [CrossRef]
27. Leandro, R.F.; Langley, R.B.; Santos, M.C. UNB3m_pack: A neutral atmosphere delay package for radiometric space techniques. *GPS Solut.* **2008**, *12*, 65–70. [CrossRef]
28. Niell, A.E. Global Mapping Functions for the Atmosphere Delay at Radio Wavelengths. *J. Geophys. Res. Solid Earth* **1996**, *101*, 3227–3246. [CrossRef]
29. Zhang, J.; Lachapelle, G. Precise estimation of residual tropospheric delays using a regional GPS network for real-time kinematic applications. *J. Geod.* **2001**, *75*, 255–266. [CrossRef]
30. Teunissen, P.J.G. The least-square ambiguity decorrelation adjustment: A method for fast GPS ambiguity estimation. *J. Geod.* **1995**, *70*, 1–2. [CrossRef]
31. Yao, Y.; Xu, X.; Xu, C.; Peng, W.; Wan, Y. Establishment of a Real-Time Local Tropospheric Fusion Model. *Remote Sens.* **2019**, *11*, 1321. [CrossRef]
32. Bartels, J. The technique of scaling indices K and Q of geomagnetic activity. *Ann. Intern. Geophys.* **1957**, *4*, 215–226.

33. Mireault, Y.; Tétreault, P.; Lahaye, F.; Héroux, P.; Kouba, J. Online precise point positioning. *GPS World* **2008**, *19*, 59–64.
34. Guo, Q. Precision comparison and analysis of four online free PPP services in static positioning and tropospheric delay estimation. *GPS Solut.* **2015**, *19*, 537–544. [CrossRef]
35. Xiao, G.; Liu, G.; Ou, J.; Liu, G.; Wang, S.; Guo, A. MG-APP: An open-source software for multi-GNSS precise point positioning and application analysis. *GPS Solut.* **2020**, *24*, 1–13. [CrossRef]

remote sensing

MDPI

Article

A New Approach for the Development of Grid Models Calculating Tropospheric Key Parameters over China

Ge Zhu [1], Liangke Huang [1,*], Lilong Liu [1], Chen Li [2], Junyu Li [1], Ling Huang [1], Lv Zhou [1] and Hongchang He [1]

[1] College of Geomatics and Geoinformation, Guilin University of Technology, Guilin 541004, China; zhuge@glut.edu.cn (G.Z.); Lllong99@glut.edu.cn (L.L.); junyu_li@whu.edu.cn (J.L.); linghuang@glut.edu.cn (L.H.); zhoulv@glut.edu.cn (L.Z.); hhe@glut.edu.cn (H.H.)

[2] Beidou Navigation Department, Natural Resources Information Center of Guangxi Zhuang Autonomous Region, Nanning 530028, China; 2120191097@glut.edu.cn

* Correspondence: lkhuang@whu.edu.cn

Abstract: Pressure, water vapor pressure, temperature, and weighted mean temperature (T_m) are tropospheric parameters that play an important role in high-precision global navigation satellite system navigation (GNSS). As accurate tropospheric parameters are obligatory in GNSS navigation and GNSS water vapor detection, high-precision modeling of tropospheric parameters has gained widespread attention in recent years. A new approach is introduced to develop an empirical tropospheric delay model named the China Tropospheric (CTrop) model, providing meteorological parameters based on the sliding window algorithm. The radiosonde data in 2017 are treated as reference values to validate the performance of the CTrop model, which is compared to the canonical Global Pressure and Temperature 3 (GPT3) model. The accuracy of the CTrop model in regards to pressure, water vapor pressure, temperature, and weighted mean temperature are 5.51 hPa, 2.60 hPa, 3.09 K, and 3.35 K, respectively, achieving an improvement of 6%, 9%, 10%, and 13%, respectively, when compared to the GPT3 model. Moreover, three different resolutions of the CTrop model based on the sliding window algorithm are also developed to reduce the amount of gridded data provided to the users, as well as to speed up the troposphere delay computation process, for which users can access model parameters of different resolutions for their requirements. With better accuracy of estimating the tropospheric parameters than that of the GPT3 model, the CTrop model is recommended to improve the performance of GNSS positioning and navigation.

Keywords: GNSS positioning; GNSS meteorology; MERRA-2; sliding window algorithm; tropospheric parameters; GNSS

Citation: Zhu, G.; Huang, L.; Liu, L.; Li, C.; Li, J.; Huang, L.; Zhou, L.; He, H. A New Approach for the Development of Grid Models Calculating Tropospheric Key Parameters over China. *Remote Sens.* **2021**, *13*, 3546. https://doi.org/10.3390/rs13173546

Academic Editor: Stefania Bonafoni

Received: 6 August 2021
Accepted: 4 September 2021
Published: 6 September 2021

1. Introduction

Tropospheric delay is one of the major factors affecting global navigation satellite system (GNSS) positioning. The vertical distribution of tropospheric parameters is strongly affected by Earth's gravity. It is difficult to accurately monitor and invert the description and modeling of tropospheric parameters under the influence of many factors. In the geodetic analysis of GNSS and Very Long Baseline Interferometry (VLBI) observations, the slant tropospheric delays are generally mapped into the zenith direction (zenith tropospheric delay, ZTD) through mapping functions. The ZTD is separated into two parts, namely, the zenith hydrostatic delay (ZHD) and the zenith wet delay (ZWD). The ZHD is usually calculated by the Saastamoinen model [1] from surface pressure measurements. The ZWD is estimated in the data analysis or approximated by models such as the Saastamoinen model, which uses parameters such as the temperature and water vapor pressure as input. Furthermore, the weighted mean temperature (T_m) is also an essential parameter that is indispensable in obtaining precipitable water vapor (PWV) from the zenith wet delay. Therefore, pressure, water vapor pressure, temperature, and T_m are key parameters that are used as input data to obtain tropospheric delay information. It is of great significance to

monitor temperature, pressure, water vapor pressure, T_m, and other tropospheric parameters for high-precision GNSS positioning and navigation, as well as GNSS meteorologic applications [2,3].

In addition, floods and droughts have been caused by extreme weather frequently. Severe weather, such as strong regional convection, and large-scale climate anomalies have brought on heavy economic losses and casualties in recent years [4–6]. With increasing requirements for high-precision GNSS positioning, and in-depth research in fields such as climate change and extreme weather generation mechanisms, the demand for real-time and high-spatiotemporal-resolution tropospheric parameters is increasing.

There are two main types of tropospheric parameter models according to the methods used for modeling. The Hopfield model [7], Saastamoinen model, and Black model [8] are the classic tropospheric delay models which are based on in situ meteorological parameters. Since conventional GNSS receivers are unavailable for measurements, the use of the aforementioned classic tropospheric delay models is restricted to a certain extent. As space technologies such as GNSS and VLBI are widely used in the navigation and guidance of various space vehicles as well as for the needs of climate change and weather forecasting, the real-time and high spatial resolution of meteorological parameters are particularly important [9].

Therefore, developing regional or global empirical tropospheric delay models based on atmosphere analysis data has attracted widespread attention [10–16]. Empirical meteorological models, such as the University of New Brunswick (UNB) models [17,18], the European Geo-stationary Navigation Overlay System (EGNOS) model [19], the TropGrid model [20,21], and the GPT models [22–25] have been developed, aimed at directly obtaining high-precision tropospheric parameters through the model without measured meteorological parameters. The UNB3 model was stored by tabulated meteorological data, which divides the latitude into five intervals. The EGNOS model was established by simplifying the UNB3 model, and the formula is different from that of the UNB3 model. Only the day of the year (DOY) and the location of the station are needed when applying this model, which is used in GNSS satellite navigation enhancement systems. The authors of [20] developed the TropGrid model considering the diurnal variations of parameters, but neglect the semiannual variations. The GPT model was established based on the ERA-40 reanalysis data. However, the GPT model only considers the annual variations of the parameters. The authors of [23] developed the GPT2 model, which considers the semiannual variations of parameters, by analyzing 10-year ECMWF ERA-Interim data with resolutions of $5^\circ \times 5^\circ$ and $1^\circ \times 1^\circ$. Considered to be the tropospheric model with the highest precision for quite a long time, two meteorological parameters were added to the GPT2w model based on GPT2. GPT3 is the latest generation model for an upgraded version of GPT2w. Two parameters of gradients in the east and north direction were added to the GPT3 model [26,27].

The aforementioned tropospheric delay models have performed well in GNSS meteorology. In this work, a new approach is introduced to develop an empirical tropospheric delay model providing meteorological parameters based on the second modern-era retrospective analysis for research and applications (MERRA-2) data. The new empirical model could be used to serve real-time GNSS positioning and navigation.

2. Data and Methods

2.1. Radiosonde Data

The radiosonde data provide measured meteorological parameters from the ground to a height of about 30 km at more than 1500 stations around the world. There are 89 radiosonde stations over China as shown in Figure 1. The radiosonde data are obtained based on the actual measurements of meteorological sensors on the sounding balloon, which has high accuracy and credibility. However, radiosonde balloons are extremely susceptible to other disturbance factors, such as weather factors and clouds, during the ascent. Different types of sounding sensors show their own system deviations, as well as

equipment failures, which lead to phenomena such as missing data. Although radiosonde data shows some disadvantages, they are still widely used to validate measurement results [27,28].

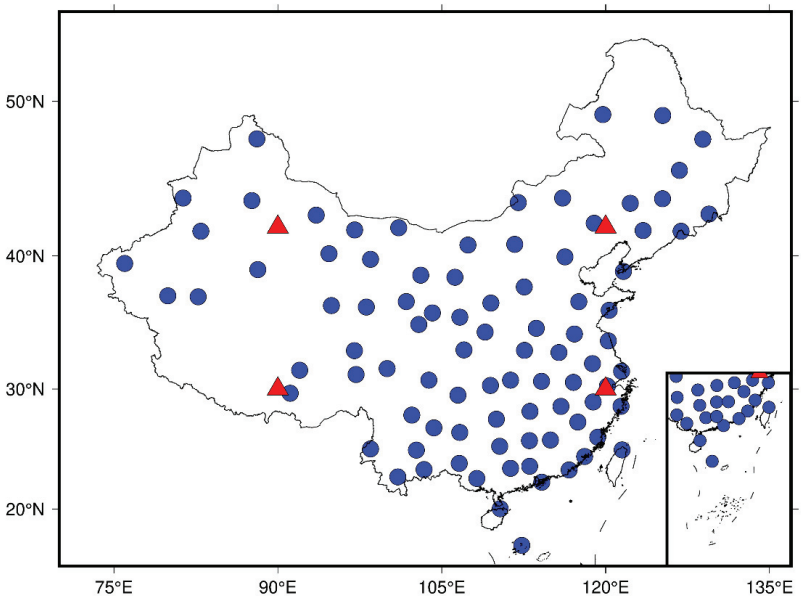

Figure 1. Distribution of 89 radiosonde stations over China. Blue dots are radiosonde stations, and red triangles are representative grid points.

2.2. MERRA-2 Reanalysis Product Data

MERRA-2 is the latest atmospheric reanalysis product comprising of data beginning in 1980. It is provided by the National Aeronautics and Space Administration (NASA) [29,30] with a spatial resolution of 0.625° × 0.5° (lon. × lat.) and a temporal resolution of 6 h. MERRA-2 replaces the original MERRA reanalysis dataset using an upgraded version of the Goddard Earth Observing System Model, Version 5 (GEOS-5) data assimilation system [31], and the Gridpoint Statistical Interpolation (GSI) analysis scheme [32–34]. It is also the first long-term global reanalysis product that assimilates space-based observations of aerosols in the climate system and represents their interactions with physical processes [34]. In addition, MERRA-2 tends to minimize the spurious variations related to inhomogeneity in the observational records and achieves a global balance between evaporation and precipitation through the mass conservation constraint [35]. Temperature, pressure, and specific humidity can be obtained by MERRA-2 data. The water vapor pressure and T_m can be calculated by the following equations:

$$e = sh \cdot P / 0.622 \tag{1}$$

$$T_m = \frac{\int_h^\infty \frac{e}{T} dh}{\int_h^\infty \frac{e}{T^2} dh} \tag{2}$$

where sh denotes the specific humidity, P is the pressure, h is the height, e is the water vapor pressure, and T is the temperature.

2.3. *Analysis of Model Parameters*

2.3.1. Analysis of Tropospheric Parameters

Analysis of the spatiotemporal characteristics of tropospheric parameters plays an important part in modeling. Some reports have suggested that T_m or temperature are related to height [36,37]. Four representative grid points over China shown in Figure 1 are chosen to determine the daily mean temperature in 2016 for analyzing the correlations between temperature and height. The temperature in each standard pressure level of MERRA-2 is interpolated upon a number of the same heights, and the result is shown in Figure 2. When geopotential height increases, the temperature decreases. There is a correlation between the temperature and the geopotential height of the four grid points over China, which can be expressed as follows:

$$T = \gamma \cdot \delta h + k \tag{3}$$

where γ denotes the temperature lapse rate, δh is the height, and k is a constant.

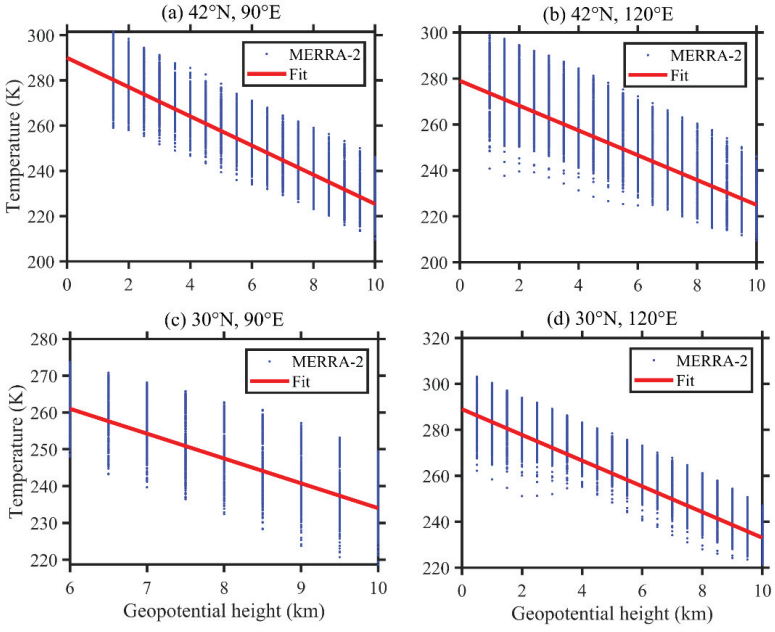

Figure 2. Relationships between temperature and geopotential height at four MERRA-2 grid points over China in 2016: (**a**) 42°N, 90°E; (**b**) 42°N, 120°E; (**c**) 30°N, 90°E; (**d**) 30°N, 120°E. Blue dots are the temperature of MERRA-2 in each height, and red lines are the linear fit to them.

The Bevis formula [38,39] shows the relationship between the surface temperature and T_m, which can be expressed as $T_m = 70.2 + 0.72T_s$; thus, the spatial and temporal characteristics of T_m are similar to those of T_s. However, the Bevis formula is only an approximate relationship, and separate models for T_m and temperature are developed in this paper.

T_m, temperature, pressure, and water vapor pressure data provided by the MERRA-2 reanalysis data from 2012 to 2016 are divided into three intervals (15°N–30°N, 30°N–40°N, and 40°N–55°N) according to latitude in order to calculate the time series and to analyze the correlations between the parameters and latitude; the result is shown in Figure 3. All the tropospheric parameters show obvious characteristics of annual and semiannual variations. The peak value of the T_m, temperature, and water vapor pressure in one year appears in the middle of the year, showing symmetrical distribution. In addition, as the latitude increases,

the aforementioned values gradually decrease, which indicates the correlation to latitude. The T_m ranges from 245 K to 280 K in the high latitude and middle latitude regions, while it ranges from 280 K to 285 K in the low latitude regions. The temperature ranges from 250 K to 295 K in the high latitude regions and middle latitude areas, while it ranges from 290 K to 300 K in the low latitude regions, which displays more stable temperatures. Pressure shows the largest value in the low latitude regions, while it appears smallest in the middle latitude regions. The water vapor pressure value ranges from 0 hPa to 20 hPa in the high latitude regions and middle latitude areas, while it ranges from 10 hPa to 30 hPa in the low latitude areas, which appears more stable.

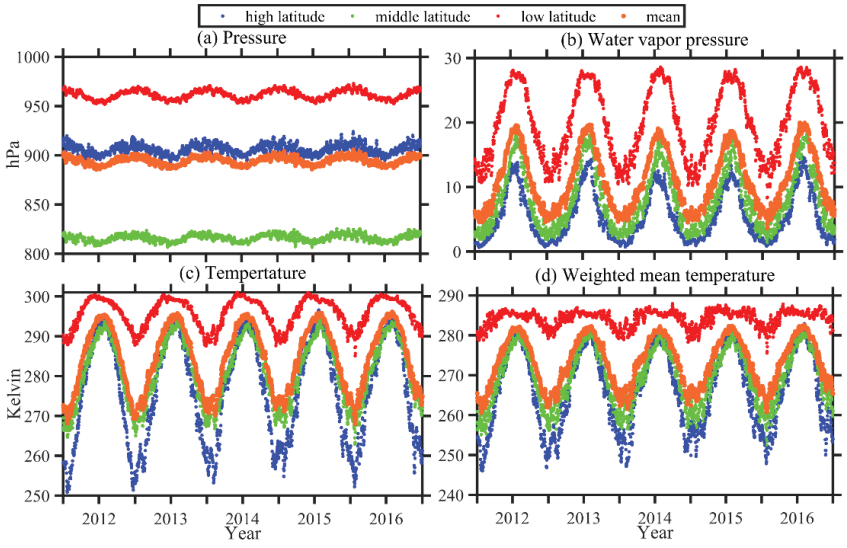

Figure 3. Time series of tropospheric parameters for pressure (**a**), parameters for water vapor pressure (**b**), parameters for temperature (**c**), and parameters for T_m (**d**) provided by MERRA-2 data from 2012 to 2016. The dots shown are the mean values of each latitude interval for each epoch. Blue dots are at high latitude, green dots are at middle latitude, red dots are at low latitude, and orange dots are the mean value.

MERRA-2 reanalysis data are used to analyze the spatial and temporal characteristics of meteorological parameters. It can be found that these tropospheric parameters are related to latitude and height, and they all have the characteristics of annual and semiannual changes. To further analyze the influence of spatial factors on the tropospheric parameters, the annual mean of the tropospheric parameters at each MERRA-2 grid point over China are determined, and the result is shown in Figure 4. The annual mean values of the tropospheric parameters in the western region are lower than those in other regions over China due to the high altitude in this area. It also has obvious characteristics indicating that the annual average values of the tropospheric parameters in high latitude areas are lower than those in the low- and middle-latitude areas. Furthermore, all the parameters show significant correlations for latitude and longitude.

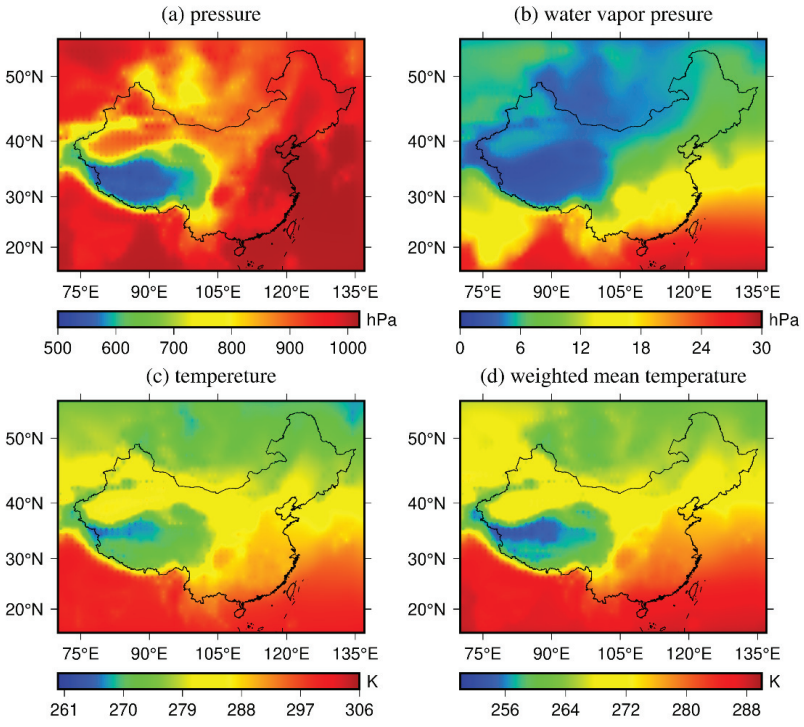

Figure 4. Distribution of the annual mean of the tropospheric parameters for pressure (**a**), parameters for water vapor pressure (**b**), parameters for temperature (**c**), and parameters for T_m (**d**) calculated from MERRA-2 data.

2.3.2. Analysis of the Characteristics of the Lapse Rate

Analysis of the spatiotemporal characteristics of the lapse rate parameters also plays an important part in modeling. When ruling out the differences in elevation data between the different data sources, such as the ellipsoidal height and the geopotential height, the elevation of GNSS and radiosonde stations is inconsistent with the height of the grid point. It must be considered that height correction in the vertical dimension plays an important role in modeling, because these tropospheric parameters are sensitive to height, showing notable changes in the vertical direction. If their vertical changes are properly considered, the model will be able to have better performance at different heights.

The changes in temperature and T_m along the vertical direction are usually adopted to be expressed by the linear function [20,40]. The exponential function is usually adopted to express the changes in pressure [24,25] and water vapor pressure along the vertical direction [21]. In this paper, conventional methods are used to carry out height correction, and they have been adopted in the GPT3 model and other tropospheric delay models. Equations (4)–(7) are for T_m, temperature, pressure, water vapor pressure, and pressure:

$$T_m^U = T_m^G - \gamma \cdot (H_U - H_G) \tag{4}$$

$$T^U = T^G - \beta \cdot (H_U - H_G) \tag{5}$$

$$e^U = e^G \cdot \left(P^U / P^G\right)^{\lambda+1} \tag{6}$$

$$P^U = P^G \left[1 - \frac{\beta}{T^G}(H_U - H_G)\right]^{\frac{g \cdot M}{R \cdot \beta}} \tag{7}$$

where T_m^U, T^U, e^U, and P^U refer to the meteorological values at the station; T_m^G, T^G, e^G, and P^G represent the meteorological values at the grid point; H_U and H_G denote the height at the station and the grid point, respectively; and γ, β, and λ are the lapse rates. M refers to the molar mass of dry air ($28.965 \cdot 10^{-3}$ kg/mol), R represents the universal gas constant (8.31432 J/K·mol), and g denotes the gravitational coefficient. A new parameter τ is introduced to show the proportion of temperature and temperature lapse rate, which can be expressed as:

$$P^U = P^G[1 - \tau(H_U - H_G)]^{\frac{g \cdot M}{R \cdot \beta}} \quad (8)$$

λ can be obtained by Equation (6) or (9). In this work, λ is obtained by fitting Equation (9):

$$ZWD = 10^{-6}\left(k_2' + k_3/T_m\right)\frac{R_\mathrm{d}}{(\lambda+1)g}e_s \quad (9)$$

where k_2' and k_3 denote the refractive index constants. R_d refers to the specific gas constant for the dry constituents [41].

To further analyze the distribution of the annual mean of the lapse rate parameters, the data over China are determined from 2012 to 2016, and the result is shown in Figure 5. The annual mean value of the pressure lapse rate, temperature lapse rate, and T_m lapse rate shows obvious geographical characteristics over China. The values are smaller in the west of China than in other regions, which is due to the higher elevation in the western region. The distribution of the water vapor decrease factor is different from the others, which shows that the values in the northeast and southwest areas are larger than that in the other regions. Furthermore, all the parameters show significant correlations for latitude and longitude.

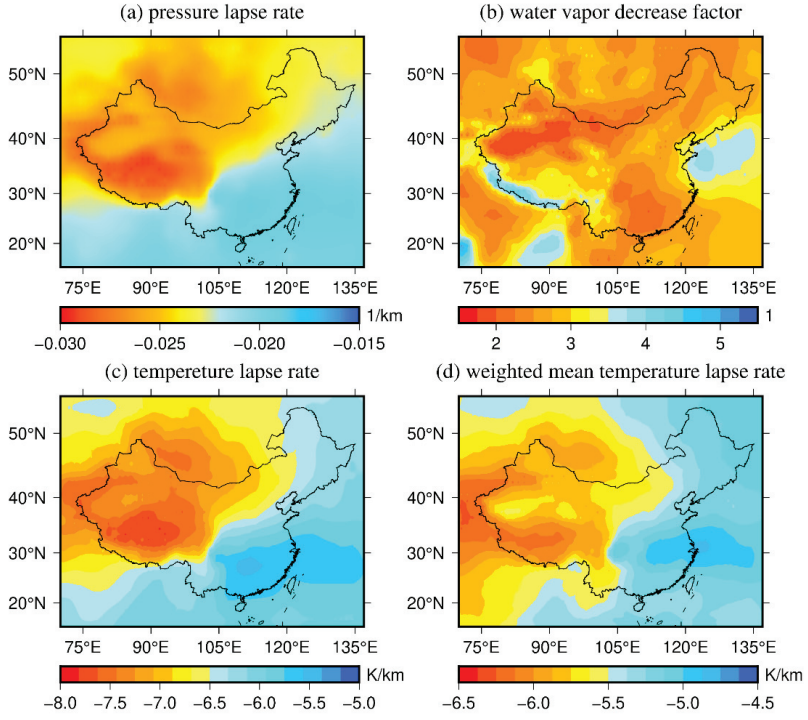

Figure 5. Distribution of the annual mean of the lapse rate for pressure (**a**), decrease factor for water vapor pressure (**b**), lapse rate for temperature (**c**), and lapse rate for T_m (**d**).

3. Development of the CTrop Model

Some shortcomings still exist in tropospheric models that have been developed, such as only single gridded data used for modeling. In this work, a sliding window algorithm is introduced to develop the tropospheric delay model, as shown in Figure 6. The new approach is instituted to divide the area of China into regular windows of the same size. Model parameters are estimated based on the data in each window to be taken as results of the center point of the sliding window. The realization process of the sliding window algorithm has been described in previous works [36,42].

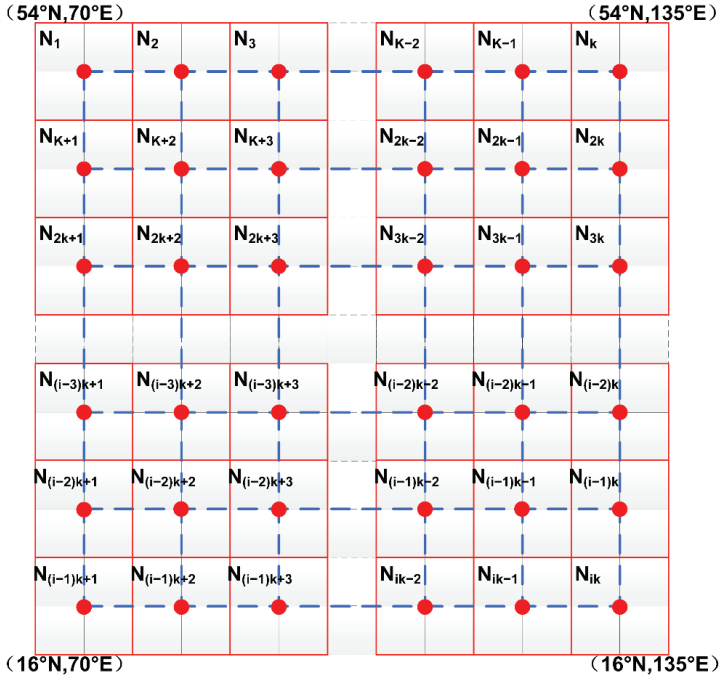

Figure 6. Realization process of the sliding window algorithm over China. The red rectangles denote the size of the sliding windows, and the red dots denote the center point of each window. The new grid over China consists of red dots and blue dashed lines.

As mentioned above, temperature, T_m, pressure, and water vapor pressure exhibit evident seasonal, latitudinal, and longitudinal characteristics over China, which should be taken into account to obtain a high-precision model. The equation in each window is expressed as follows:

$$MP(\varphi,\theta,DOY) = \alpha_1 + \alpha_2\cdot\varphi + \alpha_3\cdot\theta + \alpha_4\cdot\cos\left(2\pi\frac{DOY}{365.25}\right) + \alpha_5\cdot\sin\left(2\pi\frac{DOY}{365.25}\right) + \alpha_6\cdot\cos\left(4\pi\frac{DOY}{365.25}\right) + \alpha_7\cdot\sin\left(4\pi\frac{DOY}{365.25}\right) \quad (10)$$

where MP is the meteorological parameters, such as temperature, T_m, pressure, and water vapor pressure; φ is the latitude; θ is the longitude; α_1 is the annual average value of the meteorological parameters; α_2 is the latitude correction; α_3 is the longitude correction; α_4 and α_5 are the annual amplitude coefficients of the meteorological parameters; α_6 and α_7 are the semiannual amplitude coefficients of the meteorological parameters, and DOY is the day of the year.

The elevation of the grid points in the atmospheric reanalysis data is inconsistent with the elevation of GNSS stations. The height correction plays an important role in modeling,

for which the lapse rates of meteorological parameters should be considered for height correction in the vertical dimension. The equation is written as follows:

$$LR(\varphi,\theta,DOY) = \delta_1 + \delta_2\cdot\varphi + \delta_3\cdot\theta + \delta_4\cdot\cos\left(2\pi\frac{DOY}{365.25}\right) + \delta_5\cdot\sin\left(2\pi\frac{DOY}{365.25}\right) + \delta_6\cdot\cos\left(4\pi\frac{DOY}{365.25}\right) + \delta_7\cdot\sin\left(4\pi\frac{DOY}{365.25}\right) \quad (11)$$

where LR is the lapse rates of parameters in the vertical dimension, such as γ, β, λ, and τ; δ_1 is the annual mean value of the lapse rate of parameters; δ_2 is the latitude correction; δ_3 is the longitude correction; δ_4 and δ_5 are the annual amplitude coefficients of the lapse rate parameters; δ_6 and δ_7 are the semiannual amplitude coefficients of the meteorological parameters.

The coefficients are calculated by least-squares adjustment in each window over China from 2012 to 2016, and a grid model calculating tropospheric key parameters over China named the CTrop model is established with a spatial resolution of $1.25^\circ \times 1^\circ$.

For horizontal interpolation, the inverse distance weighted and bilinear methods are commonly used. Considering the fact that changes in latitude have an impact on tropospheric parameters when developing the model, the inverse distance weighted method can reduce the impact on the interpolation results in the latitude direction, and grid points farther from the user have less of an impact on the interpolation, so the inverse distance weighted method is used for horizontal interpolation.

Only the day of the year (DOY) and the location of the station are needed when applying this model, which makes it very convenient. First, the four grid points nearest to the location are identified. The parameters of these four points at the height are then calculated. Finally, inverse distance weighted interpolation is employed to interpolate the required parameters at the given location.

4. Results and Discussion

4.1. Analysis of the Accuracy of the CTrop Model

The performance of the CTrop model is validated by radiosonde data over China in 2017 compared with the GPT3 model at a resolution of $1^\circ \times 1^\circ$. The results are summarized in Table 1.

Table 1. Accuracy statistics of the meteorological parameters at each radiosonde site by the CTrop and GPT3 models.

Model		**CTrop/GPT3**			
Parameters		**e (hPa)**	**P (hPa)**	**T (K)**	**T_m (K)**
bias	mean	0.01/0.34	–2.35/–2.12	–0.11/–1.25	0.19/1.46
	min	–2.08/–3.83	–31.67/–31.72	–2.43/–5.03	–0.94/–1.89
	max	1.59/3.19	2.14/2.73	4.15/1.16	2.31/6.75
RMS	mean	2.60/2.86	5.51/5.83	3.09/3.44	3.35/3.87
	min	1.04/1.09	1.86/2.04	1.12/1.00	2.04/1.88
	max	4.83/5.06	32.07/42.71	5.15/6.01	5.02/7.27

Table 1 lists the accuracy of the CTrop model for meteorological parameters in comparison with the GPT3 model. In terms of water vapor pressure, the RMS of the CTrop model is 2.60 hPa and is smaller than that of the GPT3 model, which decreases by 9%. As for pressure, both models reveal a negative bias. Although the CTrop model shows a larger bias than that of the GPT3 model, it attains a smaller RMS, which decreases by 6%. In terms of temperature, it also reveals a negative bias, which indicates that the value calculated by the CTrop and GPT3 model is smaller than that of the radiosonde data. The bias of the CTrop model is –0.11 K, which decreases by 91% compared to the GPT3 model. The performance of the CTrop model is superior to that of the GPT3 model, attaining an improvement of 10%. In terms of T_m, the CTrop model exhibits a smaller error than that

of the GPT3 model. The bias of the CTrop model is 0.19 K and the RMS of the CTrop model is 3.35 K, with reductions of 87% and 13% compared with that of the GPT3 model, respectively.

To analyze the spatial characteristics of the performance of the CTrop and GPT3 models over China, the accuracy of the tropospheric parameters at each radiosonde site are calculated, and the results are shown in Figures 7–10.

As can be observed in Figure 7, the overall distribution of performance of the pressure of the CTrop model is consistent with that of the GPT3 model over China, and the accuracy of both models is high in most radiosonde sites. The largest error of radiosonde sites for the CTrop model is the same as that of the GPT3 model. Furthermore, the performance of the CTrop model in the Taibei radiosonde site (25.03°N, 121.51°E) is better than that of the GPT3 model. Figure 8 shows that the GPT3 model attains the largest positive and negative bias in terms of water vapor pressure. The CTrop model shows a smaller RMS in the western area than in the eastern area. The performance of the CTrop and GPT3 models in the coastal areas is relatively low, the reason for which may be that the rainfall in the coastal areas is high, affected by the ocean climate. Figure 9 shows that both the GPT3 and CTrop models perform well in the southeast area for T_m over China while displaying large errors in the northeast region. The CTrop model attains a smaller error than that of the GPT3 model in the west area over China. Figure 10 shows that most stations show positive bias in the southeast area and negative bias in the northwest area. As the latitude increases, the RMS accuracy shows a downward trend. The CTrop model performs better in high latitude than does the GPT3 model. In short, the CTrop model shows better accuracy in estimating the tropospheric parameters than that of the GPT3 model.

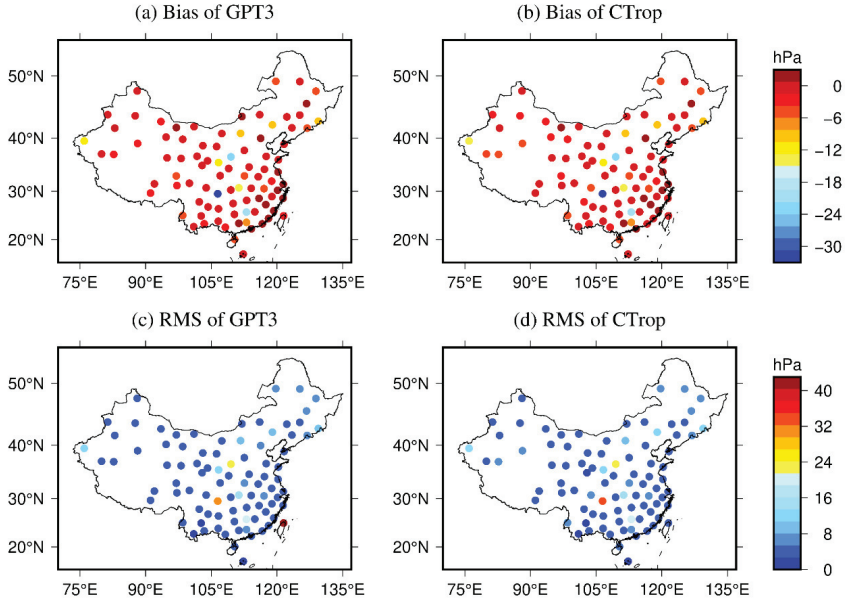

Figure 7. Distribution of the performance of pressure at each radiosonde site in 2017 by the CTrop and GPT3 models: (**a**) Bias of GPT3; (**b**) Bias of CTrop; (**c**) RMS of GPT3; (**d**) RMS of CTrop. The positive bias means the model outputs are larger than the reference values, while the negative bias means they are smaller than the reference values.

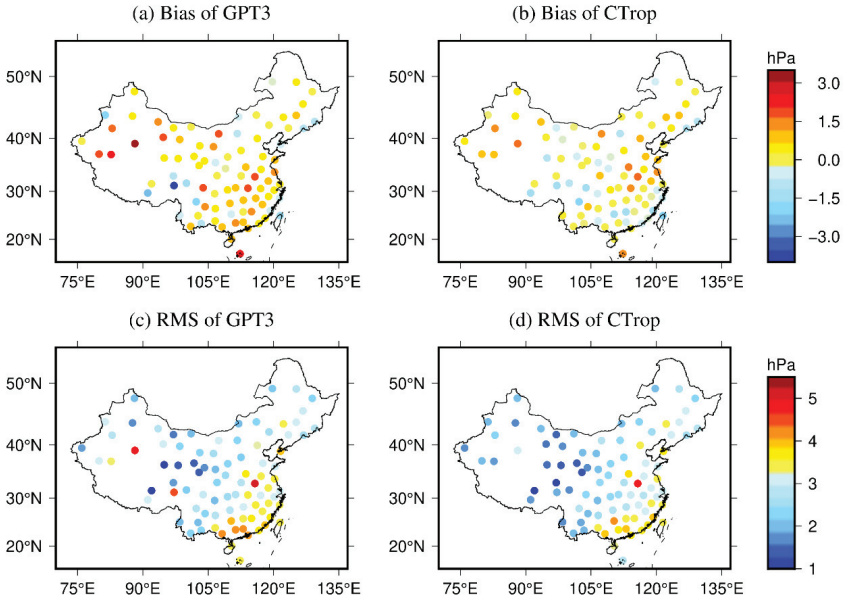

Figure 8. Distribution of the performance of water vapor pressure at each radiosonde site in 2017 by the CTrop and GPT3 models: (**a**) Bias of GPT3; (**b**) Bias of CTrop; (**c**) RMS of GPT3; (**d**) RMS of CTrop.

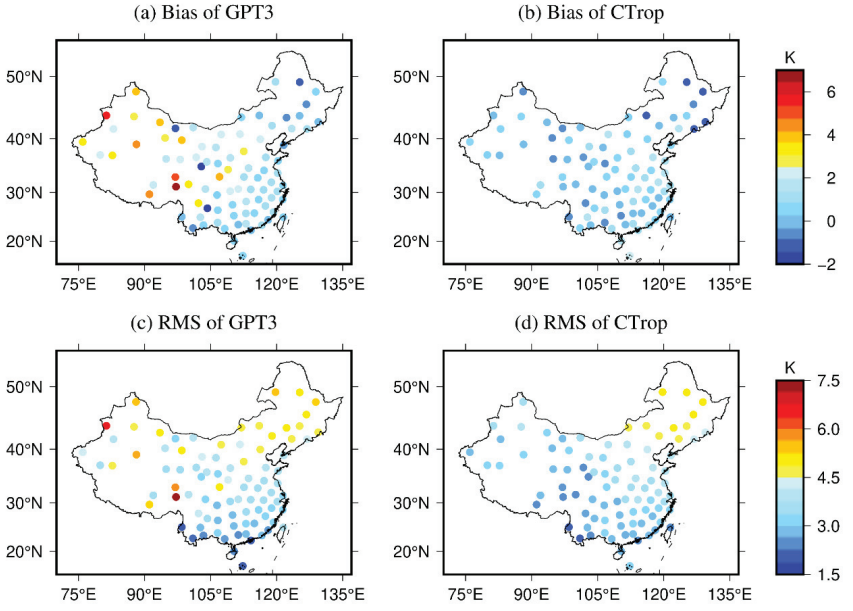

Figure 9. Distribution of the performance of T_m at each radiosonde site in 2017 by the CTrop and GPT3 models: (**a**) Bias of GPT3; (**b**) Bias of CTrop; (**c**) RMS of GPT3; (**d**) RMS of CTrop.

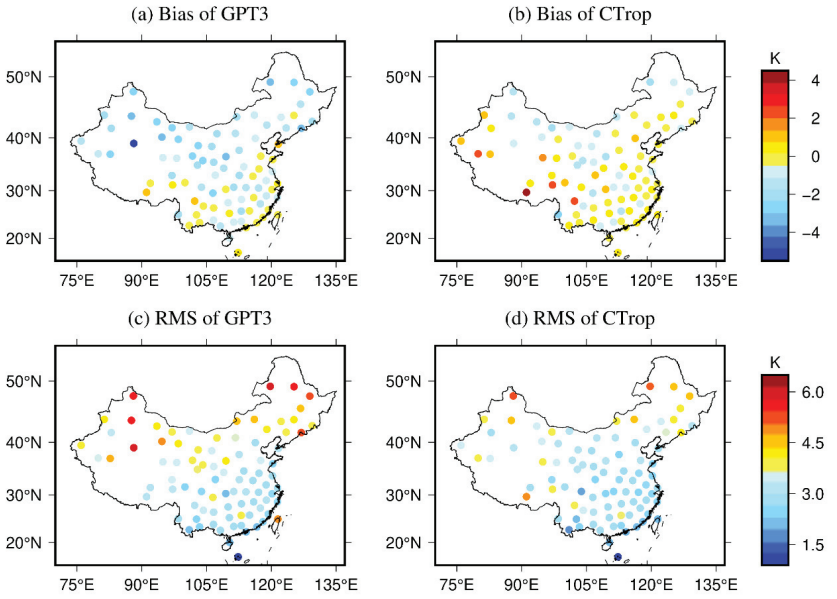

Figure 10. Distribution of the performance of temperature at each radiosonde site in 2017 by the CTrop and GPT3 models: (**a**) Bias of GPT3; (**b**) Bias of CTrop; (**c**) RMS of GPT3; (**d**) RMS of CTrop.

The height of the radiosonde site is divided into three bands, and the performance at different heights of the CTrop and GPT3 models are calculated. The results are listed in Table 2. The precision of the two models is related to height. With the increase in height, the performance of pressure and water vapor pressure is improved, but the temperature decreases. The accuracy of the T_m of the CTrop model is improved with the increase in height, which is contrary to that of the GPT3 model.

Table 2. Statistics of performance at different heights of the CTrop and GPT3 models validated by radiosonde data.

Model		CTrop/GPT3			
	Height (m)	**e (hPa)**	**P (hPa)**	**T (K)**	**T_m (K)**
bias	<500	0.07/0.47	−2.18/−2.05	−0.11/−0.88	0.53/0.88
	500~2000	0.04/0.45	−3.57/2.50	−0.37/−1.94	0.19/1.99
	>2000	−0.38/−0.57	−0.91/−1.21	0.81/−0.80	0.13/2.45
RMS	<500	3.20/3.29	5.69/6.55	2.84/3.15	3.48/3.61
	500~2000	2.09/2.47	5.96/5.51	3.32/3.91	3.37/4.13
	>2000	1.50/2.02	3.14/3.46	3.43/3.32	2.67/4.32

4.2. Analysis of the Accuracy of Different Resolutions of the CTrop Model

From the performance of the CTrop model compared with the GPT3 model, it can be observed that the CTrop model based on the sliding window algorithm performs superiorly to the GPT3 model. Since the resolutions of the GPT3 model are 1° × 1° and 5° × 5°, the applicability of the model is not sufficiently abundant. Based on the sliding window algorithm, users can access model parameters of different resolutions for their requirements, which represents one of its advantages. The goal behind the development of a lower horizontal resolution version of the CTrop model is the reduction in the amount of gridded data provided to users, as well as speeding up the troposphere delay computation process.

To analyze the influence of different resolutions of the CTrop model, window sizes of 2.5° × 2° and 5° × 4° (lon. × lat.) are proposed for the development of models, named CTrop-2 and CTrop-5, respectively. The CTrop model with sparser grids is compared to the 5-degree horizontal resolution version of the GPT3 model, named the GPT3-5 model. In view of the high resolution of the CTrop-2 model, the discussion is limited to the CTrop-5 versus the GPT3-5 model, and the result of the CTrop-2 model is only displayed without discussion. The results are shown in Tables 3 and 4 and Figures 11–14.

Table 3. Statistics of the bias of different resolutions of the CTrop model compared with the GPT3-5 model.

Models	e (hPa)	P (hPa)	T (K)	T_m (K)
	Mean [Min, Max]			
CTrop-2	–0.03 [–1.87, 2.01]	–2.83 [–32.94, 2.79]	–0.05 [–2.85, 5.04]	0.27 [–1.32, 2.39]
CTrop-5	0.32 [–1.69, 2.53]	–2.78 [–33.17, 2.38]	–0.15 [–3.25, 5.86]	0.30 [–2.32, 2.46]
GPT3-5	0.16 [–3.45, 2.84]	–0.46 [–29.90, 6.44]	1.76 [–2.22, 13.77]	–1.19 [–6.14, 3.77]

Table 4. Statistic of the RMS of different resolutions of the CTrop model compared with the GPT3-5 model.

Models	e (hPa)	P (hPa)	T (K)	T_m (K)
	Mean [Min, Max]			
CTrop-2	2.64 [1.08, 5.02]	5.59 [2.00, 33.15]	3.16 [1.17, 5.72]	3.37 [1.82, 5.11]
CTrop-5	2.71 [1.13, 5.34]	5.61 [2.00, 33.36]	3.26 [1.24, 6.41]	3.43 [1.87, 5.28]
GPT3-5	2.84 [1.05, 5.10]	6.18 [1.77, 42.89]	4.20 [2.15, 14.18]	3.52 [1.03, 7.37]

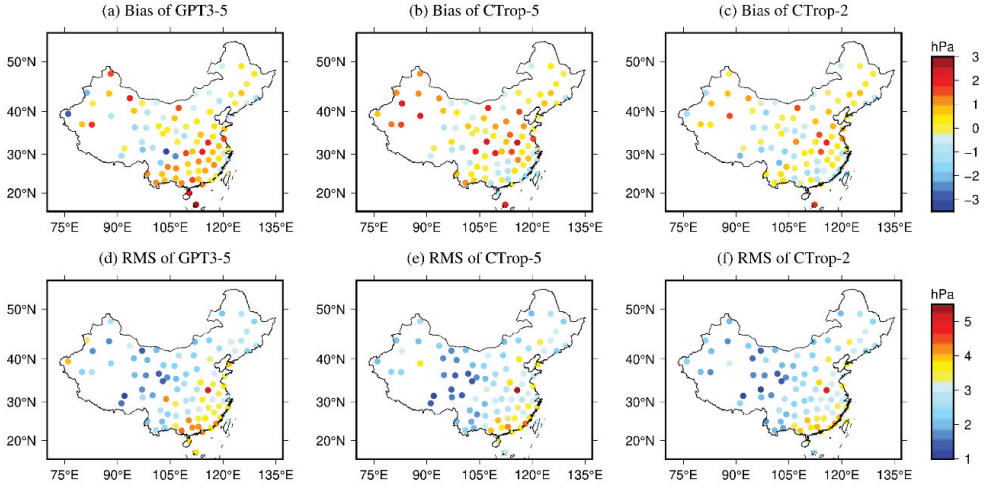

Figure 11. Distribution of the performance of water vapor pressure in different resolutions of the CTrop and GPT3 models validated by radiosonde sites in 2017: (**a**) Bias of GPT3-5; (**b**) Bias of CTrop-5; (**c**) Bias of CTrop-2; (**d**) RMS of GPT3-5; (**e**) RMS of CTrop-5; (**f**) RMS of CTrop-2. The positive bias means the model outputs are larger than the reference values, while the negative bias means they are smaller than the reference values.

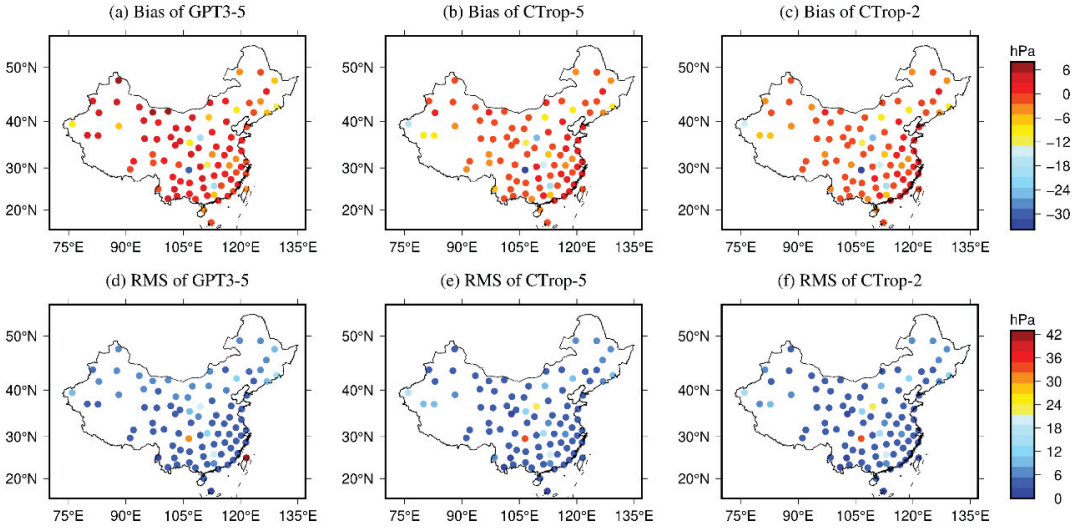

Figure 12. Distribution of the performance of pressure in different resolutions of the CTrop and GPT3 models validated by radiosonde sites in 2017: (**a**) Bias of GPT3-5; (**b**) Bias of CTrop-5; (**c**) Bias of CTrop-2; (**d**) RMS of GPT3-5; (**e**) RMS of CTrop-5; (**f**) RMS of CTrop-2.

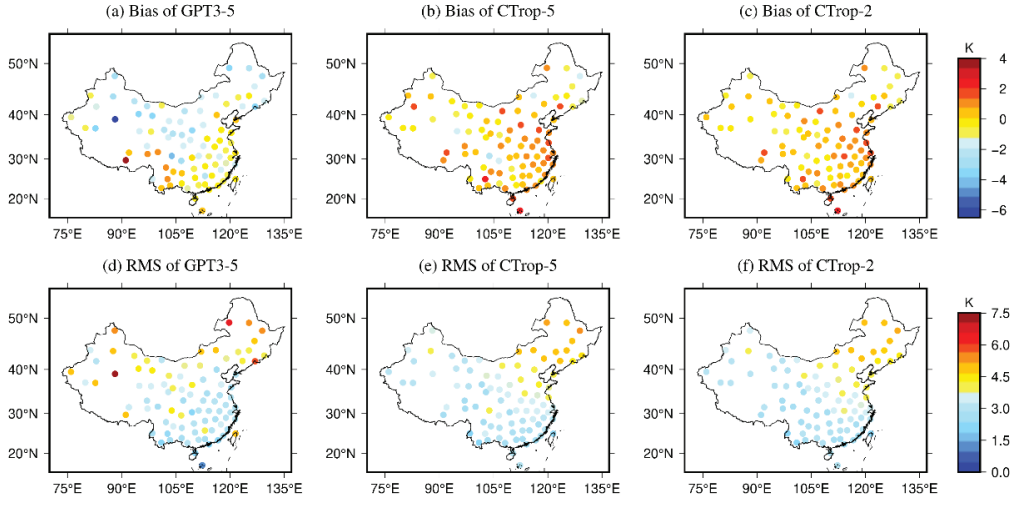

Figure 13. Distribution of the performance of T_m in different resolutions of the CTrop and GPT3 models validated by radiosonde sites in 2017: (**a**) Bias of GPT3-5; (**b**) Bias of CTrop-5; (**c**) Bias of CTrop-2; (**d**) RMS of GPT3-5; (**e**) RMS of CTrop-5; (**f**) RMS of CTrop-2.

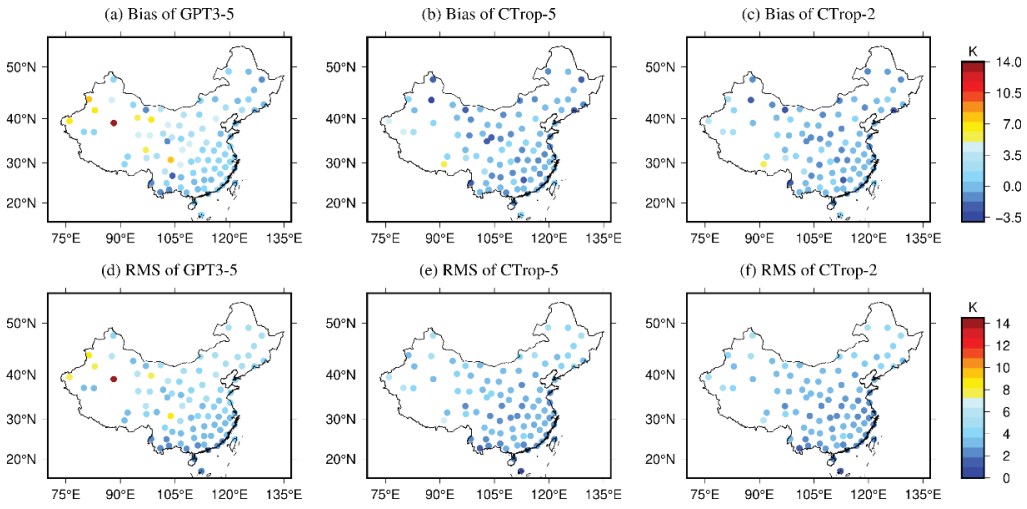

Figure 14. Distribution of the performance of temperature in different resolutions of the CTrop and GPT3 models validated by radiosonde sites in 2017: (**a**) Bias of GPT3-5; (**b**) Bias of CTrop-5; (**c**) Bias of CTrop-2; (**d**) RMS of GPT3-5; (**e**) RMS of CTrop-5; (**f**) RMS of CTrop-2.

Tables 3 and 4 indicate that as the spatial resolution of the CTrop model decreases, the accuracy gradually decreases. The Ctrop model also has better accuracy than the GPT3-5 model in lower spatial resolution. Regarding the water vapor pressure, the RMS of the Ctrop-5 model is 2.71 hPa, showing an improvement of 5% compared with the GPT3-5 model. Considering the pressure, the CTrop-5 model achieves accuracy improvements of 10% when compared to the GPT3-5 model. Regarding temperature, the bias of the CTrop-5 model appears as a negative value, while the GPT3-5 model displays a positive value. The RMS of the CTrop-5 model is 3.26 K, showing an improvement of 22% when compared with the GPT3-5 model. In terms of T_m, the precision of the CTrop-5 model is 3.43 K, also presenting a slight improvement when compared with the GPT3-5 model.

Figure 11 shows that all models display a large RMS of water vapor pressure in the southeast of China. The CTrop-5 model shows an accuracy improvement in the northeast of China when compared with the GPT3-5 model. Both models show large errors in the southeast of China, which is subject to subtropical monsoons. Water vapor is transported by monsoons from the sea to these areas, resulting in a higher error for modeling [12]. Figure 12 shows that the CTrop-5 model and the GPT3-5 model present positive and negative biases of pressure in the majority of China. The CTrop-5 model presents a slight improvement at a few stations in the northeast of China when compared with the GPT3-5 model. Figure 13 shows that all models have better accuracy of T_m in the south of China than in the north of China. The CTrop-5 model presents an improvement in the west of China when compared with the GPT3-5 model. Figure 14 shows that the CTrop-5 model has better accuracy in the west of China than that of the GPT3-5 model. Consequently, the lower horizontal resolution version of the CTrop model shows better accuracy in estimating the tropospheric parameters than that of the GPT3 model.

5. Conclusions

In this work, the distribution characteristics of meteorological parameters are analyzed, and it is observed that the meteorological parameters exhibit major annual and semiannual periodic variations that are also related to latitude and longitude. Considering the spatial distribution and time-varying characteristics of the meteorological parameters, a refined regional empirical model (CTrop) based on the sliding window algorithm is developed for the estimation of tropospheric key parameters over China. Only the day of the year (DOY)

and the location of the station are needed when applying this model, which makes it very convenient. The performance of the CTrop and GPT3 models are validated by radiosonde data. Validation results demonstrate that the CTrop model shows higher precision than that of the GPT3 model in all meteorological parameters. The improvements are 6%, 10%, 9%, and 13% for pressure, temperature, water vapor pressure, and weighted mean temperature, respectively. Three different resolutions of the CTrop model are also developed based on the sliding window algorithm, for which users can access model parameters of different resolutions for their requirements to reduce the amount of gridded data provided to the users, as well as to speed up the troposphere delay computation process. The results demonstrate that the CTrop model realizes better performance than that of the GPT3 model over China, which can meet the needs for GNSS meteorology and GNSS positioning. Although the CTrop model is only developed in regions over China with the aim of meeting the needs for GNSS positioning in China, we intend to expand the model to a global model in future work.

Author Contributions: Conceptualization, L.H. (Liangke Huang) and L.L.; methodology, G.Z. and L.H. (Liangke Huang); validation, C.L., L.H. (Liangke Huang) and L.Z.; formal analysis, G.Z.; writing—original draft preparation, G.Z. and C.L.; writing—review and editing, L.H. (Liangke Huang), J.L., L.H. (Ling Huang) and H.H.; funding acquisition, L.H. (Liangke Huang) and L.L. All authors have read and agreed to the published version of the manuscript.

Funding: This work was sponsored by the National Natural Foundation of China (41864002; 41704027); Guangxi Natural Science Foundation of China (2018GXNSFAA281182; 2020GXNSFBA297145; 2018GXNSFAA281279; 2020GXNSFBA159033); Innovation Project of Guangxi Graduate Education (YCSW2021209); Guangxi Science and Technology Base and Talent Project (AD19245060); The Guangxi Key Laboratory of Spatial Information and Geomatics (19-050-11-24), and the "Ba Gui Scholars" program of the provincial government of Guangxi.

Institutional Review Board Statement: Not applicable.

Informed Consent Statement: Not applicable.

Data Availability Statement: The MERRA-2 data can be freely accessed at https://goldsmr4.gesdisc.eosdis.nasa.gov/data/MERRA2/ (accessed on 16 May 2020). The radiosonde data can be accessed at http://www1.ncdc.noaa.gov/pub/data/igra/ (accessed on 16 May 2020). The parameters of the CTrop model, as well as codes, are available upon request to Liangke Huang (lkhuang@whu.edu.cn).

Acknowledgments: The authors would like to thank NASA for providing the MERRA-2 grid data and IGRA (Integrated Global Radiosonde Archive) for providing the radiosonde data in this study.

Conflicts of Interest: The authors declare no conflict of interest.

References

1. Saastamoinen, J. Contributions to the theory of atmospheric refraction. *Bull. Géodésique* **1972**, *105*, 279–298. [CrossRef]
2. Guo, J.; Hou, R.; Zhou, M.; Jin, X.; Li, C.; Liu, X.; Gao, H. Monitoring 2019 Forest Fires in Southeastern Australia with GNSS Technique. *Remote Sens.* **2021**, *13*, 386. [CrossRef]
3. Boutiouta, S.; Lahcene, A. Preliminary study of GNSS meteorology techniques in Algeria. *Int. J. Remote Sens.* **2013**, *34*, 5105–5118. [CrossRef]
4. Tunalı, E.; Özlüdemir, M.T. GNSS PPP with different troposphere models during severe weather conditions. *GPS Solut.* **2019**, *23*, 82. [CrossRef]
5. Li, Z.; Wen, Y.; Zhang, P.; Liu, Y.; Zhang, Y. Joint Inversion of GPS, Leveling, and InSAR Data for the 2013 Lushan (China) Earthquake and Its Seismic Hazard Implications. *Remote Sens.* **2020**, *12*, 715. [CrossRef]
6. Ning, T.; Wickert, J.; Deng, Z.; Heise, S.; Dick, G.; Vey, S.; Schöne, T. Homogenized time series of the atmospheric water vapor content obtained from the GNSS reprocessed data. *J. Clim.* **2016**, *29*, 2443–2456. [CrossRef]
7. Hopfield, H.S. Two-Quartic tropospheric refractivity profile for correcting satellite data. *J. Geophys. Res.* **1969**, *74*, 4487–4499. [CrossRef]
8. Black, H.D. An easily implemented algorithm for the tropospheric range correction. *J. Geophys. Res.* **1978**, *83*, 1825–1828. [CrossRef]

9. Lu, C.; Li, X.; Cheng, J.; Dick, G.; Ge, M.; Wickert, J.; Schuh, H. Real-time tropospheric delay retrieval from multi-GNSS PPP ambiguity resolution: Validation with final troposphere products and a numerical weather model. *Remote Sens.* **2018**, *10*, 481. [CrossRef]
10. Cao, L.; Zhang, B.; Li, J.; Yao, Y.; Liu, L.; Ran, Q.; Xiong, Z. A Regional Model for Predicting Tropospheric Delay and Weighted Mean Temperature in China Based on GRAPES_MESO Forecasting Products. *Remote Sens.* **2021**, *13*, 2644. [CrossRef]
11. Li, T.; Wang, L.; Chen, R.; Fu, W.; Xu, B.; Jiang, P.; Liu, J.; Zhou, H.; Han, Y. Refining the empirical global pressure and temperature model with the ERA5 reanalysis and radiosonde data. *J. Geod.* **2021**, *95*, 31. [CrossRef]
12. Wu, M.; Jin, S.; Li, Z.; Cao, Y.; Ping, F.; Tang, X. High-Precision GNSS PWV and Its Variation Characteristics in China Based on Individual Station Meteorological Data. *Remote Sens.* **2021**, *13*, 1296. [CrossRef]
13. Zhang, W.; Lou, Y.; Huang, J.; Liu, W. A refined regional empirical pressure and temperature model over China. *Adv. Space Res.* **2018**, *62*, 1065–1074. [CrossRef]
14. Li, J.; Zhang, B.; Yao, Y.; Liu, L.; Sun, Z.; Yan, X. A Refined Regional Model for Estimating Pressure, Temperature, and Water Vapor Pressure for Geodetic Applications in China. *Remote Sens.* **2020**, *12*, 1713. [CrossRef]
15. Huang, L.; Liu, L.; Yao, C. A zenith tropospheric delay correction model based on the regional CORS network. *Geod. Geodyn.* **2012**, *3*, 53–62.
16. Huang, L.; Xie, S.; Liu, L.; Li, J.; Chen, J.; Kang, C. SSIEGNOS: A New Asian Single Site Tropospheric Correction Model. *ISPRS Int. J. Geo-Inf.* **2017**, *6*, 20. [CrossRef]
17. Leandro, R.F.; Santos, M.C.; Langley, R.B. UNB neutral atmosphere models: Development and performance. In Proceedings of the ION NTM 2006, Monterey, CA, USA, 18–20 January 2006; pp. 564–573.
18. Leandro, R.F.; Langley, R.B.; Santos, M.C. UNB3m_pack: A neutral atmosphere delay package for radiometric space techniques. *GPS Solut.* **2008**, *12*, 65–70. [CrossRef]
19. Penna, N.; Dodson, A.; Chen, W. Assessment of EGNOS tropospheric correction model. *J. Navig.* **2001**, *54*, 37–55. [CrossRef]
20. Krueger, E.; Schüler, T.; Hein, G.; Martellucci, A.; Blarzino, G. Galileo tropospheric correction approaches developed within GSTB-V1. In Proceedings of the ENC-GNSS 2004, Rotterdam, The Netherlands, 16–19 May 2004.
21. Schüler, T. The TropGrid2 standard tropospheric correction model. *GPS Solut.* **2014**, *18*, 123–131. [CrossRef]
22. Böhm, J.; Heinkelmann, R.; Schuh, H. Short note: A global model of pressure and temperature for geodetic applications. *J. Geod.* **2007**, *81*, 679–683. [CrossRef]
23. Lagler, K.; Schindelegger, M.; Böhm, J.; Krásná, H.; Nilsson, T. GPT2: Empirical Slant Delay Modelfor Radio Space Geodetic Techniques. *Geophys. Res. Lett.* **2013**, *40*, 1069–1073. [CrossRef] [PubMed]
24. Böhm, J.; Möller, G.; Schindelegger, M.; Pain, G.; Weber, R. Development of an improved blind model for slant delays in the troposphere (GPT2w). *GPS Solut.* **2015**, *19*, 433. [CrossRef]
25. Landskron, D.; Böhm, J. VMF3/GPT3: Refined discrete and empirical troposphere mapping functions. *J. Geod.* **2018**, *92*, 349–360. [CrossRef]
26. Ding, J.; Chen, J. Assessment of Empirical Troposphere Model GPT3 Based on NGL's Global Troposphere Products. *Sensors* **2020**, *20*, 3631. [CrossRef]
27. Sun, Z.Y.; Zhang, B.; Yao, Y.B. An ERA5-based model for estimating tropospheric delay and weighted mean temperature over China with improved spatiotemporal resolutions. *Earth Space Sci.* **2019**, *6*, 1926–1941. [CrossRef]
28. Gui, K.; Che, H.; Chen, Q.; Zeng, Z.; Liu, H.; Wang, Y.; Zheng, Y.; Sun, T.; Liao, T.; Wang, H.; et al. Evaluation of radiosonde, MODIS-NIR-Clear, and AERONET precipitable water vapor using IGS ground-based GPS measurements over China. *Atmos Res.* **2017**, *197*, 461–473. [CrossRef]
29. Randles, C.A.; Da Silva, A.M.; Buchard, V.; Colarco, P.R.; Darmenov, A.; Govindaraju, R.; Smirnov, A.; Holben, B.; Ferrare, R.; Hair, J.; et al. The MERRA-2 Aerosol Reanalysis, 1980 Onward. Part I: System Description and Data Assimilation Evaluation. *J. Clim.* **2017**, *30*, 6823–6850. [CrossRef]
30. Gelaro, R.; McCarty, W.; Suárez, M.J.; Todling, R.; Molod, A.; Takacs, L.; Randles, C.A.; Darmenov, A.; Bosilovich, M.G.; Reichle, R.; et al. The Modern-Era Retrospective Analysis for Research and Applications, Version 2 (MERRA-2). *J. Clim.* **2017**, *30*, 5419–5454. [CrossRef]
31. Molod, A.; Takacs, L.; Suarez, M.; Bacmeister, J. Development of the GEOS-5 atmospheric general circulation model: Evolution from MERRA to MERRA2. *Geosci. Model Dev.* **2015**, *8*, 1339–1356. [CrossRef]
32. Kleist, D.T.; Parrish, D.F.; Derber, J.C.; Treadon, R.; Errico, R.M.; Yang, R. Improving incremental balance in the GSI 3DVAR analysis system. *Mon. Weather. Rev.* **2009**, *137*, 1046–1060. [CrossRef]
33. Wu, W.S.; Purser, R.J.; Parrish, D.F. Three-dimensional variational analysis with spatially inhomogeneous covariances. *Mon. Weather. Rev.* **2002**, *130*, 2905–2916. [CrossRef]
34. Gupta, P.; Verma, S.; Bhatla, R.; Chandel, A.S.; Singh, J.; Payra, S. Validation of surface temperature derived from MERRA-2 Reanalysis against IMD gridded data set over India. *Earth Space Sci.* **2020**, *7*, e2019EA000910. [CrossRef]
35. Huang, L.; Mo, Z.; Liu, L.; Zeng, Z.; Chen, J.; Xiong, S.; He, H. Evaluation of hourly PWV products derived from ERA5 and MERRA-2 over the Tibetan Plateau using ground-based GNSS observations by two enhanced models. *Earth Space Sci.* **2021**, *8*, e2020EA001516. [CrossRef]
36. Huang, L.K.; Jiang, W.P.; Liu, L.L.; Chen, H.; Ye, S.R. A new global grid model for the determination of atmospheric weighted mean temperature in GPS precipitable water vapor. *J. Geod.* **2019**, *93*, 159–176. [CrossRef]

37. Yao, Y.B.; Zhang, B.; Xu, C.Q.; Chen, J.J. Analysis of the global T m-T s correlation and establishment of the latitude-related linear model. *Chin. Sci. Bull.* **2014**, *59*, 2340–2347. [CrossRef]
38. Bevis, M.; Businger, S.; Herring, T.A.; Rocken, C.; Anthes, R.; Ware, R.H. GPS meteorology: Remote sensing of atmospheric water vapor using the Global Positioning System. *J. Geophys. Res.* **1992**, *97*, 15787–15801. [CrossRef]
39. Bevis, M.; Businger, S.; Chiswell, S.; Herring, T.A.; Anthes, R.A.; Rocken, C.; Ware, R.H. GPS meteorology: Mapping zenith wet delays onto precipitable water. *J. Appl. Meteorol.* **1994**, *33*, 379–386. [CrossRef]
40. Yao, Y.B.; Xu, C.Q.; Shi, J.B.; Cao, N.; Zhang, B.; Yang, J.J. ITG: A New Global GNSS Tropospheric Correction Model. *Sci. Rep.* **2015**, *5*, 10273. [CrossRef]
41. Askne, J.; Nordius, H. Estimation of tropospheric delay for microwaves from surface weather data. *Radio Sci.* **1987**, *22*, 379–386. [CrossRef]
42. Huang, L.K.; Zhu, G.; Liu, L.L.; Chen, H.; Jiang, W.P. A global grid model for the correction of the vertical zenith total delay based on a sliding window algorithm. *GPS Solut.* **2021**, *25*, 98. [CrossRef]

remote sensing

MDPI

Article

Reduced-Dynamic Precise Orbit Determination of Haiyang-2B Altimetry Satellite Using a Refined Empirical Acceleration Model

Youcun Wang [1], Min Li [1,*], Kecai Jiang [1], Wenwen Li [1], Geer Qin [1], Qile Zhao [1], Hailong Peng [2] and Mingsen Lin [2]

[1] GNSS Research Center, Wuhan University, Wuhan 430079, China; youcunwang@whu.edu.cn (Y.W.); kc.jiang@whu.edu.cn (K.J.); cheeselee@whu.edu.cn (W.L.); 2014301610210@whu.edu.cn (G.Q.); zhaoql@whu.edu.cn (Q.Z.)

[2] National Satellite Ocean Application Service, Beijing 100081, China; phl@mail.nsoas.org.cn (H.P.); mslin@mail.nsoas.org.cn (M.L.)

* Correspondence: limin@whu.edu.cn; Tel.: +86-027-6877-8767

Abstract: The Haiyang 2B (HY-2B) satellite requires precise orbit determination (POD) products for geodetic remote sensing techniques. An improved set of reduced-dynamic (RD) orbit solutions was generated from the onboard Global Positioning System (GPS) measurements over a 14-month period using refined strategies and processing techniques. The key POD strategies include a refined empirical acceleration model, in-flight calibration of the GPS antenna, and the resolution of single-receiver carrier-phase ambiguities. In this study, the potential periodicity of empirical acceleration in the HY-2B POD was identified by spectral analysis. In the along-track direction, a noticeable signal with four cycles per revolution (CPR) was significant. A mixed spectrum was observed for the cross-track direction. To better understand the real in-flight environment, a refined empirical acceleration model was used to cope with the time variability of empirical accelerations in HY-2B POD. Three POD strategies were used for the reprocessing for superior orbit quality. Validation using over one year of satellite laser ranging (SLR) measurements demonstrated a 5.2% improvement in the orbit solution of the refined model. Reliable correction for the GPS antenna phase center was obtained from an over-420-day dataset, and a trend in radial offset change was observed. After application of the in-flight calibration of the GPS antenna, a 26% reduction in the RMS SLR residuals was achieved for the RD orbit solution, and the carrier phase residuals were clearly reduced. The integer ambiguity resolution of HY-2B led to strong geometric constraints for the estimated parameters, and a 15% improvement in the SLR residuals could be inferred compared with the float solution.

Keywords: HY-2B; precise orbit determination; empirical accelerations model; satellite laser ranging; GPS antenna phase center; single-receiver ambiguity resolution

Citation: Wang, Y.; Li, M.; Jiang, K.; Li, W.; Qin, G.; Zhao, Q.; Peng, H.; Lin, M. Reduced-Dynamic Precise Orbit Determination of Haiyang-2B Altimetry Satellite Using a Refined Empirical Acceleration Model. *Remote Sens.* **2021**, *13*, 3702. https://doi.org/10.3390/rs13183702

Academic Editor: Ali Khenchaf

Received: 17 August 2021
Accepted: 13 September 2021
Published: 16 September 2021

1. Introduction

HaiYang-2B (HY-2B) is the second marine dynamic environment satellite of China [1]. It was launched on 25 October 2018, with an altitude and inclination of about 973 km and 99.3°, respectively. The major objective of the HY-2B is to monitor and investigate the marine environment. It carries various instruments, including a dual-frequency altimeter in the Ku and C-bands, a scatterometer, and a microwave imager. The HY-2B mission undertakes routine measurements of sea surface height. Its precise orbit provides a good reference for an altimetry satellite, which is very important for long-term Earth observation missions [2–4]. Moreover, the precise orbit determination (POD) function of the altimetry satellite is the basis of various oceanographic applications based on altimetry technology [5,6], such as the determination of global and regional mean sea level changes, the modeling of the mean sea height, ocean tide simulations, etc. [7–9].

To support this mission, the HY-2B spacecraft hosts a POD package, including an onboard Global Positioning System (GPS) receiver and a laser retroreflector (LRR) for

satellite laser ranging (SLR). Based on Global Navigation Satellite System (GNSS) measurements and dynamical models of satellites, three different orbit determination methods were developed, which are known as kinematic, dynamic, and reduced-dynamic. To optimize the advantages of purely geometric observations and dynamic methods, pseudo-stochastic parameters are employed to compensate for potential deficiencies of dynamic models based on reduced-dynamic concepts [5,10]. At present, the reduced-dynamic POD based on onboard GNSS observations has been widely used for most low-Earth orbit (LEO) geodetic [11–13] and remote sensing missions [14–16]. The precise orbits of GRACE [17], with an uncertainty of less than 3 cm in SLR residuals, are supported using onboard GPS data. Overall SLR validation better than 2 cm for GOCE missions can be obtained for GPS-based orbits [18]. The reduced-dynamic Swarm Precise Science Orbits (PSO) showed an accuracy of better than 2 cm by independent SLR validation [19,20]. However, the dynamic background models of the satellites involved and their data processing strategies differ slightly, and there is no unified POD strategy.

Empirical accelerations have been successfully used in LEO POD as an inherent strategy. Along with the initial state vector of LEO satellites and the scaling factors for individual force model constituents, empirical acceleration parameters are estimated in reduced-dynamic POD. The performance of this technique in high-precision orbit determination has been widely investigated by the LEO POD community [21–23]. A refined non-gravitational force model of a LEO satellite will reduce the amount of empirical acceleration [13,23,24], and many scholars have set their sights on model refinement. Some analysis has indicated the direction and the time variability of the remaining deficit [18,22]. From the perspective of spectral analysis, the potential perturbation frequency of unmodeled acceleration information can be extracted and analyzed. Better orbit determination results may be obtained when the empirical acceleration is consistent with the spectral analysis. Therefore, spectral analysis of the remaining empirical acceleration of POD was performed, and an optimized piece-wise empirical acceleration (PEA) model is proposed in this article.

The accurate known location of the GPS receiver antenna relative to the center of mass (CoM) is the premise of precise orbit determination [25,26]. This location is typically provided by the spacecraft manufacturer, with a nominal accuracy of millimeters or better, but the experience of past geodetic missions has shown that there may be inconsistencies at the level of 2–3 cm [16,27,28]. Therefore, offset calibration of the GPS antenna phase center and empirical phase center variations (PCV) corrections were performed to eliminate the systematic errors in the HY-2B POD. Single-receiver integer ambiguity resolution (IAR) has often been implemented in numerous LEO missions, and improved precision can be inferred from SLR validation [13,16,20]. Unlike the fixed double-difference ambiguity of terrestrial stations, a single-receiver IAR depends on the dedicated GNSS orbit, clocks, and wide-lane bias products [16,29,30], which were implemented in this study to improve orbit solutions. The single-receiver IAR of the Sentinel-3 and Swarm missions based on the GRG (Groupe de Recherche de Géodésie Spatiale) products of the CNES/CLS (Centre National d'Études Spatiales/Collecte Localisation Satellites) [31] analysis center is supported by previous studies [16,20]. Furthermore, GNSS orbits and an IAR-enabled clock with the accompanying Observation-Specific Bias (OSB) provided by the Center for Orbit Determination in Europe (CODE) [30] was used to implement the single-receiver IAR of LEO missions [13]. For improved orbit solutions for the HY-2B, a single-receiver IAR was implemented in this study.

This manuscript is organized as follows. Section 2 provides a brief introduction to the background dynamic model and the data process strategy used in HY-2B POD. An assessment and a discussion of the different orbit solutions are presented in Section 3. A discussion about the results is provided in in Section 4. Finally, Section 5 concludes the study and provides a general outlook.

2. Spectral Analysis of HY-2B Empirical Accelerations

The process models and strategies used for the determination of the HY-2B orbit are elaborated in this section. The GNSS Research Center of Wuhan University undertakes routine POD for the associated Haiyang-2 satellites, and the preliminary motivation of this work was to improve the accuracy of the HY-2B satellite POD. The improvements were driven primarily by offset calibration of the GPS antenna, implementation of ambiguity resolution, and a refined PEA model.

2.1. POD Processing and Models

The reduced dynamic POD method makes use of GPS observations and well-established models for computing the acceleration acting on satellites. An overview of the supporting models and data processing strategies is presented in Table 1. The undifferenced processing was adopted, and dual-frequency ionosphere-free combinations of the GPS data were used as the basic observations for the HY-2B POD. The precise GNSS orbits, clock, and wide-lane bias products provided by the CNES/CLS were used to implement a single-receiver IAR for the HY-2B satellite. In order to be consistent with the standard IGS clock product, GPS observations with a measurement interval of 30 seconds were used. For processing GPS data with a sampling interval of below 30 seconds, the high-rate GRG clock offsets based on the CODE clock product is available for single-receiver IAR. Details of this concept and its implementation are described [20]. The GPS transmitter antenna phase center offsets (PCO) and PCV of the IGS model [32,33] were taken into account. The GPS antenna offset calibration of the HY-2B and the empirical PCV corrections were considered in POD.

Table 1. Force models and datasets for HY-2B precise orbit determination and SLR validation.

Model	Description
Observation model	
Observation	Undifferenced ionosphere-free code and carrier phase combinations
Interval and arc length	30 s and 30 h
GPS orbit and clocks	CNES-CLS 'GRG' products; 30 s sampling
GPS satellite biases	CNES-CLS wide-lane satellite biases
GPS satellite PCO and PCV	IGS ATX models [33]
HY-2B attitude	Nominal
HY-2B PCO and PCV	Corrected using calibrated values
Dynamic model	
Earth gravity	EIGEN6C (120 × 120) [34]
Solid Earth and pole tides	IERS 2010 conventions [35]
Ocean tides	FES 2004 (30 × 30) [36]
N-body disturbance	JPL DE405 [37]
Relativity	IERS 2003 [38]
Solar radiation	13-plate macro-model, radiation pressure coefficients (VIS and IR) [39]
Atmospheric drag	13-plate macro-model, atmospheric density model adopting DTM-2013 [40]
Empirical acceleration	Piecewise periodic acceleration
Estimated parameters	
Initial state	Position and velocity at the initial epoch
Receiver clock offset	Each epoch as white noise
Phase ambiguities	Each continuous tracking arc as a float
Solar radiation coefficients	One per 30 h arc
Drag coefficients	One per 180 min
Empirical coefficients	One per 180 min, amplitudes of periodic accelerations acting on the along- and cross-track directions

Table 1. *Cont.*

Model	Description
SLR validation	
Station coordinates	SLRF2014 [41]
Ocean tide loading	FES 2004 [36]
Tropospheric delay	Mendes and Pavlis [42]
Relativity	Space-time curvature correction

The flat-plate macro-model is widely adopted for the LEO mission and provides a proper tool to describe the non-gravitational force on the surfaces of a satellite [5,23,43]. The 13-plate macro-model obtained from [1] was used for HY-2B POD. The scale factors were taken into account for solar radiation pressure (SRP) and atmospheric drag force. The extended analytical SRP model developed by [39] was used, and photons in the visual (VIS) and infrared (IR) were considered in SRP. We assumed that 50% of the total solar radiation pressure is caused by shortwave and longwave radiations, and indicated this contribution as 1/2. The temporal variation in the solar radiation pressure can be ignored as it causes a very small effect [44]. The density values and composition data of the Earth's thermosphere obtained from DTM-2013 [40] were employed for a precise modeling of atmospheric forces. Moreover, empirical accelerations were introduced in POD solution to compensate for deficiencies of the modeled forces.

2.2. Frequency Characteristics

Non-gravitational modeling is challenging because it does not perfectly describe the real in-flight environment encountered by a spacecraft and often relies on a variety of external products [23,24,45]. In addition to the scaling parameter, a pre-defined number of empirical accelerations, such as piecewise periodic or constant accelerations, were applied to cope with the remaining deficiencies of the satellite's prior model [21,22]. Accordingly, the piecewise constant and periodic empirical accelerations can be obtained by:

$$\ddot{r} = a_0 + a_1 \cos(k \cdot v) + a_2 \sin(k \cdot v),\ k = 1, 2 \cdots \quad (1)$$

where $\ddot{r}$ is the empirical acceleration used in POD, a_0 is the constant acceleration, a_1 and a_2 are the coefficients of periodic acceleration, and k is the frequency of periodic acceleration. Based on a high-precision force model, the unmodeled dynamic model generally occurs at a frequency of one cycle per revolution (CPR) (i.e., 1 CPR empirical acceleration), which causes empirical acceleration, which is in the form of the orbital period [45]. For a refined PEA model, the fast Fourier transform (FFT) was used in this study to identify the potential periodicity of the satellite's empirical acceleration, and the frequency of PEA was reset for orbit determination and analysis.

To fulfill our aims, an optimized periodic PEA model was proposed and implemented for the HY-2B mission. The processing flow was roughly divided into two steps. First, the piecewise constant acceleration strategy (i.e., only a constant PEA is used in Formula (1)) was used in POD to obtain a priori information for the residual acceleration and an analysis of their spectra was performed to detect the potential periodic signals. Second, a frequency test was carried out for comparison and verification. The piecewise constant accelerations of HY-2B POD on Day 8 of the year 2019 are depicted in Figure 1, clearly indicating the time variability of the remaining accelerations. Note that the periodic signals of the PEA for three directions are generally difficult to identify (see Figure 1), and thus the FFT was used in this study.

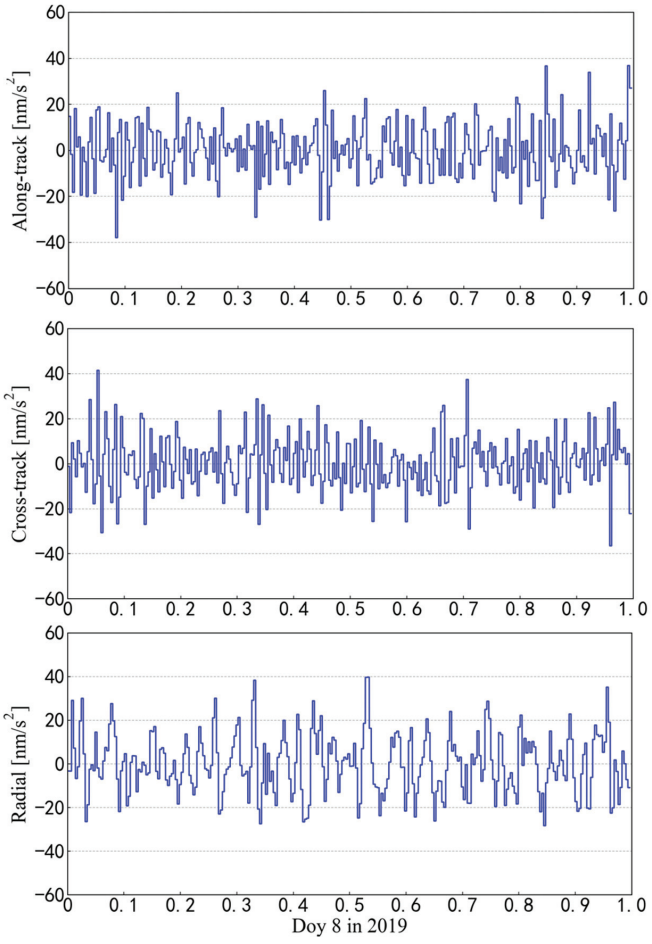

Figure 1. Piecewise constant accelerations of the reduced-dynamic orbit determination on 8 January 2019 (day of year DOY 8). These accelerations are described as constant values in the along-track (**top**), cross-track (**middle**), and radial (**bottom**) directions at consecutive intervals of 5 min.

As a starting point, estimated constant accelerations as well as reduced dynamic orbit solutions were obtained for a 14-day period, in which the acceleration value was used for spectral analysis. A power spectrum analysis of the residual accelerations in three directions is shown in Figure 2. The along-track direction and orbital radial direction show a clear periodic signal, while the results of the cross-track direction are complicated. For the along-track direction, 4 CPR is the dominant periodic signal. There is a noticeable signal of 2 CPR in the radial direction. However, a mixed spectrum is observed in the cross-track direction, and it is hard to identify the periodicity of the acceleration.

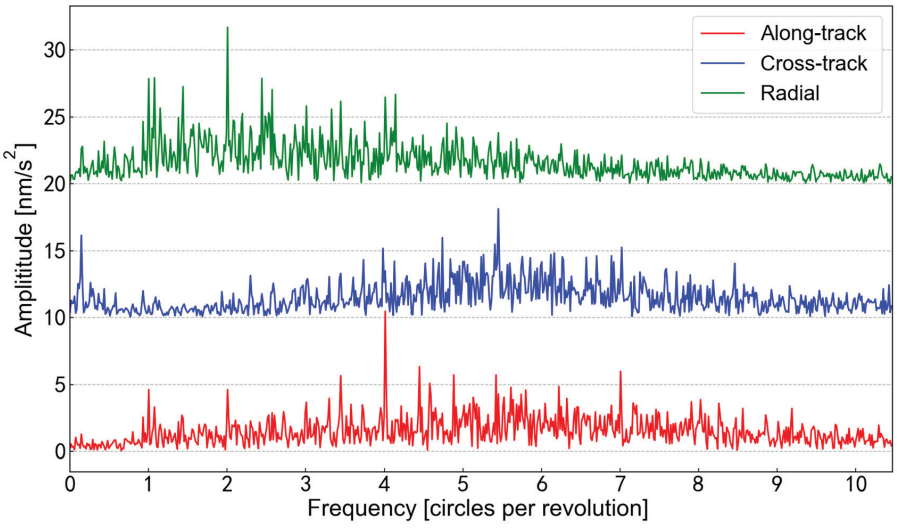

Figure 2. Amplitude spectrum of unmodeled accelerations in the along-track (red), cross-track (blue), and radial (green) directions. Values for the cross-track and radial directions are shifted by +10 nm/s^2 and +20 nm/s^2, respectively.

2.3. Refined PEA Model of HY-2B

Figure 2 shows the presence of a low-frequency signal and a 5.5 CPR signal, and the power spectrum magnitudes of the two signals are almost equivalent. Due to the existence of high- and low-frequency signals, it may be necessary to make the empirical acceleration in the cross-track direction in the form of a combination of constant and periodic signals. Moreover, the conventional 1 CPR signal in the cross-track direction can be considered as a comprehensive scheme. Based on these results, the PEA models of the empirical acceleration in the along-track and normal directions can be obtained as:

$$\begin{aligned} \ddot{r}_A &= a_1 \cos(k{\cdot}v) + a_2 \sin(k{\cdot}v),\ k = 4 \\ \ddot{r}_c &= a_0 + a_1 \cos(k{\cdot}v) + a_2 \sin(k{\cdot}v),\ k = 5.5 \end{aligned} \tag{2}$$

and:

$$\begin{aligned} \ddot{r}_A &= a_1 \cos(k{\cdot}v) + a_2 \sin(k{\cdot}v),\ k = 4 \\ \ddot{r}_C &= a_1 \cos(k{\cdot}v) + a_2 \sin(k{\cdot}v),\ k = 1 \end{aligned} \tag{3}$$

Likewise, the individual empirical accelerations in three directions can be expressed as:

$$\begin{aligned} \ddot{r}_A &= a_1 \cos(k{\cdot}v) + a_2 \sin(k{\cdot}v),\ k = 4 \\ \ddot{r}_c &= a_0 + a_1 \cos(k{\cdot}v) + a_2 \sin(k{\cdot}v),\ k = 5.5 \\ \ddot{r}_R &= a_1 \cos(k{\cdot}v) + a_2 \sin(k{\cdot}v),\ k = 2 \end{aligned} \tag{4}$$

and

$$\begin{aligned} \ddot{r}_A &= a_1 \cos(k{\cdot}v) + a_2 \sin(k{\cdot}v),\ k = 4 \\ \ddot{r}_C &= a_1 \cos(k{\cdot}v) + a_2 \sin(k{\cdot}v),\ k = 1 \\ \ddot{r}_R &= a_1 \cos(k{\cdot}v) + a_2 \sin(k{\cdot}v),\ k = 2 \end{aligned} \tag{5}$$

The periodic term of the empirical acceleration in three directions defined by the local orbital reference frame has been revealed, and the power spectrum of the cross-track direction is worth discussing. The spectrum results show that there are two differences between the normal direction and the other two directions. The power spectrum's amplitude of acceleration in the normal direction is smaller than that in the along-track and radial directions, which is related to the magnitude of acceleration and the intensity of the signal. On the other hand, there is no obvious dominant signal in the normal direction, and there are

coexisting high- and low-frequency signals. The optimal frequency combination for PEA is discussed in the following section, and a refined PEA combination can independently be inferred from the SLR validation.

3. Improvements in HY-2B POD

Based on the processing standards described in Section 2.3, assessments of each processing chain are described in this section. In addition to satellite dynamics, improving the geometric strength is a powerful means of improving the orbital accuracy of LEO satellites. GPS antenna offset calibration and an assessment of single-receiver ambiguity resolution were performed for the HY-2B satellites, as we describe in this section. An internal consistency analysis and external validations are provided for different orbit solutions. The GPS data covering the period since the initial GPS receiver operation (November 2018) to the end of 2019 were used.

3.1. Performance Analysis of the Refined PEA Model

For a clear identification, a unique identifier (ID) was introduced based on the processing strategy described in Section 2.3. The solution IDs consider the differences in the direction and frequency of PEA (see Table 2). The first digit in the code represents the along-track direction, the second digit represents the cross-track direction, and the third digit is the radial direction. The number represents the frequency of empirical acceleration in that direction. For example, the 111 solution means that the empirical acceleration is set at 1 CPR in all three directions, whereas the 110 solution means that the empirical acceleration is set at 1 CPR in the along-track and cross-track directions. The letter "C" in 110 + C represents the addition of constant acceleration in the cross-track direction to the 110 solution. To facilitate the identification, the 5.5 CPR signal is referred to as a 6 CPR signal (see Table 2). In addition to the strategies mentioned in Section 2.2, the 110 and 111 solutions were used as regular strategies for comparison.

Table 2. Three-digit codes for different PEA solutions in POD. The number represents the frequency of periodic acceleration, and the letter 'C' represents the addition of constant acceleration in the cross-track direction.

Solution Type	Along-Track		Cross-Track		Radial	
	Periodic Acc.	Constant Acc.	Periodic Acc.	Constant Acc.	Periodic Acc.	Constant Acc.
110	1 CPR	No	1 CPR	No	No	No
410	4 CPR	No	1 CPR	No	No	No
460 + C	4 CPR	No	5.5 CPR	Yes	No	No
111	1 CPR	No	1 CPR	No	1 CPR	No
412	4 CPR	No	1 CPR	No	2 CPR	No
462 + C	4 CPR	No	5.5 CPR	Yes	2 CPR	No

Spectral analysis of the unmodeled acceleration provides effective prior information for setting the frequency of the periodic PEA. The approach taken to optimize the PEA model was to change the perturbation frequency to improve the orbit's accuracy. A frequency test based on spectral analysis was used to verify whether better orbit determination results could be obtained when the empirical acceleration was consistent with the characteristic signal of the spectrum results. The SLR technique is a powerful means of evaluating a GPS-based orbit [46] and it was used to evaluate the orbit accuracy of the PEA model with different solutions. The fitting curve of the SLR residual with elevation angle and azimuth angle was used [47,48]. Eleven high-performance International Laser Ranging Service (ILRS) stations (i.e., Yarragadee (7090), Greenbelt (7105), Haleakala (7119), Hartebeest (7501), Zimmerwald (7810), Mt. Stromlo (7825), Graz (7839), Herstmonceux

(7840), Potsdam (7841), Matera (7941), and Wettzel (8834)) [46] were used for SLR validation. The relevant models used in processing are listed in Table 1.

The trend line for all stations' SLR residuals with respect to the elevation angle (see Figure 3) showed an overall dependency on the orbit solutions. The SLR residuals from the 110 orbit solution showed high dependency; much lower mean residuals were found for Solutions 410 and 460 + C. The 410 or 460 + C solutions probably represent reality well. It is worth mentioning that the empirical accelerations in the along-track direction compensated for the effect of the unmodeled part of the atmospheric drag. Both models deal with non-conservative forces in the along-track direction, and thus there is a process of mutual influence. The dependency between the SLR residuals and the azimuth angles from the stations to the satellite is shown in Figure 4. A large mean bias occurred for the 111 and 412 solutions, and a slight improvement was observed for the 462 + C solution.

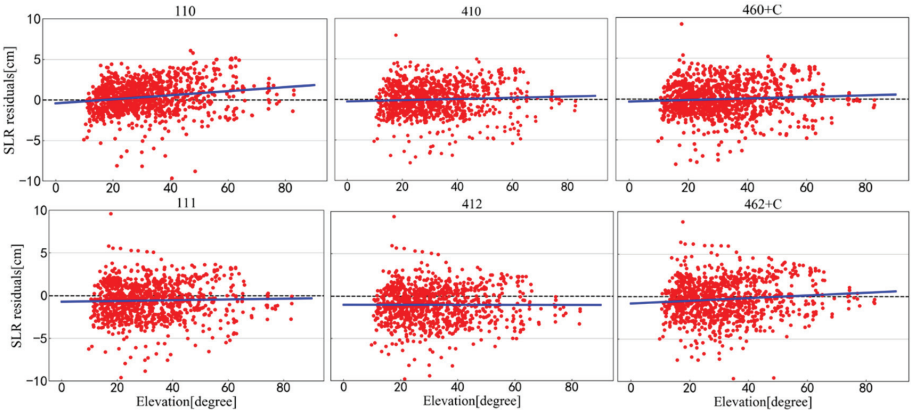

Figure 3. SLR residuals (red dot) with respect to the elevation angle for all sites, with a trend line (blue). All six PEA solutions are displayed for comparison.

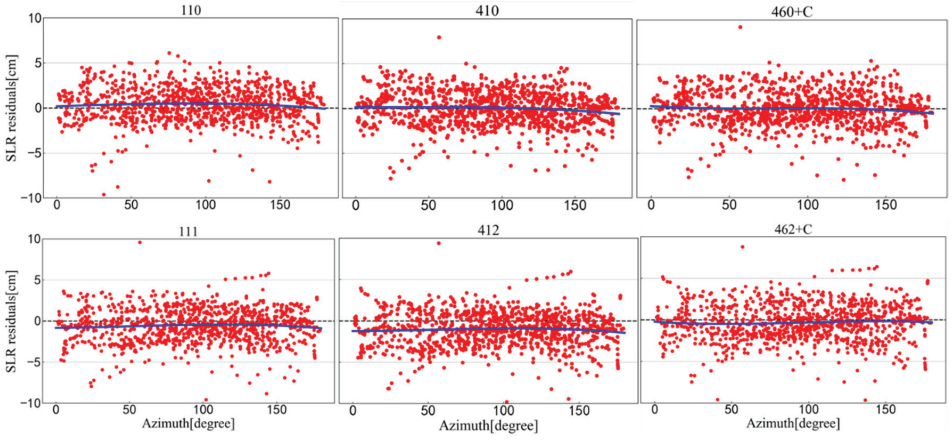

Figure 4. SLR residuals (red dot) obtained for the six PEA solutions with respect to the azimuth angle for all sites. A trend line (blue) is fitted with polynomials.

An overview of SLR validation of the different PEA solutions over a 14-day dataset is shown in Table 3. In general, the 410 orbit solution was the best for SLR validation, and the 460 + C solution closely agreed with the spectral characteristics of acceleration. The

SLR validation of this strategy was slightly worse than that of the 410 solution but it still achieved good accuracy. The SLR validation (see Table 3) showed that the 110 solution, which only estimated the acceleration in the along-track and cross-track directions, achieved the expected orbit determination accuracy. The radial direction of LEO satellites is mainly affected by conservative forces such as the gravitational field and tidal perturbation of the Earth; it is also affected by Earth radiation pressure, which results in a slight and constant acceleration. Considering the weak performance of the solutions with estimation of the radial acceleration, the related solutions (i.e., 111, 412, and 462 + C) were not used in the reprocessing of HY-2B POD.

Table 3. SLR residuals of different PEA strategies in POD. The SLR measurements were obtained from 11 individual ILRS stations and used in validations of the HY-2B orbit.

PEA Solution	Mean (mm)	RMS (mm)	Note
110	2.6	16.6	r
410	−1.5	15.7	r
460 + C	−2.0	16.5	r
111	−4.4	18.1	
412	−5.4	18.5	
462 + C	−2.1	17.5	

Note: "r" means that the PEA solution was used in the reprocessing of HY-2B POD.

Based on the spectral analysis of HY-2B empirical accelerations and orbit validation, the reprocessing arc was extended from 1 November 2018 to 1 January 2020, and three different PEA strategies were used in reprocessing (see Table 3). The SLR validation of the reprocessing of HY-2B POD is shown in Figure 5. The 110 solution participated in reprocessing as a routine strategy, while the remaining two strategies, i.e., the 410 and 460 + C solutions, performed well in the frequency test. Compared with the 110 solution, the 410 solution provided better SLR validation after changing the frequency of the along-track direction. The SLR residuals of the 11 high-performance SLR stations were improved to some extent.

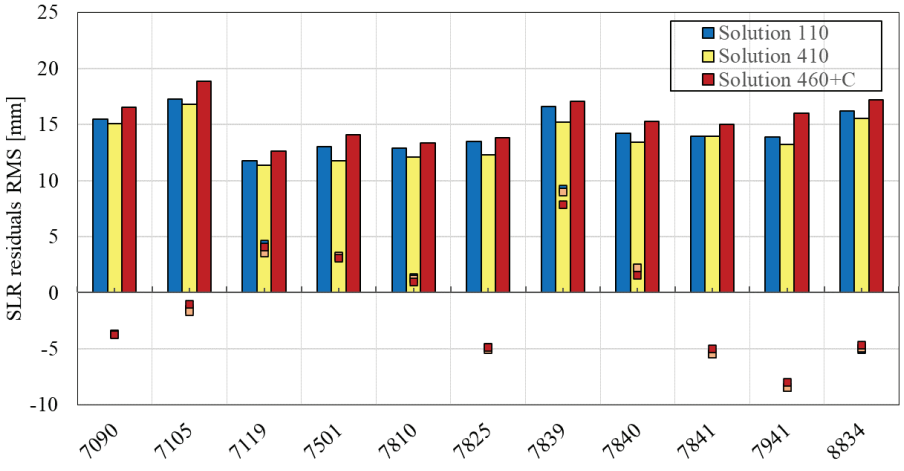

Figure 5. Statistics of the SLR residuals for individual SLR sites for three reprocessing strategies. The square is mean bias for each contributing station.

According to the SLR validation for the different PEA solutions over 14 months of the HY-2B mission, an optimized PEA strategy can be suggested. The 410 solution appeared to be the best among the three strategies in terms of SLR validation: the RMS of the SLR residuals of the 410 solution was 5.23% better than that of the 110 solution. When the frequency of the along-track direction was kept at 4 CPR, the result of the 460 + C solution with constant and periodic signals in the normal direction was slightly worse than that of the 110 solution. The 460 + C solution was the worst among those analyzed, but the average value of the SLR validation was slightly improved. For the mixed spectrum of the cross-track direction, 1 CPR as a comprehensive solution could deal with this situation well, and the validation using SLR observations proved this point.

3.2. GPS Antenna Offset Calibration

For a high-quality determination of the LEO orbit, the additional in-flight calibration of the LEO GPS antenna is essential [25,49]; the impact of unmodeled systematic errors on the HY-2B orbit is discussed. The validity of the GPS receiver antenna phase center for the HY-2B and a correction value are assessed in this section. The generation of the HY-2B GPS antenna phase center's location was based on the PCO vectors, (e.g., from the ground calibration), and no additional PCO was provided. As a starting point, the reduced-dynamic POD as well as an estimation of the PCO's z-component (i.e., the direction of the upward-facing antenna's boresight) were obtained for a 420-day period. A 20 mm systematic discrepancy in the modeled antenna phase center could be observed for the HY-2B (see Table 4). A 20 mm correction in the PCO z-component was adopted for further study, and the phase residual from POD was obviously improved, as shown in Figure 6. The negative residuals in the low-elevation area near the azimuth (0°and 180°) were significantly reduced; Figure 6 shows a typical example for this situation.

Table 4. Coordinates for the GPS receiver and CoM in the body-fixed coordinate system.

Item	Reference (x, y, z) (mm)	Notes
CoM location	(+1332.000, −8.600, +3.400)	Nov. 2018
GPS antenna location	(+347.290, −175.140, −1372.680)	Main antenna (GPS a)
GPS antenna PCO	(+0.0, +0.0, +20.0)	Estimated PCO-offset valid for ionosphere-free L1/L2

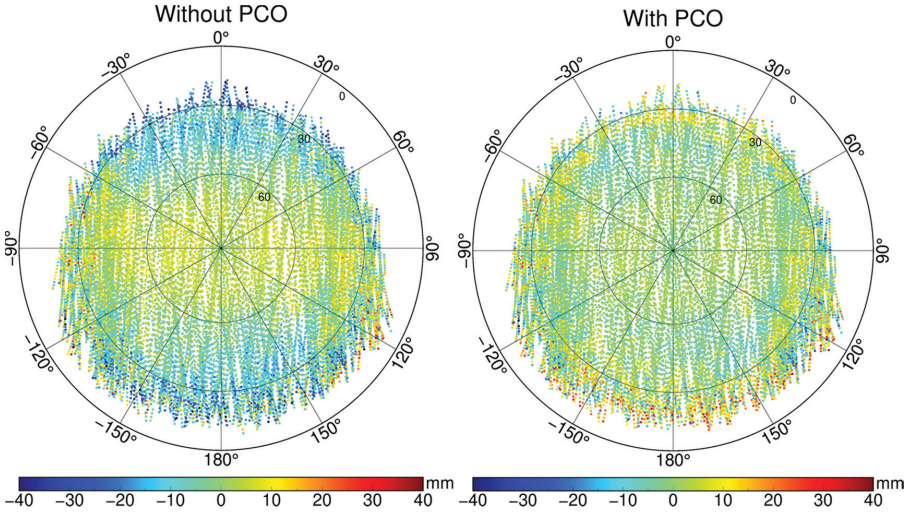

Figure 6. Sky plot of the residuals of the ionosphere-free L1/L2 carrier phase combination for HY-2B on 1 January 2019. The azimuth 0° of the antenna frame coincides with the +x-axis of the spacecraft's body, which points into the flight direction.

The residual approach [25,50] was used to obtain the phase map (see Figure 7) from the ionosphere-free carrier phase residuals over a 420-day data span. The PCV map describes the empirical phase pattern corrections around the given phase center. The static multipath or other near-field effects caused by satellite components near the GPS antenna are potential sources of these variations. Similar to other missions, flight calibration for the GPS antenna and estimation of the PCV map from actual observations have been a standard practice for POD [16,26,49].

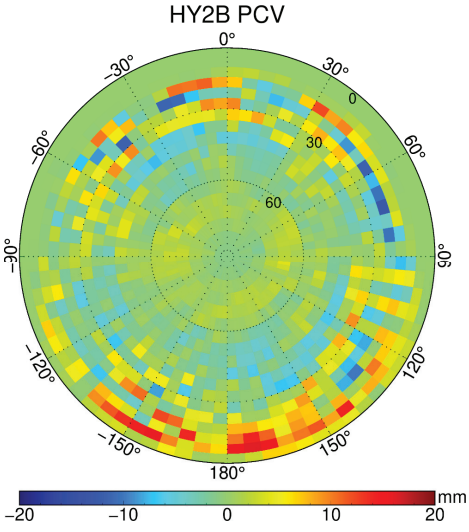

Figure 7. Estimated azimuth elevation diagrams of the 5° × 5° PCV patterns for the HY-2B satellite.

Considering fuel loss and deformation caused by in-flight temperature variations, a long-term analysis of the locations of the GPS antenna phase center was carried out. Table 4 shows the average value of the PCO z-component estimation, and the change in daily estimation is discussed (see Figure 8). The offset deviation of the PCO z-component fluctuated by about 21 mm since the start of the mission, while its offset changed by around 18 mm one year after the launch. The trend of 2–3 mm in the z-direction can be observed in Figure 8. Regular updates of the PCO of onboard receivers are indispensable to ensure high-precision orbit determination.

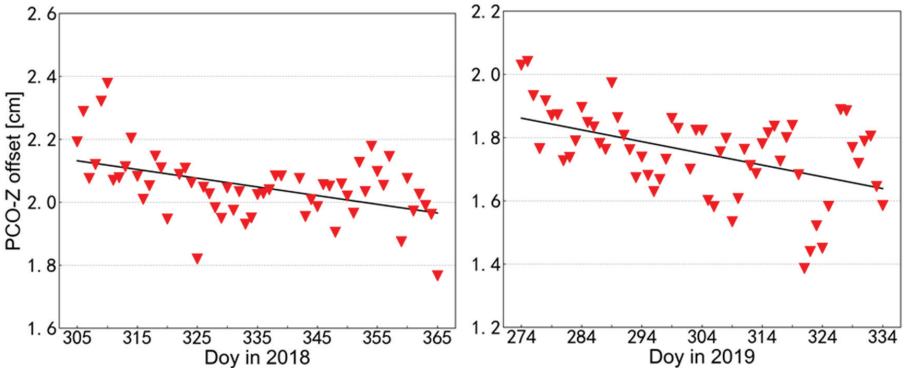

Figure 8. Estimation of the PCO z-component (red triangle) for HY-2B at the beginning of the satellite's mission (**left**) and one year later (**right**). The black line is the trend line fitted by least squares.

For an assessment of the HY-2B POD solutions with PCO/PCV correction, the uncorrected and newly corrected orbits were compared against the SLR observations. Figure 9 shows the SLR residuals of the two orbit solutions from 11 high-performance stations. It is clear that the PCO/PCV correction improved the overall accuracy of the POD solution for HY-2B. SLR validation demonstrated a 26% improvement for the orbit solution with PCO/PCV correction, and a 1.57 cm RMS of SLR residuals for the reduced-dynamic orbits was obtained. This means that the HY-2B POD product is of high quality, which is extremely important for an altimetry satellite.

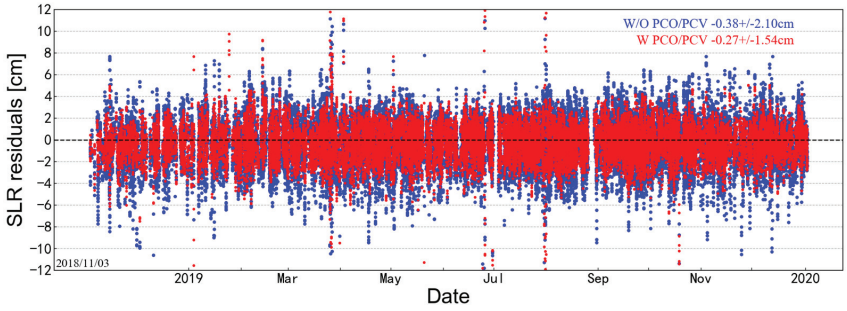

Figure 9. SLR residuals for HY-2B precise orbit determination using the nominal phase center (blue dot) and PCO/PCV correction (red dot) over a 14-month period.

3.3. *Single-Receiver Ambiguity Resolution*

Reprocessing of the raw GPS data from the HY-2B satellite covering the period from the launch (11 November 2018) to end of 2019 was performed for this study to support single-receiver ambiguity resolution. The CNES-CLS wide-lane satellite bias (WSB) product, complementary to these biases, and the CNES-CLS clock product were used in the GPS-based precise orbit determination. Details of this process and successful implementation of the Swarm GPS receiver and the Sentinel-3 GPS receiver are described in [16,29].

Over the 1-year timeframe displayed in Figure 10, average fixed rates of 92.19% for wide-lane ambiguities and 73.93% for narrow-lane ambiguities were obtained for HY-2B. Simple integer rounding is sufficient in practice to solve the mixed-integer problem [16,20], and the acceptance criterion of 0.24 and 0.12 cycles, respectively, was used. No notable variations in the success rate for wide-lane and narrow-lane ambiguity fixing could be recognized.

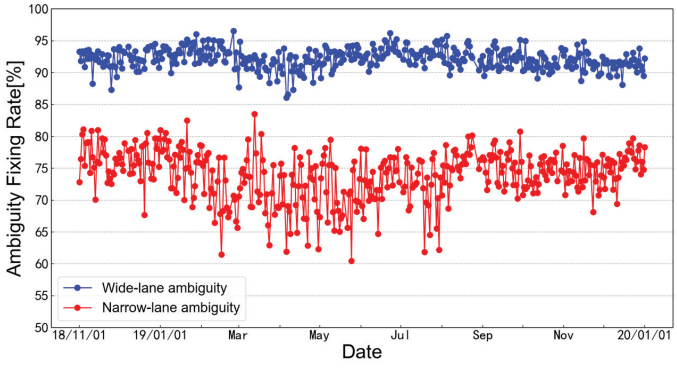

Figure 10. Fraction of passes with resolved wide-lane and narrow-lane ambiguities for the HY-2B satellite from November 2018 to the end of 2019.

SLR measurements are used as a totally independent technique to evaluate the accuracy of GPS-based orbits for the HY-2B satellite. RMS SLR residuals of 15.7 and 13.3 mm were obtained for the float ambiguity (FA) solution and the ambiguity-fixed (AF) solution, respectively (see Table 5). The overall reduction of 15.3% in the RMS SLR residuals proved that AF POD solutions are a powerful strategy for improving orbit accuracy. A well-established SLR validation depends heavily on the station coordinates and station-specific ranging biases [7,51]. For a better interpretation, the mean and standard deviation of the SLR residuals for each ILRS station are presented in Table 5. An overall mean bias of about 2 mm was found in the SLR validation. In all computations, observations above the 8° elevation were employed, and an outlier threshold of 15 cm (only 0.88% of the SLR data were rejected) was applied.

Table 5. SLR residuals and number of normal points for 11 high-performance ILRS stations used for the validation of the HY-2B orbit.

Station (ID)	N_{np}	Float Amb.		Amb. Fixed	
		Mean (mm)	STD (mm)	Mean (mm)	STD (mm)
Yarragadee (7090)	10,496	−3.3	16.0	−3.3	13.7
Greenbelt (7105)	3102	−4.2	17.3	−4.0	14.8
Haleakala (7119)	1010	3.2	11.8	3.3	10.2
Hartebeest (7501)	2265	3.4	15.6	1.9	11.3
Zimmerwald (7810)	3990	−0.4	12.4	−1.1	10.2
Mt. Stromlo (7825)	5447	−5.1	13.3	−5.5	9.9
Graz (7839)	2224	7.2	16.2	6.2	13.7
Herstmonceux (7840)	2726	−0.2	13.8	−1.4	12.2
Potsdam (7841)	1212	−8.8	13.6	−9.3	11.7
Matera (7941)	2024	−9.8	13.8	−9.7	11.4
Wettzel (8834)	1730	−8.2	17.5	−8.8	13.7
Total	36,226	−2.3	15.7	−2.7	13.3

4. Discussion

In this paper, the refined PEA strategy is proposed for superior orbital accuracy of the HY-2B satellite. A spectral analysis was performed to identify the potential periodicity of empirical acceleration in HY-2B POD. Noticeable signals were identified in the along-track and radial directions, and a mixed spectrum was observed for the cross-track direction. According to the spectral analysis of HY-2B empirical accelerations, six sets of PEA strategies were employed to assess the impact of the PEA model on the POD performance. SLR, as a completely independent space-geodetic technology, was used to evaluate the accuracy of GPS-based orbit solutions [46,52]. In order to deal with the complexity of the cross-track direction, two comprehensive PEA strategies were adopted for HY2B POD. Moreover, we found that the PEA model with empirical parameters in the along-track and cross-track directions provided satisfying orbit determination accuracy. This indicates that the forces in the radial direction of the satellite were well described by the background model. The 14 months of GPS observations are used for the reprocessing to evaluate different PEA solutions. It is worth mentioning that the optimized PEA strategy in this article is only applicable to HY2B satellites. Future work can consider investigating the POD performance of the refined PEA model for other LEO satellites and can also focus on the refinement of non-gravitational force modeling that might further reduce the uncertainty in LEO POD [13,20,24].

Similar to other LEO missions, inconsistencies at a level of 2 cm were confirmed for the HY-2B GPS antenna phase center [16,25,26]. More than one year's data were used for PCO estimation, and the change trend in the PCO z-component could be inferred from the time series of the results. The GRG provided by the CNES/CLS analysis center was used to support the implementation of HY-2B ambiguity-fixed POD solutions, which resulted in a 15% improvement of SLR residuals compared to the float solution. Similar results based on OBS-based products provided by CODE were also obtained by other LEO satellite missions [13,30]. The improvement of these GNSS products will benefit the LEO POD community.

5. Conclusions

A set of improved orbit solutions covering a period of more than a year was generated for the HY-2B satellite using a refined dynamic modeling and processing strategy. Key enhancements focused on a refined PEA strategy, GPS receiver offset calibration, and the implementation of integer ambiguity resolution. Updates to each processing strategy resulted in varying degrees of improvement for the orbit. Normally, PEA is used to absorb the uncertainties of physical modelling. To better understand the time-varying residual acceleration of spacecraft, here, we presented a refined PEA model. A spectral analysis was conducted to identify the potential periodicity of empirical acceleration in the HY-2B POD, and the main signals existing in the three dimensions (along-track, cross-track, and radial direction) were extracted and analyzed. The 4 CPR signal in the along-track direction and the 2 CPR in the radial direction were identified, and a mixed spectrum was observed for the cross-track direction. The three reprocessing strategies were applied to select an orbit solution of high quality. In the SLR validation, the refined PEA model with 4 CPR periodic acceleration in the along-track direction and 1 CPR periodic acceleration in the cross-track direction allowed a comprehensive strategy that could deal well with the mixed spectrum in the cross-track direction. Compared with regular strategies, a noticeable improvement in the SLR residuals for high-grade SLR stations was possible for orbits using the refined PEA strategy, which is still suggested as an ideal strategy for empirical acceleration modeling.

Estimation of the PCO and modeling of the PCV can effectively eliminate the systematic deviation related to signal incidence and significantly reduce the phase residuals. A systematic bias of 20 mm for the HY-2B GPS antenna phase center could be observed. Based on the PCO's z-component time series of more than 1 year, a decreasing trend appeared in this direction. For 11 high-performance SLR sites, SLR residuals with a standard deviation as low as 15.7 mm were obtained for the HY-2B POD, which produced a 25% improvement compared with the solution without PCO/PCV. Ambiguity resolution added a strong constrained geometry for other estimation parameters in POD, and better orbit precision (13.3 mm RMS) was confirmed by independent SLR measurements. Some studies related to ours are available [13,16,53]. The lean set of auxiliary data from the CNES/CLS products will be attractive for the wider LEO POD community.

Author Contributions: Conceptualization, Y.W. and M.L. (Min Li); methodology, Y.W. and K.J.; software, M.L. (Min Li) and Q.Z.; validation, K.J., W.L. and G.Q.; formal analysis, M.L. (Min Li); investigation, Y.W. and K.J.; resources, H.P. and M.L. (Mingsen Li); data curation, Y.W. and M.L. (Min Li); writing—original draft preparation, Y.W.; writing—review and editing, M.L. (Min Li); visualization, Y.W.; supervision, M.L. (Min Li); project administration, M.L. (Mingsen Li) and H.P.; funding acquisi-tion, M.L. (Min Li). All authors have read and agreed to the published version of the manuscript.

Funding: This study was supported by the National Natural Science Foundation of China (Grant Nos. 42074032, 41931075, 42030109 and 42004020) and the Wuhan Science and Technology Bureau (2019010701011391).

Data Availability Statement: The GNSS precise orbit and clock products are publicly available from ftp://igs.gnsswhu.cn/pub/gnss/products/mgex/ (accessed on 1 August 2021). The SLR observations of HY-2B is provided by ILRS at ftp://cddis.gsfc.nasa.gov/pub/slr/data/ (accessed on 1 August 2021). The SLRF2014 station coordinates is obtained from ftp://gdc.cddis.eosdis.nasa.gov/pub/slr/products/resource/ (accessed on 1 August 2021). The data that support this study are available from the corresponding author upon reasonable request.

Acknowledgments: We are grateful to the IGS for providing the GNSS products and to the ILRS for providing the SLR observations of the HY-2B satellite.

Conflicts of Interest: The authors declare no conflict of interest.

References

1. NSOAS. HY-2: A Marine Remote Sensing Satellite Series Planned by China. 2021. Available online: http://www.nsoas.org.cn/index.html (accessed on 1 August 2021).
2. Rudenko, S.; Neumayer, K.H.; Dettmering, D.; Esselborn, S.; Schone, T.; Raimondo, J.C. Improvements in Precise Orbits of Altimetry Satellites and Their Impact on Mean Sea Level Monitoring. *IEEE Trans. Geosci. Remote Sens.* **2017**, *55*, 3382–3395. [CrossRef]
3. Hackel, S.; Gisinger, C.; Balss, U.; Wermuth, M.; Montenbruck, O. Long-Term Validation of TerraSAR-X and TanDEM-X Orbit Solutions with Laser and Radar Measurements. *Remote Sens.* **2018**, *10*, 762. [CrossRef]
4. Zhang, Q.; Guo, X.; Qu, L.Z.; Zhao, Q.L. Precise Orbit Determination of FY-3C with Calibration of Orbit Biases in BeiDou GEO Satellites. *Remote Sens.* **2018**, *10*, 382. [CrossRef]
5. Tapley, B.D.; Ries, J.C.; Davis, G.W.; Eanes, R.J.; Schutz, B.E.; Shum, C.K.; Watkins, M.M.; Marshall, J.A.; Nerem, R.S.; Putney, B.H.; et al. Precision Orbit Determination for Topex/Poseidon. *J. Geophys. Res.-Oceans* **1994**, *99*, 24383–24404. [CrossRef]
6. Flohrer, C.; Otten, M.; Springer, T.; Dow, J. Generating precise and homogeneous orbits for Jason-1 and Jason-2. *Adv. Space Res.* **2011**, *48*, 152–172. [CrossRef]
7. Arnold, D.; Montenbruck, O.; Hackel, S.; Sośnica, K. Satellite laser ranging to low Earth orbiters: Orbit and network validation. *J. Geod.* **2018**, *93*, 2315–2334. [CrossRef]
8. Strugarek, D.; Sosnica, K.; Arnold, D.; Jäggi, A.; Zajdel, R.; Bury, G.; Drozdzewski, M. Determination of Global Geodetic Parameters Using Satellite Laser Ranging Measurements to Sentinel-3 Satellites. *Remote Sens.* **2019**, *11*, 2282. [CrossRef]
9. Wang, Y.C.; Guo, J.Y.; Zhou, M.S.; Jin, X.; Zhao, C.M.; Chang, X.T. Geometric solution method of SLR station coordinate based on multi-LEO satellites. *Chin. J. Geophys.* **2020**, *63*, 4333–4344. [CrossRef]
10. Wu, S.C.; Yunck, T.P.; Thornton, C.L. Reduced-dynamic technique for precise orbit determination of low earth satellites. *J. Guid. Control Dyn.* **1991**, *14*, 24–30. [CrossRef]
11. Li, M.; Li, W.W.; Shi, C.; Jiang, K.C.; Guo, X.; Dai, X.L.; Meng, X.G.; Yang, Z.D.; Yang, G.L.; Liao, M. Precise orbit determination of the Fengyun-3C satellite using onboard GPS and BDS observations. *J. Geod.* **2017**, *91*, 1313–1327. [CrossRef]
12. Kornfeld, R.P.; Arnold, B.W.; Gross, M.A.; Dahya, N.T.; Klipstein, W.M.; Gath, P.F.; Bettadpur, S. GRACE-FO: The Gravity Recovery and Climate Experiment Follow-On Mission. *J. Spacecr. Rocket.* **2019**, *56*, 931–951. [CrossRef]
13. Mao, X.; Arnold, D.; Girardin, V.; Villiger, A.; Jäggi, A. Dynamic GPS-based LEO orbit determination with 1 cm precision using the Bernese GNSS Software. *Adv. Space Res.* **2021**, *67*, 788–805. [CrossRef]
14. Montenbruck, O.; van Helleputte, T.; Kroes, R.; Gill, E. Reduced dynamic orbit determination using GPS code and carrier measurements. *Aerosp. Sci. Technol.* **2005**, *9*, 261–271. [CrossRef]
15. Jiang, K.C.; Li, M.; Wang, M.; Zhao, Q.L.; Li, W.W. TJS-2 geostationary satellite orbit determination using onboard GPS measurements. *GPS Solut.* **2018**, *22*, 87. [CrossRef]
16. Montenbruck, O.; Hackel, S.; Jäggi, A. Precise orbit determination of the Sentinel-3A altimetry satellite using ambiguity-fixed GPS carrier phase observations. *J. Geod.* **2018**, *92*, 711–726. [CrossRef]
17. Kang, Z.; Tapley, B.; Bettadpur, S.; Ries, J.; Nagel, P.; Pastor, R. Precise orbit determination for the GRACE mission using only GPS data. *J. Geod.* **2006**, *80*, 322–331. [CrossRef]
18. Bock, H.; Jäggi, A.; Beutler, G.; Meyer, U. GOCE: Precise orbit determination for the entire mission. *J. Geod.* **2014**, *88*, 1047–1060. [CrossRef]
19. Van den Ijssel, J.; Encarnação, J.; Doornbos, E.; Visser, P. Precise science orbits for the Swarm satellite constellation. *Adv. Space Res.* **2015**, *56*, 1042–1055. [CrossRef]
20. Montenbruck, O.; Hackel, S.; van den Ijssel, J.; Arnold, D. Reduced dynamic and kinematic precise orbit determination for the Swarm mission from 4 years of GPS tracking. *GPS Solut.* **2018**, *22*, 79. [CrossRef]
21. Švehla, D.; Rothacher, M. Kinematic and reduced-dynamic precise orbit determination of low earth orbiters. *Adv. Geosci.* **2003**, *1*, 47–56. [CrossRef]
22. Jäggi, A.; Hugentobler, U.; Beutler, G. Pseudo-Stochastic Orbit Modeling Techniques for Low-Earth Orbiters. *J. Geod.* **2006**, *80*, 47–60. [CrossRef]
23. Hackel, S.; Montenbruck, O.; Steigenberger, P.; Balss, U.; Gisinger, C.; Eineder, M. Model improvements and validation of TerraSAR-X precise orbit determination. *J. Geod.* **2016**, *91*, 547–562. [CrossRef]

24. Hackel, S. *Refinement of Reduced-Dynamic Orbit Determination for Low Earth Satellites*; Technische Universität München: Munich, Germany, 2019.
25. Jäggi, A.; Dach, R.; Montenbruck, O.; Hugentobler, U.; Bock, H.; Beutler, G. Phase center modeling for LEO GPS receiver antennas and its impact on precise orbit determination. *J. Geod.* **2009**, *83*, 1145–1162. [CrossRef]
26. Lu, C.X.; Zhang, Q.; Zhang, K.K.; Zhu, Y.T.; Zhang, W. Improving LEO precise orbit determination with BDS PCV calibration. *GPS Solut.* **2019**, *23*, 109. [CrossRef]
27. Visser, P.N.A.M.; van den Ijssel, J.A.A. Calibration and validation of individual GOCE accelerometers by precise orbit determination. *J. Geod.* **2015**, *90*, 1–13. [CrossRef]
28. Peter, H.; Jäggi, A.; Fernández, J.; Escobar, D.; Ayuga, F.; Arnold, D.; Wermuth, M.; Hackel, S.; Otten, M.; Simons, W.; et al. Sentinel-1A—First precise orbit determination results. *Adv. Space Res.* **2017**, *60*, 879–892. [CrossRef]
29. Laurichesse, D.; Mercier, F.; Berthias, J.P.; Broca, P.; Cerri, L. Integer ambiguity resolution on undifferenced GPS phase measurements and its application to PPP and satellite precise orbit determination. *Navigation* **2009**, *56*, 135–149. [CrossRef]
30. Schaer, S.; Villiger, A.; Arnold, D.; Dach, R.; Prange, L.; Jäggi, A. The CODE ambiguity-fixed clock and phase bias analysis products: Generation, properties, and performance. *J. Geod.* **2021**, *95*, 81. [CrossRef]
31. Loyer, S.; Perosanz, F.; Mercier, F.; Capdeville, H.; Marty, J.-C. Zero-difference GPS ambiguity resolution at CNES–CLS IGS Analysis Center. *J. Geod.* **2012**, *86*, 991–1003. [CrossRef]
32. Rebischung, P.; Schmid, R. IGS14/igs14.atx: A new framework for the IGS products. In Proceedings of the AGU Fall Meeting Abstracts, San Francisco, CA, USA, 12–16 December 2016.
33. Schmid, R.; Dach, R.; Collilieux, X.; Jäggi, A.; Schmitz, M.; Dilssner, F. Absolute IGS antenna phase center model igs08.atx: Status and potential improvements. *J. Geod.* **2016**, *90*, 343–364. [CrossRef]
34. Shako, R.; Förste, C.; Abrikosov, O.; Bruinsma, S.; Marty, J.-C.; Lemoine, J.-M.; Flechtner, F.; Neumayer, H.; Dahle, C. EIGEN-6C: A High-Resolution Global Gravity Combination Model Including GOCE Data. In *Observation of the System Earth from Space—Champ, Grace, Goce and Future Missions*; Flechtner, F., Sneeuw, N., Schuh, W.-D., Eds.; Advanced Technologies in Earth Sciences; Springer: Berlin/Heidelberg, Germany, 2014; pp. 155–161.
35. Petit, G.; Luzum, B. *IERS Conventions*; Bureau International des Poids et Mesures: Sevres, France, 2010.
36. Lyard, F.; Lefevre, F.; Letellier, T.; Francis, O. Modelling the global ocean tides: Modern insights from FES2004. *Ocean Dyn.* **2006**, *56*, 394–415. [CrossRef]
37. Standish, E.M. JPL Planetary and Lunar Ephemerides, DE405/LE405. Interoffice Memorandum: JPL IOM 312.F-98-048, 1998, August 26. Available online: ftp://ssd.jpl.nasa.gov/pub/eph/planets/ioms/de405.iom.pdf (accessed on 1 August 2021).
38. McCarthy, D.D.; Petit, G. IERS Conventions (2003). *IERS Tech. Note* **2004**, *32*, 1.
39. Vielberg, K.; Kusche, J. Extended forward and inverse modeling of radiation pressure accelerations for LEO satellites. *J. Geod.* **2020**, *94*, 43. [CrossRef]
40. Bruinsma, S. The DTM-2013 thermosphere model. *J. Space Weather Space Clim.* **2015**, *5*, A1. [CrossRef]
41. ILRS. SLRF2014 Station Coordinates. 2020. Available online: ftp://gdc.cddis.eosdis.nasa.gov/pub/slr/products/resource/SLRF2014_POS+VEL_2030.0_200325.snx (accessed on 1 August 2021).
42. Mendes, V.B.; Pavlis, E.C. High-accuracy zenith delay prediction at optical wavelengths. *Geophys. Res. Lett.* **2004**, *31*. [CrossRef]
43. Hugentobler, U.; Montenbruck, O. Satellite Orbits and Attitude. In *Springer Handbook of Global Navigation Satellite Systems*; Teunissen, P.J.G., Montenbruck, O., Eds.; Springer International Publishing: Cham, Switzerland, 2017; pp. 59–90.
44. Dewitte, S.; Clerbaux, N. Measurement of the Earth Radiation Budget at the Top of the Atmosphere—A Review. *Remote Sens.* **2017**, *9*, 1143. [CrossRef]
45. Montenbruck, O.; Gill, E.; Lutze, F.H. Satellite Orbits: Models, Methods, and Applications. *Appl. Mech. Rev.* **2002**, *55*, B27. [CrossRef]
46. Pearlman, M.R.; Degnan, J.J.; Bosworth, J.M. The international laser ranging service. *Adv. Space Res.* **2002**, *30*, 135–143. [CrossRef]
47. Strugarek, D.; Sosnica, K.; Jäggi, A. Characteristics of GOCE orbits based on Satellite Laser Ranging. *Adv. Space Res.* **2019**, *63*, 417–431. [CrossRef]
48. Strugarek, D.; Sośnica, K.; Zajdel, R.; Bury, G. Detector-specific issues in Satellite Laser Ranging to Swarm-A/B/C satellites. *Measurement* **2021**, *182*, 109786. [CrossRef]
49. Luthcke, S.B.; Zelensky, N.P.; Rowlands, D.D.; Lemoine, F.G.; Williams, T.A. The 1-Centimeter Orbit: Jason-1 Precision Orbit Determination Using GPS, SLR, DORIS, and Altimeter Data Special Issue: Jason-1 Calibration/Validation. *Mar. Geod.* **2010**, *26*, 399–421. [CrossRef]
50. Haines, B.; Bar-Sever, Y.; Bertiger, W.; Desai, S.; Willis, P. One-Centimeter Orbit Determination for Jason-1: New GPS-Based Strategies. *Mar. Geod.* **2004**, *27*, 299–318. [CrossRef]
51. Zajdel, R.; Sosnica, K.; Bury, G. A New Online Service for the Validation of Multi-GNSS Orbits Using SLR. *Remote Sens.* **2017**, *9*, 1049. [CrossRef]
52. Pearlman, M.; Arnold, D.; Davis, M.; Barlier, F.; Biancale, R.; Vasiliev, V.; Ciufolini, I.; Paolozzi, A.; Pavlis, E.C.; Sośnica, K.; et al. Laser geodetic satellites: A high-accuracy scientific tool. *J. Geod.* **2019**, *93*, 2181–2194. [CrossRef]
53. Zhou, X.; Chen, H.; Fan, W.; Zhou, X.; Chen, Q.; Jiang, W. Assessment of single-difference and track-to-track ambiguity resolution in LEO precise orbit determination. *GPS Solut.* **2021**, *25*, 62. [CrossRef]

remote sensing

MDPI

Article

GRACE-FO Antenna Phase Center Modeling and Precise Orbit Determination with Single Receiver Ambiguity Resolution

Biao Jin [1,2,3], Yuqiang Li [1,*], Kecai Jiang [4], Zhulian Li [1] and Shanshan Chen [3]

[1] Yunnan Observatories, Chinese Academy of Sciences, Kunming 650216, China; jinb@spacestar.com.cn (B.J.); lzhl@ynao.ac.cn (Z.L.)
[2] University of Chinese Academy of Sciences, Beijing 100049, China
[3] Space Star Technology Co., Ltd., Beijing 100194, China; chenss@spacestar.com.cn
[4] GNSS Research Center, Wuhan University, 129 Luoyu Road, Wuhan 430079, China; kc.jiang@whu.edu.cn
* Correspondence: lyq@ynao.ac.cn

Abstract: Precise knowledge of the phase center location of the global navigation satellite system (GNSS) antenna is a prerequisite for precise orbit determination (POD) of the low Earth orbit (LEO) satellite. The phase center offset (PCO) and phase center variation (PCV) values for the LEO antenna obtained from ground calibration cannot reflect the error sources encountered in the actual spacecraft environment. PCV corrections are estimated by ionosphere free (IF) carrier phase post-fit residuals of reduced dynamic orbit determination. Ambiguity resolution (AR) plays a crucial role in achieving the best orbit accuracy. The single receiver AR concept is realized using wide-lane (WL) and narrow-lane (NL) bias products. Single difference (SD) observations between satellites are applied to remove the receiver dependent phase bias. SD AR and traditional double difference (DD) AR methods are applied to fix the ambiguities. The recovered SD and DD IF ambiguities are taken as pseudo-observations to constrain the undifferenced IF ambiguity parameters in the POD process. The LEO orbits based on float ambiguity (FA), SD, AR, and DD AR are investigated. One year's data collected by the Gravity Recovery And Climate Experiment Follow-On (GRACE-FO) mission and GPS precise products provided by the Center for Orbit Determination in Europe (CODE) were analyzed. Precise orbit generated by the Jet Propulsion Laboratory (JPL), independent satellite laser ranging (SLR), and K-band ranging (KBR) measurements were utilized to assess the orbit accuracy. More than 98% of SD WL and 95% of SD NL ambiguities are fixed, which confirms the good quality of the bias products and correctness of the SD AR method. With PCV corrections, the average phase residuals of DD and SD AR solutions are 0.13 and 0.41 mm, which indicates improved consistency between applied models and observations. Compared with JPL's orbit, the SD AR orbits achieve the accuracy of 6.0, 6.2, and 5.1 mm in along-track, cross-track, and radial directions. The SD AR solutions show an average improvement of 18.3% related to the FA orbits while 6.3% is gained by the DD AR approach. The root mean squares (RMSs) of SLR residuals for FA, DD AR, and SD AR solutions are 11.5, 10.2, and 9.6 mm, which validate the positive effect of AR on POD. Standard deviation (STD) of KBR residuals for SD AR orbits is 1.8 mm while 0.9 mm is achieved by the DD AR method. The explanation is that the phase bias products used for SD AR are not free of errors and the errors may degrade the KBR validation. In-flight PCV calibration and ambiguity resolution improve the LEO orbit accuracy effectively.

Keywords: single receiver ambiguity resolution; phase center variation (PCV) calibration; precise orbit determination; GRACE-FO satellites

Citation: Jin, B.; Li, Y.; Jiang, K.; Li, Z.; Chen, S. GRACE-FO Antenna Phase Center Modeling and Precise Orbit Determination with Single Receiver Ambiguity Resolution. *Remote Sens.* **2021**, *13*, 4204. https://doi.org/10.3390/rs13214204

Academic Editor: Stefania Bonafoni

Received: 20 August 2021
Accepted: 14 October 2021
Published: 20 October 2021

1. Introduction

Low Earth orbit (LEO) satellites are considered as key technologies for space missions due to their advantages of flexibility, redundancy, efficiency, and low cost. To fulfill scientific mission requirements, precise absolute or relative positions are required. The precise orbit determination (POD) capability, based on spaceborne Global Positioning System (GPS)

observations, has been successfully verified on the TOPEX/Poseidon satellite [1,2]. The reduced dynamic POD technique [3,4] combined with the strength of GPS observations has shown its advantages in sampling rate and accuracy. Since then, more GPS receivers have been deployed on LEO satellites to meet the needs of various scientific missions for high precision orbit.

The quality of global navigation satellite system (GNSS) derived LEO orbits has steadily improved thanks to numerous improvements in the GNSS orbit and clock products provided by the International GNSS Service (IGS) [5], in the dynamic background models, and in modeling the carrier phase observations. LEO orbit accuracy of 1–3 cm can be fulfilled with float ambiguity (FA) [6,7]. With GPS precise orbit and clock products provided by IGS, CHAMP orbit calculated with ionosphere free (IF) observations achieves the accuracy of centimeter level [8]. GRACE orbit determined using GPS has been proven by independent satellite laser ranging (SLR) and K-band ranging (KBR) data, and 1 cm radial orbit accuracy has been achieved [9]. JASON's GPS derived orbit is evaluated based on SLR residuals, dynamic orbit produced by SLR/DORIS data, and altimeter crossover tests [10,11], and the sub-centimeter radial accuracy is verified. Similar results are also obtained in other LEO satellite missions, such as GOCE [12,13], Sentinel [14,15], TerraSAR-X [7], HY [16], and FY-3 [17,18] satellites. Ambiguity resolution (AR) and in-flight antenna phase center variation (PCV) calibration are essential to fully exploit the precision of GPS observations for POD.

In order to fix the carrier phase ambiguities, a Kalman filter modeling the relative spacecraft dynamics has been developed for the GRACE mission and the double difference (DD) ambiguities are resolved to fully exploit the inherent measurement accuracy. Finally, the resulting GRACE orbit matches the KBR measurements with an accuracy of 1 mm [19]. A GRACE POD based on undifferenced and doubly differenced GPS data is studied [6]. Different baselines, including the space baseline between two GRACE satellites, the space-ground baselines consisting of LEO satellites and ground stations, and both types of baselines together, are processed. Results show that fixing of the GPS DD ambiguities has a significant impact on the space baseline [6]. With the orbit solution constrained by resolved DD ambiguities, a GRACE baseline accuracy of 2 mm is also achieved [20].

The double difference ambiguity resolution (DD AR) approach requires two satellites to construct the baseline. Several methods have been developed to resolve the integer ambiguity for the single receiver user. The idea of a single receiver integer ambiguity resolution forms the basis of PPPRTK. Taking the ionospheric delay as the unknown parameter, the common clock model [21,22] and distinct clocks model [23,24] are proposed to perform the single receiver ambiguity resolution. For IF formulation, the integer recovery clock (IRC) model [25,26], decoupled satellite clock (DSC) model [27], and uncalibrated phase delay (UPD) or fractional cycle bias (FCB) model [28,29] are presented. The S-system theory is applied by Teunissen to establish the linkage among different PPP-RTK methods [30,31]. Their differences are shown to lie (a) in the choice of S-basis; (b) in the choice of parameterization; (c) in the choice of whether or not to eliminate the ionospheric delay.

With wide-lane (WL) and phase biases provided by the Jet Propulsion Laboratory (JPL), the single receiver AR of GRACE and JASON-2 satellites is realized [32]. GRACE baseline accuracy is improved from 6 mm of float ambiguity solution to 2 mm of ambiguity fixed solution. Based on GPS orbit, clock, and WL bias products provided by Centre National d'Études Spatiales (CNES) [26], single receiver AR is also employed to generate the orbit of Sentinel-3A satellite and the root mean square (RMS) of SLR residuals decreases from 9 to 5 mm [15]. Using the observation specific bias (OSB) products provided by the Center for Orbit Determination in Europe (CODE), AR is applied to the POD of GRACE and Sentinel-3 satellites [33]. Ambiguity fixing improves the orbit quality with validation of KBR and SLR residuals, as well as the internal consistency between the reduced dynamic and kinematic orbits. With UPDs estimated via a global distributed network, kinematic orbits of Sentinel-3A and Swarm-A satellites are determined with AR [34]. SLR residuals show an improvement of 20% for AR solution when compared with the FA solution.

Different AR solutions, including DD AR, single difference (SD) AR, and integrated SD and DD AR solutions are investigated with GRACE data to access their effects on orbit accuracy [35].

Another factor affecting the orbit accuracy of the LEO satellite is the phase center position of the spaceborne GNSS antenna. Nominal antenna models obtained from ground calibration have been made available for the antennas deployed on several space missions, such as GRACE [36], GOCE [37], Swarm [38], and TerraSAR-X [39]. Such nominal antenna models, however, do not reflect the influence of error sources, which are additionally encountered in the actual spacecraft environment, e.g., the influence of near-field multipath [36]. In-flight calibration of the LEO antenna is necessary for the stringent orbit accuracy requirement, especially for the altimeter mission. Two different approaches, the residual approach and the direct approach, can be used to determine the empirical PCV correction of the LEO antenna. Using the residual approach, the PCV map of JASON-1 satellite is created. The mean post-fit phase residual is decreased from 8 to 5 mm, and 1 cm radial accuracy is demonstrated [40]. PCV correction of the GOCE satellite is determined with 154 days of data and the consistency of reduced dynamic and kinematic orbits is improved when applying the PCV map [37]. An error in the given phase center offset (PCO) of Sentinel-1A antenna has been found by comparing different PCVs and different POD approaches [14]. The influence of relative PCV on precise baseline determination (PBD) of formation flying satellites is also studied [41]. With application of the generated relative PCVs of GRACE and GRACE-FO satellites, the consistency of KBR measurements is improved by 30%. The effects of antenna PCV on orbit determination and clock estimation for CentiSpace-1 satellite, which served as a navigation satellite, were analyzed [42].

The twin GRACE-FO satellites (named GRCC and GRCD hereafter), designed as a successor of GRACE, and jointly developed by the National Aeronautics and Space Administration (NASA) and the German Research Centre for Geosciences (GFZ), were launched from California, USA, on May 22, 2018 [43]. The main goals of GRACE-FO are to continuously provide high resolution monthly solutions of the Earth's gravity field, surface mass change, and to measure the vertical temperature and humidity profiles of the Earth's atmosphere [44]. GRACE and GRACE-FO satellites adopt the same satellite appearance design, and are equipped with the KBR system, GPS receiver, SLR retroreflector, star camera assembly (SCA), and other scientific instruments [44,45]. The appearance and instrument installation position of GRACE-FO satellites are illustrated in Figure 1 [46].

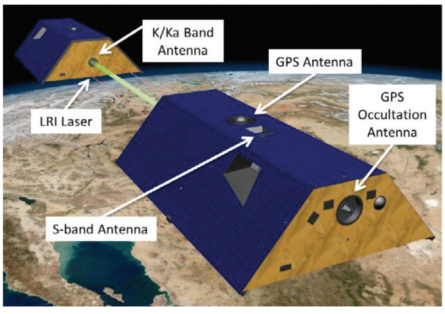

Figure 1. Appearance and instrument installation position of GRACE-FO satellites.

Effects of PCV correction on POD of GRACE-FO satellites have been explored [35,43]. However, impacts of different ambiguity resolution strategies and in-flight PCV calibration on POD and PBD still need more investigation. In this analysis, antenna PCV models of GRACE-FO satellites are developed to further exploit the POD accuracy. Single receiver and double difference integer ambiguity resolution methods are investigated and realized. With one year of data, GRACE-FO orbits based on different AR strategies, including FA, SD AR, and DD AR, are studied and evaluated with JPL's orbit, SLR, and KBR measurements.

Section 2 provides details of the strategy and data adopted for GRACE-FO POD. The antenna PCV estimation approach and related results are presented in Section 3. Section 4 introduces the GNSS observation model and focuses on the SD and DD AR. POD and PBD results with PCV corrections and different AR methods were analyzed. The necessity of in-flight antenna calibration and ambiguity resolution is verified. Finally, discussions are made, followed by conclusions.

2. POD Strategy and Data Usage

2.1. POD Strategy

The reduced dynamic approach is employed to determine the orbits of GRACE-FO satellites. The Position And Navigation Data Analyst (PANDA) software [47], developed at the GNSS research center of Wuhan University, is modified and used for the POD process. The POD strategy is listed in Table 1. The macro model of GRACE-FO satellites [44] is applied to model the non-gravitational forces, which mainly result from atmospheric drag, solar, and earth radiation pressure. The atmospheric density values required for atmospheric drag modeling are obtained with the DTM94 model [48]. To account for deficiencies in DTM94 and the macro model, drag coefficient is estimated freely once per orbital revolution. Solar radiation pressure is calculated based on the satellite macro model and a scale factor is estimated per orbit determination arc. Additionally, one cycle per revolution (CPR) empirical accelerations in along-track and cross-track directions are estimated to compensate for deficiencies in the adopted force models. Other estimated parameters include receiver clock offsets and carrier phase ambiguities. The GRACE-FO antenna PCOs are applied according to the VGN1B product [44]. PCV corrections for IF carrier phase observations are calculated using the method described in Section 3.1.

Table 1. POD strategy of GRACE-FO satellites.

Parameter	Description
Background force models	
Static gravity field model	EIGEN_06C (130 × 130) [49]
Solid earth and pole tides	IERS Conventions 2010 [50]
Ocean tides	FES2004 (30 × 30) [51]
Ocean pole tides	Desai [52] (30 × 30)
Third body perturbations	JPL's DE405
General relativistic effects	IERS Conventions 2010 [50]
Solar radiation pressure	Macro model [44]
Atmospheric drag	Macro model [44], DTM94 [48]
Input data and products	
GPS Observations	Undifferenced IF code and carrier phase
Sample interval	10 s
Elevation mask	0°
GPS orbit	CODE's final GPS orbit
GPS clock and hardware bias	CODE's 5 s clock and OSB products
GPS antenna correction	igs14.atx
GRACE-FO antenna correction	PCO applied [44]
Phase wind-up	Applied [53]

Table 1. *Cont.*

Parameter	Description
Gravitational bending	IERS Conventions 2010 [50]
Relativistic correction	IERS Conventions 2010 [50]
Estimated parameters	
Initial state vector	Position and velocity per satellite per arc
Atmospheric drag coefficient	One per orbital resolution
Scale coefficient of solar radiation pressure	One per satellite per arc
Empirical along- and cross-track accelerations	1-CPR accelerations per orbital resolution
Receiver clock errors	Epoch wise
Carrier phase ambiguities	One per satellite tracking pass

According to the ambiguity resolution methods, three kinds of orbits are calculated. The first orbit is calculated with float ambiguities (donated as FA solution hereafter), the second solution is constrained by integer DD ambiguities (DD AR solution), and the third orbit is generated with the constraint of integer SD ambiguities (SD AR solution).

2.2. Data Usage

The twin GRACE-FO satellites fly a polar orbit with an altitude of 490 km. Over the mission lifetime, the two satellites will remain in co-planar orbits and the along-track separation is about 220 km. For POD, the GRACE-FO satellites are equipped with the new generation of the GNSS space science receiver, the TriG receiver. The receiver upgrades the capabilities offered by the BlackJack receiver, which was carried on the GRACE mission. GPS C/A, P1, and P2 pseudoranges, and associated carrier phase observations, namely LA, L1, and L2 can be provided by the receiver [54]. The GPS P1 and P2 pseudoranges and L1 and L2 carrier phase observations are used in this research.

One year of data in 2019 is processed. The data can be obtained from the GRACE-FO level 1B RL04 products, which are available at ftp://isdcftp.gfz-potsdam.de/grace-fo/ (accessed on 17 October 2021). The products also include the satellite attitude (SCA1B), precise orbits provided by JPL (GNV1B), biased inter-satellite ranges measured by KBR system (KBR1B), and the positions of the GPS antenna phase center (VGN1B). The GNV1B and KBR1B data can be used to assess the orbit quality. PCOs of ionosphere free carrier phase observations and SLR reflector positions in the science reference frame (SRF) are listed in Table 2. CODE's GPS final orbits and 5 s clock products are used, and the associated OSB products are also applied to allow for SD AR [55,56].

Table 2. GPS antenna PCOs and SLR reflector Coordinates of GRACE-FO satellites.

Satellite	GPS Antenna PCO/m			SLR Reflector/m		
	X	Y	Z	X	Y	Z
GRCC	0.26023	−0.00128	−0.47697	0.60000	0.32750	0.22080
GRCD	0.26004	−0.00107	−0.47618	0.60000	0.32750	0.22080

3. Estimation of PCV Corrections

3.1. Mathematical Models

Modeling GNSS observation requires the computation of the geometric distance between the antenna phase center location of the GNSS satellite at signal emission time and the antenna phase center location of the receiving antenna at signal reception time. The phase center location usually differs from the mechanical antenna reference point (ARP). The difference vector is conventionally described by a set of phase center corrections. Such

a set of corrections consists of a PCO vector, which defines the position of the mean antenna phase center, with respect to the ARP and a consistent function, which models the azimuth and zenith dependent PCVs [36].

Phase center corrections have some inherent degrees of freedom. One set of corrections consisting of a PCO vector r_0 and an azimuth and zenith dependent function $\phi(\alpha, z)$ can be transformed into a new set, consisting of r_0' and $\phi'(\alpha, z)$, which gives the same result:

$$\begin{aligned} r_0' &= r_0 + \Delta r \\ \phi'(\alpha, z) &= \phi(\alpha, z) - \Delta r \cdot e + \Delta\phi \end{aligned} \tag{1}$$

where α and z are azimuth and zenith angles, $\Delta\phi$ is an arbitrary offset and cannot be separated from the receiver clock. The unit vector e denotes the direction from the receiver to the satellite. The offset vector Δr can be chosen arbitrarily. Preferably, PCVs should not induce a PCO and Δr should be zero. In that case, the mean antenna phase center is explicitly defined by the PCO. This convention is particularly important if one would only apply PCO and no PCV [14].

Taking computational burden into consideration, residual approach is employed in this research. The antenna PCV is represented as piecewise linear function with respect to the zenith and azimuth angles in the antenna fixed coordinate system. The model assumes that PCV is composed of different grids, and zenith and azimuth angles are equally divided. When the observation is at the point of P within the grid ABCD, its PCV value can be linearly interpolated:

$$\begin{aligned} &\Delta_{PCV,P} = (1-\gamma)(1-\beta)\Delta_{PCV,A} + \gamma(1-\beta)\Delta_{PCV,B} + \gamma\beta\Delta_{PCV,C} + (1-\gamma)\beta\Delta_{PCV,D} \\ &\gamma = (\alpha - \alpha_1)/(\alpha_2 - \alpha_1), \beta = (z - z_1)/(z_2 - z_1) \end{aligned} \tag{2}$$

where $\Delta_{PCV,P}$ is the PCV at point P and is observation, $\Delta_{PCV,i}(i = A, B, C, D)$ are the PCVs at points A, B, C, D are parameters to be estimated. γ and β are combination coefficients, α and z are azimuth and zenith angles of P, α_1 is the azimuth of point A and D, α_2 is the azimuth of B and C, z_1 is the zenith of A and B, z_2 is the zenith of C and D.

3.2. Results

The PCOs of GRACE-FO satellites provided in the VGN1B product are introduced as fixed and only the PCVs are estimated. Residual approach [36] is employed with three iterations to obtain the PCV maps. Resolutions in azimuth and zenith are 5°. Two kinds of PCV maps are created—one is generated with the phase residuals from DD AR solution and the other is derived from the SD AR solution.

Figure 2 are PCV maps of GRACE-FO satellites produced from the DD AR solution. The azimuth of 0° points into the direction of flight. A similarity exists between the PCVs of GRCC and GRCD satellites, especially in the azimuth ranges of 90°–180° and 270°–360°. The absolute maximum PCV of GRCC satellite is −14.56 mm with azimuth angle 185° and elevation angle 25°. For the GRCD satellite, the absolute maximum PCV is −14.95 mm with azimuth angle 190° and elevation angle 30°.

Figure 3 presents the PCV maps produced from the SD AR solution. The absolute maximum PCV of GRCC satellite is −12.57 mm with azimuth angle 185° and elevation angle 25°, while the GRCD satellite is −12.15 mm with azimuth angle 185° and elevation angle 30°. The PCV maps generated from DD AR and SD AR solutions have similar patterns when comparing Figure 2a with Figure 3a and comparing Figure 2b with Figure 3b. The PCVs made from the SD AR solution have less maximum values.

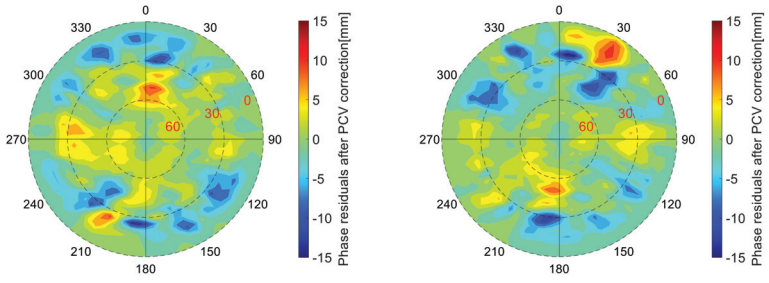

Figure 2. The 5° × 5° PCV corrections of (**a**) GRCC and (**b**) GRCD satellites based on ionosphere free carrier phase residuals from the DD AR solution.

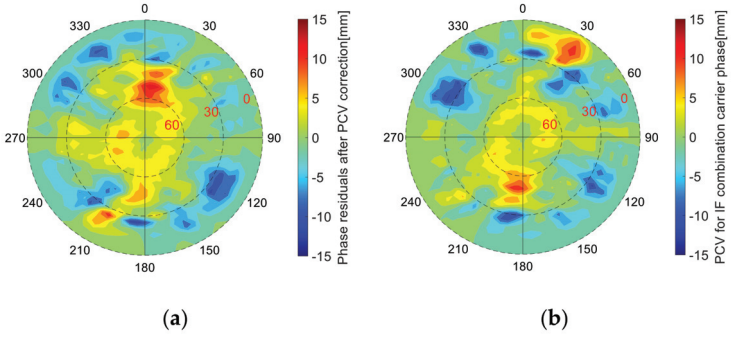

Figure 3. The 5° × 5° PCV corrections of (**a**) GRCC and (**b**) GRCD satellites based on ionosphere free carrier phase residuals from SD AR solution.

PCV maps in Figures 2 and 3 are used to correct the carrier phase observations and then to perform the POD. All available carrier phase residuals are averaged and Figure 4 illustrates the results of GRCC satellite. Figure 4a presents the carrier phase residuals from the DD AR solution while Figure 4b presents the residuals from the SD AR solution. It should be noted that the limit of the color bar is 5 mm. With application of the PCV corrections, most of the carrier phase residuals of the DD AR solution are less than 1 mm and the mean value is 0.13 mm. The carrier phase residuals of the SD AR solution are a bit larger, especially in the range with azimuth of 0°–30° and elevation of 30°–60°, the average is 0.41 mm. Similar results are obtained for the GRCD satellite and are not shown here. Carrier phase residuals can be used to measure the consistency between the applied models and GPS observations. It can be induced that the application of PCV corrections improves the orbit accuracy. The effects of PCV correction on POD and PBD will be presented in the following sections.

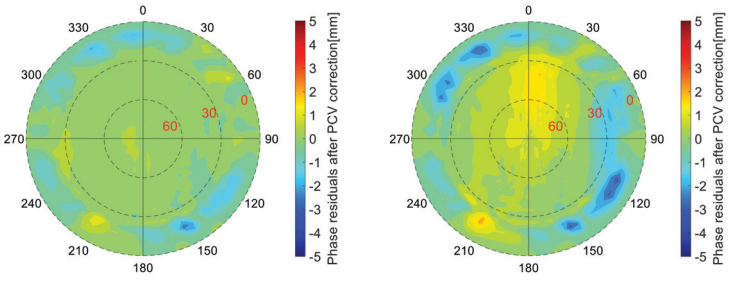

Figure 4. Carrier phase residuals of GRCC satellite derived from (**a**) DD AR solution and (**b**) SD AR solution with application of PCV corrections.

4. POD with Ambiguity Resolution

The GNSS observation model and the methods employed to resolve the SD and DD ambiguities are introduced in this part. FA, DD AR, and SD AR schemes are applied to calculate the GRACE-FO orbits. The generated orbits are assessed with JPL's orbit, SLR, and KBR data. Effects of PCV corrections on POD and PBD are also analyzed.

4.1. Mathematical Models

4.1.1. GNSS Observation Model

GNSS code and carrier phase observations between a satellite and a receiver are usually described by the following equations [35,57]:

$$\begin{aligned} P^s_{r,j} &= \rho^s_r + c(dt_r - dt^s) + I^s_{r,j} + b_{r,j} - b^s_j \\ L^s_{r,j} &= \rho^s_r + c(dt_r - dt^s) - I^s_{r,j} + \lambda_j(N^s_{r,j} + B_{r,j} - B^s_j) + \lambda_j\omega^s_r \end{aligned} \tag{3}$$

where $P^s_{r,j}$ and $L^s_{r,j}$ are code and carrier phase observations in meters, r and s represent the receiver and GNSS satellite, j is the signal frequency, ρ^s_r is the geometry distance between receiver and satellite, c is the speed of light, dt_r and dt^s are receiver and satellite clock errors, $I^s_{r,j}$ is ionospheric delay [58], $b_{r,j}$ and b^s_j are receiver and satellite hardware biases of pseudorange, $B_{r,j}$ and B^s_j are hardware biases of the carrier phase observation, λ_j is signal wavelength and $N^s_{r,j}$ is the integer ambiguity. ω^s_r is the phase wind-up error and can be corrected by model [53], in the remaining part, this item will be omitted.

Both ionosphere free and ionosphere float models can be used for POD. The first order ionospheric delay can be eliminated by the ionosphere free model, while in the ionosphere float model, the ionospheric delay is estimated as an unknown parameter. The ionosphere free approach eliminates the ionospheric delay twice and leads to smaller redundancy. The ionosphere free method owns fewer unknown parameters and it also has the drawback of lacking flexibility for further model strengthening [59]. In this investigation, the ionosphere free model is employed.

Following the IGS convention, the IF pseudorange biases will be assimilated into the receiver and satellite clock offsets. IF observations can be formulated as:

$$\begin{aligned} P^s_{r,IF} &= \rho^s_r + c(\overline{d}t_r - \overline{d}t^s) \\ L^s_{r,IF} &= \rho^s_r + c(\overline{d}t_r - \overline{d}t^s) + \lambda_1\overline{N}^s_{r,IF} \\ \overline{N}^s_{r,IF} &= N^s_{r,IF} + (B_{r,IF} - b_{r,IF}/\lambda_1) - (B^s_{IF} - b^s_{IF}/\lambda_1) \end{aligned} \tag{4}$$

where $P^s_{r,IF}$ and $L^s_{r,IF}$ are IF code and carrier phase observations, $\overline{d}t_r$ and $\overline{d}t^s$ are receiver and satellite clock errors, including the pseudorange hardware biases. $b_{r,IF}$ and b^s_{IF} are the IF pseudorange hardware biases while $B_{r,IF}$ and B^s_{IF} are the carrier phase biases. λ_1

is the wavelength of L1. $\overline{N}^s_{r,IF}$ is the IF ambiguity, which includes the hardware biases in both pseudorange and carrier phase observations, $N^s_{r,IF}$ is a combination of integer L1 and L2 ambiguities.

In order to fix the ambiguities, Blewitt presents a sequential integer ambiguity resolution method to resolve the DD ambiguities of long baseline. The integer DD WL ambiguities are firstly determined with a combination of pseudorange and carrier phase observations. Then the DD narrow-lane (NL) ambiguities are fixed using the estimated IF ambiguities and already fixed integer WL ambiguities [57]. For a single receiver integer ambiguity resolution, GNSS satellites SD observations are used to cancel the receiver based phase bias. Guo et al. provide a detailed description about the model to realize single receiver AR [35]. These methods are employed in this contribution to fix the SD and DD ambiguities.

4.1.2. Single Receiver Ambiguity Resolution

The float IF ambiguity can be rewritten as the combination of integer WL and float NL ambiguities as the following [57]:

$$\begin{array}{l} \overline{N}^s_{r,IF} = \frac{f_1 f_2}{f_1^2 - f_2^2} N^s_{r,WL} + \frac{f_1}{f_1 + f_2} \overline{N}^s_{r,NL} \\ N^s_{r,WL} = N^s_{r,1} - N^s_{r,2} \\ \overline{N}^s_{r,NL} = N^s_{r,NL} + d_{r,NL} - d^s_{NL} \end{array} \tag{5}$$

where $N^s_{r,WL}$ and $N^s_{r,NL}$ are integer WL and NL ambiguities, $\overline{N}^s_{r,NL}$ is float NL ambiguity, $d_{r,NL}$ and d^s_{NL} are the NL FCBs of the receiver and satellite.

The integer WL and NL ambiguities are fixed with two steps. Firstly, the WL ambiguity is resolved using the Hatch–Melbourne–Wübbena combination [60–62]:

$$\overline{N}^s_{r,WL} = \left(\frac{f_1 L^s_{r,1} - f_2 L^s_{r,2}}{f_1 - f_2} - \frac{f_1 P^s_{r,1} + f_2 P^s_{r,2}}{f_1 + f_2}\right) / \lambda_{WL} = N^s_{r,WL} + d_{r,WL} - d^s_{WL} \tag{6}$$

where $d_{r,WL}$ and d^s_{WL} are receiver and satellite WL FCBs, λ_{WL} is WL wavelength. After correction of the WL FCBs, the integer WL ambiguity can be determined. Then integer NL ambiguity can be derived with the fixed WL ambiguity, the estimated float IF ambiguity, and the associated NL FCBs using Equation (5).

Once the WL and NL ambiguities are resolved, the IF ambiguity can be reconstructed according to Equation (5). Usually satellite dependent WL and NL FCBs can be estimated with ground network stations or provided by GNSS analysis institutions [26,55,63]. However, receiver dependent FCBs are not available and cannot be removed from Equations (5) and (6). SD operation between satellites is suggested to cancel the receiver FCBs. The SD integer WL and NL ambiguities can be calculated using Equation (7):

$$\begin{array}{l} \Delta N^{s_1,s_2}_{r,WL} = \Delta \overline{N}^{s_1,s_2}_{r,WL} + \Delta d^{s_1,s_2}_{WL} \\ \Delta N^{s_1,s_2}_{r,NL} = \Delta \overline{N}^{s_1,s_2}_{r,NL} + \Delta d^{s_1,s_2}_{NL} \end{array} \tag{7}$$

where Δ is single difference operator, $\Delta \overline{N}^{s_1,s_2}_{r,WL}$ and $\Delta \overline{N}^{s_1,s_2}_{r,NL}$ are float SD WL and NL ambiguities of satellite s_1 and s_2 while $\Delta N^{s_1,s_2}_{r,WL}$ and $\Delta N^{s_1,s_2}_{r,NL}$ are integer ambiguities. $\Delta d^{s_1,s_2}_{WL}$ and $\Delta d^{s_1,s_2}_{NL}$ are SD hardware biases between satellites. Once SD WL and NL ambiguities are fixed, the SD IF ambiguity can be recovered as follows:

$$\Delta \overline{N}^{s_1,s_2}_{r,IF} = \frac{f_1 f_2}{f_1^2 - f_2^2} \Delta N^{s_1,s_2}_{r,WL} + \frac{f_1}{f_1 + f_2} (\Delta N^{s_1,s_2}_{r,NL} - \Delta d^{s_1,s_2}_{NL}) \tag{8}$$

The recovered SD IF ambiguity is taken as pseudo-observation to constrain the undifferenced IF ambiguity parameters in the POD estimation using Equation (9):

$$\Delta \overline{N}^{s_1,s_2}_{r,IF} = \overline{N}^{s_1}_{r,IF} - \overline{N}^{s_2}_{r,IF}, \quad W^{s_1,s_2}_r \tag{9}$$

where $W_r^{s_1,s_2}$ is the weight of the pseudo-observation and will be assigned with a large value to put a strong confidence.

4.1.3. Double Difference Ambiguity Resolution

With regard to the DD ambiguity, both receiver and satellite FCBs can be removed. The WL and NL DD ambiguities are theoretically integers according to Equations (5) and (6). The DD IF ambiguity can be reconstructed by:

$$\Delta\nabla\overline{N}^{s_1,s_2}_{r_1,r_2,IF} = \frac{f_1 f_2}{f_1^2 - f_2^2}\Delta\nabla N^{s_1,s_2}_{r_1,r_2,WL} + \frac{f_1}{f_1 + f_2}\Delta\nabla N^{s_1,s_2}_{r_1,r_2,NL} \tag{10}$$

where $\Delta\nabla$ is double difference operator, r_1 and r_2 denote a receiver pair. The DD IF ambiguity then is also treated as a pseudo-observation to constrain the undifferenced IF ambiguities.

$$\Delta\nabla\overline{N}^{s_1,s_2}_{r_1,r_2,IF} = \overline{N}^{s_2}_{r_2,IF} - \overline{N}^{s_1}_{r_2,IF} - \overline{N}^{s_2}_{r_1,IF} + \overline{N}^{s_1}_{r_1,IF}, W^{s_1,s_2}_{r_1,r_2} \tag{11}$$

$W^{s_1,s_2}_{r_1,r_2}$ is the weight of the pseudo-observation. The precision of the DD and SD IF ambiguities is set to be 1×10^{-4} L1 cycles (about 0.02 mm) to impose strong constraints.

4.1.4. Integer Ambiguity Validation

Several integer ambiguity resolution methods have been proposed including the integer rounding, integer bootstrapping, integer least squares, and partial ambiguity resolution methods [64]. The integer rounding approach is used in this research to resolve the WL and NL ambiguities. The ambiguity validation procedure is presented here for clearness. The reader can refer to [65] for more details.

Let b be the float WL or NL ambiguities and it is assumed that the probability density function for b is:

$$P(b|n) = \frac{1}{(2\pi)^{1/2}\sigma}\exp[-\frac{(b-n)^2}{2\sigma^2}] \tag{12}$$

where n is the true integer ambiguity, σ is the formal uncertainty from the adjustment. Let I be the nearest integer of b. In the ambiguity rounding procedure, it should be determined whether to fix the ambiguity to I or leave it as float. The deviation

$$x = b - I \tag{13}$$

must fall in the interval $[-0.5, 0.5]$. If the true integer ambiguity n is not equal to the nearest integer I, the probability of wrong ambiguity resolution can be calculated using Equation (14):

$$Q_0 = \sum_{m=1}^{\infty}\left[erfc(\frac{m-x}{\sqrt{2}\sigma}) - erfc(\frac{m+x}{\sqrt{2}\sigma})\right] \leq \alpha \tag{14}$$

$$erfc(x) = \frac{2}{\sqrt{\pi}}\int_x^{\infty} e^{-t^2}dt \tag{15}$$

where α is the allowable rate of wrongly fixed ambiguity, $erfc$ is the complementary error function. In order to eliminate some extremes, a decision function is defined:

$$d(x,\sigma) = T/Q_0 \tag{16}$$

$$T = \begin{cases} 0, & |x| \geq T_1 or \sigma \geq T_2 \\ (1 - \frac{|x|}{T_1})(3T_2 - 3\sigma), & otherwise \end{cases} \tag{17}$$

where T_1 is the limit for the deviation x and T_2 is the limit for σ. In this analysis, T_1 and T_2 are both 0.25 cycles for WL ambiguity resolution, and are 0.15 cycles for NL ambiguity

resolution. When $d(x, \sigma)$ is greater than 1000, the ambiguity will be fixed to the nearest integer [28,66].

4.2. Results

One year of data in 2019 collected by GRACE-FO satellites were analyzed; 38 days were excluded due to large satellite maneuvers or data gaps. The method introduced in Section 4.1.2 is used to resolve the SD WL and NL ambiguities, and the method in Section 4.1.3 is adopted to fix the DD ambiguities. Firstly, the residuals and fixing rates of WL and NL ambiguities are presented. Then the absolute orbit accuracy of each satellite and baseline accuracy between two satellites are evaluated.

4.2.1. Ambiguity Resolution Results

Ambiguity resolution performance is evaluated in terms of the residual and fixing rate. Ambiguity residual is the difference between the float ambiguity and its nearest integer. After removing the satellite and receiver FCBs, the float SD WL and NL ambiguities should be close to the integers. For DD ambiguities, the FCBs of the receiver and satellite are cancelled, which leads to an integer nature. As illustrated by Teunissen [67], the distribution of the ambiguity residuals is non-Gaussian. It is symmetric and the point of symmetry is the origin, which implies that the mean of the ambiguity residuals is zero. The distribution will become more peaked when the estimated float ambiguity is more precise. Figure 5a,b are residual distributions of SD WL and NL ambiguities while Figure 5c,d are distributions of DD ambiguities. Blue bars in the figures are percentages of the related residuals. The mean values of SD and DD WL and NL residuals are all less than 0.01 cycles and verify the symmetry of distribution. The standard deviations (STDs) of SD WL and NL residuals are 0.10 cycles and 0.07 cycles and validate the high quality of the estimated float ambiguities. For DD WL and NL ambiguities, the STDs are both 0.06 cycles. The smaller STDs of DD ambiguity residuals confirm the effectiveness of the DD operation to cancel the receiver and satellite FCBs.

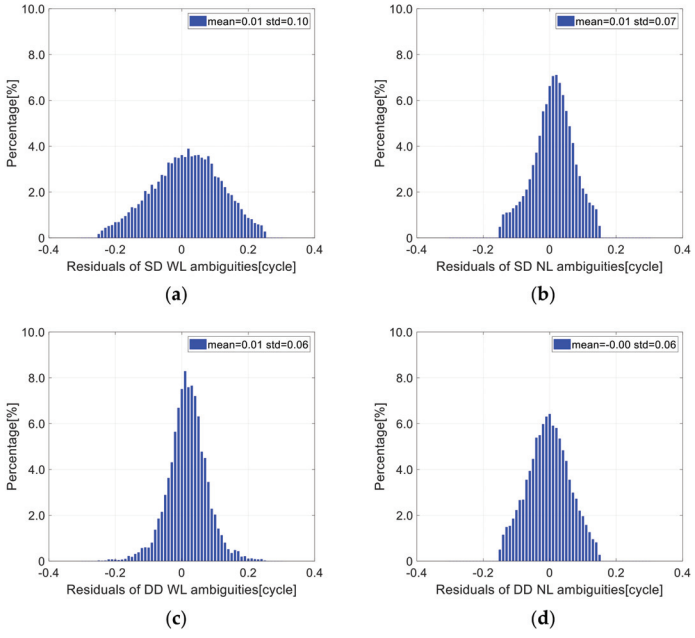

Figure 5. Residual distributions of (**a**) SD WL, (**b**) SD NL, (**c**) DD WL, and (**d**) DD NL ambiguities of GRACE-FO satellites.

The ambiguity fixing rate is the number of fixed ambiguities divided by the total number of ambiguities. Figure 6 illustrates the daily ambiguity fixing rates of SD and DD ambiguities. Figure 6a is for SD ambiguities while Figure 6b is for DD ambiguities. The upper and lower panels of Figure 6a are results of GRCC and GRCD satellites. Blue and red dots in Figure 6 are fixing rates of WL and NL ambiguities. For the GRCC satellite, one year average fixing rates of SD WL and NL ambiguities are 98.5% and 95.8%. A similar performance is observed for the GRCD satellite; the fixing rates are 98.4% and 96.5%. The excellent fixing rates confirm the good quality of applied phase bias products. For the DD case, higher fixing rates are obtained for WL and NL ambiguities, which are 99.1% and 96.7%. Gaps in day of year (DOY) 32–51, 146–149, 205–211, and 299–302 are because of data missing.

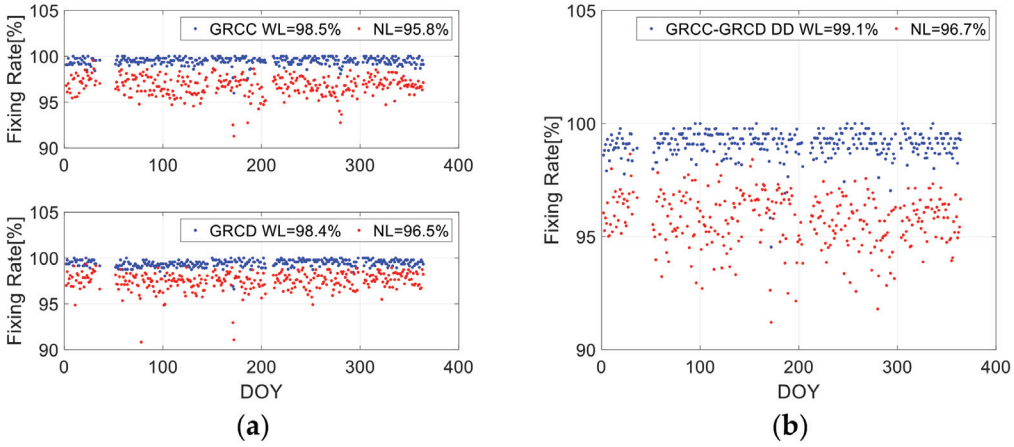

Figure 6. Fixing rates of (**a**) SD WL and NL ambiguities of GRCC and GRCD satellites and (**b**) DD WL and NL ambiguities.

4.2.2. Single Satellite Orbit Validation

JPL's precise orbit of GRACE-FO satellites is also included in the level 1B product. The orbit is calculated with single receiver ambiguity resolution [32,44] and can be used to assess the orbits generated in this investigation. The effect of PCV correction on POD is first evaluated. Figure 7 presents the along-track orbit differences between SD AR solution and JPL's orbit. The upper panel is for GRCC satellite and lower part is for GRCD satellite. The red dots are daily RMSs of differences of the orbit determined with PCV corrections while blue dots are RMSs without PCV corrections. Using created PCV maps, the RMS of the GRCC satellite decreases from 7.2 to 6.0 mm, and from 6.4 to 5.9 mm for the GRCD satellite. The detailed results for three components of SD AR and DD AR orbits can be found in Table 3. The average improvements in along-track, cross-track, and radial direction are 12.2%, 1.6%, and 1.0% for SD AR solution, and are 10.3%, 1.5%, and 3.5% for DD AR solution. The improvement of along-track orbit accuracy is the most significant, which validates the necessity of PCV calibration, especially for PBD.

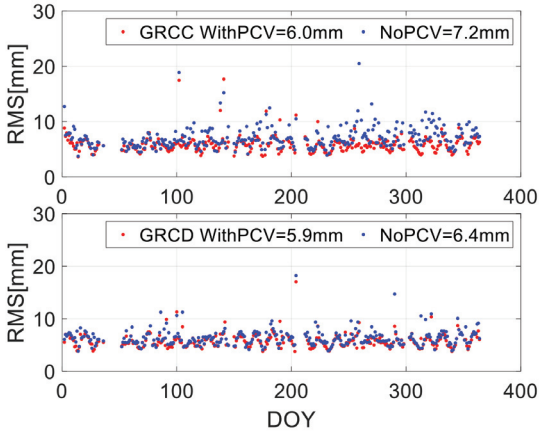

Figure 7. Daily RMSs of along-track orbit differences between JPL's orbit and SD AR solution with (red dots) and without (blue dots) PCV corrections. The upper panel is for the GRCC satellite and lower panel is for the GRCD satellite.

Table 3. Orbit improvements with application of PCV maps for SD AR and DD AR solutions.

Solution	Satellite	Orbit	No PCV/mm	With PCV/mm	Improvement
SD AR Solution	GRCC	Along-track	7.2	6.0	16.7%
		Cross-track	6.2	6.2	0
		Radial	5.2	5.1	1.9%
	GRCD	Along-track	6.4	5.9	7.8%
		Cross-track	6.3	6.1	3.2%
		Radial	5.1	5.1	0
DD AR Solution	GRCC	Along-track	9.5	8.3	12.6%
		Cross-track	6.5	6.4	1.5%
		Radial	5.8	5.6	3.4%
	GRCD	Along-track	8.8	8.1	8.0%
		Cross-track	6.4	6.3	1.6%
		Radial	5.7	5.5	3.5%

RMSs on DOY 100, 141, and 159 of GRCC satellite, and RMSs on DOY 204 and 290 of GRCD satellite are larger than other days. It has been found that sometimes, in these days, fewer GPS satellites are available, which leads to a decrease in orbit accuracy.

Orbit accuracy with different AR methods is also evaluated. Figure 8 presents the RMSs of along-track orbit differences of FA, DD AR, and SD AR solutions with JPL's orbit. For GRCC satellite, the along-track RMS of the FA solution is 8.8 mm, the RMS is improved to 8.3 mm with DD AR and further achieves 6.0 mm by using the SD AR method. Results of three orbit components of the two satellites are listed in Table 4. Compared with the FA solution, the DD AR orbit has an average improvement of 6.3% while the SD AR result has an improvement of 18.3%. Similar to PCV correction, the along-track orbit accuracy has the most significant improvement, which is more than 30%.

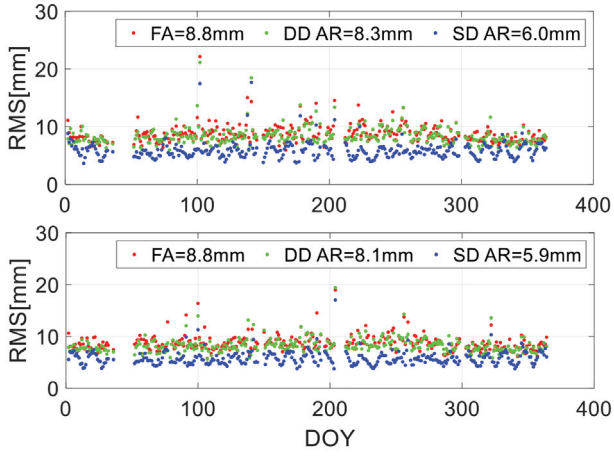

Figure 8. Daily RMSs of along-track orbit differences of FA, DD AR, and SD AR solutions with JPL's orbit. The upper panel is for the GRCC satellite and the lower panel is for the GRCD satellite.

Table 4. RMSs of differences between the FA, DD AR and SD AR orbits and JPL's orbit.

Satellite	Orbit	Solutions/mm			Improvement	
		FA	DD AR	SD AR	DD AR	SD AR
GRCC	Along-track	8.8	8.3	6.0	5.7%	31.8%
	Cross-track	6.7	6.4	6.2	4.5%	7.5%
	Radial	6.0	5.6	5.1	6.7%	15.0%
GRCD	Along-track	8.8	8.1	5.9	8.0%	33.0%
	Cross-track	6.7	6.3	6.1	6.0%	9.0%
	Radial	5.9	5.5	5.1	6.8%	13.6%

GRACE-FO satellites are equipped with SLR retroreflectors. The independent SLR data can be used as external validation. SLR normal points from nine laser stations (Yarragadee, Greenbelt, Haleakala, Zimmerwald, Mount Stromlo, Wettzell, Graz, Herstmonceux, and Potsdam) are used for orbit evaluation. Residuals larger than 10 cm are rejected and an elevation cutoff of 10° is applied. Figure 9 shows the RMSs of SLR residuals. Red, green, and blue dots are RMSs of FA, DD AR, and SD AR orbits. The RMSs of the GRCC satellite are 11.5, 10.2, and 9.6 mm, which confirms the positive impact of AR on the orbit quality. Compared with the DD AR solution, the SD AR result has better performance, which is also validated by JPL's orbit.

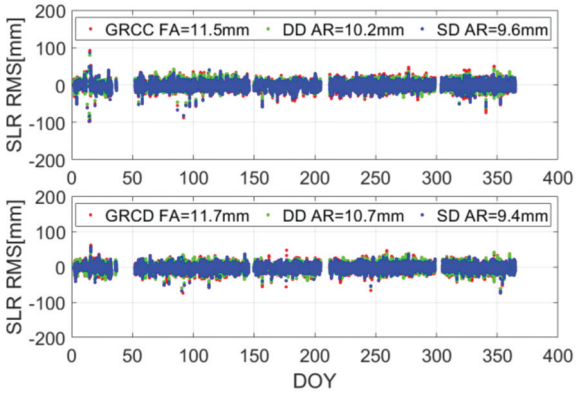

Figure 9. RMSs of SLR residuals derived from FA (red dots), DD AR (green dots), and SD AR (blue dots) solutions. The upper panel is for the GRCC satellite and the lower panel is for the GRCD satellite.

4.2.3. Baseline Validation

The GRACE-FO mission offers the possibility of validating the computed orbit, in particular, the along-track component, with the ultra-precise KBR measurements [33,68]. Figure 10 illustrates the STDs of KBR residuals (named KBR STD hereafter) calculated using FA, DD AR, and SD AR orbits. The effect of antenna PCV correction on PBD is also illustrated. Figure 10a presents the KBR STDs of the SD AR orbit with PCV corrections (blue dots), the SD AR orbit without PCV corrections (green dots), and FA orbit with PCV corrections (red dots). PCV corrections used to calculate FA orbit are generated from the SD AR solution. Figure 10b is the result of the DD AR solution.

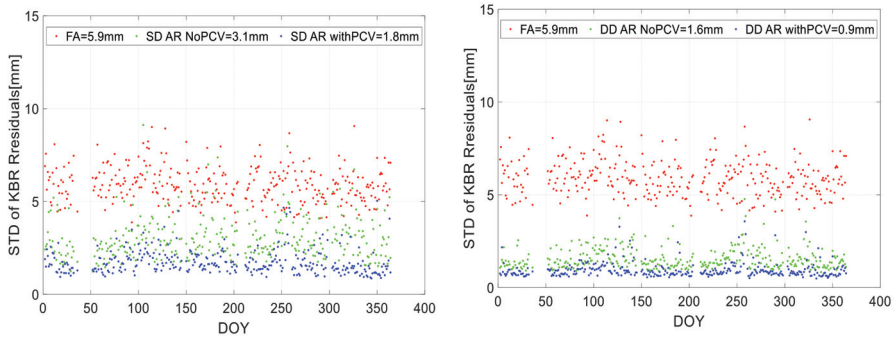

(**a**) (**b**)

Figure 10. Daily STDs of KBR residuals of (**a**) FA orbit with PCV corrections (red dots), SD AR orbit without PCV corrections (green dots), and SD AR orbit with PCV corrections (blue dots); (**b**) FA orbit with PCV corrections (red dots), DD AR orbit without PCV corrections (green dots), and DD AR orbit with PCV corrections (blue dots).

Both SD and the DD AR lead to a significant reduction in KBR residuals. Compared with the FA result, the SD AR orbit improves the KBR STD from 5.9 to 3.1 mm, and the DD AR orbit improves the STD to 1.6 mm. With PCV corrections, the KBR STD of the SD AR solution decreases from 3.1 to 1.8 mm, and the STD of the DD AR orbit decreases from 1.6 to 0.9 mm. The baseline precision of the SD AR solution gains similar performance, as presented by Arnold et al. [33]. The DD AR orbit achieves a sub-millimeter level as reported

in previous research [6,19,69]. Comparisons with JPL's orbit and SLR data show that the SD AR solution possesses better performance, while in the KBR validation, the residual STD of the DD AR orbit is smaller. In other words, the SD AR orbit has better absolute orbit accuracy, while the DD AR orbit gets better relative performance. This is explained by two facts: (a) phase bias products for SD AR are not free of errors and these errors may degrade the KBR validation [35]; (b) both JPL's orbit and the SD AR orbit in this investigation adopt the single receiver ambiguity resolution method and a better consistency can be inferred.

5. Discussions

Precise knowledge of the phase center location of the GNSS antenna is a prerequisite for high precision LEO orbit determination. PCO and PCV values of the LEO antenna obtained from ground calibration cannot reflect the influence of error sources, which are additionally encountered in the actual spacecraft environment. An in-flight calibration of the LEO antenna is thus mandatory. In this analysis, antenna PCV is represented as a piecewise linear function with respect to zenith and azimuth angles in the antenna fixed coordinate system. A residual approach is employed to estimate the PCV correction. Different ambiguity resolution strategies, including SD AR and DD AR, are investigated to fully exploit the precision of GPS observations for POD. The single receiver integer ambiguity resolution concept employed here makes use of the carrier phase biases and clock products provided by CODE. One year of GRACE-FO data in 2019 are used to demonstrate the effect of integer ambiguity resolution and PCV correction on POD.

PCV maps derived from SD AR and DD AR solutions have very similar patterns. With PCV corrections, carrier phase residuals are reduced from about 10 to 1–2 mm, which implies better consistency between the observations and applied models. The average improvements of the SD AR solution in the along-track, cross-track, and radial directions are 12.2%, 1.6%, and 1.0%, and for the DD AR solution, the improvements are 10.3%, 1.5%, and 3.5%. The great enhancement in the along-track orbit accuracy validates the necessity to calibrate the PCV errors in the relative POD.

The mean values of both SD and DD ambiguity residuals are less than 0.01 cycles and confirm the symmetry of distribution. The fixing rates of SD WL and NL ambiguities are more than 98% and 95%. Compared with the FA solution, DD AR orbit accuracy has an average improvement of 6.3% while the SD AR result gains an increase of 18.3%. For high-grade SLR stations, range residuals with RMS less than 10 mm are achieved for SD AR orbit, which marks a 17% improvement compared to the FA result. Independent KBR measurements are also used as external validations. KBR residuals STD of the SD AR solution is 1.8 mm while STD of the DD AR orbit is 0.9 mm and reaches the sub-millimeter level. The better baseline accuracy for the DD AR solution is explained by the errors in phase bias products.

6. Conclusions

Integer ambiguity resolution plays a crucial role in achieving the best positioning or orbit accuracy. Single receiver and double difference integer ambiguity resolution models are introduced in this contribution. One year of GRACE-FO data were analyzed to verify the orbit improvement with different ambiguity resolution strategies. In-flight antenna PCV maps were developed to further exploit the POD accuracy.

With PCV corrections, along-track orbit accuracy of the SD AR solution is improved by 12.6%, and that of the DD AR solution is improved by 10.3%, which verifies the necessity of in-flight antenna calibration. With phase biases cancelled by the double difference operation, fixing rates of DD ambiguities are more than 96.7%. Similar performance is achieved by SD AR, which confirms the consistency of theoretical models and bias/clock products.

JPL's orbited together with independent SLR and KBR measurements are used to assess the results of different AR strategies. Both SD AR and DD AR solutions improve the orbit accuracy. SD AR solution provides the best performance of absolute orbit. Compared with JPL's orbit, the RMS of the SD AR orbit differences is better than 6 mm and the SLR

residual RMS is less than 10 mm. The DD AR solution realizes the highest baseline accuracy and the STD of KBR residuals achieves 0.9 mm. In addition, sometimes there are fewer GPS satellites available, which leads to the reduction of orbit accuracy. With the application of multi-mode GNSS receivers and multi-GNSS phase bias products [70,71], orbit accuracy based on single receiver ambiguity resolution can be further improved.

Author Contributions: Conceptualization, B.J. and Y.L.; methodology, B.J.; software, B.J. and K.J.; validation, B.J. and S.C.; writing—original draft preparation, B.J.; writing—review and editing, S.C.; supervision, Y.L. and Z.L.; funding acquisition, Y.L. All authors have read and agreed to the published version of the manuscript.

Funding: This research was funded by the National Natural Science Foundation of China, grant number 12033009.

Data Availability Statement: GRACE-FO data in this paper can be freely accessed at ftp://isdcftp.gfz-potsdam.de/grace-fo/ (accessed on 17 October 2021). The GPS final orbit, clock, and OSB products can be found at ftp://ftp.aiub.unibe.ch/CODE/ (accessed on 17 October 2021).

Acknowledgments: The authors thank GFZ for providing GRACE-FO GPS data. The authors are grateful to the CODE for providing GPS products.

Conflicts of Interest: The authors declare no conflict of interest.

References

1. Bertiger, W.; Bar-Sever, Y.; Christensen, E.; Davis, E.; Guinn, J.; Haines, B.; Ibanez-Meier, R.; Jee, J.; Lichten, S.; Melbourne, W.; et al. GPS precise tracking of TOPEX/POSEIDON: Results and implications. *J. Geophys. Res.* **1994**, *99*, 24449–24464. [CrossRef]
2. Tapley, B.D.; Ries, J.C.; Davis, G.W.; Eanes, R.J.; Schutz, B.E.; Shum, C.K.; Watkins, M.M.; Marshall, J.A.; Nerem, R.S.; Putney, B.H.; et al. Precision orbit determination for TOPEX/POSEIDON. *J. Geophys. Res.* **1994**, *99*, 24383–24404. [CrossRef]
3. Wu, S.C.; Yunck, T.P.; Thornton, C.L. Reduced-dynamic technique for precise orbit determination of low earth satellites. *J. Guid. Control Dyn.* **1991**, *14*, 24–30. [CrossRef]
4. Jäggi, A.; Hugentobler, U.; Beutler, G. Pseudo-Stochastic Orbit Modeling Techniques for Low-Earth Orbiters. *J. Geod.* **2006**, *80*, 47–60. [CrossRef]
5. Dow, J.M.; Neilan, R.E.; Gendt, G. The International GPS Service: Celebrating the 10th anniversary and looking to the next decade. *Adv. Space Res.* **2005**, *36*, 320–326. [CrossRef]
6. Jäggi, A.; Hugentobler, U.; Bock, H.; Beutler, G. Precise orbit determination for GRACE using undifferenced or doubly differenced GPS data. *Adv. Space Res.* **2007**, *39*, 1612–1619. [CrossRef]
7. Hackel, S.; Montenbruck, O.; Steigenberger, P.; Balss, U.; Gisinger, C.; Eineder, M. Model improvements and validation of TerraSAR-X precise orbit determination. *J. Geod.* **2017**, *91*, 547–562. [CrossRef]
8. Van den Ijssel, J.; Visser, P.; Patiño Rodriguez, E. Champ precise orbit determination using GPS data. *Adv. Space Res.* **2003**, *31*, 1889–1895. [CrossRef]
9. Kang, Z.; Tapley, B.D.; Bettadpur, S.; Ries, J.C.; Nagel, P.; Pastor, R. Precise orbit determination for the GRACE mission using only GPS data. *J. Geod.* **2006**, *80*, 322–331. [CrossRef]
10. Luthcke, S.B.; Zelensky, N.P.; Rowlands, D.D.; Lemoine, F.G.; Williams, T.A. The 1-Centimeter Orbit: Jason-1 Precision Orbit Determination Using GPS, SLR, DORIS, and Altimeter Data Special Issue: Jason-1 Calibration/Validation. *Mar. Geod.* **2003**, *26*, 399–421. [CrossRef]
11. Bertiger, W.; Desai, S.D.; Dorsey, A.; Haines, B.J.; Harvey, N.; Kuang, D.; Sibthorpe, A.; Weiss, J.P. Sub-centimeter precision orbit determination with GPS for ocean altimetry. *Mar. Geod.* **2010**, *33*, 363–378. [CrossRef]
12. Bock, H.; Jäggi, A.; Meyer, U.; Visser, P.; van den IJssel, J.; van Helleputte, T.; Heinze, M.; Hugentobler, U. GPS-derived orbits for the GOCE satellite. *J. Geod.* **2011**, *85*, 807–818. [CrossRef]
13. Bock, H.; Jäggi, A.; Beutler, G.; Meyer, U. GOCE: Precise orbit determination for the entire mission. *J. Geod.* **2014**, *88*, 1047–1060. [CrossRef]
14. Peter, H.; Jäggi, A.; Fernández, J.; Escobar, D.; Ayuga, F.; Arnold, D.; Wermuth, M.; Hackel, S.; Otten, M.; Simons, W.; et al. Sentinel-1A-First precise orbit determination results. *Adv. Space Res.* **2017**, *60*, 879–892. [CrossRef]
15. Montenbruck, O.; Hackel, S.; Jäggi, A. Precise orbit determination of the Sentinel-3A altimetry satellite using ambiguity-fixed GPS carrier phase observations. *J. Geod.* **2018**, *92*, 711–726. [CrossRef]
16. Guo, J.Y.; Kong, Q.; Qin, J.; Sun, Y. On precise orbit determination of HY-2 with space geodetic techniques. *Acta Geophys.* **2013**, *61*, 752–772. [CrossRef]
17. Li, M.; Li, W.; Shi, C.; Jiang, K.; Guo, X.; Dai, X.; Meng, X.; Yang, Z.; Yang, G.; Liao, M. Precise orbit determination of the Fengyun-3C satellite using onboard GPS and BDS observations. *J. Geod.* **2017**, *91*, 1313–1327. [CrossRef]

18. Li, X.; Zhang, K.; Meng, X.; Zhang, W.; Zhang, Q.; Zhang, X.; Li, X. Precise Orbit Determination for the FY-3C Satellite Using Onboard BDS and GPS Observations from 2013, 2015, and 2017. *Engineering* **2019**, *6*, 904–912. [CrossRef]
19. Kroes, R.; Montenbruck, O.; Bertiger, W.; Visser, P. Precise GRACE baseline determination using GPS. *GPS Solut.* **2005**, *9*, 21–31. [CrossRef]
20. Zhao, Q.; Hu, Z.; Guo, J.; Li, M.; Ge, M. Precise relative orbit determination of twin GRACE satellites. *Geo Spat. Inf. Sci.* **2010**, *13*, 221–225. [CrossRef]
21. Zhang, B.; Teunissen, P.J.G.; Odijk, D. A novel un-differenced PPP-RTK concept. *J. Navig.* **2011**, *64*, S180–S191. [CrossRef]
22. Odijk, D.; Teunissen, P.J.G.; Zhang, B. Single-frequency integer ambiguity resolution enabled GPS precise point positioning. *J. Surv. Eng.* **2012**, *138*, 193–202. [CrossRef]
23. De Jonge, P.J. A processing strategy for the application of the GPS in networks. Ph.D. Thesis, Delft University of Technology, Delft, The Netherlands, 1998.
24. Teunissen, P.J.G.; Odijk, D.; Zhang, B. PPP-RTK: Results of CORS Network-Based PPP with Integer Ambiguity Resolution. *J. Aeronaut. Astronaut. Aviat. Ser.* **2010**, *42*, 223–230.
25. Laurichesse, D.; Mercier, F.; Berthias, J.P.; Broca, P.; Cerri, L. Integer ambiguity resolution on undifferenced GPS phase measurements and its application to PPP and satellite precise orbit determination. *Navigation* **2009**, *56*, 135–149. [CrossRef]
26. Loyer, S.; Perosanz, F.; Mercier, F.; Capdeville, H.; Marty, J.C. Zero-difference GPS ambiguity resolution at CNES–CLS IGS Analysis Center. *J. Geod.* **2012**, *86*, 991–1003. [CrossRef]
27. Collins, P.; Bisnath, S.; Lahaye, F.; Héroux, P. Undifferenced GPS Ambiguity Resolution Using the Decoupled Clock Model and Ambiguity Datum Fixing. *Navigation* **2010**, *57*, 123–135. [CrossRef]
28. Ge, M.; Gendt, G.; Rothacher, M.; Shi, C.; Liu, J. Resolution of GPS carrier-phase ambiguities in precise point positioning (PPP) with daily observations. *J. Geod.* **2008**, *82*, 389–399. [CrossRef]
29. Geng, J.; Bock, Y. Triple-frequency GPS precise point positioning with rapid ambiguity resolution. *J. Geod.* **2013**, *87*, 449–460. [CrossRef]
30. Teunissen, P.J.G. Zero Order Design: Generalized Inverses, Adjustment, the Datum Problem and S-Transformations. In *Optimization and Design of Geodetic Networks*; Grafarend, E., Sanso, F., Eds.; Springer: Berlin/Heidelberg, Germany, 1985; pp. 11–55.
31. Teunissen, P.J.G.; Khodabandeh, A. Review and principles of PPP-RTK methods. *J. Geod.* **2015**, *89*, 217–240. [CrossRef]
32. Bertiger, W.; Desai, S.D.; Haines, B.; Harvey, N.; Moore, A.W.; Owen, S.; Weiss, J.P. Single receiver phase ambiguity resolution with GPS data. *J. Geod.* **2010**, *84*, 327–337. [CrossRef]
33. Arnold, D.; Schaer, S.; Villiger, A.; Dach, R.; Jäggi, A. Undifferenced ambiguity resolution for GPS-based precise orbit determination of low Earth orbiters using the new CODE clock and phase bias products. In Proceedings of the International GNSS Service Workshop 2018, Wuhan, China, 29 October–2 November 2018.
34. Li, X.; Wu, J.; Zhang, K.; Li, X.; Xiong, Y.; Zhang, Q. Real-Time Kinematic Precise Orbit Determination for LEO Satellites Using Zero-Differenced Ambiguity Resolution. *Remote Sens.* **2019**, *11*, e2815. [CrossRef]
35. Guo, X.; Geng, J.; Chen, X.; Zhao, Q. Enhanced orbit determination for formation flying satellites through integrated single and double difference GPS ambiguity resolution. *GPS Solut.* **2020**, *24*, 1–12. [CrossRef]
36. Jäggi, A.; Dach, R.; Montenbruck, O.; Hugentobler, U.; Bock, H.; Beutler, G. Phase center modeling for LEO GPS receiver antennas and its impact on precise orbit determination. *J. Geod.* **2009**, *83*, 1145–1162. [CrossRef]
37. Bock, H.; Jäggi, A.; Meyer, U.; Dach, R.; Beutler, G. Impact of GPS antenna phase center variations on precise orbits of the GOCE satellite. *Adv. Space Res.* **2011**, *47*, 1885–1893. [CrossRef]
38. Van Den IJssel, J.; Encarnação, J.; Doornbos, E.; Visser, P. Precise science orbits for the Swarm satellite constellation. *Adv. Space Res.* **2015**, *56*, 1042–1055. [CrossRef]
39. Montenbruck, O.; Garcia-Fernandez, M.; Yoon, Y.; Schön, S.; Jäggi, A. Antenna phase center calibration for precise positioning of LEO satellites. *GPS Solut.* **2008**, *13*, 23–34. [CrossRef]
40. Haines, B.; Bar-Sever, Y.; Bertiger, W.; Desai, S.D.; Willis, P. One-centimeter orbit determination for Jason-1: New GPS-based strategies. *Mar. Geod.* **2004**, *27*, 299–318. [CrossRef]
41. Yi, B.; Gu, D.; Ju, B.; Shao, K.; Zhang, H. Enhanced baseline determination for formation flying LEOs by relative corrections of phase center and code residual variations. *Chin. J. Aeronaut.* **2019**, in press.
42. Yuan, J.; Zhou, S.; Hu, X.; Yang, L.; Cao, J.; Li, K.; Liao, M. Impact of Attitude Model, Phase Wind-Up and Phase Center Variation on Precise Orbit and Clock Offset Determination of GRACE-FO and CentiSpace-1. *Remote Sens.* **2021**, *13*, e2636. [CrossRef]
43. Xia, Y.; Liu, X.; Guo, J.; Yang, Z.; Qi, L.; Ji, B.; Chang, X. On GPS data quality of GRACE-FO and GRACE satellites: Effects of phase center variation and satellite attitude on precise orbit determination. *Acta Geod. Geophys.* **2021**, *56*, 93–111. [CrossRef]
44. Wen, H.; Kruizinga, G.; Paik, M.; Landerer, F.; Bertiger, W.; Sakumura, C.; Bandikova, T.; Mccullough, C. *Technical Report JPL D-56935: Grace-Fo Level-1 Data Product User Handbook*; Jet Propulsion Laboratory: Pasadena, CA, USA, 2019.
45. Tapley, B.D.; Bettadpur, S.; Watkins, M.M.; Reigber, C. The gravity recovery and climate experiment: Mission overview and early results. *Geophys. Res. Lett.* **2004**, *31*. [CrossRef]
46. Dragon, K. *Technical Report JPL D-71781: GRACE Follow-On Mission Plan*; Jet Propulsion Laboratory: Pasadena, CA, USA, 2015.
47. Liu, J.; Ge, M. PANDA software and its preliminary result of positioning and orbit determination. *Wuhan Univ. J. Nat. Sci.* **2003**, *8*, 603–609.

48. Berger, C.; Biancale, R.; Ill, M.; Barlier, F. Improvement of the empirical thermospheric model DTM: DTM94-A comparative review of various temporal variations and prospects in space geodesy applications. *J. Geod.* **1998**, *72*, 161–179. [CrossRef]
49. Förste, C.; Bruinsma, S.L.; Shako, R.; Marty, J.C.; Flechtner, F.; Abrikosov, O.; Dahle, C.; Lemoine, J.M.; Neumayer, K.H.; Biancale, R.; et al. EIGEN-6—A new combined global gravity field model including GOCE data from the collaboration of GFZ-Potsdam and GRGS Toulouse. In Proceedings of the EGU General Assembly, Vienna, Austria, 3–8 April 2011.
50. Petit, G.; Luzum, B.; Al, E. IERS Conventions. *IERS Tech. Note* **2010**, *36*, 1–95.
51. Lyard, F.; Lefevre, F.; Letellier, T.; Francis, O. Modeling the global ocean tides: Modern insights from FES2004. *Ocean Dyn.* **2006**, *56*, 394–415. [CrossRef]
52. Desai, S.D. Observing the pole tide with satellite altimetry. *J. Geophys. Res.* **2002**, *107*, 1–13. [CrossRef]
53. Wu, J.T.; Wu, S.C.; Hajj, G.A.; Bertiger, W.I.; Lichten, S.M. Effects of antenna orientation on GPS carrier phase. *Manuscr. Geod.* **1993**, *18*, 91–98.
54. Meehan, T.; Esterhuizen, S.; Franklin, G.; Tien, J.; Young, L.; Bachman, B.; Munson, T.; Robison, D.; Stecheson, T. Development status of NASA's TriG GNSS science instrument. In Proceedings of the International Radio Occultation Working Group (IROWG-2), Estes Park, CO, USA, 28 March–3 April 2012.
55. Schaer, S.; Villiger, A.; Arnold, D.; Dach, R.; Prange, L.; Jäggi, A. The CODE ambiguity-fixed clock and phase bias analysis products: Generation, properties, and performance. *J. Geod.* **2021**, *95*, 1–25. [CrossRef]
56. Villiger, A.; Schaer, S.; Dach, R.; Prange, L.; Sušnik, A.; Jäggi, A. Determination of GNSS pseudo-absolute code biases and their long-term combination. *J. Geod.* **2019**, *93*, 1487–1500. [CrossRef]
57. Blewitt, G. Carrier phase ambiguity resolution for the Global Positioning System applied to geodetic baselines up to 2000 km. *J. Geophys. Res. Solid Earth* **1989**, *94*, 10187–10203. [CrossRef]
58. Jin, B.; Chen, S.; Li, D.; Takka, E.; Li, Z.; Qu, P. Ionospheric correlation analysis and spatial threat model for SBAS in China region. *Adv. Space Res.* **2020**, *66*, 2873–2887. [CrossRef]
59. Teunissen, P.J.G. GNSS Precise Point Positioning. In *Position, Navigation, and Timing Technologies in the 21st Century: Integrated Satellite Navigation, Sensor Systems, and Civil Applications*, 1st ed.; Morton, Y.J., van Diggelen, F., Spilker, J.J., Jr., Parkinson, B.W., Lo, S., Gao, G., Eds.; Wiley-IEEE Press: Hoboken, NJ, USA, 2021; Volume 1, pp. 503–528.
60. Hatch, R. The synergism of GPS Code and carrier measurements. In Proceedings of the Third International Symposium on Satellite Doppler Positioning, Physical Sciences Laboratory of New Mexico State University, Las Cruces, NM, USA, 8–12 February 1982; pp. 1213–1231.
61. Melbourne, W. The Case for Ranging in GPS Based Geodetic Systems. In Proceedings of the 1st International Symposium on Precise Positioning with the Global Positioning System, Rockville, MD, USA, 15–19 April 1985; pp. 373–386.
62. Wubbena, G. Software developments for geodetic positioning with GPS using TI 4100 code and carrier measurements. In Proceedings of the 1st International Symposium on Precise Positioning with the Global Positioning System, Rockville, MD, USA, 15–19 April 1985; pp. 403–412.
63. Geng, J.; Chen, X.; Pan, Y.; Zhao, Q. A modified phase clock/bias model to improve PPP ambiguity resolution at Wuhan University. *J. Geod.* **2019**, *93*, 2053–2067. [CrossRef]
64. Teunissen, P.J. Carrier phase integer ambiguity resolution. In *Springer Handbook of Global Navigation Satellite Systems*, 1st ed.; Teunissen, P., Montenbruck, O., Eds.; Springer: Berlin/Heidelberg, Germany, 2017; pp. 661–685.
65. Dong, D.; Bock, Y. Global positioning system network analysis with phase ambiguity resolution applied to crustal deformation studies in California. *J. Geophys. Res.* **1989**, *94*, 3949–3966. [CrossRef]
66. Ge, M.; Gendt, G.; Dick, G.; Zhang, F.P. Improving carrier-phase ambiguity resolution in global GPS network solutions. *J. Geod.* **2005**, *79*, 103–110. [CrossRef]
67. Teunissen, P.J.G. The parameter distributions of the integer GPS model. *J. Geod.* **2002**, *76*, 41–48. [CrossRef]
68. Kang, Z.; Bettadpur, S.; Nagel, P.; Save, H.; Poole, S.; Pie, N. GRACE-FO precise orbit determination and gravity recovery. *J. Geod.* **2020**, *94*, 85. [CrossRef]
69. Gu, D.; Ju, B.; Liu, J.; Tu, J. Enhanced GPS-based GRACE baseline determination by using a new strategy for ambiguity resolution and relative phase center variation corrections. *Acta Astronaut.* **2017**, *138*, 176–184. [CrossRef]
70. Geng, J.; Yang, S.; Guo, J. Assessing IGS GPS/Galileo/BDS-2/BDS-3 phase bias products with PRIDE PPP-AR. *Satell. Navig.* **2021**, *2*, 1–15. [CrossRef]
71. Montenbruck, O.; Hackel, S.; Wermuth, M.; Zangerl, F. Sentinel-6A precise orbit determination using a combined GPS/Galileo receiver. *J. Geod.* **2021**, *95*, 109. [CrossRef]

remote sensing

MDPI

Article

Potential Contributors to Common Mode Error in Array GPS Displacement Fields in Taiwan Island

Xiaojun Ma [1,2], Bin Liu [1,2,*], Wujiao Dai [3], Cuilin Kuang [3] and Xuemin Xing [1,2]

[1] Engineering Laboratory of Spatial Information Technology of Highway Geological Disaster Early Warning in Hunan Province, Changsha University of Science & Technology, Changsha 410114, China; maxiaojun@stu.csust.edu.cn (X.M.); xuemin.xing@csust.edu.cn (X.X.)
[2] School of Traffic and Transportation Engineering, Changsha University of Science & Technology, Changsha 410114, China
[3] School of Geosciences and Info-Physics, Central South University, Changsha 410012, China; wjdai@csu.edu.cn (W.D.); kuangcuilin@csu.edu.cn (C.K.)
* Correspondence: binliu@csust.edu.cn

Abstract: The existence of the common mode error (CME) in the continuous global navigation satellite system (GNSS) coordinate time series affects geophysical studies that use GNSS observations. To understand the potential contributors of CME in GNSS networks in Taiwan and their effect on velocity estimations, we used the principal component analysis (PCA) and independent component analysis (ICA) to filter the vertical coordinate time series from 44 high-quality GNSS stations in Taiwan island in China, with a span of 10 years. The filtering effects have been evaluated and the potential causes of the CME are analyzed. The root-mean-square values decreased by approximately 14% and 17% after spatio-temporal filtering using PCA and ICA, respectively. We then discuss the relationship between the CME sources obtained by ICA and the environmental loads. The results reveal that the independent displacements extracted by ICA correlate with the atmospheric mass loading (ATML) and land water storage mass loading (LWS) of Taiwan in terms of both its amplitude and phase. We then use the white noise plus power law noise model to quantitatively estimate the noise characteristics of the pre- and post-filtered coordinate time series based on the maximum likelihood estimation criterion. The results indicate that spatio-temporal filtering reduces the amplitude of the PL and the periodic terms in the GPS time series.

Keywords: GPS time-series analysis; common mode error; independent component analysis; seasonal signals; surface mass loading

Citation: Ma, X.; Liu, B.; Dai, W.; Kuang, C.; Xing, X. Potential Contributors to Common Mode Error in Array GPS Displacement Fields in Taiwan Island. *Remote Sens.* **2021**, *13*, 4221. https://doi.org/10.3390/rs13214221

Academic Editors: Gino Dardanelli and Shuanggen Jin

Received: 19 September 2021
Accepted: 19 October 2021
Published: 21 October 2021

1. Introduction

Continuous global navigation satellite system (GNSS) networks have been widely used in the fields of geodesy and geophysics. The permanently operating ground reference stations provide not only a millimeter-level 3-D coordinate time series under a global reference frame, but also provide important observational data and quantitative constraints for studies involving crustal deformation and dynamic processes on a global and regional scale [1,2]. However, the GNSS data processing procedure is affected by many factors, and numerous errors occur in the GNSS terminal products [3–5]. Geophysical signals can be difficult to separate from noise and unknown error sources because they are hidden in a detrended residual coordinate time series. Previous studies have identified that a spatially correlated error generally exists in regional networks, caused by the reference frame, satellites orbits, ocean tide correction models, and other unknown errors. This is usually referred to as the common mode error (CME) [6–11]. The presence of this error affects the accuracy of the station coordinates and velocity solutions, and conceals many weak and transient signals in a coordinate time series (e.g., deep magma motion, fault motion).

Spatial filtering techniques can be used to mitigate the CME. There are presently two types of spatial filtering techniques, stacking [6,12] and empirical orthogonal function (EOF) decomposition [7], which have been widely used in the field of geodesy to detect transient signals. Wdowinski et al. [6] initially introduced stacking to detect co-seismic displacements in a residual position time series. However, Nikolaidis et al. [12] illustrated that stacking works satisfactorily when the CME in a regional network is essentially spatially homogeneous. Larger areas and weaker spatial correlations generally result in differences between the spatial response of the different stations to the CME. Previous studies have illustrated that the CME spatial correlation decreases with increasing distance and reaches 95% within 1000 km. For networks that exceed 2000 km, the CMEs exhibit significant differences in various regions and the spatial correlation is essentially nonexistent beyond 6000 km [13,14]. To address this problem, Tian et al. [15] proposed a correlation weighting stacking scheme. However, this algorithm is still affected by local-scale or site-specific changes, and further research is necessary to obtain the appropriate weights of all the sites at each epoch.

In comparison, Dong et al. [7] and Serpelloni et al. [16] verified that the EOF can decompose residual coordinate time series into different modes to extract the CME, which provides a stricter mathematical framework than stacking. Principal component analysis (PCA) does not require CME spatial uniformity, but adopts a uniform temporal function that affects stations across a regional network. Dong et al. [7] reviewed the spatial consistency of stations using a visual appraisal of the decomposed principal components (PCs) to extract the CME from the Southern California Integrated GPS Network (SCIGN). PCA and its extensions have been subsequently used to eliminate the CME in local area networks [8,17–24].

Previous studies focused on the effective removal of CME from a GNSS coordinate time series to improve the accuracy of coordinate solutions from regional network measurements [25], which is conducive to the study of some geophysical applications using GNSS, such as the assessment of glacial isostatic adjustment models [26] and crustal movement [27,28]. Other studies have addressed the potential contributors of CME, particularly the potential geophysical signals [18,21,29–38]. This is particularly relevant for crustal deformation caused by the redistribution of surface mass, such as strongly seasonal water movements and atmospheric pressure changes. Kumar et al. [39] extracted the CME of Taiwan using the EOF, and quantitatively analyzed the CME in the U direction and atmospheric mass loading (ATML) of Taiwan, as calculated by the International Mass Loading Service (IMLS). They found a significantly high correlation and degree of concordance between the CME and ATML residuals for the vertical component. A further regression analysis revealed that the highest 90% of the non-seasonal ATML displacements in Taiwan are present in the CME variations.

However, the extraction of the CME using PCA still experiences some limitations for geophysical interpretation. PCA is based on the second-order statistics of variance and covariance, and therefore does not make full use of the higher-order CME statistics. PCA can work effectively in cases where there is only a single source in the CME. However, when the CME contains multiple competing sources, a single principal component (PC) may contain a mixture of contributions from different sources, which can easily generate artificial features. In contrast, Liu et al. [18,19,26], Ming et al. [38], and Yan et al. [29] applied an independent component analysis (ICA) to geodetic data sets and successfully separated seasonal and long-term trend signals.

Previous studies indicated the effectiveness of ICA in studying the potential contributors of CME in a regional GNSS coordinate time series. Thus, following the work of Kumar et al. [39], we apply a combination of PCA and ICA to the vertical coordinate time series of 44 stations from Taiwan island in China, and extract the CMEs of this network. The associated effects on the stations' coordinate residuals and observed values are analyzed and compared. We discuss the relationship between the CME sources and environmental loadings, and compare GPS CMEs with vertical surface displacement predictions from the

IMLS. We determine the cause of the Taiwan GNSS network CME, except for the atmosphere pressure loading (ATML), and separate the signals related to land water storage mass loading (LWS). The results further validate the accuracy of ICA applications for CME signal separation and the geophysical interpretation of regional networks. Changes in the optimal noise model of the GNSS stations before and after the ICA filtering are analyzed, as well as the differences between the time series parameters of the GNSS stations.

2. Methods and Data Processing

2.1. GNSS Data Processing

All of the stations in Taiwan's continuous GPS (CGPS) array are equipped with dual-frequency geodetic GNSS receivers (Trimble 4000 SST Geodetic II P and 4000 SSE/SSIGeodetic Surveyor) [40]. A station was usually occupied for more than two sessions, and each session included 6–14 h of GPS observations by tracking all available satellites that had risen higher than a 15° elevation angle. The sampling interval for the data logging is 15 s. The collected data are downloaded from the internal RAM of the receivers to a PC hard disk or floppy disk. The raw data of each station are then transferred to the Receiver INdependent EXchange (RINEX) format using a transfer program for post-processing. The GNSS data in RINEX format is converted to the Bernese format, compiled and processed, and solved with respect to the Penghu Structural Stabilization Station on the west coast [40–42]. Figure 1 displays the location distribution map of CGPS sites in Taiwan Province. In this study, the GPS measurements of 44 sites in Taiwan Province (red triangle in Figure 1) from 2006 to 2016 can be obtained from the GPS Lab web application (http://gps.earth.sinica.edu.tw, accessed on 2 August 2021) of Institute of Earth Sciences, Academia Sinica, Taiwan Province, which requires a simple registration process to access data. You can download three-component continuous GPS time series data for all sites through the "download time series" button.

In this study, we first selected data from the 283 available sites in the Taiwan CGPS array that have been observed for more than 10 years, and 109 sites that have been observed for less than 10 years. We then calculated the data length ratio of each site ($Ratio_i = L_i/3652$, L is the data length of the i^{th} site, $i = 1, 2, \cdots, 392$) based on the vertical coordinate time series data of each site from January 1, 2006 to December 31, 2015 (ten-year span, totaling 3652 days). We selected 188 sites with $Ratio \geq 90\%$. We adopted the approach of visual appraisal to screen and select 44 high-quality time series sites according to the data consistency and quality. Figure 2 shows the data span of the 44 sites used for the CME estimation, with nearly all of the sites having a data cycle longer than 9.5 years.

In the time series spatio-temporal analysis, GNSS coordinate time series require a series of pre-processing steps. Coordinate series processing mainly includes outlier detection and elimination, offsets detection, missing data interpolation, etc. Kurtosis is the non-Gaussian property of random variables that can be measured by the fourth-order moment of the variables, defined as:

$$kurt(x) = E\left\{x^4\right\} - 3\left(E\left\{x^2\right\}\right)^2 \quad (1)$$

where x is an independent random variable and E is a mathematical expectation operator. In the ICA process, it is assumed that x is normalized, and $E\{y^2\} = 1$. The kurtosis is simplified to $E\{y^4\} - 3$. For Gaussian variables, the kurtosis $kurt(y) = E\{y^4\} - 3 = 3E\{y^2\} - 3 = 0$, which implies that the kurtosis of the Gaussian variable is 0, the super-Gaussian variable is positive, and the sub-Gaussian variable is negative. A stronger non-Gaussian expression of the variable is associated with a greater absolute value of kurtosis. It should be noted that the kurtosis calculation is highly sensitive to outliers [43–46]. Outliers in a GNSS time series must therefore be identified in advance. The triple standard difference method is used for outlier detection and elimination. An offset in a time series is most often caused by antenna replacements and co-seismic displacement deformation, which affects the analysis of periodic changes of the GNSS coordinate series and the estimation of some geophysical signals. Here, we use the most convenient manual visual inspection

method to eliminate the offsets [47]. The missing data in the time series are interpolated after eliminating the outliers and fitting the offsets. The initial values of the missing data are interpolated using a PCA iteration approach [26]. An initial interpolation result is obtained using an inverse distance weighting interpolation. PCA is then applied and the first several PCs for which the cumulative percentage exceeds 70% are used to reconstruct the series. The PCA reconstruction is repeated until the maximum absolute value of the difference between two iteration is less than 0.01 mm.

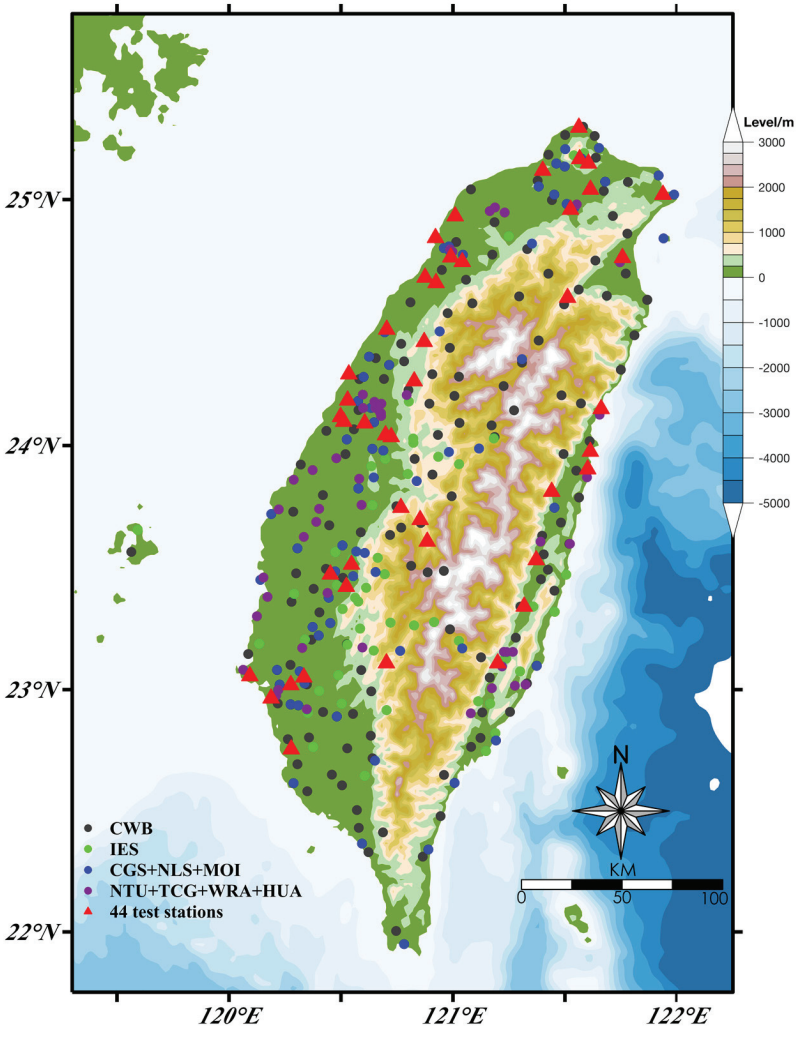

Figure 1. Taiwan continuous global positioning system (CGPS) network. The black, green, blue, and purple circles represent CGPS sites operated by the Central Weather Bureau (CWB), the Institute of Earth Sciences (IES), the Central Geological Survey (CGS) and the Water Resources Agency (WRA) and other research units. Among them, the sites represented by red triangles are used in this ICA/PCA study.

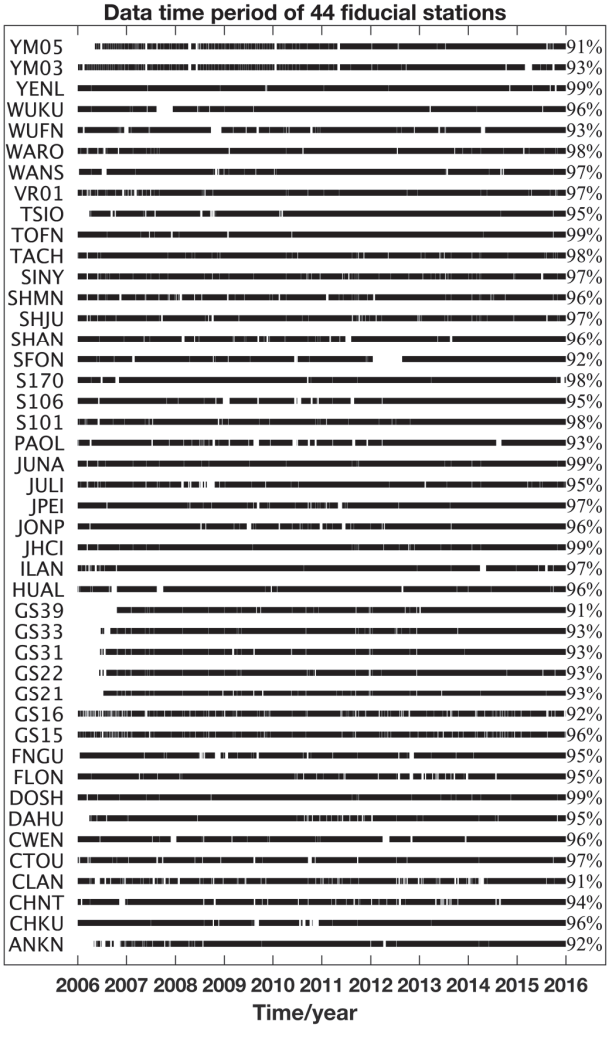

Figure 2. Data availability of the 44 GPS sites. Blanks represent the missing data.

In the data pre-processing of the 44 GNSS stations, we used Equation (2) to fit the time series of each station, and eliminated the linear term and offset term, to smoothen the observation, and input the missing data. The time series after unified treatment ranges from approximately −20 to 20 mm. We selected five stations with a notable linear term, offset term and missing data in the coordinate time series (CHKU, JUNA, S101, SFON and SHAN), as indicated on the left in Figure 3, and the pre-processed data are presented on the right. It can be seen that the linear term, offset term, and missing data are all corrected.

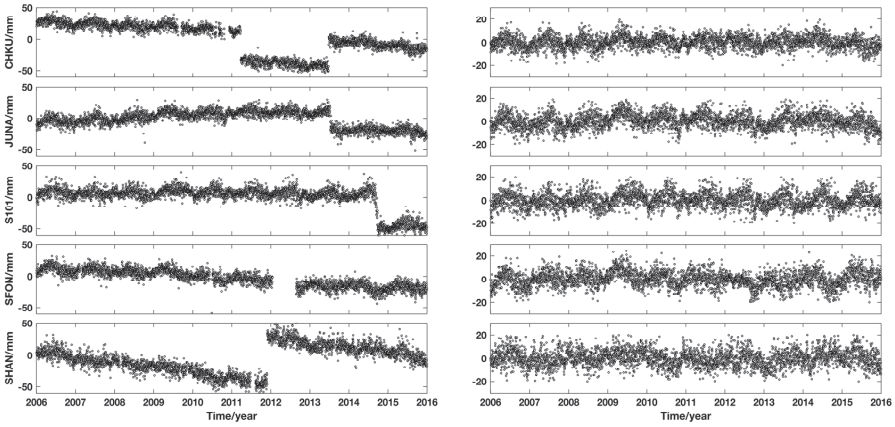

Figure 3. Original GPS time series (**left**) and preprocessing sequence of the CHKU, JUNA, S101, SFON, and SHAN stations (**right**).

The coordinate time series for each site can be modeled as follows to obtain the effects of seasonal variations and colored noise [12]:

$$y(t_i) = a + bt_i + c\sin(2\pi t_i) + d\cos(2\pi t_i) + e\sin(4\pi t_i) + f\cos(4\pi t_i) + \sum_{j=1}^{n_g} g_i H(t_i - T_{gi}) + \varepsilon_i \quad (2)$$

where t_i for $i = 1, 2, \cdots, N$ is the daily solution epoch in units of years, a and b are the site position and linear rate, respectively, c and d are the annual term coefficients, e and f are the semi-annual coefficients, $H(t_i - T_{gi})$ is a Heaviside step function (when $t_i \geq T_{gi}$, its value is 1; otherwise it is 0), g_i is the change of rate from $t_i = T_{gi}$, and ε_i is the model residual and also represents noise. It is usually assumed that ε_i is white noise; however, the analysis of a large amount of data shows that the noise in the coordinate time series obtained from GNSS continuous observation data contain both white noise and colored noise [5,48–54]. The velocity error in a GPS coordinate time series may be underestimated by factors of 5–11 if a pure white noise model is assumed [5]. If the influence of colored noise is not considered, a biased or inaccurate geophysical interpretation may be obtained.

2.2. Principal Component Analysis

PCA is an orthogonal decomposition method that combines a group of related data and decomposes the group into a group of linear uncorrelated orthogonal eigenvectors and corresponding PCs. Each of the vectors reflects some of the information from the original matrix to different degrees. The PCs are arranged in descending order of eigenvalues, and the first few PCs can generally capture most of the information from the original matrix. Therefore, the main functions of the PCA is to manage the statistical method of dimensionality reduction in mathematics, explore a small number of PCs to represent the signals of the original data, and reflect the characteristic modes contained within the original matrix as much as possible [7,20,55].

The daily station residual time series with a span of m days in a continuous GNSS network is constructed by n stations, $X(t_i, x_j)(i = 1, 2, \cdots, m; j = 1, 2, \cdots, n)$. Firstly, we preprocess each data column in matrix X with trends and outliers, and obtain its covariance matrix B using the following equation:

$$b_{ij} = \frac{1}{m-1}\sum_{k=1}^{m} x_{k,i}x_{k,j} \quad (3)$$

where $x_{k,i}, x_{k,j}$ respectively represent the time series corresponding to the i^{th} and j^{th} stations at epoch k. The symmetric matrix B can be decomposed as:

$$B = V\Lambda V^{\mathrm{T}} \tag{4}$$

where eigenvector matrix V^{T} is an $(n \times n)$ matrix and Λ is a non-zero diagonal matrix of order k. For a complete rank covariance matrix $B, k = n$. The matrix X can be expressed as:

$$X = VP \tag{5}$$

where P is a $(m \times n)$ matrix. The k-th row vector in P is the k^{th} PC for matrix X and represents a temporal signature of the mode. The k^{th} column vector in V is the k^{th} spatial response corresponding to the mapped PC, which represents the spatial distribution of the mode. The above decomposition method is known as an EOF analysis or a PCA. The matrix P can be denoted as:

$$P = V^{\mathrm{T}}X \tag{6}$$

We arrange the eigenvalues $\lambda_i (i = 1, 2, \cdots, n)$ in descending order, and the contribution of each PC to the original data set can be represented by the feature cumulative contribution rate $m_k (k = 1, 2, \cdots, n)$:

$$m_k = \frac{\sum_{i=1}^{k} \lambda_i}{\sum_{i=1}^{n} \lambda_i} \tag{7}$$

The first few PCs represent those that contribute the most to the variance of a participating time series, and are usually related to the common source of temporal function. Higher-order PCs usually relate to the influence of local or individual stations. The CME calculated by PCA can then be obtained according to:

$$\varepsilon^{\mathrm{PCA}} = \sum_{k=1}^{q} v_k p_k (1 \le q < n) \tag{8}$$

where q is the number of PCs that define the CME.

2.3. Independent Component Analysis

ICA is a data-driven approach based on blind source separation (BSS). BSS only assumes that the signal sources are independent non-Gaussian signals, and the relationship between the information of the signal sources and the linear transformation is unknown. ICA is a digital signal processing algorithm developed to solve this problem. Compared to the model-driven approaches, ICA works without prior information about the underlying sources, which allows it to effectively detect some signals that cannot be obtained when using other methods [43–46].

It is assumed that signal sources are composed of several statistically independent signals that overlap in both temporal and spatial domains, ICA synchronously observes the overlapping signals using multiple channels and decomposes the observed signals into several ICs, after the unmixing, as a set of source signal estimates (Figure 4). The channels exert no influence on the signal, and the number of observed channels is the same as the number of signals. The standard noiseless ICA mathematical model is:

$$X(t) = AS(t) \tag{9}$$

where the random vectors $X(t) = [X_1(t), \cdots, X_M(t)]^{\mathrm{T}}$ represent the observed signals and random vectors $S_i(t), i = 1, 2, \cdots, N; M \ge N$ represent the source signals, and A is a mixing matrix. The ICA decomposition process can be regarded as the inverse transformation of Equation (9):

$$Y(t) = S\hat{(t)} = BX(t) \tag{10}$$

where B is the unmixing matrix. It is assumed that the row vectors in S are statistically independent of each other, their joint probability density function (pdf) is the product of their marginal probability density function, which means that, the joint entropy of each component is the sum of the entropy of each component, such that:

$$p(S) = \prod_{i=1}^{n} p(S_i) \tag{11}$$

where p is the pdf of S, where both A and the source signal S are unknown. However, as long as the output components separated by the unmixing matrix B are statistically independent of each other, this approach is equivalent to separating the source signals.

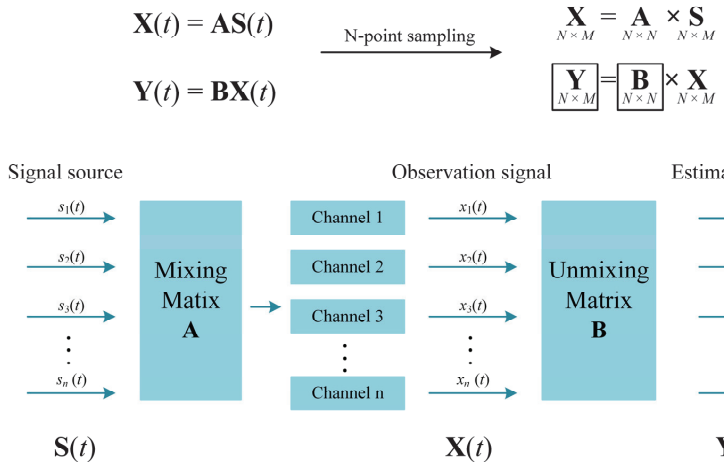

Figure 4. Schematic illustration of independent component analysis.

The basic hypothesis of ICA is that the source signals are statistically independent, allowing for no more than one source with a Gaussian distribution while describing the remaining sources with non-Gaussian distributions. Most of the deformed signals in GNSS coordinate sequences are also non-Gaussian signals, and the non-Gaussian signals are quantized by negentropy. The ICA attempts to create various linear transformations on the observed signals, and the maximum negentropy of the transformed quantity is likely to indicate the source signals [43,46]. Various ICA algorithms have been derived based on this fundamental idea. In this study, we use the FastICA algorithm based on negentropy to estimate the original signals [56,57]. The negentropy is defined as:

$$J(X) = \int_{-\infty}^{+\infty} p_G(X) \ln p_G(X) dX + \int_{-\infty}^{+\infty} p(X) \ln p(X) dX \tag{12}$$

where $p(X)$ is the pdf of X, and $p_G(X)$ is the pdf of the Gaussian distribution with the same covariance matrix as $p(X)$. The greater negentropy values are associated with stronger non-Gaussian signals [57–59].

A detailed description of the FastICA algorithm procedure is as follows:

1. Centralize and whiten the observed data.
2. Choose an initial weight vector of unit norm w.
3. Update w^+ through $w^+ = E\left[Zg\left(w^{\mathrm{T}}Z\right)\right] - E\left[g'\left(w^{\mathrm{T}}Z\right)\right]w$.
4. Normalize w by $w = w^+ / ||w||^+$.
5. Return to step 3 if w is not converged.

We can similarly reconstruct the original data set of a GNSS time series of n stations across a period of m days and calculate the CME using the source signals that have been

separated by ICA. We can obtain ICs by $Y(t) = BX(t)$, assuming that $A = B^{-1}$, and X can be obtained by:

$$X(t) = B^{-1}Y(t) = AY(t) \tag{13}$$

The CME based on ICA can thus be given as:

$$\varepsilon^{\mathrm{ICA}} = \sum_{k \in R}^{R} a_k y_k \tag{14}$$

where R is a group of temporal components in spatio-temporal filtering.

3. Results

3.1. Common Mode Error Extraction Using PCA/ICA

To intuitively compare the amplitude of each component, the corresponding spatial response is usually divided by the maximum absolute value and scaled to a variation interval of $-100\% \sim 100\%$, where the scaled amount is multiplied by the corresponding temporal components. An upward movement is a positive response and a downward is a negative response. The results of the first five PCs are shown on the left side of Figure 5, and their corresponding spatial responses are provided in the first row of Figure 6.

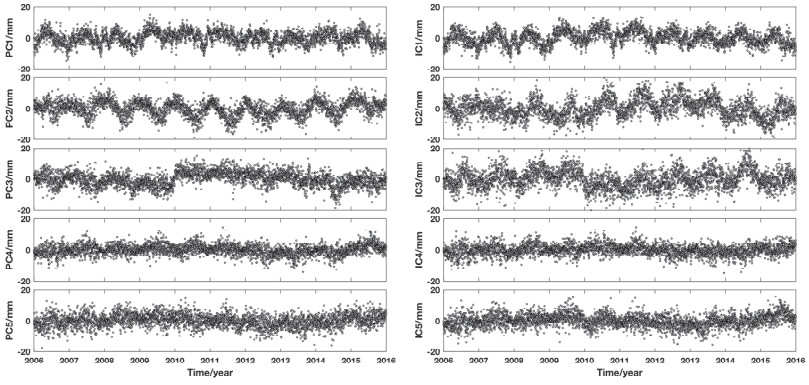

Figure 5. Five components extracted from Taiwan PCA (**left**) and ICA (**right**).

We use the standard CME definition provided by Dong et al. [7], in which most stations (50%) for a certain PC mode exhibit a clearly normalized spatial response ($> 25\%$) and the eigenvalue of the mode exceeds 1% of the collective eigenvalues; it can therefore be considered as a common mode. The spatial response corresponding to the first PC in the first line of Figure 6 displays notably good regional consistency, and its average normalized amplitude (absolute value) is 77.3%. However, the 2nd–5th. PCs do not satisfy this condition. In terms of eigenvalues, Table 1 provides the percentage of the first 10 PC eigenvalues for the total eigenvalues and the cumulative contribution rate (eigenvalues). The first PC accounts for 24.7%, the second PC accounts for 6.5%, and the cumulative contribution rate of the eigenvalues tends to stabilize after the fifth order, which indicates that the first PC is able to represent the most common-mode components. In summary, we define the displacement component caused by the first PC as the CME of the entire GPS network.

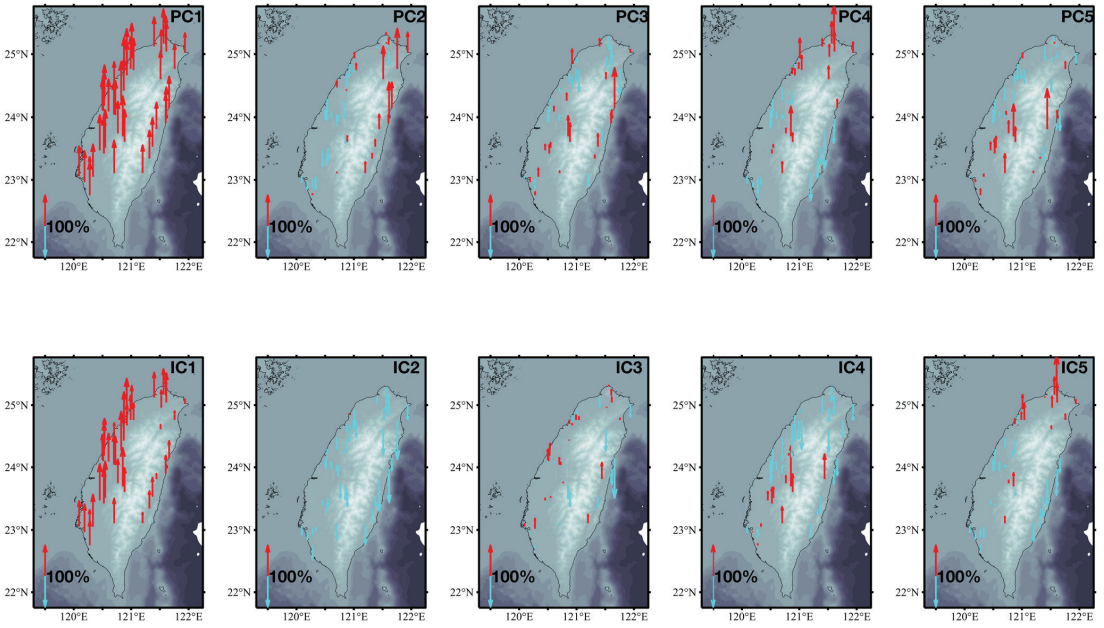

Figure 6. Spatial response of five PCs (first row) and ICs (second row) at each site in Taiwan. The red arrow represents the positive spatial response, and the blue arrow represents the negative spatial response.

Table 1. Individual contribution rate and cumulative contribution rate of the top ten PCs.

Order of PCs	Individual Contribution Rate (%)	Cumulative Contribution Rate (%)
1	24.7	24.7
2	6.5	31.2
3	4.6	35.8
4	3.7	39.5
5	3.6	43.1
6	3.0	46.1
7	2.7	48.8
8	2.5	51.3
9	2.4	53.7
10	2.3	56.0

We use ICA to process the five components from PCA. The principle is realized using ICA's fast fixed-point algorithm [57,60]. The first step of the algorithm is to centralize and whiten the observed values before processing. The mixing matrix is orthogonal so as to reduce the number of free parameters. The mixed signals are then linearly transformed to express an unrelated variable with a variance that is equal to 1 (whitening or spheroidizing). This step comprises the pretreatment process of ICA, which is realized by PCA. This is conducted because the number of PCs reserved for the ICA analysis should be lower than the data dimension. The process of trial and error is therefore used to select the appropriate quantity [61]. In this study, the effect of retaining the first five PCs becomes apparent.

The ranking of the ICs obtained by ICA does not correspond to a decrease in the variance. We therefore calculate the average ratio of the GPS_IC displacement in each GPS site calculated by the ICA filtering to the observed time series, in accordance with the procedure described by Liu et al. [19] and Milliner et al. [62]. Smaller ratios are associated with contributions that are more significant, and the ICs are reordered in ascending order. The corresponding spatial response of each IC is normalized according to the absolute

value of its maximum value so that the comparison is more accurate. The IC time series and the corresponding spatial response value, after the IC, is multiplied by the normalization factor, shown on the right in Figure 5 and in the second row of Figure 6. The first two ICs are evidently the largest of the original data according to the previous definition of the CME, and their spatial response values display the same sign. We can therefore locate the displacement caused by these two components as the CME of the entire GPS network in ICA filtering.

After calculating the CME, we subtract its influence on each station from the original time series. The filtering effect can be described by the reduction rate of the root mean square (RMS) of the residual time series (Figure 7). The results in Table 2 reveal that after PCA and ICA filtering, the average RMS values are reduced by approximately 14% and 17%, respectively. These two methods can therefore be used to effectively improve the signal-to-noise ratio of the residual time series.

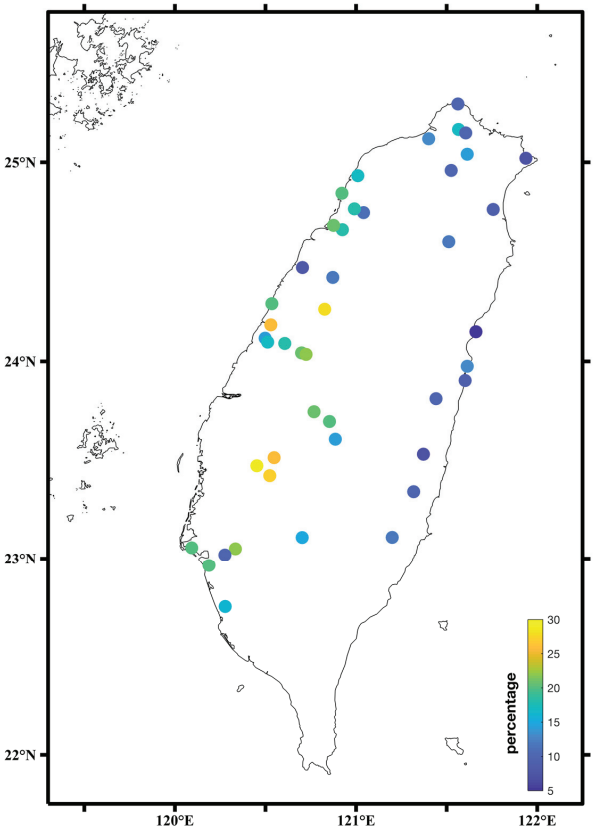

Figure 7. RMS reduction percentage of residual time series after ICA filtering.

Table 2. Mean RMS error before and after PCA/ICA filtering of GPS stations.

	Method	RMS/mm
Before		6.47
After	PCA	5.58
	ICA	5.40

Figure 7 shows the decline of the RMS value of the residual time series at each station after ICA filtering. Figure 7 also presents notable differences in the ICA filtering effect

between the east and west. The RMS reduction rate in the west is relatively large, whereas that in the east is small, which is partially due to topography. There are many mountains on the eastern side of Taiwan and the stations are sparsely distributed, whereas the western side is relatively flat and the stations are relatively dense. Another explanation is the orogenic processes, as there is topographic uplift in the eastern region [63] and sinking in the southwest region due to groundwater extraction [64]. This phenomenon can also be observed in the second-order PCs obtained via PCA filtering, and the station response indicates notable local variation characteristics, as shown in PC2 in the first line of Figure 6.

3.2. Noise Analysis of GNSS Coordinate Time Series

In the noise analysis of the Taiwan GNSS time series, for the original time series of each station, we fit the offsets in advance, interpolate the original data, and then analyze the power spectrum of the noise series. The results are presented in Figure 8. Due to the large volume of data, this study uses the GS39 station as an example to elaborate on an explanation. It can be seen that the power spectrum at low and high frequencies of the noise series presents different peaks and demonstrates a clear linear trend term. The spectral energy in the low-frequency band is higher than that in high-frequency band. The spectral exponent of this component is -0.67, which indicates that the noise of this station is influenced by colored noise. Through piecewise fitting, the slope of this component is approximately approached, yielding -1 at a low frequency and 0 at a higher frequency. The low-frequency result possesses the characteristics of flicker noise, and the high-frequency result possesses the characteristics of white noise. It can thus be estimated that the noise type of this point is a combination type of white noise and flicker noise.

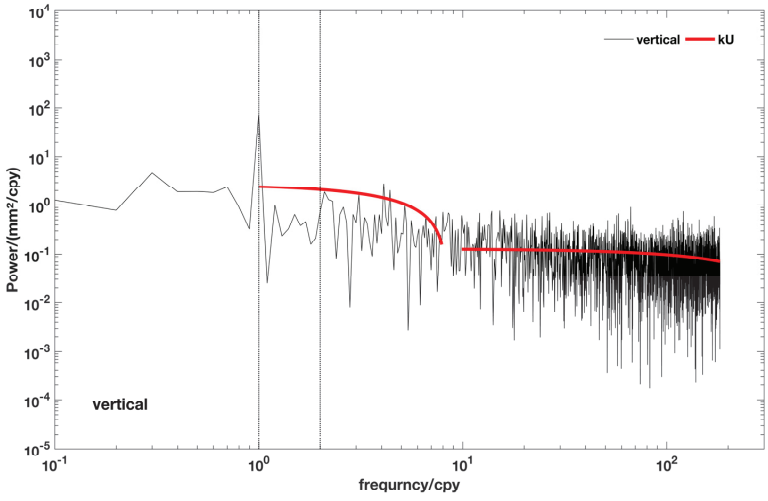

Figure 8. U component power spectrum of the GS39 site noise sequence. The black line represents the power spectrum, and the red line represents the slope.

4. Discussion

4.1. Potential Geophysical Interpretation of the CME

We note that although the RMS reduction results are similar, the PCA and ICA filtering processes exhibit different spatial and temporal patterns. Previous studies have also revealed that PCA-derived CMEs are not completely unrelated to local effects or random noise. The decomposition of similar contribution components in an actual network residual time series is difficult to achieve using PCA, and we cannot identify potential geophysical mechanisms or study the subtle signals in GPS observations [29]. In contrast, there is a high correlation between the common mode components extracted by ICA and the

simulated surface mass loading deformation. An important criterion to better understand and describe the differences between the ICA and PCA results is the extent to which the temporal and spatial patterns of annual crustal deformation, caused by mass loadings of various geophysical sources, are restored by using these two methods.

We submitted requests for real-time solutions for the ATML, and LWS 3-D displacement files from 44 stations in Taiwan between 1 January 2006 and 31 December 2015 using the online solution function of the IMLS (http://massloading.net/, accessed on 2 August 2021) [65–68]. For ATML and LWS, we used the GEOS-FPIT model developed by the Global Modeling and Assimilation Office at NASA Goddard Space Flight Center, which considers a time range from 1 January 2000 to present, that is updated several times per day. The model resolution is 0.50° × 0.625° × 72 layers × 3 h. We obtained the displacement time series in the center-of-figure frame.

We averaged all of the loading series displacements into the daily results, and we calculated the average GPS_IC1 and GPS_IC2,comparing it with the average ATML and LWS. As indicated in Figure 9, GPS_IC is the outer product of the IC and its corresponding spatial response. We note that ATML and LWS are consistent in terms of their amplitude and phase with GPS_IC1 and GPS_IC2, respectively. The correlation coefficients of these two temporal patterns are 0.58 and 0.4, respectively. We therefore suggest that atmospheric and hydrological mass loading are the main components of the CME in the Taiwan GPS network, which can be reflected by the IC extracted by ICA spatio-temporal filtering. Although IC1 and IC2 can be interpreted by ATML and LWS, other temporal components are statistically independent, and their unretrieved information still requires further study.

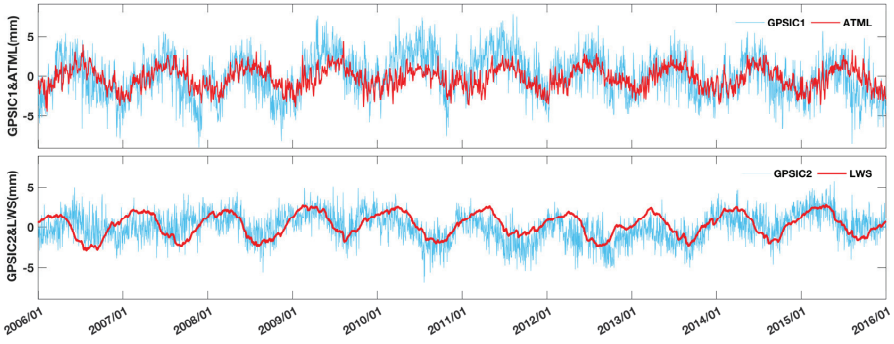

Figure 9. Comparison of the GPS_ICs (calculated with IC1 and IC2) and mass loading deformation signals (ATML and LWS). The upper figure shows GPS_IC1 and the ATML, and the lower figure shows GPS_IC2 and the LWS.

4.2. Effect of Removing the CME

We then use the Hector software [69] to analyze the 44 noise sequences with only the offsets corrected using the white-plus-power law (W + PL) model. We do not fix the spectral index, but treat it as an unknown factor, and solve it alongside the linear, annual, and semi-annual periodic terms [14]. On this basis, we subtract the CME after ICA filtering and analyze the obtained noise sequence, as shown in Table 3. We also analyze the power spectrum of the original noise sequence, PCA filtered noise sequence, and ICA filtered noise sequence of station GS39, as shown in Figure 10. The ICA filtering approach is observed is more useful than the PCA in terms of the amplitude of the annual term.

Table 3 lists the estimated parameters and noise terms of the 44 stations in Taiwan. We can see that the PL amplitude is reduced by an average of approximately 27.8% after ICA filtering, which indicates that the filtering has a certain suppression effect on noise. However, there is not an obvious change in the amplitude of the white noise (W), which indicates that it originated locally. The amplitude of annual and semi-annual periodic terms decreased by approximately 60% and 18%, respectively. Before and after the filtering,

the average spectral index shifted from −0.77 to −0.92, which is consistent with the result of Rao et al. [70], indicating that the noise model of the Taiwan GPS data is closer to the white-plus-flicker noise (W+FN) model with a spectral index of −1.

Table 3. Estimated parameters using Hector software before and after spatiotemporal filtering (ICA).

Sites	Annual Amplitude (mm)		Semi-Annual (mm)		PL Amplitude		WN Amplitude		Spectral Index κ	
	Before	After	Before	After	Before	After	Before	After	Before	After
'ANKN'	1.23 ± 0.33	0.70 ± 0.25	0.55 ± 0.25	0.50 ± 0.21	10.32	8.07	4.08	4.13	−0.47	−0.37
'CHKU'	2.41 ± 0.31	0.40 ± 0.19	0.60 ± 0.23	0.39 ± 0.15	8.63	4.94	3.50	4.00	−0.67	−0.93
'CHNT'	3.80 ± 0.83	2.80 ± 0.80	0.88 ± 0.45	0.77 ± 0.40	20.32	19.12	6.17	6.40	−0.98	−1.05
'CLAN'	4.30 ± 1.00	2.39 ± 0.94	1.58 ± 0.65	1.35 ± 0.60	24.21	23.04	6.09	6.23	−1.01	−1.10
'CTOU'	2.54 ± 0.45	0.67 ± 0.31	0.53 ± 0.26	0.59 ± 0.24	11.60	8.14	4.90	5.24	−0.85	−1.02
'CWEN'	3.41 ± 0.37	0.69 ± 0.20	0.55 ± 0.25	0.44 ± 0.16	9.99	5.37	3.88	3.75	−0.73	−0.65
'DAHU'	2.63 ± 0.45	1.58 ± 0.38	0.48 ± 0.25	0.50 ± 0.24	12.19	9.52	4.24	4.73	−0.75	−0.89
'DOSH'	3.90 ± 0.38	0.36 ± 0.18	0.40 ± 0.21	0.35 ± 0.15	10.94	5.36	3.80	4.52	−0.64	−0.68
'FLON'	2.76 ± 0.46	1.64 ± 0.42	1.58 ± 0.39	1.33 ± 0.36	15.33	14.31	0.00	0.01	−0.45	−0.43
'FNGU'	2.76 ± 0.37	0.44 ± 0.21	0.85 ± 0.27	0.64 ± 0.17	9.52	4.60	4.26	4.40	−0.82	−1.25
'GS15'	2.90 ± 0.29	0.91 ± 0.20	0.40 ± 0.19	0.31 ± 0.13	8.37	3.90	3.54	4.32	−0.60	−1.19
'GS16'	2.18 ± 0.45	0.67 ± 0.31	0.63 ± 0.30	0.42 ± 0.21	12.38	9.58	5.43	5.57	−0.73	−0.70
'GS21'	2.03 ± 0.36	0.82 ± 0.25	0.58 ± 0.24	0.37 ± 0.15	8.48	4.36	3.95	3.84	−0.94	−1.47
'GS22'	2.63 ± 0.43	1.72 ± 0.33	0.49 ± 0.25	0.43 ± 0.20	10.89	7.58	3.73	4.00	−0.85	−0.99
'GS31'	1.80 ± 0.40	2.04 ± 0.33	0.45 ± 0.23	0.30 ± 0.16	9.54	6.58	3.82	3.78	−0.99	−1.24
'GS33'	2.86 ± 0.36	0.49 ± 0.23	0.58 ± 0.24	0.50 ± 0.17	8.59	4.68	4.44	4.42	−0.93	−1.37
'GS39'	3.94 ± 0.33	1.32 ± 0.24	0.58 ± 0.24	0.42 ± 0.16	9.13	4.81	3.02	3.75	−0.67	−1.17
'HUAL'	4.06 ± 0.57	1.38 ± 0.45	0.89 ± 0.38	0.51 ± 0.25	14.22	10.14	5.96	5.68	−0.89	−1.11
'ILAN'	4.10 ± 0.70	2.35 ± 0.43	0.92 ± 0.41	0.47 ± 0.23	14.38	9.43	6.60	5.59	−1.27	−1.09
'JHCI'	3.72 ± 0.32	0.63 ± 0.18	0.56 ± 0.24	0.57 ± 0.16	10.23	5.50	2.79	3.83	−0.45	−0.37
'JONP'	3.17 ± 0.34	0.58 ± 0.18	0.51 ± 0.23	0.28 ± 0.13	9.75	4.45	3.83	4.26	−0.63	−0.76
'JPEI'	3.05 ± 0.46	1.70 ± 0.43	0.60 ± 0.29	0.68 ± 0.29	12.07	10.31	6.14	6.43	−0.78	−0.94
'JULI'	2.20 ± 0.32	0.83 ± 0.26	0.63 ± 0.25	0.57 ± 0.20	9.33	5.70	4.98	6.01	−0.51	−0.95
'JUNA'	3.16 ± 0.41	0.83 ± 0.27	0.46 ± 0.23	0.32 ± 0.16	10.38	5.75	4.56	4.66	−0.89	−1.19
'PAOL'	2.84 ± 0.47	0.65 ± 0.31	0.52 ± 0.27	0.50 ± 0.24	12.30	9.80	5.68	5.58	−0.80	−0.78
'S101'	3.50 ± 0.37	1.78 ± 0.29	0.72 ± 0.28	0.57 ± 0.23	11.76	8.98	2.63	3.96	−0.50	−0.51
'S106'	2.90 ± 0.36	0.50 ± 0.22	0.35 ± 0.18	0.29 ± 0.14	9.21	5.70	4.42	4.36	−0.82	−0.87
'S170'	2.14 ± 0.33	0.43 ± 0.20	0.96 ± 0.26	0.66 ± 0.17	9.22	5.00	3.94	4.27	−0.71	−1.00
'SFON'	3.58 ± 0.48	1.19 ± 0.38	0.52 ± 0.26	0.42 ± 0.21	11.43	8.74	5.12	5.10	−0.92	−1.00
'SHAN'	0.79 ± 0.40	1.87 ± 0.44	0.84 ± 0.37	0.63 ± 0.29	14.82	11.21	4.70	5.28	−0.75	−0.85
'SHJU'	2.97 ± 0.45	1.20 ± 0.30	0.84 ± 0.31	0.76 ± 0.21	11.27	6.04	4.56	4.80	−0.92	−1.26
'SHMN'	1.67 ± 0.34	0.36 ± 0.19	0.85 ± 0.28	0.71 ± 0.24	11.85	10.08	0.03	0.02	−0.36	−0.28
'SINY'	3.82 ± 0.49	0.50 ± 0.26	1.01 ± 0.36	0.76 ± 0.27	13.29	9.31	5.64	5.57	−0.73	−0.73
'TACH'	2.85 ± 0.49	0.68 ± 0.33	0.44 ± 0.23	0.36 ± 0.19	11.92	8.04	4.06	4.15	−0.98	−1.34
'TOFN'	2.51 ± 0.46	0.5 ± 0.26	0.59 ± 0.28	0.62 ± 0.24	11.58	8.50	4.07	4.15	−0.91	−0.98
'TSIO'	1.85 ± 0.45	0.96 ± 0.39	1.11 ± 0.33	0.96 ± 0.29	11.60	9.61	4.26	4.60	−0.86	−1.04
'VR01'	1.60 ± 0.42	0.86 ± 0.33	0.46 ± 0.23	0.31 ± 0.16	10.31	6.85	4.46	4.40	−0.97	−1.33
'WANS'	3.33 ± 0.49	2.05 ± 0.40	0.77 ± 0.32	0.83 ± 0.29	11.98	9.71	5.33	5.12	−0.95	−0.96
'WARO'	2.01 ± 0.44	0.96 ± 0.32	0.81 ± 0.33	0.38 ± 0.20	13.44	10.57	5.08	4.06	−0.55	−0.47
'WUFN'	2.61 ± 0.28	0.95 ± 0.18	0.51 ± 0.21	0.25 ± 0.12	9.00	4.00	2.43	4.46	−0.42	−0.82
'WUKU'	2.71 ± 1.07	2.65 ± 1.05	1.99 ± 0.78	1.95 ± 0.76	29.23	28.39	0.05	1.59	−0.92	−0.95
'YENL'	2.31 ± 0.36	0.73 ± 0.29	0.42 ± 0.21	0.31 ± 0.16	9.71	6.73	5.21	5.62	−0.70	−1.05
'YM03'	1.61 ± 0.51	1.80 ± 0.40	0.78 ± 0.35	0.94 ± 0.32	13.74	11.38	5.84	5.23	−0.80	−0.64
'YM05'	2.68 ± 0.47	0.77 ± 0.34	0.85 ± 0.34	0.59 ± 0.26	12.98	9.91	3.95	4.51	−0.72	−0.83
Mean	2.77 ± 0.45	1.12 ± 0.34	0.72 ± 0.30	0.59 ± 0.23	12.08	8.72	4.21	4.46	−0.77	−0.92

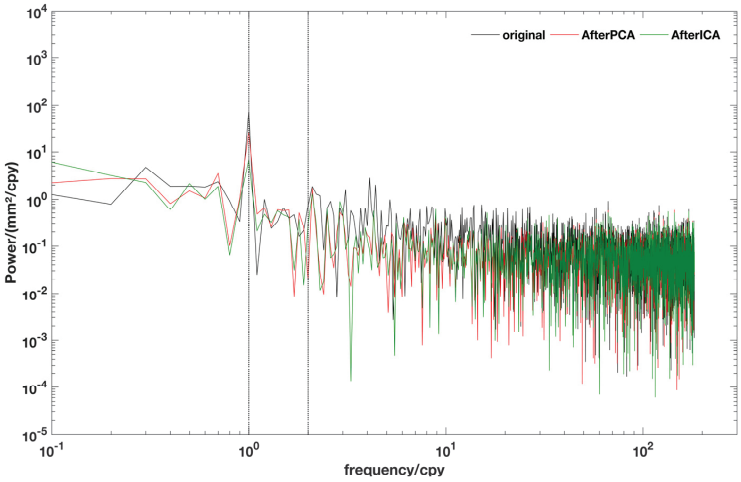

Figure 10. Comparison of the power spectrum of the GS39 site noise sequence and noise sequence filtered by PCA and ICA.

5. Conclusions

We use PCA and ICA approaches to analyze the vertical coordinate time series of 44 sites in Taiwan island in China from 2006 to 2016. The results are summarized as follows.

1. Both PCA and ICA can effectively remove the CME. The average RMS of PCA and ICA in the U direction shifted from 6.47 mm to 5.58 mm and 5.40 mm, respectively, a decreased by approximately 14% and 17%. However, the CMEs of the two approaches reveal notable differences in their temporal and spatial characteristics. Figure 6 shows that the PCA separates only one CME and the ICA separates two CMEs. We therefore believe that PCA may eliminate the original site information, whereas ICA retains more original site information.
2. There are notable differences in the ICA filtering effect between the east and west of Taiwan. The RMS reduction rate in the west is relatively large, whereas that in the east small, which is partially due to topography. There are many mountains on the eastern side of Taiwan and the stations are sparsely distributed, whereas the western side is relatively flat and the stations are relatively dense. Another explanation is the orogenic processes, as there is a topographic uplift in the eastern region and sinking in the southwest region due to groundwater extraction.
3. To explore the possible geophysical sources of ICA's CMEs, we compare the CMEs of ICA with the predicted average loading displacements caused by changes in the atmospheric and hydrological loadings. It is found that GPS_IC1 and ATML, and GPS_IC2 and LWS are consistent in terms of amplitude and characteristics. The correlation between GPS_IC1 and ATML is 0.55, and the correlation coefficient between GPS_IC2 and LWS is 0.40. This indicates that seasonal changes in Taiwan are related to the movement of water in addition to atmospheric pressure.
4. We used Hector software to analyze the noise characteristics of the time series of all stations prior to filtering. The average spectral index shifted from -0.72 to -0.92, which indicates that the most suitable noise model in Taiwan is W + FN. Filtering can also effectively reduce PL noise. After filtering, PL noise is reduced by an average of approximately 28%. The average annual cycle item is also significantly reduced by approximately 60%. ICA filtration is more advantageous than PCA filtration. The noise sequence filtered by ICA and PCA at the GS39 station was analyzed to verify the above conclusions.

Author Contributions: All authors contributed significantly to the manuscript. Conceptualization, X.M., B.L. and W.D.; methodology, X.M. and B.L.; validation, X.M. and B.L.; formal analysis, X.M.; investigation, X.M.; resources, B.L. and W.D.; data curation, X.X.; writing—original draft preparation, X.M.; writing—review and editing, B.L., W.D., C.K. and X.X.; supervision, W.D., C.K. and X.X.; funding acquisition, B.L. All authors have read and agreed to the published version of the manuscript.

Funding: This work is funded by the National Natural Science Foundation of China (Grant No. 41904003, 41774040, 41674011), the Natural Science Foundation of Hunan Province, China (Grant No. 2020JJ5571) and Open Fund of Engineering Laboratory of Spatial Information Technology of Highway Geological Disaster Early Warning in Hunan Province (Changsha University of Science & Technology) (Grant No. KFJ190602).

Data Availability Statement: The GPS data used in this work can be obtained from the GPS Lab web application (http://gps.earth.sinica.edu.tw, accessed on 2 August 2021) of the Institute of Earth Sciences, Academia Sinica, Taiwan. This application requires a simple registration process to access the data. You can download the three-component continuous GPS time series data of all the sites through the "download time series" button. The pre-calculated ATML and LWS displacement data sets were obtained from the International Mass Loading Service Web application (http://massloading.net/, accessed on 2 August 2021) Explore individual loadings, used in the "GEOS-FPIT" model, the "Center of figure" frame, and the time range is in "Between 2006.01.01_00:00" and "2016.01.01_00:00". Site file uses our solved XYZ coordinate file. The displacement is provided every 3 h and is stored in a total of 120 .eph files at all 44 sites. The file name contains the corresponding timestamp. We extract the U-component displacement from each file to form the original time series data set for our spatio-temporal analysis. The time series of the GPS stations used in this paper are uploaded to Figshare, and readers can download the data from: https://figshare.com/articles/dataset/data_for_EES_rar/13490442, accessed on 2 August 2021.

Conflicts of Interest: The authors declare no conflict of interest.

References

1. Bock, Y.; Melgar, D. Physical applications of GPS geodesy: A review. *Rep. Prog. Phys.* **2016**, *79*, 106801. [CrossRef]
2. He, X.; Montillet, J.P.; Fernandes, R.; Bos, M.; Yu, K.; Hua, X.; Jiang, W. Review of current GPS methodologies for producing accurate time series and their error sources. *J. Geodyn.* **2017**, *106*, 12–29. [CrossRef]
3. Li, Z.; Jiang, W.; Liu, H. Noise Model Establishment and Analysis of IGS Reference Station Coordinate Time Series inside China. *Acta Geod. Cartogr. Sin.* **2012**, *41*, 496–503.
4. Huang, L. Noise properties in time series of coordinate component at gps fiducial stations. *J. Geod. Geodyn.* **2006**, *26*, 31–34.
5. Mao, A.; Harrison, C.G.A.; Dixon, T.H. Noise in GPS coordinate time series. *J. Geophys. Res.* **1999**, *104*, 2797–2816. [CrossRef]
6. Wdowinski, S.; Bock, Y.; Zhang, J.; Fang, P.; Genrich, J. Southern California permanent GPS geodetic array: Spatial filtering of daily positions for estimating coseismic and postseismic displacements induced by the 1992 Landers earthquake. *J. Geophys. Res. Solid Earth* **1997**, *102*, 18057–18070. [CrossRef]
7. Dong, D.; Fang, P.; Bock, Y.; Webb, F.; Prawirodirdjo, L.; Kedar, S.; Jamason, P. Spatiotemporal filtering using principal component analysis and Karhunen-Loeve expansion approaches for regional GPS network analysis. *J. Geophys. Res. Solid Earth* **2006**, *111*, B03405. [CrossRef]
8. Gruszczynski, M.; Klos, A.; Bogusz, J. A Filtering of Incomplete GNSS Position Time Series with Probabilistic Principal Component Analysis. *Pure. Appl. Geophys.* **2018**, *175*, 1841–1867. [CrossRef]
9. King, M.A.; Altamimi, Z.; Boehm, J.; Bos, M.; Dach, R.; Elosegui, P.; Fund, F.; Hernández-Pajares, M.; Lavallee, D.; Cerveira, P.J.M. Improved constraints on models of glacial isostatic adjustment: A review of the contribution of ground-based geodetic observations. *Surv. Geophys.* **2010**, *31*, 465–507. [CrossRef]
10. Zhu, Z.; Zhou, X.; Deng, L.; Wang, K.; Zhou, B. Quantitative analysis of geophysical sources of common mode component in CMONOC GPS coordinate time series. *Adv. Space Res.* **2017**, *60*, 2896–2909. [CrossRef]
11. Bogusz, J.; Gruszczynski, M.; Figurski, M.; Klos, A. Spatio-temporal filtering for determination of common mode error in regional GNSS networks. *Open Geosci.* **2015**, *7*, 140–148. [CrossRef]
12. Nikolaidis, R. Observation of Geodetic and Seismic Deformation with the Global Positioning System. Ph.D. Thesis, University of California, San Diego, CA, USA, 2002.
13. Márquez-Azúa, B.; DeMets, C. Crustal velocity field of Mexico from continuous GPS measurements, 1993 to June 2001: Implications for the neotectonics of Mexico. *J. Geophys. Res. Solid Earth* **2003**, *108*, 2450. [CrossRef]
14. Williams, S.D.P.; Bock, Y.; Fang, P.; Jamason, P.; Nikolaidis, R.M.; Prawirodirdjo, L.; Miller, M.; Johnson, D.J. Error analysis of continuous GPS position time series. *J. Geophys. Res. Solid Earth* **2004**, *109*, B03412. [CrossRef]
15. Tian, Y.; Shen, Z.-K. Extracting the regional common-mode component of GPS station position time series from dense continuous network. *J. Geophys. Res. Solid Earth* **2016**, *121*, 1080–1096. [CrossRef]

16. Serpelloni, E.; Faccenna, C.; Spada, G.; Dong, D.; Williams, S.D.P. Vertical GPS ground motion rates in the Euro-Mediterranean region: New evidence of velocity gradients at different spatial scales along the Nubia-Eurasia plate boundary. *J. Geophys. Res. Solid Earth* **2013**, *118*, 6003–6024. [CrossRef]
17. He, X.; Hua, X.; Yu, K.; Xuan, W.; Lu, T.; Zhang, W.; Chen, X. Accuracy enhancement of GPS time series using principal component analysis and block spatial filtering. *Adv. Space Res.* **2015**, *55*, 1316–1327. [CrossRef]
18. Liu, B.; Dai, W.; Peng, W.; Meng, X. Spatiotemporal analysis of GPS time series in vertical direction using independent component analysis. *Earth Planets Space* **2015**, *67*, 189. [CrossRef]
19. Liu, B.; Dai, W.; Liu, N. Extracting seasonal deformations of the Nepal Himalaya region from vertical GPS position time series using Independent Component Analysis. *Adv. Space Res.* **2017**, *60*, 2910–2917. [CrossRef]
20. Li, W.; Shen, Y. The Consideration of Formal Errors in Spatiotemporal Filtering Using Principal Component Analysis for Regional GNSS Position Time Series. *Remote Sens.* **2018**, *10*, 534. [CrossRef]
21. Tan, W.; Chen, J.; Dong, D.; Qu, W.; Xu, X. Analysis of the Potential Contributors to Common Mode Error in Chuandian Region of China. *Remote. Sens.* **2020**, *12*, 751. [CrossRef]
22. Yuan, L.G.; Dong, X.; Chen, W.; Guo, Z.; Chen, S.; Hong, B.; Zhou, J. Characteristics of daily position time series from the Hong Kong GPS fiducial network. *Chin. J. Geophys.* **2008**, *51*, 1372–1384. [CrossRef]
23. Shen, Y.; Li, W.; Xu, G.; Li, B. Spatiotemporal filtering of regional GNSS network's position time series with missing data using principle component analysis. *J. Geod.* **2014**, *88*, 1–12. [CrossRef]
24. Li, W.; Shen, Y.; Li, B. Weighted spatiotemporal filtering using principal component analysis for analyzing regional GNSS position time series. *Acta Geod. Geophys.* **2015**, *50*, 419–436. [CrossRef]
25. Kreemer, C.; Blewitt, G. Robust estimation of spatially varying common-mode components in GPS time-series. *J. Geod.* **2021**, *95*, 1–19. [CrossRef]
26. Liu, B.; King, M.; Dai, W. Common mode error in Antarctic GPS coordinate time-series on its effect on bedrock-uplift estimates. *Geophys. J. Int.* **2018**, *214*, 1652–1664. [CrossRef]
27. Zhou, M.; Guo, J.; Liu, X.; Shen, Y.; Zhao, C. Crustal movement derived by GNSS technique considering common mode error with MSSA. *Adv. Space Res.* **2020**, *66*, 1819–1828. [CrossRef]
28. Pan, Y.; Chen, R.; Ding, H.; Xu, X.; Zheng, G.; Shen, W.; Xiao, Y.; Li, S. Common Mode Component and Its Potential Effect on GPS-Inferred Three-Dimensional Crustal Deformations in the Eastern Tibetan Plateau. *Remote. Sens.* **2019**, *11*, 1975. [CrossRef]
29. Yan, J.; Dong, D.; Burgmann, R.; Materna, K.; Tan, W.; Peng, Y.; Chen, J. Separation of Sources of Seasonal Uplift in China Using Independent Component Analysis of GNSS Time Series. *J. Geophys. Res. Solid Earth* **2019**, *124*, 11951–11971. [CrossRef]
30. Gualandi, A.; Serpelloni, E.; Belardinelli, M.E. Blind source separation problem in GPS time series. *J. Geod.* **2016**, *90*, 323–341. [CrossRef]
31. Gualandi, A.; Avouac, J.P.; Galetzka, J.; Genrich, J.F.; Blewitt, G.; Adhikari, L.B.; Koirala, B.P.; Gupta, R.; Upreti, B.N.; Pratt-Sitaula, B.J.T. Pre-and post-seismic deformation related to the 2015, Mw7. 8 Gorkha earthquake, Nepal. *Tectonophysics* **2017**, *714*, 90–106. [CrossRef]
32. Bian, Y.; Yue, J.; Ferreira, V.G.; Cong, K.; Cai, D. Common Mode Component and Its Potential Effect on GPS-Inferred Crustal Deformations in Greenland. *Pure. Appl. Geophys.* **2021**, *178*, 1805–1823. [CrossRef]
33. Deng, L.; Chen, H.; Ren, J.; Liao, Y. Long-term and seasonal displacements inferred from the regional GPS coordinate time series: Case study in Central China Hefei City. *Earth Sci. Inform.* **2020**, *13*, 71–81. [CrossRef]
34. An, J.; Zhang, B.; Ai, S.; Wang, Z.; Feng, Y. Evaluation of vertical crustal movements and sea level changes around Greenland from GPS and tide gauge observations. *Acta Oceanol. Sin.* **2021**, *40*, 4–12. [CrossRef]
35. Zhang, T.; Shen, W.; Pan, Y.; Luan, W. Study of seasonal and long-term vertical deformation in Nepal based on GPS and GRACE observations. *Adv. Space Res.* **2018**, *61*, 1005–1016. [CrossRef]
36. Ma, C.; Li, F.; Zhang, S.; Lei, J.; Dong-Chen, E.; Hao, W.; Zhang, Q. The coordinate time series analysis of continuous GPS stations in the Antarctic Peninsula with consideration of common mode error. *Chin. J. Geophys.* **2016**, *59*, 2783–2795.
37. Zhang, K.; Wang, Y.; Gan, W.; Liang, S. Impacts of Local Effects and Surface Loads on the Common Mode Error Filtering in Continuous GPS Measurements in the Northwest of Yunnan Province, China. *Sensors* **2020**, *20*, 5408. [CrossRef]
38. Ming, F.; Yang, Y.; Zeng, A.; Zhao, B. Spatiotemporal filtering for regional GPS network in China using independent component analysis. *J. Geod.* **2017**, *91*, 419–440. [CrossRef]
39. Kumar, U.; Chao, B.F.; Chang, E.T.Y. What Causes the Common-Mode Error in Array GPS Displacement Fields: Case Study for Taiwan in Relation to Atmospheric Mass Loading. *Earth Space Sci.* **2020**, *7*, e2020EA001159. [CrossRef]
40. Yu, S.; Chen, H.; Kuo, L. Velocity field of GPS stations in the Taiwan area. *Tectonophysics* **1997**, *274*, 41–59. [CrossRef]
41. Yu, S.; Hsu, Y.; Kuo, L.; Chen, H.; Liu, C. GPS measurement of postseismic deformation following the 1999 Chi-Chi, Taiwan, earthquake. *J. Geophys. Res.* **2003**, *108*, 2520–2539. [CrossRef]
42. Yi-Ben, T. Seismotectonics of Taiwan. *Tectonophysics* **1986**, *125*, 17–37. [CrossRef]
43. Comon, P. Independent component analysis, a new concept? *Signal. Process.* **1994**, *36*, 287–314. [CrossRef]
44. Comon, P.; Jutten, C.; Herault, J. Blind separation of sources, Part II: Problems statement. *Signal. Process.* **1991**, *24*, 11–20. [CrossRef]
45. Herault, J.; Jutten, C. Space or time adaptive signal processing by neural network models. *Am. Inst. Phys.* **1986**, *151*, 206–211.

46. Jutten, C.; Herault, J. Blind separation of sources, part I: An adaptive algorithm based on neuromimetic architecture. *Signal. Process.* **1991**, *24*, 1–10. [CrossRef]
47. Gazeaux, J.; Williams, S.; King, M.; Bos, M.; Dach, R.; Deo, M.; Moore, A.; Ostini, L.; Petrie, E.; Roggero, M.; et al. Detecting offsets in GPS time series: First results from the detection of offsets in GPS experiment. *J. Geophys. Res. Solid Earth* **2013**, *118*, 2397–2407. [CrossRef]
48. Wang, W.; Qiao, X.; Wang, D.; Chen, Z.; Yu, P.; Lin, M.; Chen, W. Spatiotemporal noise in GPS position time-series from Crustal Movement Observation Network of China. *Geophys. J. Int.* **2019**, *216*, 1560–1577. [CrossRef]
49. Wang, F.; Zhang, P.; Sun, Z.; Zhang, Q.; Liu, J. Analysis the Influence of Modulated Amplitude on Common Mode Error Based on GPS Data. *ISPRS-Int. Arch. Photogramm. Remote. Sesing Spat. Inf. Sci.* **2021**, *43*, 153–158. [CrossRef]
50. Zhu, Z.; Zhou, X.; Liu, J. Noise analysis of common mode error in CMONOC GPS coordinate time series. In Proceedings of the 2017 Forum on Cooperative Positioning and Service (CPGPS), Harbin, China, 19–21 May 2017; IEEE: Piscataway, NJ, USA, 2017; pp. 190–193.
51. Klos, A.; Olivares, G.; Teferle, F.N.; Hunegnaw, A.; Bogusz, J. On the combined effect of periodic signals and colored noise on velocity uncertainties. *Gps Solut.* **2017**, *22*, 1–13. [CrossRef]
52. Jiang, W.; Ma, J.; Li, Z.; Zhou, X.; Zhou, B. Effect of removing the common mode errors on linear regression analysis of noise amplitudes in position time series of a regional GPS network & a case study of GPS stations in Southern California. *Adv. Space Res.* **2018**, *61*, 2521–2530.
53. He, X.; Bos, M.S.; Montillet, J.P.; Fernandes, R.M.S. Investigation of the noise properties at low frequencies in long GNSS time series. *J. Geod.* **2019**, *93*, 1271–1282. [CrossRef]
54. Santamaría-Gómez, A.; Ray, J. Chameleonic Noise in GPS Position Time Series. *J. Geophys. Res. Solid Earth* **2021**, *126*, e2020JB019541. [CrossRef]
55. Dong, D.; Chen, J.; Wang, J. *The GNSS High. Precision Positioning Principle*; Science Press: Beijing, China, 2018; pp. 253–260.
56. Hyvärinen, A. Fast and robust fixed-point algorithms for independent component analysis. *IEEE Trans. Neural Netw.* **1999**, *10*, 626–634. [CrossRef] [PubMed]
57. Hyvärinen, A.; Oja, E. A fast fixed-point algorithm for independent component analysis. *Neural Comput.* **1997**, *9*, 1483–1492. [CrossRef]
58. Bell, A.; Sejnowski, T. An information-maximization approach to blind separation and blind deconvolution. *Neural Comput.* **1995**, *7*, 1129–1159. [CrossRef]
59. Yang, F.; Hong, B. *Theory and Application of Independent Component Analysis*; Tsinghua University Press: Beijing, China, 2006.
60. Hyvärinen, A.; Oja, E. Independent component analysis: Algorithms and applications. *Neural Comput.* **2000**, *13*, 411–430. [CrossRef]
61. Barnie, T.; Oppenheimer, C. Extracting high temperature event radiance from satellite images and correcting for saturation using independent component analysis. *Remote. Sens. Env.* **2015**, *158*, 56–68. [CrossRef]
62. Milliner, C.; Materna, K.; Burgmann, R.; Fu, Y.; Moore, A.; Bekaert, D.; Adhikari, S.; Argus, D. Tracking the weight of Hurricane Harvey's stormwater using GPS data. *Sci. Adv.* **2018**, *4*, eaau2477. [CrossRef]
63. Hsu, Y.; Lai, Y.; You, R.; Chen, H.; Teng, L.; Tsai, Y.; Tang, C.; Su, H. Detecting rock uplift across southern Taiwan mountain belt by integrated GPS and leveling data. *Tectonophysics* **2018**, *744*, 275–284. [CrossRef]
64. Hu, J.; Chu, H.; Hou, C.; Lai, T.; Chen, R.; Nien, P. The contribution to tectonic subsidence by groundwater abstraction in the Pingtung area, southwestern Taiwan as determined by GPS measurements. *Quat. Int.* **2006**, *147*, 62–69. [CrossRef]
65. Dobslaw, H.; Bergmann-Wolf, I.; Dill, R.; Poropat, L.; Thomas, M.; Dahle, C.; Esselborn, S.; Koenig, R.; Flechtner, F. A new high-resolution model of non-tidal atmosphere and ocean mass variability for de-aliasing of satellite gravity observations: AOD1B RL06. *Geophys. J. Int.* **2017**, *211*, 263–269. [CrossRef]
66. Petrov, L. The International Mass Loading Service. In *REFAG 2014*; Springer: Cham, Switzerland, 2015; pp. 79–83.
67. Petrov, L.; Boy, J. Study of the atmospheric pressure loading signal in very long baseline interferometry observations. *J. Geophys. Res.* **2004**, *109*, 409. [CrossRef]
68. Rienecker, M.; Suarez, M.; Todling, R.; Bacmeister, J.; Takacs, L.; Liu, H.; Gu, W.; Sienkiewicz, M.; Koster, R.; Gelaro, R. *The GEOS-5 Data Assimilation System: Documentation of Versions 5.0. 1, 5.1. 0, and 5.2. 0*; Technical Report Series on Global Modeling and Data Assimilation Volume 27; NASA: Washington, DC, USA, December 2008.
69. Bos, M.; Fernandes, R.; Williams, S.; Bastos, L. Fast error analysis of continuous GNSS observations with missing data. *J. Geod.* **2013**, *87*, 351–360. [CrossRef]
70. Rao, R. Noise in GPS coordinate time series II. Compilation by the Central Weather Bureau of the Ministry of Communications. 2014; Volume 64, pp. 281–327. Available online: https://scweb.cwb.gov.tw/Uploads/Reports/MOTC-CWB-103-E-04.pdf (accessed on 2 August 2021). (In Chinese)

remote sensing

MDPI

Article

Improving the iGNSS-R Ocean Altimetric Precision Based on the Coherent Integration Time Optimization Model

Xuezhi Sun [1,†], Wei Zheng [1,2,*,†], Fan Wu [1,†] and Zongqiang Liu [1,3]

[1] Qian Xuesen Laboratory of Space Technology, China Academy of Space Technology, Beijing 100094, China; sunxuezhi@qxslab.cn (X.S.); wufan@qxslab.cn (F.W.); bestlzq@nuaa.edu.cn (Z.L.)
[2] School of Geomatics, Liaoning Technical University, Fuxin 123000, China
[3] School of Astronautics, Nanjing University of Aeronautics and Astronautics, Nanjing 210016, China
* Correspondence: zhengwei1@qxslab.cn; Tel.: +86-010-6811-1077
† Those authors contributed equally to this paper.

Abstract: Improving the altimetric precision under the requirement of ensuring the along-track resolution is of great significance to the application of iGNSS-R satellite ocean altimetry. The results obtained by using the empirical integration time need to be improved. Optimizing the integration time can suppress the noise interference from different sources to the greatest extent, thereby improving the altimetric precision. The inverse relationship between along-track resolution and signal integration time leads to the latter not being infinite. To obtain the optimal combination of integral parameters, this study first constructs an analytical model whose precision varies with coherent integration time. Second, the model is verified using airborne experimental data. The result shows that the average deviation between the model and the measured precision is about 0.16 m. The two are consistent. Third, we apply the model to obtain the optimal coherent integration time of the airborne experimental scenario. Compared with the empirical coherent integration parameters, the measured precision is improved by about 0.1 m. Fourth, the verified model is extrapolated to different spaceborne scenarios. Then, the optimal coherent integration time and the improvement of measured precision under various conditions are estimated. It was found that the optimal coherent integration time of the spaceborne scene is shorter than that of the airborne scene. Depending on the orbital altitude and the roughness of the sea surface, its value may also vary. Moreover, the model can significantly improve the precision for low signal-to-noise ratios. The coherent integration time optimization model proposed in this paper can enhance the altimetric precision. It would provide theoretical support for the signal optimization processing and sea surface height retrieval of iGNSS-R altimetry satellites with high precision and high along-track resolution in the future.

Keywords: coherent integration time optimization model; global navigation satellite systems reflectometry (GNSS-R); ocean altimetry precision; waveform correlation; signal optimization processing

Citation: Sun, X.; Zheng, W.; Wu, F.; Liu, Z. Improving the iGNSS-R Ocean Altimetric Precision Based on the Coherent Integration Time Optimization Model. *Remote Sens.* **2021**, *13*, 4715. https://doi.org/10.3390/rs13224715

Academic Editors: Shuanggen Jin and Gino Dardanelli

Received: 19 October 2021
Accepted: 17 November 2021
Published: 22 November 2021

1. Introduction

Accurately measured sea surface height (SSH) is one of the critical parameters of marine ecosystem monitoring, which is of paramount significance to applications such as fishery, oil drilling, and commercial navigation. Global navigation satellite systems reflectometry (GNSS-R) or the passive reflection and interference system (PARIS) can perform ocean altimetry as a passive remote sensing technique [1]. It has some unique advantages compared with the traditional tide gauge station and monostatic radar ocean altimetry. On the one hand, the receiver can capture multiple global navigation satellite system (GNSS) signals simultaneously, which increases the spatial coverage. On the other hand, as a novel bistatic passive remote sensing method, it has the characteristics of low cost, low power consumption, all-weather and high time revisit rate, which can make up for the shortcomings of the existing technology to a large extent. Since the technology

was proposed, ground-based, air-based, and space-based altimetry experiments have been conducted successively to verify its feasibility [2–4].

Some signal processing techniques for GNSS-R ocean altimetry have been proposed. Conventionally, GNSS-R altimetry involves cross-correlating the reflected signals with the local replicas of the open navigation signals (cGNSS-R) [5]. The encrypted signal (e.g., P(Y)) has a broader bandwidth, which will bring a sharper autocorrelation function (ACF) and a higher range precision. With it, the reconstructed code GNSS-R (r-GNSS-R) altimetry improves the precision by reproducing the encrypted signals [6]. The interferometric altimetry (iGNSS-R) utilizes the full composite components of the direct signal to correlate with the reflected signal [5]. The partial interferometric GNSS-R (piGNSS-R) altimetry extracts a portion of the encrypted signal from the full composite components to obtain a sharper ACF, which is an extension of iGNSS-R [7]. Nevertheless, in the case of iGNSS-R and piGNSS-R, the loss of signal-to-noise ratio (SNR) caused by dual-channel noise is more severe than that of cGNSS-R, which leads to a two-fold improvement in precision only [8]. The SNR should be improved by increasing the signal processing time, as this will diminish the influence of thermal noise and speckle noise on altimetric precision [9]. However, a longer integration time corresponds to a longer specular point (SP) movement distance. Considering the moving speed of the sub-satellite point (km/s) and the size of the spatial footprint (~10 km), the actual inverted single height represents the average over the larger sea area which further reduces the along-track resolution [10]. The previous study has shown that in the spaceborne iGNSS-R altimetry scenario, in order to achieve an altimetric precision better than 20 cm, the signal processing time required for a single height retrieval is approximately 10 s, and the along-track spatial resolution is about 65 km [8]. If the iGNSS-R ocean altimetry with high precision and high along-track spatial resolution can be realized, it would provide critical data and information resources for small and medium scale ocean phenomena monitoring, high temporal and spatial resolution ocean gravity field model establishment, and other earth science research.

One of the data products of GNSS-R observation is the delay-Doppler maps (DDM). Fernando et al. detailed the corresponding relationship between the DDM and its spatial location [11]. The waveform corresponding to zero Doppler is extracted from the calibrated DDM waveform for GNSS-R code-delay altimetry, and the delay information of the reflected signal is extracted from this waveform. Commonly used retrieval algorithms include the peak point of the first derivative (DER), the peak of the waveform (MAX), and the half-power point (HALF) [8,12,13]. Obtaining the inversion delay requires correction of numerous parameters including the receiver and transmitter orbits, ionospheric errors, tropospheric errors, and antenna baseline offsets [14]. For the evaluation of the altimetry performance, Li et al. considered both the altimetric precision and the altimetric accuracy. Altimetric accuracy is primarily affected by systematic errors. The altimetric precision is mainly induced by the randomness of the received signal caused by thermal noise and speckle noise. Theoretically, the higher the SNR of the signal, the more accurate the SP delay information extracted from the waveform, and the better the altimetric precision [15].

It is possible to increase the altimetric precision by optimizing the payload and signal post-processing. Payload optimization includes increasing antenna gain, refining antenna pointing and receiver bandwidth, etc. [16,17]. For signal post-processing, one method to improve the altimetric precision is to increase the signal's coherent integration time and incoherent average number. Both methods inhibit the noise introduced in different ways. The former is to suppress the thermal noise introduced at the receiver end, while the latter is to suppress the speckle noise introduced in the glistening area near the SP. The total integration time of signal processing is the product of the coherent integration time and incoherent average number. In theory, high precision requires an increased integration time. Despite this, the inverse relationship between the along-track resolution and the integration time prevents the latter from increasing indefinitely. It is typically necessary to sacrifice a certain degree of precision when performing altimetry tasks requiring high spatial resolution along the orbit. To achieve an optimal altimetric precision for a given

spatial resolution along track, it is necessary to optimize the combination of coherent and incoherent parameters. Accordingly, Martin-Neira et al. derived an altimetric precision prediction model with coherent integration time as a variable [18], but this model overlooked the influence of the correlation between the waveforms. You et al. constructed a waveform correlation model from the time domain and frequency domain to predict the upper limit of the waveform coherence time [19,20]. Li et al., reconstructed the altimetric precision model by considering the correlation of the waveforms which had reasonable consistency with the measured results [21], but the influence of the coherent integration time on the precision was not discussed in detail. Currently, traditional intermediate frequency (IF) data processing uses empirical parameters to approximate an optimal precision. The coherent integration time normally takes 10 ms in airborne scenarios [21] and 1 ms in spaceborne scenarios [22]. However, the actual optimal coherent integration processing depends on factors such as the position and relative motion of the transmitter and receiver. This needs to be estimated through accurate modelling.

Different from previous studies, in order to improve the precision of iGNSS-R ocean altimetry, this study constructs a coherent integration time optimization model by deducing the conversion relationship among coherent integration time, waveform correlation, and altimetric precision. Furthermore, the model can more accurately estimate the variation of precision with coherent integration time in different iGNSS-R altimetry applications so as to optimize the final precision result.

2. Signal Processing and Height Inversion

In order to examine the accuracy of the coherent integration optimization model, we use the data obtained by the Institute for Space Studies of Catalonia (IEEC) through an airborne experiment on the Baltic Sea on the 3 December 2015, for verification. The delay difference between direct and reflected signals is calculated using interference processing. The raw IF datasets are processed on the ground with the software receiver, including data acquisition, processing, height retrieval, and precision calculation.

The aircraft's altitude was about 3 km during the experiment, and the velocity was about 50 m/s. The direct and reflected signals are captured by the 8-element phased array antennas of RHCP (right-handed circular polarization) and LHCP (left HCP) respectively. The radiofrequency (RF) signals received by the antenna elements are filtered, amplified, and down-converted into IF signals. The IF signals are quantized by a comparator, and the quantized signals are connected to a field-programmable gate array (FPGA) through D-type flip-flops whose parallel processing capability is used for sampling. Analogue signals received by an element are quantized into one-bit in-phase components and one-bit quadrature components per sample. The sampling frequency is 80 MHz. Finally, the sampled digital signal is transmitted into the ground receiving station through the PCIe bus [23]. The acquired data is processed by a software-defined receiver. A simplified diagram of data processing and altimetry retrieval is depicted in Figure 1.

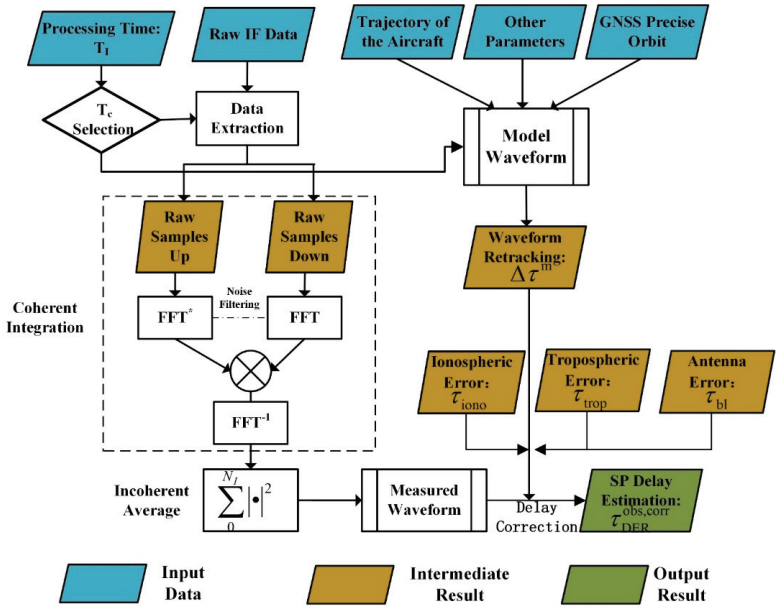

Figure 1. Simplified flowchart of airborne IF data processing.

2.1. Signal Processing

2.1.1. Data Fetch

The IF data is read in 4 bytes at a time, which correspond to the in-phase and quadrature components of the 16 antenna elements sampled at a time. The binary data is converted from 0, 1 code to 1, −1 code. That means the logic level is converted to a polarity non-return-to-zero level. The direct signal and the reflected signal sampled each time can be expressed as [24]:

$$\begin{aligned} S_{\mathrm{up}}^{nT_c}(k) &= \sum_{i=1}^{8} s_{i,\mathrm{up\_I}}(k) + j\sum_{i=1}^{8} s_{i,\mathrm{up\_Q}}(k) \\ S_{\mathrm{down}}^{nT_c}(k) &= \sum_{i=9}^{16} s_{i,\mathrm{down\_I}}(k) + j\sum_{i=9}^{16} s_{i,\mathrm{down\_Q}}(k) \end{aligned} \tag{1}$$

where $S_{\mathrm{up}}^{nT_c}(k)$ and $S_{\mathrm{down}}^{nT_c}(k)$ are the amplitudes of the kth sample of the direct signal and the reflected signal during the nth coherent integration, s is the signal component of each antenna element, i is the antenna element number, up_I and up_Q respectively represent the in-phase and quadrature components of the zenith pointing antenna, and down_I and down_Q denote the in-phase and quadrature components of the nadir pointing antenna respectively.

2.1.2. Coherent Integration

The coherent integration time is set to T_c and the sampling frequency f_s is 80 MHz. In this case, $f_s \times T_c$ samples constitute the sequence of each coherent integration, which is expressed as $S_{\mathrm{up}}^{nT_c}[K] = [S_{\mathrm{up}}^{nT_c}(1), S_{\mathrm{up}}^{nT_c}(2) \ldots S_{\mathrm{up}}^{nT_c}(f_s \times T_c)]$. Removing single-frequency interference is essential before coherent integration can be performed to prevent it from influencing the measurement result. Through fast Fourier transform (FFT), the time domain signal $S_{\mathrm{up}}^{nT_c}[K]$ and $S_{\mathrm{down}}^{nT_c}[K]$ are transformed into the frequency domain $S_{\mathrm{up}}^{nT_c}[f]$ and $S_{\mathrm{down}}^{nT_c}[f]$, and the amplitude anomalies in the frequency spectrum are identified and filtered out. The filtered direct signal and the reflected signal are cross-correlated in the frequency domain to obtain the complex waveform $y(nT_c, \tau) = F^{-1}(S_{\mathrm{up}}^{*nT_c}[f] \times S_{\mathrm{down}}^{nT_c}[f])$. It should

be declared that the phased array antenna is used in this experiment, and beamforming is usually employed to improve the SNR in the signal post-processing. However, the effect of beamforming may submerge the influence of the coherent integration time on the SNR of power waveforms. To reveal the role of coherent integration time, this research abandons beamforming.

2.1.3. Retracking and Incoherent Average

The complex waveforms after coherent integration need to be incoherently averaged to degrade the influence of speckle noise. With the vertical drift of the aircraft during this period, the waveform series need to be compensated with respect to the first one (retracking) [25]. Figure 2A shows a power waveform obtained after incoherent averaging.

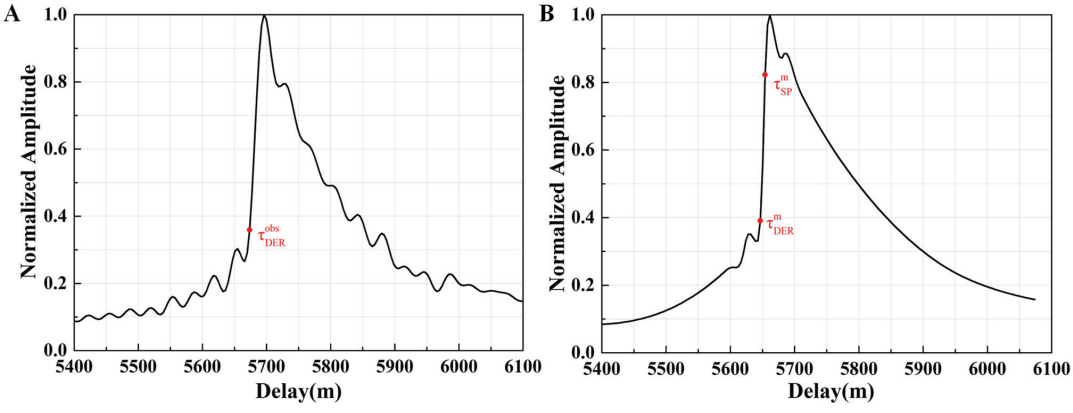

Figure 2. Examples of measured and simulated power waveforms. (**A**) Normalized measured power waveform processed from the IF data. The τ_{DER}^{obs} is the maximum point of the first derivative. (**B**) Normalized simulated power waveform generated based on the Z-V model. The τ_{DER}^{m} is the maximum point of the first derivative. The τ_{sp}^{m} is the nominal SP calculated based on the WGS-84 reference ellipsoid.

2.2. Height Inversion

2.2.1. Delay Estimation and Error Correction

The delay of the reflected signal through the SP can be estimated from the power waveform. The delay estimation can be divided into two types: fixed-point tracking and model fitting. Fixed-point tracking involves tracking a given point of the waveform, such as DER, MAX, and HALF. The DER delay estimation is applied in this study, which can be expressed as [15]:

$$\tau_{DER}^{obs,corr} = \tau_{DER}^{obs} + (\tau_{sp}^{m} - \tau_{DER}^{m}) \quad (2)$$

where τ_{DER}^{obs} is the delay corresponding to the maximum of the measured waveform's first derivative (Figure 2A), and τ_{sp}^{m} and τ_{DER}^{m} correspond to the nominal SP delay and the maximum of the simulated waveform's first derivative. The nominal SP τ_{sp}^{m} is the minimum of the reflection path calculated from the WGS-84 reference coordinate when the positions of the transmitter and the receiver are known. The simulated waveform (Figure 2B) is generated according to the Zavorotny and Voronovich (Z-V) model, which takes into account the influence of geometry, instrument configuration, and ocean state [26]. The difference between τ_{sp}^{m} and τ_{DER}^{m} obtained from the simulated waveform is used as the deviation correction for DER tracking.

The estimated bistatic delay information of the SP also needs error correction, including tropospheric error ρ_{trop}, ionospheric error ρ_{iono}, and antenna baseline error ρ_{bl} [12,14]. As the ionosphere is located above 60 km, both direct and reflected signals received by the airborne platform go through the same data path for downlink transmission, so the

delay deviation can be ignored. The tropospheric error correction is derived from the Saastamoinen model [21]:

$$\rho_{\text{trop}} = \frac{4.6}{\sin e}\left(1 - e^{-H_{\text{R}}/H_{\text{trop}}}\right) \tag{3}$$

where e is the satellite elevation angle, H_{R} is the receiver height, and H_{trop} is the average tropospheric height. The antenna baseline offset is calculated from the path difference between the zenith pointing antenna and the nadir pointing antenna relative to the SP under the known airborne position and attitude information. The corrected SP delay can be converted to the actual height from the receiver to the sea surface [15].

$$H_e^{\text{obs}} = \frac{\tau_{\text{DER}}^{\text{obs,corr}} - (p_{\text{iono}} + p_{\text{trop}} + p_{\text{bl}})}{2 \times \sin(e)} \tag{4}$$

2.2.2. Height Retrieval and Precision Calculation

After delay estimation and error correction, the vertical distance from the sea surface to the reference ellipsoid can be computed as:

$$\text{SSH} = H_e^{\text{obs}} - H_e^{\text{m}} = H_e^{\text{obs}} - \frac{\tau_{\text{sp}}^{\text{m}}}{2 \times \sin(e)} \tag{5}$$

where H_e^{m} is the height of the aircraft on the WGS84 reference ellipsoid obtained by using bistatic geometry. A fitted piecewise linear function is subtracted from the measured SSH sequence to generate zero mean, near-white noise residuals. The precision is obtained by calculating the standard deviation of the SSH residuals for each trajectory.

$$\sigma_h^{\text{obs}}(T_c) = \sqrt{\left\langle \left| \text{SSH}_{\text{residual}}^{\text{k}} - \left\langle \text{SSH}_{\text{residual}}^{\text{k}} \right\rangle \right|^2 \right\rangle} \tag{6}$$

It is primarily due to the following considerations that linear fitting is used instead of the geoid model. The altimetry precision is affected by zero-mean random error, which is mainly due to the random nature of the received signals caused by thermal noise and speckle noise. The SSH residual after subtracting the linear fit can be used to evaluate randomness. In contrast, precision will be affected by the errors in the geoid model [27].

3. Construction of Coherent Integration Time Optimization Model

The altimetric precision is related to the power uncertainty of the incoherent average waveform at the SP. The uncertainty value of the incoherent average waveform will be affected by the correlation between the waveforms. To more accurately reflect the variation of precision with the coherent integration time, the waveform correlation is considered in the precision prediction model. Since the correlation between the waveforms varies with the coherent integration parameters, variable conversion is performed on the reconstructed precision model to obtain the coherent integration time optimization model whose precision varies with the coherent integration time in this section.

3.1. The Reconstruction of Altimetric Precision Model

According to [18], the estimated altimetric precision can be converted by the uncertainty of the incoherent average power waveform at SP.

$$\sigma_h^{\text{m}}(\tau) = \frac{c}{2 \times \cos(i)} \frac{\sigma_Z(\tau)}{\overline{Z}'(\tau)} = \frac{1}{2 \times \cos(i)} \frac{1}{S_h(\tau)} \frac{\sigma_Z(\tau)}{\overline{Z}(\tau)} \tag{7}$$

where i is the incident angle, c is the speed of light in vacuum, $\overline{Z}(\tau) = \langle Z(t,\tau) \rangle$ is the average of the power waveform, and the derivative of which corresponds to $\overline{Z}'(\tau)$. $S_h = \overline{Z}'(\tau)/c\overline{Z}(\tau)$ indicates the logarithmic derivative of the power waveform at SP which

is defined as the altimetric sensitivity. $\sigma_Z(\tau)/\overline{Z}(\tau)$ is the ratio of the standard deviation to power amplitude which is defined as the effective independent incoherent average number [21]. Since $\sigma_Z(\tau)$ depends on the correlation between the waveforms, the ratio is derived analytically in this section.

As introduced in Section 2, the complex waveform after coherent integration of direct and reflected signals can be represented by a discrete array $y(nT_c, \tau)$:

$$y(nT_c, \tau) = [y(nT_c, \tau_1), y(nT_c, \tau_2) \ldots\ldots y(nT_c, \tau_n)] \tag{8}$$

where nT_c is the nth coherent integration process, T_c is the coherent integration time which is usually in milliseconds, and τ_n is the code delay whose resolution is inversely proportional to the signal sampling rate. The square of each complex waveform results in a one-shot power waveform expressed as [21]:

$$z(nT_c, \tau) = y(nT_c, \tau)y^*(nT_c, \tau) \tag{9}$$

In the case of an incoherent average of N_I one-shot power waveforms, the power waveform can be expressed as:

$$Z(\tau) = \frac{1}{N_\mathrm{I}} \sum_{n=0}^{N_\mathrm{I}-1} z(nT_c, \tau) = \langle z(nT_c, \tau) \rangle \tag{10}$$

where $\langle\rangle$ stands for the ensemble average. A power waveform is usually processed in seconds, which can be expressed as:

$$T_\mathrm{I} = T_c \times N_\mathrm{I} \tag{11}$$

Due to the relative motion of the transmitter and the receiver, the correlation between two complex waveforms separated by $\widetilde{n}T_c$ in time is determined by the coherence of the signals from two ocean contribution areas. These regions are elliptical, and the length of the semi-axis is related to τ_n. The correlation between complex waveforms is defined as [19]:

$$C_y(\widetilde{n}T_c, \tau) = \langle y(nT_c, \tau)y^*(nT_c + \widetilde{n}T_c, \tau) \rangle \tag{12}$$

where $\widetilde{n}T_c$ is the time interval between complex waveforms. The spatial geometry of correlation function is illustrated in Figure 3. It can be seen that the correlation between the two sea surface scattering signals gradually decreases as $\widetilde{n}T_c$ increases. An analogous correlation between one-shot power waveforms can also be derived as:

$$C_z(\widetilde{n}T_c, \tau) = \langle [z(nT_c, \tau) - \langle z(nT_c, \tau) \rangle][z(nT_c + \widetilde{n}T_c, \tau) - \langle z(nT_c + \widetilde{n}T_c, \tau) \rangle] \rangle \tag{13}$$

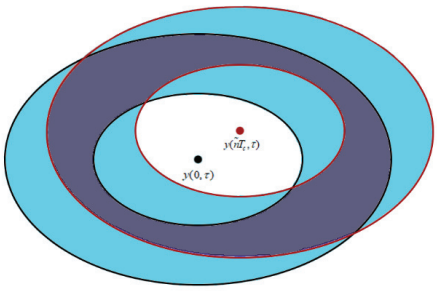

Figure 3. Sea surface contribution area corresponding to $\langle y(nT_c, \tau)y^*(nT_c + \widetilde{n}T_c, \tau) \rangle$.

The correlation time of the signal is usually measured in milliseconds, while the time of incoherent averaging can reach the order of seconds. Thus, it can be assumed that there

is no correlation between the incoherent average power waveforms, i.e., $C_Z(\widetilde{t},\tau) = 0\widetilde{t} \neq 0$. The variance of the power waveform can be expressed as [21]:

$$\sigma_Z^2(\tau) = C_Z(0,\tau) = \left\langle \left[Z(t,\tau) - \langle Z(t,\tau) \rangle \right]^2 \right\rangle \tag{14}$$

The effective incoherent average number can be reconstructed following Appendix A as [21]:

$$\frac{1}{N_{\text{eff}}} = \frac{\sigma_Z^2(\tau)}{\overline{Z}^2(\tau)} = \frac{\frac{1}{N_{\text{I}}} \sum_{\widetilde{n}=-(N_{\text{I}}-1)}^{N_I-1} \left| C_y(\widetilde{n}T_c,\tau) \right|^2}{\left| C_y(0,\tau) \right|^2} \tag{15}$$

3.2. The Relationship between Model Parameters and Coherent Integration Time

As discussed in Section 3.1, the altimetric precision is determined mainly by two parameters, S_h and N_{eff}. In this section, the variables of these two parameters are derived to be expressed in terms of coherent integration time. The re-derived parameters are brought into Equation (7) to construct the coherent integration time optimization model.

3.2.1. Altimetric Sensitivity

As discussed in [28], the complex waveform is composed of useful signal and noise components

$$y(nT_c,\tau) = y_{\text{s}}(nT_c,\tau) + y_{\text{nd}}(nT_c,\tau) + y_{\text{nr}}(nT_c,\tau) + y_{\text{ndr}}(nT_c,\tau) \tag{16}$$

where $y_{\text{s}}(t,\tau)$ is the cross-correlation value for the useful signal term, and $y_{\text{nd}}(t,\tau)$,$y_{\text{nr}}(t,\tau)$ and $y_{\text{ndr}}(t,\tau)$ are the cross-correlation values of the direct and reflected noise terms.

Assuming that the signal component has no correlation with the noise components, the power waveform can be expressed as [29]:

$$Z(\tau) = \left\langle \left| y_{\text{s}}(nT_c,\tau) \right|^2 \right\rangle + \left\langle \left| y_{\text{nr}}(nT_c,\tau) \right|^2 \right\rangle + \left\langle \left| y_{\text{nd}}(nT_c,\tau) \right|^2 \right\rangle + \left\langle \left| y_{\text{ndr}}(nT_c,\tau) \right|^2 \right\rangle \tag{17}$$

The components above can be interpreted as the expression for the coherent integration time [18,20]:

$$\begin{aligned}
&\left\langle \left| y_{\text{s}}(nT_{\text{c}},\tau) \right|^2 \right\rangle = 2P_{\text{d}} \iint \frac{2P_{\text{t}}G_{\text{r}}(\vec{p})\sigma_0}{4\pi R_{\text{t}}^2(\vec{p})R_{\text{r}}^2(\vec{p})} \times \Lambda^2(\Delta\tau) \times \text{sinc}^2(\Delta f T_{\text{c}}) d^2p \\
&\left\langle \left| y_{\text{nr}}(nT_{\text{c}},\tau) \right|^2 \right\rangle = \frac{2kT_{\text{rec_r}}}{T_c} 2P_{\text{d}} \\
&\left\langle \left| y_{\text{nd}}(nT_{\text{c}},\tau) \right|^2 \right\rangle = \frac{2kT_{\text{rec_d}}}{T_{\text{c}}} 2P_{\text{r}} \\
&\left\langle \left| y_{\text{ndr}}(nT_{\text{c}},\tau) \right|^2 \right\rangle = \frac{2kT_{\text{rec_r}}}{T_{\text{c}}} 2kT_{\text{rec_d}}B
\end{aligned} \tag{18}$$

where B represents the equivalent noise bandwidth of the receiver, $T_{\text{rec\_d}}$ and $T_{\text{rec\_r}}$ represent the equivalent input noise temperature of the up-looking and down-looking chains, P_{r} represents the total power of the reflected signal at the input of the correlator, P_{d} represents the total power of the direct signal at the input of the correlator, P_{t} represents the power of the transmitted signal, and G_{r} represents the antenna gain [30,31]. Based on Equations (17) and (18), the altimetric sensitivity can be represented by the coherent integration time [5].

3.2.2. Effective Incoherent Average Number

As discussed in Equation (15), the effective incoherent average at the SP is closely related to the waveform correlation [32]. Therefore, when the processing time of the incoherent average power waveform is T_{I}, the variation of N_{eff} with the coherent integration time can be approximated following Appendix B as:

$$\frac{1}{N_{\text{eff}}} = \frac{T_c \sum_{\tilde{n}=-(N_I-1)}^{N_I-1} \left(2P_d \iint \frac{2P_t G_r(\vec{p})\sigma_0}{4\pi R_t^2(\vec{p}) R_r^2(\vec{p})} \Lambda^2(\Delta\tau)\text{sinc}^2(\Delta f T_c) \exp^{-j2\pi\Delta f(\tilde{n}T_c)} d^2p + \frac{2P_d n_0^d}{T_c}\text{tri}(\frac{\tilde{n}T_c}{T_c}) + \frac{Bn_0^d n_0^u}{T_c}\text{tri}(\frac{\tilde{n}T_c}{T_c}) \right)}{T_I \left(2P_d \iint \frac{2P_t G_r(\vec{p})\sigma_0}{4\pi R_t^2(\vec{p}) R_r^2(\vec{p})} \Lambda^2(\Delta\tau)\text{sinc}^2(\Delta f T_c) d^2p + \frac{2P_d n_0^d}{T_c} + \frac{Bn_0^d n_0^u}{T_c} \right)} \quad (19)$$

where $n_0^d = 2kT_d$ and $n_0^u = 2kT_u$ are the power spectral density of thermal noise from the up-looking and down-looking chains respectively, tri() is the triangular function, $\Delta\tau$ is the difference between τ_n and the scattering point delay $\tau(\vec{p})$, and Δf is the difference between 0 Doppler and the scattering point Doppler $f(\vec{p})$.

Accordingly, the coherent integration time optimization model can be derived by simultaneously applying Equations (7) and (17)–(19). In accordance with Equation (17), a larger coherent integration time is needed to improve the altimetric sensitivity and precision. Nevertheless, the limitation of N_{eff} on the altimetric precision leads to a relatively smaller expected value of the coherent integration time. As a consequence, the best precision result is achieved by balancing the time required for the coherent integration of both aspects.

4. Results and Application

4.1. Validation of Coherent Integration Time Optimization Model

The proposed model precision results are compared with the experimental results to verify the effectiveness of the coherent integration time optimization model in this section. The measured precision is calculated as described in Section 2. With the power waveform processing time $T_I = 1$ s unchanged, the precision variation $\sigma_h^{\text{obs}}(T_c)$ with coherent integration time can be determined by varying the value of T_c. To avoid the error interference caused by aircraft turning, two straight flight trajectories are selected for precision calculations. Figure 4B illustrates the inverted SSH sequence when T_c is 10 ms during the experiment. The corresponding SSH residual sequence is shown in Figure 4C.

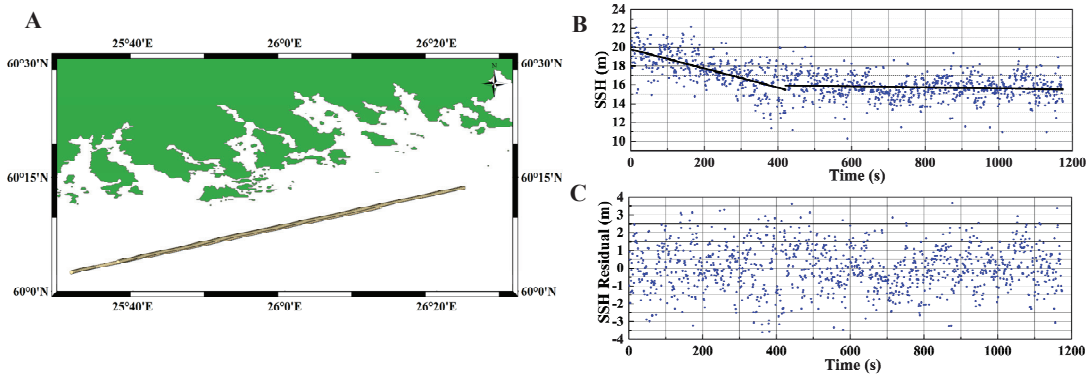

Figure 4. Experimental area and IF data processing results. (**A**) The specular points tracks of the raw IF data. (**B**) Measured SSH relative to the WGS84 reference ellipsoid. (**C**) SSH residual after subtracting the fitted value.

The coherent integration time optimization model has been acquired in the following steps as described in Section 3. Obtain auxiliary data during the experiment, including the position and velocity information of the receiver after dual-frequency orbit determination, the GPS satellite position and velocity using the IGS precision ephemeris interpolation method, wind speed (~7 m/s) and payload parameters. These simulation parameters are listed in Table 1. The elevation angle is computed with the bistatic geometry. The computation of the variations in the effective incoherent average number and altimeric sensitivity with coherent integration time can be obtained by applying Equations (17)–(19).

By substituting the intermediate results into Equation (7), the coherent integration time optimization model can be calculated.

Table 1. Air-based simulation parameters that are consistent with those for the experiment described in Section 2.

Design Parameter	Value
Receiver height	~3000 m
Transmitter altitude	20,200 km
Receiver velocity	50 m/s
Antenna temperature	200 K
Antenna gain	15 dBi
Elevation angle	70°
Processing interval	39,102–40,721
Power waveform processing time	1 s
Wind speed	7 m/s
Process method	iGNSS-R
Sampling frequency	80 MHz
Carrier frequency	1575.42 MHz (GPS L1)
Receiver bandwidth	35 MHz
Waveform retracking method	DER
Filter bandwidth	12 MHz

A comparison between the variance of the model and the measured result is shown in Figure 5. To evaluate the effectiveness of the model, the mean deviation of precision $\left\langle \left| \sigma_h^{\mathrm{m}}(T_c) - \sigma_h^{\mathrm{obs}}(T_c) \right| \right\rangle$ is used. $\sigma_h^{\mathrm{m}}(T_c)$ is the precision calculated by the model, whereas $\sigma_h^{\mathrm{obs}}(T_c)$ is the measured precision. The results show that the average deviation between the red and blue curves is 0.85 m, and the average deviation between the red and black curves is 0.16 m. Therefore, the proposed model considering the correlation of the waveforms is in good agreement with the measured result.

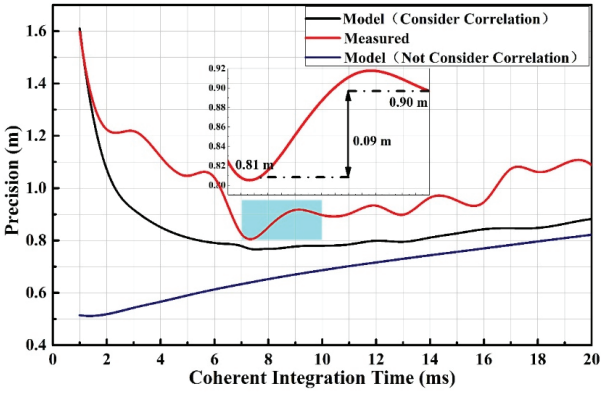

Figure 5. The variation of the precision with coherent integration time under different conditions. Red indicates the measured result. Black indicates the model result considering the correlation between the waveforms. Blue indicates the model result without considering the correlation between the waveforms.

The model curve and the measured curve differ by a certain amount. On the one hand, the measured precision result is generally worse than that of the model, with an average of 0.16 m. This may be due to the lack of beamforming in the signal processing, which causes the SNR to decrease. On the other hand, the trend of the measured curve fluctuates. As opposed to the simulated results, the actual measurement results may contain other stochastic factors such as aircraft mechanical vibrations, attitude changes,

and antenna pointing, etc. These random factors can be used to optimize the model by obtaining recorded data of aircraft attitude and vibration in the future.

4.1.1. Altimetric Sensitivity

The reciprocal of the altimetric sensitivity simulation is compared with the measured result, as shown in Figure 6. It can be appreciated that the measured and the simulated curves are in good agreement. As the coherent integration time increases, the reciprocal of the sensitivity approaches a limit value. The difference between the curves may be caused by unaccounted noises [33,34].

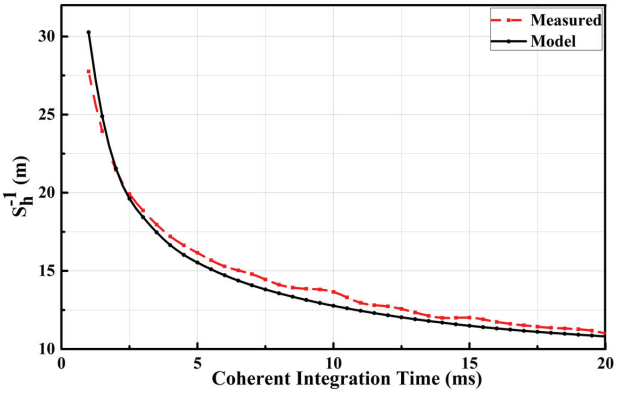

Figure 6. A comparison of the reciprocal value of altimetric sensitivity between measured (red) and simulated data (black).

4.1.2. Effective Incoherent Average Number

It can be seen from Equation (19) that the effective incoherent average is a nonlinear function of the coherent integration time. The variations of N_{I} and N_{eff} with the coherent integration time are compared, as shown in Figure 7. It reveals that when T_{I} is constant, N_{I} and T_c are inversely proportional. However, N_{eff} and T_c are non-linearly related. The difference between N_{eff} and N_{I} will gradually decrease as the coherent integration time increases. If there were no correlation between the waveforms i.e., $C_y(\widetilde{n}T_c, \tau) = 0, \widetilde{n} \neq 0$, then N_{eff} would be equal to N_{I}. N_{eff} also varies with the length delay $c\tau_n$ as shown in Figure 8. It is a hybrid effect of SNR and Doppler bandwidth at different delays [35].

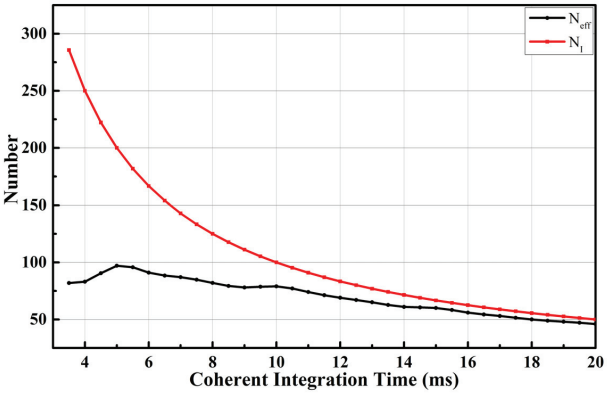

Figure 7. Comparison of the effective incoherent average number (black) and the incoherent average number (red).

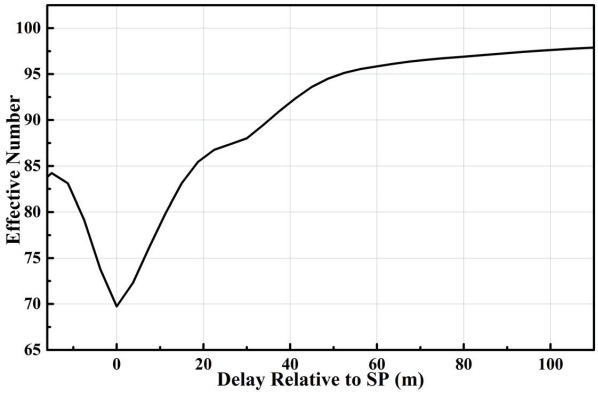

Figure 8. Effective incoherent average number relative to SP.

4.2. Application of Coherent Integration Time Optimization Model

The conformity between the model and the measured results indicates that the proposed model can better reflect the influence of coherent integration time on the altimetric precision. Consequently, the model can be used to determine the optimal coherent integration time to improve experimental data processing. In addition, the model can be applied to a variety of altimetry situations to provide a theoretical reference for data optimization processing.

4.2.1. Model Application: Airborne Experiment Scenario

In the airborne altimetry scene described in Section 4.1, the traditional integration parameters cannot yield the optimal precision. In constructing a coherent integration time optimization model based on the same experimental parameters, the optimal coherent integration time is calculated to be 7.5 ms, as shown in Figure 5. By applying this integral parameter to the processing of the measured data, the precision is 0.81 m. As compared to the empirical coherent integration (10 ms) [21], the altimetric precision is improved by 0.09 m.

4.2.2. Model Application: Extrapolation to Spaceborne Scenario

Given the reasonable levels of agreement between the simulated model and the airborne experimental data, the proposed coherent integration time optimization model has been implemented to simulate spaceborne iGNSS-R data. Since there is no dedicated iGNSS-R altimetry satellite at present, the results of model optimization can provide a theoretical reference for improving the in-orbit performance of an iGNSS-R-based ocean altimeter in the future. The altimetric precision is mainly determined by the system instrument parameters and observation geometry. These factors will lead to different model optimization results. According to the model's expression, the main parameters that affect the precision are respectively analyzed, including the receiver's orbital altitude, sea surface roughness, elevation angle, and antenna gain. Previously, these parameters were discussed, and this section re-evaluates them in light of the novel model [31,36]. It needs to be clarified that the Z-V model does not account for the influence of coherent scattering under low wind speed conditions; the minimum wind speed is set to 4 m/s to avoid errors caused by the simulation waveform. The fixed system parameters are summarized in Table 2. The dependence of the precision variation and the optimal coherent integration time on different parameters is analyzed as follows.

Table 2. The common simulation parameters for spaceborne altimetry scenarios.

Design Parameter	Value
Receiver bandwidth	35 MHz
Antenna temperature	200 K
Transmitter altitude	20,200 km
Process method	iGNSS-R
Sampling rate	80 MHz
Carrier frequency	1575.42 MHz (GPS L1)
Waveform retracking method	DER
Filter bandwidth	12 MHz
Power waveform processing time	1 s

As can be seen from Figure 9:

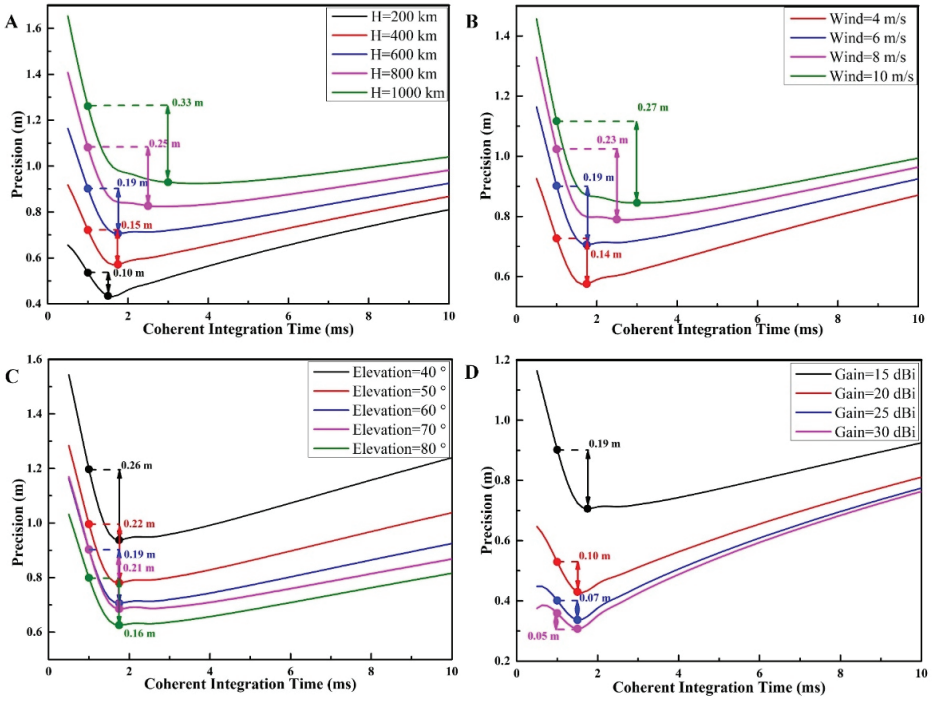

Figure 9. The simulation variation curves of the estimated altimetric precision with the coherent integration time under different conditions. (**A**) When the wind speed is 6 m/s, the elevation is 60°, the antenna gain is 15 dBi, and the orbit altitude varies. (**B**) When the orbit altitude is 600 km, the elevation is 60°, the antenna gain is 15 dBi, and the wind speed varies. (**C**) When the orbit altitude is 600 km, the wind speed is 6 m/s, the antenna gain is 15 dBi, and the elevation varies. (**D**) When the orbit altitude is 600 km, the wind speed is 6 m/s, the elevation is 60°, and the antenna gain varies.

(1) As shown in Figure 9A, the precision decreases with the altitude of the orbit. When the orbit altitude increases from 200 km to 1000 km, the optimal precision decreases from 0.43 m to 0.94 m. This is because, according to Equation (17), the signal power decreases squarely with the transmission distance, causing the SNR to decrease. On the other hand, the receiver velocity decreases with altitude, resulting in increased waveform correlation and decreased effective incoherent average.

As the orbital altitude increases, the optimal coherent integration time increases from 1.5 ms to 3 ms. Higher altitude results in greater energy loss, which calls for a longer time for coherent integration, which improves the SNR and therefore the altimetric sensitiv-

ity. The higher the orbital altitude of the receiver, the more noticeable the improvement in precision of the optimal coherent integration time when compared to the empirical spaceborne coherent integration parameters (1 ms). Therefore, the coherent integration time optimization model is preferred for improving the altimetric precision under the low SNR conditions.

(2) As shown in Figure 9B, the precision decreases with wind speed. With an increase in wind speed from 4 m/s to 10 m/s, the optimal precision decreases from 0.57 m to 0.85 m. At low wind speeds, the sea surface is smooth, the waveform coherence is strong, and the effective incoherent average is small. However, the SNR is high, which enhances precision.

The optimal coherent integration time will increase from 1.6 ms to 3 ms with wind speed. This is because high wind speed increases ocean scattering. Simultaneously, the higher the wind speed, the worse the SNR, and the greater the precision improved by the optimal coherent integration time.

(3) In Figure 9C, the optimal precision increases from 0.94 m to 0.63 m as the elevation angle changes from 40° to 80°. On the one hand, increasing the elevation angle shortens the propagation path of the navigation signal, which reduces the signal energy loss. On the other hand, according to Figure 3, the iso-delay area decreases with the elevation angle, thereby increasing the effective incoherent average.

Since both the altimetric sensitivity and the effective incoherent average decrease with the elevation angle, the balance between the two leads to little change in the optimal coherent integration time. Accordingly, as the elevation angle increases, the SNR of the reflected signal upgrades and the improvement of the precision by the optimal coherent integration time becomes insignificant.

(4) As illustrated in Figure 9D, when the antenna gain is increased from 15 dBi to 30 dBi, the optimal precision improves from 0.72 m to 0.31 m. The high gain antenna can increase signal energy and upgrade the SNR. When the antenna gain is increased from 25 dBi to 30 dBi, the optimal precision is only improved from 0.34 m to 0.31 m. This indicates that an increase in antenna gain will not be sufficient to improve precision at high SNRs.

Similarly, the optimal coherent integration time does not greatly improve the precision in the case of high gain. Since the change of the antenna gain does not affect the effective incoherent average, the optimal coherent integration time does not change much with the antenna gain.

(5) In general, the optimal coherent integration time calculated in the spaceborne simulation is shorter than that for the airborne scenario. This is because the satellite receiver has a high velocity, making the Doppler bandwidth and the effective incoherent average large. The shorter coherent integration time can effectively reduce the influence of speckle noise.

The simulation analysis of the above parameters indicates that the coherent integration time optimization model improves the precision more significantly when the SNR of the reflected waveform is relatively weak. Limited by the code bandwidth, improving the SNR of the signal does not increase the precision infinitely but approaches the limit value. Additionally, the optimal coherent integration time varies with the simulation parameters, and the spaceborne scenario tends to be shorter than the airborne scenario. Increasing the altitude of the orbit and the wind speed will also increase the optimal coherent integration time.

5. Conclusions

This paper constructs a coherent integration time optimization model from the perspective of signal processing to improve iGNSS-R ocean altimetric precision. The research mainly involves three aspects: the processing of IF data and the extraction of precision information; the derivation and verification of the coherent integration time optimization model; and the application of the validated model to airborne and spaceborne altimetry mission scenarios to predict the optimal solution for precision.

(1) To estimate the SP delay for airborne data processing, we use the DER method. The altimetric precision is evaluated based on the random characteristics of the SSH. (2) For the purpose of optimizing the precision performance, we consider the influence of the correlation between waveforms on the covariance of the power waveform, and derive the coherent integration time optimization model from the statistical properties of the waveform. The model is verified by airborne measurements. Results indicate that the average deviation between model and measurement precisions is 0.16 m, which is acceptable. (3) Based on the optimal coherent integration time of the model solution, we processed the experimental data, and the precision is improved by about 0.1 m relative to that obtained using the empirical parameters. The positive validation of the coherent integration time optimization model provides a tool for evaluating the optimal coherent integration time and its precision under different orbital altitudes, sea surface roughness, elevation angles, and antenna gains in spaceborne iGNSS-R altimetry scenarios. The results show that the optimal coherent integration time for the spaceborne scene is shorter than that for the airborne scene. In the case of low SNR, the model can improve the precision to the decimeter level. Due to the combined effect of the SNR and the Doppler bandwidth, the optimal coherent integration time increases with the orbit altitude and the sea surface roughness.

The coherent integration time optimization model developed in this paper is capable of optimizing the waveform processing parameters and improving the altimetric precision. It can be applied to the optimization of data processing and high-precision retrieval for future spaceborne iGNSS-R altimetry missions. In future research, we will also analyze and evaluate the influence of the calibration errors of the instrument, the receiver orbit, and the atmosphere on the precision.

Author Contributions: Writing—original draft, X.S.; Writing—review and editing, W.Z., F.W. and Z.L.; X.S., W.Z. and F.W. contributed equally to this paper. All authors have read and agreed to the published version of the manuscript.

Funding: This work was supported by the National Natural Science Foundation of China under Grant (41774014, 41574014), the Liaoning Revitalization Talents Program under Grant (XLYC2002082), the Frontier Science and Technology Innovation Project and the Innovation Workstation Project of Science and Technology Commission of the Central Military Commission under Grant (085015), the Independent Research and Development Start-up Fund of Qian Xuesen Laboratory of Space Technology (Y-KC-WY-99-ZY-000-025), and the Outstanding Youth Fund of the China Academy of Space Technology.

Institutional Review Board Statement: Not applicable.

Informed Consent Statement: Not applicable.

Data Availability Statement: Not applicable.

Acknowledgments: We would like to thank the Institute of Space Sciences (ICE, CSIC) and the Institute for Space Studies of Catalonia (IEEC) for providing the raw data processing results of the airborne experiment. We would also like to thank IGS for providing SP3 precise orbit documents.

Conflicts of Interest: The authors declare no conflict of interest.

Appendix A

Simultaneous Equations (8) and (13), $C_z(\widetilde{n}T_c, \tau)$ can be derived as [21]:

$$\begin{aligned} C_z(\widetilde{n}T_c,\tau) &= \langle [z(nT_c,\tau) - \langle z(nT_c,\tau)\rangle][z(nT_c+\widetilde{n}T_c,\tau) - \langle z(nT_c+\widetilde{n}T_c,\tau)\rangle]\rangle \\ &= \langle [y(nT_c,\tau)y^*(nT_c,\tau) - \langle y(nT_c,\tau)y^*(nT_c,\tau)\rangle] \\ &\quad \times [y(nT+\widetilde{n}T_c,\tau)y^*(nT_c+\widetilde{n}T_c,\tau) - \langle y(nT_c+\widetilde{n}T_c,\tau)y^*(nT_c+\widetilde{n}T_c,\tau)\rangle]\rangle \\ &= \langle y(nT_c,\tau)y^*(nT_c,\tau)y(nT+\widetilde{n}T_c,\tau)y^*(nT_c+\widetilde{n}T_c,\tau)\rangle \\ &\quad - \langle y(nT_c,\tau)y^*(nT_c,\tau)\rangle\langle y(nT+\widetilde{n}T_c,\tau)y^*(nT_c+\widetilde{n}T_c,\tau)\rangle \end{aligned} \tag{A1}$$

In general, the complex waveforms follow the circular complex Gaussian statistics. The correlation function of the one-shot power waveforms can be simplified by using the complex Gaussian moment theorem [37]:

$$\begin{array}{l}\langle y(nT_c,\tau)y^*(nT_c,\tau)y(nT+\widetilde{n}T_c,\tau)y^*(nT_c+\widetilde{n}T_c,\tau)\rangle \\ =\langle y(nT_c,\tau)y^*(nT_c,\tau)\rangle\langle y(nT+\widetilde{n}T_c,\tau)y^*(nT_c+\widetilde{n}T_c,\tau)\rangle \\ +\langle y(nT_c,\tau)y^*(nT_c+\widetilde{n}T_c,\tau)\rangle\langle y^*(nT_c,\tau)y(nT+\widetilde{n}T_c,\tau)\rangle\end{array} \tag{A2}$$

Substituting Equation (A2) into Equation (A1), we can get:

$$\begin{array}{rcl}C_z(\widetilde{n}T_c,\tau) & = & \langle y(nT_c,\tau)y^*(nT_c+\widetilde{n}T_c,\tau)\rangle\langle y^*(nT_c,\tau)y(nT+\widetilde{n}T_c,\tau)\rangle \\ & = & \left|C_y(\widetilde{n}T_c,\tau)\right|^2\end{array} \tag{A3}$$

$$\begin{array}{rcl}C_z(0,\tau) & = & \left|C_y(0,\tau)\right|^2 \\ & = & \langle y(nT_c,\tau)y^*(nT_c,\tau)\rangle\langle y^*(nT_c,\tau)y(nT_c,\tau)\rangle \\ & = & \langle y(nT_c,\tau)y^*(nT_c,\tau)\rangle\langle y^*(nT_c,\tau)y(nT_c,\tau)\rangle \\ & = & \langle z(nT_c,\tau)\rangle\langle z(nT_c,\tau)\rangle\end{array} \tag{A4}$$

According to Equations (10) and (14), the variance of the power waveforms after incoherent average can be expressed as [21]:

$$\begin{array}{rcl}\sigma_Z^2(\tau) & = & C_Z(0,\tau) \\ & = & \langle[Z(t,\tau)-\langle Z(t,\tau)\rangle][Z(t,\tau)-\langle Z(t,\tau)\rangle]\rangle \\ & = & \langle Z(t,\tau)Z(t,\tau)\rangle-\langle Z(t,\tau)\rangle\langle Z(t,\tau)\rangle \\ & = & \langle Z(t,\tau)Z(t,\tau)\rangle-\langle z(t,\tau)\rangle\langle z(t,\tau)\rangle\end{array} \tag{A5}$$

Substitute Equation (10) into the first term of Equation (A5), we can get:

$$\begin{array}{rcl}\langle Z(t,\tau)Z(t,\tau)\rangle & = & \frac{1}{N_I^2}\left\langle\sum\limits_{i=0}^{N_I-1}z(iT_c,\tau)\sum\limits_{j=0}^{N_I-1}z(jT_c,\tau)\right\rangle \\ & = & \frac{1}{N_I^2}\sum\limits_{i=0}^{N_I-1}\sum\limits_{j=0}^{N_I-1}\langle z(iT_c,\tau)z(jT_c,\tau)\rangle\end{array} \tag{A6}$$

According to Equation (A1), $\langle z(iT_c,\tau)z(jT_c,\tau)\rangle$ can be represented as:

$$\langle z(iT_c,\tau)z(jT_c,\tau)\rangle = C_z((i-j)T_c,\tau)+\langle z(nT_c,\tau)\rangle\langle z(nT_c,\tau)\rangle \tag{A7}$$

$$\begin{array}{rcl}\sigma_Z^2(\tau) & = & C_Z(0,\tau) \\ & = & \frac{1}{N_I^2}\sum\limits_{i=0}^{N_I-1}\sum\limits_{j=0}^{N_I-1}C_z((i-j)T_c,\tau) \\ & = & \sum\limits_{k=-(N_I-1)}^{N_I-1}\frac{N_I-k}{N_I^2}C_z(kT_c,\tau) \\ & = & \frac{1}{N_I}\sum\limits_{\widetilde{n}=-(N_I-1)}^{N_I-1}C_z(\widetilde{n}T_c,\tau)\end{array} \tag{A8}$$

Simultaneous Equations (A3), (A4) and (A8), we can get:

$$\begin{array}{rcl}\frac{1}{N_{\text{eff}}} & = & \frac{\sigma_Z^2(\tau)}{Z^2(\tau)} \\ & = & \frac{\sigma_Z^2(\tau)}{\langle z(nT_c,\tau)\rangle\langle z(nT_c,\tau)\rangle} \\ & = & \frac{\sum\limits_{n=-(N_I-1)}^{N_I-1}\left|C_y(\widetilde{n}T_c,\tau)\right|^2}{N_I\left|C_y(0,\tau)\right|^2}\end{array} \tag{A9}$$

B.

Assuming that there is no correlation between the signal term and noise term, the complex waveforms of iGNSS-R can include the following four items [18]:

$$C_y(\widetilde{n}T_c,\tau) = C_{y,\mathrm{s}}(\widetilde{n}T_c,\tau) + C_{y,\mathrm{nd}}(\widetilde{n}T_c,\tau) + C_{y,\mathrm{nu}}(\widetilde{n}T_c,\tau) + C_{y,\mathrm{ndu}}(\widetilde{n}T_c,\tau) \tag{A10}$$

Since the noise of the reflected signal is much larger than that of the direct signal, can be assumed. According to [20], the covariance of signal components can be simplified as:

$$\begin{aligned} C_{y,\mathrm{s}}(\widetilde{n}T_c,\tau) &= \langle y_\mathrm{s}(nT_c,\tau) {y_\mathrm{s}}^*(nT_c+\widetilde{n}T_c,\tau)\rangle \\ &= 2P_\mathrm{d}\iint \frac{2P_\mathrm{t}G_\mathrm{r}(\vec{p})\sigma_0}{4\pi R_\mathrm{t}^2(\vec{p})R_\mathrm{r}^2(\vec{p})}\Lambda^2(\Delta\tau)\mathrm{sinc}^2(\Delta f T_c)\exp^{-\mathrm{j}2\pi\Delta f(\widetilde{n}T_c)}\,d^2p \end{aligned} \tag{A11}$$

According to [21], the covariance of the noise component can be simplified as:

$$\begin{aligned} C_{y,\mathrm{nd}}(\widetilde{n}T_c,\tau) &= \frac{2P_\mathrm{d}n_0^\mathrm{d}}{T_c}\mathrm{tri}(\frac{\widetilde{n}T_c}{T_c}) \\ C_{y,\mathrm{ndu}}(\widetilde{n}T_c,\tau) &= \frac{Bn_0^\mathrm{d}n_0^\mathrm{u}}{T_c}\mathrm{tri}(\frac{\widetilde{n}T_c}{T_c}) \end{aligned} \tag{A12}$$

Simultaneous Equations (A10)–(A12), $C_y(\widetilde{n}T_c,\tau)$ can be converted as:

$$\begin{aligned} C_y(\widetilde{n}T_\mathrm{c},\tau) &= 2P_\mathrm{d}\iint \frac{2P_\mathrm{t}G_\mathrm{r}(\vec{p})\sigma_0}{4\pi R_\mathrm{t}^2(\vec{p})R_\mathrm{r}^2(\vec{p})}\Lambda^2(\Delta\tau)\times\mathrm{sinc}^2(\Delta f T_\mathrm{c})\exp^{-\mathrm{j}2\pi\Delta f(\widetilde{n}T_\mathrm{c})}\,d^2p \\ &\quad + \frac{2P_\mathrm{d}n_0^\mathrm{d}}{T_\mathrm{c}}\mathrm{tri}(\frac{\widetilde{n}T_\mathrm{c}}{T_\mathrm{c}}) + \frac{Bn_0^\mathrm{d}n_0^\mathrm{u}}{T_\mathrm{c}}\mathrm{tri}(\frac{\widetilde{n}T_\mathrm{c}}{T_\mathrm{c}}) \end{aligned} \tag{A13}$$

Simultaneous Equations (A9) and (A13), the relationship between the reciprocal of the effective incoherent average number and the coherent integration time can be derived as Equation (19).

References

1. Martin-Neira, M. A Passive Reflectometry and Interferometry System (PARIS): Application to ocean altimetry. *ESA J.* **1993**, *17*, 331–355.
2. Lowe, S.T.; Zuffada, C.; LaBrecque, J.L.; Lough, M.; Lerma, J.; Young, L.E. An ocean-altimetry measurement using reflected GPS signals observed from a low-altitude aircraft. *IEEE Int. Geosci. Remote Sens. Symp.* **2000**, *5*, 2185–2187. [CrossRef]
3. Beyerle, G.; Hocke, K. Observation and simulation of direct and reflected GPS signals in radio occultation experiments. *Geophys. Res. Lett.* **2001**, *28*, 1895–1898. [CrossRef]
4. Foti, G.; Gommenginger, C.; Jales, P.; Unwin, M.; Shaw, A.; Robertson, C.; Rosello, J. Spaceborne GNSS reflectometry for ocean winds: First results from the UK TechDemoSat-1 mission. *Geophys. Res. Lett.* **2015**, *42*, 5435–5441. [CrossRef]
5. Martin-Neira, M.; Caparrini, M.; Font-Rossello, J.; Lannelongue, S.; Vallmitjana, C.S. The PARIS concept: An experimental demonstration of sea surface altimetry using GPS reflected signals. *IEEE Trans. Geosci. Remote Sens.* **2001**, *39*, 142–150. [CrossRef]
6. Carreno-Luengo, H.; Camps, A.; Ramos-Perez, I.; Rius, A. Experimental evaluation of GNSS reflectometry altimetric precision using the P(Y) and C/A signals. *IEEE J. Sel. Top. Appl. Earth Obs. Remote Sens.* **2014**, *7*, 1493–1500. [CrossRef]
7. Li, W.; Yang, D.; D'Addio, S.; Martin-Neira, M. Partial interferometric processing of reflected GNSS signals for ocean altimetry. *Geophys. Res. Lett.* **2014**, *11*, 1509–1513. [CrossRef]
8. Cardellach, E.; Rius, A.; Martin-Neira, M.; Fabra, F.; Nogues-Correig, O.; Ribo, S.; Kainulainen, J.; Camps, A.; D'Addio, S. Consolidating the precision of interferometric GNSS-R ocean altimetry using airborne experimental data. *IEEE Trans. Geosci. Remote Sens.* **2014**, *52*, 4992–5004. [CrossRef]
9. Feng, W.; Yang, D.; Li, W.; Wei, Y. On-ground retracking to correct distorted waveform in spaceborne global navigation satellite system-reflectometry. *Remote Sens.* **2017**, *9*, 643. [CrossRef]
10. Hajj, G.A. Theoretical description of a bistatic system for ocean altimetry using the GPS signa. *Radio Sci.* **2003**, *38*, 1001–1019. [CrossRef]
11. Fernando Marchan-Hernandez, J.; Camps, A.; Rodriguez-Alvarez, N.; Valencia, E.; Bosch-Lluis, X.; Ramos-Perez, I. An efficient algorithm to the simulation of delay-Doppler maps of reflected global navigation satellite system signals. *IEEE Trans. Geosci. Remote Sens.* **2009**, *47*, 2733–2740. [CrossRef]
12. Rius, A.; Cardellach, E.; Martin-Neira, M. Altimetric analysis of the sea-surface GPS-reflected signals. *IEEE Trans. Geosci. Remote Sens.* **2010**, *48*, 2119–2127. [CrossRef]
13. Rodríguez, E. Altimetry for non-Gaussian oceans: Height biases and estimation of parameters. *J. Geophys. Res.* **1988**, *93*, 14107–14120. [CrossRef]

14. Mashburn, J.; Axelrad, P.; Lowe, S.T.; Larson, K.M. Global ocean altimetry with GNSS reflections from TechDemoSat-1. *IEEE Trans. Geosci. Remote Sens.* **2018**, *56*, 4088–4097. [CrossRef]
15. Li, W.; Cardellach, E.; Fabra, F.; Ribo, S.; Rius, A. Assessment of spaceborne GNSS-R ocean altimetry performance using CYGNSS mission raw data. *IEEE Trans. Geosci. Remote Sens.* **2019**, *58*, 238–250. [CrossRef]
16. Liu, Z.; Zheng, W.; Wu, F.; Cui, Z.; Kang, G. A necessary model to quantify the scanning loss effect in spaceborne iGNSS-R ocean altimetry. *IEEE J. Sel. Top. Appl. Earth Obs. Remote Sens.* **2021**, *14*, 1619–1627. [CrossRef]
17. Liu, Z.; Zheng, W.; Wu, F.; Kang, G.; Li, Z.; Wang, Q.; Cui, Z. Increasing the number of sea surface reflected signals received by GNSS-Reflectometry altimetry satellite using the nadir antenna observation capability optimization method. *Remote Sens.* **2019**, *11*, 2473. [CrossRef]
18. Martin-Neira, M.; D'Addio, S.; Buck, C.; Floury, N.; Prieto-Cerdeira, R. The PARIS ocean altimeter in-orbit demonstrator. *IEEE Trans. Geosci. Remote Sens.* **2011**, *49*, 2209–2237. [CrossRef]
19. You, H.I.; Garrison, J.L.; Heckler, G.; Zavorotny, V.U. Stochastic voltage model and experimental measurement of ocean-scattered GPS signal statistics. *IEEE Trans. Geosci. Remote Sens.* **2004**, *42*, 2160–2169. [CrossRef]
20. Garrison, J.L. A statistical model and simulator for ocean-reflected GNSS signals. *IEEE Trans. Geosci. Remote Sens.* **2016**, *54*, 6007–6019. [CrossRef]
21. Li, W.; Rius, A.; Fabra, F.; Cardellach, E.; Ribo, S.; Martin-Neira, M. Revisiting the GNSS-R waveform statistics and its impact on altimetric retrievals. *IEEE Trans. Geosci. Remote Sens.* **2018**, *56*, 2854–2871. [CrossRef]
22. Jing, C.; Niu, X.; Duan, C.; Lu, F.; Di, G.; Yang, X. Sea surface wind speed retrieval from the first Chinese GNSS-R mission: Technique and preliminary results. *Remote Sens.* **2019**, *11*, 3013. [CrossRef]
23. Fabra, F.; Cardellach, E.; Ribo, S.; Li, W.; Rius, A.; Carlos Arco-Fernandez, J.; Nogués-Correig, O.; Praks, J.; Rouhe, E.; Seppänen, J.; et al. Is accurate synoptic altimetry achievable by means of interferometric GNSS-R? *Remote Sens.* **2019**, *11*, 505. [CrossRef]
24. Ribo, S.; Arco-Fernandez, J.C.; Cardellach, E.; Fabra, F.; Li, W.; Nogues-Correig, O.; Rius, A.; Martín-Neira, M. A software-defined GNSS reflectometry recording receiver with wide-bandwidth, multi-band capability and digital beam-forming. *Remote Sens.* **2017**, *9*, 450. [CrossRef]
25. Park, H.; Camps, A.; Valencia, E.; Rodriguez-Alvarez, N.; Bosch-Lluis, X.; Ramos-Perez, I.; Carreno-Luengo, H. Retracking considerations in spaceborne GNSS-R altimetry. *GPS Solut.* **2012**, *16*, 507–518. [CrossRef]
26. Zavorotny, V.U.; Voronovich, A.G. Scattering of GPS signals from the ocean with wind remote sensing application. *IEEE Trans. Geosci. Remote Sens.* **2000**, *38*, 951–964. [CrossRef]
27. Mashburn, J.; Axelrad, P.; Lowe, S.T.; Larson, K.M. An assessment of the precision and accuracy of altimetry retrievals for a monterey bay GNSS-R experiment. *IEEE J. Sel. Top. Appl. Earth Observ. Remote Sens.* **2016**, *9*, 4660–4668. [CrossRef]
28. D'Addio, S.; Martin-Neira, M.; di Bisceglie, M.; Galdi, C.; Martin Alemany, F. GNSS-R altimeter based on Doppler multi-looking. *IEEE J. Sel. Top. Appl. Earth Obs. Remote Sens.* **2014**, *7*, 1452–1460. [CrossRef]
29. D'Addio, S.; Martin-Neira, M. Comparison of processing techniques for remote sensing of earth-exploiting reflected radio-navigation signals. *Electron. Lett.* **2013**, *49*, 292–293. [CrossRef]
30. Fan, M.; Zhang, B.; Wang, F. Semi-codeless based P(Y) code autocorrelation GNSS-R sea surface altimetry method. *J. Beijing Univ. Aeronaut. Astronaut.* **2019**, *45*, 398–404. [CrossRef]
31. Martin, F.; Camps, A.; Park, H.; D'Addio, S.; Martin-Neira, M.; Pascual, D. Cross-correlation waveform analysis for conventional and interferometric GNSS-R approaches. *IEEE J. Sel. Top. Appl. Earth Obs. Remote Sens.* **2014**, *7*, 1560–1572. [CrossRef]
32. Camps, A.; Park, H.; Domènech, E.V.; Pascual, D.; Martin, F.; Rius, A.; Ribo, S.; Benito, J.; Andrés-Beivide, A.; Saameno, P.; et al. Optimization and performance analysis of interferometric GNSS-R altimeters: Application to the Paris IoD mission. *IEEE J. Sel. Top. Appl. Earth Obs. Remote Sens.* **2014**, *7*, 1436–1451. [CrossRef]
33. Wu, F.; Zheng, W.; Li, Z.; Liu, Z. Improving the GNSS-R specular reflection point positioning accuracy using the gravity field normal projection reflection reference surface combination correction method. *Remote Sens.* **2018**, *11*, 33. [CrossRef]
34. Wu, F.; Zheng, W.; Li, Z.; Liu, Z. Improving the positioning accuracy of satellite-borne GNSS-R specular reflection point on sea surface based on the ocean tidal correction positioning method. *Remote Sens.* **2019**, *11*, 1626. [CrossRef]
35. Zavorotny, V.U.; Gleason, S.; Cardellach, E.; Camps, A. Tutorial on remote sensing using GNSS bistatic radar of opportunity. *IEEE Geosci. Remote Sens. Mag.* **2014**, *2*, 8–45. [CrossRef]
36. Carreno-Luengo, H.; Park, H.; Camps, A.; Fabra, F.; Rius, A. GNSS-R Derived Centimetric Sea Topography: An Airborne Experiment Demonstration. *IEEE J. Sel. Top. Appl. Earth Observ. Remote Sens.* **2013**, *6*, 1468–1478. [CrossRef]
37. Goodman, J.W.; Narducci, L.M. Statistical Optics. *Phys. Today* **1986**, *39*, 126. [CrossRef]

remote sensing

MDPI

Article

Maritime Multiple Moving Target Detection Using Multiple-BDS-Based Radar: Doppler Phase Compensation and Resolution Improvement

Xiang Lan [1], Liuying Wang [2], Jinxing Li [1], Wangqiang Jiang [1] and Min Zhang [1,*]

[1] The School of Physics and Optoelectronic Engineering, Xidian University, Xi'an 710000, China; xianglan@stu.xidian.edu.cn (X.L.); jxli@xidian.edu.cn (J.L.); wqjiang@mail.xidian.edu.cn (W.J.)
[2] Xi'an Research Institute of High Technology, Xi'an 710000, China; lywangxa@163.com
* Correspondence: mzhang@mail.xidian.edu.cn; Tel.: +86-29-88202663

Abstract: With the realization of global navigation satellite system (GNSS) completion, GNSS reflectometry (GNSS-R) has become increasingly popular due to the advantages of global coverage and the availability of multiple sources in terms of earth remote sensing. This paper analyzes the Beidou navigation satellite system (BDS) signal reflection detection of multiple satellites and multiple moving targets under multiple-input and multiple-output (MIMO) radar systems and proposes a series of methods to suppress multiple Doppler phase influences and improve the range detection property. The simulation results show the restored target peaks, which match the RCS data more accurately, with the GNSS-R Doppler phase influence removed, which proves the proposed method can improve target recognition and detection resolution performance.

Keywords: global navigation satellite system reflectometry (GNSS-R); Beidou navigation satellite system (BDS); Doppler compensation; range resolution

Citation: Lan, X.; Wang, L.; Li, J.; Jiang, W.; Zhang, M. Maritime Multiple Moving Target Detection Using Multiple-BDS-Based Radar: Doppler Phase Compensation and Resolution Improvement. *Remote Sens.* **2021**, *13*, 4963. https://doi.org/10.3390/rs13244963

Academic Editors: Shuanggen Jin and Gino Dardanelli

Received: 8 November 2021
Accepted: 3 December 2021
Published: 7 December 2021

1. Introduction

At the moment more than 70 satellites are already in view; this brings great opportunities and challenges for both scientific and engineering applications. The different global navigation satellite system (GNSS) signals are compared and analyzed in the literature [1] in terms of detection performance and signal characteristics. A four-system positioning model for multi-satellite detection is proposed in the literature [2].

Global navigation satellite system reflectometry (GNSS-R) detection has become a popular tool for earth remote sensing, such as multiple maritime targets detection, with its gradual improvement in observation technology. Based on GNSS-R delay–Doppler map (DDM) imaging, an effective method of expression based on GNSS-R signals, the literature [3–5] shows an incoherent range walk compensation method and accurate realization methods to improve the DDM imaging effectiveness. The waveform and detection models were analyzed in [6,7] for GNSS-R detection. With the gradual maturity of the Beidou navigation satellite system (BDS), BDS satellite remote sensing studies have become increasingly widespread. The single-frequency PPP time transfer performance of BDS-2/3 is evaluated for excellent performance and BDS-3's is expected for better accuracy with the continuous development of real-time products of BDS [8]. Time–frequency-transfer and time performance technology based on BDS systems have been implemented and evaluated [9,10]. With the increase in the demand for precise positioning, an increasing number of observational reports have been proposed with constant improvement of the positioning method. The literature [11,12] presents a real-time detection and point position method based on the combination of GPS and BDS observations.

BDS-R detection still leaves some problems to be solved. Due to the low reflected signal power, it is difficult to obtain complete target information with a background of

strong clutter and noise. Reference [13] notes that for large and medium-sized targets on the sea surface, GNSS-R detection can acquire a sufficient signal-to-noise ratio (SNR) of 20~25 dB [14] after several seconds of accumulation. Next, one study in the literature [14,15] simulated a delay–Doppler map (DDM) of large-scale targets and verified the effectiveness of large-scale target detection based on short time accumulation signals using the range–Doppler Fourier method. In terms of theoretical construction and system model, reference [16] gives an extremum approximation algorithm for advanced receiver autonomous integrity monitoring, and triple-frequency combining observation models have been studied for precise point positioning [17]. Moreover, real-time, direction-constrained determination methods were proposed for point velocity detection studies [18–20]. In order to better interpret the target information of the GNSS-R signal and obtain the images that match the detected target, many signal processing methods were proposed. The incoherent range walk compensation method was proposed for spaceborne GNSS-R imaging [3], and GNSS-R-based moving target indication is studied in the literature [21]. In terms of marine target detection, ocean surface target detection and positioning were discussed [22], the delay and Doppler tracking errors were analyzed [15], and the feasibility analysis of ship detection by DDM was simulated [23]. In order to distinguish sea targets from sea clutter, the blind sea clutter suppression method was discussed [24]. Moreover, the data of TDS-1 were used to prove the effectiveness of the proposed target detection method [25], and the anomalous artifacts of TDS-1 DDM were analyzed in [26].

In this paper, multiple-BDS signal reflection detection for multiple moving targets was studied. We propose the multiple targets Doppler compensation (MTDC) method to keep target peaks from the influence of the Doppler phase and provide a target peak identification method and range inversion methods to realize the specific scatter information detection of targets. The contributions of this paper can be summarized as follows: (1) The target peak reduction problem existing in multiple-BDS signal detection was analyzed by echo formulas, and solutions are proposed for two situations: when target estimation information is acquired and when it is not. In the simulation, a difference of more than 400 Hz in the Doppler frequency was set among the detected targets, which further verifies that the proposed method is effective; (2) The target peak identification method is proposed based on 33 m sampling at the echoes, and the improved target detection peaks can express the target information more accurately in terms of amplitude and range point; (3) A range inversion method is proposed to acquire the specific scatter information in the case of low-resolution BDS signals. The results are in good agreement with the corresponding RCS data in the ship target simulation; (4) In terms of practicability, the proposed MTDC method 1 and range inverse method 1 can remove the Doppler phase influence and further acquire the targets' RCS distribution without target estimation. The target peak identification results based on 33 m echo sampling can be utilized to verify target recognition. Moreover, the results were simulated and analyzed under clutter and noise backgrounds.

The rest of the sections in this paper are organized as follows. Section 2 discusses the MIMO BDS signal detection model and lists existing problems. The Doppler compensation methods and range detection resolution design of the BDS signal based on MIMO multiple-target detection are discussed in Section 3. In Section 4, the simulation results and analysis are obtained. Finally, the paper is concluded in Section 5.

2. Detection Model and Existing Problems

2.1. Detection Model

The detection model of multiple GNSS-R signals for multiple targets was firstly outlined. The BDS signals, which are transmitted by MEO (medium earth orbit) satellites in the Beidou No. 3 system fixed at 2.1528×10^4 km above the Earth's surface, were used as detection sources. The detection simulated maritime multiple moving target detection under space-based observation. The geometry of the model is given in Figure 1, where a rectangular coordinate system is established and the XOY level coincides with the sea level. The satellites, targets, and receiver positions are marked in red.

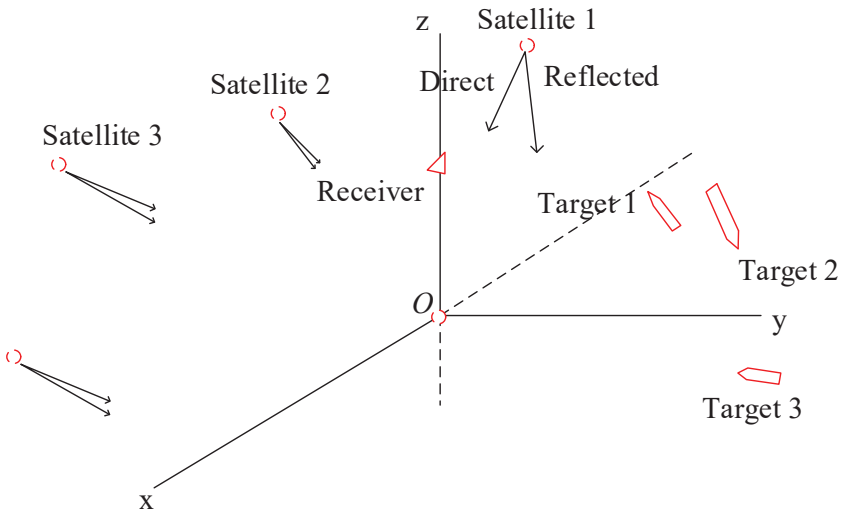

Figure 1. MIMO and multiple target BDS signal detection geometric model.

2.2. Signal Structure

During the detection model, several sets of B1I and B3I signals transmitted by MEO satellites with corresponding pseudo-random noise (PRN) codes were used. A part of the signals reaches the airborne-based receiver directly, and the other part of the signals is reflected by the ship targets and arrives at the latter receiver. The received echo is the sum of all echoes transmitted by each satellite and reflected by each target. In the simulation experiment, we found the echo modulation information through the proposed geometric model with satellite ephemeris, receiver motion information and target position, altitude, and velocity information. The BDS signals' model structures are expressed as formulae with changes and states in the propagation and receivers, as follows.

In the formula expression, we set '*i*' as the satellite number and '*j*' as the target number. The transmitting BDS signal [27,28] of satellite *i* is expressed as:

$$s^i(t) = AC^iD^i\cos(2\pi f_0 t + \varphi^i) \tag{1}$$

where $s^i(t)$ contains B1I and B3I signals. A is the signal amplitude, C^i the signal ranging code, and D^i the signal data code. During the cosine function, f_0 is the carrier frequency, and φ^i is the original phase. The echoes after propagation and receiving can be expressed as follows:

$$R_d^i = a_d^i \cdot s^i(t - \tau_d^i, fd_d^i) \tag{2}$$

$$R_r^{i,j} = a_r^{i,j} \cdot s^i(t - \tau_r^{i,j}, fd_r^{i,j}) \tag{3}$$

where the subscripts '*d*' and '*r*' are direct signals and reflected signals, respectively. a_d^i is the propagation coefficient and scattering coefficient of direct signals, and $a_r^{i,j}$ is the reflected signal reflected by target *j*. τ and fd are the responding transmitted delay and Doppler frequency, which are related to the carrier frequency and show different values between the B1I and B3I signals. Finally, the total received B1I and B3I signals transmitted by multiple satellites and propagated through the direct and multiple targets reflection approach is expressed as

$$R = \sum_{i=1}^{M}(R_{\mathrm{B1I},d}^i + \sum_{j=1}^{N} R_{\mathrm{B1I},r}^{i,j}) + \sum_{i=1}^{M}(R_{\mathrm{B3I},d}^i + \sum_{j=1}^{N} R_{\mathrm{B3I},r}^{i,j}) \tag{4}$$

For pulse accumulation and slow-time Doppler frequency detection, the echoes expressed in Q ranging code periods is (5), after data code demodulation processing.

$$ {}^{Q}R = \sum_{q=1}^{Q} u_{T_P}(t - q \cdot T_P) \cdot R \tag{5} $$

where ${}^{Q}R$ represents the echoes in Q ranging code periods, and $u_{T_P}(t - q \cdot T_P) = 1$, $q \cdot T_P < t < (q+1)T_P$ is the window function. T_P is the ranging code cycle period.

2.3. Existing Problems

Based on the detection model, there exist several problems which promote the development of the proposed methods:

- First, the satellites and receiver are moving fast, which will produce a large Doppler frequency. With different dual-station angle of targets, the Doppler frequencies among the targets shows big differences, which weakened target detection peaks to varying degrees. A Doppler compensation method should be given to restore and unify the target peaks.
- Second, since the BDS signal was not devised for GNSS-R detection, its range resolution is not sufficient to detect ship targets well. Further RCS distribution information of targets needs to be detected for target recognition.

3. Methods

3.1. Multiple Targets Detection Doppler Compensation

In order to remove the Doppler phase influence during multiple targets detection, we further studied echo processing. The B3I signal is set as an example to express the formula, and the B1I signal has the same form. Take Formulas (1) and (3) into (5) as

$$ \begin{aligned} {}^{Q}R^{i,j}_{\mathrm{B3I,r}} &= \sum_{q=1}^{Q} u_{T_P}(t - q * T_P) \cdot R^{i,j}_{\mathrm{B3I,r}} \\ &= a^{i,j}_{\mathrm{B3I,r}} A^{i}_{\mathrm{B3I}} C^{i}_{\mathrm{B3I}} \cdot \sum_{q=1}^{Q} \Big\{ u\Big(t - \tau^{i}_{rj} - q \cdot T_P\Big) \\ &\quad \cdot \cos(2\pi f d^{i,j}_{\mathrm{B3I,r}}(t - \tau^{i,j}_{\mathrm{B1I,r}} - q \cdot T_P) + \varphi^{i}_{\mathrm{B3I}}) \Big\} \end{aligned} \tag{6} $$

where ${}^{Q}R^{i,j}_{\mathrm{B3I,r}}$ is the received reflected B3I signals transmitted by satellite i and reflected by target j during Q ranging code periods. According to the ranging code C^{i}_{B3I}, we find the duty ratio of the signal to be 1 in a ranging code period. Therefore, the Doppler phase changes during a signal ranging code period cannot be ignored. The echoes model (6) is improved as

$$ \begin{aligned} {}^{Q}R^{i,j}_{\mathrm{B3I,r}} = a^{i,j}_{\mathrm{B3I,r}} A^{i}_{\mathrm{B3I}} C^{i}_{\mathrm{B3I}} \cdot \sum_{q=1}^{Q} \sum_{n=1}^{N_C} \{ u_{T_c}\Big(t - \tau^{i,j}_{\mathrm{r}} - qT_P - nT_c\Big) \\ \cdot \cos(2\pi f d^{i,j}_{\mathrm{B3I,r}}(t - \tau^{i,j}_{\mathrm{B3I,r}} - qT_P - nT_c) + \varphi^{i}_{\mathrm{B3I}}) \} \end{aligned} \tag{7} $$

where N_c is the number of range code elements, and T_c is the range code element period. In (7), the Doppler phase of echoes changes with each ranging code element, and it influences the target range peak result level of the matched filter. The normalized autocorrelation peak level changing with Doppler frequency is shown in Figure 2, where the peak level reduces slowly first and then drops quickly to lower than 0.1 when the Doppler frequency

is more than 1000 Hz. Moreover, the relevant parameters are described in the simulation section. Focusing on the Doppler phase influence, we express (7) as

$$\begin{aligned} {}^{Q}R^{i,j}_{\mathrm{B3I,r}} &= {}^{Q}R^{i,j}_{\mathrm{B3I,r}}(Ph^{i,j}_{\mathrm{B3I,r}}) \\ {}^{Q}Ph^{i,j}_{\mathrm{B3I,r}} &= \sum_{q=1}^{Q}\sum_{n=1}^{N_C} u_{T_c}(t-qT_P-nT_c)\cdot 2\pi fd^{i,j}_{\mathrm{B3I,r}}(t-qT_P-nT_c) \\ &= {}^{Q}Ph^{i,j}_{\mathrm{B3I,r}}(fd^{i,j}_{\mathrm{B3I,r}}) \end{aligned} \tag{8}$$

where we can find that ${}^{Q}Ph^{i,j}_{\mathrm{B3I,r}}$ is the sequence with a length of $Q \cdot N_c$ and is up to $fd^{i,j}_{\mathrm{B3I,r}}$. Moreover, each target reflects echo carriers with different Doppler frequencies, and we needed to reduce multiple Doppler phase influences for better detection of the target peak.

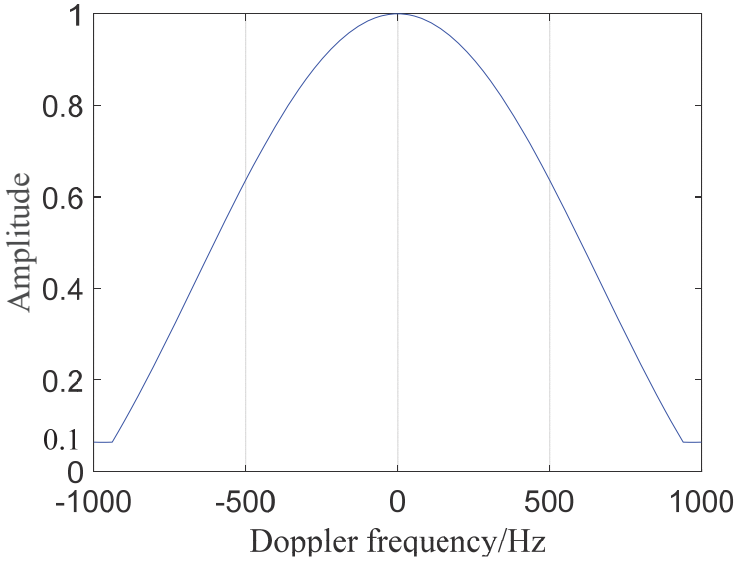

Figure 2. Target peak curves with the Doppler channel in the detection of BDS signals.

Before the Doppler phase compensation, the compensatory Doppler frequency of target echoes needed to be acquired. We propose two methods: method 1, without estimation and method 2, with estimation. In method 1, we acquired the Doppler frequency range of targets by satellite navigation code data and receiver data as

$$\begin{aligned} &fd^{i}_{\mathrm{B1I,min}} = \\ &\min(fd^{i}_{\mathrm{B1I,sat\_rec}} + fd^{i}_{\mathrm{B1I,rec\_tar\_max}}, fd^{i}_{\mathrm{B1I,sat\_rec}} - fd^{i}_{\mathrm{B1I,rec\_tar\_max}}) \\ &fd^{i}_{\mathrm{B1I,max}} = \\ &\max(fd^{i}_{\mathrm{B1I,sat\_rec}} + fd^{i}_{\mathrm{B1I,rec\_tar\_max}}, fd^{i}_{\mathrm{B1I,sat\_rec}} - fd^{i}_{\mathrm{B1I,rec\_tar\_max}}) \end{aligned} \tag{9}$$

and the compensated Doppler frequencies are acquired by sampling in the range with an interval of 125 Hz as

$$\begin{aligned} {}^{1}fd^{i,j'}_{\mathrm{B1I,r}} &= {}^{1}fd^{i}_{\mathrm{B1I,min}} + 250 * (j'-1) \\ {}^{1}fd^{i}_{\mathrm{B1I,min}} &\le {}^{1}fd^{i,j'}_{\mathrm{B1I,r}} \le {}^{1}fd^{i}_{\mathrm{B1I,max}} \end{aligned} \tag{10}$$

where ${}^{1}fd^{i}_{\mathrm{B1I},rj'}$ is the compensation Doppler frequency of method 1 and j' is the compensation number. Using the estimated information of targets, the compensated Doppler frequencies are set as Doppler frequency estimation values in method 2.

$$ {}^{2}fd^{i,j'}_{\mathrm{B1I,r}} = {}^{2}fd^{i,j'}_{\mathrm{B1I,e}} \tag{11} $$

where ${}^{2}fd^{i,j'}_{\mathrm{B1I,r}}$ is the compensation Doppler frequency of method 2. After acquiring the corresponding Doppler frequency, the compensation phase is expressed as

$$ \begin{aligned} {}^{Q}CPh^{i,j'}_{\mathrm{B3I,r}} &= \sum_{q=1}^{Q}\sum_{n=1}^{N_C} u_{T_c}(t - qT_P - nT_c)\cdot 2\pi fd^{i,j'}_{\mathrm{B3I,r}}(t - qT_P - nT_c) \\ &= {}^{Q}CPh^{i,j'}_{\mathrm{B3I,r}}(fd^{i,j'}_{\mathrm{B3I,r}}) \end{aligned} \tag{12} $$

To solve the multiple Doppler phase influences and restore the weakened target peak, we propose the multiple target Doppler compensation (MTDC) method, which compensates for the echoes with multiple Doppler phase sequences at the corresponding range code period position of targets and fetches the maximum value of the filter outputs as the compensation result. Next, (13) expresses the compensated echo.

$$ {}^{Q}CR^{i,j,j'}_{\mathrm{B3I,r}} = {}^{Q}R^{i,j}_{\mathrm{B3I,r}}({}^{Q}Ph^{i,j}_{\mathrm{B3I,r}} + {}^{Q}CPh^{i,j'}_{\mathrm{B3I,r}}) \tag{13} $$

where ${}^{Q}CR^{i,j,j'}_{\mathrm{B3I,r}}$ denotes the echoes of satellite i and target j with compensation j'. The echoes from satellite i with multiple-target Doppler compensation can be expressed as

$$ {}^{Q}CR^{i,j'}_{\mathrm{B3I}} = {}^{Q}CR^{i}_{\mathrm{B3I,d}} + \sum_{j=1}^{N} {}^{Q}CR^{i,j,j'}_{\mathrm{B3I,r}} \tag{14} $$

Next, we matched echoes with the corresponding satellite signal as

$$ {}^{Q}CM^{i,j'}_{\mathrm{B1I}} = {}^{Q}CR^{i,j'}_{\mathrm{B3I}} \otimes s^{i}_{\mathrm{B3I}}(t) \tag{15} $$

Finally, (16) shows the selected maximum of each compensation as the result.

$$ {}^{Q}CM^{i}_{\mathrm{B1I}}c = \max({}^{Q}CM^{i,1}_{\mathrm{B1I}}, \ldots, {}^{Q}CM^{i,j'}_{\mathrm{B1I}}, \ldots, {}^{Q}CM^{i,N'}_{\mathrm{B1I}}) \tag{16} $$

The formula mentioned above is the one-dimensional range–Doppler compensation of multiple target reflections. In the next part, we show the Doppler and the delay two-dimensional Doppler compensation methods for Doppler delay image target peak compensation. To better express the Doppler phase changes among code element periods ranging code periods in a discrete time system, we express the Doppler phase in the form of a matrix as (17), where each row expresses a period of T_P, and its range is from 0 to $Q \cdot T_P$.

$$ \begin{aligned} &ph^{i}_{\mathrm{B1I},rj} = fd^{i}_{\mathrm{B1I},rj}\cdot \\ &\begin{bmatrix} 0+0, & \ldots, & 0+nT_c, & \ldots, & 0+(N_c-1)T_c \\ \vdots & & \vdots & & \vdots \\ qT_P+0, & \ldots, & qT_P+nT_c, & \ldots, & qT_P+(N_c-1)T_c \\ \vdots & & \vdots & & \vdots \\ (Q-1)T_P+0, & \ldots, & (Q-1)T_P+nT_c, & \ldots, & (Q-1)T_P+(N_c-1)T_c \end{bmatrix} \end{aligned} \tag{17} $$

where we can find that the number column is incremented by T_c in each row and is incremented by T_P in each column. Therefore, we can take the FFT in the columns of the matrix to first acquire the Doppler information of targets. Next, we compensate the matrix

in each T_P row for the duration based on the compensation phase. Finally, we can obtain the compensated DDM results by the proposed MTDC method.

3.2. Resolution Study and Peaks Identifying Methods

In this part, we study the resolution performance of the BDS signal. As shown in Table 1 in the simulation section, the B3I signal is transmitted with a bandwidth of 20.46 MHz. Figure 3 shows the autocorrelation curves of the B3I signal and two chirp signals with bandwidths of 10.23 MHz and 20.46 MHz.

Table 1. System parameter.

Signals	**B3I**	
Bandwidth (B)/MHz	20.46	
Carrier frequency f_0/Hz	1.268×10^9	
Satellite1 PRN	19	
Satellite2 PRN	26	
Satellite3 PRN	21	
Satellite4 PRN	22	
Receiver label/km	(0, 0, 6.5)	
Receiver velocity/m/s	250	
Receiver velocity angle	$\varphi = 135°, \theta = 90°$	
Simulation serial number	1	2
Accumulation time/s	0.128	10

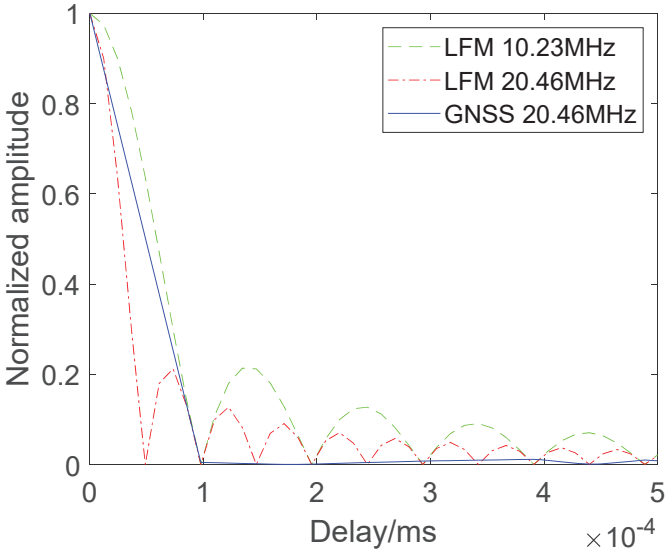

Figure 3. Autocorrelation curves of GNSS B3I and chirp signals.

In Figure 3, we find that the main lobe of the B3I signal is wider than that of the chirp signal at 20.46 MHz. According to Formula (18), where C is the electromagnetic wave velocity and B is the signal bandwidth, the range resolution of the two chirp signals can be calculated as 29.32 m. The resolution of the B3I signal is approximately 30 m, as shown in Figure 3.

$$\Delta r = \mathrm{C}/B \tag{18}$$

To further study the resolution of the B3I signal, we simulated two-point target detection with interval of 29 m and 33 m by using the B3I signal, setting the chirp signal at a 10.23 MHz bandwidth as a comparison. Figure 4a shows the detection peaks of the GNSS B3I signal and chirp signal reflected by two-point targets with a distance of 29 m. We found that the solid line peaks overlap completely, which means that the B3I signal cannot distinguish the two-point targets. The chirp signal, with a bandwidth of 10.23 MHz, can clearly detect two-point target peaks. Next, in Figure 4b, where the distance between two-point targets is 33 m, two signals show two target peaks, and the sidelobe of the B3I signal in the center is higher, while its sidelobes on both sides are lower than those of the chirp signal.

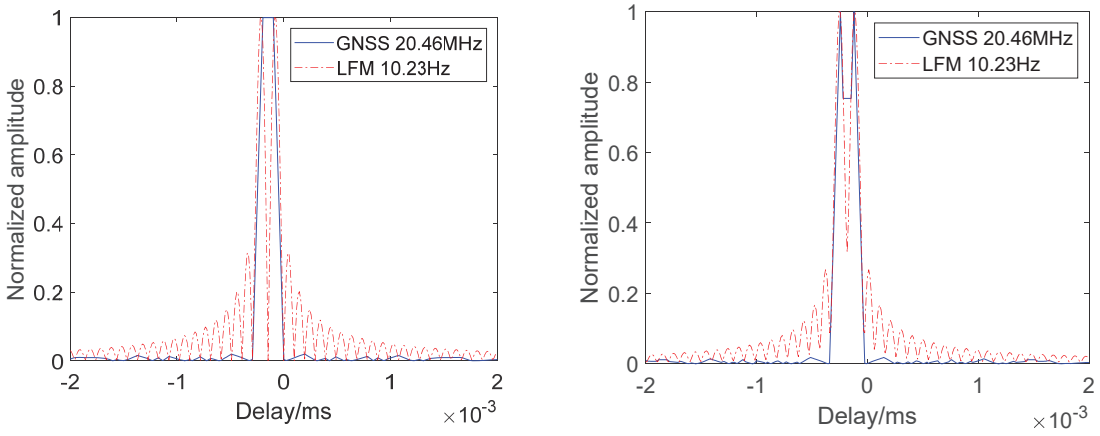

Figure 4. Two-point target detection main lobe curves of GNSS B3I and chirp signals: (**a**) The distance between the two targets is 29 m; (**b**) the distance between two targets is 33 m.

Next, we studied the sidelobe between the two target peaks of the B3I signal detection curves. Figure 5 shows the normalized sidelobe peak curves between two target peaks of the GNSS B3I signal as the distance between two targets. We found that the sidelobe peaks gradually decreased until the distance was more than 30 m, and in the range of 30~60 m, they had a linear decline as the distance increased. The results show that the GNSS B3I signal can realize a clear target peak resolution with an interval of targets near 30 m. After further simulation, we found that 33 m is the suitable interval for B3I signals with clear and smaller peak resolutions.

In BDS-R detection, the echo intervals are smaller than the resolution of the B3I signal, and in the case of bistatic detection, intervals of targets vary with the bistatic angle. To acquire a clear and stable resolution, we propose sampling the echoes with an interval of 33 m, and the RCS data for comparative verification can also be processed with an interval of 33 m.

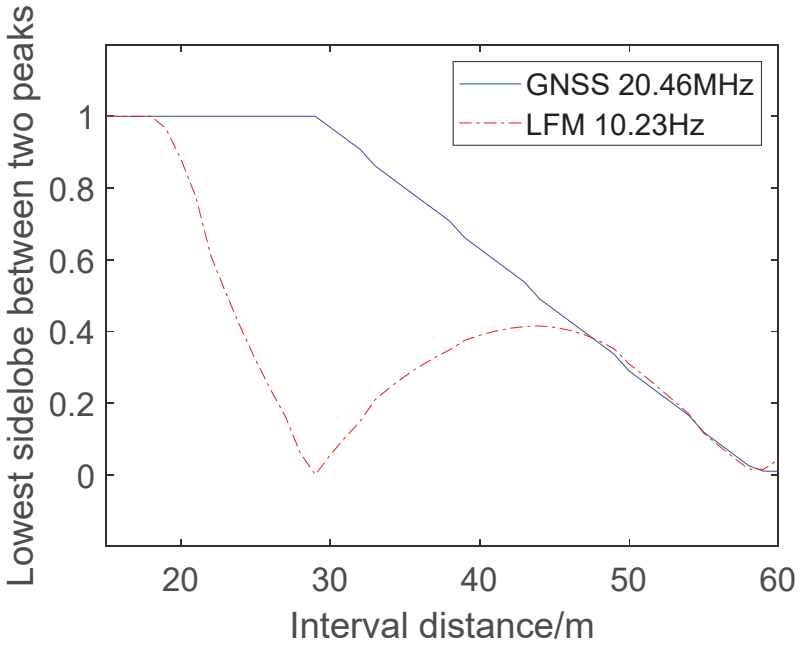

Figure 5. Sidelobe between two main lobe peak ratios of the B3I and chirp signals.

3.3. Resolution Study and Range Inversion Methods

In this section, we study the peak inversion methods. For the limited resolution problem, we propose a correlation peak inversion method to determine the specific range information of targets based on one-dimensional detection data and the corresponding signal autocorrelation function. Moreover, the inversion result accuracy is related to the sampling frequency of the echoes. We propose two methods to find the approximate ranges of target positions in the time domain. In method 1, without target estimation information, we found the range as follows: (1) Acquiring matched filter results, we filtered it with a normalized amplitude > a_0. (2) Next, we divided the results into small segments, between each pair of segments. There is a low amplitude period with a length of b_0, where a_0 and b_0 can be utilized to adjust the target range for better adaptability of detecting targets. In method 2, we can obtain the rough target position in the echoes by rough detection. The inversion ranges can be expressed as $\boldsymbol{Range} = [range_1, range_2, \ldots, range_m, \ldots, range_M]$, and the corresponding sampling points can be expressed as $\boldsymbol{N} = [n_1, n_2, \ldots, n_{\mathrm{m}}, \ldots, n_{\mathrm{M}}]$. The inversion in $range_m$ can be expressed as

$$\sum_{q=1}^{n_m} (s(n - n_m + q) - s(n + q))Amp(q) = M(range_m) \tag{19}$$

where Amp is the modulating amplitude of the received signals. When clutter, noise, and the correlation sidelobe have little influence, the specific radar cross-section (RCS) distribution can be expressed as

$$RCS(range_m) = Amp \tag{20}$$

According to the literature [28], clutter and noise influence can be suppressed effectively during long-term accumulation. Because the RCS of the simulation ship is large, we accumulated 10 s to effectively suppress the clutter and noise in simulation 2 and corrected

the distance and velocity migration. Therefore, we can utilize the inversion method to acquire the specific range information of targets.

3.4. Target Information Inversion Method Based on GNSS-R Detection

In signal processing, the detection results of different satellites can be separated by signal range codes. After acquiring multiple satellite detection results for the targets, the different target peaks in the range dimension can be distinguished when the targets keep a sufficiently large distance. Additionally, we can also distinguish them by the difference in beam direction. To acquire the precise coordinate information of targets in bistatic detection, we can determine the target coordinates by detecting the target range and velocity information, satellite information, and receiver information.

$$N^{i,j} \cdot T_P \cdot \mathrm{C} + r^{i,j} = \sqrt{\left(x_s^i - x_t^j\right)^2 + \left(y_s^i - y_t^j\right)^2 + \left(z_r^i - z_t^j\right)^2} + \sqrt{\left(x_r - x_t^j\right)^2 + \left(y_r - y_t^j\right)^2 + \left(z_r - z_t^j\right)^2} \tag{21}$$

$$\begin{aligned} &\left(\mathbf{v}_r \cdot \theta_r^{i,1} + \mathbf{v}_s^i \cdot \theta_r^{i,2}\right)/\lambda + \left(\mathbf{v}_t^{i,j} \cdot \theta^{i,j,1} + \mathbf{v}_s^i \cdot \theta^{i,j,2}\right)/\lambda \\ &= M^{i,j} \cdot PRF + fd^{i,j} \end{aligned} \tag{22}$$

The target coordinate information can be acquired by the satellite coordinate information from the signal data and the range detection results, as shown in Formula (21). We can also obtain the target velocities through the Doppler detection results as (22), where x_s^i, y_s^i, z_s^i are the coordinates of satellite i, and x_t^j, y_t^j, z_t^j are the coordinates of target j. $N^{i,j}$, and $r^{i,j}$ are the cycle number and distance during a cycle of detected results of target j and satellite i,, respectively. In (22), $\mathbf{v}_t^{i,j} \cdot \theta^{i,j,1}$ expresses the component of the velocity of target i in the direction of the bistatic angular bisector between satellite i and the receiver, and $\mathbf{v}_s^i \cdot \theta^{i,j,2}$ is the component of the velocity of satellite i in the direction of target j. $\mathbf{v}_r \cdot \theta_r^{i,1}$ and $\mathbf{v}_s^i \cdot \theta_r^{i,2}$ are the corresponding velocity components between target i and the receiver. $M^{i,j}$ and $fd^{i,j}$ are the Doppler cycle number and Doppler value of the detected results of target j and satellite i, respectively.

3.5. Experimental Technical Scheme

Figure 6 shows the experimental technical scheme of multiple targets and multiple-GNSS-R-signal detection. The technical route of the detection can be divided into three parts: (1) The BDS MEO satellite information can be obtained from the database [29] and the signal can simulate the parameter, as observed in the literature [27,28]. We found the ship model using the physical optics scattering method and simulated the sea clutter with the weibull distribution model; (2) After establishing the detection model, the echo was simulated and preprocessed. Where the echo was sampled, the distance migration and velocity migration were corrected, and the direct part of echo was suppressed; (3) For the third part, we simulated the DDM, 33-meter one-dimensional range image, and inverse image with multiple-target Doppler compensation, 33-meter peak identifying methods, and inverse methods. The proposed method has been bolded in the picture.

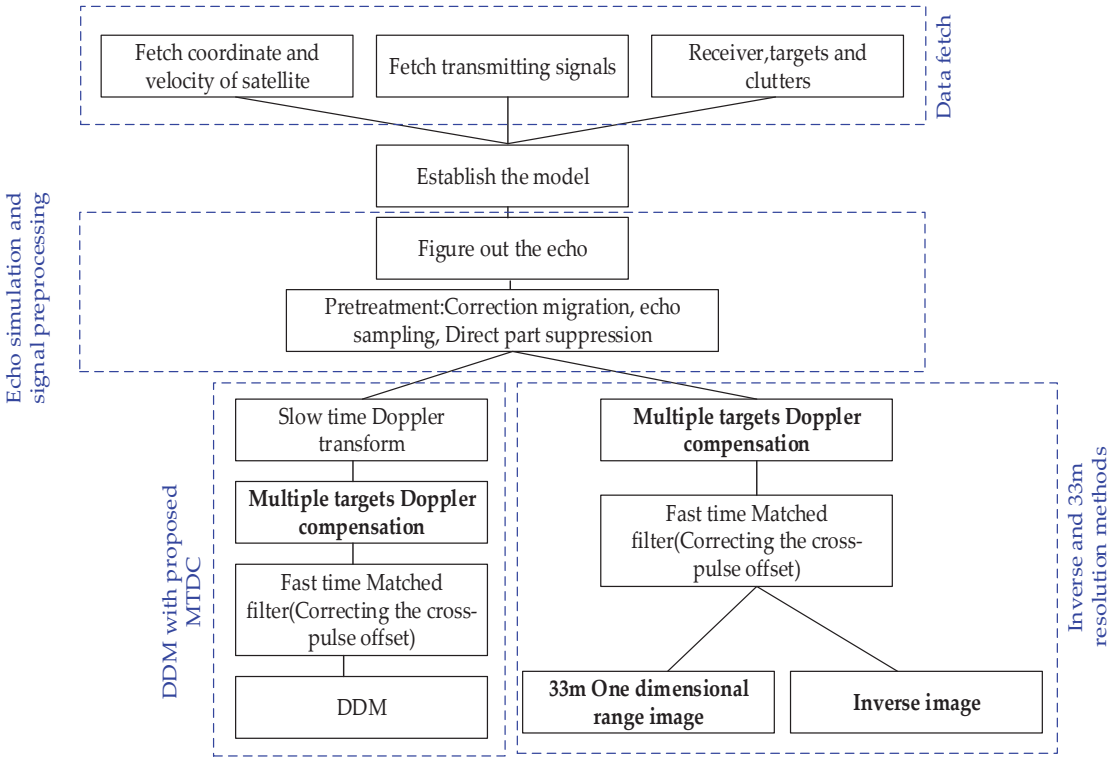

Figure 6. The technical process of multiple GNSS-R signals and multiple-targets detection.

4. Simulation Results and Discussion

In this section, two sets of simulation results are given to evaluate the effectiveness of the proposed MTDC method, the target peaks resolution method and the target peaks range inversion method based on the B3I signal of four BDS satellites and the MIMO system. The system parameters and target parameters are listed in Tables 1 and 2. The geometry schematic diagram of the simulation is plotted in Figure 6, where the receiver was set as airborne-based to better reflect the Doppler frequency difference of each target during GNSS-R detection. During the 10 s pulse accumulation time in simulation 2, we set the receiver plane to move horizontally and at a constant speed according to the given direction and speed, and the ship does not change its track. The influence of the Doppler and distance values instigated by the aircraft movement can be compensated for by the known aircraft movement parameters combined with the geometric model. Additionally, we set the linear delay compensation to be once per pulse period to remove the delay effect caused by ship motion.

4.1. Simulation 1

In simulation 1, we detected three sets of point targets based on the B3I signals of four BDS satellites without considering clutter and noise. The point target information is expressed in Table 2, where the points were set with an interval of 30 m, and its geometric distribution was plotted in Figure 7. In particular, to better study the detection property, the RCS ratios of target 1, target 2, and target 3 were set to 2:5:15.

Table 2. Target parameter.

Simulation 1 Point	***r*/km**	φ_r	**v/m/s**	φ_v	**Interval/m**	**Number**
Target 1	1	150°	15	−120°	30	1
Target 2	1.5	135°	20	−135°	30	5
Target 3	2	60°	20	−120°	30	3
Simulation 2 Ship	***r*/km**	φ_r	**v/m/s**	φ_v	**Length/Width(m)**	
Target 1	1	150°	15	−120°	141/20	
Target 2	1.5	135°	20	−135°	314.6/40.8	
Target 3	2	60°	20	−120°	142/18	

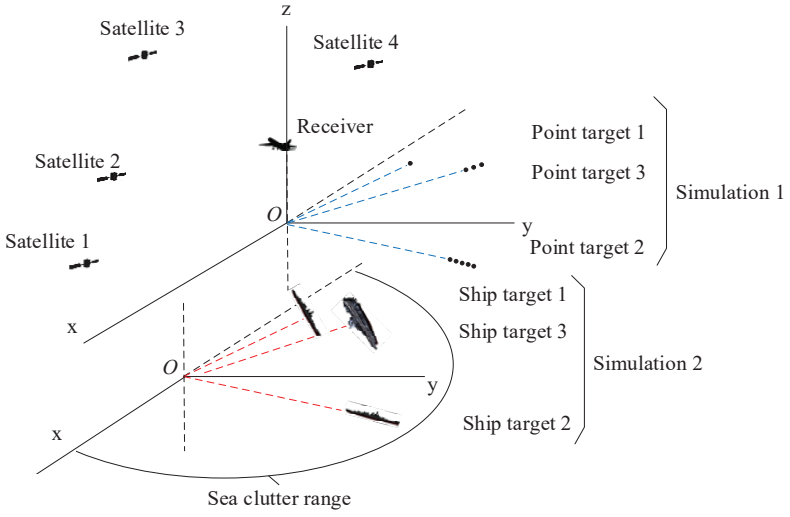

Figure 7. Geometry schematic diagram of multi-signal and multi-target detection simulation.

To study the target peak resolution effectiveness of the sampling method at 33 m, Figures 8 and 9 show the RCS data distribution and one-dimensional range detection results with sampling at 33 m. In Figure 8, the circle line expresses the original RCS distribution of point target 3 under each satellite, and the star line represents the data with a sample at 33 m. In Figure 9, the curves are the detection peaks of point target 3 under each satellite, and its direction and length vary with the detection angle. Taking Figure 8 as a comparison, we found that the small peaks in the detection results of Figure 9 are in good agreement with the sampling data at 33 m in terms of amplitude and range point. The results can be utilized to estimate the RCS distribution of targets and verify target recognition.

To research the Doppler and range information of detection by four satellites, the simulation shows the DDM results of three sets of point targets of the B3I signal from four satellites separately in Figure 10. Because the resolution of B3I is near 30 m, each set of point targets was detected as a few light points in the DDM, and according to the number of points set in each target, we identified that the highlights are target 3, target 2, and target 1, in order from the strongest to the weakest. Among the four detection results, the Doppler frequency of each target ranged from −1000 to 1900 Hz for the high speed and different radiation angle of the satellites, but the difference in the Doppler value among targets was stable at approximately 400 Hz on account of the target points and receiver location. The motion of the receiver and the target determine the Doppler difference among targets. Moreover, the range and velocity information of the detection of four satellites can

determine the target coordinate information using the target information inversion method mentioned previously.

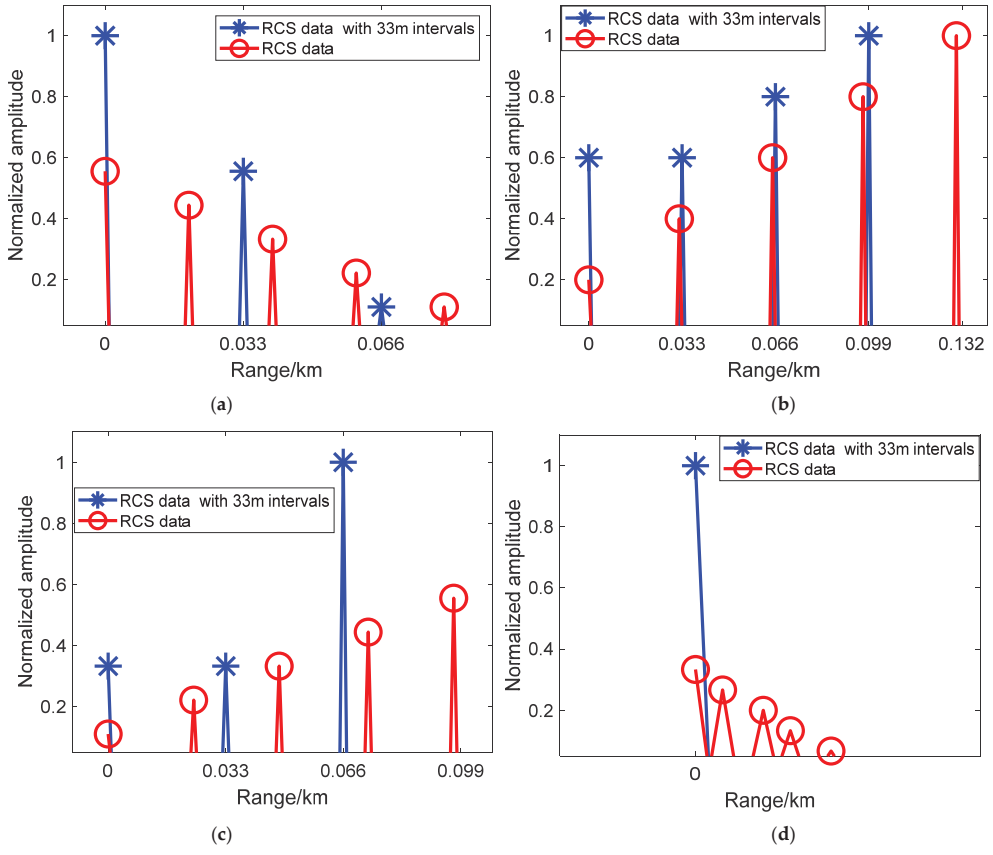

Figure 8. RCS data of point target 3 under the detection of 4 BDS satellites: (**a**) satellite 1; (**b**) satellite 2; (**c**) satellite 3; and (**d**) satellite 4.

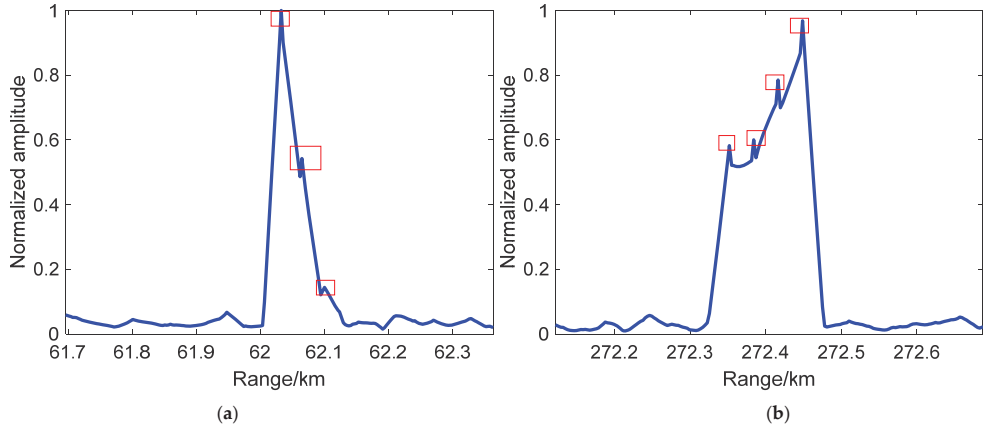

Figure 9. *Cont.*

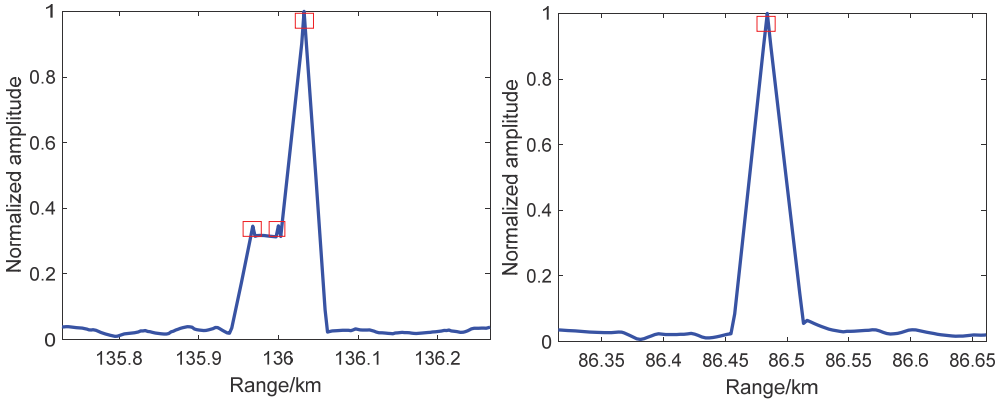

Figure 9. One-dimensional range detection results of point target 3 under the detection of 4 BDS satellites with 33-meter echo sampling: (**a**) satellite 1; (**b**) satellite 2; (**c**) satellite 3; and (**d**) satellite 4.

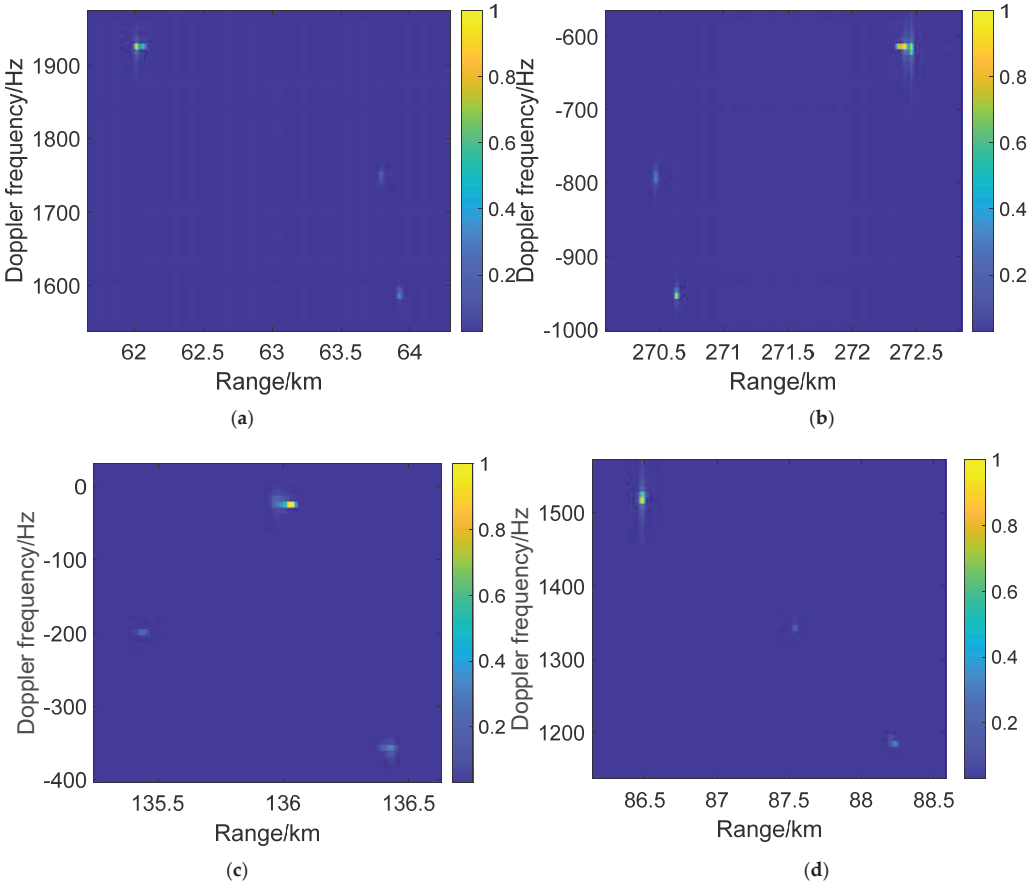

Figure 10. DDM of point targets under the detection of 4 BDS satellites: (**a**) satellite 1; (**b**) satellite 2; (**c**) satellite 3; and (**d**) satellite 4.

4.2. Simulation 2

In simulation 2, we designed a simulation to detect three sets of ship targets based on the B3I signals of satellite 3 considering Gaussian noise and sea clutter based on the Weibull model. The ship target information and geometric diagram are also expressed in Table 2 and Figure 7.

In Figures 11 and 12, we show the Doppler compensation effectiveness comparison of the two compensation methods. In Figure 11, we simulated the one-dimensional range detection compensated results of three ship targets without target estimation information, and the results are compensated for with single Doppler channels and the MTDC method. Figure 11a–c show the incomplete peak amplitudes of three ship targets, and Figure 11d shows the target peaks without Doppler phase influence, which shows the effectiveness of MTDC in estimating no-target information situations. Figure 12 shows the compensation results with acquired target estimation information. Figure 12a–c show that each target peak can return to the normal level under the corresponding Doppler compensation and that other target peaks lose part of their amplitudes. Figure 12d shows the MTDC method compensation results expressing all target peaks, obtaining their maximum level. The results of Figures 11 and 12 verify that the proposed MTDC method can remove the Doppler phase influence of multiple target detection.

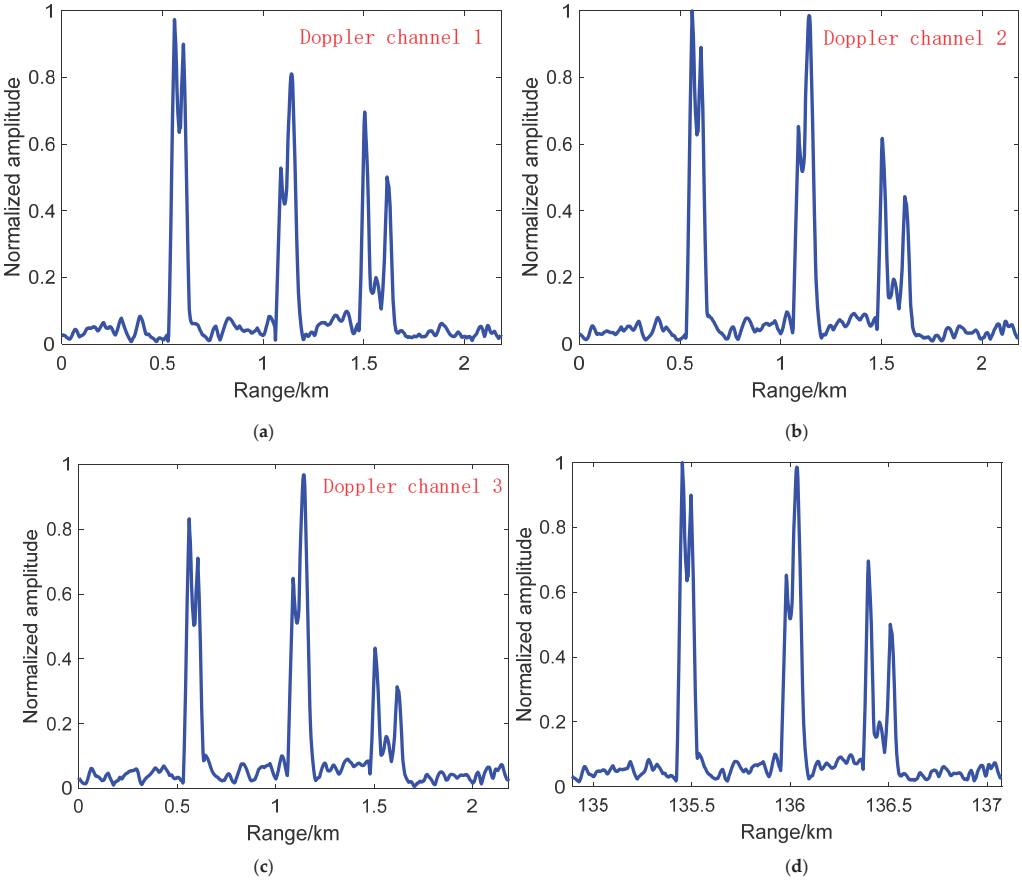

Figure 11. Doppler compensation comparison of method 1 in a one-dimensional range image using B3I signals of satellite 3: (**a**) Results with Doppler channel 1 compensation; (**b**) results with Doppler channel 2 compensation; (**c**) results with Doppler channel 3 compensation; (**d**) results with the proposed MTDC method based on multiple Doppler channels.

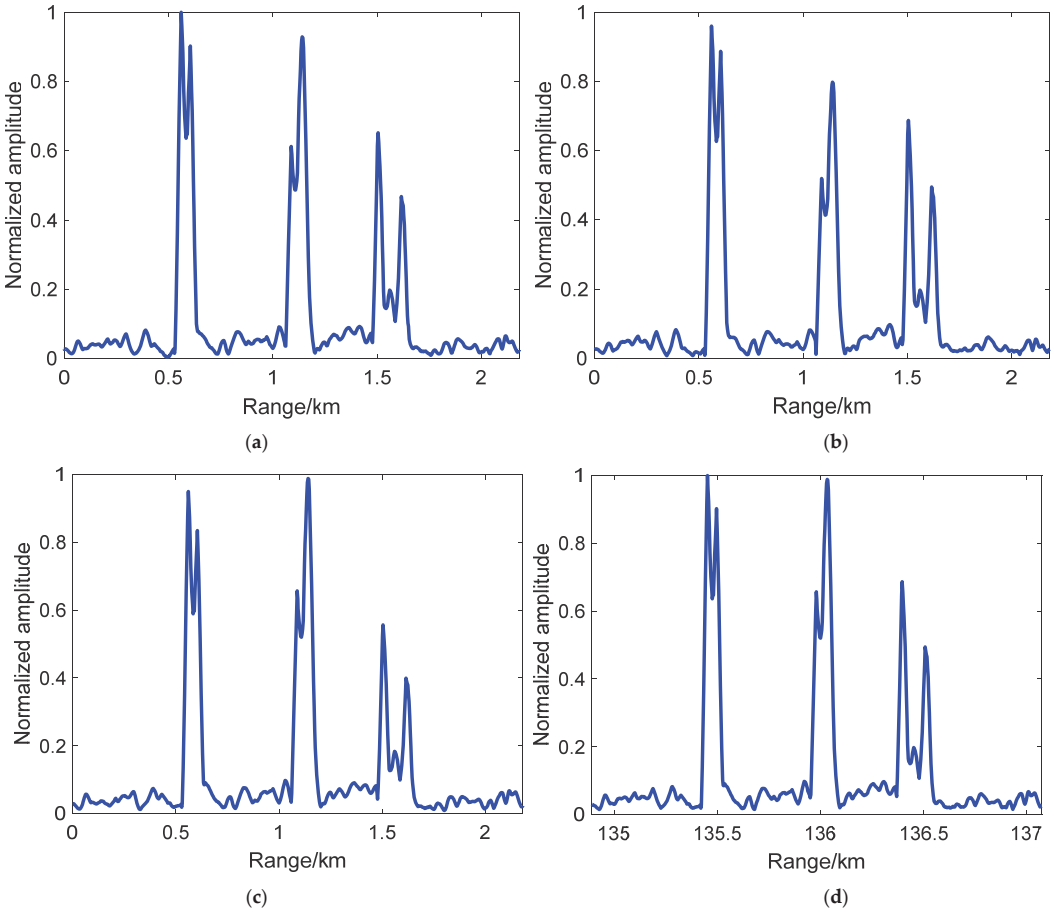

Figure 12. Doppler compensation comparison of method 2 in a one-dimensional range image by B3I signals of satellite 3: (**a**) results with first target Doppler compensation; (**b**) results with second target Doppler compensation; (**c**) results with third target Doppler compensation; (**d**) results with the proposed MTDC method based on multiple estimated target Dopplers.

Based on the same sampling at 33 m, we plotted the one-dimensional range detection results of three ship targets by satellite 3 in Figure 13, where Figure 13a,c,e show the sampling detection results at 3 m and the sampling detection results at 33 m for ships 1, 2, and 3, respectively. Compared with the RCS data of Figure 13b,d,f, we found that the sampling detection at 3 m can express the general outline of the ship's target RCS without accurate amplitude and range point information. The small peaks in the sampling results at 33 m, which are in good agreement with the sampling data obtained at 33 m, express segmented scattering strong points with accurate amplitude and computable range points. The results can be more accurate in the service of target recognition.

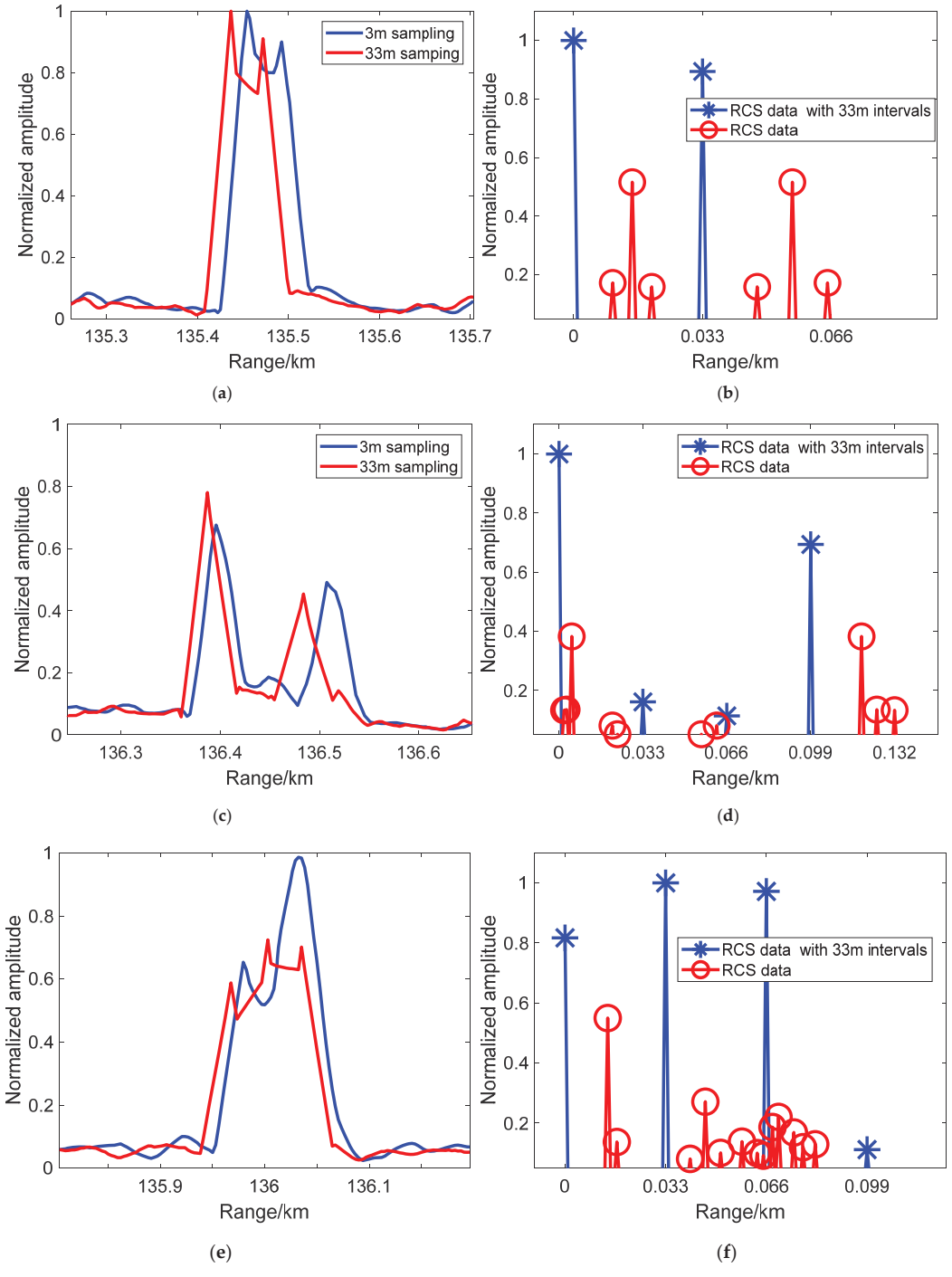

Figure 13. One-dimensional range detection results of 3 ship targets under the detection of satellite 3 with 33-meter echo sampling and 3-meter echo sampling and the corresponding RCS data distribution: (**a**) ship 1 detection result; (**b**) ship 1 RCS data; (**c**) ship 2 detection result; (**d**) ship 2 RCS data; (**e**) ship 3 detection result; (**f**) ship 3 RCS data.

To further study the resolution improvement method, we simulated the detection results of satellite 3 with range inverse methods to acquire the more delicate RCS distribution of targets based on the sampling frequency $fs = 10*B$. Figure 14 shows the range inverse results of method 1, in which we screened the probable target information by amplitude and segment; the results are given by a certain length in the low-amplitude region. The dotted line in Figure 14 expresses the RCS data, and the circle line, which is the inverse result, which does not consider clutter, is in good agreement with the data in terms of the amplitude and range point, especially at strong scattering points. Moreover, we utilized the small square line to express the inverse results with clutter and noise backgrounds with 10 s pulse accumulation. It shows that target peaks can be recognized from clutter and noise backgrounds with the proposed inverse method.

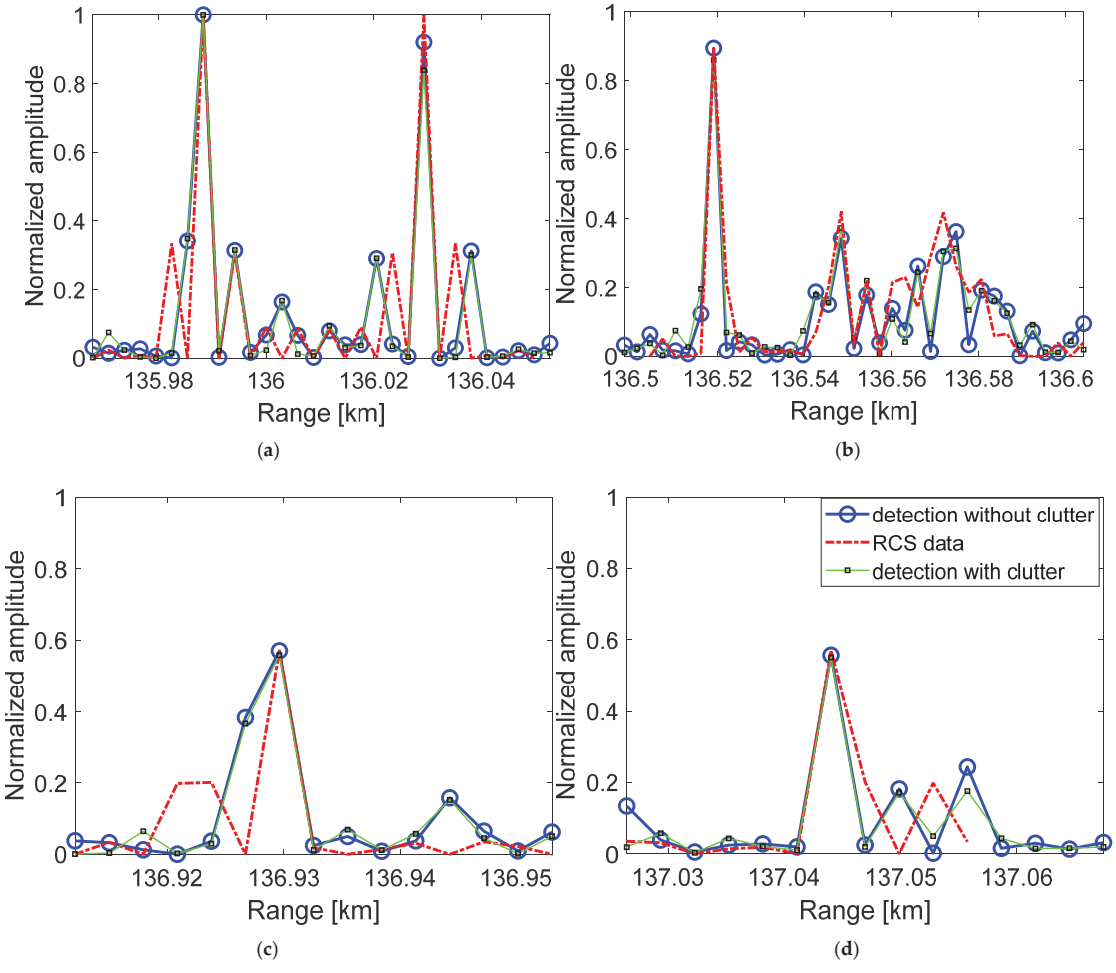

Figure 14. Range inversion results of 3 ship targets under the detection of BDS satellite 3 with range inversion method 1: (**a**) ship 1; (**b**) ship 3; (**c**) left part of ship 2; (**d**) right part of ship 2.

In the other situation, since we have estimated the target information, we can acquire rough target distance ranges and reverse them using the range inverse method 2. Figure 15 shows the range inverse results based on target estimation information, where ship 2 can notably be expressed more completely and accurately than with method 1.

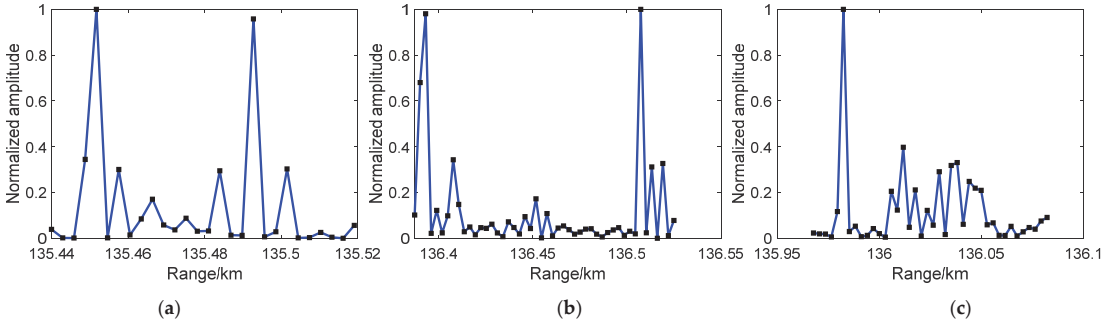

Figure 15. Range inversion results of 3 ship targets under the detection of BDS satellite 3 with target estimation information by range inversion method 2: (**a**) ship 1; (**b**) ship 2; (**c**) ship 3.

Starting from the two dimensions of Doppler and range, Figure 16 plots the DDM results of three ship targets under the detection of the B3I signal of satellite 3, where pictures (a) and (b) express whether the results consider clutter and noise. In Figure 16a, combined with target peak identification and target range inverse results, we found that the highlight groups were target 1, target 3, and target 2 from left to right. The ship targets can be detected as several highlights with a range resolution of near 30 m and a Doppler frequency resolution of approximately 8 Hz. Due to the high speed of the receiver and different received angles, the targets' Doppler frequency varies in the range of 400 Hz, and there are 8 Hz offsets in the scattered point in a target. After introducing clutter and noise backgrounds, Figure 16b shows the detection results with clutter distribution, as shown in Figure 7, with 10 s pulse accumulation. We found a clutter highlight group near the 0 Hz Doppler channel with a normalized amplitude of 0.6. In the range dimension, a few clutter peaks overlapped target 1, which protected the detection of target 1 from clutter influence. Some cluttered peaks overlapped target 2 and target 3, but the cluttered peaks are small and dispersed, which reduces the influence of the detection of the two targets. Moreover, the cluttered strong scatter point does not overlap in the simulation, supporting better detection results for the signal process. This situation has a large probability of overlapping since the scattering intensity of sea clutter is random.

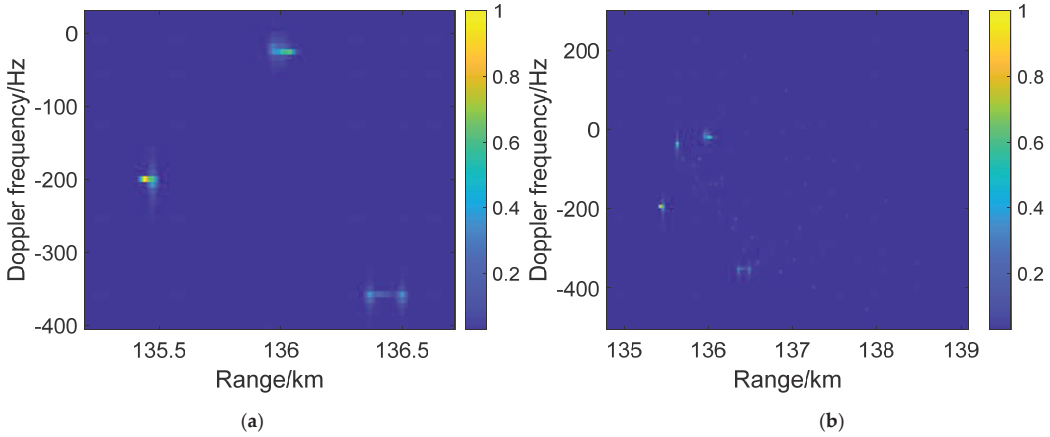

Figure 16. DDM detection results of 3 ship targets under the detection of satellite 3: (**a**) without clutter and noise influence; (**b**) with clutter background.

Figures 12–16 show the one-dimensional range image Doppler compensation results, one-dimensional range image target peak identification results, range inverse results, and DDM results of three ship targets in simulation 2, which verify that multiple fetched ship targets can be detected with better strength using the MDTC method with noise and sea clutter backgrounds in a 10 s accumulation, and the ship RCS distribution structure can be further acquired by the proposed target peak identification method and range inversion method.

5. Conclusions

This paper studies multiple-BDS signal reflection detection for multiple moving targets in the sea. It analyzes the influence of multiple-target Doppler phases and proposes the MDTC method to suppress influence under target estimation and not under target estimation. The results show the proposed method can effectively restore target peaks under the influence of four kinds of Doppler frequencies in GNSS-R detection, where the Doppler frequency variation range is −1000–1900 Hz. For further study of target peak detection, simulations of point target and ship target detection were performed to verify the effectiveness of the proposed peak identification method and range inversion methods. The peak identification results of four satellites and three ship targets showed corresponding peaks which matched the RCS data of detected targets. The range inversion results show a better resolution of target peak detection results, which can obtain the specific RCS distribution of ships in the hundred-meter class. At last, noise and clutter backgrounds were added to simulation 2 under 10 s pulse accumulation, which shows some influence on the sidelobe of target 2 and target 3, and the three target main peaks can still be detected relatively clearly. In the future, we will study the detection simulation of small-scale targets in the sea and detection with various satellite detection angles.

Author Contributions: Conceptualization, methodology, formal analysis, writing—original draft preparation, X.L.; data curation, L.W. and W.J.; writing—review and editing, X.L., J.L. and M.Z.; supervision, M.Z. All authors have read and agreed to the published version of the manuscript.

Funding: This work was supported in part by the National Natural Science Foundation of China under Grant No. 62171351, No. 6217011640, No. 62001343, No. 41901267, and No. 41701386 and the China Postdoctoral Science Foundation under Grant No. 2021T140532.

Data Availability Statement: The satellite coordinates based on the geodetic coordinate system were obtained from http://www.csno-tarc.cn/datacenter/ephemeris (accessed on 1 January 2021). The signal PRN parameters were obtained from literature [27,28].

Conflicts of Interest: The authors declare no conflict of interest.

References

1. Ansari, K.; Bae, T.S.; Seok, H.W.; Kim, M.S. Multiconstellation global navigation satellite systems signal analysis over the Asia-Pacific region. *Int. J. Satell. Commun. Netw.* **2020**, *39*, 280–293. [CrossRef]
2. Li, X.; Zhang, X.; Ren, X.; Fritsche, M.; Wickert, J.; Schuh, H. Precise positioning with current multi-constellation global navigation satellite systems: GPS, GLONASS, Galileo and BeiDou. *Sci. Rep.* **2015**, *5*, 8328. [CrossRef] [PubMed]
3. Southwell, B.J.; Dempster, A.G. Incoherent Range Walk Compensation for Spaceborne GNSS-R Imaging. *IEEE Trans. Geosci. Remote Sens.* **2019**, *57*, 2535–2542. [CrossRef]
4. Huang, F.X.; Garrison, J.L.; Leidner, S.M.; Annane, B.; Hoffman, R.N.; Grieco, G.; Stoffelen, A. A Forward Model for Data Assimilation of GNSS Ocean Reflectometry Delay-Doppler Maps. *IEEE Trans. Geosci. Remote Sens.* **2021**, *59*, 2643–2656. [CrossRef]
5. Giangregorio, G.; Bisceglie, M.D.; Addabbo, P. Stochastic Modeling and Simulation of Delay–Doppler Maps in GNSS-R Over the Ocean. *IEEE Trans. Geosci. Remote Sens.* **2016**, *54*, 2056–2069. [CrossRef]
6. Martin, F.; Camps, A.; Park, H.; DaAddio, S.; Martín-Neira, M.; Pascual, D. Cross-correlation waveform analysis for conventional and interferometric GNSS-R approaches. *IEEE J. Sel. Top. Appl. Earth Observ. Remote Sens.* **2014**, *7*, 1560–1572. [CrossRef]
7. Martin, F.; D'Addio, S.; Camps, A.; Martín-Neira, M. Modeling and analysis of GNSS-R waveforms sample-to-sample correlation. *IEEE J. Sel. Top. Appl. Earth Observ. Remote Sens.* **2014**, *7*, 1545–1559. [CrossRef]
8. Xiao, X.; Shen, F.; Lu, X.C.; Shen, P.L.; Ge, Y.L. Performance of BDS-2/3, GPS, and Galileo Time Transfer with Real-Time Single-Frequency Precise Point Positioning. *Remote Sens.* **2020**, *13*, 4192. [CrossRef]

9. Zhang, P.F.; Tui, R.; Zhang, R.; Liu, N.; Gao, Y. Time and frequency transfer using BDS-2 and BDS-3 carrier-phase observations. *IET Radar Sonar Navig.* **2019**, *13*, 1249–1255. [CrossRef]
10. Feng, Z.; Li, X.-H.; Zhang, H.-J.; Huang, L.-X.; Xu, L.-X. Timing performance evaluation of BDS IGSO-6 and GEO-7 satellite Network. In Proceedings of the Joint Conference of the European Frequency and Time Forum and IEEE International Frequency Control Symposium (EFTF/IFCS), Besancon, France, 9–13 July 2017; pp. 817–820.
11. Tu, R.; Zhang, R.; Liu, Z.K. Real-time detection of BDS orbit manoeuvres based on the combination of GPS and BDS observations. *IET Radar Sonar Navig.* **2020**, *14*, 1603–1609. [CrossRef]
12. Pei, T.D.; Pan, W.; Liu, Y. Research on BDS/GPS dual-mode single point positioning. In Proceedings of the Chinese Automation Congress (CAC), Jinan, China, 20–22 October 2017; pp. 1163–1168.
13. Li, Z.Y.; Huang, C.; Wu, J.; Yang, H.; Yang, J. Over view of maritime target detection techniques using GNSS-Based passive radar (in Chinese). *Radar Sci. Technol.* **2020**, *18*, 404–413.
14. Ma, H.; Antoniou, M.; Pastina, D.; Santi, F.; Pieralice, F.; Bucciarelli, M.; Cherniakov, M. Maritime Moving Target Indication Using Passive GNSS-Based Bistatic Radar. *IEEE Trans. Aerosp. Electron. Syst.* **2018**, *54*, 115–128. [CrossRef]
15. Beltramonte, T.; Braca, P.; Bisceglie, M.D.; Di Simone, A.; Galdi, C.; Iodice, A.; Millefiori, L.M.; Riccio, D.; Willett, P.K. Simulation-Based Feasibility Analysis of Ship Detection Using GNSS-R Delay-Doppler Maps. *IEEE J. Sel. Top. Appl. Earth Observ. Remote Sens.* **2020**, *13*, 1385–1399. [CrossRef]
16. Sun, X.Y.; Xu, L.Z.; Ji, Y.F. An Extremum Approximation ARAIM Algorithm Based on GPS and BDS. *IEEE Access* **2020**, *8*, 30027–30036. [CrossRef]
17. Qin, H.; Liu, P.; Cong, L.; Ji, W. Triple-Frequency Combining Observation Models and Performance in Precise Point Positioning Using Real BDS Data. *IEEE Access* **2019**, *7*, 69826–69836. [CrossRef]
18. Liu, G.J.; Guo, J. Real-time determination of a bds satellite's velocity using the broadcast ephemeris. In Proceedings of the Fourth International Conference on Instrumentation and Measurement, Computer, Communication and Control, Harbin, China, 18–20 September 2014; pp. 478–483.
19. Zhang, B.Q. Research on GPS/BDS single point velocity measurement considering direction constraints. In Proceedings of the IEEE 8th Data Driven Control and Learning System Conference, Dali, China, 24–27 May 2019; pp. 982–986.
20. Ding, W.D.; Wang, J.L. Precise velocity estimation with s stand-alone GPS receiver. *J. Navig.* **2011**, *64*, 311–325. [CrossRef]
21. Zhou, X.K.; Wang, J.C.; Zeng, H.C.; Pei, Z.C. Experimental results for GNSS-R based moving target indication. In Proceedings of the IEEE International Geoscience and Remote Sensing Symposium (IGARSS), Waikoloa, HI, USA, 26 September–2 October 2020; pp. 2819–2822.
22. Park, H.; Camps, A.; Valencia, E.; Carreno-Luengo, H.; Martin, F.; Alonso, A.; Pascual, D. Analysis of gnss-r delay and doppler tracking errors. *IEEE J. Sel. Top. Appl. Earth Obs. Remote Sens.* **2014**, *7*, 1481–1492. [CrossRef]
23. Ji, W.X.; Xiu, C.D.; Li, W.Q.; Wang, L.J. Ocean surface target detection and positioning using the spaceborne GNSS-R delay-Doppler maps. In Proceedings of the IEEE International Geoscience and Remote Sensing Symposium (IGARSS), Quebec City, QC, Canada, 13–18 July 2014; pp. 3806–3809.
24. Cheong, J.W.; Southwell, B.J.; Dempster, A.G. Blind sea clutter suppression for spaceborne GNSS-R target detection. *IEEE J. Sel. Top. Appl. Earth Obs. Remote Sens.* **2019**, *12*, 5373–5378. [CrossRef]
25. Simone, A.D.; Park, H.; Riccio, D.; Camps, A. Sea target detection using spaceborne gnss-r delay-doppler maps theory and experimental proof of concept using TDS-1 data. *IEEE J. Sel. Top. Appl. Earth Obs. Remote Sens.* **2017**, *10*, 4237–4255. [CrossRef]
26. Hu, C.J.; Benson, C.; Park, H.; Camps, A.; Qiao, L.; Rizos, C. Analyzing anomalous artefacts in TDS-1 delay doppler maps. In Proceedings of the IEEE International Geoscience and Remote Sensing Symposium (IGARSS), Yokohama, Japan, 28 July–2 August 2019; pp. 8366–8369.
27. Open Service Signal B3I (Version 1.0). Available online: http://www.beidou.gov.cn/xt/gfxz/201802/P020180209620480385743.pdf (accessed on 1 January 2021).
28. Open Service Signal B1I (Version 1.0). Available online: http://www.beidou.gov.cn/xt/gfxz/201902/P020190227592987952674.pdf (accessed on 1 January 2021).
29. Test and Assessment Research Center of China Satellite Navigation Office. Available online: http://www.csno-tarc.cn/datacenter/ephemeris (accessed on 1 January 2021).

remote sensing

MDPI

Article

Variation Characteristics of Multi-Channel Differential Code Biases from New BDS-3 Signal Observations

Qiqi Shi [1,2] and Shuanggen Jin [1,3,4,*]

[1] Shanghai Astronomical Observatory, Chinese Academy of Sciences, Shanghai 200030, China; qiqishi@shao.ac.cn
[2] University of Chinese Academy of Sciences, Beijing 100049, China
[3] School of Remote Sensing and Geomatics Engineering, Nanjing University of Information Science and Technology, Nanjing 210044, China
[4] School of Surveying and Land Information Engineering, Henan Polytechnic University, Jiaozuo 454000, China
* Correspondence: sgjin@shao.ac.cn; Tel.: +86-021-34775292

Abstract: A multi-frequency Global Navigation Satellite System (GNSS) provides greater opportunities for positioning and navigation applications, particularly the BeiDou Global Navigation Satellite System (BDS-3) satellites. However, multi-frequency signals import more pseudorange channels, which introduce more multi-channel Differential Code Biases (DCBs). The satellite and receiver DCBs from the new BDS-3 signals are not clear. In this study, 9 DCB types of the new BDS-3 signals from 30-days Multi-GNSS Experiment (MGEX) observations are estimated and investigated. Compared with the DCB values provided by the Chinese Academy of Science (CAS) products, the mean bias and root mean squares (RMS) error of new BDS-3 satellite DCBs are within ±0.20 and 0.30 ns, respectively. The satellite DCBs are mostly within ±0.40 ns with respect to the product of the Deutsches Zentrum für Luft- und Raumfahrt (DLR). The four sets of constructed closure errors and their mean values are within ±0.30 ns and ±0.15 ns, respectively. The mean standard deviation (STD) of the estimated satellite DCBs is less than 0.10 ns. In particular, our estimated satellite DCBs are more stable than DCB products provided by CAS and DLR. Unlike satellite DCBs, the receiver DCBs have poor compliance and show an obvious relationship with the geographic latitude when compared to the CAS products. The STDs of our estimated receiver DCBs are less than 1.00 ns. According to different types of receiver DCBs, the distribution of STDs indicates that the coefficient of the ionospheric correction has an influence on the stability of the receiver DCBs under the ionosphere with the same accuracy level. In addition, the type of receiver shows no regular effects on the stability of receiver DCBs.

Keywords: BeiDou Global Navigation Satellite System (BDS-3); Differential Code Biases (DCBs); multi-channel; ionospheric correction

Citation: Shi, Q.; Jin, S. Variation Characteristics of Multi-Channel Differential Code Biases from New BDS-3 Signal Observations. *Remote Sens.* **2022**, *14*, 594. https://doi.org/10.3390/rs14030594

Academic Editor: José Fernández

Received: 11 December 2021
Accepted: 25 January 2022
Published: 26 January 2022

1. Introduction

The Global Navigation Satellite System (GNSS) has been widely used in geosciences and life [1,2]. In particular, China's BeiDou Global Navigation Satellite System (BDS-3) was officially operated for global users on July 31, 2020 [3]. As the first hybrid constellation of navigation satellite systems in the world, BDS-3 has been developing rapidly and providing global services, and can provide positioning, navigation, and timing (PNT) services [4]. BDS-3 transmits other new signals of multiple frequency bands, which is compatible with signals of B1 and B3 provided by the BeiDou regional navigation satellite system (BDS-2). Multi-frequency signals provide plentiful observations for satellite applications but also introduce new errors in the positioning process [5,6]. For example, the difference of hardware delay between the signals of double-frequency bands is designated as the differential code bias (DCB), which affects the accuracies of the ionospheric modeling and GNSS precise positioning [7,8]. There are multiple channels for BDS observations on the same frequency, which are summarized in Table 1 from the Receiver Independent Exchange

(RINEX) format (https://files.igs.org/pub/data/format/rinex305.pdf). Therefore, the multiple DCBs caused by multi-channel signals of BDS-3 should be estimated and analyzed accurately.

Table 1. The pseudorange channels of BDS multi-frequency signals.

System	Freq. Band	Frequency/MHz	Channel Codes of Pseudorange
BDS-2	B2	1207.140	C7I C7Q C7X
BDS-2/3	B1	1561.098	C2I C2Q C2X
	B3	1268.52	C6I C6Q C6X
BDS-3	B1C	1575.42	C1D C1P C1X
	B2a	1176.45	C5D C5P C5X
	B2b	1207.140	C7D C7P C7Z
	B2(a+b)	1191.795	C8D C8P C8X

Generally, the ionospheric total electron content (TEC) and DCB need to be considered simultaneously during the estimation process. Carrier-to-code leveling (CCL) is a common estimation method to extract ionospheric TEC and DCB. It exhibits suitable accuracy and simple implementation with the dual-frequency geometry-free (GF) observation combination [9,10]. Moreover, the method of undifferenced and uncombined precise point positioning (PPP) shows higher estimation accuracy when compared with the CCL [11]. However, the PPP approach introduces external constraints on the receiver coordinates, orbits, and clock errors [12,13]. The above-mentioned methods are only used to extract the ionospheric observations, while DCB estimation should be further considered. Ionospheric correction generally includes two components: external ionospheric models and simultaneous estimation [14]. The empirical ionospheric models and the global ionospheric map (GIM) can be used as external ionospheric models to correct the ionosphere. The empirical ionospheric models mainly include the Klobuchar model, NeQuick model, and BeiDou Global Ionospheric delay correction Model (BDGIM) [15–17]. Since the Ionosphere Working Group (IWG) was created by IGS in 1998, many Ionosphere Associate Analysis Centers (IAACs) continue to generate GIMs with high-precision for GNSS users [18]. To achieve simultaneous estimation, the ionospheric modeling is performed, including the global spherical harmonics (SH) and regional generalized trigonometric series function (GTSF) [19,20]. The Multi-GNSS Experiment (MGEX) network of the International GNSS Service (IGS) has been developed [21] so that more and more stations can track multi-frequency new BDS-3 signals. However, the number of these stations is insufficient for global ionospheric modeling and DCB estimation of BDS-3 signals.

Recently, the ionosphere and DCB of BDS-2/3 have been analyzed and discussed. Xue et al. [22] analyzed the stability of BDS-2 B1I-B2I and B1I-B3I DCBs by using multi-GNSS observations. Zhu et al. [23] verified and analyzed satellite and receiver DCB by employing the BDGIM. MGEX observations are utilized to analyze the stability and systematic bias of BDS-2 and BDS-3 DCBs [24,25]. Deng et al. [26] also estimated multiple satellite DCBs of BDS-3 and compared with the Chinese Academy of Sciences (CAS) and the Deutsches Zentrum für Luft- und Raumfahrt (DLR) products. However, most studies have focused on the DCBs estimation and analysis of BDS B1 and B3 frequency, or between B1/B3 and other frequencies. It has a lack of variation characteristics of satellite and receiver DCBs from new BDS-3 signal observations.

This paper aims to estimate and analyze the satellite and receiver DCBs of the new BDS-3 signals (B1C/B2a/B2b/B2(a+b)). The method of DCB estimation and data are introduced in Section 2. Results are presented in Section 3. Nine DCB types from the MGEX network are estimated and compared with DCB products provided by the CAS/DLR. Besides, four sets of closure errors of satellite DCBs are analyzed in detail, including the distribution and the mean values of closure errors. The accuracy and stability of the BDS-3 receiver DCBs are analyzed. Finally, some discussion and conclusions are given in Sections 4 and 5.

2. Methods and Data

2.1. Ionospheric Estimation Equation

Observations obtained from the files of RINEX format generally include pseudorange and carrier-phase observations. Considering multiple errors, the general observation equations can be expressed as follows [27]:

$$\begin{cases} P^s_{i,j} = \rho^s_i + dt_i - dt^s + d^s_{tro,i} + \mu_j \cdot d^s_{ion,i,1} + d_{i,j} - d^s_{,j} + \varepsilon_P \\ \Phi^s_{i,j} = \rho^s_i + dt_i - dt^s + d^s_{tro,i} - \mu_j \cdot d^s_{ion,i,1} + b_{i,j} - b^s_{,j} + N^s_{i,j} + \varepsilon_\Phi \\ \mu_j = f_1^2 / f_j^2 \end{cases} \quad (1)$$

where P and Φ are the pseudorange and carrier-phase observations, respectively; i and j refer to the receiver and the frequency index, respectively; s denotes the BDS satellite; ρ is the geometric range between the receiver and satellite; dt_i and dt^s are the receiver and satellite clock offsets, respectively; d_{tro} and d_{ion} are the slant tropospheric and ionospheric delays, respectively; μ_j denotes the frequency-dependent multiplier factor; $d_{i,j}$ and $d^s_{,j}$ are the receiver and satellite pseudorange instrumental delays at f_j frequency, respectively; $b_{i,j}$ and $b^s_{,j}$ are the receiver and satellite the carrier-phase hardware delays at f_j frequency, respectively; N denotes the integer ambiguity; and ε_P and ε_Φ are the noises of pseudorange and carrier-phase observations, including multipath, respectively.

For any dual-frequency observations of BDS-3, ionospheric observable can be obtained from GF combined observations, which can be expressed as [28]:

$$\begin{cases} P_4 = P^s_{i,1} - P^s_{i,2} & = (\mu_1 \cdot d_{ion,i,1} - \mu_2 \cdot d_{ion,i,1}) + (d_{i,1} - d_{i,2}) - \left(d^s_{,1} - d^s_{,2}\right) + \varepsilon_{P,4} \\ & = (\mu_1 \cdot d_{ion,i,1} - \mu_2 \cdot d_{ion,i,1}) + DCB_i - DCB^s + \varepsilon_{P,4} \\ \Phi_4 = \Phi^s_{i,1} - \Phi^s_{i,2} = & -(\mu_1 \cdot d_{ion,i,1} - \mu_2 \cdot d_{ion,i,1}) + (b_{i,1} - b_{i,2}) - \left(b^s_{,1} - b^s_{,2}\right) + \left(N^s_{i,1} - N^s_{i,2}\right) + \varepsilon_{\Phi,4} \end{cases} \quad (2)$$

where P_4 and Φ_4 are the GF pseudorange and carrier-phase observations, respectively; DCB_i and DCB^s are the corresponding receiver and satellite DCB, respectively; and $\varepsilon_{P,4}$ and $\varepsilon_{\Phi,4}$ are the noises of GF pseudorange and carrier-phase observations, respectively.

To eliminate the large noise of pseudorange observations P_4 [29], the CCL approach is adopted during one observation arc with no cycle slips. The pseudorange instrumental delay and integer ambiguity remain the same constant in such arcs, so the ionospheric observables after smoothing can be expressed as [14]:

$$P_s = \Phi_4(t_i) - \frac{1}{n}\sum_{n=t_1}^{t_n}\left[P_4(t_i) + \Phi_4(t_i)\right] = -(\mu_1 - \mu_2) \cdot d^s_{ion,i,1} - DCB_i + DCB^s \quad (3)$$

where n refers to the number of measurements during one observation arc.

2.2. Ionospheric Correction Based on GIM

Due to the insufficient distribution of BDS-3 stations, the external ionospheric correction is introduced from GIM provided by the Center for Orbit Determination in Europe (CODE). Then, the single-layer mapping function is used for converting slant TEC (STEC) to VTEC. It can be expressed as follows [30]:

$$\begin{cases} d^s_{ion,i,1} = \frac{40.30}{f_1^2}\mathrm{STEC}^s_i \\ \mathrm{STEC}^s_i = \mathrm{MF} \cdot \mathrm{VTEC}^s_i \\ \mathrm{MF} = \frac{1}{\cos\left[\arcsin\left(\frac{R}{R+H}\sin(\alpha \cdot \mathrm{E})\right)\right]} \end{cases} \quad (4)$$

where MF denotes the mapping function, R is the average radius (6371 km) of the Earth, H is the assumed height (450 km) of the single layer ionosphere, α refers to the model coefficient (0.9782), and E is the satellite elevation angle. VTEC can be obtained by linear

interpolation based on GIM, involving interpolations of two-dimensional space and time series [31].

2.3. DCB Separation and Estimation

After correcting the ionosphere, Equation (3) contains only satellite and receiver DCB. For one-day observation, the DCBs of each satellite and receiver are estimated as one constant, respectively. To solve the singular problem of the equation, the zero-mean condition is adopted to separate the DCBs of satellites and receivers. Namely the sum of the DCBs of all satellites is zero on one day, so Equation (3) can reach full rank [32]. Under this constraint condition, the DCB variations are not affected [33]. The zero-mean condition for BDS-3 satellites can be expressed as:

$$\sum_{s=1}^{N} DCB^s = 0 \tag{5}$$

where N denotes to the total number of BDS-3 satellites observed per day. When the satellites observed are different per day, the zero-mean condition will be inconsistent. In that case, the conversion method needs to be implemented for unified zero-mean condition [25].

Based on Equations (3)–(5), the DCB estimation by employing CODE's GIM can be rewritten as:

$$\begin{cases} P_s - \frac{40.30\left(f_1^2 - f_2^2\right)}{f_1^2 f_2^2} \cdot \mathrm{MF} \cdot \mathrm{VTEC}_i^s = -DCB_i + DCB^s \\ \sum\limits_{s=1}^{N} DCB^s = 0 \end{cases} \tag{6}$$

Finally, the cut-off elevation angle is set to 15° to reduce the impact of multipath noise and mapping function errors [10]. To get an arc without cycle slips, the MW (Melbourne–Wübbena combination) and ionospheric residual observations are used to process the sequence of GF observations [28].

2.4. Experimental Data

With the development and updating of MGEX stations, increasingly more stations can track the BDS-3 new signals. Eighty-eight stations of the MGEX network collected from a period of 30 days, corresponding to the day of year (DOY) 060-089 in 2021, were processed to estimate DCBs of BDS-3. Figure 1 shows the distribution of the MGEX stations with tracking the BDS-3. It can be seen from Figure 1 that the distribution of the stations tracking the BDS-3 new signals is inadequate and uneven, so a single BDS-3 system cannot implement the global ionospheric modeling yet. According to the multi-channel type of BDS-3 in the observation file, we estimate 9 DCB types of BDS-3 new signals. The channel type depends on the type of station receiver. Table 2 shows pseudorange observation channels and corresponding frequency bands used to estimate 9 DCB types in our study. As we can see from Table 2, the number of stations with receiving new BDS-3 signals is still less than GPS stations in the hundreds. In particular, the C7Z-C8X combination has only 19 stations that can be used for DCB estimation.

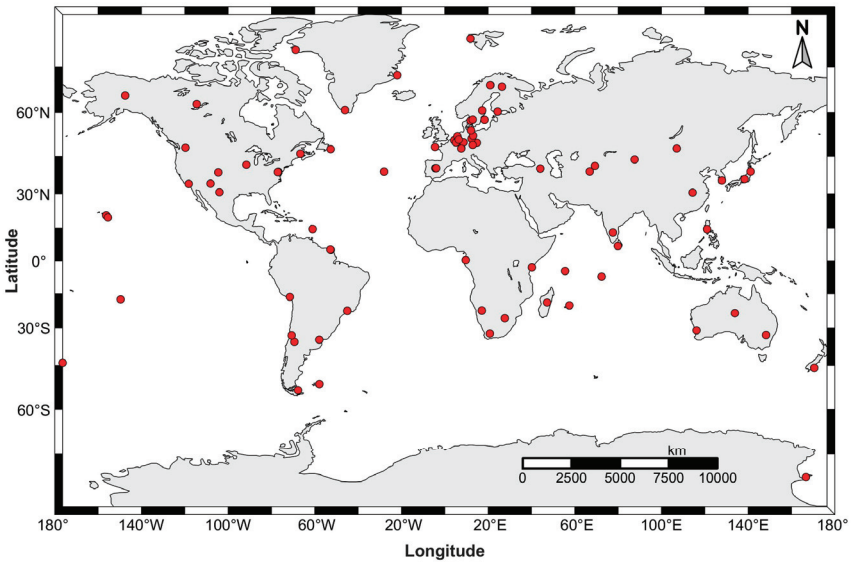

Figure 1. Distribution of MGEX stations with tracking the new BDS-3 signals.

Table 2. Nine types in the DCB estimation of BDS-3.

Freq. Band	Pseudorange Observation Channels			
	Combination 1	Stations Number	Combination 2	Stations Number
B1C-B2a	C1P-C5P	60	C1X-C5X	28
B1C-B2b	C1P-C7D	43	C1X-C7Z	23
B2a-B2b	C5P-C7D	42	C5X-C7Z	23
B1C-B2(a + b)			C1X-C8X	21
B2a-B2(a + b)			C5X-C8X	23
B2b-B2(a + b)			C7Z-C8X	19

3. Results and Analysis

3.1. Quality Analysis of New BDS-3 Signal

To assess the quality of the new BDS-3 signals, we analyze the multipath (MP) combination of multi-channel signals. Figure 2 shows MP values of BDS-3 C19, C37, C38, and C45 satellites during the DOY 60–89, 2021, which are observed at stations PTGG and FFMJ. The digits represent the root mean squares (RMS) of MP. As shown, the MP values vary within ±2 m. The signal quality of C1P/C5P/C7D channels is not significantly different. The RMS of C1X(B1C) MP is significantly larger than the other three channels. Nevertheless, MP of the C8X (B2) channel has satisfying signal performance. Thus, it can be seen the signal quality of B1C frequency is the worst and that of B2(a+b) frequency is the best.

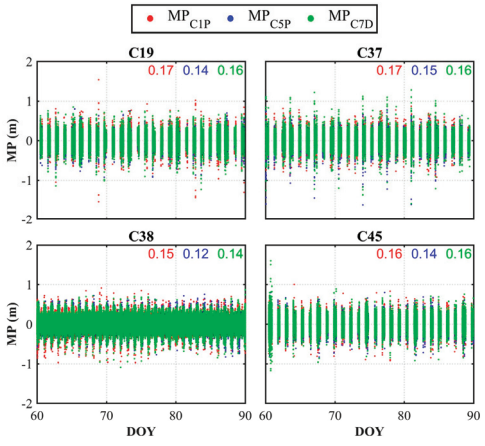

(**a**) PTGG

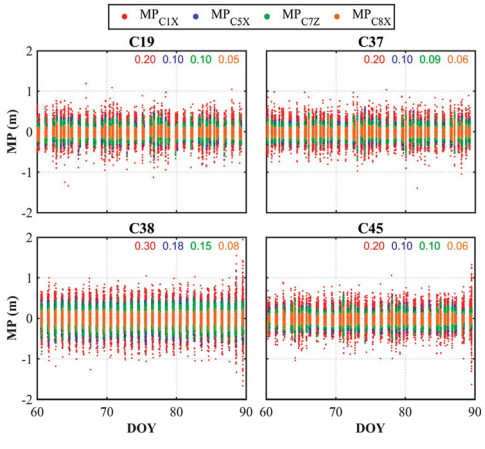

(**b**) FFMJ

Figure 2. MP of the BDS-3 C19, C37, C38, and C45 satellites at stations PTGG (**a**) and FFMJ (**b**) during a period of 30 days.

3.2. Validation of Satellite DCBs

CAS and DLR analysis centers (ACs) provide DCB products for BDS-3 signals but do not include all DCB types. To validate the accuracy of DCBs within the 30 days estimated in this paper, we analyzed statistics of the DCBs, including mean bias and RMS, with CAS and DLR products. Figure 3 depicts the statistical results of 4 DCB types with the direct value provided by CAS products. The mean bias and RMS of satellite DCBs vary within ±0.20 ns and 0.30 ns, respectively. The results show our estimated DCBs have better consistency with the direct DCB value provided by CAS products. Owing to the DLR only provides DCB types between C2I and other channels, we calculated the conversion value of DCBs between the channels of BDS-3 new signal by using DLR products. The mean bias and RMS of 6 satellite DCB types are shown in Figure 4. The results of comparison with DLR products are inferior to the previous result with CAS and are mostly within ±0.40 ns. According to the error propagation principle, the cumulative error of the converted value can lead to a larger deviation of the result. In particular, C45 and C46 are obviously difference. Compared with CAS products and our estimated results, it is found that the values of DLR products deviate. This may be related to corresponding satellite stability and observation

quality. Finally, the time series of C1P-C5P of DCB and the differences with respect to CAS products are shown in Figure 5. The estimated DCB of C1P-C5P varies between the −79.00 and 23.00 ns, and the differences vary within ±0.30 ns. It can be seen that the time series DCB of C1P-C5P are stable and consistent with the DCB provided by CAS products.

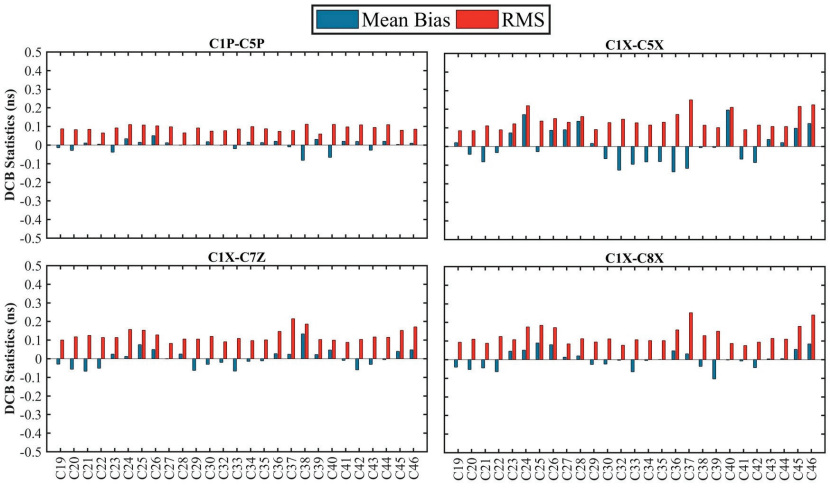

Figure 3. The mean bias and RMS of our estimated C1P-C5P, C1X-C5X, C1X-C7Z, and C1X-C8X, of BDS-3 satellite DCBs, with respect to the direct values provided by CAS products.

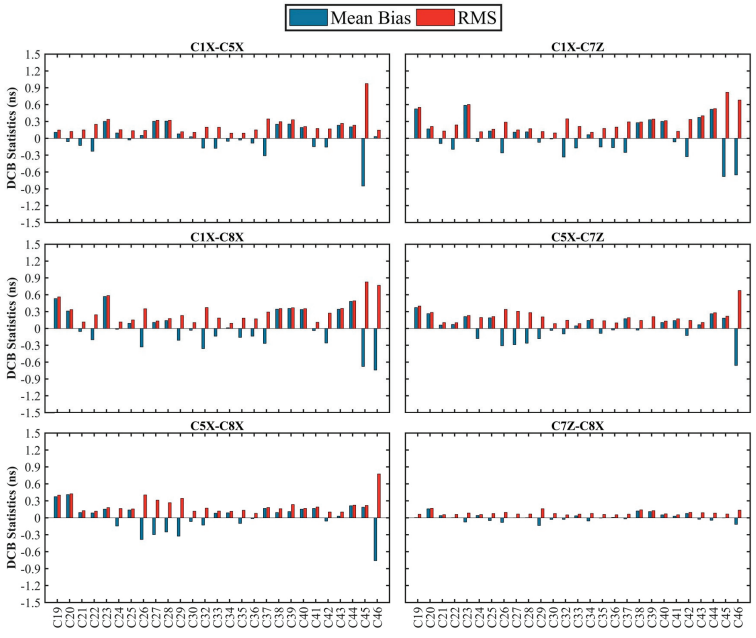

Figure 4. The mean bias and RMS of our estimated C1X-C5X, C1X-C7Z, C1X-C8X, C5X-C7Z, C5X-C8X, and C7Z-C8X, of BDS-3 satellite DCBs, with respect to the conversion values provided by DLR products.

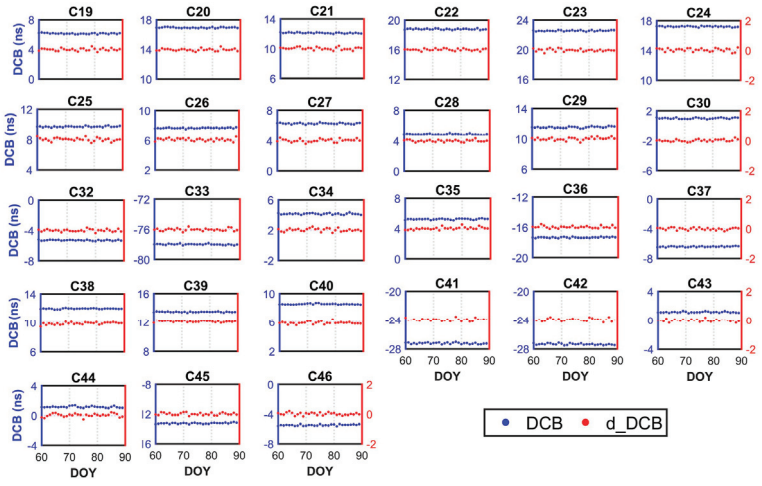

Figure 5. DCB time series of BDS-3 C1P-C5P during a period of 30 days, and the differences time series with respect to CAS products.

The stability of satellites during long time series is an important index to evaluate the accuracy of DCBs. Figure 6 shows the distribution of deviation between 9 DCB types of BDS-3 satellites and the corresponding mean values. The deviations of 9 DCB types vary within ±0.30 ns for the whole distribution. The optimal deviation is less than 0.10 ns, particularly for the C5P-C7D and C7Z-C8X. Table 3 summarizes the mean values of the standard deviation (STD) of BDS-3 DCBs of DLR, CAS, and our results. Our results are consistent with the stability of DCBs provided by CAS products. The conversion values of DCB provided by CAS and DLR products are less stable than our estimated DCBs. DCBs provided by DLR products related to C1X and C5X channels exhibit instability in C45 and C37 satellites. Our estimated DCBs of C37 satellites show instability in the C1X channel. This indicates that the stability levels of our estimated DCB and CAS are the same, but the conversion values of DCB provided by DLR products are slightly less stable.

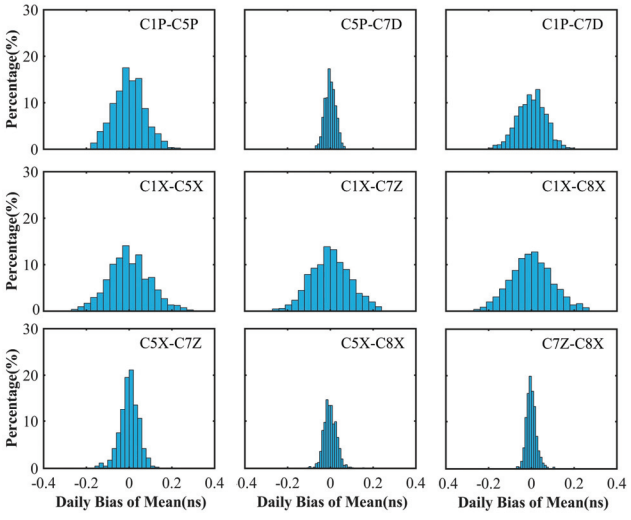

Figure 6. Distribution of deviations between nine DCB types of BDS-3 satellites and the corresponding mean values.

Table 3. Mean STD of BDS-3 DCBs of DLR, CAS, and our results, showing the corresponding satellite psuedo random noise (PRN); the bold types are the direct values provided by CAS products.

Type	CAS			DLR			Our Results		
	Max	Min	Mean	Max	Min	Mean	Max	Min	Mean
C1P-C5P	**0.115 (C42)**	**0.040 (C39)**	**0.076**				0.100 (C42)	0.049 (C39)	0.072
C1P-C7D							0.087 (C34)	0.045 (C38)	0.066
C5P-C7D							0.036 (C43)	0.013 (C26)	0.025
C1X-C5X	**0.128 (C30)**	**0.050 (C40)**	**0.087**	0.470 (C45)	0.065 (C40)	0.125	0.195 (C37)	0.050 (C27)	0.092
C1X-C7Z	**0.118 (C36)**	**0.056 (C40)**	**0.092**	0.465 (C45)	0.079 (C44)	0.130	0.168 (C37)	0.049 (C30)	0.091
C5X-C7Z	0.120 (C36)	0.035 (C40)	0.075	0.215 (C39)	0.073 (C36)	0.111	0.075 (C37)	0.023 (C27)	0.042
C1X-C8X	**0.131 (C46)**	**0.066 (C40)**	**0.097**	0.490 (C45)	0.080 (C35)	0.129	0.191 (C37)	0.043 (C27)	0.095
C5X-C8X	0.117 (C44)	0.039 (C40)	0.071	0.213 (C39)	0.065 (C36)	0.104	0.052 (C22)	0.016 (C23)	0.029
C7Z-C8X	0.085 (C22)	0.021 (C40)	0.055	0.093 (C43)	0.040 (C24)	0.060	0.051 (C29)	0.011 (C40)	0.022

3.3. Internal Coincidence of Satellite DCB

According to the nine estimated DCB types, four sets of closure errors can be constructed, including C1P-C5P-C7D, C1X-C5X-C7Z, C1X-C5X-C8X, and C1X-C7Z-C8X. Figure 7 shows the distribution of four sets of closure errors for all BDS-3 satellites. The fluctuation in closure error is within ±0.30 ns. The closure errors of C1P-C5P-C7D are less than 0.10 ns by using more stations. From the normal distribution curve, the distribution of BDS-3 satellites closure error conforms to the condition under the influence of random noise. Moreover, the corresponding mean closure error is also depicted in Figure 8. The mean closure errors of all DCB types are less than 0.15 ns. Echoing the conclusion above, the C1P-C5P-C7D set has the smallest closure error, which relates to the use of more stations. The closure errors of the C37 satellite related to the C1X channel are larger, indicating its poor stability.

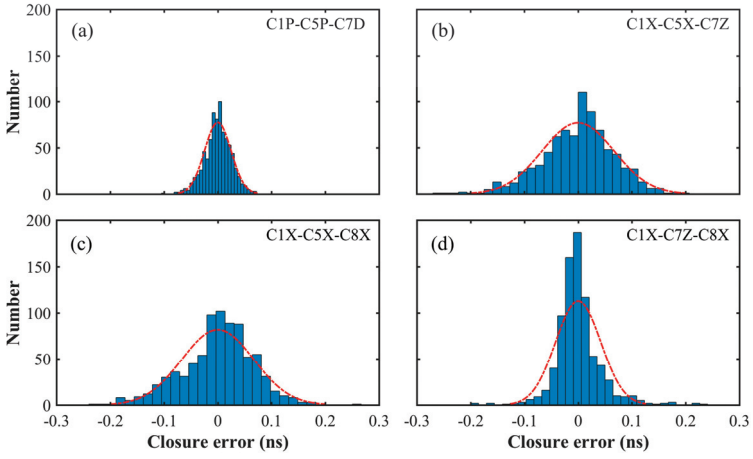

Figure 7. Distribution of BDS-3 satellites C1P-C5P-C7D (**a**), C1X-C5X-C7Z (**b**), C1X-C5X-C8X (**c**), and C1X-C7Z-C8X (**d**) closure errors. The red line denotes the fitted normal distribution curve.

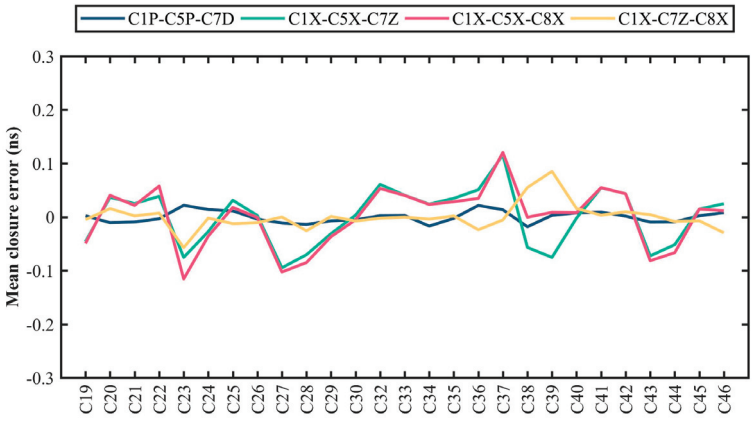

Figure 8. Mean closure error of BDS-3 satellites C1P-C5P-C7D, C1X-C5X-C7Z, C1X-C5X-C8X, and C1X-C7Z-C8X.

3.4. Validation and Variation of Receiver DCBs

To evaluate variation characteristics of receiver DCBs, we classify experimental stations in terms of receiver types, which are summarized in Table 4. According to the receiver tracking the channel types of BDS-3 new signals, the observation channels consist of two sets, i.e., C1P/C5P/C7D and C1X/C5X/C7Z/C8X. The former receiver types belong to Septentrio (SEPT), and the latter receiver types belong to TRIMBLE and JAVAD (https://files.igs.org/pub/station/general/IGSNetwork.csv) [21]. The corresponding station names are also given. As a matter of common knowledge, the stability of receiver DCBs is not as good as satellite DCBs, and it is susceptible to receiver hardware and changes in the external environment. Besides, receiver DCBs provided by CAS tracking BDS-3 new signals are not continuous for 30 days. Thus, we only compare our estimated receiver DCBs with their corresponding values provided by CAS products during 30 days.

Table 4. Station and receiver information for BDS-3 DCB estimation.

Observation Channels	Receiver Type	Station					
C1P/C5P/C7D	SEPT POLARX5TR	AMC4	BREW	BRUX	CEBR	GAMG	GODE
		HARB	KOUG	MGUE	NLIB	NNOR	ONSA
		PARK	SPT0	STJ3	THTG	USN7	YEL2
	SEPT POLARX5	ABPO	ALIC	AREG	ARUC	CHPI	DGAR
		FAA1	FALK	GOP6	HAL1	IISC	JPLM
		KIR0	KIRU	KITG	KOUR	MAL2	MAO0
		MAR6	MDO1	METG	MIZU	MKEA	NKLG
		NYA2	OUS2	PTGG	QAQ1	REDU	SANT
		SCOR	SEYG	SUTH	THU2	USUD	VACS
		VILL	VIS0				
	SEPT POLARX5E	KOS1					
	SEPT ASTERX4	KIT3	RIO2	TASH			
C1X/C5X/C7Z/C8X	TRIMBLE ALLOY	BRST	CHPG	LMMF	OWMG	UNB3	
		ARHT	BRMG	FFMJ	GCGO	GODN	GODS
	JAVAD TRE_3 DELTA	HUEG	LEIJ	MET3	PIE1	SOD3	TIT2
		WARN	WTZZ				
	JAVAD TRE_3	ENAO	LPGS	POTS	SGOC	SUTM	ULAB
		URUM	WIND	WUH2			

When the estimated results of satellite DCBs are relatively stable, the estimation of receiver DCBs is also directly subject to ionospheric delay estimation or correction. The accuracy of the ionospheric modeling is also closely related to geographic latitude.

Hence, the geographic latitude is taken as the horizontal axis to analyze receiver DCBs. Figure 9 shows the RMS of four receiver DCB types, including C1P-C5P, C1X-C5X, C1X-C7Z, and C1X-C8X, which are dotted in different colors. Overall, the RMS of receiver DCBs vary within 2.50 ns. The RMS show an obvious relationship with the geographic latitude. The RMS mostly exceed 1.00 ns at low latitudes between −30° and 30°. However, higher consistency exists between our estimated receiver DCBs and CAS products in middle and high latitudes. Statistics for RMS of four receiver DCB types are depicted in Figure 10, including the maximum, minimum, and mean for each DCB type. The RMS of our estimated receiver DCBs is mostly less than 1.50 ns with respect to CAS. There is an equivalent accuracy among C1X-C5X, C1X-C7Z, and C1X-C8X DCBs. Because there are more low-latitude stations used to estimate C1P-C5P, the RMS values are relatively large. Finally, we calculate the mean value for RMS of our estimated receiver DCBs, which is about 0.68 ns. Considering the previous satellite DCB analysis, this phenomenon is caused by higher ionospheric activity at lower latitudes and the different ionospheric modeling strategies from CODE and CAS.

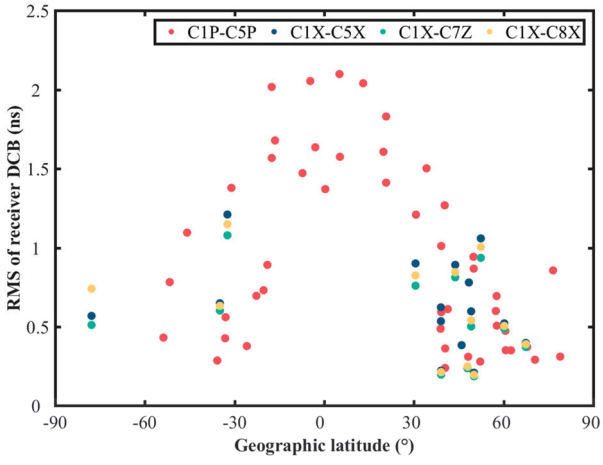

Figure 9. RMS error of the estimated BDS-3 receiver DCBs with respect to the products provided by CAS during the period of DOY 60–89 in 2021.

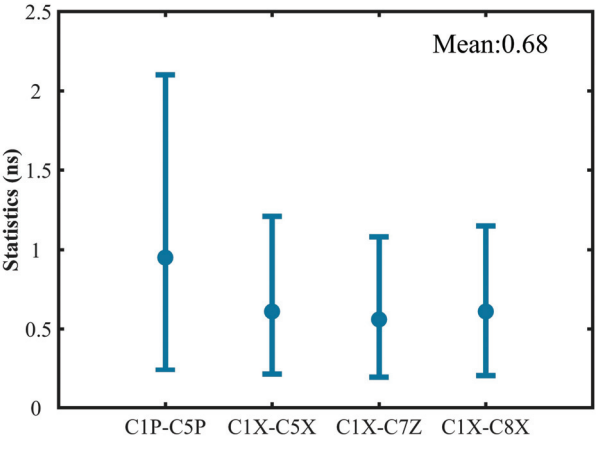

Figure 10. Statistics for RMS error of the estimated BDS-3 receiver DCBs with respect to the products provided by CAS during the period of DOY 60–89 in 2021.

Figure 11 shows the STDs for all BDS-3 receiver DCB types in our study. Most STD values are less than 0.50 ns, and all of them are less than 1.00 ns. This indicates the receiver DCBs have poor stability compared with satellite DCBs. In addition, it can be seen that the receiver DCB types associated with the B1C(C1P/C1X) frequency are less stable than other types. As shown by the digitals in this figure, the absolute values of coefficient for ionospheric correction term increase due to the use of the dual-frequency observation with a larger frequency difference. The accuracy of ionospheric products provided by CODE is 2-8 TEC Unit (TECU) [34]. Coefficients with large absolute values can amplify the ionospheric errors under the ionospheric corrections with the same accuracy level, thus leading to the unstable estimated receiver DCBs. In terms of different colored dots, there is not a significant regularity. Thus, it can be explained that the type of receiver has no critical determinant for its stability.

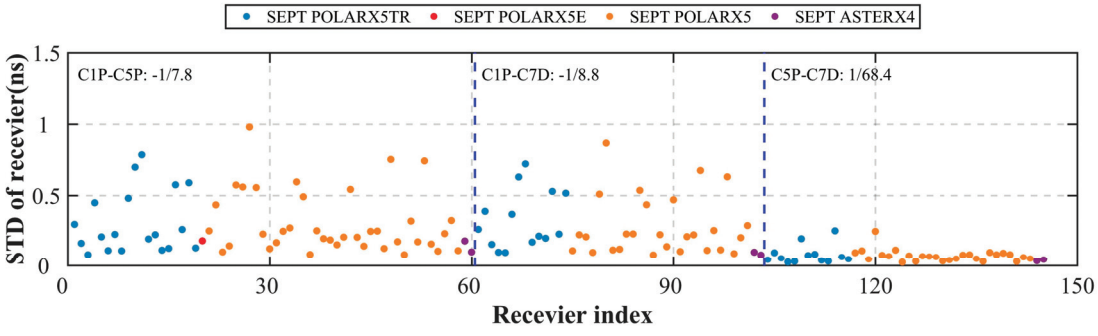

(**a**) Receivers of C1P/C5P/C7D channels.

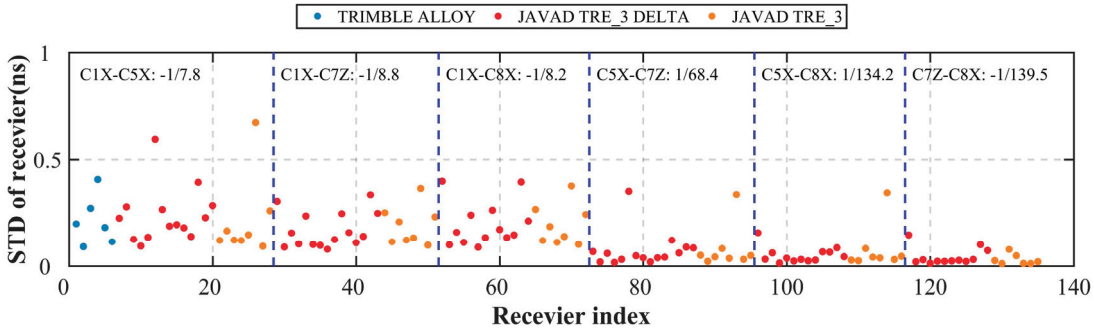

(**b**) Receivers of C1X/C5X/C7Z/C8X channels.

Figure 11. Distribution of STDs for all BDS-3 receiver DCB types of C1P/C5P/C7D channels (**a**) and C1X/C5X/C7Z/C8X channels (**b**) during the period of DOY 60–89 in 2021. Receiver index is arranged according to the classification and order in Table 4. The digitals represent coefficients of the ionospheric correction with corresponding DCB types.

4. Discussion

The satellite and receiver DCBs of new BDS-3 signals are estimated and analyzed in this paper. The MP values of BDS-3 new signals show that the B1C signal quality is slightly worse at the highest frequency, which is significantly affected by MP and other noises. Comparing our estimated results with CAS and DLR products, the DCB values with respect to the C45 and C46 satellites in DLR products have a deviation. When fewer available stations are used to estimate DCB products, the quantity and quality of observables have

a large impact on the stability of satellite DCB estimates. Satellite DCB estimates are susceptible to poor quality observations and thus result in systematical bias and instability.

The receiver DCBs of the new BDS-3 signals exhibit an obvious relationship with the geographic latitude. The latitudinal dependence of receiver DCB estimates is consistent with Li et al. [24] and Wang et al [25]. Different ionospheric coefficients have a significant influence on the stability of receiver DCBs. Under the ionospheric corrections with the same accuracy level, the ionospheric coefficient with a larger absolute value will amplify the errors in the process of error propagation. Although the STDs of receiver DCBs show no obvious relationship between the type of receiver and its stability, this relationship also needs to be further analyzed and validated for latitude, temperature, and other influencing factors [22,35].

Because there are only a few MGEX stations with tracking such channel codes of observation, the DCB estimation does not cover all the channel codes, such as C1X-C7D and C5X-C7D. The DCB types can be further estimated and analyzed when more stations are established by tracking the relevant channel codes of observation in the future.

5. Conclusions

As the main error source of multi-frequency BDS signal applications, the DCBs of new BDS-3 signals (B1C/B2a/B2b/B2(a+b)) are estimated and analyzed systematically in this paper. The nine sets of DCB types are constructed using the 88 stations from the MGEX network for 30 days. The main conclusions are summarized as follows:

1. Compared to the direct DCB values provided by CAS products, the mean bias and RMS of satellite DCBs are within $\pm$0.20 and 0.30 ns, respectively, while the results are mostly within $\pm$0.40 ns when compared with the DLR products.
2. By analyzing STD values for each DCB type, our estimated DCBs are more stable than CAS and DLR products. In particular, DCBs of DLR products related to the C1X channel of the C45 satellite have poor stability, leading to a deviation from our estimation and CAS product.
3. Four sets of constructed closure errors are within 0.30 ns, and their mean values are less than 0.15 ns, indicating that our estimated satellite DCBs of BDS-3 have high precision.
4. The RMS of receiver DCBs is mostly less than 1.50 ns with respect to CAS products. An obvious relationship is found between RMS values and the geographic latitude, e.g., the RMS of C1P-C5P DCB with more than 1.00 ns for stations in low latitude areas. Almost all the receivers of C1X/C5X/C7Z/C8X channels are located at middle and high latitudes, so the receiver DCBs are better consistent with CAS products.
5. The STDs of BDS-3 receiver DCBs are within 1.00 ns, which are not as stable as satellite DCBs. The STDs of different receiver types show no significant differences. However, the coefficients of ionospheric correction obtained by different frequencies differ significantly.

Although the BDS-2/3 system has been fully built, the number of stations with tracking new BDS-3 signals is far less than GPS. To promote precise applications of multi-frequency BDS-3, more stations with tracking full frequencies of BDS-3 signals need to be established, which will contribute to ionospheric modeling and DCBs estimation.

Author Contributions: Conceptualization of the Manuscript Idea: S.J. and Q.S. Methodology and Software: Q.S.; Supervision and Funding Acquisition: S.J.; Q.S. wrote the original draft preparation; S.J. reviewed and edited this paper. All authors have read and agreed to the published version of the manuscript.

Funding: This research was funded by National Natural Science Foundation of China (NSFC) Project, grant number 12073012.

Data Availability Statement: The BDS observation data from IGS MGEX networks can be obtained https://cddis.nasa.gov/archive/gps/data/daily/. The precise orbit products from GFZ are available at https://www.gfzpotsdam.de/GNSS/products/mgex/. The GIM products from CODE are

available at https://cddis.nasa.gov/archive/gnss/products/ionex/. The DCB products provided by CAS and DLR can be obtained at https://cddis.nasa.gov/archive/gnss/products/bias/.

Acknowledgments: The authors thank IGS for providing the BDS observation data of MGEX networks, DLR/CAS for providing the DCB products, CODE for providing the GIM products, and GFZ for providing precise orbit products, as well as Ke Su and Zhenchuan Huang for their help with the English-language aspects of writing this paper.

Conflicts of Interest: The authors declare no conflict of interest.

References

1. Wu, X.; Jin, S. GNSS-Reflectometry: Forest canopies polarization scattering properties and modeling. *Adv. Space Res.* **2014**, *54*, 863–870. [CrossRef]
2. Jin, S.; Zhang, T. Terrestrial Water Storage Anomalies Associated with Drought in Southwestern USA from GPS Observations. *Surv. Geophys.* **2016**, *37*, 1139–1156. [CrossRef]
3. Li, G.; Guo, S.; Lv, J.; Zhao, K.; He, Z. Introduction to global short message communication service of BeiDou-3 navigation satellite system. *Adv. Space Res.* **2021**, *67*, 1701–1708. [CrossRef]
4. Yang, Y.; Mao, Y.; Sun, B. Basic performance and future developments of BeiDou global navigation satellite system. *Satell. Navig.* **2020**, *1*, 1. [CrossRef]
5. Jin, S.; Su, K. PPP models and performances from single- to quad-frequency BDS observations. *Satell. Navig.* **2020**, *1*, 16. [CrossRef]
6. Okoh, D.; Onwuneme, S.; Seemala, G.; Jin, S.; Rabiu, B.; Nava, B.; Uwamahoro, J. Assessment of the NeQuick-2 and IRI-Plas 2017 models using global and long-term GNSS measurements. *J. Atmos. Sol.-Terr. Phys.* **2018**, *170*, 1–10. [CrossRef]
7. Li, M.; Yuan, Y.; Zhang, X.; Zha, J. A multi-frequency and multi-GNSS method for the retrieval of the ionospheric TEC and intraday variability of receiver DCBs. *J. Geod.* **2020**, *94*, 102. [CrossRef]
8. Montenbruck, O.; Hauschild, A.; Steigenberger, P. Differential code bias estimation using multi-GNSS observations and global ionosphere maps. In Proceedings of the 2014 International Technical Meeting of the Institute of Navigation, San Diego, CA, USA, 27–29 January 2014; pp. 802–812.
9. Chen, L.; Yi, W.; Song, W.; Shi, C.; Lou, Y.; Cao, C. Evaluation of three ionospheric delay computation methods for ground-based GNSS receivers. *GPS Solut.* **2018**, *22*, 125. [CrossRef]
10. Li, W.; Wang, G.; Mi, J.; Zhang, S. Calibration errors in determining slant Total Electron Content (TEC) from multi-GNSS data. *Adv. Space Res.* **2019**, *63*, 1670–1680. [CrossRef]
11. Zhang, B.; Ou, J.; Yuan, Y.; Li, Z. Extraction of line-of-sight ionospheric observables from GPS data using precise point positioning. *Sci. China Earth Sci.* **2012**, *55*, 1919–1928. [CrossRef]
12. Liu, T.; Zhang, B.; Yuan, Y.; Zhang, X. On the application of the raw-observation-based PPP to global ionosphere VTEC modeling: An advantage demonstration in the multi-frequency and multi-GNSS context. *J. Geod.* **2019**, *94*, 1. [CrossRef]
13. Zhang, B.; Teunissen, P.J.; Yuan, Y.; Zhang, X.; Li, M. A modified carrier-to-code leveling method for retrieving ionospheric observables and detecting short-term temporal variability of receiver differential code biases. *J. Geod.* **2019**, *93*, 19–28. [CrossRef]
14. Su, K.; Jin, S.; Jiang, J.; Hoque, M.; Yuan, L. Ionospheric VTEC and satellite DCB estimated from single-frequency BDS observations with multi-layer mapping function. *GPS Solut.* **2021**, *25*, 68. [CrossRef]
15. Klobuchar, J.A. Ionospheric Time-Delay Algorithm for Single-Frequency GPS Users. *IEEE Trans. Aerosp. Electron. Syst.* **1987**, *AES-23*, 325–331. [CrossRef]
16. Nava, B.; Coïsson, P.; Radicella, S.M. A new version of the NeQuick ionosphere electron density model. *J. Atmos. Sol.-Terr. Phys.* **2008**, *70*, 1856. [CrossRef]
17. Yuan, Y.; Wang, N.; Li, Z.; Huo, X. The BeiDou global broadcast ionospheric delay correction model (BDGIM) and its preliminary performance evaluation results. *NAVIGATION-J. Inst. Navig.* **2019**, *66*, 55–69. [CrossRef]
18. Li, Z.; Wang, N.; Liu, A.; Yuan, Y.; Wang, L.; Hernández-Pajares, M.; Krankowski, A.; Yuan, H. Status of CAS global ionospheric maps after the maximum of solar cycle 24. *Satell. Navig.* **2021**, *2*, 19. [CrossRef]
19. Orus-Perez, R.; Nava, B.; Parro, J.; Kashcheyev, A. ESA UGI (Unified-GNSS-Ionosphere): An open-source software to compute precise ionosphere estimates. *Adv. Space Res.* **2021**, *67*, 56–65. [CrossRef]
20. Yuan, Y.; Ou, J. A generalized trigonometric series function model for determining ionospheric delay. *Prog. Nat. Sci.* **2004**, *14*, 1010–1014. [CrossRef]
21. Montenbruck, O.; Steigenberger, P.; Prange, L.; Deng, Z.; Zhao, Q.; Perosanz, F.; Romero, I.; Noll, C.; Stürze, A.; Weber, G.; et al. The Multi-GNSS Experiment (MGEX) of the International GNSS Service (IGS)—Achievements, prospects and challenges. *Adv. Space Res.* **2017**, *59*, 1671–1697. [CrossRef]
22. Xue, J.; Song, S.; Zhu, W. Estimation of differential code biases for Beidou navigation system using multi-GNSS observations: How stable are the differential satellite and receiver code biases? *J. Geod.* **2016**, *90*, 309–321. [CrossRef]
23. Zhu, Y.; Tan, S.; Feng, L.; Cui, X.; Zhang, Q.; Jia, X. Estimation of the DCB for the BDS-3 new signals based on BDGIM constraints. *Adv. Space Res.* **2020**, *66*, 1405–1414. [CrossRef]
24. Li, M.; Yuan, Y. Estimation and Analysis of BDS2 and BDS3 Differential Code Biases and Global Ionospheric Maps Using BDS Observations. *Remote Sens.* **2021**, *13*, 370. [CrossRef]

25. Wang, Q.; Jin, S.; Yuan, L.; Hu, Y.; Chen, J.; Guo, J. Estimation and Analysis of BDS-3 Differential Code Biases from MGEX Observations. *Remote Sens.* **2020**, *12*, 68. [CrossRef]
26. Deng, Y.; Guo, F.; Zhang, X.; Liu, W. Estimation and analysis of the multi-frequency and multi-channel DCB for BDS-3. *Acta Geod. Cartogr. Sin.* **2021**, *50*, 448.
27. Leick, A.; Rapoport, L.; Tatarnikov, D. *GPS Satellite Surveying*; John Wiley & Sons: Hoboken, NJ, USA, 2015.
28. Jin, R.; Jin, S.; Feng, G. M_DCB: Matlab code for estimating GNSS satellite and receiver differential code biases. *GPS Solut.* **2012**, *16*, 541–548. [CrossRef]
29. Ma, G.; Gao, W.; Li, J.; Chen, Y.; Shen, H. Estimation of GPS instrumental biases from small scale network. *Adv. Space Res.* **2014**, *54*, 871–882. [CrossRef]
30. Schaer, S. *Mapping and Predicting the Earth's Ionosphere Using the Global Positioning System*; Astronomical Institute, University of Berne: Bern, Switzerland, 1999.
31. Schaer, S.; Gurtner, W.; Feltens, J. IONEX: The ionosphere map exchange format version 1. In Proceedings of the IGS AC workshop, Darmstadt, Germany, 9–11 February 1998.
32. Wang, N.; Yuan, Y.; Li, Z.; Montenbruck, O.; Tan, B. Determination of differential code biases with multi-GNSS observations. *J. Geod.* **2016**, *90*, 209–228. [CrossRef]
33. Jin, S.G.; Jin, R.; Li, D. Assessment of BeiDou differential code bias variations from multi-GNSS network observations. *Ann. Geophys.* **2016**, *34*, 259–269. [CrossRef]
34. Ren, X.; Zhang, X.; Xie, W.; Zhang, K.; Yuan, Y.; Li, X. Global Ionospheric Modelling using Multi-GNSS: BeiDou, Galileo, GLONASS and GPS. *Sci. Rep.* **2016**, *6*, 33499. [CrossRef]
35. Zhang, B.; Teunissen, P.J.G. Characterization of multi-GNSS between-receiver differential code biases using zero and short baselines. *Sci. Bull.* **2015**, *60*, 1840–1849. [CrossRef]

remote sensing

MDPI

Article

A Study of Possible Correlations between Seismo-Ionospheric Anomalies of GNSS Total Electron Content and Earthquake Energy

Yung-Chih Su [1,2,3] and Jinming Sha [1,2,3,*]

[1] Postdoctoral Research Station of Geography, Fujian Normal University, Fuzhou 350007, China; surdrew@yahoo.com.tw
[2] State Key Laboratory of Subtropical Mountain Ecology of the Ministry of Science and Technology and Fujian Province, Fujian Normal University, Fuzhou 350007, China
[3] School of Geographical Sciences, Fujian Normal University, Fuzhou 350007, China
* Correspondence: jmsha@fjnu.edu.cn

Abstract: In this study, we conduct a correlation analysis between the daily occurrence times of the increase and decrease anomalies in the global total electron content (TEC) in the ionosphere, and the daily earthquake energy release within 110–130°E longitude over the following three latitude regions: A: 13°S–0.5°S (22.3°S–10°S geomagnetic), B: 0.5°S–19.5°N (10°S–10°N geomagnetic), and C: 19.5°N–32.1°N (10°N–22.5°N geomagnetic). The TEC data from global ionosphere maps (GIMs) during earthquake events of $M \geq 2.5$ that occurred in 2015–2018 are used in this study. The time series of daily seismic wave energy releases within the three regions and the daily occurrence times of the TEC anomalies in each GIM grid are computed. By time-shifting the time series, the correlations are calculated and compared globally, and the temporal characteristics are also examined. The disturbance storm time (Dst) index, planetary geomagnetic index Kp, and daily observed 10.7 cm solar flux (F10.7) are used to remove data associated with space weather variations. Although the seismo-ionospheric precursor is not confirmed by the statistical investigations, the greater occurrence times of TEC decrease anomalies are observed in the southeast in Region A, and the conjugate point 13 days prior to a *M*6.9 earthquake in Region A, which occurred on 5 August 2018, in accordance with the statistical results. Therefore, it is required to apply more parameters to understand the causes of the ionospheric TEC variations and investigate whether ionospheric variations are caused by earthquakes.

Keywords: earthquake energy; total electron content; global ionosphere maps; seismo-ionospheric anomaly

Citation: Su, Y.-C.; Sha, J. A Study of Possible Correlations between Seismo-Ionospheric Anomalies of GNSS Total Electron Content and Earthquake Energy. *Remote Sens.* **2022**, *14*, 1155. https://doi.org/10.3390/rs14051155

Academic Editors: Shuanggen Jin and Gino Dardanelli

Received: 3 December 2021
Accepted: 22 February 2022
Published: 26 February 2022

1. Introduction

Earthquakes are one of the most devastating types of natural disasters, and large earthquakes can cause great damage to life and property. Therefore, predicting the occurrence of earthquakes in advance has been of interest to researchers and the general public. Scientific attempts related to earthquake prediction include monitoring variations in the geomagnetic field, surface displacements, groundwater levels, etc. [1–5]. In addition, many studies have shown that the electron density in the Earth's ionosphere might vary anomalously within approximately 7 days prior to earthquakes [6–11]. Liu et al. [6,7] conducted regional ionospheric observations using the Chung-Li ionosonde (25.0°N, 121.2°E) and the Global Positioning System (GPS) network in the Taiwan area to observe the maximum plasma frequency foF_2 in the ionospheric F_2 region and the total electron content (TEC), respectively, and detected ionospheric variations before the 1999 *M*7.7 Chi-Chi earthquake, which occurred in central Taiwan. The results show that the ionospheric electron density over the epicenter anomalously decreased 1, 3, and 4 days before the Chi-Chi earthquake.

To understand the ionospheric precursor signatures, it is important to examine global ionospheric variations prior to earthquakes. Global ionosphere maps (GIMs) provided by the Center for Orbit Determination in Europe (CODE) are based on time-continuous observations with global coverage and can be used to investigate the global distributions of ionospheric anomalies. Liu et al. [8–10] employed GIMs to investigate the seismo-ionospheric precursors (SIPs) for the 2008 *M* 8.0 Wenchuan, China, the 2004 *M* 9.1 Sumatra, and the 2010 *M* 7.0 Haiti earthquakes, respectively. They found that ionospheric TEC anomalies appeared around the epicenters 1–6 days prior to the three earthquakes. Furthermore, satellite observations have detected ionospheric variations before earthquakes. For example, Liu et al. [11] utilized data obtained by the French satellite Detection of Electro-Magnetic Emissions Transmitted from Earthquake Regions (DEMETER) to analyze the differences between the observed ionospheric parameters before and after the 2008 Wenchuan earthquake and found that the ionospheric nighttime electron density and ion density decreased significantly over the epicenter 1–6 days before the earthquake. On 2 February 2018, the China Seismo-Electromagnetic Satellite (CSES) was launched. It measures the electric field, magnetic field, electron density, ion density, and other important parameters. Yan et al. [12] showed that the ionospheric parameters observed by CSES around the epicenters of four earthquakes with a $M > 7.0$ during August 2018 were perturbed prior to the earthquakes. Statistical results also support pre-earthquake anomalous variations in the ionospheric electron density [6,8,9,13–15]. Several mechanisms have been proposed to explain the occurrence of SIPs, including atmospheric conductivity changes in the global electric circuit (GEC) related to ionization caused by an increase in the radon emanations before earthquakes [16], amplification of internal gravity waves (IGWs) produced due to surface motion through interaction with planetary waves and their subsequent propagation to the ionosphere where they modify the dynamo electric fields [17], and large-scale electric field-induced ionospheric perturbations [18,19].

There are also studies showing the opposite findings. For example, Masci et al. [20] analyzed ionospheric TEC during the 6 April 2009 *M*6.1 L'Aquila (Italy) earthquake and showed that the hump-like shape in the TEC difference (DTEC) time series calculated from two GPS receivers in central Italy, which was interpreted as a possible earthquake effect by Nenovski et al. [21], appears to be a diurnal variation and cannot be considered an earthquake-related effect. Dautermann et al. [22] and Thomas et al. [23] investigated long periods of data; the former used 2 years (2003–2004) of TEC data from the Southern California Integrated GPS Network (SCIGN) for earthquakes in southern California, and the latter used GIMs for the 1279 $M \geq 6.0$ earthquakes globally during the years 2000–2014. Both studies showed no evidence to support ionospheric perturbations prior to earthquakes. The supporting and opposite results might be because the variability in SIPs might be large, making them sometimes difficult to detect.

Many studies have shown that the ionospheric anomalies in GIM TEC associated with earthquakes might have frequent or prolonged occurrence times (e.g., Liu et al. [10]). In this study, we would like to investigate the possibility of establishing an earthquake prediction model by using GIM TEC, considering the frequent or prolonged feature of SIPs. This study focuses on earthquakes that occurred during 2015–2018 within three selected low geomagnetic latitude regions in the 110–130°E longitude sector. The day is used as a unit, and the daily seismic energy released within the three latitude regions is computed. The correlation coefficients between the seismic energy and the daily occurrence times of GIM TEC anomalies within each GIM grid for ± 15 days from the energy release are calculated. Thus, we could compare the correlations globally and examine the temporal characteristics. The data that are associated with geomagnetic disturbances by using the disturbance storm time (Dst) index are removed. In addition, the results of using declustered seismic energy and removing data by using Dst and considering the planetary geomagnetic index Kp and daily observed 10.7 cm solar flux (F10.7) are investigated.

2. Materials and Methods

2.1. Earthquake Data

In this study, the earthquake data from U.S. Geological Survey (USGS, https://earthquake.usgs.gov/earthquakes/search/, last accessed on 26 January 2022) and GIM TEC from CODE (ftp://ftp.aiub.unibe.ch/CODE/, last accessed on 29 August 2021) are used. All earthquakes that occurred within a longitude range of 110–130°E and during 1 January 2015, to 31 December 2018, with $M \geq 2.5$ from the USGS are included in this study. We presumed that the uncertainties, which might be associated with the pre-earthquake effects near the Earth's surface and their coupling to the ionosphere, such as magnetic dip, and the geographically related conditions (for example, ocean, urban area, etc.), might produce different ionospheric variations, and the selected longitude sector is subdivided into three latitude regions, which are A: 13°S–0.5°S (22.3°S–10°S geomagnetic), B: 0.5°S–19.5°N (10°S–10°N geomagnetic), and C: 19.5°N–32.1°N (10°N–22.5°N geomagnetic). The three regions are separated mainly according to the magnetic dip angle. The distribution of the earthquakes used is shown in Figure 1.

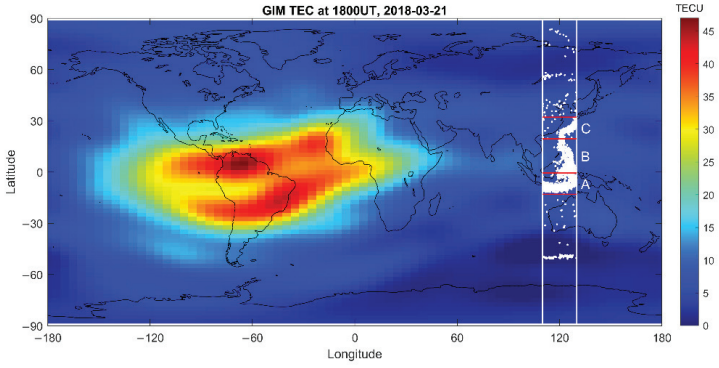

Figure 1. The distribution of earthquakes of magnitude ≥ 2.5 occurring within 110–130°E longitude from 1 January 2015 to 31 December 2018 (white dots), and the global distribution of GIM TEC observed at 1800 UT on 21 March 2018 in TEC units (1 TECU = 10^{16} electron/m^2). Two vertical white lines denote longitudes of 110 and 130°E. The three study Regions A (13°S–0.5°S), B (0.5°S–19.5°N), and C (19.5°N–32.1°N) are divided by four red lines. The equatorial ionization anomaly (EIA) can be seen between approximately −150 and 30°E longitudes.

It is shown that SIPs might be related to earthquake energy [13,14]. One of the variables used in computing the correlation coefficient is the daily total energy of seismic waves radiated by earthquakes in a given latitude region. The seismic wave energy released by an earthquake of magnitude M was estimated using the following relationship developed by Gutenberg and Richter [24]:

$$\log E = 11.8 + 1.5\,M \quad (1)$$

where E is seismic wave energy in erg (10^{-7} J). The total seismic wave energy released within a region by all the earthquakes was then summed for each day during 2015–2018. The time series of daily seismic energy and the temporal distributions of earthquakes with different magnitude ranges within 110–130°E and in Regions A, B, and C are provided in Figure S1 in Supplementary Material S1. There were 123,505 seismic events with $M \geq 2.5$ in total worldwide, releasing a total seismic wave energy of 1.28×10^{25} erg during 2015–2018. Table 1 shows that there were 8080 earthquakes with $M \geq 2.5$ in 110–130°E during 2015–2018, with four $M \geq 7$ earthquakes among them, among which one occurred in Region A and three in Region B. The total seismic wave energy of the 8080 earthquakes was 3.43% of the net seismic energy released worldwide during 2015–2018. Among the three Regions A–C, Region B spans the widest latitude range and has the largest earthquake

number and total seismic energy, while Region C has the smallest earthquake number and energy.

Table 1. Earthquake number and energy of $M \geq 2.5$ within 110–130°E in 2015–2018.

	EQK Number				Total EQK Number	Total Energy Release (erg)	% of Global EQK Number	% of Global Energy Release
	$M < 5$	$5 \leq M < 6$	$6 \leq M < 7$	$7 \leq M < 8$				
All	7307	711	58	4	8080	4.40×10^{23}	6.54%	3.43%
A	2652	244	26	1	2923	1.37×10^{23}	2.37%	1.07%
B	3392	343	21	3	3759	2.66×10^{23}	3.04%	2.07%
C	1000	93	10	0	1103	3.26×10^{22}	0.89%	0.25%

Note: The earthquake catalog: USGS (https://earthquake.usgs.gov/earthquakes/search/, last accessed on 26 January 2022).

2.2. GIM TEC

TEC is the integral of electron density along the signal path from the global navigation satellite system (GNSS) satellite to the receiver. Since the signal path to the ground-based receiver is tilted, the following measured TEC is called slant TEC (STEC):

$$STEC = \int_{\text{Sat}}^{\text{Rx}} N_e ds, \tag{2}$$

where *Ne* is the electron density and Sat and Rx are the locations of the GNSS satellite and ground-based receiver, respectively. As the satellite's zenith angle changes, the length of the path of the signal through the ionosphere changes, and hence, STECs have to be converted into vertical TECs (VTECs) to eliminate the zenith angle effect. The GIM TECs provided by CODE are generated by using data from approximately 300 GNSS sites worldwide using spherical harmonics expansion. The GIM covers a range of ±87.5°N latitude and ±180°E longitude, with spatial resolutions of 2.5° and 5°, respectively. During the study period, the CODE GIM provides 24-h global TEC distributions (from 00 to 23 UT) each day [25]. Please note that the accuracy of GIM is lower over the ocean areas. However, the GIM data are suitable statistical data for global analysis and to investigate the possible obvious and prolonged SIPs. The global distribution of GIM TEC at 1800 UT on 21 March 2018, is displayed in Figure 1.

2.3. TEC Anomalies

We use the method used in Liu et al. [8] and Chen et al. [13] to define anomalies in the GIM TEC variations. For an observation (O) at a certain time and location (GIM grid), the median TEC and the corresponding first and third quartiles, denoted by M, LQ, and UQ, respectively, are computed based on the TECs of the previous 15 days at the same time and location. The upper bound (UB) and lower bound (LB) are defined as the following:

$$\begin{aligned} UB &= M + k(UQ - M), \\ LB &= M - k(M - LQ). \end{aligned} \tag{3}$$

We set k to be 1.5 [8–10,13]. If $O > UB$ ($O < LB$), then an anomalous increase (decrease) in the TEC observation at this time and location is declared. Under the assumption of a normal distribution, the probability of an observed TEC in the interval (LB, UB) is approximately 69%. The occurrence times of the increase anomaly and decrease anomaly and the sum of the two are counted separately for each day. The daily occurrence times of TEC anomalies (the maximum is 24 times), together with the daily seismic wave energy release, are used to compute the correlation coefficients.

2.4. Removing Storm Effects and Other Experimental Designs

When magnetic disturbances or magnetic storms occur, the ionospheric electron density is perturbed and could anomalously increase and/or decrease relative to that in a quiet time period. Liu et al. [26] showed that storm-related ionospheric perturbations can last as long as 4 days after storm onset. The Dst index, obtained from the average of the horizontal component of the low-latitude magnetic field, can be used to identify storm onset. The Dst temporal variations from the World Data Center (WDC) for Geomagnetism in Kyoto (http://wdc.kugi.kyoto-u.ac.jp/dstdir/index.html, last accessed on 24 January 2022) during the study period were employed. In this study, we refer to Zhu et al. [27], and if Dst < −40 nT or the absolute value of the Dst difference from the previous 1-h value > 40 nT, the occurrence times of TEC anomalies from 1 day before to 4 days after this UT day (6 days in total) were not considered. Figure S1 in Supplementary Material S1 shows the days that were not considered in this study.

To investigate the temporal correlation, the time series of occurrence times of TEC increase anomalies, decrease anomalies, and both anomalies together at each GIM grid were shifted ±15 days forward and backward relative to the time series of daily seismic energy release. Therefore, the correlation coefficients between the daily seismic wave energy release within 110–130°E in Regions A, B, and C and the occurrence times of TEC anomalies in each GIM grid prior to and after energy release could be computed. During the study period, the average sample size used in calculating correlation coefficients is 905 days (with a minimum of 893 and a maximum of 917 days depending on the day shifts) after removing the storm effects by using the Dst index.

To test whether the two variables are correlated (population correlation coefficient $\varrho \neq 0$), the *t*-test was applied. The *t*-value (t) is given by the following:

$$t = r\sqrt{\frac{n-2}{1-r^2}}, \tag{4}$$

where r is the correlation coefficient and n is the sample size. The null hypothesis is that ϱ is not significantly different from zero, i.e., there is not a significant linear relationship between the occurrence times of TEC anomalies and the earthquake energy in the population [28]. Setting a significance level (α) of 0.01, the critical value $t_{\alpha=0.01}$ for the two-tailed test with a sample size of 905 is approximately 2.581, and the associated r is 0.086. If $r > 0.086$ ($r < -0.086$), we consider the occurrence times of TEC anomalies to be positively (negatively) correlated with the earthquake energy. In addition, the p value (p), which is defined as the probability that t is greater than the observed t with a degree of freedom of $n - 2$, was also computed. The minimum p was found to further examine the spatial relationships between the positive correlations and earthquakes.

Since larger earthquakes are more likely to produce SIPs [13,14], for Regions A, B, and C, the sample pairs with daily seismic wave energy < 1.1220×10^{20} erg (equivalent to an M5.5 earthquake) were removed in the following analyses. In addition, a 1-unit difference in M corresponds to a difference of approximately 32 times in earthquake energy, and 2 units correspond to 1000 times (Equation (1)). Thus, there could be effects from the outliers. In the analyses of Regions A, B, and C, the outliers were found from seismic wave energies that were ≥ M5.5 by using a 1.5 interquartile range above or below the associated two quartiles, and the associated sample pairs were further removed to eliminate the possible effects from outliers. The outliers were removed, and the ranges of seismic energy were fixed before eliminating the storm effects. Table 2 lists the parameters of the samples with daily seismic wave energy release ≥ M5.5 with/without outliers in Regions A, B, and C. The threshold of the correlation coefficient is $\alpha = 0.01$ ($r_{\alpha=0.01}$), and maximum daily seismic wave energy releases for samples with energy release ≥ M5.5 and with/without outliers for Regions A, B, and C are computed. The parameters vary depending on whether the storm effect is significant when the days are shifted.

Table 2. Parameters for daily energy release equivalent to $M \geq 5.5$ earthquakes.

Region	With Outliers			Without Outliers		
	Sample Size	$r_{\alpha = 0.01}$	Max. Daily Energy Release in M	Sample Size	$r_{\alpha = 0.01}$	Max. Daily Energy Release in M
A	34–44	0.384–0.436	6.906–7.000	29–37	0.418–0.471	6.480–6.512
B	41–52	0.354–0.398	7.300–7.505	35–45	0.380–0.430	6.201–6.201
C	14–20	0.561–0.661	6.429–6.701	10–16	0.623–0.765	6.154–6.200

Note: The $r_{\alpha = 0.01}$ represents the threshold value of r at significance level $\alpha = 0.01$.

3. Results

3.1. 110–130°E

In this section, we briefly describe the results of the correlation analyses. The results are presented in Supplementary Material S2. The figures which are of more importance or could be used as examples are also shown in the paper. Figures 2–4 (Figures S1–S3 in Supplementary Material S2) show the temporal and spatial distributions of r between the daily released seismic wave energy within 110–130°E (all the earthquakes in Figure 1 were considered) and its associated occurrence times of TEC anomalies 15 days before and after the energy release. Panels from left to right denote the days from daily energy release (D); for example, D = −7 represents the 7 days before the energy release. The main focus of the study is over 120°E longitude. However, we also wanted to examine whether similar variations existed in other longitude sectors for the same selected earthquakes. From top to bottom, the four longitude sectors of 120 (the study area of earthquakes), 30, −60, and −150°E, with a width of ±20° and separated by 90°, are displayed. Each panel displays an area of a 40° longitude range (x-axis) and a ±90°N latitude range (y-axis). Note that the results of the −150°E sector have a lower accuracy since most areas in this sector are ocean areas, and the results are provided for comparisons and references. For the decrease anomaly (Figure 2), a larger area of positive correlation is seen in the 120°E sector from approximately 30–60°N at D = −13, and many positive correlations appear in northern higher latitudes and other latitudes at approximately D = −14 to −7. The positive correlations are more apparent from D = −6 to −1 over the 120 and 30°E sectors with changing latitudes. After the energy release, there were fewer positive correlations in the four longitudinal sectors. For the increase anomaly (Figure 3), positive correlations mainly appear at approximately D = 3 to 12, with D = 3 to 7 in the southern higher latitudes and D = 8 and 9 in all four sectors. For the occurrence times of both increase and decrease anomalies (Figure 4), positive correlations are relatively rare and sporadic in time and space. There are only a few negative correlations for all three types of anomalies in Figures 2–4.

3.2. Region A

Figure 5 shows the temporal and spatial distributions of r between the daily seismic wave energy released within Region A and its associated occurrence times of TEC decrease anomalies in ±15 days. Positive correlations are evident mainly in the northern mid- and high latitudes, and roughly during D = −14 to −10, −7 to −5, and −3 to 0 in Figure 5. There are only a few correlations for D > 0. In contrast, the distributions of the positive correlation for the increase anomalies are relatively irregular, and the possible precursory information is not as clear as shown in Figure S5, which is provided in Supplementary Material S2. In addition, no specific feature in the temporal and spatial distribution of the correlation for both increase and decrease anomalies counted together could be identified. The results for using all energy releases available within Region A are provided as Figures S4–S6 in Supplementary Material S2.

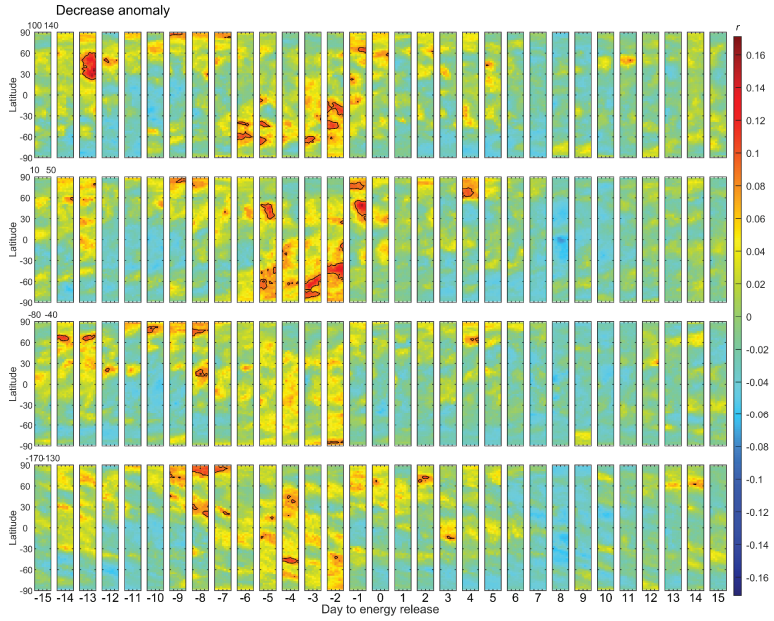

Figure 2. Temporal and spatial distributions of correlation coefficient between daily seismic wave energy release within 110–130°E and occurrence times of TEC decrease anomalies. Panels from left to right represent −15 to 15 days from the seismic wave energy release (D). Top to bottom panels display four selected longitude sectors centered over 120, 30, −60, and −150°E, respectively, each with a width of ±20°. The x-axis of each panel denotes the 40° longitude range, and the y-axis denotes latitude. The contour denotes $r_{\alpha = 0.01} = \pm 0.086$.

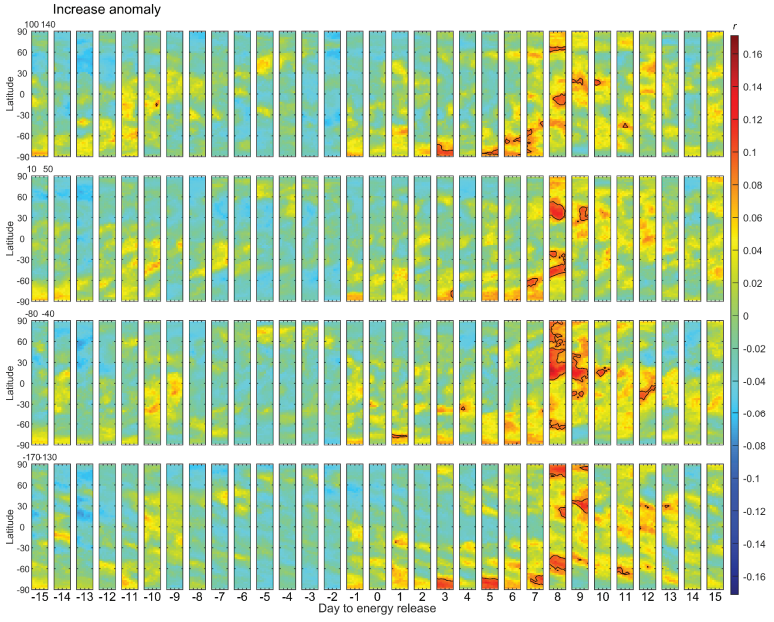

Figure 3. Same as Figure 2 for the results of occurrence times of TEC increase anomalies.

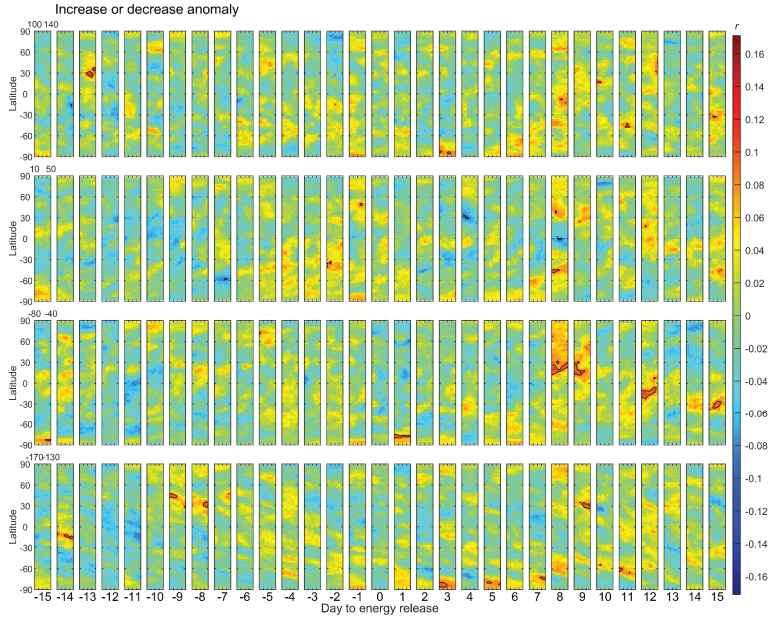

Figure 4. Same as Figure 2 for the results of occurrence times of both the TEC increase and decrease anomalies counted together.

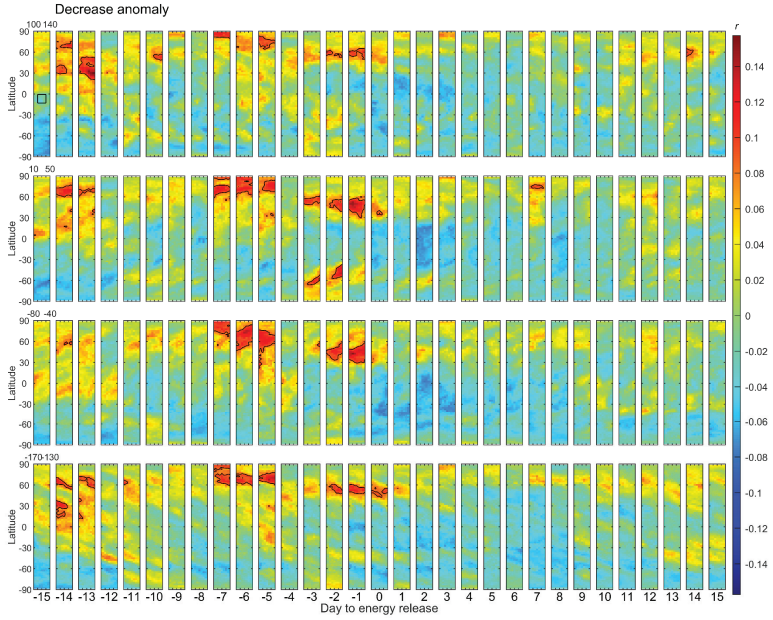

Figure 5. Temporal and spatial distributions of correlation coefficient between the daily seismic wave energy release within Region A and the occurrence times of the TEC decrease anomalies. Panels from left to right represent −15 to 15 days from the seismic wave energy release (D). Top to bottom panels display four selected longitude sectors centered over 120, 30, −60, and −150°E, respectively, each with a width of ± 20°. The contour denotes $r_{\alpha = 0.01} = \pm 0.086$. The black box on the top first panel indicates Region A.

Figure 6 shows the temporal and spatial distributions of r for samples with daily seismic wave energy $\geq M5.5$ (1.1220×10^{20} erg) released within Region A. As the sample size is reduced, the required correlation coefficients for significance at the 99% level increase. On D = −13, there is a larger area of positive correlation for the occurrence times of decreasing anomalies around the northern mid-latitudes of the 120°E sector. Positive correlations in the northern mid- and high latitudes can be seen when D = −7 to 0. They also appear at other latitudes and longitudes and after energy release. Figure 7 shows the results of the decrease anomaly when outliers of daily seismic wave energy $\geq M5.5$ were removed. Positive correlations can be found in the mid- and high latitudes of both hemispheres, as well as in the low latitudes, during D = −2 to 5. There are fewer correlations and no obvious pattern for the TEC increase anomaly for energy release $\geq M5.5$. After removing outliers of larger energy releases and for increase anomalies, positive correlations appear on D = −12 to −11 and −8 to −4 in the four sectors. The results for energy releases $\geq M5.5$ with/without outliers within Region A are provided as Figures S7–S10.

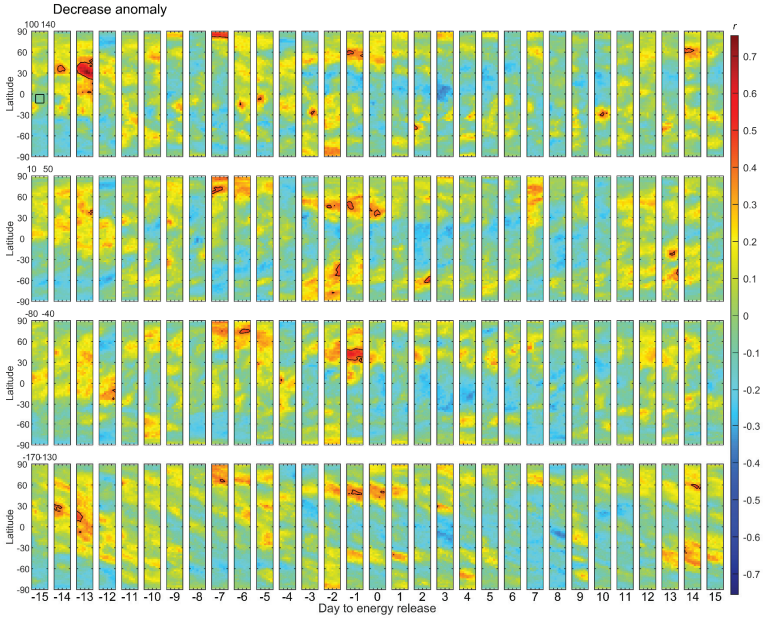

Figure 6. Same as Figure 5 for daily seismic wave energy release $\geq M5.5$ with outliers within Region A and for the TEC decrease anomalies. The contour denotes $r_{\alpha = 0.01}$ according to the sample size at each D.

3.3. Region B

The temporal and spatial distributions of r between the seismic wave energy released within Region B and the associated occurrence times of the TEC decrease anomalies and increase anomalies in a period of ±15 days are similar to those obtained from all the earthquakes occurring within 110–130°E during the four years, as shown in Figures 2 and 3. The correlation features between the occurrence times of both increase and decrease anomalies counted together and earthquake energy are fewer. The results are provided in Figures S11–S13 in Supplementary Material S2.

Figure 8 shows the results for samples with an energy release $\geq M5.5$ and for the decrease anomalies. It is revealed that apparent positive correlations of the decrease anomaly appear between D = −6 and 0. Correlations are also seen up to D = 6 after energy release. After removing outliers with large energy releases, the apparent correlations from D = −6 to 0 in Figure 8 disappear. Positive correlations appear during D = −14 to −11, and the possible

precursory information becomes less clear. The distributions of positive correlations of increase anomalies with energy release $\geq M5.5$ are more similar to those in Figure 3 (apparent patterns between approximately D = 3 and 12). After the outliers were removed, there were positive correlations on D = −10 to −3, but the precursory information is less clear. The positive correlations obtained with outliers shown in Figures 8 and S16 could be caused by the outlier with a large energy release. The results for energy releases $\geq M5.5$ with/without outliers within Region B are shown in Figures S14–S17.

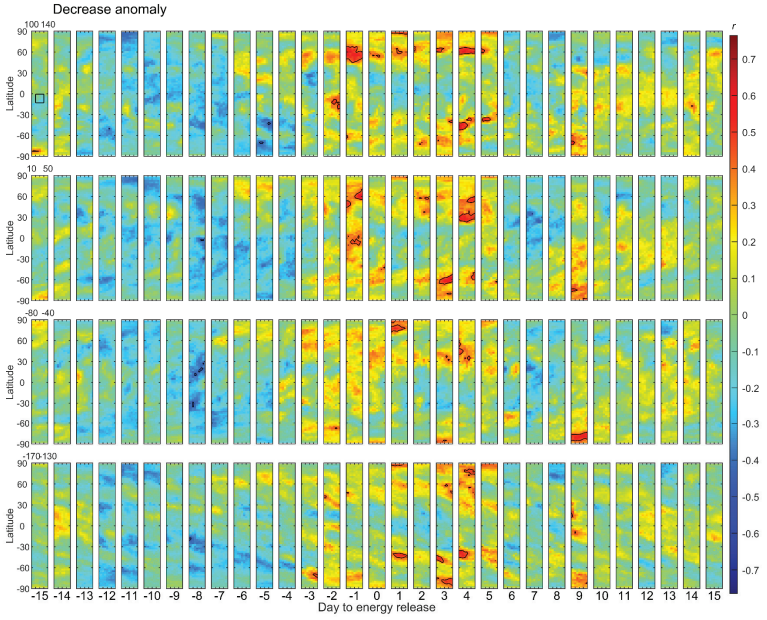

Figure 7. Same as Figure 5 for the daily seismic wave energy release $\geq M5.5$ without outliers within Region A and for the TEC decrease anomalies. The contour denotes $r_{\alpha = 0.01}$ according to sample size at each D.

3.4. Region C

The temporal and spatial distributions of *r* for the seismic wave energy released within Region C using all the samples available during the study period show that there is no clear precursory information that could be directly identified for the TEC decrease anomalies and increase anomalies since the positive correlations appear in the four sectors and after energy release. There are also fewer precursory features associated with both the increase and decrease anomalies counted together based on the correlation coefficients (Figures S18–S20).

The results for samples with an energy release $\geq M5.5$ with outliers and for decrease anomalies and increase anomalies are presented in Figures 9 and 10, respectively, because we also reference them in the following analyses. The sample size for an energy release $\geq M5.5$ in Region C is relatively small (14–20, see Table 2), and the correlation coefficients could be very large. Figure 9 shows that positive correlations for the decrease anomalies appear in large areas over the globe at approximately D = −13 to −11 and D = −5. There are also positive correlations at approximately D = 9 to 15. On the other hand, Figure 10 shows that more apparent positive correlations for the increase anomalies appear at approximately D = −6 to 3 and on D = 7. After the outliers with large energy releases are removed, for the decrease anomalies, positive correlations can be seen at approximately D = −11 to −7 in the four sectors. For the increase anomalies, there are apparent correlations during D = −15 to −14 and −6 to −2 in the four sectors. The results for energy releases $\geq M5.5$ with/without outliers within Region C are provided in Figures S21–S24.

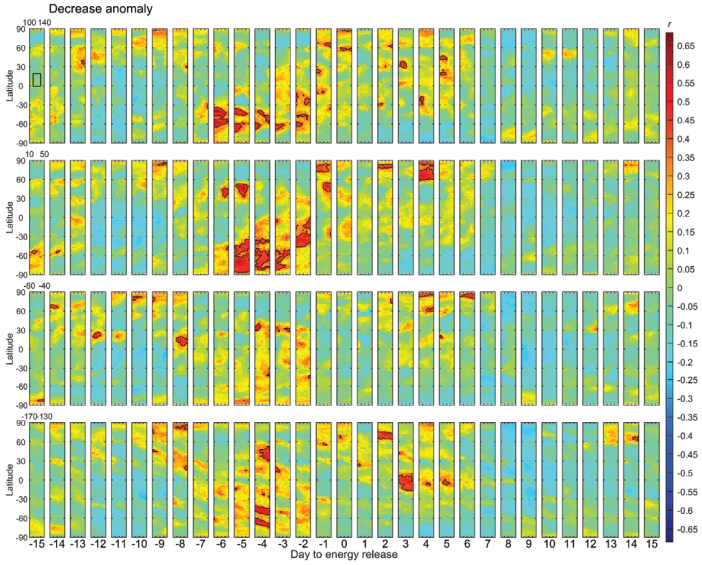

Figure 8. Temporal and spatial distributions of correlation coefficient between the daily seismic wave energy release $\geq M5.5$ with the outliers within Region B and the occurrence times of the TEC decrease anomalies. Panels from left to right represent −15 to 15 days from the seismic wave energy release (D). Top to bottom panels display the four selected longitude sectors centered over 120, 30, −60, and −150°E, respectively, each with a width of ±20°. The contour denotes $r_{\alpha = 0.01}$ according to sample size at each D. The black box on the top first panel indicates Region B.

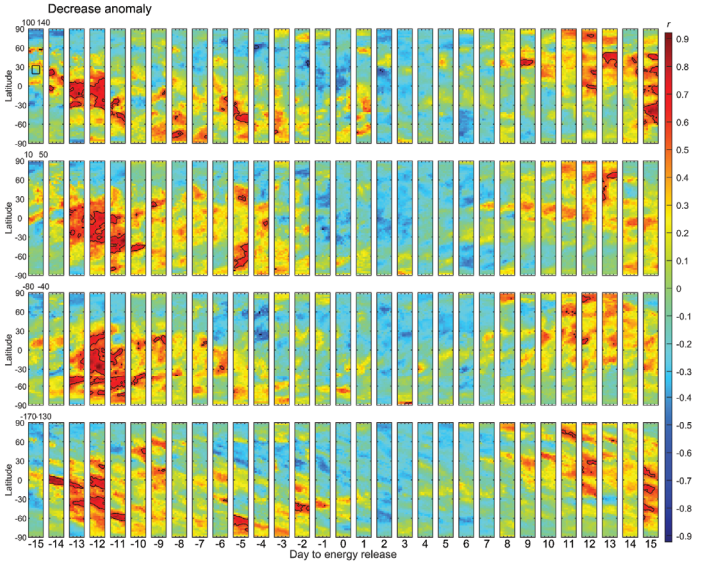

Figure 9. Temporal and spatial distributions of correlation coefficient between the daily seismic wave energy release $\geq M5.5$ with the outliers within Region B and the occurrence times of the TEC decrease anomalies. Panels from left to right represent −15 to 15 days from the seismic wave energy release (D). Top to bottom panels display the four selected longitude sectors centered over 120, 30, −60, and −150 °E, respectively, each with a width of ±20°. The contour denotes $r_{\alpha = 0.01}$ according to sample size at each D. The black box on the top first panel indicates Region C.

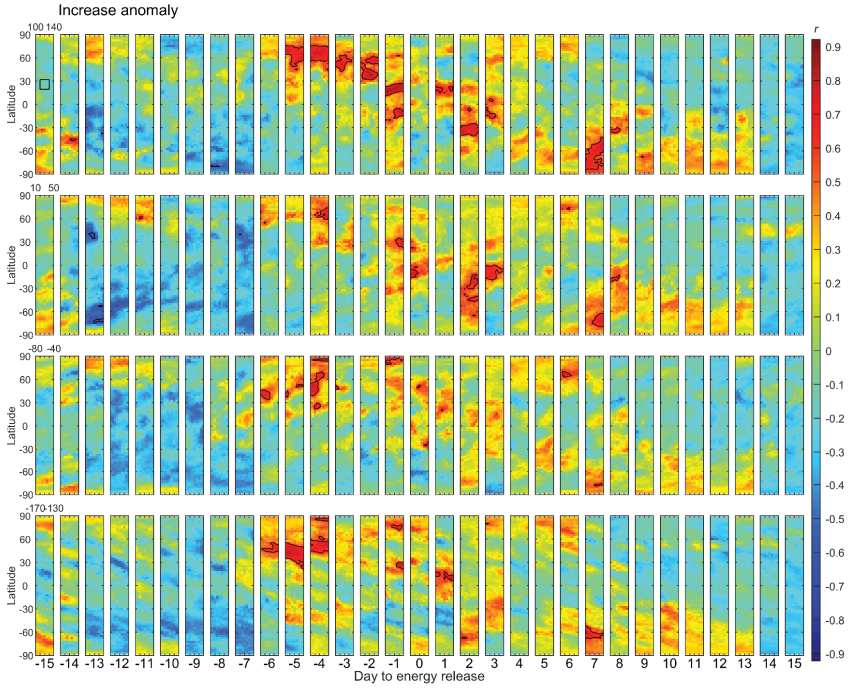

Figure 10. Same as Figure 9 for the results of occurrence times of the TEC increase anomalies.

3.5. Geographical Dependence

To further investigate the possible precursory information, the p value (p), which is defined as the probability that t is greater than the observed t (Equation (4)) with a degree of freedom of sample size–2 under the hypothesis of no correlation, was computed from the r values of the decrease and increase anomalies shown in Supplementary Material S2, and the minimum p values during D = −15 to 15 and over the global 71 × 73 (5183) GIM grids were extracted. The D, location, and r of the minimum p were also extracted in order to examine the possible geographical dependence (Table 3). The results reveal that the minimum p of the decrease anomaly is D = −13 in the 120°E sector and approximately 30–35°N, when all samples available from 110–130°E and Region A and those with energy releases $\geq$ M5.5 with outliers in Region A were used. In addition, the minimum p of the decrease anomaly appears at D = −6 in the 120°E sector for energy releases $\geq$ M5.5 with outliers in Region B. For energy releases in Regions A and B, the minimum p values, which appear before the energy release and in the 120°E sector, are not above the latitude ranges of the two regions. We search for the minimum p and wish to find the time and locations where the SIPs are most likely to appear, and also expect that it would be more efficient in earthquake prediction by using GIM.

Table 3. The minimum p, associated D, locations, and r in analyses of this study shown in Supplementary Material S2.

			Min. p	D	Lat.	Long.	r
110–130 °E (all samples)		Decrease anomaly	$\mathbf{2.025 \times 10^{-7}}$	**−13**	**35**	**135**	**0.169 ***
		Increase anomaly	8.448×10^{-7}	8	15	−90	0.158 *
Region A	All samples	Decrease anomaly	$\mathbf{1.382 \times 10^{-6}}$	**−13**	**30**	**135**	**0.156 ***
		Increase anomaly	7.497×10^{-6}	−15	−87.5	30	0.144 *
	$E \geq M5.5$	Decrease anomaly	$\mathbf{8.411 \times 10^{-9}}$	**−13**	**32.5**	**125**	**0.750 ***
		Increase anomaly	8.951×10^{-6}	9	−12.5	70	0.650 *
	$E \geq M5.5$ and outliers removed	Decrease anomaly	4.617×10^{-8}	3	−45	165	0.764 *
		Increase anomaly	1.741×10^{-5}	−12	55	40	0.633 *
Region B	All samples	Decrease anomaly	1.753×10^{-5}	−5	−70	95	0.138 *
		Increase anomaly	1.136×10^{-6}	9	15	−70	0.156 *
	$E \geq M5.5$	Decrease anomaly	$\mathbf{2.295 \times 10^{-7}}$	**−6**	**−40**	**110**	**0.689 ***
		Increase anomaly	9.674×10^{-7}	8	62.5	−100	0.637 *
	$E \geq M5.5$ and outliers removed	Decrease anomaly	1.641×10^{-6}	1	−77.5	50	0.669 *
		Increase anomaly	4.097×10^{-5}	10	7.5	−160	0.553
Region C	All samples	Decrease anomaly	6.410×10^{-9}	15	−35	140	0.187 *
		Increase anomaly	1.171×10^{-6}	2	−5	90	0.156 *
	$E \geq M5.5$	Decrease anomaly	1.454×10^{-8}	−11	−35	65	0.947 *
		Increase anomaly	1.624×10^{-7}	−3	50	−80	0.902 *
	$E \geq M5.5$ and outliers removed	Decrease anomaly	3.089×10^{-7}	−9	−50	−165	0.940
		Increase anomaly	2.102×10^{-8}	−4	85	−65	0.944

Note: The minimum p during D = −15 to 15 and over the 5183 GIM grids were extracted for occurrence times of the decrease anomalies and increase anomalies, respectively. The bold font denotes the minimum p appearing before the energy release and in the 120°E sector. The asterisk near r denotes that the associated r is the maximum r during D = −15 to 15 and over the 5183 GIM grids.

4. Discussions

First, the positive correlations that appear before the earthquake energy release are summarized. For all the samples of energy released within 110–130°E longitude during the years 2015–2018, the most apparent correlations for decrease anomalies are around D = −6 to −1 over 120 and 30°E sectors, and this pattern is similar to the results of Region B. The minimum p of the decrease anomalies is found at D = −13 in the 120°E sector. One of the features of Region A is that positive correlations of decrease anomalies occur in the northern, higher latitudes. The minimum p of the decrease anomalies is also found at D = −13 in the 120°E sector when using all samples and those with energy releases $\geq M5.5$ with outliers. In Region B, the apparent correlations of the decrease anomalies appear at approximately D = −6 to −1 in the longitude sectors of 120 and 30°E, as obtained with all samples and those with energy releases $\geq M5.5$. These should be produced by the outliers with large energy releases. The minimum p of decrease anomalies is found at D = −6 in the 120°E sector for energy releases $\geq M5.5$ with outliers. For Region C, apparent correlations of the decrease anomalies are seen in all four sectors for energy releases $\geq M5.5$ with and without outliers. Positive correlations of the increase anomalies appear a few days before energy releases for energy releases $\geq M5.5$ with and without outliers.

Since positive correlations appear in the four sectors and after energy release, the possible precursory information cannot be confirmed. In addition, the minimum p values occurring before energy release and in the 120°E sector are characterized by samples that have not been declustered and have outliers. In Supplementary Material S3, we first examine the results of the declustered samples with energy releases of $\geq M5.5$ and without outliers. The advantage of the declustering process is that is avoids the influence of consecutive larger energy releases during a space weather event. The declustering method was as follows: if there were two energy releases of $\geq M5.5$ separated by ≤ 6 days, the larger energy release was retained. Moreover, two methods were used to eliminate space weather effects. The first one involved the Dst index, which was identical to that used in the paper. The second method involved considering Kp and F10.7. The condition that for days with at least one Kp > 3 (3o), the occurrence times of the TEC anomalies were not

considered as set. In addition, five periods of strengthening solar activity were found by using F10.7 and excluded (please see Supplementary Material S3 for details).

In Supplementary Material S3, Figures S1–S12 show that, for Region A (Figures S1–S4), one obvious characteristic of the decrease anomalies is that a large area of positive correlation appears at D = −2 around Region A when using Dst (the odd figures) and using Kp and F10.7 (the even figures), which are also provided in Figures 11 and 12, respectively. The apparent correlations of the increase anomalies mainly appear at D ≤ −4. When applying Kp and F10.7, the minimum p of the decrease anomalies appears at D = −2 and in the 120°E sector at −20°N (Table 4; Table S2). For Region B, the precursory features of the decrease and increase anomalies seem difficult to identify when using Dst and using Kp and F10.7, since the correlations occur in the four sectors and after the energy release (Figures S5–S8), and no minimum p of the decrease or increase anomalies appears before the energy release in the 120°E sector. For Region C, some of the temporal characteristics of the positive correlation of decrease and increase anomalies are closer to the results than the samples without the declustering process and including the outliers were used (Figures S9–S12), as shown in Figures 9 and 10. When applying Kp and F10.7, the minimum p of the increase anomalies appears at D = −1 in the 120°E sector; however, at D = −1, larger areas of correlation are also observed in the four sectors in the distributions of Figure S12. The parameters for the declustered samples of energy release ≥ M5.5 without outliers are shown in Table S1 (similar to Table 2). The results of the declustered samples of energy release ≥ M5.5 and with outliers are provided in Supplementary Material S4 (Figures S1–S12 and Tables S1–S2). For daily seismic wave energy released within Regions A, B, and C with the use of the Dst index to eliminate the space weather effects and within Region C with the use of Kp and F10.7, the results for the decrease and increase anomalies are similar to those of energy releases ≥ M5.5 with outliers in the paper and Supplementary Material S2. When applying Kp and F10.7, the correlations of the decrease anomalies improve between D = −13 and −6 in Region A (Figure S2), while in Region B, frequent positive correlations can be seen in the northern higher latitudes at approximately D ≤ 2 (Figure S6). On the other hand, there is no explicit precursory information in the correlation coefficients of the increase anomalies for Regions A and B (Figures S4 and S8). Only in Region A with the use of the Dst index does the minimum p of the decrease anomalies occur on D = −13 in the 120°E sector (Tables 5 and S2).

Furthermore, the results of the declustered samples with energy releases ≥ M5.5 over the entire area of Regions A–C (13°S–32.1°N) are also examined in Supplementary Material S3. The results of retaining and excluding the outliers, as well as using the same two methods to remove the space weather effects, are presented in Figures S13–S20. In addition, the results might show a large variability in the occurrence times of the TEC anomalies when using k = 1.5 in the definition of TEC anomalies, and k = 3 (a probability of 0.043 for an increase or decrease anomaly under a normal distribution) was used for the energy release within the entire area of Regions A–C. Figures S13–S16 show the results of retaining the outliers. The distributions of the decrease anomalies and increase anomalies are similar to or resemble some of the features found in Region B, as shown in Supplementary Materials S2 and S4. After removing the outliers, more sporadic correlations are shown in Figures S17–S20, and the minimum p values of the increase anomalies are found at D = −4 and −15 in the 120°E sector at −47.5°N and −72.5°N when using Dst and using Kp and F10.7, respectively (Table S4). Nevertheless, in the associated distributions of Figures S19 and S20, correlations also appear at higher latitudes in other sectors. The parameters for the declustered samples with energy releases ≥ M5.5 over the entire area of Regions A–C are shown in Table S3.

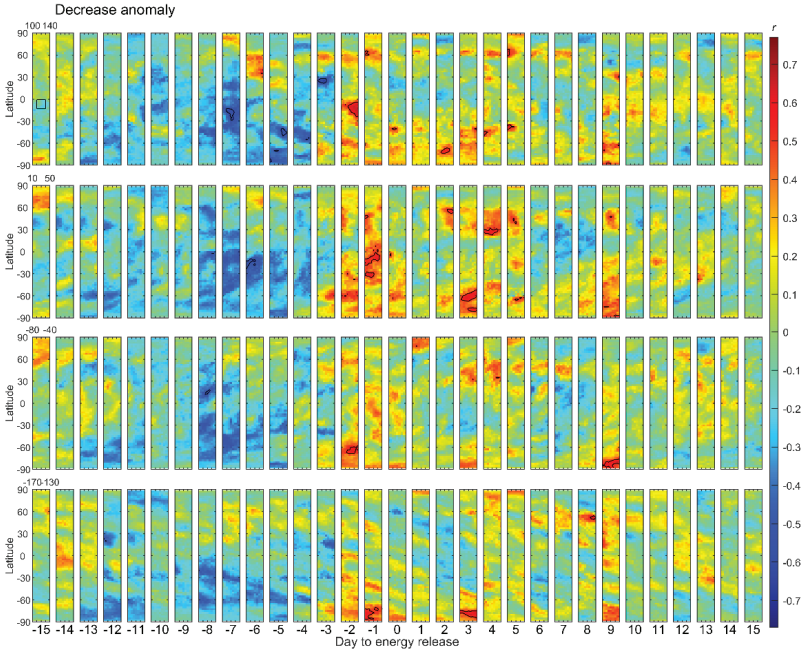

Figure 11. Distributions of the correlation coefficient of the TEC decrease anomaly for the declustered samples with energy releases $\geq M5.5$ within Region A and without outliers. Data are removed using the Dst index.

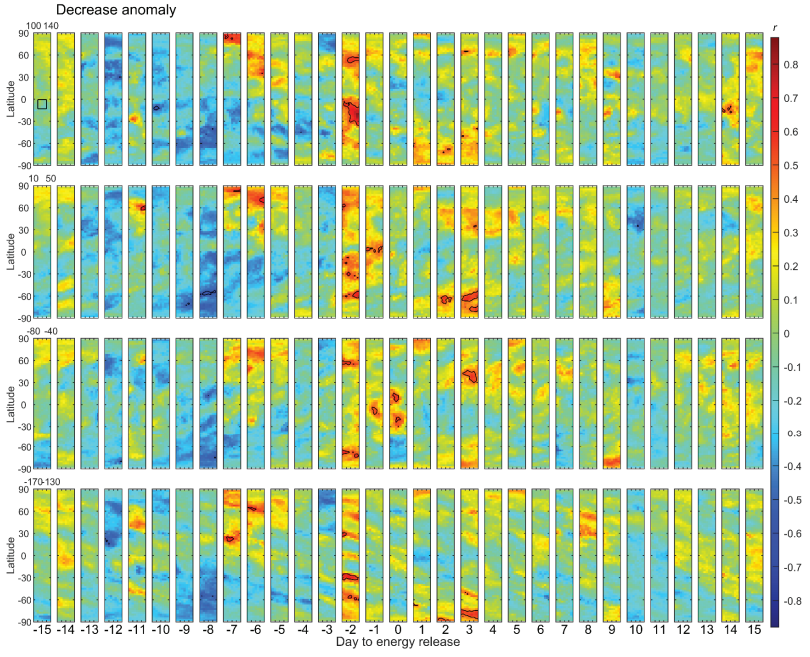

Figure 12. Same as Figure 11, but data are removed using Kp and F10.7.

Table 4. The minimum p, associated D, locations, and r for the results of the declustered samples with energy releases $\geq M5.5$ without outliers shown in Supplementary Material S3.

			Min. p	D	Lat.	Long.	r
Region A	Using Dst index	Decrease anomaly	2.929×10^{-5}	4	−47.5	95	0.726
		Increase anomaly	7.909×10^{-6}	−12	55	40	0.750
	Using Kp and F107	Decrease anomaly	$\mathbf{3.391 \times 10^{-7}}$	**−2**	**−20**	**135**	**0.847 ***
		Increase anomaly	7.988×10^{-7}	−11	40	−45	0.879 *
Region B	Using Dst index	Decrease anomaly	2.716×10^{-5}	8	52.5	−15	0.677
		Increase anomaly	1.607×10^{-6}	10	27.5	55	0.698 *
	Using Kp and F107	Decrease anomaly	1.589×10^{-5}	2	−47.5	−20	0.692
		Increase anomaly	3.129×10^{-8}	13	5	25	0.763 *
Region C	Using Dst index	Decrease anomaly	1.088×10^{-7}	−11	−35	10	0.959
		Increase anomaly	1.525×10^{-6}	−4	47.5	−75	0.934
	Using Kp and F107	Decrease anomaly	4.741×10^{-8}	−12	−50	−170	0.965
		Increase anomaly	$\mathbf{1.236 \times 10^{-7}}$	**−1**	**17.5**	**105**	**0.968**

Note: The minimum p during D = −15 to 15 and over the 5183 GIM grids were extracted for occurrence times of decrease anomalies and increase anomalies, respectively. The bold font denotes the minimum p appearing before energy release and in the 120°E sector. The asterisk near r denotes that the associated r is the maximum r during D = −15 to 15 and over the 5183 GIM grids.

Table 5. Same as Table 4 for the results of the declustered samples with energy releases $\geq M5.5$ with outliers shown in Supplementary Material S4.

			Min. p	D	Lat.	Long.	r
Region A	Using Dst index	Decrease anomaly	$\mathbf{1.598 \times 10^{-7}}$	**−13**	**32.5**	**125**	**0.783**
		Increase anomaly	6.166×10^{-5}	−7	−32.5	95	0.704 *
	Using Kp and F107	Decrease anomaly	4.036×10^{-6}	−8	−17.5	65	0.756 *
		Increase anomaly	7.127×10^{-7}	7	0	95	0.823 *
Region B	Using Dst index	Decrease anomaly	1.792×10^{-7}	−4	−50	−130	0.756 *
		Increase anomaly	2.243×10^{-7}	8	−10	155	0.744 *
	Using Kp and F107	Decrease anomaly	1.842×10^{-7}	−4	60	35	0.706
		Increase anomaly	7.943×10^{-14}	13	7.5	−135	0.875 *
Region C	Using Dst index	Decrease anomaly	4.196×10^{-10}	15	−35	125	0.980 *
		Increase anomaly	1.525×10^{-6}	−4	47.5	−75	0.934
	Using Kp and F107	Decrease anomaly	3.849×10^{-9}	−11	−30	60	0.984
		Increase anomaly	7.780×10^{-9}	0	7.5	−145	0.988 *

Note: The minimum p during D = −15 to 15 and over the 5183 GIM grids were extracted for occurrence times of decrease anomalies and increase anomalies, respectively. The bold font denotes the minimum p appearing before energy release and in the 120°E sector. The asterisk near r denotes that the associated r is the maximum r during D = −15 to 15 and over the 5183 GIM grids.

Since the correlations appear frequently, to examine whether the possible precursory information, such as the minimum p appearing before an energy release in the 120°E sector, could be accidental, we performed three times of random tests for Region A. The time series of daily seismic wave energy releases for 2015–2018 within Region A were permuted randomly. Then, the dates with energy release $\geq M5.5$ were selected, and the declustering process and removal of outliers were implemented. The results show that regardless of using Dst or using Kp and F10.7, there are positive correlations of TEC anomalies in the four sectors and after energy release. The minimum p values are all quite small, the same as those shown in Table 4, and the minimum p values could also appear in the 120°E sector and before energy release. These indicate that the precursory information in this study might be accidental. The results of random permutations are shown in Figures S1–S12 and Tables S1–S2 in Supplementary Material S5.

Although the precursory information could be coincidental, some interesting results might be seen from this study. For example, the results of Region B show that larger areas of correlation appear before energy release when including the outliers, and the minimum p of decrease anomaly for energy releases $\geq M5.5$ with outliers occurs on D = −6 and in the 120°E sector (Table 3). This possibly indicates an SIP event has appeared with other ionospheric disturbances. Another interesting result is that for Region A, the minimum p values of the decrease anomaly are on D = −13 and in the 120°E sector when including the

outliers and using the Dst index, and the minimum p appears on D = −2 and in the 120°E sector for the declustered samples with energy releases ≥ M5.5 without outliers when using Kp and F10.7. This possibly indicates that the SIPs might not only appear closer to the epicenter region, but also occur along the earthquake longitude.

Linear regression models were fitted to samples for which the minimum p values appear in the 120°E sector and before energy release in Tables 3–5 and Table S4 in Supplementary Material S3. The results are shown in Figure 13. The top panels, from left to right, are the results of using all samples, energy releases ≥ M5.5 with outliers, and declustered samples with energy releases ≥ M5.5 with outliers for Region A, respectively. The time and locations of samples, anomaly types, and the methods used to eliminate the space weather effects are indicated in the title. When using all samples, the R^2 is merely 0.0244 (= r^2), because when the seismic energies are smaller, there are still larger occurrence times of the TEC decrease anomaly. After removing samples with energy releases < M5.5, the R^2 values increase in the other two panels. There are four energy releases ≥ M6.9 with the occurrence times of the decrease anomaly ≥ 12 times on D = −13 and at (32.5°N, 125°E). The result of declustered samples with energy releases ≥ M5.5 without outliers within Region A, and using Kp and F10.7, shows that the R^2 is the greatest (0.7168) among six panels on D = −2 and at (–20°N, 135°E) for the decrease anomaly (bottom left panel). For energy releases ≥ M5.5 with outliers within Region B, there is an energy release of approximately M7.3 that has 20 occurrence times of the decrease anomaly (bottom middle panel). The regression line is affected by the sample, with an energy release of approximately M7.3. However, since the possible precursory information shown in this study cannot be confirmed to be related to the earthquakes, the regression models can only be provided as references.

Because the CODE GIM has provided TEC maps of 1-h resolution since 19 October 2014 (day of year 292), the period around 2015–2018 was selected as the study period. Earlier and later years of data might be included in the analysis to include a greater number of earthquakes and larger earthquakes. Moreover, the earthquake depth is one of the factors that possibly influences SIPs. The earthquake depth could be considered in future studies. Since there are positive correlations at higher latitudes, removing possible high-latitude effects might also be considered.

The TEC derived from the Jet Propulsion Laboratory (JPL) GIM was used to examine the daily occurrence times of TEC anomalies during a 30-day period from 21 July to 19 August 2018. The time resolution of JPL GIM is 2 h. During this period, there were six $M \geq 6.0$ earthquakes occurring on the four days, and two events with M6.9 among the six earthquakes, which occurred on 5 August and 19 August, respectively. Figure 14 shows the temporal variations of Dst, Kp, and F10.7 between 16 July and 23 August 2018. The Kp index reveals that the geomagnetic disturbances with Kp ≥ 3o occurred around 17, 21, and 24–25 July and 7, 11, and 15–20 August. The Dst variations show that a weaker magnetic storm occurred on 14 August. Figures 15 and 16 show the daily occurrence times of the TEC decrease anomaly and increase anomaly from JPL with k = 1.5, respectively. Frequent ionospheric positive effects are observed in the associated periods with Kp ≥ 3o at higher latitudes and over the globe, which are followed by the ionospheric negative effects. These effects should be associated with the magnetic disturbances. On the other hand, despite the ionospheric negative effects over the northern higher latitudes on 23 July (D = −13 for the M6.9 earthquake on 5 August), larger occurrence times of the decrease anomaly also appear in the southeast of Region A and the associated conjugate point. In addition, on 6 August (D = 1 and D = −13 for another M6.9 event on 19 August), greater occurrence times of the decrease anomaly appear between approximately 120 and 180°E in the northern mid-latitudes. It is noted that the greater occurrence times of the increase anomaly are seen between 29 July and 4 August (D = −7 to −1) around Region A. In fact, the TEC increase and decrease anomalies with k = 1.5 tend to appear globally. The larger occurrence times of TEC anomalies observed prior to the earthquakes might be only the natural variability; however, there is also the possibility of existence of the earthquake effects.

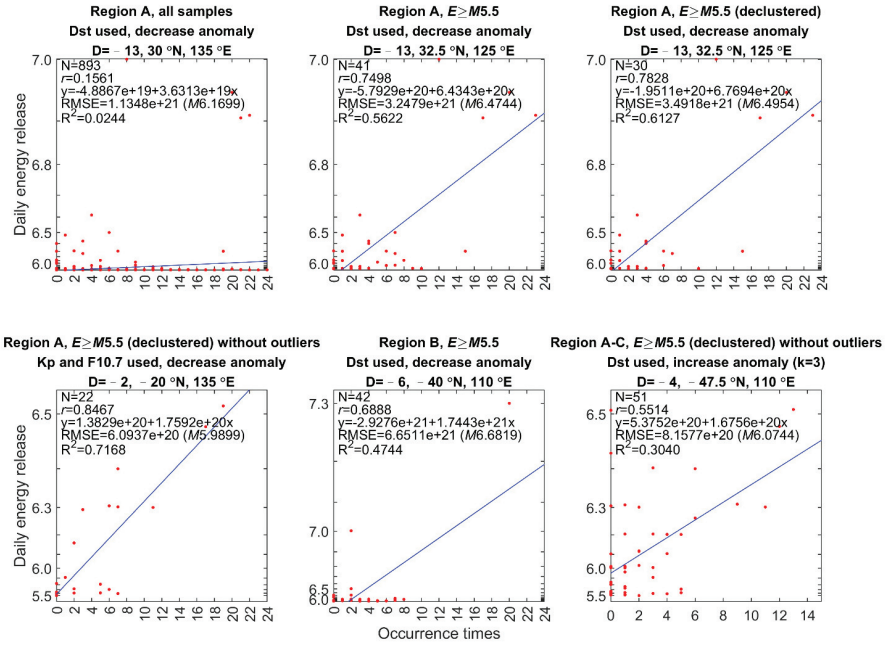

Figure 13. Linear regression models for samples with the minimum p values appearing in the 120°E sector and before the energy release. The time and locations of samples, anomaly types, and the methods used to eliminate the space weather effects are indicated in title. The sample size (N), r, equation of best fit line (x: occurrence times of TEC anomaly, y: daily seismic wave energy release in erg), RMSE (in erg and magnitude), and R^2 are shown in each panel. The unit of y-axis is erg, and the values and ticks are displayed with the corresponding magnitudes.

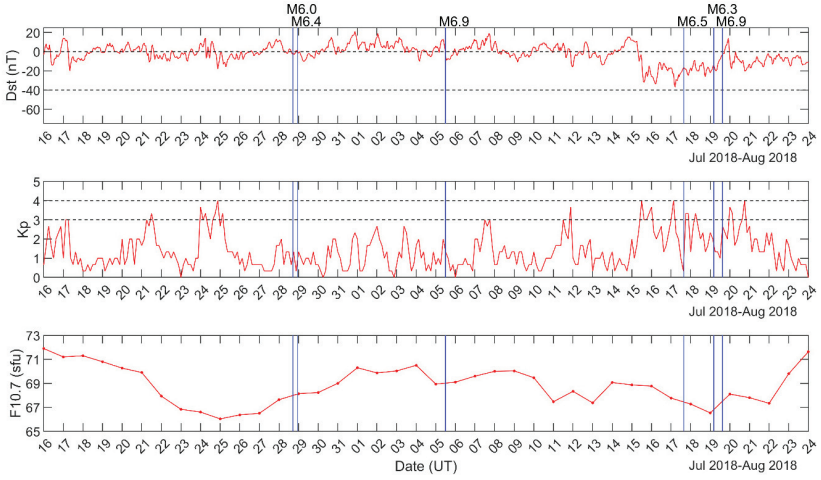

Figure 14. Temporal variations of Dst, Kp, and F10.7 during 16 July to 23 August 2018. The blue lines denote the time of six earthquakes during the period (1. *M*6 at 17:07:23 on 28 July, 7.10°S, 122.73°E. 2. *M*6.4 at 22:47:38 on 28 July, 8.24°S, 116.51°E. 3. *M*6.9 at 11:46:38 on 5 August, 8.26°S, 116.44°E. 4. *M*6.5 at 15:35:01 on 17 August, 7.37°S, 119.80°E. 5. *M*6.3 at 04:10:22 on 19 August, and 8.34°S, 116.60°E. 6. *M*6.9 at 14:56:27 on 19 August, 8.32°S, 116.63°E.). The time of the earthquake catalog is in UTC.

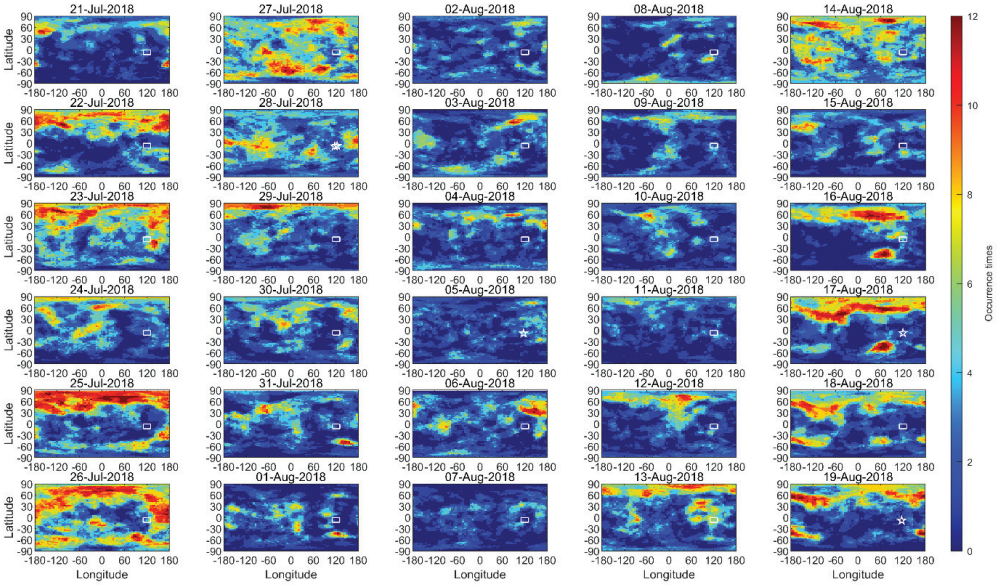

Figure 15. Daily occurrence times of the TEC decrease anomaly from JPL. The time resolution of JPL GIM is 2 h. The UT date is noted on top of each panel. The white box denotes Region A, and the stars denote the earthquakes occurring on the four days.

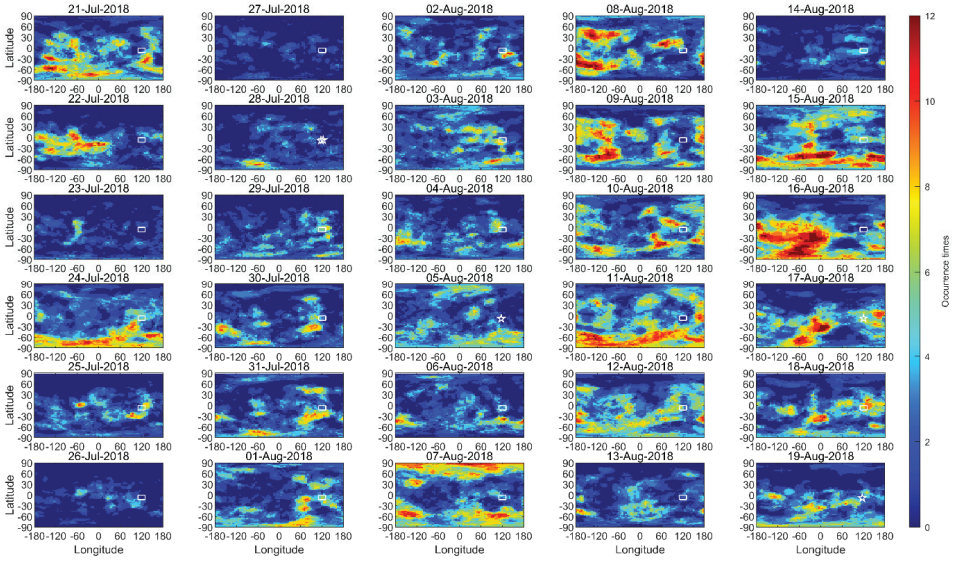

Figure 16. Same as Figure 15 for the daily occurrence times of the TEC increase anomaly.

Due to the conjugate effects of the ionospheric variations observed prior to the earthquakes, the electric field perturbations could be important. The origin of the electric field perturbations might be associated with the neutral wind modification. For example, Oyama et al. [17] proposed that the internal gravity waves (IGWs) of extremely small amplitude produced by small-amplitude ground motion before a large earthquake could be one of the possible origins. The IGWs interact with planetary-scale waves below 10 km and are amplified. When the amplified IGWs propagate to the dynamo region, they modify the

wind system or conductivity and, in turn, modify the electric field. Due to the frequent occurrences of ionospheric anomalies, the earthquake signals must constantly interact with the ionosphere. In addition, the statistical results in this study show a possibility of earthquake effects at higher latitudes; therefore, the area of neutral wind modification should be quite large. To understand the ionospheric variability, it is required to apply more parameters to the analyses and investigate the possibility of connections with earthquakes.

5. Conclusions

In conclusion, the temporal and spatial correlation between the seismic wave energy releases within the three low geomagnetic latitude regions in 110–130°E and the occurrence times of the ionospheric TEC anomalies have been examined. Four longitude sectors of 120, 30, −60, and −150°E are investigated, and there is no clear difference in the distributions of correlation coefficients between 120°E and the other sectors. Although the statistical results do not show sufficient evidence for the specific SIPs for the three study regions, the greater occurrence times of the TEC decrease anomaly are found on D = −13 prior to two *M*6.9 earthquakes in August 2018 in the southeast of Region A and the conjugate point by using JPL GIM, according to the results of statistical investigations. Therefore, it is required to apply more parameters to analyze the causes of the ionospheric TEC variations and investigate the possible connections with earthquakes.

Supplementary Materials: The following are available online at https://www.mdpi.com/article/10.3390/rs14051155/s1, Supplementary Material S1 (Figure S1): Dst variations, temporal distributions of earthquake events and variations in daily total seismic wave energy release during 2015–2018 for earthquakes and energy releases within 110–130°E, Region A, Region B, and Region C, Supplementary Material S2 (Figures S1–S24): results of correlation analyses shown in Section 3, Supplementary Material S3 (Figures S1–S20, Tables S1–S4): results of correlation analyses for the declustered samples with energy releases $\geq$ *M*5.5 without outliers for Regions A, B, and C, and for the declustered samples with energy releases $\geq$ *M*5.5 from the entire area of Regions A–C, Supplementary Material S4 (Figures S1–S12, Tables S1–S2): results of correlation analyses for the declustered samples with energy releases $\geq$ *M*5.5 with outliers for Regions A, B, and C. Supplementary Material S5 (Figures S1–S12, Tables S1–S2): results of correlation analyses for the declustered samples with energy releases $\geq$ *M*5.5 without outliers from three times of random permutations of energy releases within Region A.

Author Contributions: Conceptualization, Y.-C.S. and J.S.; methodology, Y.-C.S.; software, Y.-C.S.; validation, Y.-C.S. and J.S.; formal analysis, Y.-C.S.; investigation, Y.-C.S.; resources, J.S.; data curation, Y.-C.S.; writing—original draft preparation, Y.-C.S.; writing—review and editing, Y.-C.S.; visualization, Y.-C.S.; supervision, J.S.; project administration, J.S.; funding acquisition, J.S. All authors have read and agreed to the published version of the manuscript.

Funding: This research was funded by the Multigovernment International Science and Technology Innovation Cooperation Key Project of the National Key Research and Development Program of China (grant number 2018YFE0184300), EU Erasmus+ Project "Innovation on Remote Sensing Education and Learning (IRSEL)" (586037-EPP-1-2017-1-HU-EPPKA2-CBHE-JP), EU Erasmus+ Project "GIS and Remote Sensing for Sustainable Forestry and Ecology (SUFOGIS)" (598838-EPP-1-2018-EL-EPPKA2-CBHE-JP), Fujian Provincial Department of Science and Technology (2018I0005), and Fujian Provincial Department of Human Resources and Social Security (2017 strait postdoctoral exchange funding project).

Institutional Review Board Statement: Not applicable.

Informed Consent Statement: Not applicable.

Data Availability Statement: The GIM data is obtained from the Center for Orbit Determination in Europe (CODE) (http://www.aiub.unibe.ch/download/CODE, last accessed on 24 February 2022). The earthquake catalog is obtained from the U.S. Geological Survey (https://earthquake.usgs.gov/earthquakes/search/, last accessed on 26 January 2022). The Dst index is obtained from the World Data Center for Geomagnetism in Kyoto (http://wdc.kugi.kyoto-u.ac.jp/dstdir/, last accessed on 24 January 2022). The results presented in this paper rely on the Kp index, calculated and made available by ISGI Collaborating Institutes from data collected at magnetic observatories. We thank

the involved national institutes, the INTERMAGNET network, and ISGI (isgi.unistra.fr, last accessed on 30 January 2022). The F10.7 is obtained from Natural Resources Canada (https://spaceweather.gc.ca/solarflux/sx-5-en.php, last accessed on 30 January 2022). The GIM TEC data published by JPL is downloaded from the Crustal Dynamics Data Information System (ftp://gdc.cddis.eosdis.nasa.gov/, last accessed on 26 January 2022).

Acknowledgments: The authors are grateful to J.Y. Liu (Department of Space Sciences & Engineering, National Central University) for his guidance. The authors are grateful to P.K. Rajesh (Department of Earth Sciences, National Cheng Kung University) for his help in correcting the manuscript. The authors are also deeply grateful to the anonymous reviewers for their critical comments and suggestions.

Conflicts of Interest: The authors declare no conflict of interest.

References

1. Yen, H.Y.; Chen, C.H.; Yeh, Y.H.; Liu, J.Y.; Lin, C.R.; Tsai, Y.B. Geomagnetic Fluctuations during the 1999 Chi-Chi Earthquake in Taiwan. *Earth Planets Space* **2004**, *56*, 39–45. [CrossRef]
2. Chen, C.H.; Liu, J.Y.; Yen, H.Y.; Zeng, X.; Yeh, Y.H. Changes of Geomagnetic Total Field and Occurrences of Earthquakes in Taiwan. *Terr. Atmos. Ocean. Sci.* **2004**, *15*, 361–370. [CrossRef]
3. Chen, C.H.; Liu, J.Y.; Lin, P.Y.; Yen, H.Y.; Hattori, K.; Liang, W.T.; Chen, Y.I.; Yeh, Y.H.; Zeng, X. Pre-Seismic Geomagnetic Anomaly and Earthquake Location. *Tectonophysics* **2010**, *489*, 240–247. [CrossRef]
4. Chen, C.H.; Wang, C.H.; Wen, S.; Yeh, T.K.; Lin, C.H.; Liu, J.Y.; Yen, H.Y.; Lin, C.; Rau, R.J.; Lin, T.W. Anomalous Frequency Characteristics of Groundwater Level before Major Earthquakes in Taiwan. *Hydrol. Earth Syst. Sci.* **2013**, *17*, 1693–1703. [CrossRef]
5. Chen, C.H.; Wen, S.; Yeh, T.K.; Wang, C.H.; Yen, H.Y.; Liu, J.Y.; Hobara, Y.; Han, P. Observation of Surface Displacements from GPS Analyses before and after the Jiashian Earthquake (M = 6.4) in Taiwan. *J. Asian Earth Sci.* **2013**, *62*, 662–671. [CrossRef]
6. Liu, J.Y.; Chen, Y.I.; Pulinets, S.A.; Tsai, Y.B.; Chuo, Y.J. Seismo-Ionospheric Signatures Prior to M $\geq$ 6.0 Taiwan Earthquakes. *Geophys. Res. Lett.* **2000**, *27*, 3113–3116. [CrossRef]
7. Liu, J.Y.; Chen, Y.I.; Chuo, Y.J.; Tsai, H.F. Variations of Ionospheric Total Electron Content during the Chi-Chi Earthquake. *Geophys. Res. Lett.* **2001**, *28*, 1383–1386. [CrossRef]
8. Liu, J.Y.; Chen, Y.I.; Chen, C.H.; Liu, C.Y.; Nishihashi, M.; Li, J.Z.; Xia, Y.Q.; Oyama, K.I.; Hattori, K.; Lin, C.C.H. Seismoionospheric GPS Total Electron Content Anomalies Observed before the 12 May 2008 M_w 7.9 Wenchuan Earthquake. *J. Geophys. Res. Space Phys.* **2009**, *114*, A04320. [CrossRef]
9. Liu, J.Y.; Chen, Y.I.; Chen, C.H.; Hattori, K. Temporal and Spatial Precursors in the Ionospheric Global Positioning System (GPS) Total Electron Content Observed before the 26 December 2004 M 9.3 Sumatra-Andaman Earthquake. *J. Geophys. Res. Space Phys.* **2010**, *115*, A09312. [CrossRef]
10. Liu, J.Y.; Le, H.; Chen, Y.I.; Chen, C.H.; Liu, L.; Wan, W.; Su, Y.Z.; Sun, Y.Y.; Lin, C.H.; Chen, M.Q. Observations and Simulations of Seismoionospheric GPS Total Electron Content Anomalies before the 12 January 2010 M 7 Haiti Earthquake. *J. Geophys. Res. Space Phys.* **2011**, *116*, A04302. [CrossRef]
11. Liu, J.Y.; Chen, Y.I.; Huang, C.C.; Parrot, M.; Shen, X.H.; Pulinets, S.A.; Yang, Q.S.; Ho, Y.Y. A Spatial Analysis on Seismo-Ionospheric Anomalies Observed by DEMETER during the 2008 M 8.0 Wenchuan Earthquake. *J. Asian Earth Sci.* **2015**, *114*, 414–419. [CrossRef]
12. Yan, R.; Shen, X.; Huang, J.; Wang, Q.; Chu, W.; Liu, D.; Yang, Y.; Lu, H.; Xu, S. Examples of Unusual Ionospheric Observations by the CSES Prior to Earthquakes. *Earth Planet. Phys.* **2018**, *2*, 515–526. [CrossRef]
13. Chen, Y.I.; Huang, C.S.; Liu, J.Y. Statistical Evidences of Seismo-Ionospheric Precursors Applying Receiver Operating Characteristic (ROC) Curve on the GPS Total Electron Content in China. *J. Asian Earth Sci.* **2015**, *114*, 393–402. [CrossRef]
14. Liu, J.Y.; Chen, Y.I.; Chuo, Y.J.; Chen, C.S. A Statistical Investigation of Preearthquake Ionospheric Anomaly. *J. Geophys. Res.* **2006**, *111*, A05304. [CrossRef]
15. Liu, J.Y.; Chen, C.H.; Chen, Y.I.; Yang, W.H.; Oyama, K.I.; Kuo, K.W. A Statistical Study of Ionospheric Earthquake Precursors Monitored by Using Equatorial Ionization Anomaly of GPS TEC in Taiwan during 2001–2007. *J. Asian Earth Sci.* **2010**, *39*, 76–80. [CrossRef]
16. Pulinets, S.; Davidenko, D. Ionospheric Precursors of Earthquakes and Global Electric Circuit. *Adv. Space Res.* **2014**, *53*, 709–723. [CrossRef]
17. Oyama, K.I.; Chen, C.H.; Bankov, L.; Minakshi, D.; Ryu, K.; Liu, J.Y.; Liu, H. Precursor Effect of 11 March 2011 off the Coast of Tohoku Earthquake on High and Low Latitude Ionospheres and Its Possible Disturbing Mechanism. *Adv. Space Res.* **2019**, *63*, 2623–2637. [CrossRef]
18. Kelley, M.C.; Swartz, W.E.; Heki, K. Apparent Ionospheric Total Electron Content Variations Prior to Major Earthquakes Due to Electric Fields Created by Tectonic Stresses. *J. Geophys. Res. Space Phys.* **2017**, *122*, 6689–6695. [CrossRef]
19. Kim, V.P.; Hegai, V.V.; Liu, J.Y.; Ryu, K.; Chung, J.K. Time-Varying Seismogenic Coulomb Electric Fields as a Probable Source for Pre-Earthquake Variation in the Ionospheric F2-Layer. *J. Astron. Space Sci.* **2017**, *34*, 251–256. [CrossRef]

20. Masci, F.; Thomas, J.N.; Secan, J.A. On a Reported Effect in Ionospheric TEC around the Time of the 6 April 2009 L'Aquila Earthquake. *Nat. Hazards Earth Syst. Sci.* **2017**, *17*, 1461–1468. [CrossRef]
21. Nenovski, P.I.; Pezzopane, M.; Ciraolo, L.; Vellante, M.; Villante, U.; de Lauretis, M. Local Changes in the Total Electron Content Immediately before the 2009 Abruzzo Earthquake. *Adv. Space Res.* **2015**, *55*, 243–258. [CrossRef]
22. Dautermann, T.; Calais, E.; Haase, J.; Garrison, J. Investigation of Ionospheric Electron Content Variations before Earthquakes in Southern California, 2003–2004. *J. Geophys. Res.* **2007**, *112*, B02106. [CrossRef]
23. Thomas, J.N.; Huard, J.; Masci, F. A Statistical Study of Global Ionospheric Map Total Electron Content Changes Prior to Occurrences of $M \geq 6.0$ Earthquakes during 2000–2014. *J. Geophys. Res. Space Phys.* **2017**, *122*, 2151–2161. [CrossRef]
24. Gutenberg, B.; Richter, C.F. Earthquake Magnitude, Intensity, Energy, and Acceleration. *Bull. Seismol. Soc. Am.* **1956**, *46*, 105–145. [CrossRef]
25. *CODE Final Product Series for the IGS*; Astronomical Institute, University of Bern: Bern, Switzerland, 2020. [CrossRef]
26. Liu, J.Y.; Yang, W.H.; Lin, C.H.; Chen, Y.I.; Lee, I.T. A Statistical Study on the Characteristics of Ionospheric Storms in the Equatorial Ionization Anomaly Region: GPS-TEC Observed over Taiwan. *J. Geophys. Res. Space Phys.* **2013**, *118*, 3856–3865. [CrossRef]
27. Zhu, F.; Su, F.; Lin, J. Statistical Analysis of TEC Anomalies Prior to M 6.0 + Earthquakes During 2003–2014. *Pure Appl. Geophys.* **2018**, *175*, 3441–3450. [CrossRef]
28. Illowsky, B.; Dean, S. Testing the Significance of the Correlation Coefficient. In *Introductory Statistics*; OpenStax: Houston, TX, USA, 2013; Available online: https://opentextbc.ca/introstatopenstax/chapter/testing-the-significance-of-the-correlation-coefficient/ (accessed on 30 November 2021).

remote sensing

MDPI

Article

A Novel Method to Estimate Multi-GNSS Differential Code Bias without Using Ionospheric Function Model and Global Ionosphere Map

Qisheng Wang [1], Shuanggen Jin [2,3,*] and Xianfeng Ye [1]

[1] College of Civil Engineering and Mechanics, Xiangtan University, Xiangtan 411105, China; qswang@xtu.edu.cn (Q.W.); yexianfeng3422@xtu.edu.cn (X.Y.)
[2] School of Surveying and Land Information Engineering, Henan Polytechnic University, Jiaozuo 454000, China
[3] Shanghai Astronomical Observatory, Chinese Academy of Sciences, Shanghai 200030, China
* Correspondence: sgjin@shao.ac.cn or sg.jin@yahoo.com; Tel.: +86-21-34775292

Abstract: Global navigation satellite system (GNSS) differential code bias (DCB) is one of main errors in ionospheric modeling and applications. Accurate estimation of multiple types of GNSS DCBs is important for GNSS positioning, navigation, and timing, as well as ionospheric modeling. In this study, a novel method of multi-GNSS DCB estimation is proposed without using an ionospheric function model and global ionosphere map (GIM), namely independent GNSS DCB estimation (IGDE). Firstly, ionospheric observations are extracted based on the geometry-free combination of dual-frequency multi-GNSS code observations. Secondly, the VTEC of the station represented by the weighted mean VTEC value of the ionospheric pierce points (IPPs) at each epoch is estimated as a parameter together with the combined receiver and satellite DCBs (RSDCBs). Last, the estimated RSDCBs are used as new observations, whose weight is calculated from estimated covariances, and thus the satellite and receiver DCBs of multi-GNSS are estimated. Nineteen types of multi-GNSS satellite DCBs are estimated based on 200-day observations from more than 300 multi-GNSS experiment (MGEX) stations, and the performance of the proposed method is evaluated by comparing with MGEX products. The results show that the mean RMS value is 0.12, 0.23, 0.21, 0.13, and 0.11 ns for GPS, GLONASS, BDS, Galileo, and QZSS DCBs, respectively, with respect to MGEX products, and the stability of estimated GPS, GLONASS, BDS, Galileo, and QZSS DCBs is 0.07, 0.06, 0.13, 0.11, and 0.11 ns, respectively. The proposed method shows good performance of multi-GNSS DCB estimation in low-solar-activity periods.

Keywords: differential code bias (DCB); global navigation satellite systems (GNSS); multi-GNSS experiments (MGEX); total electron content (TEC)

Citation: Wang, Q.; Jin, S.; Ye, X. A Novel Method to Estimate Multi-GNSS Differential Code Bias without Using Ionospheric Function Model and Global Ionosphere Map. *Remote Sens.* **2022**, *14*, 2002. https://doi.org/10.3390/rs14092002

Academic Editors: Ali Khenchaf and José Fernández

Received: 30 January 2022
Accepted: 20 April 2022
Published: 21 April 2022

1. Introduction

Global navigation satellite system (GNSS) differential code bias (DCB) is the difference between a hardware delay bias of two code observations [1,2]. According to the frequency of two code observations, DCBs can be divided into inter-frequency and intra-frequency DCBs, which are the error sources in the GNSS ionospheric modeling and the application of positioning, navigation, and timing [3–6]. Generally, the intra-frequency DCBs can be directly determined by the mean value of differences between the corresponding code observations [7]. However, the inter-frequency DCBs are the parameters of the ionospheric observation equation obtained through dual-frequency code observations, which need to be estimated through the corresponding methods. Therefore, most of the attention on DCB is focused on inter-frequency DCB [8]. Similarly, the estimated DCB in this study is referred to as the inter-frequency DCB.

Generally, mainly two approaches are used to calculate the DCB parameter. The first method is to model regional or global total electron content (TEC) through a definite

mathematical function, e.g., a spherical harmonic function for global TEC modeling and a generalized triangular series function or polynomial function for regional TEC modeling [7,9–13]. Then the DCB parameter can be obtained together with the TEC modeling. The second method is to eliminate the TEC parameter through the existing global ionospheric map (GIM) [3,14,15], and then we can calculate the DCB. Because of the high correlation between DCB and TEC, DCB, as a by-product of ionosphere modeling, is regularly produced along with the GIM by the International GNSS Service (IGS) Analysis Center (IAC) [1,10,16–18]. These IACs, e.g., the Center for Orbit Determination in Europe (CODE), mainly provide the DCB products of GPS and GLONASS through the first method mentioned above. Due to the good coverage of GPS and GLONASS satellites, more observations can be used, and the estimated satellite DCBs present good stability. Thus, the monthly DCB products, including GPS P1-P2 (C1W-C2W) DCB and GLONASS P1-P2 (C1P-C2P) DCB, are provided by CODE.

In recent years, the rapid development of multi-GNSS accounts for the strong demand for multiple types of DCBs, instead of just a single type from GPS and GLONASS [19–23]. In the current IACs, only two agencies, namely, the Chinese Academy of Sciences (CAS) and Deutsches Zentrum Für Luft-und Raumfahrt (DLR), provide multi-GNSS (GPS, GLONASS, BDS, Galileo, and QZSS) DCB products [7,15]. In terms of the DCB estimation method, the CAS produces the MGEX DCB products through the IGGDCB method proposed by Li et al. [24], in which single-station TEC modeling based on a generalized triangular series function was used [7], whereas MGEX DCB from DLR was estimated through the second method mentioned above [15]. Their products can be obtained from ftp://cddis.gsfc.nasa.gov/pub/gps/products/mgex/dcb/ (accessed on 1 June 2020). The information on MGEX DCB products provided by CAS and DLR is listed in Table 1, which includes 19 types of DCBs in total. It should be noted that GPS C1W-C2W DCB and GLONASS C1P-C2P DCB are not directly provided by DLR, whose value can be derived from the combined value of the other two types of DCBs [25], i.e., $DCB_{C1W-C2W} = DCB_{C1C-C2W} - DCB_{C1C-C1W}$ and $DCB_{C1P-C2P} = DCB_{C1C-C2P} - DCB_{C1C-C1P}$.

Table 1. Information on the MGEX DCB products provided by CAS and DLR.

No.	System	Bias Type	CAS	DLR	No.	System	Bias Type	CAS	DLR
1	GPS	C1C-C2W	✓	✓	10	Galileo	C1X-C5X	✓	✓
2		C1W-C2W	✓		11		C1X-C7X	✓	✓
3		C1C-C5X	✓	✓	12		C1X-C8X	✓	✓
4		C1C-C5Q	✓	✓	13		C1C-C5Q	✓	✓
5	GLONASS	C1C-C2P	✓	✓	14		C1C-C7Q	✓	✓
6		C1P-C2P	✓		15		C1C-C8Q	✓	✓
7		C1C-C2C	✓	✓	16	QZSS	C1X-C2X	✓	✓
8	BDS	C2I-C7I	✓	✓	17		C1X-C5X	✓	✓
9		C2I-C6I	✓	✓	18		C1C-C2L	✓	✓
10					19		C1C-C5Q	✓	✓

In terms of most DCB estimation methods, including those currently used in the CAS and DLR, the ionospheric observations are extracted based on the geometry-free combination of dual-frequency code measures, since the extraction method is simple to implement without relying on other external products. In addition, some studies on DCB estimation through the precise point-positioning (PPP) method have also been carried out [5,19,25,26]. However, these methods of DCB estimation rely on ionospheric function models and global ionosphere maps.

In this study, to estimate multi-GNSS DCB efficiently and accurately, a new method of multi-GNSS DCB estimation is proposed without relying on the ionospheric function model and existing global ionosphere map (GIM). In the following, the proposed new method is described in detail in Section 2. In Section 3, 200 days of observations from more than 300 multi-GNSS experiment (MGEX) stations are collected for the estimation of the types of multi-GNSS satellite DCBs. The estimated DCBs are compared with the MGEX

DCB products for validation and evaluation. Finally, the corresponding discussion and conclusion are given in Sections 4 and 5, respectively.

2. Methods and Data

2.1. A New Method of Multi-GNSS DCB Estimation

The GNSS satellite and receiver DCB is the parameter to be estimated in the ionospheric observation equation together with the ionospheric TEC. The ionospheric observation equation can be obtained based on the geometry-free linear combination of dual-frequency GNSS code observations. Generally, the code observation is smoothed through the carrier phases, since it is susceptible to noises and multipath errors [1,27]. The smoothed code observation equation can be expressed as:

$$\begin{cases} \overline{P}_{4,r,k} = RS^j_{r,k} + \frac{1}{F_k} \cdot VTEC_k + \varepsilon \\ RS^i_{r,k} = c \cdot \left(DCB^j + DCB_r\right) \end{cases} \tag{1}$$

where $\overline{P}_{4,r,k}$ is the smoothed code observation of epoch k at station r; c is the speed of light; $RS^i_{r,k}$ is the combined value of satellite and receiver DCB of epoch k at station r; DCB^j and DCB_r are the satellite and receiver DCB, respectively; $VTEC_k$ is the vertical total electron content (VTEC) of the corresponding the ionospheric pierce point (IPP) at epoch k; ε is the ionospheric observation error; $F^j_k = f_1^2 \cdot f_2^2 / (40.28 \times (f_1^2 - f_2^2)) \cdot M(z)$, where f_1 and f_2 are the first and second frequency of the observations, respectively; and $M(z)$ is the mapping function used to convert the slant total electron content (STEC) to the VTEC. The mapping function used in this study is the modified single-layer model (MSLM), which can be expressed as [1]:

$$M(z) = \cos\left(\arcsin\left(\frac{R}{R+H}\sin(az)\right)\right) \tag{2}$$

where R is the mean radius of the Earth (R = 6371 km), H is the height of the assumed single-layer ionosphere (H = 506.7 km), a is a correction factor (a = 0.9782), and z is the satellite zenith angle of a satellite at the receiver.

According to Equation (1), there are two parameters, namely, RS and TEC, in the observation equation of each available epoch. Thus, it is impossible to obtain the solution of parameters directly through the least-square adjustment. As mentioned above, two methods, namely, TEC function modeling for regional or global and TEC eliminating through existing global ionosphere maps, can also be adopted to estimate the DCBs. Concerning Equation (1), the DCB parameter can be obtained directly if the TEC parameter can be determined. In fact, the VTEC of IPPs can be converted into the VTEC of a station if the relationship between them is established. As can be seen from the sketch of the IPP distribution shown in Figure 1, the red dot represents the station and the black dots represent IPPs, and the location of the station can be regarded as the center of the limited distribution area of the IPPs. This means that the variation of TEC in this area is relatively small, and the TEC value of the IPP is close to that of the station when the distance between them is short. Thus, the VTEC of the station and the IPPs can be expressed as follows:

$$\Delta^j_k = VTEC^s_k - VTEC^j_k \tag{3}$$

where $VTEC^s_k$ is the VTEC of the station at epoch k, $VTEC^i_k$ is the VTEC of ith IPP at epoch k, and Δ^j_k is the difference between them. Obviously, the difference is small when the distance between them is small. Thus, it can be regarded as a virtual observation close to 0.

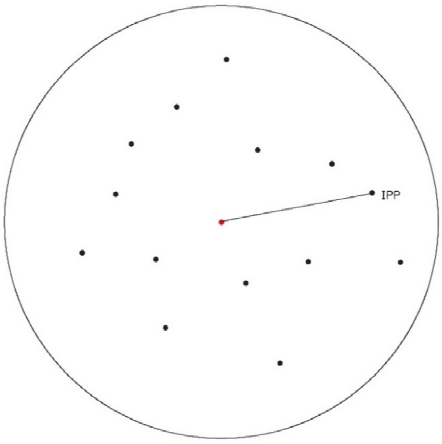

Figure 1. Sketch of the ionospheric pierce point (IPP) distribution.

Combining Equations (1) and (3), a joint observation equation can be obtained:

$$\begin{cases} LP_{r,k}^{j} = F_k^j \cdot RS_{r,k}^j + VTEC_k^s + \Delta_k^j + \varepsilon_{LP} \\ L\Delta_k^j = \Delta_k^j + \varepsilon_{L\Delta} \end{cases} \tag{4}$$

where $LP_{r,k}^{j} = F_k^j \cdot \overline{P}_{4,r,k}^{j}$ is regarded as the original observation, $L\Delta_k^j$ is the virtual observation and $L\Delta_k^j = 0$, and ε_{LP} and $\varepsilon_{L\Delta}$ are the original and virtual observation error, respectively. The weight of the original observation can be determined by the height angle, and the weight of virtual observation is related to the distance, since the weight is larger when the distance between them is very close, which means that the estimated Δ_k^j is close to 0 when the weight is larger. In this paper, we considered that the TEC difference between the IPPs and the station is relatively small in a single-station area. Thus, the used weight is set as a large value. In other words, the second formula of Equation (4) does not act in the adjustment. Thus, the VTEC of the station is represented by the weighted mean VTEC values of the IPPs.

In fact, the TEC difference between the IPPs and the station is not equal to 0, and there may be a large difference among some IPPs far away from the station, especially for those stations located at a low latitude. However, Equation (4) is still available, which can be adjusted with priori right obtained by an inverse ratio of distance. Note that the priori right is an empirical value that needs to be further analyzed. It should be noted that a lager TEC difference may occur at low-latitude stations through our method. Our purpose is to estimate DCB rather than TEC. Stations with large error may remove or reduce their role in the adjustment through the variance of estimation introduced later.

Moreover, the variation in TEC of the station is slow among adjacent epochs. Thus, a random walk can be used to describe the variations, which is regarded as a virtual observation equation to add into the adjustment solution.

$$LS_k = VTEC_{k+1}^s - VTEC_k^s + \varepsilon_{LS} \tag{5}$$

where LS_k is the virtual observation and $LS_k = 0, k = 1, 2, \cdots$, and ε is the random error. The weight of virtual observation is an empirical value and used to balance the random walk and the observations' contribution to the adjustment solution [28]. The value is set as 1/0.03 TECu for all its elements in this study, which is proper in our text experiment.

Considering multi-GNSS observation and combining Equations (4) and (5), it can be expressed in the matrix as:

$$\begin{cases} A \cdot X = L \\ A = \begin{bmatrix} A_{LP} & A_{L\Delta} & A_{LS} \end{bmatrix} \\ X = \begin{bmatrix} RS & VTEC^s & \Delta \end{bmatrix}^T \\ L = \begin{bmatrix} LP & L\Delta & LS \end{bmatrix}^T \end{cases} \tag{6}$$

Based on Equation (6), the RS and VTEC can be solved through the least-square adjustment. Then, the covariance of the parameters can be obtained as:

$$D_{XX} = \begin{bmatrix} D_{RS} & \\ & D_{VTEC} \end{bmatrix} \tag{7}$$

The correlation between parameters was not considered in Equation (7). Therefore, the combined value of satellite and receiver DCB of multi-GNSS and its covariance for each station can be obtained. Then, satellite and receiver DCB of multi-GNSS can be separated based on the RS value of all stations. The separation of satellite and receiver DCB can be expressed in the matrix as:

$$\begin{cases} RS = A_{RS} \cdot X_{DCB} \\ X_{DCB} = \begin{bmatrix} X_R & X_S \end{bmatrix} \\ A_{RS} = \begin{bmatrix} A_R & A_S \end{bmatrix} \end{cases} \tag{8}$$

where A_{RS} is the design matrix of DCB and consists of A_R and A_S, and X_{DCB} is the DCB estimate and consists of satellite DCB X_S and receiver DCB X_R. Considering the different accuracy of the combined value of satellite and receiver DCB obtained at different stations, a weight is used in the adjustment of Equation (8), which can be defined as:

$$P_{RS} = D_{RS}^{-1} \tag{9}$$

Because of the correlation between receiver and satellite DCBs, a zero-mean satellite reference needs to be added to the adjustment of Equation (8), which can be expressed as:

$$\begin{cases} 0 = C \cdot X_{DCB} \\ X_{DCB} = \begin{bmatrix} X_R & X_S \end{bmatrix} \\ C = \begin{bmatrix} 0 & e_S \end{bmatrix} \end{cases} \tag{10}$$

Thus, by combining Equations (8)–(10), the satellite and receiver DCBs of multi-GNSS can be obtained. According to the above derivation, the new method can be implemented in three steps. The first step is to extract ionospheric observations through the approach of carrier smooth pseudo-distance with the geometry-free linear combination of dual-frequency multi-GNSS code observations. Then, the VTEC of the station, represented by the weighted mean VTEC values of the IPPs of each epoch, is estimated as a parameter together with the combined value of satellite and receiver DCBs at the epoch. Last, the previously estimated RS DCBs are used as new observations, whose weight is calculated with the use of the estimated covariances, and then the satellite and receiver DCBs of multi-GNSS are estimated. The corresponding flowchart of the new method of multi-GNSS DCB estimation is illustrated in Figure 2.

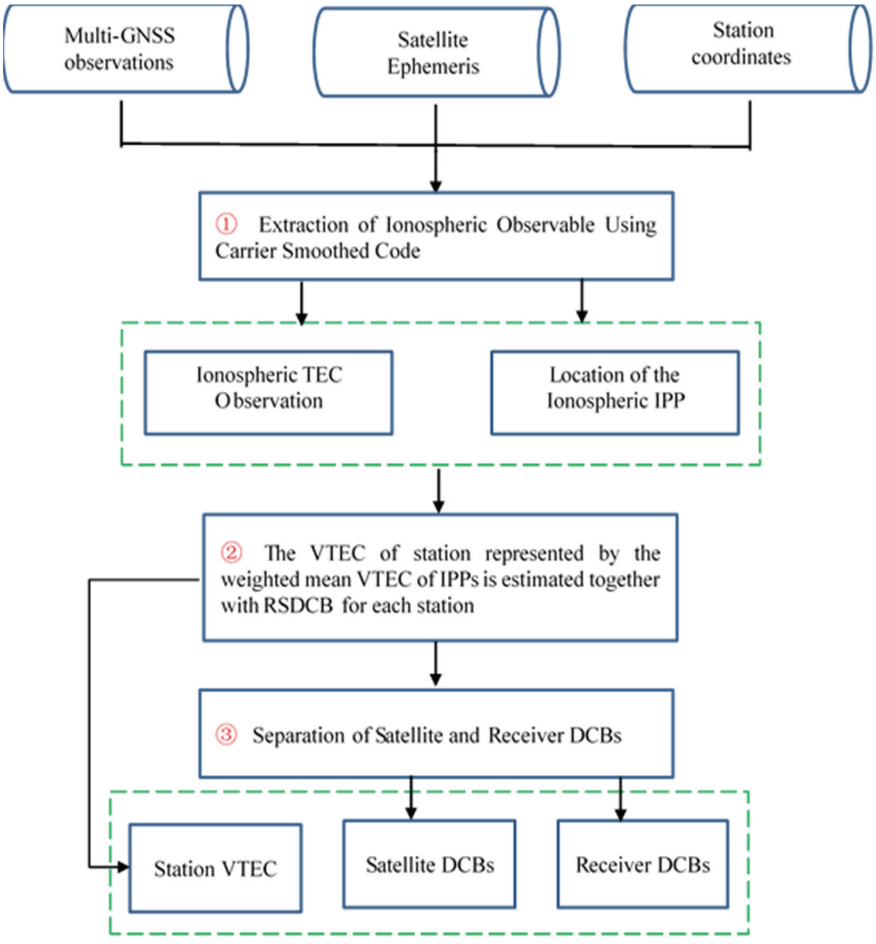

Figure 2. Flowchart of the new method of multi-GNSS DCB estimation.

For convenience in the following analysis, the proposed method is named IGDE (independent GNSS DCB estimation), which can be found to determine the satellite and receiver DCB values by estimating VTEC directly, instead of modeling TEC by function or eliminating TEC parameters by GIM. In addition, in order to reduce multipath error and mapping function error, a 20° cutoff elevation is used in this IGDE method. It is feasible to represent the VTEC of the station by the average value of the VTEC of the IPP, because we consider that the VTEC value is not much different in the limited area, and the position of the station can be regarded as the center of the area. The observations of multi-GNSS can be marked as full use through the IGDE method, and the observations from GPS as well as GLONASS with a good quality can be used to strengthen the adjustment.

2.2. Experimental Data

In order to better verify the performance of the new method proposed in this study, more than 300 MGEX stations were selected, which are shown in Figure 3. It can be clearly seen that these stations roughly show the global distribution. It was sufficient to use these MGEX stations for DCB estimation. Figure 4 shows the number of available stations for different DCB type estimation. The serial numbers of the *x*-axis in the figure corresponds to

the serial number in Table 1—e.g., 1 corresponds to C1C-C2W of the GPS in Table 1. As is shown in Figure 4, the number of stations tracking the GPS was the largest, whereas that of stations tracking QZSS was the smallest. Due to the wide distribution of GPS tracking stations, all selected stations could be used to track the C1C-C2W observations of GPS. About 290 and 170 stations were available for GLONASS and BDS, respectively. However, the number of stations available for GAIEO and QZSS was smaller than 100. A total of 200 days (DOY 001 to 200, 2019) of data from selected MGEX stations were collected in this study. In addition, the corresponding DCB products provided by CAS, DLR, and CODE were downloaded for verification and comparison.

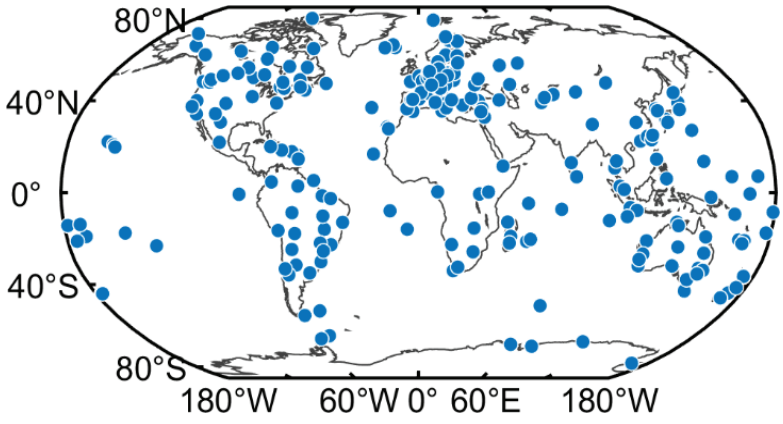

Figure 3. Distribution of the MGEX stations used in this study.

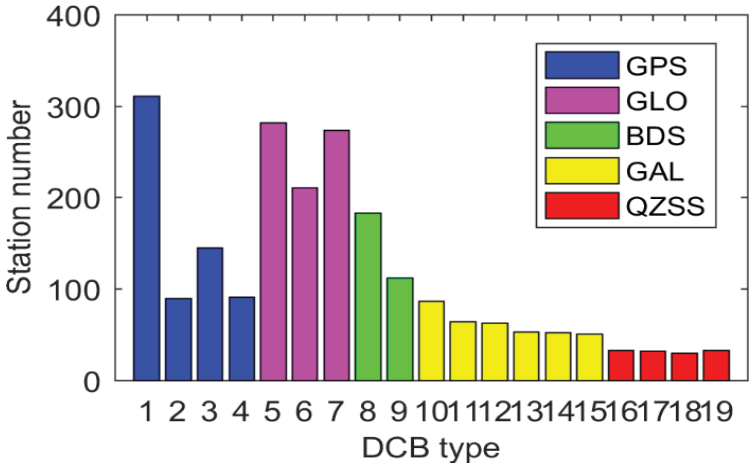

Figure 4. Number of available stations for different DCB type estimation.

3. Results and Analysis

In this section, the proposed new method is first verified, in which the estimated VTEC value of station is compared with that provided by CODE. Then, a difference analysis between the estimated DCB and the MGEX DCB product is implemented. The stability of multi-GNSS DCB through the proposed new method and the MGEX DCB product are finally compared.

3.1. Validation of the New Method

In the proposed new method, the VTEC value of the station can be obtained together with the combined value of the satellite and receiver DCB for each station. Therefore, the evaluation of the VTEC of the station can reflect the performance of the proposed method. Taking four stations as an example, i.e., ZIMJ, RDSD, MAYG, and KERG, the VTEC of the station obtained by IGDE and CODE are compared on DOY 011, 2019. Figure 5 shows the VTEC series value of the IGDE and CODE product at the four stations, two of which are located in the Northern Hemisphere, and the other two in the Southern Hemisphere. In terms of latitude, two of them at a middle latitude and the others are at a low latitude.

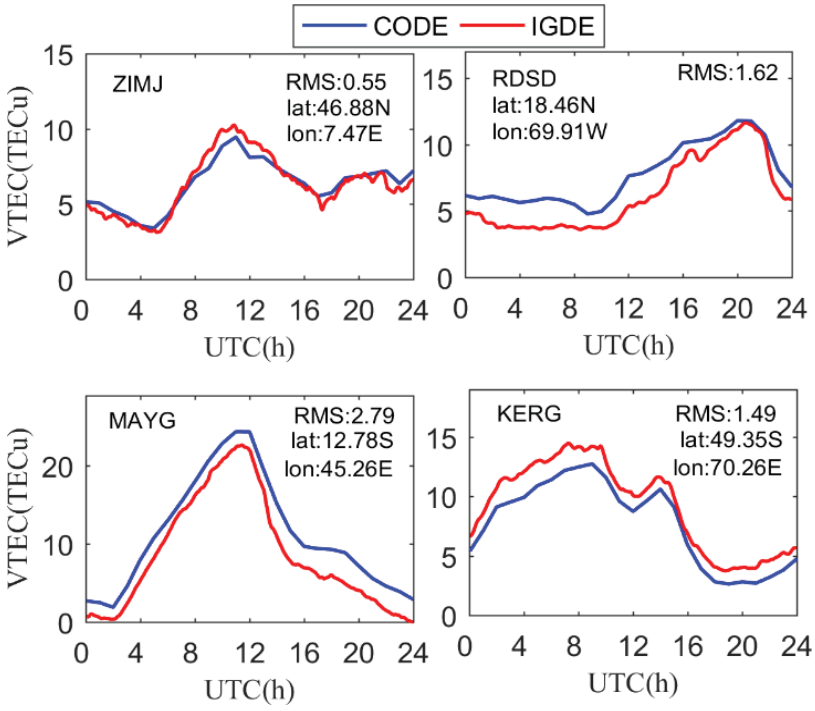

Figure 5. VTEC series value of the IGDE and CODE product for the four stations on DOY 011.

As can be seen from Figure 5, the series value of VTEC obtained by IGDE and CODE showed the same trend throughout the whole day, which indicates that the VTEC of the station obtained by IGDE can show the variation in TEC at the station. However, the performance of IGDE may have been different at different stations. It is obvious that for stations ZIMJ and KERG, the RMS of VTEC was within 1.5 TECU. However, the RMS of RDSD and MAYG was larger than that of other stations, mainly since they are in the equator area with active ionospheric variation. Figure 6 shows the mean difference and RMS of VTEC between the IGDE and CODE product at all MGEX stations on DOY 011, 2019. For most stations, the mean difference and RMS were within ±3 TECu and 3 TECu, respectively. However, the stations located in the low-latitude area, whose mean difference and RMS showed a larger value, showed the same phenomenon, as depicted in Figure 5. Moreover, some large values also appeared at high latitudes, which may be related to the few observations at those stations. The accuracy of TEC from CODE was 2–8 TECu [10], and the mean values of the difference and RMS were −0.25 and 2.28 TECu for all stations, respectively, indicating good performance of the proposed method in VTEC estimating for those stations.

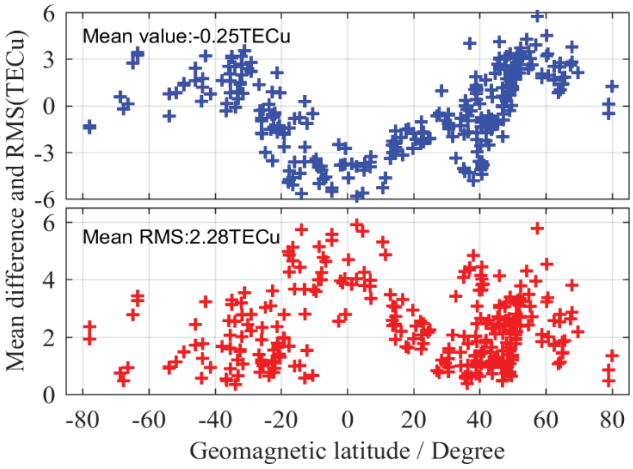

Figure 6. Mean difference and RMS of VTEC between the IGDE and CODE product for all MGEX stations on DOY 011.

3.2. Difference Analysis between Estimated DCB and MGEX DCB Product

As mentioned above, 19 types of multi-GNSS DCBs, which were from GPS, GLONASS, BDS, Galileo, and QZSS, needed to be estimated and analyzed. In order to verify the accuracy and reliability of the DCBs estimated by IGDE, a difference analysis between estimated DCB and the MGEX DCB product was performed in this section. The MGEX DCB products were from CAS and DLR, and the GPS C1W-C2W DCB and GLONASS C1P-C2P DCB provided by CODE were also used as the reference for a better comparison. Because the different satellite DCB reference datum may be used for different DCB estimation methods, the corresponding satellite DCB reference datum needed to be unified before DCB comparison. Different reference benchmarks mean that the number of satellites participating in the zero-mean constraint is different, so they needed to be unified [4,29]. In the following analysis, the mean difference and standard deviation (STD) of multi-GNSS DCB between IGDE and MGEX products are shown in Figures 7–11, and the corresponding root mean square (RMS) values are listed in Table 2.

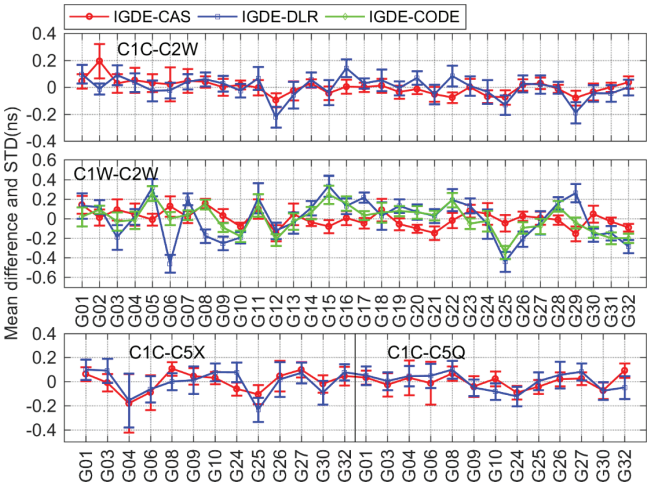

Figure 7. Mean difference and STD of GPS DCB between IGDE and MGEX products.

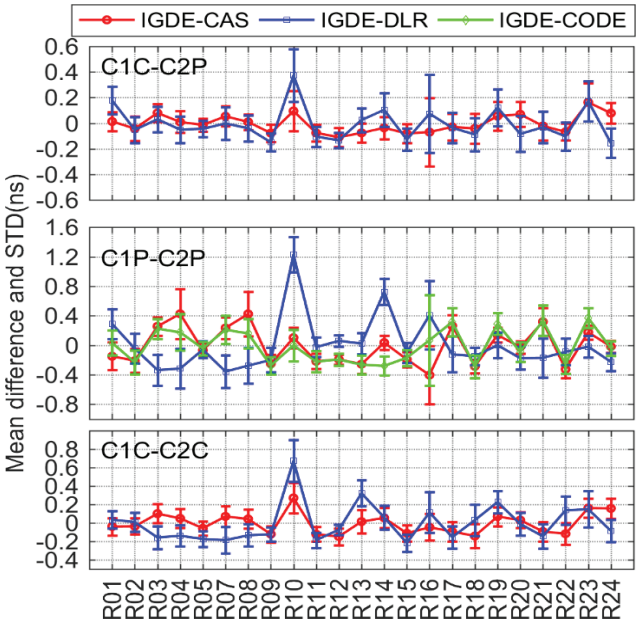

Figure 8. Mean difference and STD of GLONASS DCB between IGDE and MGEX products.

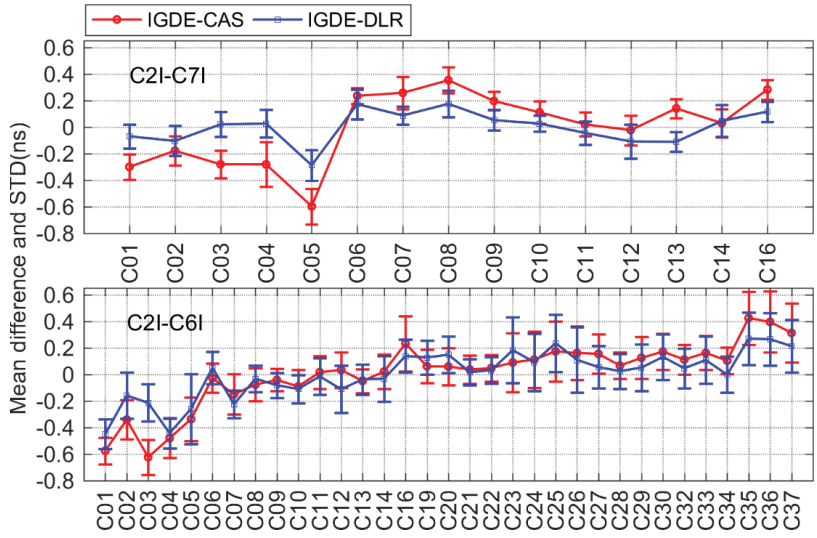

Figure 9. Mean difference and STD of BDS DCB between IGDE and MGEX products.

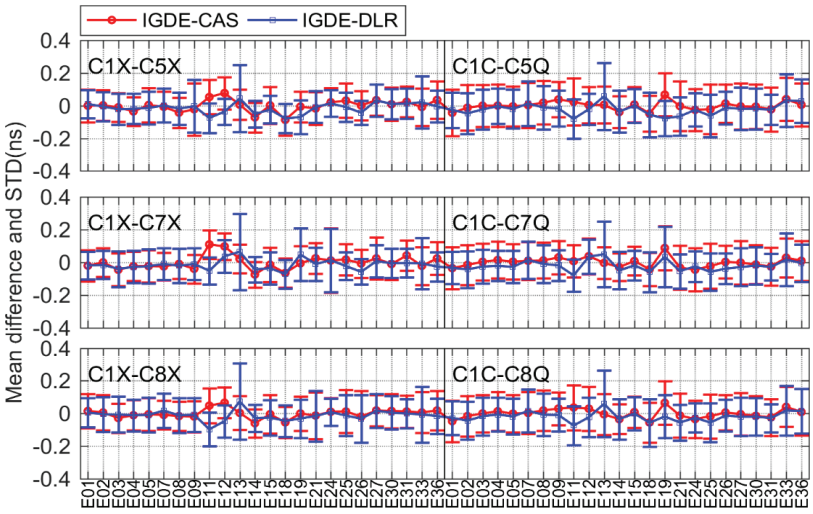

Figure 10. Mean difference and STD of GAILEO DCB between IGDE and MGEX products.

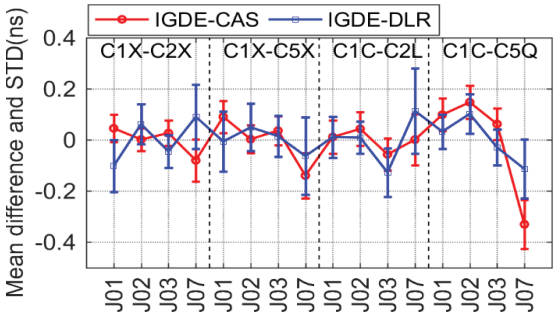

Figure 11. Mean difference and STD of QZSS DCB between IGDE and MGEX products.

Table 2. Mean RMS value of all DCBs between IGDE and MGEX products.

System	DCB Type	CAS	DLR	CODE	System	DCB Type	CAS	DLR
GPS	C1C-C2W	0.07	0.10	0.14	GAL	C1X-C5X	0.11	0.11
	C1W-C2W	0.10	0.20			C1X-C7X	0.11	0.11
	C1C-C5X	0.12	0.14			C1X-C8X	0.11	0.12
	C1C-C5Q	0.10	0.10			C1C-C5Q	0.13	0.13
GLO	C1C-C2P	0.12	0.17	0.28		C1C-C7Q	0.12	0.12
	C1P-C2P	0.27	0.33			C1C-C8Q	0.12	0.12
	C1C-C2C	0.16	0.21		QZSS	C1X-C2X	0.07	0.12
BDS	C2I-C7I	0.25	0.14			C1X-C5X	0.10	0.12
	C2I-C6I	0.24	0.22			C1C-C2L	0.08	0.13
						C1C-C5Q	0.18	0.11

For GPS, four types of DCB, namely, C1C-C2W, C1W-C2W, C1C-C5X, and C1C-C5Q, were compared with CAS, DLR, and CODE. It should be noted that the value of all four types of daily DCB can be provided by CAS and just C1W-C2W daily DCB values can be provided by CODE, whereas the C1W-C2W DCB of DLR can be obtained from $DCB_{C1W-C2W} = DCB_{C1C-C2W} - DCB_{C1C-C1W}$ and the other three types of DCBs from DLR can be obtained directly. As can be seen from the mean difference in Figure 7, the value of four types of DCBs with respect to the products from CAS, DLR, and CODE was

mostly with ±0.4 ns, the largest value of which was near −0.6 ns. Especially for C1W-C2W DCB, the mean difference with respect to CAS and CODE was within ±0.2 ns, and the mean RMS values were 0.10 and 0.14 ns, respectively. As is shown in Table 2, the mean RMS values were 0.07/0.09, 0.12/0.14, and 0.10/0.10 ns for C1C-C2W, C1C-C5X, and C1C-C5Q, respectively, with respect to CAS/DLR.

According to the comparison results of GLONASS DCB shown in Figure 8, three types of DCBs (C1C-C2C, C1P-C2P, and C1C-C2C) were compared with CAS, DLR, and CODE. Similar to GPS C1W-C2W, C1P-C2P DCB was also compared with CODE, and the products from DLR were also derived from $DCB_{C1P-C2P} = DCB_{C1C-C2P} - DCB_{C1C-C1P}$. The other two types of DCBs were compared with CAS and DLR, whose products can be obtained directly. Obviously, the value of difference in GLONASS DCBs was larger than those of the GPS, which may be related to the use of frequency division multiple access (FDMA) technology through GLONASS [7]. The mean difference between C1C-C2P and C1C-C2C DCB with respect to CAS/DLR was mostly within ±0.4 ns, whose mean RMS values were 0.12/0.16 and 0.15/0.21 ns, respectively. For C1P-C2P, the mean difference with respect to CAS, DLR, and CODE was within ±0.8, ±1.2, and ±0.4 ns respectively, whose mean RMS values were 0.27, 0.33, and 0.28 ns, respectively.

For BDS, only two types of DCB (C2I-C7I for BDS-2 and C2I-C6I for BDS-2 and BDS-3) observations could be tracked by satellites based on the current MGEX network. The corresponding DCB products could be obtained from CAS and DLR, and the comparison result is shown in Figure 9. It can be seen that the mean difference between two types of DCB with respect to CAS and DLR was within ±0.6 ns. For C2I-C7I and C2I-C6I, there was a mean RMS of 0.25/0.14 and 0.24/0.22 ns, respectively, with respect to CAS/DLR.

For Galileo, there were six types of DCBs compared with CAS and DLR, including C1X-C5X, C1X-C7X, and C1X-C8X, as well as C1C-C5Q, C1C-C7Q, and C1C-C8Q. Figure 10 shows the corresponding comparison result. As is shown in the figure, the mean difference of all DCBs was within ±0.2 ns. The mean RMS values were 0.11/0.11, 0.11/0.11, and 0.11/0.12 ns, as well as 0.13/0.13, 0.12/0.12, and 0.12/0.12 ns, for C1X-C5X, C1X-C7X, and C1X-C8X, respectively, and C1C-C5Q, C1C-C7Q, and C1C-C8Q, respectively, with respect to CAS/DLR.

For QZSS, only four satellites could be tracked in the current MGEX network, and four types of DCBs, namely, C1X-C2X, C1X-C5X, C1C-C2L, and C1C-C5Q, needed to be estimated. All DCB products could be obtained by CAS and DLR, and the comparison result is shown in Figure 11. It can be seen that the mean difference of all DCBs for all satellites (except J07) with respect to CAS/DLR was within ±0.2 ns. The mean RMS values of the four types of DCBs with respect to CAS/DLR were 0.07/0.12, 0.10/0.12, 0.08/0.13, and 0.18/0.11 ns, respectively.

As is shown in the above results, the mean difference among most types of DCB with respect to CAS/DLR was within ±0.4 ns. The comparison results of 19 types of DCBs estimated by IGDE show good agreement with the MGEX DCB products, indicating good performance of IGDE in multi-GNSS DCB estimating. Especially for GPS C1W-C2W and GLONASS C1P-C2P DCB, the difference with our estimated DCB and CODE products was small, whose value was less than that between IGDE and CAS/DLR products. This may be related to the larger number of stations used in DCB estimation of GPS and GLONASS. In addition, some difference in the mean, with a larger value for GPS C1W-C2W and GLONASS C1P-C2P DCB with respect to DLR, could be found, e.g., the value of G06 near −0.6 ns and that of R10 near 1 ns, mainly due to the fact that the two types of DCB of DLR product could not be obtained directly but were calculated based on the other DCBs. In terms of BDS DCB, there seemed to be some difference in mean of a large value for GEO satellites, e.g., a value of C2I-C7I for C05 and that of C2I-C6I for C01 near −0.6 ns, which may be due to the fact that GEO satellite observations are more susceptible to multipath errors. As can be seen from the STD of the difference, the value of GPS and GLONASS was obviously smaller than that of BDS, Galileo, and QZSS, mainly since more continuous observations could be observed through GPS and GLONASS. Some larger STDs could be

found in BDS-3, Galileo, and QZSS, e.g., C37 of BDS, E33 of Galileo, and J07 of QZSS, which is mainly related to the fact that fewer observations could be tracked from those satellites. Overall, mean RMS values were 0.12, 0.22, 0.21, 0.12, and 0.12 ns, for GPS, GLONASS, BDS, Galileo, and QZSS DCBs, respectively, with respect to MGEX products.

3.3. Stability Analysis of Multi-GNSS DCB

As two important indicators of comparison between the proposed method (IGDE) and MGEX products, the mean difference and STD were analyzed in the previous section, between which good agreement was found. In this section, we mainly analyze the stability of DCBs estimated through different methods, as the stability of DCBs reflects the stability and reliability of DCB estimation to a certain extent, which can be expressed as [7,29,30]:

$$S^j = \sqrt{\frac{\sum_{d=1}^{D} \left(b_d^j - \overline{b}^j\right)^2}{D-1}} \tag{11}$$

where S^j is the stability of DCB for satellite j, b_d^j is the daily DCB of satellite j on day d, $\overline{b}^j$ is the mean DCB of satellite j, and D is the number of days.

Figure 12 shows the stability of GPS satellite DCBs obtained by IGDE, CAS, DLR, and CODE. The C1W-C2W DCB of CODE was relatively stable, whose stability was within 0.05 ns, which is mainly due to the observations at about 300 IGS stations for three consecutive days used by CODE for DCB estimation. The stability of C1W-C2W DCB from IGDE, CAS, and DLR was within 0.1 ns. In terms of the other three types of DCB, the stability of the DCB obtained by IGDE, CAS, and DLR was almost same, with values mostly within 0.1 ns, indicating reasonable stability of GPS DCBs estimated by IGDE.

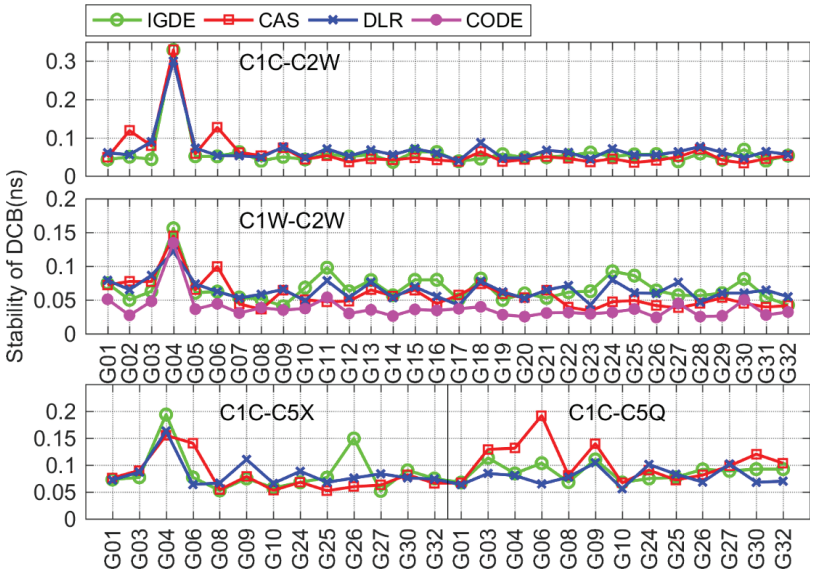

Figure 12. Stability of the GPS DCB obtained by IGDE, CAS, DLR, and CODE.

For GLONASS, the comparison of DCB stability through IGDE, CAS, and DLR is shown in Figure 13. Note that the stability of C1P-C2P DCB through CODE could not be obtained due to just the monthly mean value that can be provided by CODE. Obviously, the overall stability of GLONASS DCB satellite was not as good as that of GPS satellite, and the values of three types of DCB were within 0.2 ns. However, some larger values could

be seen, e.g., the values of R07, R10, and R16, mainly because few observations could be tracked through these satellites.

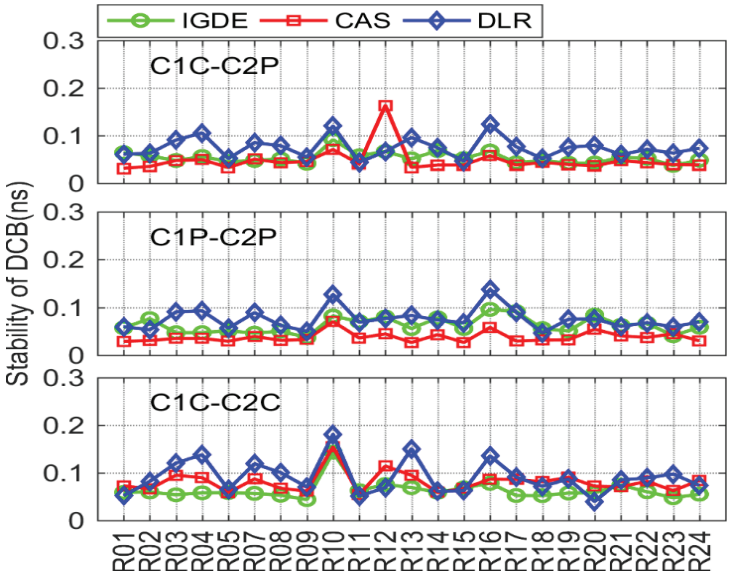

Figure 13. Stability of the GLONASS DCB obtained by IGDE, CAS, and DLR.

Figure 14 shows the stability of BDS DCB obtained by IGDE, CAS, and DLR, including the results of two types of DCB for BDS-2 and C2I-C6I DCB for BDS-3. As is shown in the figure, the stability of DCB estimated by IGDE was basically consistent with that of the DCB provided by CAS and DLR. The stability of the two types of DCB were mostly within 0.2 ns, with the value of some satellites, including the GEO satellite and some BDS-3 satellites, seeming larger than 0.2 ns, which is mainly related to the observation from the satellite.

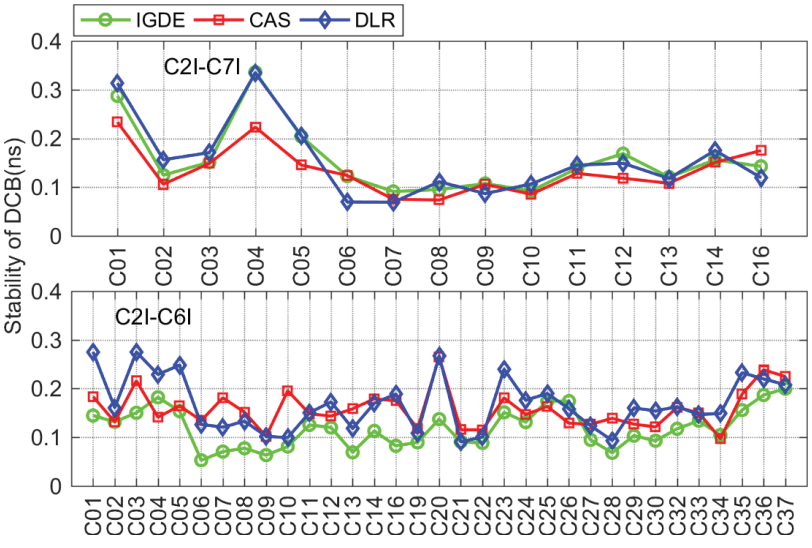

Figure 14. Stability of the BDS DCB obtained by IGDE, CAS, and DLR.

For Galileo and QZSS, the comparison of DCB stability with IGDE, CAS, and DLR is shown in Figures 15 and 16. The DCB stability of most satellites was around 0.1 ns, except for a few satellites, i.e., E33 of Galileo and J07 of QZSS. In particular, the DCB stability of E33 from the DLR product presented a larger value, which may be related to its solution. The value of DCB stability of J07 was larger than that of other satellites, which is mainly related to the few observations of J07.

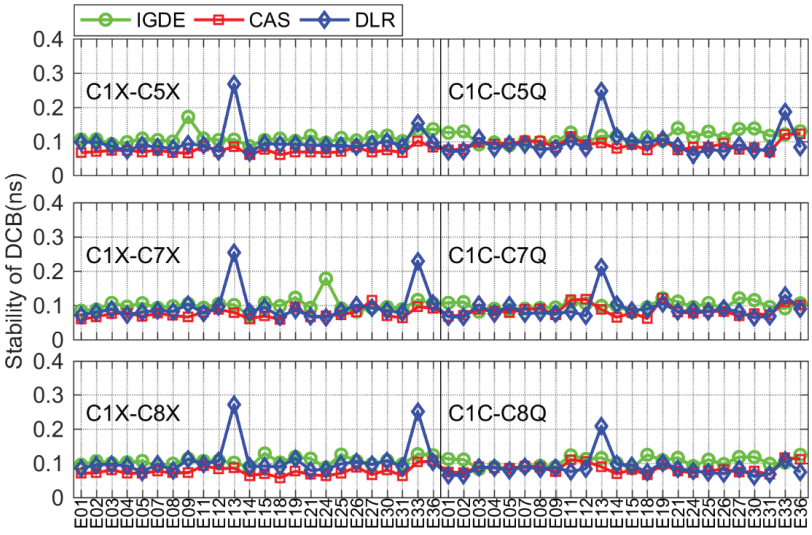

Figure 15. Stability of the Gaileo DCB obtained by IGDE, CAS, and DLR.

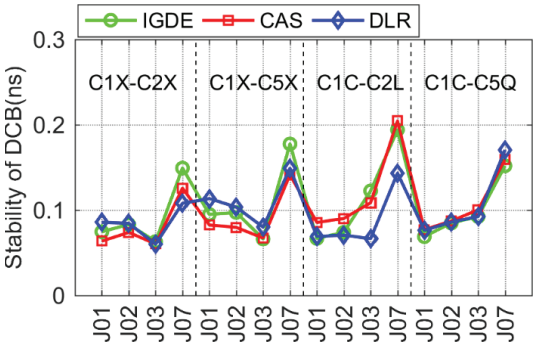

Figure 16. Stability of the QZSS DCB obtained by IGDE, CAS, and DLR.

It can be seen from the above analysis results that the stability of multi-GNSS DCB through the proposed estimation method (IGDE) and the MGEX DCB product was at the same level. The mean values of stability of DCB estimated by IGDE were 0.07, 0.06, 0.13, 0.11, and 0.11 ns, for GPS, GLONASS, BDS, Galileo, and QZSS, respectively. The good performance of the stability of multi-GNSS DCB estimated by IGDE can be concluded based on the above comparison results.

4. Discussion

A new method is proposed in this study to estimate multi-GNSS DCB based on the consideration that TEC variation is small in single-station areas. A total of 200 days of observations from more than 300 MGEX stations in low-solar-activity periods was collected for experimentation. The verification results from the TEC station in Figures 3 and 4

indicate that good performance of the proposed method was shown at most stations. Thus, it can be said that the processing strategy for the TEC of IPPs in the proposed method is feasible. Although we directly used the TEC of the station instead of the TEC of the IPPs for estimation, many observation data can play the role of adjustment for each station. This means that the TEC of the station is represented by the weighted mean TEC values of the IPPs. However, if the station is in the low-latitude area with active ionospheric variations or there is less observation data from the station, there may be a large deviation in estimated TEC. Since the variance can play a controlling role in the next DCB estimation, the role of the data from these stations may be removed or reduced in the adjustment. Thus, the proposed method shows good performance in multi-GNSS DCB estimation in low-solar-activity periods.

For different systems, the stability of estimated satellite DCB was obviously different; there were also some satellites with large values of stability of DCBs that can be found in the figures, e.g., G04, R10, C01, C04, E13, E33, and J07, which may mainly have been caused by the quality and quantity of data from the satellites.

However, we also tested the DCB estimation during the period of high solar activity in 2015. The result of the estimated GPS DCB is shown in Figure 17; the bias was larger than that in 2019, especially for C1C-C5X. In addition to GPS, DCB estimation of other systems may have had some deviations on some days, which may mainly have been caused by insufficient observation data, because some data were removed due to the failure of the TEC estimation. The method proposed in this paper will continue being studied and improved in the next step to fit the DCB estimation in periods of high solar activity.

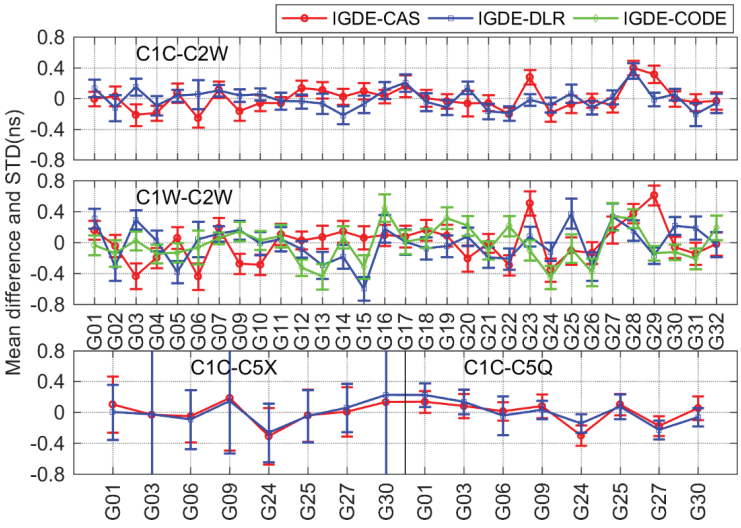

Figure 17. Mean difference and STD of the GPS DCB between IGDE and MGEX products.

5. Conclusions

In recent years, the rapid development of multi-GNSS has accounted for the strong demand for multiple types of DCBs, instead of just a single type of them from GPS and GLONASS. To estimate multi-GNSS DCB efficiently and accurately, a new method of multi-GNSS DCB estimation without relying on the ionospheric function model and GIM is proposed, which can be implemented in three steps. The first is to extract ionospheric observations based on the geometry-free combination of dual-frequency multi-GNSS code observations. Then, the VTEC of the station represented by the weighted mean VTEC value of the ionospheric pierce points (IPPs) at each epoch is estimated as a parameter together with the combined receiver and satellite DCBs (RSDCBs). Last, the estimated RSDCBs are

used as new observations, whose weight is calculated with the use of estimated covariances, and thus the satellite and receiver DCBs of multi-GNSS are estimated.

Nineteen types of multi-GNSS satellite DCBs are estimated based on 200-day observations from more than 300 multi-GNSS experiment (MGEX) stations, and the performance of the proposed method is evaluated by comparing with MGEX products. The results show that the mean RMS values were 0.12, 0.23, 0.21, 0.13, and 0.11 ns for GPS, GLONASS, BDS, Galileo, and QZSS DCBs, respectively, with respect to MGEX products, and the stability of estimated GPS, GLONASS, BDS, Galileo, and QZSS DCBs as 0.07, 0.06, 0.13, 0.11, and 0.11 ns, respectively. The proposed method shows a good performance in multi-GNSS DCB estimation in low-solar-activity periods. The method proposed in this paper will continue being studied and improved in the next step to fit the DCB estimation in periods of high solar activity.

Author Contributions: Conceptualization of the manuscript idea: Q.W. and S.J.; methodology and software: Q.W.; writing—original draft preparation: Q.W. and X.Y.; writing—review and editing: S.J.; supervision and funding acquisition: Q.W. and S.J. All authors have read and agreed to the published version of the manuscript.

Funding: This research was funded by the National Natural Science Foundation of China (NSFC) Project (Grant No. 12073012) and the Scientific Research Foundation for Doctor of Xiangtan University (No. 21QDZ55).

Data Availability Statement: The GNSS observation data from the IGS MGEX networks can be obtained at https://cddis.nasa.gov/archive/gps/data/daily/ (accessed on 1 June 2020). The precise orbit products from GFZ are available at https://www.gfzpotsdam.de/GNSS/products/mgex/ (accessed on 1 June 2020) The GIM products from CODE are available at https://cddis.nasa.gov/archive/gnss/products/ionex/ (accessed on 1 June 2020). The DCB products provided by CAS and DLR can be obtained at https://cddis.nasa.gov/archive/gnss/products/bias/ (accessed on 1 June 2020).

Acknowledgments: The authors gratefully acknowledged the DLR and CAS for providing the products and IGS for providing the MGEX data.

Conflicts of Interest: The authors declare no conflict of interest.

References

1. Schaer, S. *Mapping and Predicting the Earth's Ionosphere Using the Global Positioning System*; Astronomical Institute, University of Berne: Bern, Switzerland, 1999.
2. Li, M.; Yuan, Y.; Wang, N.; Li, Z.; Li, Y.; Huo, X. Estimation and analysis of Galileo differential code biases. *J. Geodesy* **2017**, *91*, 279–293. [CrossRef]
3. Jin, S.G.; Jin, R.; Li, D. Assessment of BeiDou differential code bias variations from multi-GNSS network observations. *Ann. Geophys.* **2016**, *34*, 259–269. [CrossRef]
4. Wang, Q.; Jin, S.; Yuan, L.; Hu, Y.; Chen, J.; Guo, J. Estimation and Analysis of BDS-3 Differential Code Biases from MGEX Observations. *Remote Sens.* **2020**, *12*, 68. [CrossRef]
5. Shi, C.; Fan, L.; Li, M.; Liu, Z.; Gu, S.; Zhong, S.; Song, W. An enhanced algorithm to estimate BDS satellite's differential code biases. *J. Geodesy* **2015**, *90*, 161–177. [CrossRef]
6. Jin, S.; Jin, R.; Kutoglu, H. Positive and negative ionospheric responses to the March 2015 geomagnetic storm from BDS observations. *J. Geodesy* **2017**, *91*, 613–626. [CrossRef]
7. Wang, N.; Yuan, Y.; Li, Z.; Montenbruck, O.; Tan, B. Determination of differential code biases with multi-GNSS observations. *J. Geod.* **2016**, *90*, 209–228. [CrossRef]
8. Zhao, C.; Zhang, B.; Odolinski, R.; Yuan, Y. Combined use of single-frequency data and global ionosphere maps to estimate BDS and Galileo satellite differential code biases. *Meas. Sci. Technol.* **2020**, *31*, 015002. [CrossRef]
9. Choi, B.-K.; Lee, S.J. The influence of grounding on GPS receiver differential code biases. *Adv. Space Res.* **2018**, *62*, 457–463. [CrossRef]
10. Hernández-Pajares, M.; Juan, J.M.; Sanz, J.; Orus, R.; Garcia-Rigo, A.; Feltens, J.; Komjathy, A.; Schaer, S.C.; Krankowski, A. The IGS VTEC maps: A reliable source of ionospheric information since 1998. *J. Geodesy* **2009**, *83*, 263–275. [CrossRef]
11. Jin, R.; Jin, S.; Feng, G. M_DCB: Matlab code for estimating GNSS satellite and receiver differential code biases. *GPS Solutions* **2012**, *16*, 541–548. [CrossRef]

12. Li, Z.; Yuan, Y.; Wang, N.; Hernandez-Pajares, M.; Huo, X. SHPTS: Towards a new method for generating precise global ionospheric TEC map based on spherical harmonic and generalized trigonometric series functions. *J. Geod.* **2015**, *89*, 331–345. [CrossRef]
13. Sardón, E.; Rius, A.; Zarraoa, N. Estimation of the transmitter and receiver differential biases and the ionospheric total electron content from Global Positioning System observations. *Radio Sci.* **1994**, *29*, 577–586. [CrossRef]
14. Li, X.; Xie, W.; Huang, J.; Ma, T.; Zhang, X.; Yuan, Y. Estimation and analysis of differential code biases for BDS3/BDS2 using iGMAS and MGEX observations. *J. Geodesy* **2019**, *93*, 419–435. [CrossRef]
15. Montenbruck, O.; Hauschild, A.; Steigenberger, P. Differential Code Bias Estimation Using Multi-GNSS Observations and Global Ionosphere Maps. *J. Inst. Navig.* **2014**, *61*, 191–201. [CrossRef]
16. Hernández-Pajares, M.; Juan, J.; Sanz, J. New approaches in global ionospheric determination using ground GPS data. *J. Atmos. Sol-Terr. Phys.* **1999**, *61*, 1237–1247. [CrossRef]
17. Hernández-Pajares, M.; Juan, J.M.; Sanz, J.; Aragón-Àngel, À.; García-Rigo, A.; Salazar, D.; Escudero, M. The ionosphere: Effects, GPS modeling and the benefits for space geodetic techniques. *J. Geod.* **2011**, *85*, 887–907. [CrossRef]
18. Okoh, D.; Onwuneme, S.; Seemala, G.; Jin, S.; Rabiu, B.; Nava, B.; Uwamahoro, J. Assessment of the NeQuick-2 and IRI-Plas 2017 models using global and long-term GNSS measurements. *J. Atmos. Solar-Terrestrial Phys.* **2018**, *170*, 1–10. [CrossRef]
19. Liu, T.; Zhang, B.; Yuan, Y.; Li, Z.; Wang, N. Multi-GNSS triple-frequency differential code bias (DCB) determination with precise point positioning (PPP). *J. Geodesy* **2019**, *93*, 765–784. [CrossRef]
20. Prange, L.; Orliac, E.; Dach, R.; Arnold, D.; Beutler, G.; Schaer, S.; Jäggi, A. CODE's five-system orbit and clock solution—the challenges of multi-GNSS data analysis. *J. Geodesy* **2016**, *91*, 345–360. [CrossRef]
21. Montenbruck, O.; Steigenberger, P.; Prange, L.; Deng, Z.; Zhao, Q.; Perosanz, F.; Romero, I.; Noll, C.; Stürze, A.; Weber, G. The Multi-GNSS Experiment (MGEX) of the International GNSS Service (IGS)–achievements, prospects and challenges. *Adv. Space Res.* **2017**, *59*, 1671–1697. [CrossRef]
22. Montenbruck, O.; Steigenberger, P.; Khachikyan, R.; Weber, G.; Langley, R.; Mervart, L.; Hugentobler, U. IGS-MGEX: Preparing the ground for multi-constellation GNSS science. *Inside Gnss* **2014**, *9*, 42–49.
23. Jin, S.; Su, K. PPP models and performances from single- to quad-frequency BDS observations. *Satell. Navig.* **2020**, *1*, 1–13. [CrossRef]
24. Li, Z.; Yuan, Y.; Li, H.; Ou, J.; Huo, X. Two-step method for the determination of the differential code biases of COMPASS satellites. *J. Geodesy* **2012**, *86*, 1059–1076. [CrossRef]
25. Gu, S.; Wang, Y.; Zhao, Q.; Zheng, F.; Gong, X. BDS-3 differential code bias estimation with undifferenced uncombined model based on triple-frequency observation. *J. Geodesy* **2020**, *94*, 1–13. [CrossRef]
26. Liu, T.; Zhang, B.; Yuan, Y.; Zhang, X. On the application of the raw-observation-based PPP to global ionosphere VTEC modeling: An advantage demonstration in the multi-frequency and multi-GNSS context. *J. Geodesy* **2019**, *94*, 1. [CrossRef]
27. Wellenhof, B.H.; Lichtenegger, H.; Collins, J. *Global Positioning System: Theory and Practice*; Springer: Berlin/Heidelberg, Germany, 1992.
28. Zhang, H.; Xu, P.; Han, W.; Ge, M.; Shi, C. Eliminating negative VTEC in global ionosphere maps using inequality-constrained least squares. *Adv. Space Res.* **2013**, *51*, 988–1000. [CrossRef]
29. Ren, X.; Chen, J.; Li, X.; Zhang, X. Multi-GNSS contributions to differential code biases determination and regional ionospheric modeling in China. *Adv. Space Res.* **2020**, *65*, 221–234. [CrossRef]
30. Wilson, B. Instrumental Biases in Ionospheric Measurements derived from GPS data. In Proceedings of the ION GPS'93, Salt Lake City, UT, USA, 22 September 1993.

remote sensing

MDPI

Article

Recovering Regional Groundwater Storage Anomalies by Combining GNSS and Surface Mass Load Data: A Case Study in Western Yunnan

Pengfei Xu [1,2], Tao Jiang [2,*], Chuanyin Zhang [2], Ke Shi [3] and Wanqiu Li [4]

[1] School of Civil and Architectural Engineering, Shandong University of Technology, Zibo 255000, China
[2] Chinese Academy of Surveying and Mapping, Beijing 100830, China
[3] Yunnan Technical Center of Base Surveying and Mapping, Kunming 650032, China
[4] School of Surveying and Geo-Informatics, Shandong Jianzhu University, Jinan 250101, China
* Correspondence: jiangtao@casm.ac.cn; Tel.: +86-010-63-880-705

Abstract: The redistribution of surface mass (e.g., atmosphere, soil water, oceans, and groundwater) can cause load responses, resulting in vertical deformations of the crust. Indeed, the global navigation satellite system (GNSS)-based continuously operating reference stations (CORS) are able to accurately measure the vertical deformation caused by surface mass loads. In this study, the CORS was used to invert groundwater storage anomalies (GWSA), represented by the equivalent water height (EWH), after removing the effect of the non-groundwater surface mass load (atmospheric, groundwater, and non-tidal oceanic loads) from the vertical deformation monitored by CORS. In addition, the global and regional high-resolution surface mass models were combined to calculate the high-precision load deformation field in in western Yunnan using the remove–restore method, thereby obtaining more accurate surface mass load data and improving the accuracy of the inverted GWSA results. In order to assess the feasibility of the CORS inversion for the GWSA used, 66 CORS stations in western Yunnan Province were considered, presenting weekly GWSA data from 10 January 2018 to 31 December 2020. The results revealed significant seasonal variation in GWSA in the study area, showing an amplitude range of −200–200 mm. This approach is based on the already-established CORS network without requiring additional set-up costs. In addition, the reliability of CORS inverse results was assessed using Gravity Recovery and Climate Experiment (GRACE) inverse results and actual groundwater monitoring data. According to the obtained results, GWSA can be monitored by both CORS and GRACE data; however, CORS provided a more effective spatiotemporal resolution of GWSA. Therefore, the CORS network combined with surface mass load data is able to effectively monitor the spatiotemporal dynamics of GWSA in small-scale areas and provides important references for the study of hydrology.

Keywords: ground water storage; surface mass load; groundwater monitoring station; GNSS; remove-restore method

Citation: Xu, P.; Jiang, T.; Zhang, C.; Shi, K.; Li, W. Recovering Regional Groundwater Storage Anomalies by Combining GNSS and Surface Mass Load Data: A Case Study in Western Yunnan. *Remote Sens.* **2022**, *14*, 4032. https://doi.org/10.3390/rs14164032

Academic Editors: Gino Dardanelli and Shuanggen Jin

Received: 27 June 2022
Accepted: 16 August 2022
Published: 18 August 2022

1. Introduction

As a densely populated country, China is relatively poor in water resources per capita [1]. Moreover, China is characterized by an uneven spatiotemporal distribution of water resources due to the impacts of climatic and topographic characteristics. The GWSA (groundwater storage anomalies) aims to estimate groundwater storage, thereby maintaining the ecological balance of groundwater systems. The overexploitation of groundwater resources has seriously restrained sustainable development in many regions [2,3]. Therefore, the assessment of the spatiotemporal distribution of regional GWS (groundwater storage) is of great scientific importance for studying water circulation and groundwater allocation as well as for preventing groundwater droughts [4,5].

At present, the two main GWS monitoring approaches consist of in situ monitoring of groundwater level fluctuations and using Gravity Recovery and Climate Experiment (GRACE) and Global Land Data Assimilation System (GLDAS) data to invert the spatiotemporal characteristics of GWS [6,7]. In fact, consecutive groundwater level data, with relatively high accuracies, can be obtained at monitoring well stations using the first approach. However, this approach is costly since it requires several monitoring stations with high density to ensure accurate regional monitoring. Moreover, most well stations can be located in plains regions, making it challenging to monitor groundwater storage in mountainous areas. Meanwhile, due to the complex regional geological structures, some parameters (e.g., specific yield) are difficult to determine, making it difficult to effectively assess GWSA using discretely distributed well stations. On the other hand, the GRACE and GLDAS data-based approach is often applied to large-scale regional GWSA monitoring [8,9]. Although the quality of gravity satellite data is relatively high, there is considerable interference upon high-order spherical harmonic coefficients, resulting in low spatial resolutions. Furthermore, these satellite data have been lacking since 2011, with a data gap of nearly one year between GRACE/GRACE Follow-on (GRACE-FO), explaining the inability of GRACE data to provide high-resolution continuous monitoring the GWSA data in small-scale regions [10,11]. Therefore, given the complex physical conditions, high cost of monitoring groundwater storage through well stations, and the low-resolution GRACE monitoring data, the continuously operating reference system (CORS) inversion method for GWSA in small-scale areas requires further study and discussion.

The CORS is a ground observation system based on the global navigation satellite system (GNSS) observation system. These data are derived from long consecutive monitoring data of satellite navigation signals, providing real-time and periodic data through communication facilities. The CORS can monitor the dynamics of regional geodetic heights and their consecutive long-time series [12,13]. Indeed, several researchers have demonstrated the ability of the CORS network to obtain real-time information from selected monitoring stations in certain regions, providing references for monitoring spatial dynamics as well as comprehensive continuous regional observation data [14–16]. In addition, the load-deformation theory demonstrated that changes in the surface environmental mass (e.g., atmosphere, surface water, groundwater, and ocean) lead to load vertical deformation, thereby influencing the seasonal periodic signals in the geodesic height variations of CORS stations [17–19]. Argus [20] used the seasonal signals of GNSS vertical data to invert the terrestrial water storage anomalies (TWSA) in California, showing consistent spatial distribution data with that inverted using GRACE. In addition, He [21] inverted the changes in the TWSA in Yunnan Province from 2010 to 2014 and compared the GNSS data with those of GRACE and GLDAS, discussing the possibility of GNSS to separately operate and monitor the TWSA. Several studies have revealed consistent findings with the hypothesis that the seasonal vertical displacement of GNSS is strongly related to the load-deformation caused by TWSA and have assessed the reliability of GNSS data to invert the TWSA [22–28]. However, studies on groundwater inversion have only assessed the correlation between seasonal GNSS and GWSA data due to the complexity of seasonal signals of GNSS vertical displacements, while only a few studies have inverted GWSA data using the CORS.

To address this challenge, this study aims to verify the feasibility and reliability of the combined CORS high-resolution surface mass load inversion for GWSA based on an already-established CORS network, thus avoiding additional establishment costs. Moreover, the density of CORS stations and their continuous and immediate high-precision observation make it possible to perform high-resolution GWSA monitoring in a small-scale region. Yunnan Province in China has experienced a severe water shortage and continuous drought. Indeed, the GWSAs have directly affected the regional economy and local ecological environment in Yunnan Province. Therefore, assessing the spatiotemporal distribution characteristics of the GWSA can provide important reference significance for human production activities as well as for relevant decision-makers in the regions. In order to improve the precision and stability of the CORS inversion, the global and regional

high-resolution surface mass models were combined in this study to calculate the high-precision load deformation field in Yunnan Province based on the remove-restore method. Indeed, researchers have eliminated three surface mass loads (atmospheric, soil water, and non-tidal oceanic loads) from the non-linear time series of CORS geodetic heights through data processing, and then the CORS data were used to invert the GWSAs based on load deformation theory and inversion models [29,30]. To assess the applicability of the method, researchers have used data from 66 CORS stations in Western Yunnan Province and high-resolution surface mass load results and performed a weekly GWSA grid in the study area from 10 January 2018 to 31 December 2020 to assess the effectiveness and reliability of CORS inverse results using GRACE inverse results and groundwater monitoring station data.

2. Materials and Methods

2.1. Data Used

2.1.1. CORS Network Data

As is shown in Figure 1, the study region is circled by red lines. The data were collected from 66 CORS stations located in the study region, covering the 2018–2020 period. In addition, 15 international GNSS service (IGS) stations were selected in this study to obtain high-precision CORS coordinate time series and to resolve the solution of CORS data. The longitude and latitude coordinates of the IGS stations are reported in Table 1. GAMIT and GLOBK were also used in this study to process the collected data [31]. On the other hand, by correcting the daily errors of GNSS data for each station, a solution was achieved in some zones of the study region through GAMIT (Table 2). GLOBK was used for a global adjustment of the network and to present the time series of station coordinates in the international terrestrial reference frame (ITRF) [32]. As is shown in Table 2, the CORS data solution removed the influences of the solid, sea, and atmospheric tides, while the influences of non-tidal elements (e.g., atmosphere pressure, soil water, and sea level) were maintained.

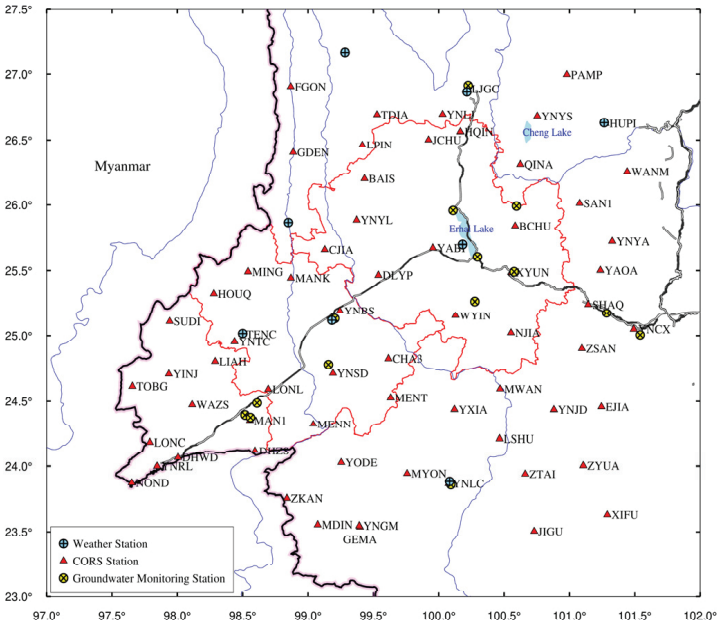

Figure 1. Geographic location of the study region.

Table 1. The 15 IGS sites used for the calculation of the CORS network in Western Yunnan Province.

IGS	Longitude and Latitude	IGS	Longitude and Latitude	IGS	Longitude and Latitude
AIRA	130.59/31.82	ARTU	58.56/56.42	BJFS	115.89/39.60
DAEJ	127.37/36.39	HYDE	78.55/17.41	IISC	77.57/13.02
IRKJ	104.31/52.21	KIT3	66.88/39.13	LHAZ	91.10/29.65
NVSK	83.23/54.84	PIMO	121.07/14.63	POL2	74.69/42.67
TCMS	120.98/24.79	TIXI	128.86/71.63	YSSK	142.71/47.02

Table 2. The main parameters used in the GAMIT calculation.

Parameters	Processing Modes
Sampling interval data	15 s
Satellite elevation cut-off angle (°)	10
Baseline processing mode	BASELINE
Ionosphere delay model	LC_AUTCLN
Satellite clock error model	Precise clock offset and orbit products of IGS
Tropospheric model	Saastamoinen + GPT2w + estimation
Solar radiation pressure model	ECOMC model
Solid tide model	IERS2010
Ocean tide model	FES2004(otl_FES2004.grid)
Atmospheric mapping function	VMF1
Inertial framework	J2000
Framework of prior coordinates	ITRF2014
PCO/PCV	IGS14 atx
Ambiguity resolution	LAMBDA method
A priori IGS station coordinates	Coordinates under ITRF20008

2.1.2. Atmospheric Pressure Data

In order to calculate the effect of atmospheric load, the global atmospheric pressure data were derived in this study from ECMWF's (European Centre for Medium-Range Weather Forecasts) re-analysis of the 0.25° × 0.25° ERA-interim surface pressure product data (https://www.ecmwf.int/, accessed on 15 May 2021), covering the 3 January 2018–30 December 2020 period [33]. The original data were averaged by week, which is reported by Wednesday of each week. Similar to the solutions of non-tidal oceanic and soil water loadings, the weekly grid time series of atmospheric loading were obtained using Equations (1) and (2).

On the other hand, the regional high-resolution atmospheric pressure data were downloaded from the CLDAS-V2.0 data (CLDAS Atmospheric Driving Field) product of the China Meteorological Administration Land Data Assimilation System (CLDAS) from the China Meteorological Data Network (http://data.cma.cn/, accessed on 15 May 2021). The product data consist of temperature, pressure, humidity, wind speed, precipitation, and other meteorological parameter data. The hourly product data cover the Asian region (0°~65°N, 60°~160°E), with a spatial resolution of 0.0625° × 0.0625°. The dataset includes data observed at over 2400 and 40,000 national and regional automatic meteorological stations, respectively, for operational assessment. By combining global and regional atmospheric pressure data, a high-resolution atmospheric loading deformation field of the study area was determined using the remove–restore method. The soil water loading was calculated using the same method.

2.1.3. Sea Level Anomaly Data

In order to calculate the effect of Non-tidal ocean load, the daily global sea-level anomaly (SLA) data were derived from the 0.25° × 0.25° archiving validation and interpretation of satellite oceanography (AVISO) data (https://www.aviso.altimetry.fr/, accessed on 15 May 2021), covering the 2 January 2018–30 December 2020 period. The AVISO data

integrate not only multi-satellite-derived sea-level data (e.g., TOPEX/Poseidon, Jason-1/2, and Envisat) but also the associated geophysical correction, including tidal and inverse barometer corrections, thereby representing the effects of non-tidal ocean loading [34,35].

2.1.4. Soil Water Data

Calculation of soil water load requires soil water data. In this study, the V2.1 GLDAS/Noah model, provided by the National Aeronautics and Space Administration (NASA) and National Centers for Environmental Prediction (NCEP), was used to obtain the soil water data, with a spatial resolution of 0.25° × 0.25° (https://mirador.gsfc.nasa.gov, accessed on 15 May 2021) [36]. The GLDAS model takes into account soil water, canopy water, and snow water (ranging from 0 to 200 cm), while groundwater is excluded. The temporal resolutions of the data are 3-hourly and monthly. In this study, the 3-hourly resolution GLDAS data, from 3 January 2018 to 30 December 2020, were first downloaded, then averaged by week to obtain weekly soil water data. These data were used to determine the influence of soil water loading, whereas the monthly soil water data covered the January 2018–December 2020 period. Indeed, the monthly GLDAS data combined with the monthly GRACE data can be used to determine GWSA as well as to assess the validity and feasibility of the CORS inversion for GWSA.

On the other hand, the regional high-resolution surface water height data were downloaded in this study from the CLDAS data product of the China Meteorological Data Network, which consists of hourly soil moisture data covering the Asian region (0°–65°N, 60°–160°E), with a spatial resolution of 0.0625° × 0.0625°.

2.2. GRACE-FO Mascon Solutions

To compare and analyze the CORS and GRACE inverse results for GWSA, GRACE-FO RL06 mascon solutions, provided by the Center for Space Research (CSR) with a spatial resolution of 0.25° × 0.25°, were used to reflect the monthly changes in terrestrial water storage (http://www2.csr.utexas.edu/grace/RL06_mascons.html, accessed on 15 May 2021) [37]. The data covered the October 2018–December 2020 period. The collected data were corrected for degree-1, C20 (degree 2 order 0), C30 (degree 3 order 0), and GIA to reflect the dynamics of terrestrial water storage (Table 3). It should be noted that in comparison with GRACE, the GRACE-FO data processing added the C30 correction into its procedure. Therefore, the regional GWSA could be calculated through the combination of monthly data of terrestrial water storage and the monthly data of soil water provided by GLDAS.

Table 3. The main corrections used in Mascon solutions.

Corrections	Processing Mode
C20 Replacement	C20 solutions from SLR in TN14
C30 Replacement	C30 solutions from SLR in TN14
Degree 1 Corrections	Estimated value in TN-13a
GIA Correction	ICE6G-D Model

2.3. Groundwater Monitoring Station Data

The daily data observed at 15 groundwater monitoring stations (Figure 1) from 26 September 2018 to 25 November 2020 were used in this study to assess the accuracy of the CORS inverse results for the GWSA. The collected data were averaged by week. The applicability and reliability of the integrated solution method can be assessed by comparing the observed data with those of the CORS inversion for the GWSA.

2.4. Precipitation Data from Weather Stations

To analyze the influences of precipitation on the spatiotemporal distribution of GWSA in the study region, daily precipitation data observed at eight weather stations in Yunnan Province from (Figure 1) 1 January 2018 to 31 December 2020 were used in this study (http://data.cma.cn, accessed on 15 May 2021).

3. Method

3.1. High-Resolution Surface Mass Load Based on the Remove–Restore Method

The spherical harmonic analysis method was expressed using Equation (1), reflecting the medium- and long-wave components at global scales, while Equation (2) is the load Green's function method, which mainly reflects the short-wave components at small scales. Since equivalent water height (EWH) can reflect the changes in the mass of the surface environment (e.g., atmosphere, soil water, oceans, and groundwater) based on the load theory of spherical harmonic coefficients, the changes in geodetic heights caused by loads can be calculated using the following equation [17,38]:

$$H(\varphi,\lambda,t) = 3\frac{\rho_w}{\rho_e}\frac{GM}{\gamma R}\sum_{l=2}^{L}\frac{h'_l}{2l+1}\sum_{m=0}^{l}\left[\Delta C^q_{lm}\cos m\lambda + \Delta S^q_{lm}\sin m\lambda\right]\overline{P}_{lm}(\sin\varphi) \quad (1)$$

where $\rho_e \approx 5.5\times10^3$ kg·m^{-3} denotes the average density of the solid earth; G is the gravitational constant; and γ is the average gravity of the ground.

On the other hand, the changes in the geodetic heights of CORS stations resulting from the changes in surface mass load can be expressed using the load Green's function equation [17,38]:

$$H(\varphi,\lambda,t) = \int_0^{2\pi} d\lambda' \int_0^{\pi} \rho_w \Delta h_w G(\psi) a^2 \sin\lambda' d\varphi' \quad (2)$$

where $H(\varphi,\lambda,t)$ denotes the geodetic height; t represents time; (φ,λ) denotes the longitude and latitude of the calculated point; and (φ',λ') denotes the load point on the ground. The density of water was considered as $\rho_w \approx 10^3$ kg·m^{-3}; ψ denotes the spherical angular distance between the calculated and load points; $G(\psi)$ denotes the green function of the radial loads; and R denotes the average earth radius.

The green function of the radial loads can be expressed as follows [17,38]:

$$G(\psi) = \frac{Rh'_\infty}{2M\sin(\psi/2)} + \frac{a}{M}\sum_{n=0}^{N}(h'_l - h'_\infty)P_n(\cos\psi) \quad (3)$$

where h'_l is radial load Love number; M denotes the earth mass; and P_n denotes the Legendre function.

In this study, the global and regional high-resolution models were combined to calculate the high-precision load deformation field in the study area using the remove–restore method. Figure 2 shows the procedure used in this study [12,19].

First, the global EWH model was used to estimate the reference EWH and load vertical deformation in the study area using the spherical harmonic analysis method, thus obtaining the spatial long-wave component information. Second, the high-resolution regional EWH model was encrypted into a $1' \times 1'$ grid before removing the reference EWH grid from the regional high-resolution EWH grid to obtain the residual EWH using the remove method. Third, the load impact of the residual EWH change on the geodetic height was estimated using the load Green's function method, introducing the short wave components of the study area. Finally, the load impacts obtained in the first and third steps were added using the restore method. By using these steps, the high-resolution and high-precision load deformation field of the study area was obtained. This approach not only introduces the short-wave component of the study area and improves the applicability of the model in the small-scale study area but also effectively removes the truncation error generated during the spherical harmonic expansion and reduces the calculation uncertainties.

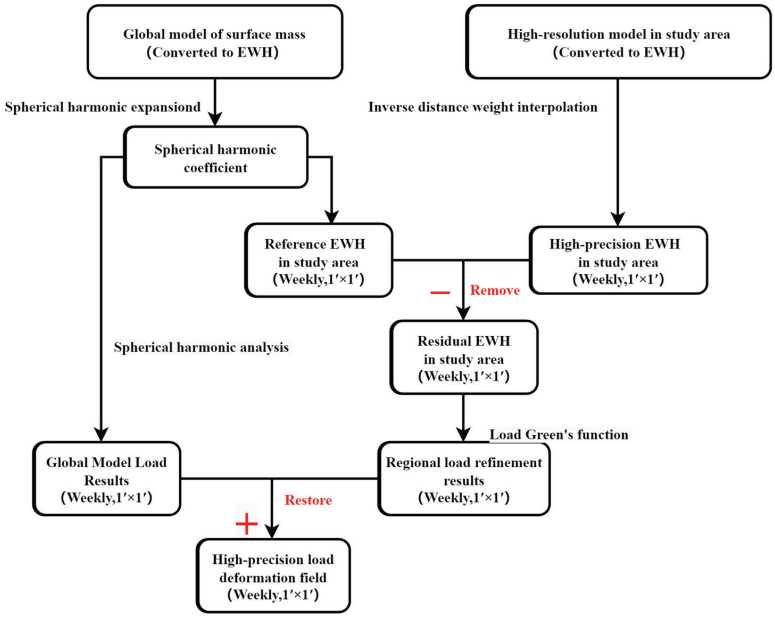

Figure 2. Flowchart of the high-precision load deformation field solution.

3.2. GWSA Inversion Using the Combined CORS and Surface Mass Load Method

EWH was used in this study to reflect the mass changes in the surface environment (atmospheric pressure, sea level, soil water, and groundwater levels) [17]. Based on load deformation theory, the normalized expansion formula of the spherical harmonic load was determined using the load-deformation theory, according to the following equations [17,38,39]:

$$\Delta h_w(\varphi,\lambda) = R\sum_{l=1}^{L}\sum_{m=0}^{l}\left[\Delta C_{lm}^{q}\cos m\lambda + \Delta S_{lm}^{q}\sin m\lambda\right]\overline{P}_{lm}(\sin\varphi) \quad (4)$$

where (φ,λ) denotes the geocentric latitude and longitude of the ground calculation point; ΔC_{lm}^{q}, ΔS_{lm}^{q} are the load sphere harmonic coefficients, with l degree and m order; and $\overline{P}_{lm}(\sin\varphi)$ denotes the associated Legendre function, with l degree and m order.

Different thicknesses and radius disks of the same mass were placed on the surface. Figure 3 shows the related load deformation and its relationship with distance, indicating clear load responses near fields. The load-deformation was 1/10 of that of the center at a distance from the center of the disk equal to three times its radius, while no load-deformation was observed at a distance from the center of disk equation to 10 times its radius. Therefore, the vertical displacement and load-deformation were mainly influenced by the load points within a limited distance range. The use of GNSS in the inversion of the regional GWS showed that stations on the edges of the study area tended to be simultaneously influenced by the inside and outside loads of the study area. By neglecting the influence of the outside mass changes, the outside loads can be restrained to the border region, thus leading to false inversion on the edges of the study area, explaining the larger inverted region than the study area. The expansion should consider the sensitive range of load responses. Therefore, the 66 CORS stations covered the study region and its peripheral areas.

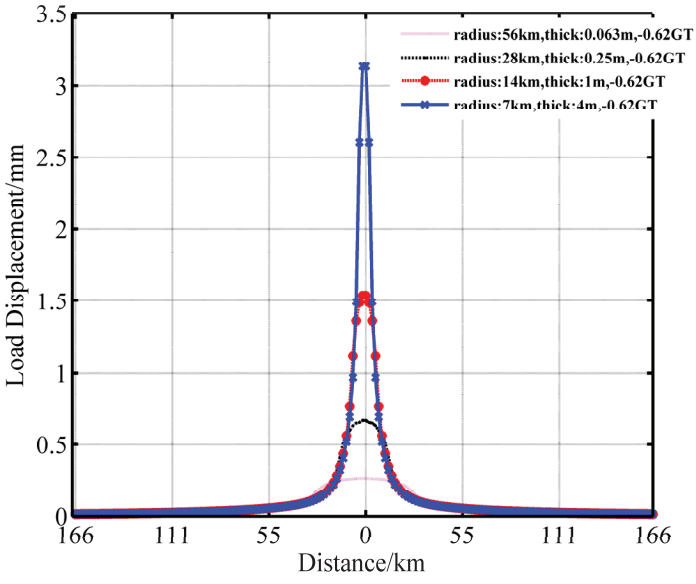

Figure 3. Vertical deformation caused by disks of different masses.

The inversion model of Argus [20] used in this paper:

$$((Ax - b)/\sigma)^2 + \beta^2(L(x))^2 \rightarrow \min \tag{5}$$

where σ denotes the standard deviation of the observation value vector of geodetic height changes; A denotes the coefficient matrix of the green function, which can be calculated using Equation (3); x is the EWH of the corresponding grid point; b denotes the observation value of the GNSS geodetic height changes of CORS stations; β denotes the smoothing factor; and L denotes the Laplace operator.

Due to the limited number of GPS observation stations in the study area, the number of equations is smaller than the number of unknowns, resulting in a rank loss of the coefficient matrix of the normal equation. The inversion of the equivalent water height changes using GNSS observation data is, therefore, an ill-posed equation problem. To address this challenge, the ridge estimation reported by Hoerl [40] was used in this study, which is a classical regularized approach, to determine the solution of β in Equation (5). Indeed, the L-curve method was used in previous studies to select the best-regularized parameters [41].

The influence of surface mass changes was calculated using the load-deformation theory in Equation (1). Besides the impact of groundwater changes, atmospheric pressure, sea level, and soil water changes were considered in the present study, while other less influential factors (e.g., rivers, lakes, and reservoirs) were neglected. Based on the weekly geodetic height values, the non-linear time series of each CORS station were obtained. After removing the influences of the non-groundwater data, the residual time series were obtained, including load and non-load vertical deformations of groundwater. Afterward, Equations (2) and (5) were used to invert GWSA from the residual time series. The method used is illustrated in Figure 4. In this study, the integral radius of the load Green's function and the smoothing factor (β) were set to 2° and 0.01, respectively.

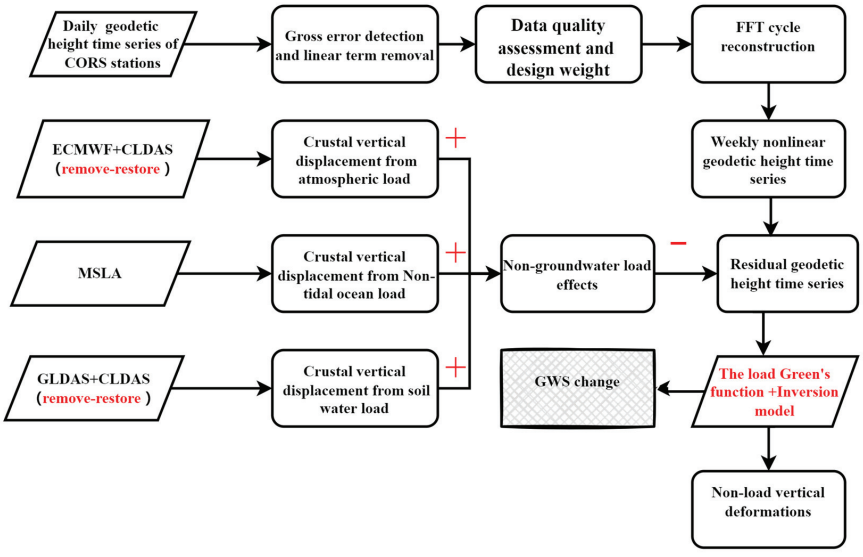

Figure 4. Flowchart of CORS inversion for GWSA.

3.3. GWSA Inversion Using GRACE Product Data

The terrestrial water storages (TWS) are the summation of soi l water, groundwater, surface runoff, snow, and canopy water. Contrary to soil water and groundwater, the contributions of surface runoff and canopy water changes to TWS are minor, and thus they can be neglected. Indeed, TWS in the study region is mainly affected by soil water, snow water, and groundwater [10]. ΔGWS was calculated in this study using the following formula:

$$\Delta GWS = \Delta TWS - (\Delta SM + \Delta SWE) \quad (6)$$

where ΔGWS is the groundwater storage; ΔTWS denotes the changes in TWS obtained from GRACE data; ΔSM and ΔSWE denote the changes in soil water and snow water, respectively, obtained from GLDAS product data.

4. Results

4.1. GWSA Inversion Results Using CORS Data

The time series of non-linear geodetic height changes were first processed using gross error detection and linear item removal, as shown by the red points in Figure 5. The black curve in Figure 5 shows the time series of geodetic heights after the periodic fast Fourier transformation (FFT) reconstruction. According to the magnitude of the power spectral density, this paper uses the first eight periodic signals to reconstruct [42,43]. Indeed, the periodic FFT reconstruction is a low-pass filtering method used to decrease or inhibit the high-frequency noise of the time series, thus improving the stability of the inversion results. The geodetic heights of CORS stations corresponded to the temporal resolution of surface mass loads. In order to improve the accuracy of the CORS inversion, the influences of high-resolution surface mass loads, including atmospheric, soil water, and non-tidal oceanic loads, were removed from the reconstructed time series of non-linear geodetic heights, as shown by the purple, blue and green curves in Figure 5. The residual time series obtained after the removal process, according to Equations (2) and (5), can therefore be used to invert GWSA within the coverage of the CORS network, which is reflected by EWH.

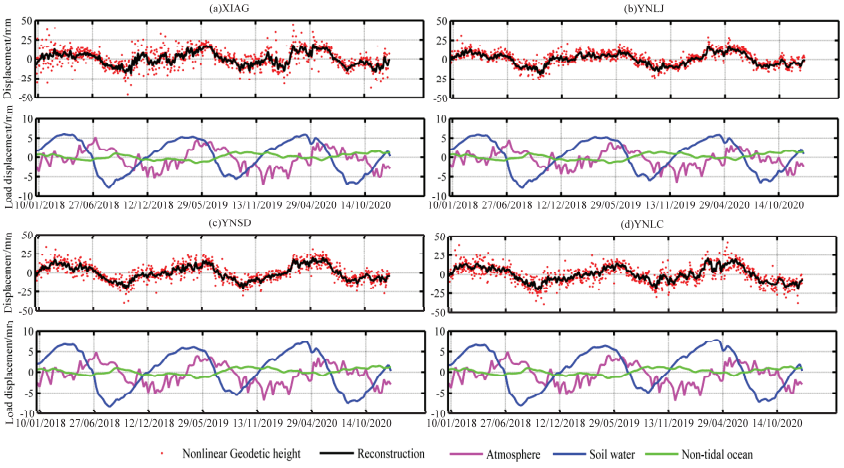

Figure 5. Processed geodetic height changes of different CORS stations and surface mass loads.

Figure 6 shows the annual differences between the maximum and minimum values of the reconstructed geodetic height time series at the 66 CORS stations, ranging from 15 to 35 mm. According to Figure 5, the atmospheric and soil water loads revealed the highest effects among the three types of loads. The results revealed that the vertical deformation, caused by the soil water loads, ranged from −8 to 8 mm, while non-tidal oceanic load showed the lowest effect, with a vertical deformation range of −2–2 mm.

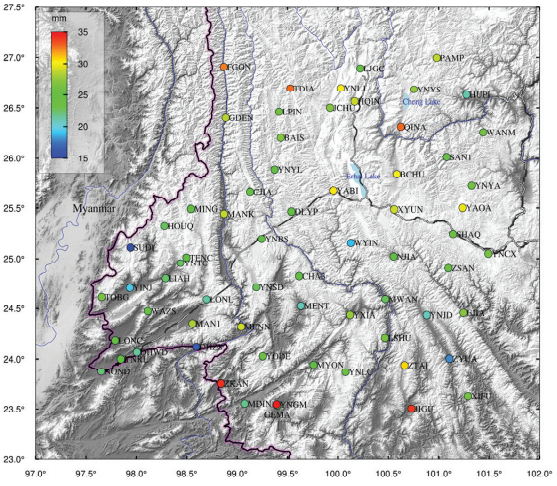

Figure 6. Range of the reconstructed geodetic heights at each CORS station in the study area.

Surface mass loads, namely atmospheric, non-tidal oceanic, and soil water loads, showed different correlations with the geodetic height time series of CORS stations, demonstrating the influences of these surface mass loads. Therefore, in order to compare the obtained results, the influences of loads were first removed, then the WRMS ratio of the GNSS time series was calculated according to the following formula [44]:

$$WRMS(\%) = \frac{WRMS_{GNSS} - WRMS_{GNSS-load}}{WRMS_{GNSS}} \quad (7)$$

where $WRMS_{GNSS}$ is the WRMS of the reconstructed GNSS geodetic height time series. Positive and negative values of $WRMS(\%)$ indicate a decrease and increase in the WRMS of the GNSS time series, respectively. It should be noted that the absolute value of $WRMS(\%)$ can reflect the load influences on the GNSS's non-linear geodetic height time series.

On the other hand, the Pearson correlation coefficient (R) was computed in this study according to the following equation. It is widely used to measure the degree of correlation between two variables [45,46]:

$$R = \frac{Cov(X, Y)}{\sqrt{Var(X), Var(Y)}} \tag{8}$$

where $X = (x_1, x_2, \cdots, x_N)$ denotes the reconstructed time series of the observed GNSS geodetic heights; $Y = (y_1, y_2, \cdots, y_N)$ denotes the time series of the vertical deformation caused by surface mass loads. The R values range from -1 to 1, indicating strong negative and positive correlations, respectively, between the periodic phases of the two series.

In total, 12 stations were selected to assess the influences of the three surface mass loads on the reconstructed time series of CORS geodetic heights using R and $WRMS$ values (Table 4). Unlike the non-tidal oceanic load, the R and $WRMS$ values of atmospheric and soil water loads were all positive. According to the obtained results, the R and $WRMS$ values of the atmospheric load ranged from 0.50 and 0.66 and 7.61 to 12.80%, respectively, whereas the R and $WRMS$ values of the soil water load ranged from 0.64 to 0.81 and 20.54 to 34.80%, respectively. On the other hand, the non-tidal oceanic load was negatively correlated with the reconstructed time series of the CORS geodetic heights, which is consistent with the reported by Munekane and Nordman [47,48]. However, the absolute $WRMS$ value of the non-tidal oceanic load ranged from 3.24 to 6.39%, suggesting a low influence on the CORS geodetic heights. This result was due to the offsetting effects of the atmospheric and soil water loads, making the influence of the non-tidal oceanic load difficult to reflect in the time series of the CORS geodetic heights. In other words, atmospheric and soil water loads exhibited stronger influences than that of the non-tidal oceanic load. The R and $WRMS$ values of total loads ranged from 0.81 to 0.89 and 33.84 and 43.93%, respectively (Table 4). On the other hand, by removing the surface mass loads, decreases in the $WRMS_{GNSS-load}$ values were observed. This finding demonstrates not only the reliability of the reconstructed CORS geodetic height time series and surface mass load deformations but also the effectiveness of the integrated solving process used in the present study.

Table 4. Correlation coefficient and WRMS values between different loads and the reconstructed geodetic height time series.

CORS Stations	Atmospheric Load		Soil Water Load		Non-Tidal Ocean Load		Total Load	
	R	WRMS (%)	*R*	WRMS (%)	*R*	WRMS (%)	*R*	WRMS (%)
XIAG	0.60	11.03%	0.66	24.08%	−0.62	−4.31%	0.82	37.70%
YNCX	0.62	12.80%	0.64	20.50%	−0.66	−5.10%	0.84	34.31%
YNGM	0.61	12.63%	0.67	21.27%	−0.54	−3.24%	0.81	33.84%
YNJD	0.58	8.53%	0.69	24.99%	−0.58	−3.81%	0.82	34.04%
YNLC	0.66	10.26%	0.71	25.91%	−0.52	−4.25%	0.86	38.74%
YNLJ	0.62	9.45%	0.79	34.80%	−0.63	−6.39%	0.87	43.93%
YNRL	0.56	7.46%	0.77	33.74%	−0.61	−5.77%	0.87	43.85%
YNSD	0.62	10.22%	0.75	30.08%	−0.60	−4.96%	0.88	40.58%
YNTC	0.50	7.61%	0.81	33.56%	−0.66	−5.53%	0.89	39.35%
YNYA	0.58	9.01%	0.78	30.98%	−0.63	−5.97%	0.86	38.71%
YNYL	0.66	10.24%	0.77	27.73%	−0.63	−5.27%	0.86	36.43%
YNYS	0.64	10.88%	0.78	31.82%	−0.62	−4.42%	0.87	41.48%

In order to ensure the reliability of the inversion and reduce the influence of the low-quality CORS data, the quality of each CORS dataset was first evaluated before inversion, and then different weights were assigned to CORS stations. The initial weight of every station was set at 1, while the weight of the low-quality stations was decreased based on the entire time series data and their RMS values.

It was demonstrated earlier that the integration solution of the CORS data revealed a weekly GWSA grid over the 3 January 2018–30 December 2020 period was established, with the GWSA expressed in EWH. As is shown in Figure 7, the GWSA showed significant spatial and seasonal variations. The results revealed decreases in GWS from February to June each year, which might be due to the significant seasonal and spatial decreases in groundwater recharge (e.g., rainfall infiltration). From August to the next January, however, increases in GWS were observed in the study area from August to January due to the increase in rainfall amounts. In addition, the inverted GWS using the CORS network showed a relatively high spatial resolution (Figure 7).

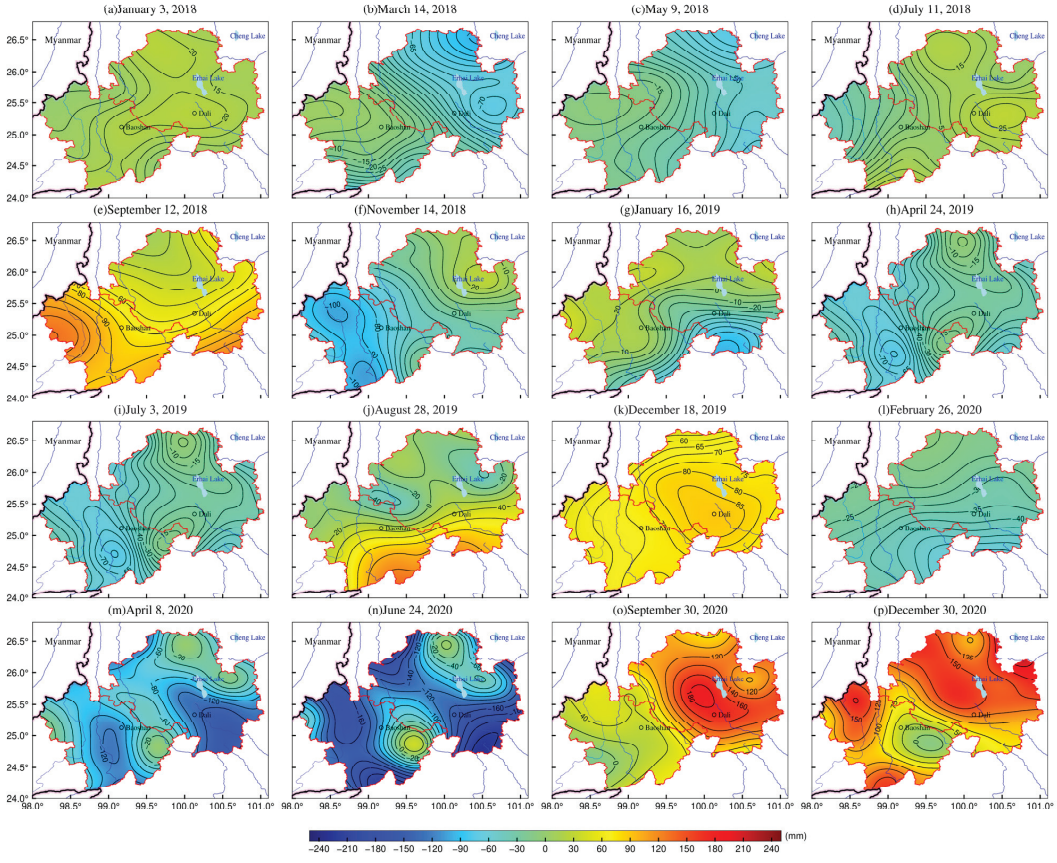

Figure 7. Weekly GWSA over the January 2018-December 2020 period.

The errors generated from the GNSS data processing, the surface mass model, and the uncertainty in the CORS inversion model may affect the accuracy of the GWSA inversion. The inverse distance weight interpolation method was used in this study to map the time series of the GWSA of CORS stations. Table 5 shows the statistical results of the interpolated GWSA time series of 12 CORS stations. The maximum and minimum values of the inverted GWSA were −200 and 200 mm, respectively. In addition, there were some differences in the

amplitude variation of GWSA at different CORS stations, indicating that the CORS inverse results had a high resolution. The mean and standard deviation (SD) values of GWSA at all CORS stations ranged from 3.16 to 15.03 mm and 55.87 to 110.39 mm, respectively. The reliability of the CORS inverse results was assessed in the subsequent part using the GRACE inverse results and groundwater monitoring station data.

Table 5. Statistics of CORS inverse results for GWSA (mm).

	Max	Min	Mean	SD
XIAG	221.65	−254.34	12.05	95.30
YNCX	194.21	−187.55	3.16	83.02
YNGM	195.89	−220.71	3.71	98.74
YNJD	238.94	−163.37	9.32	86.38
YNLC	269.79	−196.11	15.03	98.91
YNLJ	177.70	−117.27	8.25	61.45
YNRL	247.96	−106.43	12.97	55.87
YNSD	184.97	−141.54	9.58	65.27
YNTC	228.84	−129.08	12.70	69.09
YNYA	234.34	−251.67	3.17	110.39
YNYL	184.23	−179.98	6.39	76.58
YNYS	269.98	−222.53	7.96	106.81

In order to further analyze the temporal features of GWSA based on the sequence data of the GWSA grids, the study area was first divided into four sub-study areas, namely the eastern (BCHU, SYUN, and NJIA), northern (BAIS, YNYL, and JCHU), western (SUDI, YINJ, and TOBG), and southern (CHA3, MENT, and YNSD) sub-study areas, and then four CORS stations were selected randomly as examples. In Figure 8, the curves show the time series of GWSA at the corresponding stations, while the bar charts indicate the precipitation amounts in certain sub-study areas observed at nearby weather stations (Figure 1). In comparison with Figure 7, Figure 8 more directly reflects the temporal features of GWSA. The GWSA dynamics in different sub-study areas were relatively similar. Indeed, since groundwater recharge is derived mainly from precipitation in the study region, GWSA was strongly correlated with precipitation and exhibited significant seasonal differences. According to the obtained results, GWS exhibited main wave crest shapes. From February and March of each year, GWS showed the lowest values from February/March to June/July, then increased significantly from July to October due to the significant increase in the precipitation amounts, followed by a decrease in GWS in December and January. Therefore, precipitation was the main influencing factor on the GWSA in the study region.

In order to quantitatively analyze the groundwater drought in the study area within 3 years, the groundwater severity index (DSI) [49] was used in this study. This index was calculated using the following formula:

$$CORS - DSI_{i,j} = \frac{GWSA_{i,j} - \overline{GWSA_j}}{\sigma_j} \quad (9)$$

where i denotes the year from 2018 to 2020; j represents the month from January to December; $CORS - DSI_{i,j}$ represents the groundwater drought index DSI; $\overline{GWSA_j}$ and σ_j represent the mean and standard deviation of GWSA, respectively. The classification results of groundwater drought, derived from DSI, are reported in Table 6. As reported above, the monthly GWSA data were obtained from the monthly average of the weekly GWSA time series.

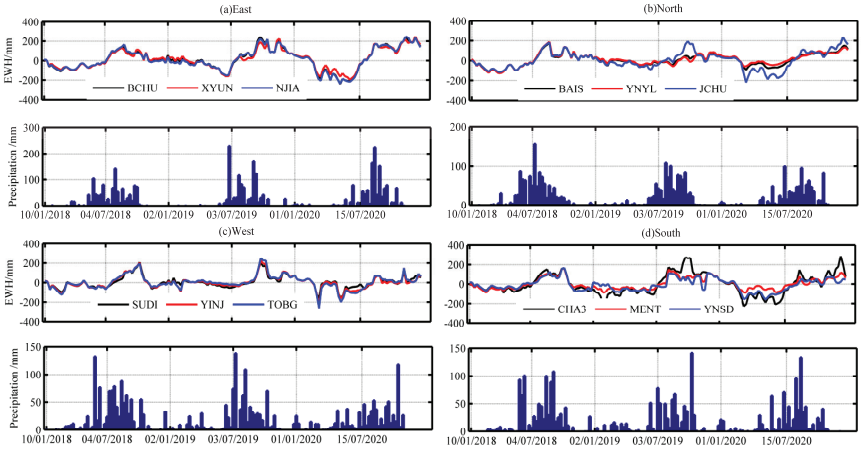

Figure 8. GWSA at Different CORS stations and precipitation amounts in different sub-study areas.

Figure 9 shows the temporal variation of CORS-DSI in the study area from 2018 to 2020. The results showed a significant seasonal variation in CORS-DSI. In addition, the CORS-DSI values in the eastern and northern sub-regions of the study area were above 0.8 in most months, while only a few months showed CORS-DSI values slightly below 0.8, indicating a mild groundwater drought (Figure 9a,b). On the other hand, the western and southern sub-regions of the study area showed several months with CORS-DSI values below −0.8, while the southern sub-region exhibited relatively significant groundwater drought, with CORS-DSI close to −1.3 over the November 2018–February 2019 and April 2020–August 2020 periods (Figure 9c,d). It is worth noting that the groundwater drought analysis requires more than 10 years of observation data, while only 3 years of CORS station data were used in this study to invert the GWSA. Therefore, to obtain more detailed and accurate drought analysis results, it is suggested to consider long-term observation data in future groundwater drought analyses.

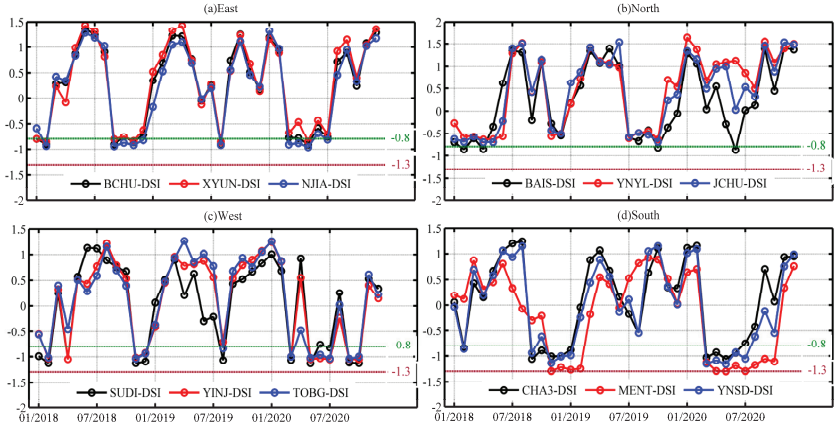

Figure 9. CORS-DSI in different sub-study areas.

Table 6. Correlation coefficients and WRMS (%) between different mass surface loads and the reconstructed geodetic height time series.

Drought Ranges	Drought Severity	CORS-DSI Range Values
L1	No drought	[−0.79, −0.50]
L2	Mild drought	[−1.29, −0.80]
L3	Moderate drought	[−1.59, −1.30]
L4	Severe drought	[−1.99, −1.60]
L5	Extreme drought	≤2.0

4.2. Comparison with GRACE Data

In order to assess the reliability of the CORS inverse results for GWSA, the GRACE inverse results for GWSA and the observed groundwater level data were used in this study. EWH is considered in the GRACE data to reflect the TWS. GWSA can be computed by removing soil water storage provided by the GLDAS data product. In this study, the period between October 2018 and December 2020 was considered due to the loss of data between GRACE and GRACE-FO. The monthly GRACE data were compared in this study with the monthly inverted CORS-based GWSA data during the year 2019. The obtained results are shown in Figure 10.

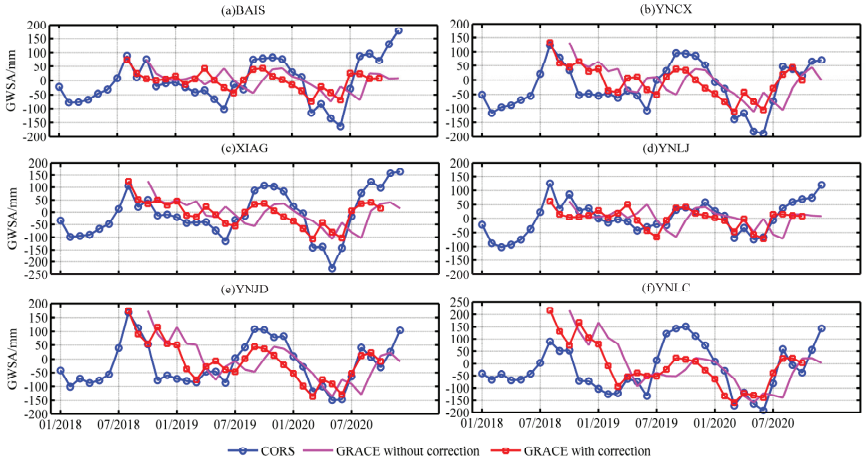

Figure 10. Comparison between CORS and GRACE inverse results.

Feng [50] showed a delay in the GRACE-based land water storage changes by 2 months compared to precipitation changes. Therefore, a 2-month phase delay was performed for the GRACE time series. As can be seen from Figure 10, relatively consistent GRACE- and CORS-based GWSA trends were obtained following the phase delay correction.

In total, 15 CORS were selected randomly as examples. The values in Table 7 indicate the correlation coefficients of the CORS- and GRACE-based GWSA results. Due to the missing data in 2018, the correlation coefficients were computed in this study based on the 2019 data. Compared with the inversion CORS-based data, the GRACE data had a 2-month phase delay. After phase delay correction, the coefficients were significantly improved. Except for FGON, LJGC, and YNRL, showing correlation coefficients of 0.68, 0.69, and 0.65, respectively, the correlation coefficients of all other stations were above 0.7. The highest correlation coefficient was 0.85 in YNJD, indicating a strong correlation. The computed correlation coefficients showed a spatial variation due to the low spatial resolution of the inversion GRACE-based on data. As is shown in Figure 10, the interpolation method used in this study resulted in relatively consistent trends of GRACE monitoring results at different sites without showing significant spatial differences. In addition, the CORS-based

GWSA results were based on long-term monitoring GNSS data. Indeed, the density of the CORS stations in the study region allowed us to obtain a higher spatial resolution (Figure 7), showing clear differences in the GWSA time series that are also clearer (Figure 10).

Table 7. Correlation coefficients between CORS and GRACE inverse results.

CORS Stations	GRACE		CORS	GRACE		CORS	GRACE	
	Raw Data	Correction		Raw Data	Correction		Raw Data	Correction
BAIS	0.44	0.73	FGON	0.36	0.68	LJGC	0.23	0.69
XIAG	0.57	0.76	YNCX	0.53	0.79	YNGM	0.66	0.75
YNJD	0.56	0.85	YNLC	0.53	0.81	YNLJ	0.19	0.80
YNRL	0.33	0.65	YNSD	0.59	0.74	YNTC	0.37	0.72
YNYA	0.36	0.70	YNYL	0.61	0.72	YNYS	0.11	0.72

Figure 11 shows the annual variation in CORS- and GRACE-based GWSA from 2018 to 2020. The spatial distribution characteristics of the two monitoring results were slightly consistent, showing relatively large annual changes in GWSA in the eastern and southern parts of the study area. The main spatial differences between the two monitoring results were observed in the south-central part of the study area. Overall, the amplitude of the annual variation in CORS-based GWSA was greater than that of GRACE-based GWSA. This finding may be due to the different monitoring methods of the two data products. Indeed, GRACE measures the integrated regional effect of mass redistribution. Its low spatial resolution makes it difficult to comprehensively reflect the effective information of the small-scale region, whereas the CORS data product is based on GNSS measurement methods, which provides real-time geometric deformation information at different locations in the study area, thereby fully reflecting the signal changes in the region.

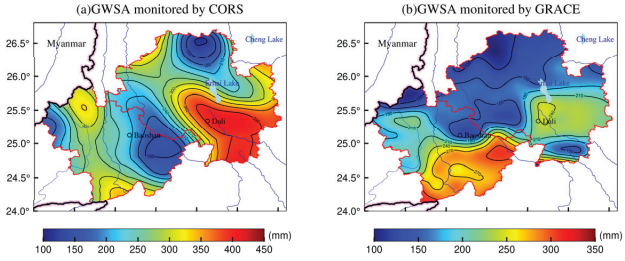

Figure 11. Annual variation in CORS- and GRACE-based GWSA results.

In summary, both inverse results reflected the changes in GWSA. The results indicate that the GNSS-based CORS data are more sensitive to GWSA, showing obvious local spatial characteristics compared to those of the GRACE data.

4.3. Comparison with Groundwater Monitoring Data

In order to further assess the reliability of CORS-based GWSA results, the inverted GWSA data were interpolated and compared to groundwater levels observed at groundwater monitoring stations. The daily groundwater level data were collected from September 2018 to December 2020. These data were processed for gross error detection and weekly averaging. In order to quantitatively compare the groundwater level data with GWSA, it is necessary to convert the groundwater level data to equivalent water height by considering the specific yield of the area [10]. The specific yield value for the study area was set to 0.05 [51,52].

The blue curves in Figure 12 indicate the CORS-based GWSA results observed in four stations, while the red line indicates the result of multiplying the groundwater level by the specific yield value. Both results are the average values of data observed over the year 2019.

The results revealed consistent trends of CORS-based GWSA and groundwater levels, showing the same order of amplitude changes. On the other hand, the correlation coefficients between the two data ranged from 0.62 to 0.82, indicating strong positive correlations (Table 8). Therefore, the results demonstrated that the combined CORS and high-resolution surface mass load data effectively invert GWSA in small-scale areas, providing accurate seasonal trends for GWSA.

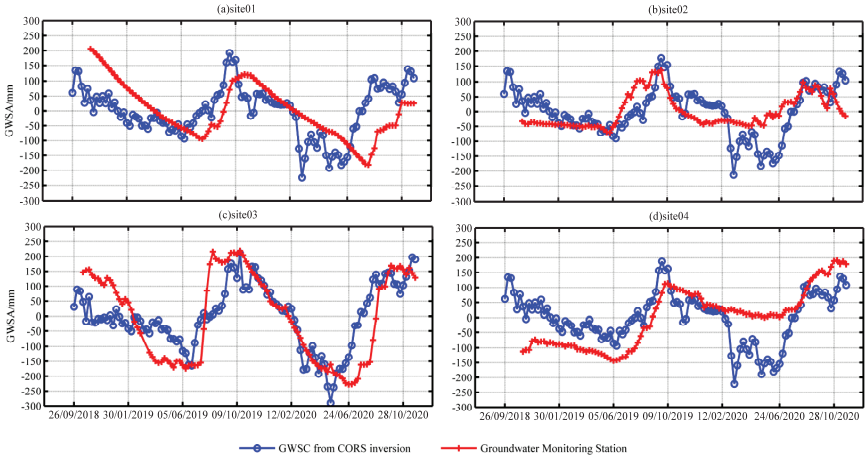

Figure 12. Comparison between CORS-based GWSA and groundwater monitoring results.

Table 8. Correlation coefficients between CORS-based GWSA and observed GWSA at groundwater monitoring stations.

Station	Correlation Coefficient	Station	Correlation Coefficient	Station	Correlation Coefficient
Site 01	0.82	Site 02	0.63	Site 03	0.74
Site 04	0.82	Site 05	0.62	Site 06	0.62
Site 07	0.64	Site 08	0.64	Site 09	0.64
Site 10	0.69	Site 11	0.66	Site12	0.65
Site13	0.63	Site14	0.67	Site15	0.66

5. Discussion

Considering the difficult physical conditions and high cost of constructing groundwater monitoring stations, as well as the low-resolution problem of the GRACE inversion results, the present study aims to assess the feasibility and reliability of CORS for GWSA inversion. Numerous studies have analyzed the correlation of TWSA or GWSA with GNSS vertical displacement [24,26,27]. In addition, He [21] inverted TWSA using GNSS vertical displacement. However, few studies have directly inverted GWSA using the CORS data product. Therefore, to improve the accuracy and stability of the inversion results, global and regional high-resolution surface mass models were combined to determine the high-precision load deformation field in western Yunnan using the remove–restore method. In addition, the reliability of CORS-based GWSA results was assessed using the observed groundwater levels. Although the obtained results showed accurate GWSA and demonstrated the validity and reliability of the methods used in this study, there are still some challenges to address. Data covering a period longer than 2.5 years were observed only at 15 stations among the 66 CORS stations, thereby affecting the accuracy of the inverse results for some months. Since the data processing is complicated, the study period considered in this study was only 3 years, resulting in non-obvious drought characteristics and trends. Therefore, this study focused mainly on the seasonal variation in GWSA in the

study area. In addition, the specific yield in this study was set to 0.05 for the entire study area. It should be noted that the specific yield can vary significantly depending on the depth of groundwater wells and the lithological characteristic of the aquifers. Therefore, different specific yield values need to be provided for different groundwater wells to obtain more accurate GWSA results using groundwater monitoring data.

The correlation coefficients between GRACE- and CORS-based GWSA were above 0.65 following the 2-month delay phase correction. The variation in the EWH of GRACE- and CORS-based GWSA showed a consistent magnitude of variation. In addition, the annual variation in CORS-based GWSA results was slightly larger than that of GRACE-based GWSA results. Although the principles of GRACE and CORS methods used in the GWSA inversion are different, the results suggested that both methods can effectively reflect the seasonal trend of GWSA in the study area. Indeed, GRACE product data are based on remote sensing techniques to comprehensively reflect the regional effects with redistributed mass, resulting in a low spatial resolution and difficulties in effectively transmitting small-scale regional information. Moreover, the filtering process used in the GRACE data processing might affect the real signal. On the other hand, the CORS data product is derived from GNSS-based monitoring data, allowing us to obtain in real time the geodetic height changes at a certain location, thus assuring faster response and better performance in reflecting the inter-region signal dynamics. Both methods can reflect the GWSA trends. However, the signal intensity and GRACE trend monitoring results at different locations can be basically the same in small-scale areas, while the differences in CORS network monitoring results are more obvious. GRACE is ineffective in determining features of small-scale study areas due to its limited spatial resolution, while CORS network monitoring results exhibit higher spatiotemporal resolution, with continuous and high-precision observation data, making the CORS method advantageous. Moreover, the CORS method can capture local area signals that are difficult to monitor by remote sensing techniques (e.g., GRACE). In summary, the CORS-based GWSA results revealed higher spatiotemporal resolution than that of GRACE-based GWSA results and are more sensitive to groundwater storage changes.

6. Conclusions

The present study aims to invert GWSA in western Yunnan using CORS and high-precision surface mass load data. This approach is based on the already-established CORS network without requiring extra construction costs. This approach is, indeed, able to provide a high-resolution GWSA grid sequence within the coverage of the CORS network due to the high density of CORS stations and consecutive high-precision GNSS monitoring data. Western Yunnan Province was considered in the present study to assess the validity of the approach used. The results demonstrated that the approach is able to independently and effectively invert a high-resolution GWSA grid within the CORS network. In addition, the spatiotemporal distribution characteristics of GWSA were analyzed in this study using the precipitation data observed at meteorological stations in western Yunnan. Moreover, to test the reliability of the obtained results, the GRACE and groundwater monitoring data were used in the present study. The main conclusions are as follows:

1. The correlation coefficients between the CORS geodetic height time series and the vertical deformation of the surface mass loads were all above 0.8, indicating strong positive correlations. In addition, the percentage of WRMS decreased from 33.84 to 43.93% following the load removal, demonstrating the effectiveness of the data processing used in the present study and the feasibility of CORS inversion for GWSA. The vertical deformations caused by surface mass loads contributed significantly to the seasonal signals of CORS geodetic height changes. Among the three surface mass loads, atmospheric and soil water loads were more influential, with an amplitude ranging from −8 to 8 mm, while the non-tidal oceanic load showed the lowest influence with an amplitude range of −2–2 mm.

2. The GWSA results exhibited clear seasonal variations in the study area from January 2018 to December 2020. In addition, GWS values decreased and increased from February to July and from July to September due to the significant decrease and increase in precipitation, respectively, observed during these periods. These findings indicated that precipitation is the major factor influencing GWS in the study region. In addition, the GWSA trends were similar in the different sub-study areas, while differences were mainly observed in the annual variation magnitude of GWSA. The largest annual variation was observed mainly in the eastern part of the study area, reaching 450 mm.
3. After performing a 2-month phase delay correction for GRACE inverse results, the correlation coefficient between GRACE- and CORS-GWSA results was over 0.65. Both methods were able to reflect the dynamics of GWSA in the study area. However, the CORS-based GWSA results reflected more accurately the GWSA changes in the study area, with a higher spatiotemporal resolution than those obtained using the GRACE data product.
4. The CORS-based GWSA showed high positive correlations with those determined using groundwater monitoring stations, with a correlation coefficient range of 0.62–0.82. The amplitudes of both GWSA results were on the same order of magnitude. These findings demonstrated the effectiveness and reliability of the CORS inversion for GWSA.

Author Contributions: P.X., T.J. and C.Z. conceived and designed the experiments; P.X. performed the experiments, analyzed the data, and wrote the paper; T.J., W.L. and C.Z. helped in the discussion and revision. K.S. provided the data from the CORS network. All authors have read and agreed to the published version of the manuscript.

Funding: This work was supported by the National Natural Science Foundation of China (No. 42074020), the Open Fund Project of the Key Laboratory of Marine Environmental Survey Technology and Application of the Ministry of Natural Resources (MESTA-2020-A001), and the Comprehensive CORS network and multi-source data monitoring of surface stability changes and pilot analysis of geological disaster precursor capture (AR2114).

Data Availability Statement: The raw/processed CORS network and groundwater level data are available from the author upon reasonable request. Correspondence and requests for data should be addressed to T.J.

Acknowledgments: Thanks to the CORS network data provided by the Yunnan Technical Center of Base Surveying and Mapping and the data from groundwater monitoring stations provided by the China Geological Environment Monitoring Institute.

Conflicts of Interest: The authors declare no conflict of interest.

References

1. Zheng, C.; Liu, J.; Cao, G.; Kendy, E.; Wang, H.; Jia, Y. Can China cope with its water crisis?—Perspectives from the North China Plain. *Groundwater* **2010**, *48*, 350–354. [CrossRef] [PubMed]
2. Doell, P.; Hoffmann-Dobrev, H.; Portmann, F.T.; Siebert, S.; Eicker, A.; Rodell, M.; Strassberg, G.; Scanlon, B.R. Impact of water withdrawals from groundwater and surface water on continental water storage variations. *J. Geodyn.* **2012**, *59*, 143–156. [CrossRef]
3. Andermann, C.; Longuevergne, L.; Bonnet, L.; Crave, A.; Davy, P.; Gloaguen, R. Impact of transient groundwater storage on the discharge of Himalayan rivers. *Nat. Geosci.* **2012**, *5*, 127–132. [CrossRef]
4. Hodnett, M.G.; Vendrame, I.; Filho, A.O.M.; Oyama, M.D.; Tomasella, J. Soil water storage and groundwater behaviour in a catenary sequence beneath forest in central Amazonia: I. Comparisons between plateau, slope and valley floor. *Hydrol. Earth Syst. Sci.* **1997**, *1*, 265–277. [CrossRef]
5. Bakalowicz, M. Karst groundwater: A challenge for new resources. *Hydrogeol. J.* **2005**, *13*, 148–160. [CrossRef]
6. Sharda, V.N.; Kurothe, R.S.; Sena, D.R.; Pande, V.C.; Tiwari, S.P. Estimation of groundwater recharge from water storage structures in a semi-arid climate of India. *J. Hydrol.* **2006**, *329*, 224–243. [CrossRef]
7. Kim, G.B.; Lee, K.K.; Lee, J.Y.; Yi, M.J. Case study for determination of a water level monitoring frequency for nationwide groundwater monitoring networks in Korea. *J. Hydrol.* **2007**, *342*, 223–237. [CrossRef]
8. Strassberg, G. Evaluation of groundwater storage monitoring with the GRACE satellite: Case study of the High Plains aquifer, central United States. *Water Resour. Res.* **2009**, *45*, W05410. [CrossRef]

9. Rodell, M.; Famiglietti, J.S. An analysis of terrestrial water storage variations in Illinois with implications for the Gravity Recovery and Climate Experiment (GRACE). *Water Resour.* **2001**, *37*, 1327–1339. [CrossRef]
10. Wei, F.; Wang, C.; Mu, D.; Min, Z.; Xu, H. Groundwater storage variations in the North China Plain from GRACE with spatial constraints. *Chin. J. Geophys.* **2017**, *60*, 1630–1642. [CrossRef]
11. Flechtner, F.; Neumayer, K.H.; Dahle, C.; Dobslaw, H.; Güntner, A.; Raimondo, J.C.; Fagiolini, E. What Can be Expected from the GRACE-FO Laser Ranging Interferometer for Earth Science Applications? *Surv. Geophys. Int. Rev. J. Geophys. Planet. Sci.* **2016**, *37*, 263–280.
12. Zhang, C.Y.; Wang, W.; Gan, W.J. Monitoring temporal and spatial changes of crustal deformation and gravity field caused by environmental load in the Three Gorges Reservoir Region based on CORS network. *Geomat. Inf. Sci. Wuhan Univ.* **2018**, *43*, 1287–1294. [CrossRef]
13. Baniulis, R.; Galinauskas, K.; Marozas, L.; Parseliunas, E.; Puskorius, V. An Analysis of the Performance and Coordinates Time Series of CORS Network LitPOS. In Proceedings of the 2017 Baltic Geodetic Congress (BGC Geomatics), Gdansk, Poland, 22–25 June 2017; pp. 22–25.
14. Métois, M.; Socquet, A.; Vigny, C.; Carrizo, D.; Peyrat, S.; Delorme, A.; Maureira, E.; Valderas-Bermejo, M.-C.; Ortega, I. Revisiting the North Chile seismic gap segmentation using GPS-derived interseismic coupling. *Geophys. J. Int.* **2013**, *194*, 1283–1294. [CrossRef]
15. Daniélyan, Y.S.; Yanitskii, P.A. Stability of the interphase surface in the freezing of moist ground. *J. Eng. Phys.* **1980**, *39*, 781–785. [CrossRef]
16. Zhang, C.Y.; Jiang, T.; Ke, B.G.; Wang, W. The Analysis of Height System Definition and the High Precision GNSS Replacing Leveling Method. *Acta Geod. Cartogr. Sin.* **2017**, *46*, 11–17. [CrossRef]
17. Farrell, W.E. Deformation of the Earth by surface loads. *Rev. Geophys.* **1972**, *10*, 761–791. [CrossRef]
18. Blewitt, G.; Clarke, P. Inversion of Earth's changing shape to weigh sea level in static equilibrium with surface mass redistribution. *J. Geophys. Res.* **2003**, *108*, 2311. [CrossRef]
19. Wang, W.; Zhang, C.Y.; Hu, M.Z.; Yang, Q.; Liang, S.M.; Kang, S.J. Monitoring and analysis of geological hazards in Three Gorges area based on load impact change. *Nat. Hazards* **2019**, *97*, 611–622. [CrossRef]
20. Argus, D.F.; Fu, Y.; Landerer, F.W. Seasonal variation in total water storage in California inferred from GPS observations of vertical land motion. *Geophys. Res. Lett.* **2014**, *41*, 1971–1980. [CrossRef]
21. He, S.Y.; Gu, Y.C.; Fan, D.M.; Zhao, H.; Zheng, R. Seasonal Variation of Terrestrial Water Storage in Yunnan Province lmferredfrom GPS Vertical Observations. *Acta Geod. Cartogr. Sin.* **2018**, *47*, 332–340. [CrossRef]
22. Amos, C.B.; Audet, P.; Hammond, W.C.; Bürgmann, R.; Johanson, I.A.; Blewitt, G. Uplift and seismicity driven by groundwater depletion in central California. *Nature* **2014**, *509*, 483–486. [CrossRef] [PubMed]
23. Gross, R.S.; Blewitt, G.; Clarke, P.J.; Lavallée, D. Degree-2 harmonics of the Earth's mass load estimated from GPS and Earth rotation data. *Geophys. Res. Lett.* **2004**, *31*, L07601. [CrossRef]
24. Liu, R.L.; Zou, R.; Li, J.C.; Zhang, C.H.; Zhao, B.; Zhang, Y.K. Vertical Displacements Driven by Groundwater Storage Changes in the North China Plain Detected by GPS Observations. *Remote Sens.* **2018**, *10*, 259. [CrossRef]
25. Chanard, K.; Avouac, J.P.; Ramillien, G.; Genrich, J. Modeling deformation induced by seasonal variations of continental water in the Himalaya region: Sensitivity to Earth elastic structure. *J. Geophys. Res. Solid Earth* **2014**, *119*, 5097–5113. [CrossRef]
26. Hew, C.C.; Small, E.E. Terrestrial water storage response to the 2012 drought estimated from GPS vertical position anomalies. *Geophys. Res. Lett.* **2014**, *41*, 6145–6151. [CrossRef]
27. Davis, J.L. Climate-driven deformation of the solid Earth from GRACE and GPS. *Geophys. Res. Lett.* **2004**, *31*, L24605. [CrossRef]
28. Nahmani, S.; Bock, O.; Bouin, M.N.; Santamaría-Gómez, A.; Boy, J.P.; Collilieux, X.; Métivier, L.; Panet, I.; Genthon, P.; Linage, C.D.; et al. Hydrological deformation induced by the West African Monsoon: Comparison of GPS, GRACE and loading models. *J. Geophys. Res. Solid Earth* **2012**, *117*, 5409. [CrossRef]
29. Dardanelli, G.; Brutto, M.L.; Pipitone, C. GNSS CORS network of the University of Palermo: Design and first analysis of data. *Geogr. Tech.* **2020**, *15*, 43–69. [CrossRef]
30. Kenyeres, A.; Bellet, J.G.; Bruyninx, C.; Caporali, A.; Doncker, F.D.; Droscak, B.; Duret, A.; Franke, P.; Georgiec, I.; Bingley, R.; et al. Regional integration of long-term national dense GNSS network solutions. *GPS Solut.* **2019**, *23*, 122. [CrossRef]
31. Herring, T.A.; King, R.W.; Floyd, M.A.; McClusky, S.C. *Introduction to GAMIT/GLOBK*; Massachusetts Institute of Technology: Cambridge, MA, USA, 2018. Available online: http://geoweb.mit.edu/gg/Intro_GG.pdf (accessed on 15 May 2021).
32. Altamimi, Z.; Collilieux, X.; Métiver, L. ITRF2008: An improved solution of the international terrestrial reference frame. *J. Geod.* **2011**, *85*, 457–473. [CrossRef]
33. Dee, D.P.; Uppala, S.M.; Simmons, A.J.; Berrisford, P.; Poli, P.; Kobayashi, S.; Andrae, U.; Balmaseda, M.A.; Balsamo, G.; Bauer, P. The ERA-Interim reanalysis: Configuration and performance of the data assimilation system. *Q. J. R. Meteorol. Soc.* **2011**, *137*, 553–597. [CrossRef]
34. Sheng, C. Characteristics of non-tectonic crustal deformation from surface loads around Chinese mainland and correction model. *Recent Dev. World Seism.* **2014**, *11*, 45–48.
35. Lombard, A.; Garcia, D.; Ramillien, G.; Cazenave, A.; Biancale, R.; Lemoine, J.M.; Flechtner, F.; Schmidt, R.; Ishii, M. Estimation of steric sea level variations from combined GRACE and Jason-1 data. *Earth Planet. Sci. Lett.* **2007**, *254*, 194–202. [CrossRef]

36. Rodell, M.; Beaudoing, H.K. *NASA/GSFC/HSL. GLDAS Noah Land Surface Model L4 Monthly 0.25 × 0.25 Degree V2.1*; Goddard Space Flight Center Earth Sciences Data and Information Services Center (GES DISC): Greenbelt, MD, USA, 2016. [CrossRef]
37. Save, H.; Bettadpur, S.; Tapley, B.D. High-resolution CSR GRACE RL05 mascons. *J. Geophys. Res. Solid Earth* **2016**, *121*, 7547–7569. [CrossRef]
38. Dong, D.; Fang, P.; Bock, Y.; Cheng, M.K. Anatomy of apparent seasonal variations from GPS-derived site position time series. *J. Geophys. Res. Solid Earth* **2002**, *107*, 2075. [CrossRef]
39. Blais, J.A.R.; Provins, D.A.; Soofi, M.A. Spherical harmonic transforms for discrete multiresolution applications. *J. Supercomput.* **2006**, *38*, 173–187. [CrossRef]
40. Hoerl, A.E.; Kennard, R.W. Ridge Regression: Biased Estimation for Nonorthogonal Problems. *Technometric* **1970**, *12*, 55–67. [CrossRef]
41. Wang, Z.J.; Ou, J.K. Determining the RidgeParameter in a Ridge Estimation Using L-curve Method. *Geomat. Inf. Sci. Wuhan Univ.* **2004**, *29*, 235–238. [CrossRef]
42. Nussbaumer, H.J. *Fast Fourier Transform and Convolution Algorithms*; Springer: Berlin/Heidelberg, Germany, 1981.
43. Tao, R.; Li, B.-Z.; Wang, Y. Spectral Analysis and Reconstruction for Periodic Nonuniformly Sampled Signals in Fractional Fourier Domain. *IEEE Trans. Signal Process.* **2007**, *55*, 3541–3547. [CrossRef]
44. Dam, T.V.; Wahr, J.; Lavallée, D. A comparison of annual vertical crustal displacements from GPS and Gravity Recovery and Climate Experiment (GRACE) over Europe. *J. Geophys. Res. Solid Earth* **2007**, *112*, B03404. [CrossRef]
45. Kostadinov, T.S.; Lookingbill, T.R. Snow cover variability in a forest ecotone of the Oregon Cascades via MODIS Terra products. *Remote Sens. Environ.* **2015**, *164*, 55–169. [CrossRef]
46. Muhuri, A.; Gascoin, S.; Menzel, L.; Kostadinov, T.; Moreno, J.I.L. Performance Assessment of Optical Satellite-Based Operational Snow Cover Monitoring Algorithms in Forested Landscapes. *IEEE J. Sel. Top. Appl. Earth Obs. Remote Sens.* **2021**, *14*, 7159–7178. [CrossRef]
47. Munekane, H.; Matsuzaka, S. Nontidal ocean mass loading detected by GPS observations in the tropical Pacific region. *Geophys. Res. Lett.* **2004**, *31*, 289–291. [CrossRef]
48. Nordman, M.; Mäkinen, J.; Virtanen, H.; Johansson, J.; Bilker-Koivula, M.; Virtanen, J. Crustal loading in vertical GPS time series in Fennoscandia. *J. Geodyn.* **2009**, *48*, 144–150. [CrossRef]
49. Han, Z.M.; Hhuang, S.Z.; Huang, Q.; Leng, G.Y.; Wang, H.; Bai, Q.J.; Zhao, J.; Ma, L.; Wang, L.; Du, M. Propagation dynamics from meteorological to groundwater drought and their possible influence factors. *J. Hydrol.* **2019**, *578*, 124102. [CrossRef]
50. Feng, W.; Lemoine, J.M.; Zhong, M.; Tou-Tse, H. Terrestrial water storage changes in the Amazon basin measured by GRACE during 2002–2010. *Chin. J. Geophys.* **2012**, *55*, 814–821. (In Chinese) [CrossRef]
51. Gehlin, S.E.A.; Hellstrm, G. Influence on thermal response test by groundwater flow in vertical fractures in hard rock. *Renew. Energy* **2003**, *28*, 2221–2238. [CrossRef]
52. Zhou, Y.Y.; CHEN, X.; Zhang, Z.C. Numerical groundwater modeling in a small karst watershed of the Southwest China. *Geotech. Investig. Surv.* **2011**, *4*, 43–51.

remote sensing

MDPI

Article

Modelling and Assessment of a New Triple-Frequency IF1213 PPP with BDS/GPS

Zhongyuan Wang [1], Ruiguang Wang [1,*], Yangyang Wang [1,2], Chao Hu [3] and Bingyu Liu [1]

[1] School of Environmental and Spatial Informatics, China University of Mining and Technology, Xuzhou 221116, China
[2] Qianxun Spatial Intelligence Inc., Shanghai 200082, China
[3] School of Spatial Information and Geomatics Engineering, Anhui University of Science and Technology, Huainan 232001, China
* Correspondence: ragwang@cumt.edu.cn

Abstract: The currently available triple-frequency signals give rise to new prospects for precise point positioning (PPP). However, they also bring new bias, such as time-varying parts of the phase bias in the hardware of receivers and satellites due to the fact that dual-frequency precise clock products cannot be directly applied to triple-frequency observation. These parameters generate phase-based inter-frequency clock bias (PIFCB), which impacts the PPP. However, the PIFCBs of satellites are not present in all GNSSs. In this paper, various IF1213 PPP models are constructed for these parts, namely, the triple-frequency PIFCB (TF-C) model with PIFCB estimation, the TF inter-frequency bias (IFB) (TF-F) model ignoring the PIFCB, and the TF-PIFCB-IFB (TF-CF) model with one system PIFCB estimation. Additionally, this study compares these IF1213 PPP models with the dual-frequency ionosphere-free (DF) model. We conducted single system static PPP, dual-system static and kinematic PPP experiments based on BDS/GPS observation data. The GPS static PPP experiment demonstrates the reliability of the TF-C model, as well as the non-negligibility of the GPS PIFCB. The BDS static PPP experiment demonstrates the reliability of the TF-F and TF-CF models, and that the influence of the BDS-2 PIFCB can be neglected in BDS. The BDS/GPS PPP experimental results show that the third frequency does not significantly improve the positioning accuracy but shortens the convergence time. The positioning accuracy of TF-C and TF-CF for static PPP is better than 1.0 cm, while that for kinematic PPP is better than 2.0 cm and 4.0 cm in the horizontal and vertical components, respectively. Compared with the DF model, the convergence time of the TF-C and TF-CF models for static PPP is improved by approximately 23.5%/18.1%, 13.6%/9.7%, and 19.8%/12.1%, while that for kinematic PPP is improved by approximately 46.2%/49.6%, 33.5%/32.4%, and 35.1%/36.1% in the E, N and U directions, respectively. For dual-system PPP based on BDS/GPS observations, the TF-C model is recommended.

Keywords: GPS; BDS; triple-frequency signals; IFCB; PPP

Citation: Wang, Z.; Wang, R.; Wang, Y.; Hu, C.; Liu, B. Modelling and Assessment of a New Triple-Frequency IF1213 PPP with BDS/GPS. *Remote Sens.* **2022**, *14*, 4509. https://doi.org/10.3390/rs14184509

Academic Editors: Shuanggen Jin and Gino Dardanelli

Received: 19 July 2022
Accepted: 7 September 2022
Published: 9 September 2022

1. Introduction

In the late 1990s, precise point positioning (PPP) technology was proposed by Zumberge et al. [1] and implemented [2]. With the modernization of GPS and the completion of BDS, an increasing number of navigation satellites provide signals at three or more frequencies, and the research and application of triple-frequency PPP has become increasingly extensive and in depth [3–6]. The available triple-frequency signals create new prospects for integrity monitoring [7], for facilitating cycle slip detection and repairing [8,9], for fast ambiguity resolution (AR) [10] and for ionospheric analysis [11]. While triple-frequency signals have many benefits, new bias has also been introduced. Montenbruck et al. [12] first demonstrated the existence of a bias between L1/L2 and L1/L5 in ionosphere-free (IF) combination, including a periodic line bias between the satellite and the signal, based on geometry-free and ionosphere-free (GFIF) phase combination. The inconsistency of L1/L2/L5 was defined as inter-frequency clock bias (IFCB) [13]. Precise clock estimation

(PCE) is obtained through dual-frequency IF combination. When using signals of different frequencies for the dual-frequency IF combination PCE, the satellite clock estimation will have a bias, which is the IFCB [14]. The bias consists of the receiver and satellite code hardware bias and phase hardware bias time-varying components, which generate the code-based IFCB (CIFCB) and PIFCB, respectively. The PIFCB consists of a satellite PIFCB and a receiver PIFCB. However, not all satellites of constellations have PIFCB, e.g., BDS-3, Galileo and QZSS constellations could ignore the satellite PIFCB [15,16].

GPS Block IIF satellite PIFCB varies throughout the day, with peak-to-peak amplitudes of a few to several tens of centimeters [13]. Pan et al. [14] proposed a satellite PIFCB estimation method for triple-frequency PPP for GPS and established an uncombined (UC) and IF123 PPP model with satellite PIFCB estimations followed by corrections. The experimental results showed that after GPS satellite PIFCB corrections, the corresponding positioning accuracy of the UC123 and IF123 PPP models could be improved to 5, 4, and 9 mm and 4, 3, and 10 mm in the E, N and U directions, respectively. For BDS-2, there was a small bias in B1I/B2I/B3I, and its satellite PIFCB varied throughout the day with a peak-to-peak amplitude of approximately 2 cm [17,18]. Fan et al. [19] proposed a GNSS IFCB estimation and correction generic model, which was implemented and validated using BDS-2 and BDS-3 data. It was experimentally demonstrated that the BDS-2 satellite PIFCB showed a periodic variation and with some of the satellites corrected by PIFCB, the mean root mean square error (RMS) value of the GFIF phase combination was 5 mm, which was an improvement of 50%. Gong et al. [20] and Pan et al. [21] systematically studied the long-term characteristics of the GNSS satellite PIFCB through GFIF phase combination.

In addition to the study of the characteristics of the satellite PIFCB, a number of researchers have analyzed different triple-frequency PPP models based on the consideration of the satellite PIFCB [3,22]. Guo et al. [23] conducted a systematic study of the UC123, IF1213 and IF123 PPP models based on BDS-2 B1I/B2I/B3I triple-frequency observation data. Pan et al. [24] systematically analyzed different triple-frequency PPP models based on GPS triple-frequency observation data. Different studies have shown that triple-frequency PPP positioning performance considering satellite PIFCB could reach the level of dual-frequency PPP. As GPS, GLONASS, BDS and Galileo continue to improve and modernize, an increasing number of researchers are focusing on multi-constellation combinations [25–28], while multi-constellation multifrequency PPP is also a new trend. Li et al. [29] investigated the performance of BDS/Galileo for triple-frequency PPP AR, and Li et al. [10] investigated the performance of GPS/Galileo/BDS-2 for triple-frequency PPP AR. Different studies have shown that multi-GNSS positioning performance is not only better than single GNSS, but further improves position estimation and can be applied to complex environmental conditions.

In summary, the short- and long-term characteristics of the satellite PIFCB have been studied, as well as the triple-frequency PPP in the case of satellite PIFCB correction. In this study, we focus on the precision modeling of the dual-system triple-frequency IF1213 PPP and validate it using GPS and BDS observations. First, the IF1213 PPP models with different treatments for the PIFCB are presented, namely, triple-frequency PIFCB (TF-C) with the PIFCB estimation, triple-frequency IFB (TF-F) ignoring the PIFCB, and the triple-frequency PIFCB-IFB (TF-CF) model without the full estimation of PIFCB, which only estimates the PIFCB in one system. Additionally, we also present the IF1213 PPP model using the IGMAS [30] product corrected by the satellite PIFCB, namely, the triple-frequency IFB-product (TF-FP). The relationships between these models are also analyzed. Next, the deduced models are validated using BDS and GPS triple-frequency observations, respectively. GPS triple-frequency observations are also used to validate the influence of GPS PIFCB. BDS triple-frequency observations are also used to validate the influence of BDS-2 PIFCB in BDS. Static and kinematic experiments are then conducted using BDS/GPS triple-frequency data. Finally, the main conclusions are given.

2. Materials and Methods

In this section, the functional models of three IF1213 models (TF-C, TF-F, and TF-CF) are described based on the general observation model. Additionally, the TF–FP model is also presented. For convenience, the three frequencies are numbered 1, 2 and 3. The specific frequencies indicated by the numbers are shown in Table 1, and the values in parentheses are in MHz. For BDS-3, the IF combination of B1I/B1C causes the noise amplification factor to be much larger than that of B3I/B1C. Therefore, the IF13 combination utilizes the IF combination of B3I/B1C; this means that for BDS-3, the IF combination is IF1223 in the experiment, but it is still noted as IF1213 during the derivation of the model below for ease of expression.

Table 1. BDS/GPS frequency number.

Number	GPS	BDS-2	BDS-3
1	L1 (1575.42)	B1I (1561.01)	B1I (1561.01)
2	L2 (1227.60)	B3I (1268.52)	B3I (1268.52)
3	L5 (1176.45)	B2I (1207.14)	B1C (1575.42)

2.1. General Observation Model

The code and carrier phase observations on a single frequency are as follows [31]:

$$\begin{cases} p_{r,j}^{s,Q} = \mu_r^{s,Q} \cdot x + dt_r - dt^{s,Q} + m^{s,Q} \cdot Z_r + \gamma_j \cdot I_{r,1}^{s,Q} + d_{r,j} - d_j^{s,Q} + \varepsilon_{r,j}^{s,Q} \\ l_{r,j}^{s,Q} = \mu_r^{s,Q} \cdot x + dt_r - dt^{s,Q} + m^{s,Q} \cdot Z_r - \gamma_j \cdot I_{r,1}^{s,Q} + N_{r,j}^{s,Q} + \varphi_{r,j} - \varphi_j^{s,Q} + \xi_{r,j}^{s,Q} \end{cases} \quad (1)$$

where the superscript s, Q and subscript r represent the satellite, constellation and receiver, respectively; in this paper Q can be G, C2, C3 and C for GPS, BDS-2, BDS-3 and BDS, respectively, where BDS means that BDS-2 and BDS-3 are considered as one constellation; $p_{r,j}^{s,Q}$ and $l_{r,j}^{s,Q}$ are the code and phase observed-minus-computed (OMC) values, respectively; j denotes the frequency ($j = 1, 2, 3$); $\mu_r^{s,Q}$ is the unit vector of direction; x represents the vector of position correction to the a priori position; and dt_r and $dt^{s,Q}$ indicate the receiver and satellite clock offsets, respectively. Furthermore, Z_r is the wet troposphere delay at zenith; $\gamma_j = f_1^2/f_j^2$ is the ionospheric factor; f indicates the carrier phase frequency; $I_{r,1}^{s,Q}$ denotes the slant ionospheric delay at the first frequency; and $N_{r,j}^{s,Q}$ represents the integer phase ambiguity. The parameters $d_{r,j}$ and $d_j^{s,Q}$ are the code hardware delays from the receiver and satellite, respectively. $\varphi_{r,j}$ and $\varphi_j^{s,Q}$ are the receiver-dependent and satellite-dependent carrier phase hardware delays, respectively. $\varepsilon_{r,j}^{s,Q}$ and $\xi_{r,j}^{s,Q}$ are the measurement noise of the code and carrier phase, respectively. Other error items include the phase center offset (PCO) and variation (PCV), dry slant troposphere delay, phase wind-up, and relativistic effect. For simplicity, they are precisely corrected with their corresponding models and are not listed in the equations. It should be noted that in the case of lacking the precise PCO/PCV information of the third frequency, we use the PCO/PCV corrections of the first frequency instead due to the adjacent frequency.

For code and phase hardware bias, the code hardware bias is generally considered to be relatively stable and can be considered constant over the course of a day [32]. The phase hardware bias has a clear time-varying character and can be decomposed into a constant part and a time-varying part [13,14].

$$\begin{cases} \varphi_{r,j} = \overline{\varphi}_{r,j} + \delta\varphi_{r,j} \\ \varphi_j^{s,Q} = \overline{\varphi}_j^{s,Q} + \delta\varphi_j^{s,Q} \end{cases} \quad (2)$$

where $\overline{\varphi}_{r,j}$ and $\overline{\varphi}_j^{s,Q}$ are the phase hardware bias constant parts of the receiver and satellite, respectively; $\delta\varphi_{r,j}$ and $\delta\varphi_j^{s,Q}$ are the corresponding time-varying parts. The constant part

can be completely absorbed by the ambiguity $\overline{N}_{r,j}^{s,Q} = N_{r,j}^{s,Q} + \overline{\varphi}_{r,j} + \overline{\varphi}_{j}^{s,Q}$. Moreover, the following variables are defined herein for ease of expression:

$$\begin{cases} \alpha_{ij} = \frac{f_i^2}{f_i^2 - f_j^2} \\ \beta_{ij} = -\frac{f_j^2}{f_i^2 - f_j^2} \\ DCB_{r,ij} = d_{r,i} - d_{r,j} \\ DCB_{ij}^{s,Q} = d_i^{s,Q} - d_j^{s,Q} \\ DPB_{r,ij} = \delta\varphi_{r,i} - \delta\varphi_{r,j} \\ DPB_{ij}^{s,Q} = \delta\varphi_i^{s,Q} - \delta\varphi_j^{s,Q} \\ DCB_{r,ij}^{s,Q} = DCB_{r,ij} - DCB_{ij}^{s,Q} \\ DPB_{r,ij}^{s,Q} = DPB_{r,ij} - DPB_{ij}^{s,Q} \end{cases} \tag{3}$$

where i, j are the phase frequencies $(i, j = 1, 2, 3; i \neq j)$, α_{ij} and β_{ij} are the coefficients of the IF combination; $DCB_{r,ij}$ and $DCB_{ij}^{s,Q}$ are the differential code biases (DCBs) of the receiver and satellite; and $DPB_{r,ij}$ and $DPB_{ij}^{s,Q}$ are the differential phase biases (DPBs) of the receiver and satellite.

2.2. IF1213 Observation Model

The IF combination can eliminate the ionospheric first-order term from the original observation equation. Using the IF combination and ignoring the ionospheric second-order term and above, the number of parameters that need to be estimated in the equation can be effectively reduced. A single-system dual-frequency IF combined observation equation is formed by Equation (1), which can be expressed as follows:

$$\begin{cases} p_{r,IFij}^{s,Q} &= \alpha_{ij} \cdot p_{r,i}^{s,Q} + \beta_{ij} \cdot p_{r,j}^{s,Q} \\ &= \mu_r^{s,Q} \cdot x + dt_r - dt^{s,Q} + m^{s,Q} \cdot Z_r + d_{r,IFij} - d_{IFij}^{s,Q} + \varepsilon_{r,IFij}^{s,Q} \\ l_{r,IFij}^{s,Q} &= \alpha_{ij} \cdot l_{r,i}^{s,Q} + \beta_{ij} \cdot l_{r,j}^{s,Q} \\ &= \mu_r^{s,Q} \cdot x + dt_r - dt^{s,Q} + m^{s,Q} \cdot Z_r + \overline{N}_{r,IFij}^{s,Q} + \delta\varphi_{r,IFij} - \delta\varphi_{IFij}^{s,Q} + \xi_{r,IFij}^{s,Q} \end{cases} \tag{4}$$

where

$$\begin{cases} d_{r,IFij} &= \alpha_{ij} \cdot d_{r,i} + \beta_{ij} \cdot d_{r,j} \\ d_{IFij}^{s,Q} &= \alpha_{ij} \cdot d_i^{s,Q} + \beta_{ij} \cdot d_j^{s,Q} \\ \delta\varphi_{r,IFij} &= \alpha_{ij} \cdot \delta\varphi_{r,i} + \beta_{ij} \cdot \delta\varphi_{r,j} \\ \delta\varphi_{IFij}^{s,Q} &= \alpha_{ij} \cdot \delta\varphi_i^{s,Q} + \beta_{ij} \cdot \delta\varphi_j^{s,Q} \\ \overline{N}_{r,IFij}^{s,Q} &= \alpha_{ij} \cdot \overline{N}_{r,i}^{s,Q} + \beta_{ij} \cdot \overline{N}_{r,j}^{s,Q} \end{cases} \tag{5}$$

and $d_{r,IFij}$ and $d_{IFij}^{s,Q}$ are IF combinations of the code hardware bias of the receiver and satellite, respectively. Furthermore, $\delta\varphi_{r,IFij}$ and $\delta\varphi_{IFij}^{s,Q}$ are the IF combinations of the phase hardware bias time-varying part of the receiver and satellite, respectively. $\overline{N}_{r,IFij}^{s,Q}$ is the ambiguity IF combination.

The IF1213 observation equation is based on Equation (4), which consists of the IF12 and IF13 observation equations and can be expressed as follows:

$$\begin{cases} p_{r,IF12}^{s,Q} &= \mu_r^{s,Q} \cdot x + dt_r - dt^{s,Q} + m^{s,Q} \cdot Z_r + d_{r,IF12} - d_{IF12}^{s,Q} + \varepsilon_{r,IF12}^{s,Q} \\ l_{r,IF12}^{s,Q} &= \mu_r^{s,Q} \cdot x + dt_r - dt^{s,Q} + m^{s,Q} \cdot Z_r + \overline{N}_{r,IF12}^{s,Q} + \delta\varphi_{r,IF12} - \delta\varphi_{IF12}^{s,Q} + \xi_{r,IF12}^{s,Q} \\ p_{r,IF13}^{s,Q} &= \mu_r^{s,Q} \cdot x + dt_r - dt^{s,Q} + m^{s,Q} \cdot Z_r + d_{r,IF13} - d_{IF13}^{s,Q} + \varepsilon_{r,IF13}^{s,Q} \\ l_{r,IF13}^{s,Q} &= \mu_r^{s,Q} \cdot x + dt_r - dt^{s,Q} + m^{s,Q} \cdot Z_r + \overline{N}_{r,IF13}^{s,Q} + \delta\varphi_{r,IF13} - \delta\varphi_{IF13}^{s,Q} + \xi_{r,IF13}^{s,Q} \end{cases} \tag{6}$$

2.3. TF-C: IF1213 PPP Model with PIFCB Estimation

The TF-C model is an IF1213 PPP model that fully considers the time-varying part of the phase hardware bias of the receiver and satellite. The GNSS precise satellite clock products are based on the dual frequency IF combined code and phase observations solved for the first and second frequencies (e.g., GPS L1/L2 and BDS B1I/B3I) [33]. Thus, the precise satellite clock is a linear combination of the time-varying components of the dual-frequency code and phase hardware bias and is expressed as follows:

$$dt_{IF12}^{s,Q} = dt^{s,Q} + d_{IF12}^{s,Q} + \delta\varphi_{IF12}^{s,Q} \tag{7}$$

Combining Equation (6) with Equation (7) and considering the consistency of the receiver clock difference, the TF-C model can be deduced after correcting for the satellite clock difference

$$\begin{cases} p_{r,IF12}^{s,Q} &= \mu_r^{s,Q} \cdot x + d\bar{t}_r + m^{s,Q} \cdot Z_r + B_{12} + \varepsilon_{r,IF12}^{s,Q} \\ l_{r,IF12}^{s,Q} &= \mu_r^{s,Q} \cdot x + d\bar{t}_r + m^{s,Q} \cdot Z_r + \overline{N}_{r,IF12}^{s,Q} + \xi_{r,IF12}^{s,Q} \\ p_{r,IF13}^{s,Q} &= \mu_r^{s,Q} \cdot x + d\bar{t}_r + m^{s,Q} \cdot Z_r + IFCB_r^{s,Q} + B_{13} + \varepsilon_{r,IF13}^{s,Q} \\ l_{r,IF13}^{s,Q} &= \mu_r^{s,Q} \cdot x + d\bar{t}_r + m^{s,Q} \cdot Z_r - IFCB_r^{s,Q} + \overline{N}_{r,IF13}^{s,Q} + \xi_{r,IF13}^{s,Q} \end{cases} \tag{8}$$

where

$$\begin{cases} d\bar{t}_r &= dt_r + d_{r,IF12} + \delta\varphi_{r,IF12} \\ \overline{N}_{r,IFij}^{s,Q} &= \alpha_{ij} \cdot \overline{N}_{r,i}^{s,Q} + \beta_{ij} \cdot \overline{N}_{r,j}^{s,Q} + M_{1j} \\ B_{1j} &= \begin{cases} \beta_{12} \cdot DPB_{r,12}^{s,Q} - \delta\varphi_{r,1}^{s,Q}, & j = 2 \\ -\beta_{13} \cdot DPB_{r,13}^{s,Q} + 2 \cdot \beta_{12} \cdot DPB_{r,12}^{s,Q} - \delta\varphi_{r,1}^{s,Q}, & j = 3 \end{cases} \\ M_{1j} &= \begin{cases} \beta_{12} \cdot DCB_{r,12}^{s,Q} - d_{r,1}^{s,Q}, & j = 2 \\ -\beta_{13} \cdot DCB_{r,13}^{s,Q} + 2 \cdot \beta_{12} \cdot DCB_{r,12}^{s,Q} - d_{r,1}^{s,Q}, & j = 3 \end{cases} \\ CIFCB &= \beta_{12} \cdot DCB_{r,12}^{s,Q} - \beta_{13} \cdot DCB_{r,13}^{s,Q} \\ PIFCB &= \beta_{12} \cdot DPB_{r,12}^{s,Q} - \beta_{13} \cdot DPB_{r,13}^{s,Q} \\ IFCB_r^{s,Q} &= CIFCB - PIFCB \end{cases} \tag{9}$$

and $d\bar{t}_r$ and $\overline{N}_{r,IFij}^{s,Q}$ are the reparametrized receiver clock difference and ambiguity parameters, respectively. B_{1j} is the combined time-varying part of the receiver and satellite phase hardware bias, which can be absorbed by the code observation residuals, M_{1j} is the combined receiver and satellite code hardware bias, which is constant throughout the day and will be completely absorbed by the ambiguity. $IFCB_r^{s,Q}$ denotes IFCB, which consists mainly of CIFCB and PIFCB, corresponding to DCB synthesis and DPB synthesis for receivers and satellites, respectively. Additionally, the time-varying part of the hardware bias gives rise to PIFCB.

All the estimated parameters in TF-C PPP models include

$$X = [x \quad d\bar{t}_r \quad Z_r \quad IFCB_r^{s,Q} \quad \overline{N}_{r,IF12}^{s,Q} \quad \overline{N}_{r,IF13}^{s,Q}] \tag{10}$$

It is worth noting that the TF-C model does not need to be corrected by DCB, as the CIFCB in IFCB contains the DCB of the satellite and the receiver.

2.4. TF-F: IF1213 PPP Model Ignoring the PIFCB

The TF-F model is an IF1213 PPP model that disregards the time-varying part of the phase hardware bias of the receiver and satellite. The effect of the time-varying part of the phase hardware bias of the receiver can be ignored, owing to its small magnitude [34]. In this case, the precise satellite clock including only the satellite code hardware bias is expressed as follows:

$$dt_{IF12}^{s,Q} = dt^{s,Q} + d_{IF12}^{s,Q} \tag{11}$$

The code and phase hardware delay from the receiver and satellite were fully absorbed by the receiver clock, ionosphere, and ambiguity parameter [35]. Combining Equation (11) with Equation (6) and considering the consistency of the receiver clock difference, the TF-F model was derived by correcting the satellite DCB product $\widetilde{p}_{r,IF13}^{s,Q} = p_{r,IF13}^{s,Q} + \beta_{12} \cdot DCB_{12}^{s,Q} - \beta_{13} \cdot DCB_{13}^{s,Q}$ and then correcting the precise satellite clock product. TF-F is expressed as follows:

$$\begin{cases} p_{r,IF12}^{s,Q} = \mu_r^{s,Q} \cdot x + d\bar{t}_r + m^{s,Q} \cdot Z_r + \varepsilon_{r,IF12}^{s,Q} \\ l_{r,IF12}^{s,Q} = \mu_r^{s,Q} \cdot x + d\bar{t}_r + m^{s,Q} \cdot Z_r + \overline{\overline{N}}_{r,IF12}^{s,Q} + \xi_{r,IF12}^{s,Q} \\ \widetilde{p}_{r,IF13}^{s,Q} = \mu_r^{s,Q} \cdot x + d\bar{t}_r + m^{s,Q} \cdot Z_r + IFB_r + \varepsilon_{r,IF13}^{s,Q} \\ l_{r,IF13}^{s,Q} = \mu_r^{s,Q} \cdot x + d\bar{t}_r + m^{s,Q} \cdot Z_r + \overline{\overline{N}}_{r,IF13}^{s,Q} + \xi_{r,IF13}^{s,Q} \end{cases} \tag{12}$$

where

$$\begin{cases} IFB_r = \beta_{12} \cdot DCB_{r,12} - \beta_{13} \cdot DCB_{r,13} \\ \overline{\overline{N}}_{r,IF12}^{s,Q} = \overline{N}_{r,IF12}^{s,Q} + d_{IF12}^{s,Q} - d_{r,IF12} \\ \overline{\overline{N}}_{r,IF13}^{s,Q} = \overline{N}_{r,IF13}^{s,Q} + d_{IF12}^{s,Q} - d_{r,IF12} \end{cases} \tag{13}$$

and IFB_r is the inter-frequency bias (IFB) between IF12 and IF13. All the estimated parameters in the TF-F PPP models include the following:

$$X = [x \quad d\bar{t}_r \quad Z_r \quad IFB_r \quad \overline{\overline{N}}_{r,IF12}^{s,Q} \quad \overline{\overline{N}}_{r,IF13}^{s,Q}] \tag{14}$$

2.5. TF-CF: IF1213 PPP Model without the Full Estimation of PIFCB

The TF-CF model, which is an IF1213 PPP model applied to a dual-system, was constructed by considering that the time-varying part of the phase bias of the first system cannot be ignored and the second one can be ignored. For inter-system bias (ISB), other systems estimate the difference between the receiver clock of that system and the GPS receiver clock used as a reference [36]. The TF-CF model can be expressed as follows:

$$\begin{cases} p_{r,IF12}^{s,Q1} = \mu_r^{s,Q1} \cdot x + d\bar{t}_r + m^{s,Q1} \cdot Z_r + \varepsilon_{r,IF12}^{s,Q1} \\ l_{r,IF12}^{s,Q1} = \mu_r^{s,Q1} \cdot x + d\bar{t}_r + m^{s,Q1} \cdot Z_r + \overline{N}_{r,IF12}^{s,Q1} + \xi_{r,IF12}^{s,Q1} \\ p_{r,IF13}^{s,Q1} = \mu_r^{s,Q1} \cdot x + d\bar{t}_r + m^{s,Q1} \cdot Z_r + IFCB_r^{s,Q1} + \varepsilon_{r,IF13}^{s,Q1} \\ l_{r,IF13}^{s,Q1} = \mu_r^{s,Q1} \cdot x + d\bar{t}_r + m^{s,Q1} \cdot Z_r - IFCB_r^{s,Q1} + \overline{N}_{r,IF13}^{s,Q1} + \xi_{r,IF13}^{s,Q1} \\ p_{r,IF12}^{s,Q2} = \mu_r^{s,Q2} \cdot x + d\bar{t}_r + m^{s,Q2} \cdot Z_r + \varepsilon_{r,IF12}^{s,Q2} \\ l_{r,IF12}^{s,Q2} = \mu_r^{s,Q2} \cdot x + d\bar{t}_r + m^{s,Q2} \cdot Z_r + \overline{\overline{N}}_{r,IF12}^{s,Q2} + \xi_{r,IF12}^{s,Q2} \\ p_{r,IF13}^{s,Q2} = \mu_r^{s,Q2} \cdot x + d\bar{t}_r + m^{s,Q2} \cdot Z_r + IFB_r + \varepsilon_{r,IF13}^{s,Q2} \\ l_{r,IF13}^{s,Q2} = \mu_r^{s,Q2} \cdot x + d\bar{t}_r + m^{s,Q2} \cdot Z_r + \overline{\overline{N}}_{r,IF13}^{s,Q2} + \xi_{r,IF13}^{s,Q2} \end{cases} \tag{15}$$

All the estimated parameters in the TF-CF PPP models include the following:

$$X = [x \quad d\bar{t}_r \quad Z_r \quad IFCB_r^{s,Q1} \quad IFB_r \quad \overline{N}_{r,IF12}^{s,Q1} \quad \overline{N}_{r,IF13}^{s,Q1} \quad \overline{\overline{N}}_{r,IF12}^{s,Q2} \quad \overline{\overline{N}}_{r,IF13}^{s,Q2}] \tag{16}$$

2.6. TF-FP: IF1213 PPP Model with IGMAS Product Correction

The TF-FP model, which is an IF1213 PPP model, can be applied to IGMAS PIFCB product correction. In this case, the time-varying part of the phase hardware bias of the receiver is ignored, and the satellite part is not. The precise satellite clock is the same as in Equation (7). Combining Equation (7) with Equation (6) corrects the satellite DCB product and the precise satellite clock. The TF-FP is expressed as follows:

$$\begin{cases} p_{r,IF12}^{s,Q} = \mu_r^{s,Q} \cdot x + d\bar{t}_r + m^{s,Q} \cdot Z_r + \varepsilon_{r,IF12}^{s,Q} \\ l_{r,IF12}^{s,Q} = \mu_r^{s,Q} \cdot x + d\bar{t}_r + m^{s,Q} \cdot Z_r + \overline{\overline{N}}_{r,IF12}^{s,Q} + \xi_{r,IF12}^{s,Q} \\ \widetilde{p}_{r,IF13}^{s,Q} = \mu_r^{s,Q} \cdot x + d\bar{t}_r + m^{s,Q} \cdot Z_r + IFB_r + \varepsilon_{r,IF13}^{s,Q} \\ l_{r,IF13}^{s,Q} = \mu_r^{s,Q} \cdot x + d\bar{t}_r + m^{s,Q} \cdot Z_r - pifcb_{r,IF13}^{s,Q} + \overline{\overline{N}}_{r,IF13}^{s,Q} + \xi_{r,IF13}^{s,Q} \end{cases} \tag{17}$$

where $pifcb_{r,IF13}^{s,Q} = \delta\varphi_{r,IF12} - \delta\varphi_{IF12}^{s,Q} - \delta\varphi_{r,IF13} + \delta\varphi_{IF13}^{s,Q}$ is the content of the IGMAS PIFCB product. Other parameters are the same as described above. After correction by IGMAS PIFCB products, Equation (17) is the same as Equation (12) in GPS.

2.7. Relationships in the IF1213 PPP Models

Both the TF-C and TF-F models are derived on the basis of the IF1213 observation model. The TF-CF model is derived from the TF-C and TF-F models. The TF-C model is applied to GNSS with the time-varying part of the phase hardware bias of the satellite, but the TF-F model is not. The TF-C model parameterizes the part of the receiver and the satellite named PIFCB, as well as the code hardware delays of the receiver and the satellite named CIFCB, which contains the components of IFB. The TF-F model is applied to GNSS without the satellite PIFCB and ignores the effect of the receiver PIFCB. The TF-CF model is applied to a dual system, the first with satellite PIFCB and the second without it. The TF-FP model is applied to GPS, which corrects the $pifcb_{r,IF13}^{s,Q}$ in the TF-FP model by means of the IGMAS product. After the correction of the $pifcb_{r,IF13}^{s,Q}$, it is consistent with the TF-F model.

The three IF1213 PPP models have different parameters to estimate. The TF-C model needs to estimate the IFCB parameters, the TF-F model needs to estimate the IFB parameters, and the TF-CF model needs to estimate both of them. In addition, the three models do not have exactly the same ambiguity parameters to be estimated. The TF-C model does not require the DCB product and IFCB product to correct the corresponding deviation terms. However, an increase in the number of parameters to be estimated may increase the convergence time.

3. Results and Discussion

3.1. Data Processing Strategies

This study used 60 stations provided by the MGEX of the IGS organization and the observation data with a 30 s sample interval for a week-long period of day of the year (DOY) 121–127, 2022. Figure 1 shows the geographical distribution of the selected stations. Table 2 shows the GPS and BDS satellites that can broadcast triple-frequency observations, including some GPS satellites and all BDS satellites, except for the experimental satellites.

Table 2. BDS/GPS satellites transmitting triple frequency signals.

System	PRN	Orbit Type
GPS	G01, G03, G04, G06, G08, G09, G10, G14, G18, G23, G24, G25, G26, G27, G30, G32.	Medium Earth Orbit (MEO)
BDS-2	C01, C02, C03, C04, C05;	Geostationary Earth Orbit (GEO)
	C06, C07, C08, C09, C10, C13, C16;	Inclined Geo-Synchronous Orbit (IGSO)
	C11, C12, C14;	MEO
BDS-3	C19, C20, C21, C22, C23, C24, C25, C26, C27, C28, C29, C30, C32, C33, C34, C35, C36, C37, C41, C42, C43, C44, C45, C46;	MEO
	C38, C39, C40.	IGSO

Table 3 provides an in-depth summary of the processing strategy of IF1213 PPP models, including the DF PPP model. In static PPP, if the east (E) and north (N) directions are less than 5 cm and the upwards (U) direction is less than 10 cm at the current epoch and the following 20 epochs, the positioning error satisfies convergence. In the kinematic PPP, the E and N directions are less than 10 cm, and the U direction is less than 20 cm. The time taken to reach the first epoch that satisfies the convergence condition is defined as the convergence time.

Table 3. Data-processing strategies.

Items	Strategy
Model	DF, TF-C, TF-F, TF-CF, TF-FP(GPS)
Satellite elevation mask	15°
Estimator	Kalman filter
Weighting scheme	Elevation-dependent weight; 0.003 m and 0.3 m for raw phase and code, respectively
PCO/PCV	igs14_2196.atx according to Schmid et al. [37]
Phase windup	Corrected [38]
Satellite DCB corrections	Corrected with MGEX DCB products except TF-C model
Satellite orbit and clock	Products from WUM
Tropospheric delay	Zenith Hydrostatic Delays (ZHD) are corrected using the Saastamoinen model, and Zenith Wet Delays (ZWD) are estimated using random walk [39]
Tide effect	Solid Earth, pole and ocean tide [40]
Relativistic effect	Corrected [41]
Station coordinates	Static: estimated using constants; kinematic: estimated using white noise process
Receiver clock	Estimated using white noises
Receiver inter-frequency bias	Estimated using random walk
Inter-frequency clock bias	Estimated using random walk
Ambiguity	Estimated using a constant

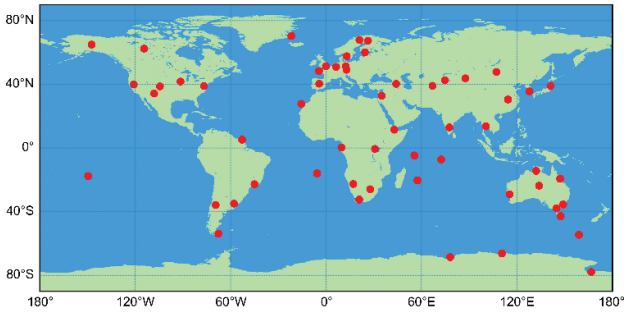

Figure 1. Geographical distribution of the 60 selected MGEX stations.

3.2. Influence of the Satellite PIFCB

In this section, static experiments using single GPS and BDS data with the TF-C, TF-F, and TF-CF models to carry out a comparison with the dual-frequency IF combination PPP model (DF) of the first and second frequency are described. The main validations are the reliability of the models, the influence of the GPS satellite PIFCB and the influence of the BDS-2 PIFCB in BDS.

3.2.1. Influence of the GPS PIFCB

GPS satellites have significant time-varying characteristics of phase hardware bias [14,42]. This section describes the four GPS static PPP models for positioning. Figure 2 shows the static positioning error curves of the stations KOUR and WIND on DOY127. It is observed that the TF-F models perform slightly worse in the convergence process, compared to the other triple-frequency PPP models. After convergence, the positioning error curves of the positioning error curves of the three PPP models, except for the TF-F model, largely overlap. For the PIFCB values throughout the day, the PIFCB estimated by the TF-C model was output, and Figure 3 shows the PIFCB values observed by the KOUR station on DOY121–127, where each color represents a GPS triple-frequency satellite. It is observed that the PIFCB values can reach the decimeter level [43]. Additionally, there are clear time-varying features within each day.

A boxplot of the distribution of positioning accuracy and convergence time for the 60 selected stations for different static PPP models within DOY121–127 is shown in Figure 4. In the boxplot, the upper and lower edge line distributions represent the 99% and 0% quantiles, and the upper and lower end lines of the rectangular box represent the 75% and 25% quantiles, respectively. The inner lines of the rectangular box represent the 50% quantile. The median positioning accuracy and convergence times, representing the positioning performance of this model, are presented in Table 4. From Figure 4, ignoring the GPS PIFCB has a greater impact on the positioning accuracy, and the TF-F and TF-FP models take longer to converge. The TF-FP model has a long convergence time, probably due to the number of stations used by the IGMAS product and the fact that the stations are not exactly the same as in the experiments. The reason for the long convergence time of the TF-F model is that the GPS PIFCB cannot be neglected and also proves that the TF-F model is not applicable to the GPS PPP. As shown in Table 4, the convergence accuracies of DF and TF-C are similar: better than 1.0 cm in the E and U directions and better than 1.5 cm in the U direction. The convergence accuracy of the TF-FP model is slightly worse than that of the TF-C model and better than that of the TF-F model. The convergence time of the TF-FP model is significantly worse than that of the DF and TF-C models.

The PPP convergence accuracy of the DF and TF-C models is largely consistent. This demonstrates that a reliable convergence accuracy can be obtained when the TF-C model is applied to GPS PPP as demonstrated by the PPP results of the TF-FP model. The average convergence time is 20.39 min for the DF model and 24.38 min for the TF-C model, which is consistent with previous studies [43]. This phenomenon prolongs the convergence

time, due to the higher number of parameters to be estimated in the TF-C model and fewer degrees of freedom in the observation equation. The inclusion of triple frequency observations did not improve the convergence accuracy, which is consistent with previous studies [3]. However, its increased convergence time may be due to the increase in the number of parameters to be estimated.

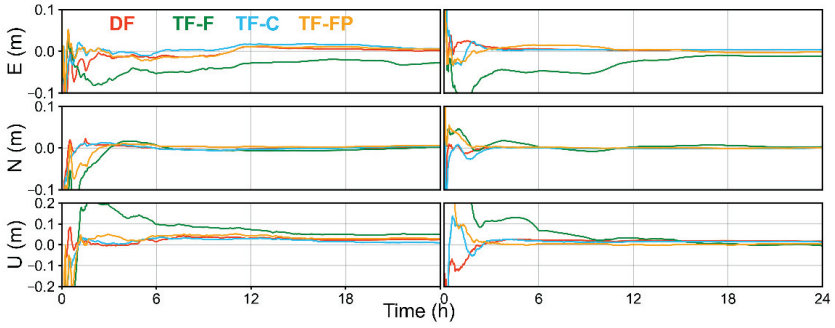

(**a**) (**b**)

Figure 2. Positioning error of the four GPS static PPP models (DOY127, 2022). The stations are (**a**) KOUR and (**b**) WIND, respectively.

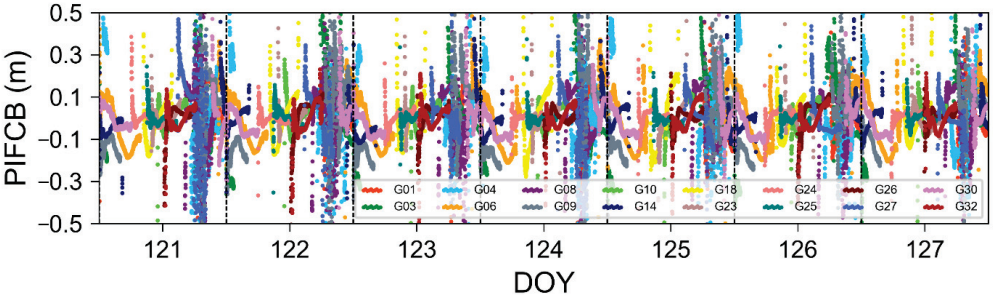

Figure 3. Variation in the PIFCB values from the GPS satellites at the KOUR station.

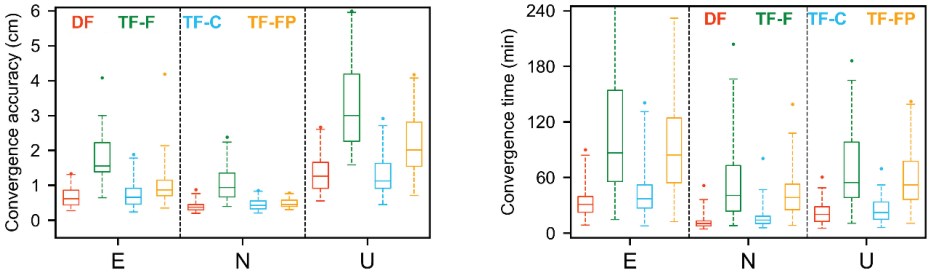

(**a**) (**b**)

Figure 4. Positioning accuracy and convergence time distribution of the four GPS static PPP models. (**a**) Convergence accuracy. (**b**) Convergence time.

Table 4. Statistics on the positioning results of the four GPS static PPP models.

Model	Convergence Accuracy (CM)			Convergence Time (Min)		
	E	N	U	E	N	U
DF	0.61	0.37	1.26	30.86	10.17	20.14
TF-F	1.56	0.94	3.00	86.36	40.64	54.43
TF-C	0.66	0.42	1.12	36.93	14.00	22.21
TF-FP	0.86	0.45	2.01	84.25	38.21	51.79

3.2.2. Influence of the BDS-2 PIFCB in BDS

BDS-2 satellites have time-varying characteristics of phase hardware bias [19]. However, this section demonstrates that the influence of BDS-2 PIFCB can be ignored when BDS-2 and BDS-3 are used as BDS. The TF-CF model is shown in Table 3 with BDS-2 as the first system and BDS-3 as the second system.

This section describes four BDS static PPP models for positioning. Figure 5 shows the static positioning error curves of stations SUTH and ULAB on DOY127. It is observed that the positioning error curves of the four PPP models largely overlap after convergence. A boxplot of the distribution of positioning accuracy and convergence time for the 60 selected stations for different static PPP models within DOY121–127 is shown in Figure 6. The median positioning accuracy and convergence times, representing the positioning performance of this model, are presented in Table 5. From Figure 6, the positioning performance of the four PPP models is similar. From Table 5, the accuracy of the four static PPP models after convergence is better than 1.0 cm in the horizontal direction and 1.5 cm in the elevation direction. The convergence accuracy of the TF-F, TF-C and TF-CF models deviates from 0.05 cm, and the convergence time deviates from 2 min. The experimental results demonstrate that the influence of BDS-2 PIFCB is negligible when BDS-2 and BDS-3 are used as the BDS.

Table 5. Statistics on the positioning results of the four BDS static PPP models.

Model	Convergence Accuracy (CM)			Convergence Time (Min)		
	E	N	U	E	N	U
DF	0.74	0.46	1.31	51.64	29.57	33.64
TF-F	0.93	0.54	1.46	47.59	21.69	30.36
TF-C	0.96	0.56	1.46	46.14	21.00	28.29
TF-CF	0.98	0.53	1.44	47.89	22.75	29.96

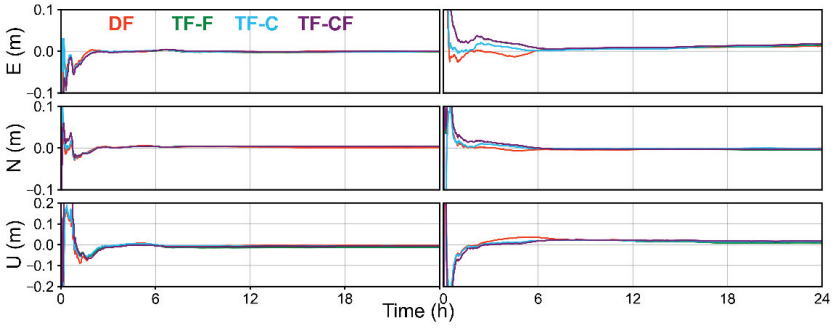

Figure 5. Positioning error of the four BDS static PPP models (DOY127, 2022). The stations are (**a**) SUTH and (**b**) ULAB, respectively.

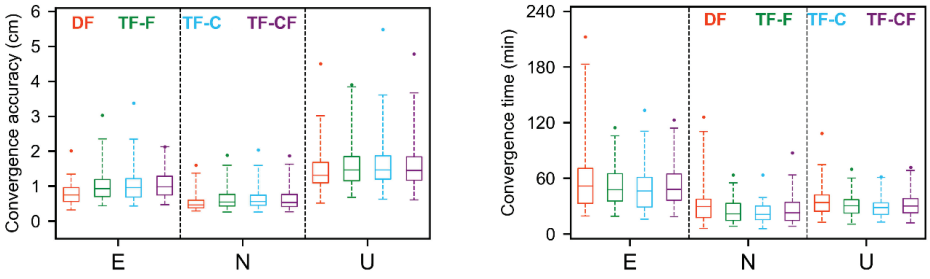

(**a**) (**b**)

Figure 6. Positioning accuracy and convergence time distribution of the four BDS static PPP models. (**a**) Convergence accuracy. (**b**) Convergence time.

3.3. BDS/GPS PPP Performance

This section describes the BDS/GPS dual-system experiment with the same data sources as described in Section 3.1. The PPP models are the DF, TF-F, TF-C and TF-CF models. In the TF-CF model, the GPS is the first system, and the BDS is the second system. The other data-processing strategies are consistent with those given in Table 3.

3.3.1. Static Mode

This section gives four BDS/GPS static PPP models for positioning. Figure 7 shows the static positioning error curves of stations CUSV, DGAR, GAMG, MIZU, SEYG and MOBS on DOY121. The positioning accuracy of the TF-F model for the CUSV and DGAR stations is less than their median, while it is greater than their median for the GAMG, MIZU, SEYG and MOBS stations. It can be observed that the DF and TF-F models perform slightly worse in the convergence process compared to the other three frequency models. After convergence in the E, N and U directions, the positioning error curves of the four PPP models basically coincide.

Figure 8 shows that, except for the TF-F model, the positioning accuracy of the stations does not improve significantly with the addition of the third frequency [34], but the convergence time is slightly reduced. Table 6 demonstrates that the positioning accuracy is better than 1.0 cm, except for the TF-F model's U direction, and better than 1.5 cm for the TF-F model's U direction. In terms of convergence time, the convergence time of the TF-CF model is improved by 18.1%, 9.7% and 12.1% in the E, N and U directions, respectively. The convergence time of TF-C model is the shortest among the triple-frequency PPP models. It is 28.43, 11.61 and 16.68 min in the E, N and U directions with improvements of 23.5%, 13.6% and 19.8%, respectively.

In contrast to the experiment above, in the dual-system static PPP experiment, ignoring the GPS PIFCB had a slight effect on the PPP results; this is because the BDS plays a major role in the PPP process, as the BDS can ignore the PIFCB [43].

Table 6. Statistics on the positioning results of the four BDS/GPS static PPP models.

Model	Convergence Accuracy (CM)			Convergence Time (Min)		
	E	N	U	E	N	U
DF	0.56	0.38	1.00	37.18	13.43	20.80
TF-F	0.81	0.49	1.39	35.18	15.04	19.54
TF-C	0.54	0.39	0.93	28.43	11.61	16.68
TF-CF	0.56	0.39	0.93	30.46	12.12	18.29

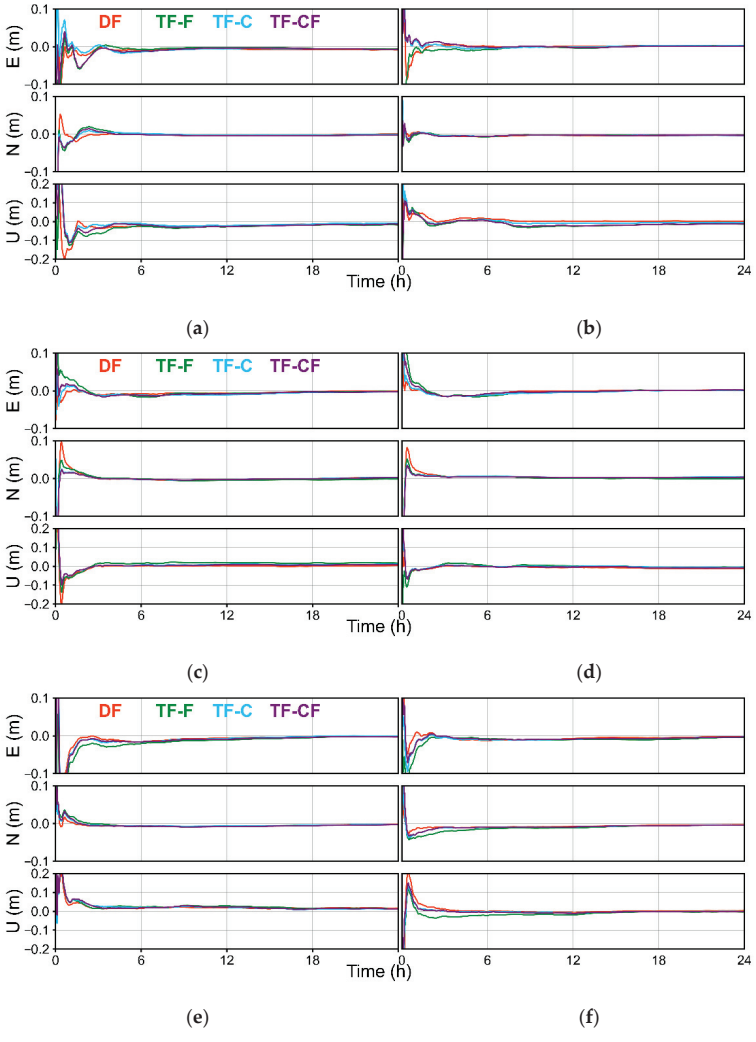

Figure 7. Positioning error of the four BDS/GPS static PPP models (DOY121, 2022). The stations are (**a**) CUSV, (**b**) DGAR, (**c**) GAMG, (**d**) MIZU (**e**) SEYG and (**f**) MOBS, respectively.

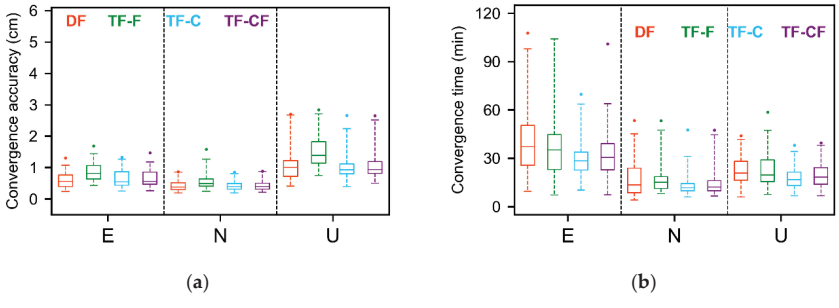

Figure 8. Positioning accuracy and convergence time distribution of the four BDS/GPS static PPP models. (**a**) Convergence accuracy. (**b**) Convergence time.

3.3.2. Kinematic Mode

This section describes four BDS/GPS kinematic PPP models for positioning. In Figure 9, the kinematic PPP results differ from the BDS/GPS static PPP results. Ignoring the GPS PIFCB significantly affects the convergence time. Additionally, the triple-frequency PPP models in addition to the TF-F model make the convergence much faster than the DF PPP model.

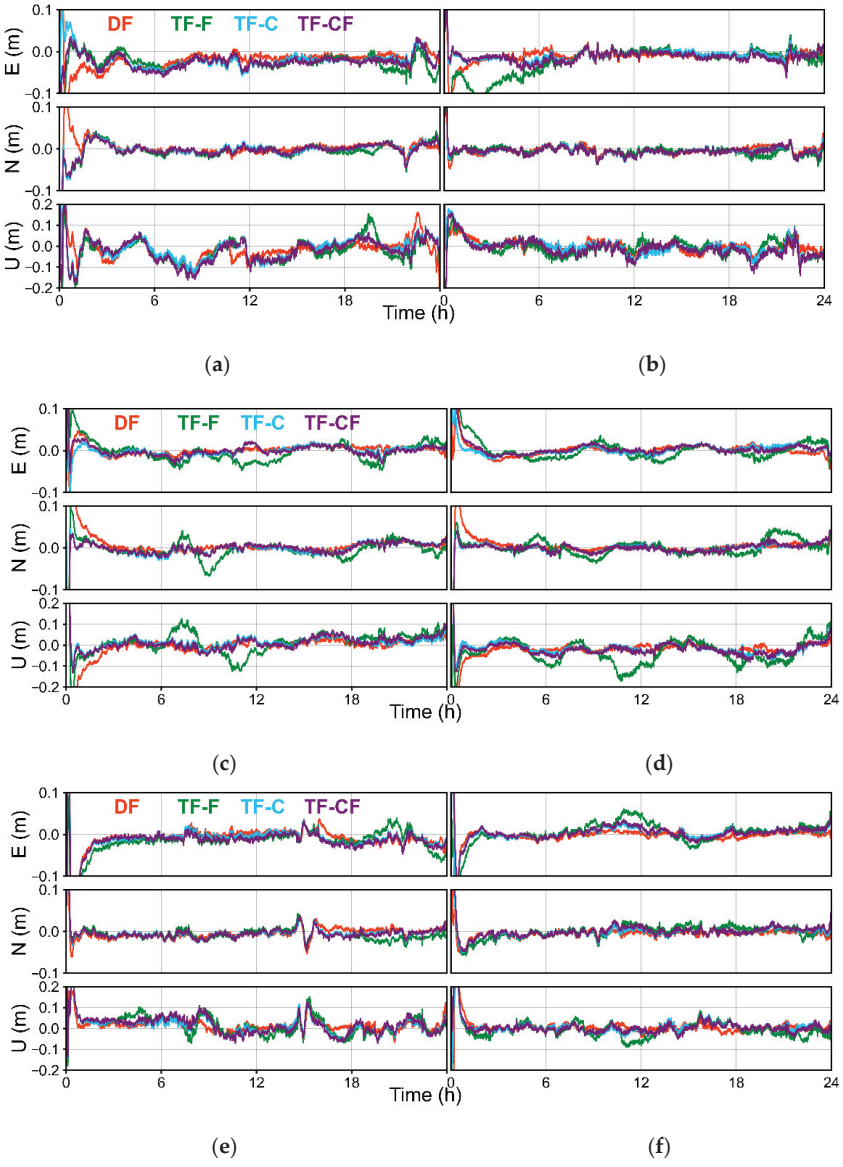

Figure 9. Positioning error of the four BDS/GPS kinematic PPP models (DOY121, 2022). The stations are (**a**) CUSV, (**b**) DGAR, (**c**) GAMG, (**d**) MIZU, (**e**) SEYG and (**f**) MOBS, respectively.

Figure 10 and Table 7 show that the positioning performance of the models is similar, except for the TF-F model, where the horizontal positioning accuracy is better than 2.0 cm and the U-direction accuracy is better than 4.0 cm. In terms of convergence time, the TF-C

model is improved by 46.2%, 33.5% and 35.1% in the E, N and U directions, respectively, and the TF-CF model is improved by 49.6%, 32.4% and 36.1%, respectively.

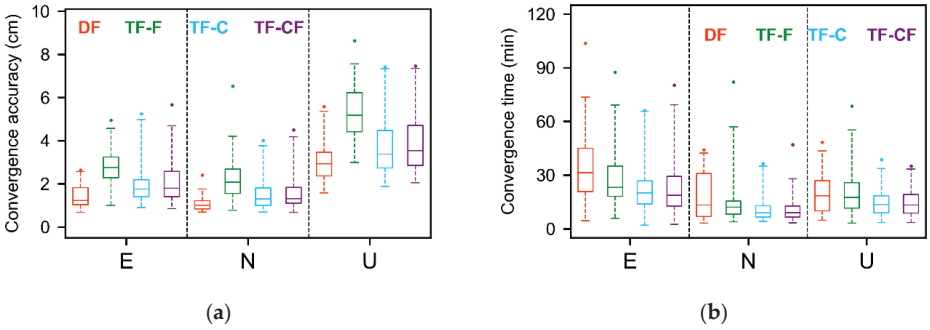

Figure 10. Positioning accuracy and convergence time distribution of the four BDS/GPS kinematic PPP models. (**a**) Convergence accuracy. (**b**) Convergence time.

Table 7. Statistics on the positioning results of the four BDS/GPS kinematic PPP models.

Model	Convergence Accuracy (CM)			Convergence Time (Min)		
	E	N	U	E	N	U
DF	1.23	1.01	2.93	31.24	13.33	18.39
TF-F	2.75	2.08	5.17	23.07	12.13	17.47
TF-C	1.75	1.29	3.37	20.02	8.93	13.50
TF-CF	1.79	1.31	3.53	18.74	9.08	13.29

4. Conclusions

This study focuses on the precision modeling of the dual-system triple-frequency IF1213 PPP based on BDS/GPS triple-frequency observations. The TF-C model is able to estimate the IFCB. This was deduced by considering the time-varying part of the phase hardware bias of the receiver and satellite. The TF-CF model is able to estimate the IFCB of the first GNSS. This was deduced by considering that the time-varying part of the phase bias of the receiver and the satellite in the first system, and the second one can be ignored. The advantage of the TF-C model is that it does not require the DCB product and IFCB product to correct the corresponding deviation terms. The disadvantage is that it has a large number of parameters to be estimated, which can reduce the degrees of freedom of the observation equation and lead to an increased convergence time when applied to GPS. The reliability of the deduced models was demonstrated using static PPP experiments for a single system. GPS PPP experiments demonstrated the reliability of the models, except for the TF-CF model, and the fact that GPS PIFCB has a bad influence on the GPS PPP. The BDS PPP experiments demonstrated the reliability of the TF-CF model and the negligible effect of the BDS-2 PIFCB when BDS-2 and BDS-3 are used as the BDS.

Using one week of observation from 60 stations provided by the MGEX of the IGS organization, we conducted a BDS/GPS dual-system static and kinematic experiment. The results show that the GPS PIFCB had less of an influence in the static experiment, while the influence was greater in the kinematic experiment. The performance of the DF, TF-C and TF-CF models is similar; the positioning accuracy is better than 1.0 cm in the three directions in the static experiment, and in the kinematic experiment, the horizontal positioning accuracy is better than 2.0 cm, while the U directional positioning accuracy is better than 4.0 cm. The addition of third-frequency data does not significantly improve the positioning accuracy [34], but the convergence time is reduced. Compared with the DF model, the TF-C model improves the convergence time by approximately 23.5%, 13.6% and 19.8% in the E, N and U directions, respectively, and the TF-CF model improves

by approximately 18.1%, 9.7% and 12.1%, respectively, in the static experiment. In the kinematic experiment, the TF-C model improves by approximately 46.2%, 33.5% and 35.1% in the E, N and U directions, respectively, and the TF-CF model improves by approximately 49.6%, 32.4% and 36.1%, respectively. The positioning performance of the TF-C model is slightly better than that of the TF-CF model, probably because the IFCB parameters in the TF-C model can absorb the residuals. However, one should be aware that the positioning performance of IF1213 PPP models is limited due to the limitations of the float ambiguity solution. Therefore, we will focus on finding a multi-frequency solution to integer ambiguity in the future.

For dual-system PPP based on BDS/GPS observations, the TF-C model is the most rigorous; therefore, the TF-C model is recommended.

Author Contributions: Conceptualization, Z.W. and R.W.; methodology, R.W.; software, R.W.; validation, Z.W., R.W. and Y.W.; formal analysis, R.W.; investigation, Z.W. and Y.W.; resources, Z.W. and C.H.; data curation, C.H. and B.L.; writing—original draft preparation, R.W.; writing—review and editing, Z.W., R.W., Y.W., C.H. and B.L.; visualization, R.W.; supervision, Z.W. and C.H.; project administration, Z.W. and Y.W.; funding acquisition, Z.W. All authors have read and agreed to the published version of the manuscript.

Funding: This research was funded by Natural Science Foundation of Jiangsu Province, No. BK20181361; Natural Science Foundation of Jiangsu Province, No. BK20191342, the Natural Science Foundation of Anhui Colleges (Grant No. KJ2020A0310) and Anhui Natural Science Foundation (Grant No. 2108085QD173).

Data Availability Statement: The observation data and precise products used in the research are available on the FTP of Wuhan University (ftp://igs.gnsswhu.cn/pub/, accessed on 20 May 2022). The GPS satellite PIFCB products were obtained from iGMAS Innovation Application Center (http://igmas.users.sgg.whu.edu.cn/products/download/directory/products/upd/2022/, accessed on 20 May 2022).

Acknowledgments: The authors gratefully acknowledge WUM for providing the observation data, the precise products and iGMAS Innovation Application Center for providing GPS satellite PIFCB products.

Conflicts of Interest: The authors declare no conflict of interest.

References

1. Zumberge, J.F.; Heflin, M.B.; Jefferson, D.C.; Watkins, M.M.; Webb, F.H. Precise point positioning for the efficient and robust analysis of GPS data from large networks. *J. Geophys. Res. Solid Earth* **1997**, *102*, 5005–5017. [CrossRef]
2. Malys, S.; Jensen, P.A. Geodetic point positioning with GPS carrier beat phase data from the CASA UNO Experiment. *Geophys. Res. Lett.* **1990**, *17*, 651–654. [CrossRef]
3. Deo, M.; El-Mowafy, A. Triple-frequency GNSS models for PPP with float ambiguity estimation: Performance comparison using GPS. *Surv. Rev.* **2018**, *50*, 249–261. [CrossRef]
4. Xiao, G.R.; Li, P.; Gao, Y.; Heck, B. A Unified Model for Multi-Frequency PPP Ambiguity Resolution and Test Results with Galileo and BeiDou Triple-Frequency Observations. *Remote Sens.* **2019**, *11*, 116. [CrossRef]
5. Liu, G.; Guo, F.; Wang, J.; Du, M.Y.; Qu, L.Z. Triple-Frequency GPS Un-Differenced and Uncombined PPP Ambiguity Resolution Using Observable-Specific Satellite Signal Biases. *Remote Sens.* **2020**, *12*, 2310. [CrossRef]
6. Naciri, N.; Bisnath, S. An uncombined triple-frequency user implementation of the decoupled clock model for PPP-AR. *J. Geod.* **2021**, *95*, 1–17. [CrossRef]
7. Tsai, Y.-H.; Yang, W.-C.; Chang, F.-R.; Ma, C.-L. Using multi-frequency for GPS positioning and receiver autonomous integrity monitoring. In Proceedings of the 2004 IEEE International Conference on Control Applications, Taipei, Taiwan, 2–4 September 2004; pp. 205–210.
8. Zhao, Q.L.; Sun, B.Z.; Dai, Z.Q.; Hu, Z.G.; Shi, C.; Liu, J.N. Real-time detection and repair of cycle slips in triple-frequency GNSS measurements. *GPS Solut.* **2015**, *19*, 381–391. [CrossRef]
9. Gu, X.Y.; Zhu, B.C. Detection and Correction of Cycle Slip in Triple-Frequency GNSS Positioning. *IEEE Access* **2017**, *5*, 12584–12595. [CrossRef]
10. Li, P.; Jiang, X.; Zhang, X.; Ge, M.; Schuh, H. GPS + Galileo + BeiDou precise point positioning with triple-frequency ambiguity resolution. *GPS Solut.* **2020**, *24*, 78. [CrossRef]
11. Spits, J.; Warnant, R. Total electron content monitoring using triple frequency GNSS data: A three-step approach. *J. Atmos. Sol. Terr. Phys.* **2008**, *70*, 1885–1893. [CrossRef]
12. Montenbruck, O.; Hauschild, A.; Steigenberger, P.; Langley, R. Three's the challenge: A close look at GPS SVN62 triple-frequency signal combinations finds carrier-phase variations on the new L5. *GPS World* **2010**, *21*, 8–19.

13. Montenbruck, O.; Hugentobler, U.; Dach, R.; Steigenberger, P.; Hauschild, A. Apparent clock variations of the Block IIF-1 (SVN62) GPS satellite. *GPS Solut.* **2012**, *16*, 303–313. [CrossRef]
14. Pan, L.; Zhang, X.; Guo, F.; Liu, J. GPS inter-frequency clock bias estimation for both uncombined and ionospheric-free combined triple-frequency precise point positioning. *J. Geod.* **2019**, *93*, 473–487. [CrossRef]
15. Steigenberger, P.; Hauschild, A.; Montenbruck, O.; Rodriguez-Solano, C.; Hugentobler, U. Orbit and Clock Determination of QZS-1 Based on the CONGO Network. *Navigation* **2013**, *60*, 31–40. [CrossRef]
16. Cai, C.S.; He, C.; Santerre, R.; Pan, L.; Cui, X.Q.; Zhu, J.J. A comparative analysis of measurement noise and multipath for four constellations: GPS, BeiDou, GLONASS and Galileo. *Surv. Rev.* **2016**, *48*, 287–295. [CrossRef]
17. Montenbruck, O.; Hauschild, A.; Steigenberger, P.; Hugentobler, U.; Teunissen, P.; Nakamura, S. Initial assessment of the COMPASS/BeiDou-2 regional navigation satellite system. *GPS Solut.* **2013**, *17*, 211–222. [CrossRef]
18. Zhao, Q.; Wang, G.X.; Liu, Z.Z.; Hu, Z.G.; Dai, Z.Q.; Liu, J.N. Analysis of BeiDou Satellite Measurements with Code Multipath and Geometry-Free Ionosphere-Free Combinations. *Sensors* **2016**, *16*, 123. [CrossRef]
19. Fan, L.; Wang, C.; Guo, S.; Fang, X.; Jing, G.; Shi, C. GNSS satellite inter-frequency clock bias estimation and correction based on IGS clock datum: A unified model and result validation using BDS-2 and BDS-3 multi-frequency data. *J. Geod.* **2021**, *95*, 135. [CrossRef]
20. Gong, X.; Gu, S.; Lou, Y.; Zheng, F.; Yang, X.; Wang, Z.; Liu, J. Research on empirical correction models of GPS Block IIF and BDS satellite inter-frequency clock bias. *J. Geod.* **2020**, *94*, 36. [CrossRef]
21. Pan, L.; Zhang, X.H.; Li, X.X.; Liu, J.N.; Li, X. Characteristics of inter-frequency clock bias for Block IIF satellites and its effect on triple-frequency GPS precise point positioning. *GPS Solut.* **2017**, *21*, 811–822. [CrossRef]
22. Lu, X.F.; Zhang, S.L.; Bao, Y.C. A New Method of Ambiguity Resolution for Triple-Frequency GPS PPP. *ITM Web Conf.* **2016**, *7*, 01010. [CrossRef]
23. Guo, F.; Zhang, X.H.; Wang, J.L.; Ren, X.D. Modeling and assessment of triple-frequency BDS precise point positioning. *J. Geod.* **2016**, *90*, 1223–1235. [CrossRef]
24. Pan, L.; Zhang, X.H.; Liu, J.N. A comparison of three widely used GPS triple-frequency precise point positioning models. *GPS Solut.* **2019**, *23*, 1–13. [CrossRef]
25. Cai, C.S.; Gao, Y.; Pan, L.; Zhu, J.J. Precise point positioning with quad-constellations: GPS, BeiDou, GLONASS and Galileo. *Adv. Space Res.* **2015**, *56*, 133–143. [CrossRef]
26. Ren, X.D.; Zhang, X.H.; Xie, W.L.; Zhang, K.K.; Yuan, Y.Q.; Li, X.X. Global Ionospheric Modelling using Multi-GNSS: BeiDou, Galileo, GLONASS and GPS. *Sci. Rep.* **2016**, *6*, 1–11. [CrossRef]
27. Gao, X.; Dai, W.J.; Song, Z.Y.; Cai, C.S. Reference satellite selection method for GNSS high-precision relative positioning. *Geod. Geodyn.* **2017**, *8*, 125–129. [CrossRef]
28. Pan, L.; Zhang, X.H.; Liu, J.N.; Li, X.X.; Li, X. Performance Evaluation of Single-frequency Precise Point Positioning with GPS, GLONASS, BeiDou and Galileo. *J. Navig.* **2017**, *70*, 465–482. [CrossRef]
29. Li, X.X.; Li, X.; Liu, G.G.; Feng, G.L.; Yuan, Y.Q.; Zhang, K.K.; Ren, X.D. Triple-frequency PPP ambiguity resolution with multi-constellation GNSS: BDS and Galileo. *J. Geod.* **2019**, *93*, 1105–1122. [CrossRef]
30. Hu, C. *An Investigation of Key Technologies Related to Combining BDS-2 and BDS-3 Observations in Data Processing*; China University of Mining and Technology: Xuzhou, China, 2020.
31. Leick, A.; Rapoport, L.; Tatarnikov, D. *GPS Satellite Surveying*, 1st ed.; John Wiley & Sons, Ltd.: Hoboken, NJ, USA, 2015.
32. Liu, T.; Zhang, B.; Yuan, Y.; Li, Z.; Wang, N. Multi-GNSS triple-frequency differential code bias (DCB) determination with precise point positioning (PPP). *J. Geod.* **2019**, *93*, 765–784. [CrossRef]
33. Chen, L.; Li, M.; Zhao, Y.; Hu, Z.; Zheng, F.; Shi, C. Multi-GNSS real-time precise clock estimation considering the correction of inter-satellite code biases. *GPS Solut.* **2021**, *25*, 32. [CrossRef]
34. Zhou, F.; Xu, T. Modeling and assessment of GPS/BDS/Galileo treple-frequency precise point positioning. *Acta Geod. Cartogr. Sin.* **2021**, *50*, 61–70.
35. Li, P.; Zhang, X.H.; Ge, M.R.; Schuh, H. Three-frequency BDS precise point positioning ambiguity resolution based on raw observables. *J. Geod.* **2018**, *92*, 1357–1369. [CrossRef]
36. Zhou, F.; Dong, D.; Li, P.; Li, X.; Schuh, H. Influence of stochastic modeling for inter-system biases on multi-GNSS undifferenced and uncombined precise point positioning. *GPS Solut.* **2019**, *23*, 59. [CrossRef]
37. Schmid, R.; Steigenberger, P.; Gendt, G.; Ge, M.; Rothacher, M. Generation of a consistent absolute phase-center correction model for GPS receiver and satellite antennas. *J. Geod.* **2007**, *81*, 781–798. [CrossRef]
38. Wu, J.-T.; Wu, S.-C.; Hajj, G.; Bertiger, W.; Lichten, S.M. Effects of antenna orientation on GPS carrier phase. *Astrodynamics 1991* **1992**, 91–98.
39. Saastamoinen, J. Contributions to the theory of atmospheric refraction. *Bulletin Géodésique (1946–1975)* **1973**, *107*, 13–34. [CrossRef]
40. Petit, G.; Luzum, B.; Conventions, I. *IERS Conventions (2010)*; Bundesamts für Kartographie und Geodäsie: Frankfurt am Main, Germany, 2010.
41. Ashby, N. Relativity in the Global Positioning System. *Living Rev. Relativ.* **2003**, *6*, 1. [CrossRef] [PubMed]

42. Fan, L.; Shi, C.; Li, M.; Wang, C.; Zheng, F.; Jing, G.; Zhang, J. GPS satellite inter-frequency clock bias estimation using triple-frequency raw observations. *J. Geod.* **2019**, *93*, 2465–2479. [CrossRef]
43. Chen, Y.; Mi, J.; Gu, S.; Li, B.; Li, H.; Yang, L.; Pang, Y. GPS, BDS-3, and Galileo Inter-Frequency Clock Bias Deviation Time-Varying Characteristics and Positioning Performance Analysis. *Remote Sens.* **2022**, *14*, 3991. [CrossRef]

remote sensing

MDPI

Review

A Review on Multi-GNSS for Earth Observation and Emerging Applications

Shuanggen Jin [1,2], Qisheng Wang [3] and Gino Dardanelli [4,*]

[1] School of Surveying and Land Information Engineering, Henan Polytechnic University, Jiaozuo 454000, China
[2] Shanghai Astronomical Observatory, Chinese Academy of Sciences, Shanghai 200030, China
[3] College of Civil Engineering, Xiangtan University, Xiangtan 411105, China
[4] Department of Engineering, University of Palermo, Viale delle Scienze, 90128 Palermo, Italy
* Correspondence: gino.dardanelli@unipa.it; Tel.: +39-019-2389-6228

Abstract: Global Navigation Satellite System (GNSS) has drawn the attention of scientists and users all over the world for its wide-ranging Earth observations and applications. Since the end of May 2022, more than 130 satellites are available for fully global operational satellite navigation systems, such as BeiDou Navigation Satellite System (BDS), Galileo, GLONASS and GPS, which have been widely used in positioning, navigation, and timing (PNT), e.g., precise orbit determination and location-based services. Recently, the refracted, reflected, and scattered signals from GNSS can remotely sense the Earth's surface and atmosphere with potential applications in environmental remote sensing. In this paper, a review of multi-GNSS for Earth Observation and emerging application progress is presented, including GNSS positioning and orbiting, GNSS meteorology, GNSS ionosphere and space weather, GNSS-Reflectometry and GNSS earthquake monitoring, as well as GNSS integrated techniques for land and structural health monitoring. One of the most significant findings from this review is that, nowadays, GNSS is one of the best techniques in the field of Earth observation, not only for traditional positioning applications, but also for integrated remote sensing applications. With continuous improvements and developments in terms of performance, availability, modernization, and hybridizing, multi-GNSS will become a milestone for Earth observations and future applications.

Keywords: GNSS; GNSS meteorology; GNSS ionosphere; GNSS-Reflectometry; GeoHazards

Citation: Jin, S.; Wang, Q.; Dardanelli, G. A Review on Multi-GNSS for Earth Observation and Emerging Applications. *Remote Sens.* **2022**, *14*, 3930. https://doi.org/10.3390/rs14163930

Academic Editor: Yunbin Yuan

Received: 1 August 2022
Accepted: 7 August 2022
Published: 13 August 2022

1. Introduction

The Global Navigation Satellite System (GNSS) has been developed rapidly and attracted increasing global attentions for its wide-ranging Earth monitoring and investigatory applications. Since the end of May 2022, more than 130 satellites of fully global operational satellite navigation systems are available, such as China's BeiDou Navigation Satellite System (BDS) [1], the European Union's Galileo [2], Russia's GLObal NAvigation Satellite System (GLONASS) [3] and the United States' Global Positioning System (GPS) [4]. Furthermore, many other regional GNSS systems are available, e.g., the Indian Regional Navigation Satellite System (IRNSS/NavIC), the Japanese Quasi-Zenith Satellite System (QZSS), and the Regional South Korean Positioning System (KPS), which hold massive potential applications in the scientific community. In terms of applications, the ground-based and space-borne GNSS receivers can measure the ionospheric total electron content (TEC) for the global ionospheric climate and space weather (GNSS-Ionosphere). The dense TEC observations can record ionospheric perturbations, due to earthquakes, tsunamis, volcanos, typhoons, or geomagnetic storms, and eclipses [5–7]. The GNSS Reflectometry (GNSS-R) from a low Earth-orbiting satellite can retrieve environmental parameters over the sea ice, lands, and oceans [8,9].

Nowadays, multi-GNSS represents one of the best techniques in the field of Earth observations. Of course, with continuous improvements and developments in terms of performance, availability, modernization, and hybridizing, GNSSs will be involved in

more future applications. The aim of this review is to present the latest state of multi-GNSS for Earth observations and emerging applications, including the following, not fully exhaustive, troposphere and ionosphere observations; modeling and assimilation from ground-based and space-borne GNSS observations; theory and methods of multi-GNSS near real-time kinematic (RTK) positioning; precise point positioning (PPP) and PPP-RTK; GNSS-Reflectometry applications; geohazard observation and warning from GNSS; errors, systematic effects and noise in GNSS solutions; and surface-loading GNSS observations from atmosphere, hydrology and loading.

In this paper, a review of multi-GNSS for Earth Observation and emerging application progress is presented, including GNSS positioning and orbiting, GNSS meteorology, GNSS ionosphere and space weather, and GNSS-Reflectometry as well as GNSS earthquake monitoring and GNSS integrated techniques for land and structural health monitoring. In Section 2, BDS/GNSS theory, methods and error resources are presented, as well as multi-GNSS observations. GNSS emerging applications are reviewed in details in Section 3. A summary and prospective are given in Section 4.

2. BDS/GNSS Techniques and Observations

2.1. BDS/GNSS Techniques

As it is widely known, GPS and GLONASS were the first two global positioning systems used in different fields. Their Earth observation comes mainly from dual frequency signals. Global Positioning System (GPS) was originally Navstar GPS, which is a satellite-based radionavigation system by USA. GPS provides geolocation and time information to a GPS receiver anywhere on or near the Earth with four or more GPS satellites. GPS can provide precise positioning capabilities to military, civil, and commercial users around the world. GPS uses code division multiple access (CDMA), while GLONASS uses frequency division multiple access (FDMA). With the development of science, technology and society, GPS and GLONASS were implemented with a new generation of satellites, and three frequency signals were established. In particular, CDMA technology was used by GLONASS for its new signals [10]. Moreover, Galileo, as the main provider of civil services, has quickly developed in recent years to provide global services with multi-frequency signals [11]. After three-step strategic developments, China's BeiDou Global Navigation Satellite System (BDS-3) has been able to provide global services with more signals [12,13]. All constellations of GPS, GLONASS and Galileo adopt the constellation of medium Earth orbit (MEO), while the constellation of BDS is composed of MEO satellites, geostationary orbit (GEO) satellites and inclined geosynchronous orbit (IGSO) satellites [1–4]. Based on existing global services, BDS has improved service performances within the region and the global. The number of GNSS satellites are shown in Table 1 with satellites types and signals. Nowadays, multi-frequency multi-GNSS technology is used for Earth observation. Table 2 shows the GNSS multi-frequency signals from the Receiver Independent Exchange (RINEX) format [14]. Note that this study only presents and discusses the publicly available signals.

Table 1. Number of multi-GNSS satellites in orbit (until 2022) [1–4].

System	Block	Signal	Number of Operational Satellites
GPS	IIR	L1 L2	7
	IIR-M	L1 L2	7
	IIF	L1 L2 L5	12
	III/IIIF	L1 L2	5
GLONASS	M	G1 G2	22
	K	G1 G2 G3	1
Galileo	IOV	E1 E6 E5a/b/ab	3
	FOC	E1 E6 E5a/b/ab	19

Table 1. *Cont.*

System	Block	Signal	Number of Operational Satellites
BDS-2	MEO	B1 B2 B3	3
	IGSO	B1 B2 B3	7
	GEO	B1 B2 B3	5
BDS-3	MEO	B1 B3 B1C B2 a/b	24
	IGSO	B1 B3 B1C B2 a/b	3
	GEO	B1 B3	2

Table 2. Multi-frequency multi-GNSS signals [14].

System	Freq. Band	Frequency/MHz	Observation Codes
GPS	L1	1575.42	C1C C1S C1L C1X C1P C1W C1Y C1M
	L2	1227.60	C2C C2D C2S C2L C2X C2P C2W C2Y C2M
	L5	1176.45	C5I C5Q C5X
GLONASS	G1	1602 + k × 9/16 k = −7 . . . + 12	C1C C1P
	G2	1246 + k × 7/16	C2C C2P
	G3	1202.025	C3I C3Q C3X
Galileo	E1	1575.42	C1A C1B C1C C1X C1Z
	E5a	1176.45	C5I C5Q C5X
	E5b	1207.140	C7I C7Q C7X
	E5 (E5a + E5b)	1191.795	C8I C8Q C8X
	E6	1278.75	C6A C6B C6C C6X C6Z
BDS-2	B2	1207.140	C7I C7Q C7X
BDS-2/3	B1	1561.098	C2I C2Q C2X
	B3	1268.52	C6I C6Q C6X
BDS-3	B1C	1575.42	C1D C1P C1X
	B1A	1575.42	C1S C1L C1Z
	B2a	1176.45	C5D C5P C5X
	B2b	1207.140	C7D C7P C7Z
	B2 (B2a + B2b)	1191.795	C8D C8P C8X
	B3A	1268.52	C6D C6P C6Z

2.2. GNSS Observation Equations

The GNSS pseudo-range and carrier phase observations can be expressed as [15]

$$\begin{cases} p^s_{r,j} = \rho^s_r + c(dt_r - dt^s) + T^s_r + I^s_{r,j} + c(d_{r,j} - d^s_j) + \varepsilon_p \\ \varphi^s_{r,j} = \rho^s_r + c(dt_r - dt^s) + T^s_r - I^s_{r,j} + \lambda_j w^s_r + \lambda_j N^s_{r,j} + \lambda_j (b_{r,j} - b^s_j) + \varepsilon_\varphi \end{cases} \quad (1)$$

where the superscript s denotes a GNSS satellite; the subscript r and j denote the receiver and the frequency; $P^s_{r,j}$ denotes the observed pseudo-range on jth frequency in meters; $\varphi^s_{r,j}$ is the corresponding carrier phase; ρ^s_r denotes the geometrical range from phase centers of the satellite to receiver antennas at the signal transmitting and receive time in meters; c denotes the vacuum speed of light in meters per second; $d$tr is the receiver clock offset in seconds; $d$ts is the satellite clock offset in seconds; T^s_r is the slant tropospheric delay in meters; $I^s_{r,j}$ is the ionospheric delay on jth frequency in meters; $d_{r,j}$ and d^s_j are the code biases of the receiver and the satellite in seconds; λ_j is the wavelength of carrier phase on the jth frequency in meters; w^s_r is the phase wind-up delay in cycles; $N^s_{r,j}$ is the integer ambiguity on the jth frequency in cycles; $b_{r,j}$ and b^s_j are the uncalibrated phase delays (UPDs) for receiver and satellites in cycles, respectively; ε_p and ε_φ are the pseudo range and carrier phase observation noises including multipath in meters, respectively.

In order to eliminate some parameters, the original observations of GNSS can be linearly combined. There are several common combinations, such as geometry-free (GF) [16], ionosphere-free (IF) [17], wide lane (WL) and narrow lane (NL) [18] combinations. GF combination eliminates the frequency independent parameters and it is used for ionospheric modeling. The IF combination is often used for precise single point positioning, while WL and NL combinations can be used for cycle-slip detection [16–18].

2.3. GNSS Positioning Methods

There are two common methods for GNSS positioning, namely differential positioning, and precise point positioning (PPP). Differential positioning is a relative positioning technology, which needs to set up a reference station with a known position and observes synchronously with the user [19]. PPP is an absolute positioning technique with removing or estimating GNSS errors, which provides a high level of position accuracy by a single receiver observation [20].

For GNSS differential positioning, there are four different types of position differentials: pseudo range differential, carrier phase smoothing, pseudo range differential and carrier phase differential. Real Time Kinematic (RTK), used to obtain precise positioning results, adopts carrier phase differential technology. However, the base stations need to be set up for RTK, so the operation mode is not flexible and the cost is relatively high. Moreover, with increase of the distance between users and reference stations, its positioning accuracy becomes significantly reduced. Comparing the two methods, since non-difference observation is used in PPP, the latter provides more advantages in terms of operation mode and cost [21,22].

The GNSS PPP method is based on three common models, the ionosphere-free combination mode, the Uofc model and the uncombined model [23]. Among these, the most used ionospheric-free model is able to eliminate the ionospheric parameters through the combination of dual frequency pseudo range and carrier phase observations [17]:

$$\begin{cases} P_{IF} = \alpha \cdot p^s_{r,i} + \beta \cdot p^s_{r,j} \\ \Phi_{IF} = \alpha \cdot \varphi^s_{r,i} + \beta \cdot \varphi^s_{r,j} \end{cases} \tag{2}$$

where $\alpha = f_i^2/(f_i^2 - f_j^2)$, $\beta = -f_j^2/(f_i^2 - f_j^2)$.

The Uofc model, based on the ionospheric-free model with two frequency phase observations, involves the ionospheric free combination composed of phase and pseudo range observations at each frequency [22–25]:

$$\begin{cases} P_{UofC,i} = (p^s_{r,i} + \varphi^s_{r,i})/2 \\ P_{UofC,j} = (p^s_{r,j} + \varphi^s_{r,j})/2 \\ \Phi_{UofC,ij} = \Phi_{IF} \end{cases} \tag{3}$$

The above two models both eliminate the ionospheric parameters through the combination of observation equations, but also enlarge the observation errors. In the last few years, the uncombined model, by using the original observation equation shown in Equation (1), has received more attentions, and thus has been involved in several applications, such as positioning, timing, and tropospheric retrieval applications [26,27]. The three PPP models are theoretically equivalent [22,25]. With the development of multi-frequency and multi-GNSS, the ionospheric-free model and Uofc model have been extended to handle multi-frequency signals. More PPP models can be extended based on the above three models, considering ionospheric parameter corrections or weight [11,28–30].

2.4. Main Error Sources

The main errors in GNSS observations [31,32] are, for instance, those related to the GNSS satellite, to the GNSS receiver, to signal propagation among others, as shown in Figure 1, including satellite orbit error, satellite clock offset, phase center offset, receiver

clock offset, receiver hardware delay, antenna phase center offset, ionospheric and tropospheric delay, relativistic effect and multipath.

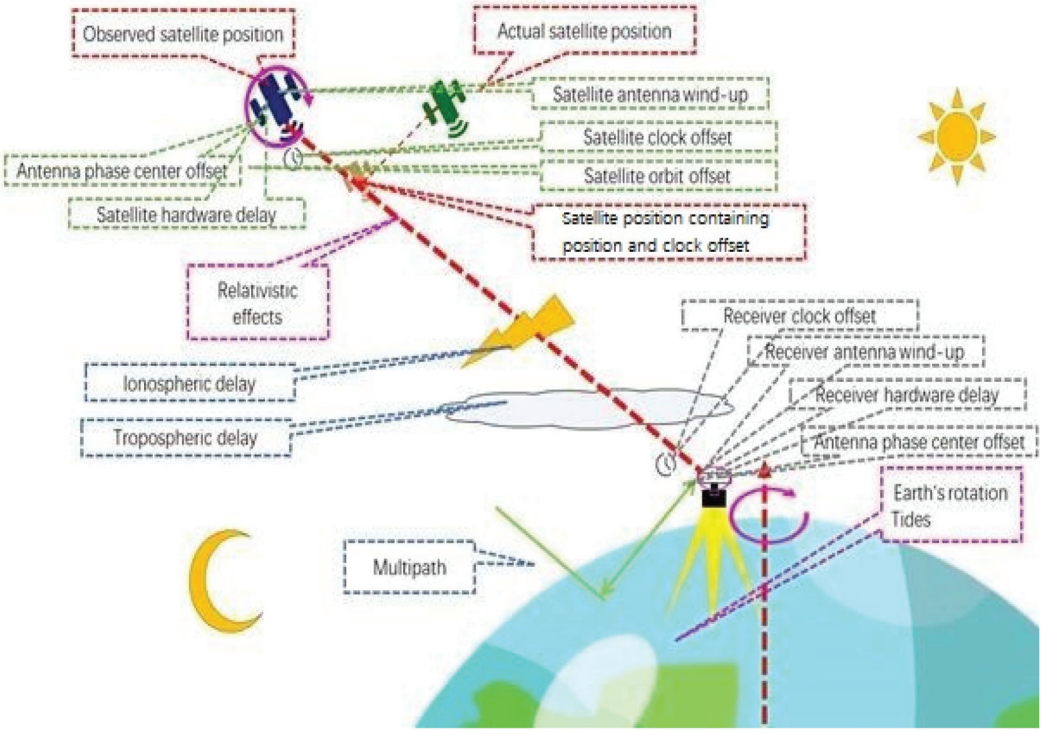

Figure 1. GNSS error source.

2.5. Multi-GNSS Observations

As a volunteer association, the International GNSS Service (IGS) has provided the highest-quality GNSS data to users for the last twenty years. With the development of newly established global and regional navigation satellite systems, IGS conducted the multi-GNSS experiment (MGEX) project to collect and analyze observations of the new systems and signals [33,34]. The MGEX network started in 2012, and grew rapidly in the following years. In May 2022, the number of IGS and MGEX stations rose to more than 500 (Figure 2). All stations can track GPS, while about 450 stations are available for GLONASS. There are approximately 370 and 310 stations to track Galileo and BDS, respectively. Table 3 summarizes the information of GNSS receivers in MGEX (until May 2022). As shown, most of the available receivers can track multiple GNSS. These stations provide sufficient guarantee for GNSS Earth observation data. Note that there are other public agencies and some private vendors, which can provide single- or multi-GNSS observations, such as the GPS Earth Observation Network System (GEONET), operated by the Geospatial Information Authority of Japan (GSI).

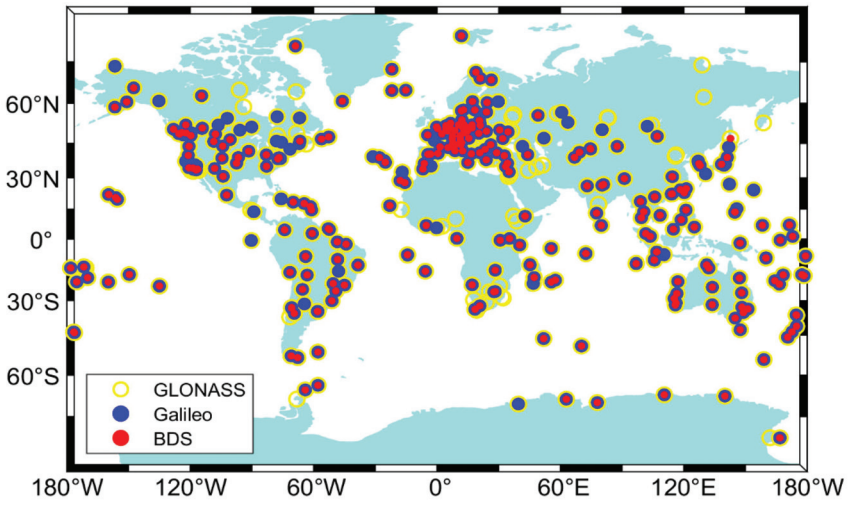

Figure 2. IGS/MGEX stations in May 2022.

Table 3. Information of GNSS receiver in MGEX (until May 2022).

ID	Receiver	Type	Trackable Satellite	Stations
1	ASHTECH	UZ-12, Z-XII3, Z-XII3T	GPS	16
4	CHC	P5E	GPS + GLO + GAL + BDS	1
5	JAVAD	TR_G3TH, TRE_3, TRE_3 DELTA, TRE_3L DELTA, TRE_3N DELTA, TRE_G2T DELTA, TRE_G3T DELTA, TRE_G3TH DELTA,	GPS + GLO + GAL + BDS	74
6	JPS	EGGDT, LEGACY	GPS + GLO	7
7	LEICA	GR10, GR25, GR30, GR50, GRX1200	GPS + GLO + GAL + BDS	57
8	NOV	OEM4-G2, OEM6, OEMV3	GPS	23
9	SEPT	ASTERX4, POLARX2, POLARX3ETR, POLARX4TR, POLARX5, POLARX5E, POLARX5S, POLARX5TR,	GPS + GLO + GAL + BDS	153
10	STONEX	SC2200	GPS + GLO + GAL + BDS	1
11	TPS	LEGACY, NETG3, NET-G3A, NET-G5	GPS + GLO	20
12	TRIMBLE	5700, ALLOY, NETR5, NETR8, NETR9, NETRS, R9S	GPS + GLO + GAL + BDS	160
			Total	512

3. GNSS Emerging Applications

3.1. GNSS Positioning and Orbiting

Single-frequency GNSS Precise Point Positioning (PPP) can achieve a centimeter-decimeter accuracy level and multi-frequency GNSS PPP can obtain a millimeter-centimeter level when the carrier phase ambiguities converge. Figure 3 shows the errors of single-, dual-, triple- and quad-frequency static BDS PPP at the iGMAS station KUN1 in the north, east and vertical directions on DOY 16, 2019 [28]. The positioning performance

was compared with the iGMAS products. From the comparison of single-, dual-, triple- and quad-frequency BDS PPP performances, the multi-frequency BDS signals were able to greatly improve the positioning performance, particularly for quad-frequency BDS observations. It also showed that the positioning errors were decreased with increasing observation time.

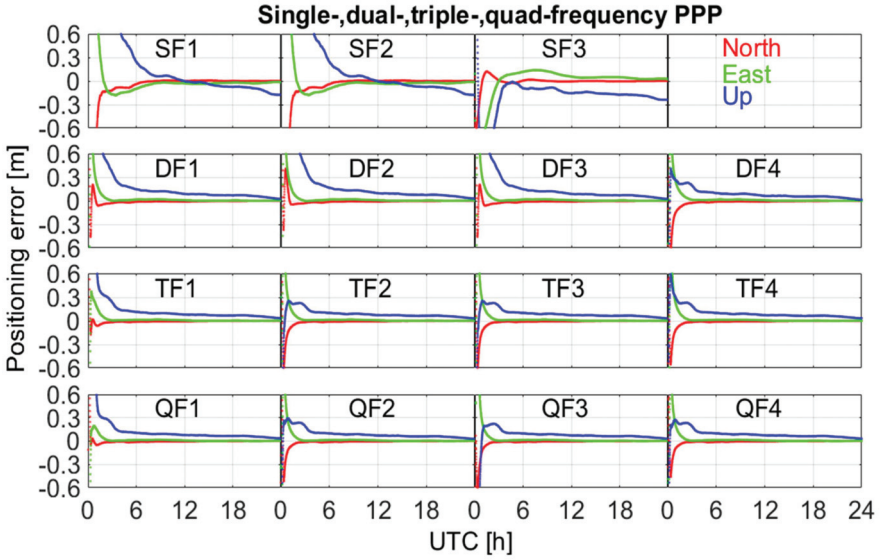

Figure 3. Errors of single-, dual-, triple- and quad-frequency BDS PPP at the iGMAS station KUN1 in the north, east and vertical direction on DOY 16, 2019 [28].

Precise positioning and precise orbit determination (POD) can be estimated from GNSS observations. For example, the potential periodicity of empirical acceleration in the Haiyang 2B (HY-2B) POD was identified by spectral analysis. Using over one year of satellite laser ranging (SLR) measurements, a 5.2% improvement in the orbit solution of the refined model was demonstrated and validated. After application of the in-flight calibration of the GPS antenna, a 26% reduction in the root mean square (RMS) of SLR residuals was achieved for the reduced-dynamic (RD) orbit solutions, and the carrier phase residuals were clearly reduced. The integer ambiguity resolution of HY-2B led to strong geometric constraints for the estimated parameters, and a 15% improvement in the SLR residuals could be inferred when compared with the float solution [35].

One year's data collected by the Gravity Recovery and Climate Experiment Follow-On (GRACE-FO) mission and GPS precise products provided by the Center for Orbit Determination in Europe (CODE) were analyzed. The precise orbit, generated by the Jet Propulsion Laboratory (JPL), independent SLR, and K-band ranging (KBR), measurements were utilized to assess the orbit accuracy. More than 98% of single difference (SD) wide-lane (WL) and 95% of SD narrow-lane (NL) ambiguities were fixed, which confirmed the good quality of the bias products and the correctness of the SD ambiguity resolution (AR) method [36,37].

3.2. GNSS Meteorology

Tropospheric delay is one of the most common GNSS positioning errors. Nowadays, the zenith tropospheric delay (ZTD) can be estimated from GNSS observations, which can be transferred into precipitable water vapor (PWV) for meteorological applications. Recently, PWV was estimated and analyzed at 377 GNSS stations from the infrastructure construction of national geodetic datum modernization and Crustal Movement Observation

Network of China (CMONC), which is one of the most important Continuously Operating Reference Station (CORS) networks in the world. Further PWV was obtained from GPS observations and meteorological data from 2011 to 2019. The PWV had improved accuracy when compared with the Bevis model. Bevis et al. [38] pioneered the concept of GPS meteorology and obtained global surface temperature and weighted average temperature from more than 8000 radiosonde stations in America. They also described the linear relationship coefficient and the specific process of GPS water vapour inversion on the ground. Furthermore, the daily and monthly average values, long-term trend, and change characteristics of the PWV were analyzed, using the high-precision inversion model. The results showed that the averaged PWV was higher in Central–Eastern China and Southern China and lower in Northwest China, Northeast China, and North China (Figure 4). The PWV was increasing in most parts of China, while some PWVs in North China showed a downward trend [39].

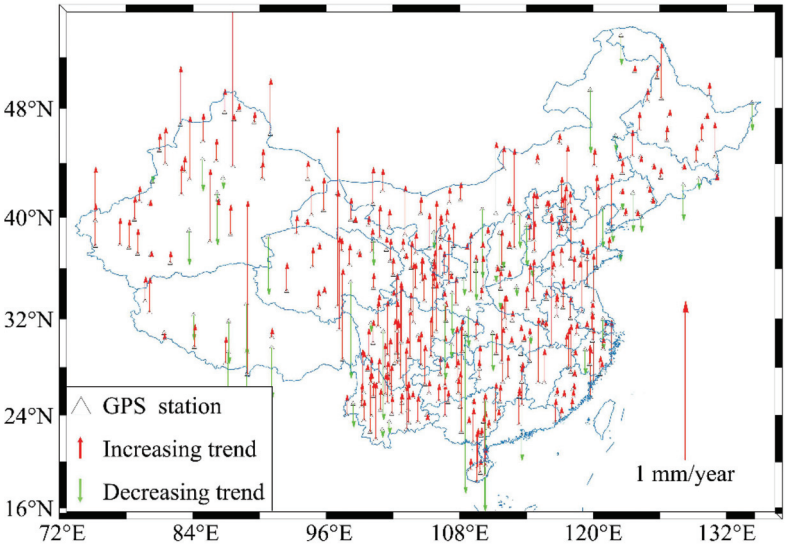

Figure 4. Long-term variation trend of the GNSS PWV from 2011 to 2018 [39].

In addition, pressure, water vapor pressure, temperature, and weighted mean temperature (Tm) play an important role in GNSS meteorological applications. A new approach was introduced to develop an empirical tropospheric delay model, named the China Tropospheric (CTrop) model, to provide meteorological parameters based on the sliding window algorithm, using radiosonde data as reference values to validate the performance of the CTrop model, which was compared to the canonical Global Pressure and Temperature 3 (GPT3) model. The accuracy of the CTrop model in regards to pressure, water vapor pressure, temperature, and weighted mean temperature were 5.51 hPa, 2.60 hPa, 3.09 K, and 3.35 K, respectively, achieving an improvement of 6%, 9%, 10%, and 13%, respectively, when compared to the GPT3 model, as reported in [40].

3.3. GNSS Ionosphere and Space Weather

Ionospheric delay is an important and concerning error source in GNSS navigation and positioning systems, which has been widely analyzed [41–44]. Even though it affects the accuracy of GNSS navigation and positioning, it is well known that it can be modeled by GNSS Earth observation [45]. The ionospheric delay can be parameterized as the total

electron content (TEC) on the observation path. The relationship between ionospheric delay and TEC can be expressed as [45]:

$$I_{ion} = \frac{40.28}{f^2}\text{TEC} \quad (4)$$

where I_{ion} is the ionosohric delay and f is the frequency. In the ionospheric TEC modeling, the code bias, generally represented by differential code bias (DCB), is an important error affecting the accuracy of TEC. To estimate ionospheric TEC and DCB by GNSS observations, two basic assumptions are established [45,46]. The first one is the single-layer model, in which TEC is assumed to be concentrated in a thin layer between 300–500 km. The second one is the zero-mean condition, in which the sum of satellite DCB is zero. Ionospheric modeling can be divided into three steps. Firstly, the ionospheric slant TEC (STEC) is extracted, then the STEC is transformed into vertical TEC by using an ionospheric mapping function, and finally TEC and differential code bias are estimated. Therefore, ionospheric TEC estimation and modelling are mainly focused on the following aspects, extraction of the slant TEC observables, ionospheric thin layer height and mapping function, TEC estimation and GNSS code bias handing [45,46].

The carrier-to-code leveling (CCL) method is the most used method to extract STEC [47] due to its simple implementation. A modified CCL (MCCL) method was proposed to retrieve ionospheric observables when considering the intra-day fluctuation of receiver DCB [48,49]. The MCCL method has also been extended to multi-frequency multi-GNSS [49,50]. The GF combination of GNSS observation is used in the CCL method, which affects the accuracy of TEC extraction. Therefore, the PPP method is used to improve the accuracy [51–53]. The methods of extracting ionospheric observations by PPP can be divided into single-, dual- and multi-frequency methods [54]. In addition, PPP fixed-ambiguity solutions for extracting STEC has also been proposed, instead of the more common PPP float-ambiguity solutions [55]. To take advantage of the high accuracy carrier phase observation, a method of extracting STEC by using phase observations directly was proposed [56].

Generally, for ionospheric TEC modeling, a fixed height of ionospheric thin layer and a mapping function are commonly selected [45]. However, these selections affect the accuracy of ionospheric modeling. An enhanced mapping function with ionospheric varying height was proposed in [57]. Moreover, a multi-layer mapping function was analyzed in order to reduce the ionospheric mapping errors in [58,59].

The ionospheric TEC is generally modeled through a definite mathematical function, such as spherical harmonic function, for global, generalized triangular series function, or polynomial function for regional. The DCB can be estimated together with the TEC modeling [60–63]. Moreover, the DCB can be obtained by using a global ionosphere map. Table 4 shows the mean RMS of estimated satellite DCB relative to the DCB products provided by MGEX, in which the DCB was estimated by spherical harmonic function modeling for global. Acronyms are given as: Chinese Academy of Sciences (CAS), Center for Orbit Determination in Europe (CODE), and Deutsches Zentrum für Luft- und Raumfahrt (DLR).

To handle more types of differential code bias from multi-frequency multi-GNSS, the observable-specific Signal Bias (OSB) was proposed. Several studies on the estimation and processing of GNSS OSB have been carried out [64–66].

A very interesting case study has been developed regarding plasma-spheric total electron content (PTEC). Its long-term variations have been estimated and studied from GPS observations onboard the Constellation Observing System for Meteorology, Ionosphere, and Climate (COSMIC). As it is known, the plasmasphere, or inner magnetosphere, is a region of the Earth's magnetosphere consisting of low-energy (cool) plasma and is located above the ionosphere. The long-term variation in PTEC was further analyzed using a decade-long dataset of COSMIC GPS observation data from 2007 to 2017 (Figure 5), and a high correlation was found between PTEC and the solar flux (F10.7) in the range 0.88–0.93 [67].

Table 4. The mean RMS of estimated satellite DCB relative to the DCB product provided by MGEX.

System	DCB Type	CAS	DLR	CODE	System	DCB Type	CAS	DLR
GPS	C1C-C2W	0.06	0.09	0.07	GAL	C1X-C5X	0.06	0.11
	C1W-C2W	0.06	0.16			C1X-C7X	0.07	0.11
	C1C-C5X	0.07	0.08			C1X-C8X	0.08	0.12
	C1C-C5Q	0.10	0.13			C1C-C5Q	0.10	0.11
GLO	C1C-C2P	0.12	0.12	0.15		C1C-C7Q	0.07	0.10
	C1P-C2P	0.14	0.22			C1C-C8Q	0.08	0.10
	C1C-C2C	0.17	0.13		QZSS	C1X-C2X	0.07	0.16
BDS	C2I-C7I	0.15	0.14			C1X-C5X	0.07	0.10
	C2I-C6I	0.19	0.13			C1C-C2L	0.11	0.12
						C1C-C5Q	0.09	0.18

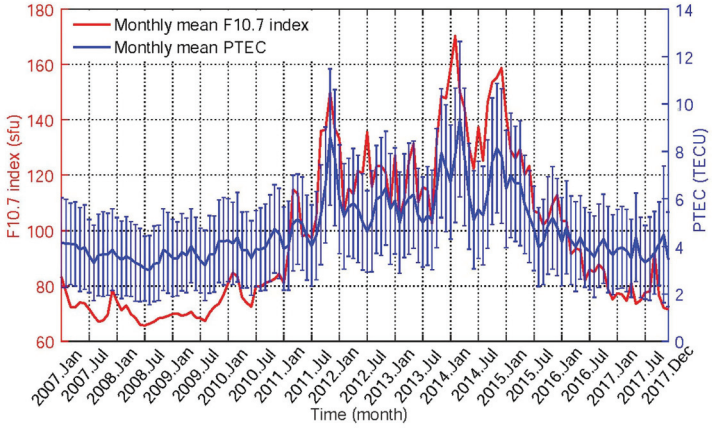

Figure 5. Monthly mean F10.7 index and monthly mean PTEC from January 2007 to December 2017 [67].

An analysis of the ionospheric TEC disturbances from global ionosphere maps (GIMs) was conducted during earthquakes with magnitude ≥2.5, which occurred in 2015–2018, in different latitude regions and, in particular, in A: 13° S–0.5° S (22.3° S–10° S geomagnetic), B: 0.5° S–19.5° N (10° S–10° N geomagnetic), and C: 19.5° N–32.1° N (10° N–22.5° N geomagnetic, Figure 6). The greater occurrence times of TEC decrease anomalies were observed in the southeast in Region A [68].

The thin layer ionospheric height (TLIH) was further analysed, which plays a role in mapping function (MF), and affects the accuracy of the conversion between the slant total electron content (STEC) and vertical total electron content (VTEC). In particular, a new method for determining the optimal TLIH was proposed [69], which compares the mapping function values (MFVs) from the MF at different given TLIHs with the "truth" mapping values from the UQRG global ionospheric maps (GIMs) and the differential TEC (dSTEC) method, namely, the dSTEC- and GIM-based thin layer ionospheric height (dG-TLIH) techniques. The optimal TLIH was determined using the dG-TLIH method based on GNSS data over the Antarctic and Arctic. An innovative method was recently proposed regarding multi-GNSS DCB estimation as one of the main errors in ionospheric modeling and applications. This innovative method uses independent GNSS DCB estimation (IGDE), without using the ionospheric function model and global ionosphere map (GIM). Firstly, ionospheric observations are extracted, based on the geometry-free combination of dual-frequency multi-GNSS code observations. Secondly, the VTEC of the station, represented by the weighted mean VTEC value of the ionospheric pierce points (IPPs) at each epoch, is

estimated as a parameter, together with the combined receiver and satellite DCBs (RSDCBs). Finally, the estimated RSDCBs are used as new observations, the weights of which are calculated from estimated covariances, and, thus, the satellite and receiver DCBs of multi-GNSS are estimated. Nineteen types of multi-GNSS satellite DCBs are estimated based on 200-day observations from more than 300 multi-GNSS experiment (MGEX) stations. The performance of the proposed method was evaluated by comparing it with MGEX products. The results showed that the mean RMS values were 0.12, 0.23, 0.21, 0.13, and 0.11 ns for GPS, GLONASS, BDS, Galileo, and QZSS DCBs, respectively, with respect to MGEX products, and the stabilities of estimated GPS, GLONASS, BDS, Galileo, and QZSS DCBs were 0.07, 0.06, 0.13, 0.11, and 0.11 ns, respectively, as reported on in [70].

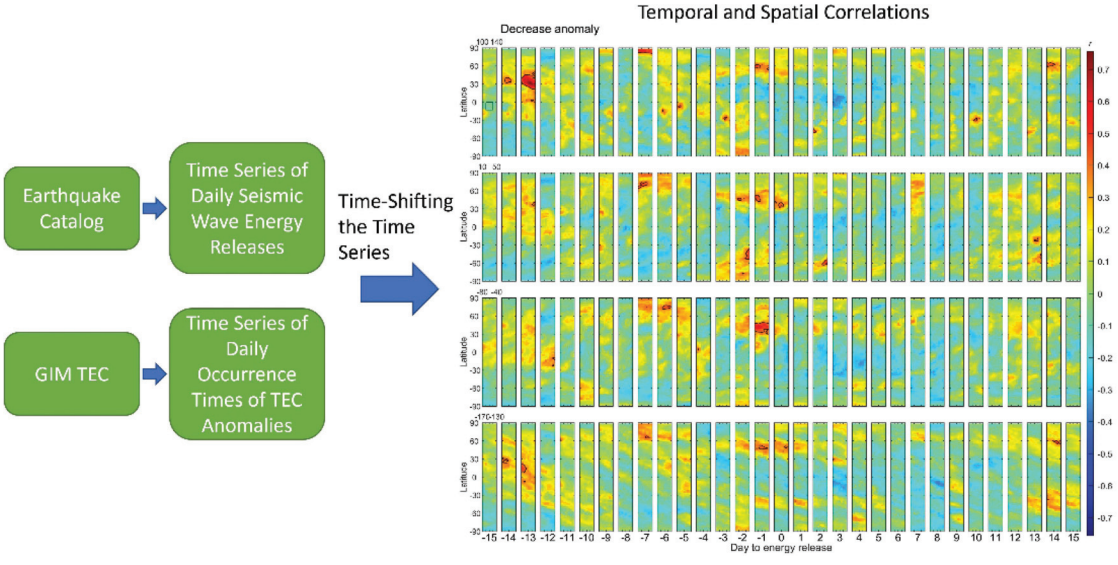

Figure 6. Temporal and spatial correlations [68].

Other interesting progress concerns the greater opportunities for positioning offered by Beidou (BDS) GNSS with precise ionospheric delay corrections. The BDS reflection signal detects multiple moving targets under multiple-input and multiple-output (MIMO) radar systems and proposes a series of methods to suppress multiple Doppler phase influences and improve the range detection property. The simulation results showed restored target peaks, which matched the RCS data more accurately, with the GNSS-R Doppler phase influence removed, which proved the proposed method could improve target recognition and detection resolution performance [71]. Many Differential Code Biases, DCBs and DCB types of the new BDS-3 signals from 30-days Multi-GNSS Experiment (MGEX) observations, were estimated and investigated. Compared with the DCB values provided by the Chinese Academy of Science (CAS) products, the mean bias and root mean squares (RMS) error of the new BDS-3 satellite DCBs were within ±0.20 and 0.30 ns, respectively. The satellite DCBs were mostly within ±0.40 ns with respects to the Deutsches Zentrum für Luft- und Raumfahrt (DLR). The four sets of constructed closure errors and their mean values were within ±0.30 ns and ±0.15 ns, respectively. The mean standard deviation (STD) of the estimated satellite DCBs was less than 0.10 ns (Figure 7). Of particular note was the fact that the estimated satellite DCBs were more stable than DCB products provided by CAS and DLR [72].

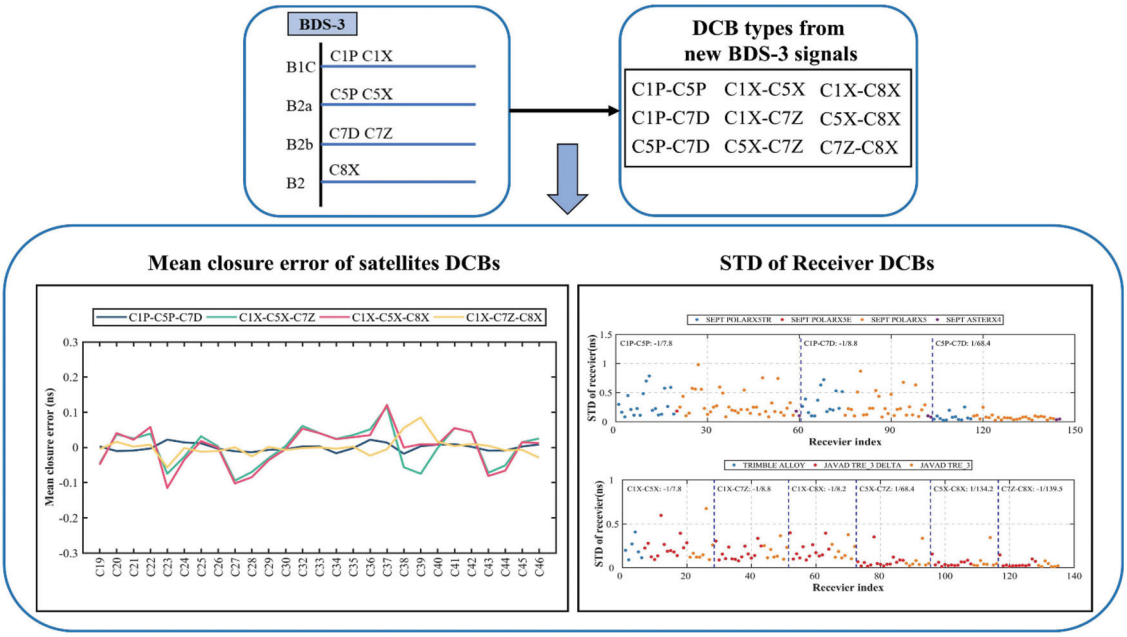

Figure 7. Mean closure error of BDS-3 satellites DCBs and STD of recilver DCBs [72].

3.4. GNSS-Reflectometry

GNSS reflectometry (GNSS-R) is a very useful tool for remote sensing and plays a key role in various applications. Signals reflected from the Earth's surface are analyzed to measure various geophysical parameters. Multipath delay is one of the main error sources in GNSS navigation and positioning. The changes in the polarization characteristics, amplitude, phase, and frequency of the reflected signal reflect the roughness of the reflecting surface, such as changes in coastal water levels and snow thickness. Therefore, accurate estimations of the multipath delay can invert the physical properties and geophysical parameters of the reflecting surface. One of the available solutions is to use the upward-facing GNSS right-handed antenna to receive the direct signal and the downward-facing GNSS left-handed antenna to receive the reflected signal. Using GNSS precise single-point positioning, the delay of the direct and reflected signals can be estimated, and then the water level and snow thickness changes can be inversed. Another solution is to use the signal-to-noise ratio (SNR) of GNSS observations to estimate soil and snow thickness changes, but not all receivers have SNR observations. Qian and Jin [73] used geometry-free linear combination of GNSS code and carry phase observations (L4 observations) to estimate snow thickness. The L4 observations were not affected by geometrical factors and contained multipath residuals, which could effectively represent the multipath. The snow thickness was inverted according to the relationship between the changes of the L4 observations and the measured snow thickness. The snow thickness obtained by using the L4 observations was in good agreement with the results obtained from the signal-to-noise ratio data. However, a single system sometimes has limited observation satellites, and multiple systems improve space coverage. Qian and Jin [73] combined GPS and GLONASS observations from the IGS station GANP (Slovenia) to estimate the snow thickness variation in 2012 and 2013 from GNSS geometry-free linear combination observations (L4 observations) and signal-to-noise ratio (SNR), respectively (Figure 8). The accuracy was improved for a single system, but the L4 method needed to be further improved when compared to the SNR method, because of ionospheric delay and other unremoved errors.

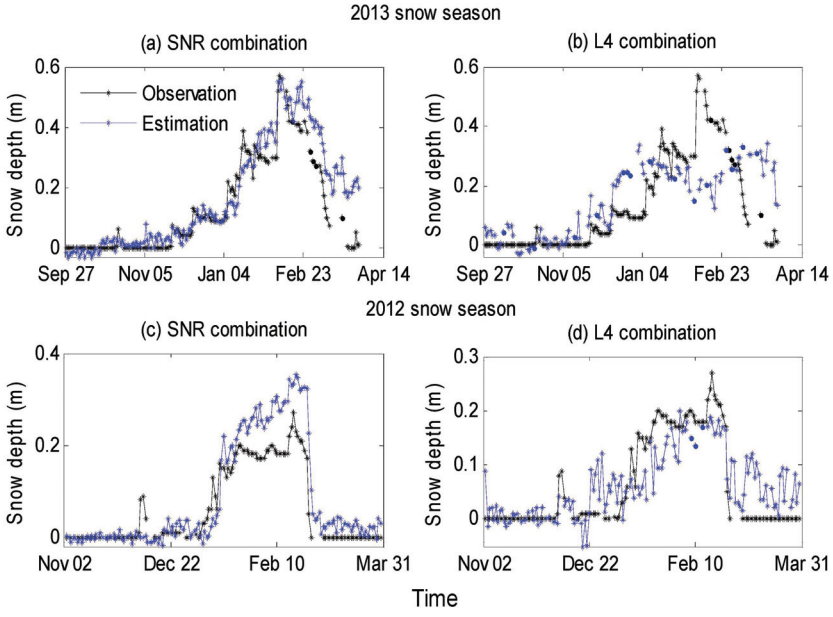

Figure 8. Snow thickness changes at IGS station GANP in 2012 and 2013 from the combined GPS and GLONASS observations with geometric-free combination (L4) and signal-to-noise ratio (SNR), respectively [73].

3.5. Earthquake Monitoring by GNSS

Traditional earthquake magnitude and rupture are inverted using seismograph or accelerometer observation data. However, seismograph data often has missing saturation and data, which cannot completely record the seismic co-seismic displacement amplitude. Although the accelerometer data is not missing, the seismic displacement obtained by integrating the accelerometer data can be distorted by the tilt and rotation of the instrument. Nowadays, GNSS can perform precise single-point positioning and estimate absolute seismic displacement, as well as inverse the rupture, with high accuracy. For example, using the 1 Hz GPS, BDS, GLONASS and Galileo observation data at the LASA station provided by Beidou Experiment Tracking Station (BETS), the displacement of the 25 April 2015 Mw 7.8 Nepal earthquake was estimated and compared with the strong-seismic records near the Tibet area. Figure 9 shows acceleration, velocity, and displacement time series based on constant velocity (CV) dynamic PPP (CVDPPP) with BDS single system, GPS single system, BDS + GPS dual system, GPS + GLONASS dual system and BDS + GPS + GLONASS + Galileo four system during the 300 s period of the initial earthquake occurrence [74]. GNSS results showed high consistency with the displacement time series obtained by the strong motion instrument. The seismic waves estimated by CVDPPP were not affected by the distortion caused by the rotation and tilt of the instrument. By combining multi-system observation data, the velocity and acceleration waves obtained by the CVDPPP model were smoother, which also verified the advantages of multi-system GNSS in monitoring earthquake co-seismic displacements.

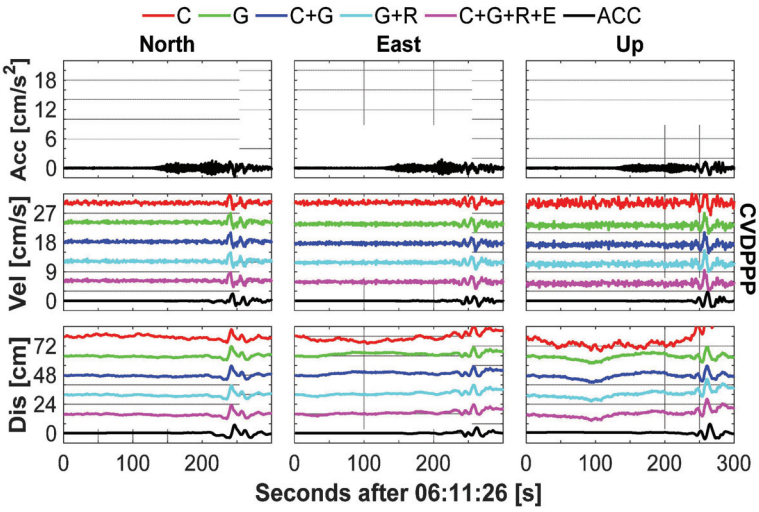

Figure 9. Acceleration, velocity, and displacement time series based on constant velocity (CV) dynamic PPP (CVDPPP) for BDS, GPS, BDS + GPS, GPS + GLONASS and BDS + GPS + GLONASS + Galileo four system during 300 s after UTC 06:11:26 [74].

3.6. GNSS Integrated Techniques for Land and Structural Health Monitoring (SHM)

Real-time monitoring of the engineering structures safety is necessary, since these structures play economic, social and environmental roles. The assessment of the coherence between the expected displacements and those affecting the structures could provide feedback about their behavior in the elastic field, complying with safety regulations. GNSS monitoring systems, used in combination with geotechnical, hydraulic, and structural systems, could allow the monitoring of real-time displacements, with high accuracy, even remotely.

Among the emerging applications of GNSS, those related to monitoring through low-cost mobile smartphone type instruments play a very important role because of the wide availability of these instruments. With Xiaomi Mi8, the first GNSS dual-frequency smartphone embedded with the Broadcom BCM47755 GNSS chip, tests using both VADASE (Variometric Approach for Displacement Analysis Stand-alone Engine) and VARION (Variometric Approach for Real-Time Ionosphere Observations) algorithms were even able to derive real-time STEC variations [75]. Other authors using smartphone accelerometer (Bosch BMI160) and a low-cost dual frequency GNSS reference-rover pair (u-blox ZED-F9P) have achieved high precision values (σ) of ±7.7, 8.1 and 9.6 mm in the East, North and Up (ENU), respectively, which were comparable with the declared precision potential (σ) of the smartphone accelerometer of ±8.8 mm [76].

The interaction between GNSS and Remote Sensing produces excellent results for the monitoring of strategic structures, such as dams. Dam structures can be monitored via traditional contact sensors (extensometers, accelerometers, tiltmeters), ground-based methods (ground-based SAR, ground-based photogrammetry, terrestrial laser scanning, robotic total stations), and GNSS. Remotely based methods include airborne Light Detection and Ranging (LiDAR) and space-borne InSAR. The pros and cons of these methods are summarized in [77].

Furthermore, other new techniques have been developed and tested. The first of these was based on an unsupervised classification and was suitable for automating of the process. The second was based on visual matching with contour lines, with the aim of fully exploiting the dataset. Their performances were evaluated by comparison with water levels measured in situ (r^2 = 0.97 using the unsupervised classification, and r^2 = 0.95 using visual matching), demonstrating that both techniques were suitable to quantify reservoir surface extension. However, ~90% of available images were analyzed using the visual

matching method, and just 37 images are out of 58 using the other method. The evaluation of the water level from the water surface, using both techniques, could be easily extended to un-gauged reservoirs to manage the variations of the levels during normal operation. In addition, during the period of investigation, the use of GNSS allowed the estimation of dam displacements. By comparing results from both techniques, relationships between the orthogonal displacement component via GNSS, estimated water levels via remote sensing and in situ measurements were investigated. In fact, the moving average of the displacement time series (middle section on the dam crest) showed a range of variability of ±2 mm (Figures 10 and 11). The dam deformation versus reservoir water level behavior was different during the reservoir emptying and filling periods, indicating a kind of hysteresis loop [78,79].

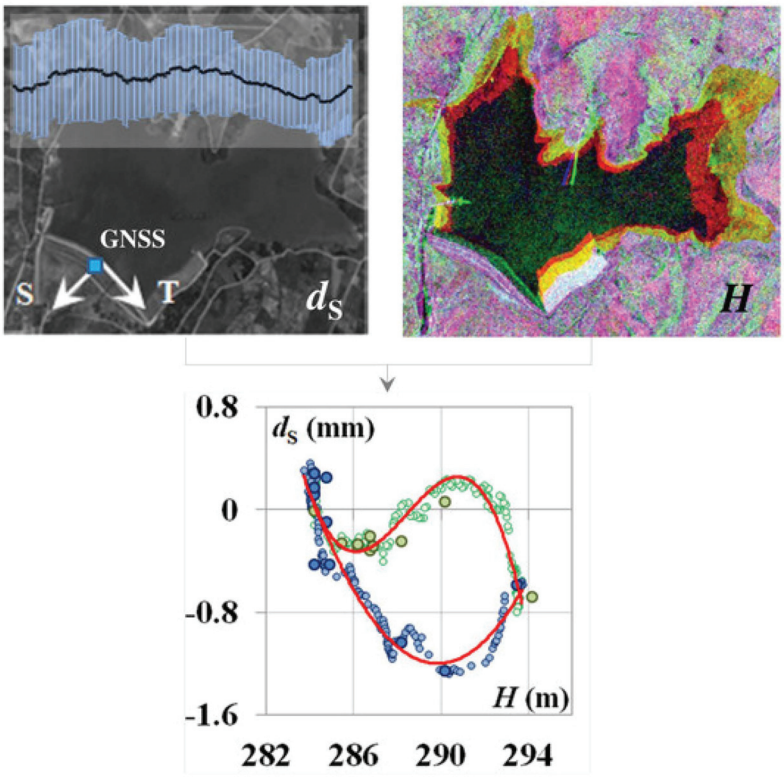

Figure 10. Water surface and level of a reservoir from different remote sensing approaches and comparison with dam displacements evaluated via GNSS [78]. Top left: The Castello dam on Magazzolo reservoir (37°34′51″ N, 13°24′48″ E, WGS84) with local reference system (T and S indicate directions tangential and orthogonal to the dam) and temporal behavior of timely averaged GNSS displacements of the central section along S-axis (black dots) with over imposed ± the standard deviation within the 2-month moving window (blue bars). The black dot indicates *d*s occurring with minimum the water. Top right: diachronic CSK false-color composition for increasing Hm, (281.10, 285.31 and 291.40 m represented in red, gran and blue color scales, respectively). Downwards: He, and Hm, vs. *d*s. during the emptying (green circles) and filling (blue circles) phase, over-imposed two interpolation curves (red continuous lines).

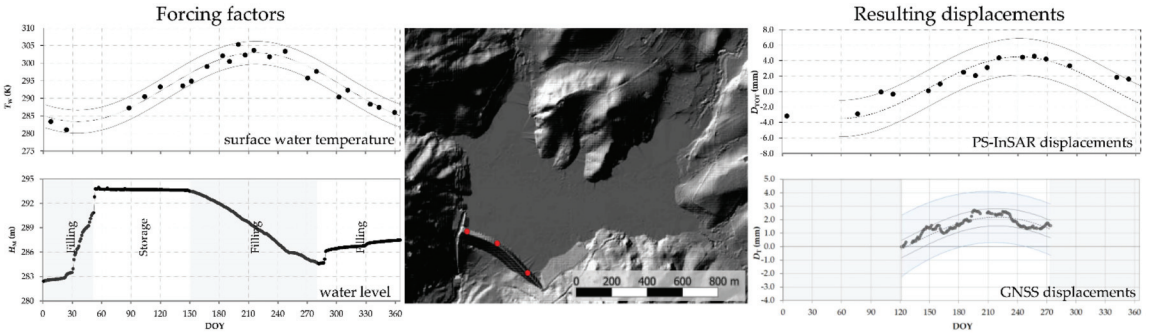

Figure 11. Comprehensive dam monitoring with on-site and remote-retrieved forcing factors and resulting displacements [79]. Top left: Daily water levels measured in situ, H_{IS} (m a.s.l.). A linear interpolation curve is superimposed–imposed (continuous line); Up left: the temporal behavior of the water surface temperature, T_W (K), retrieved by Landsat 8 data, using both 189-034 and 190-034 scenes. A sinusoidal interpolation curve (continuous dashed line) and a confidence band of $\pm 2 \times \sigma_{XY}$ between measured and interpolated values (dark grey lines) are reported to facilitate the interpretation of the phenomenon. Center: hill shade of the dam–reservoir system derived from a digital surface model by setting azimuth and elevation of the incident light at 315 and 45 degrees, respectively). Superimposed the positions of the GNSS stations (red points). Top right: the temporal behavior (DOY in x-axis) of the horizontal total displacements orthogonal to the dam (D_{TOT}, mm) is estimated via PS–InSAR (red dots). A sinusoidal interpolation curve (continuous dashed line) and a confidence band of $\pm 2 \times \sigma_{XY}$ between measured and interpolated values (dark grey). Up right: the temporal behavior (DOY in x-axis) of the horizontal total displacements orthogonal to the dam (D_{TOT}, mm) is estimated via Global Navigation Satellite System (GNSS) (grey dots). A sinusoidal interpolation curve and confidence band of $\pm 2 \times \sigma_{XY}$ between measured and interpolated values (dark grey lines) were reported to facilitate the interpretation of the phenomenon (continuous line). The interpolation curves at the 10th and 90th percentiles of the raw data were reported (pale blue band) as a measure of its variability.

Many studies have focused on the SHM of other composite structures, such as bridges. Yigit and Gurlek [80] proposed some testing of a high-rate GNSS precise point positioning (PPP) method for detecting dynamic vertical displacement response. In particular, the usability of PPP for evaluating the dynamic displacement response of a structure was analyzed with different experiments on cantilever beam structures. Four cases with different vibration frequencies between 0.94 and 2.90 Hz were selected to compare the PPP and relative precise methods in the time, position and frequency domains. In addition, the effects of the ultra-fast products and the final precise orbits on the PPP kinematic solution, in terms of vertical oscillation detection, were examined. Xi et al. [81] used the BDS/GNSS system to conduct an experiment on a bridge in China to evaluate the performance of BDS through comparing with GPS, and found that the accuracy of BDS in static mode could be up to 2–3 mm and 5–7 mm in the horizontal and vertical components. With the monitoring data of a bridge, BDS had the same, or even better, monitoring performance and data quality as GPS. Meng et al. [82] carried out a system for large bridge monitoring, while Xi et al. [81] proposed a multi-GNSS integration processing method and presented a case study on bridge monitoring using multi-GNSS observations (BDS, GPS and GLONASS) with high cutoff heights. Based on the experiments conducted, it was shown that, with more available satellites and stronger satellite geometry, the GPS/BDS/GLONASS combination showed the highest accuracy with 1–2 mm horizontal accuracy and 2–5 mm vertical accuracy. With the integration of GPS/BDS/GLONASS, different cutoff values were set in the data processing in the bridge monitoring application. The results showed that the accuracy in the horizontal component could always reach 1–2 mm with increasing cutoff elevation angles (10° to 40°), even when the upper limit of 40° was selected [83]. More

recently, Manzini et al. [84] evaluated the use of low-cost GNSS stations for SHM, through different combinations of GNSS receivers and antennas. Several sets of parameters and processing requirements were also evaluated using the open-source software RTKLib. The performance of the proposed solution was evaluated through two dynamic experimental scenarios, and results showed its ability to track rapid displacements of up to 4 mm and oscillations of 1 cm with a frequency of up to 0.25 Hz with a 1 Hz receiver. Finally, a two-week dataset, acquired from a network of low-cost GNSS stations distributed on a suspension bridge, was used to validate the in-situ performance. The results showed good agreement between GNSS time series, conventional displacement sensors and numerical simulations [84]. A very interesting review has been published in recent years concerning the use of GNSS with Based Dynamic Monitoring Technologies for SHM. For more details the reader should refer to the work [85].

3.7. GNSS Congruence with Different Modes' Solutions (NRTK, PPP, Static)

Other GNSS emerging applications are related to uses with different modes' solutions, such as Network Real Time Kinematic (NRTK) or PPP, or also static. As an example, Baybura et al. [86] suggested examining the accuracy of Network RTK (NRTK) and Long Base RTK (LBRTK) methods with repetitive measurements. The NRTK and LBRTK measurements were performed on different days between 2015 and 2018 with various survey campaigns, and considered the results of the static measurements as true coordinates. The results of the NRTK and LBRTK methods showed that the LBRTK and NRTK methods provided similar results for baseline lengths up to 40 km, with differences of less than 3 cm horizontally and 4 cm vertically. Lu et al. [87] compared static and dynamic PPP measurements, and the numerical results during the static and dynamic tests showed that the proposed positioning study could achieve a positioning accuracy of a few centimeters within one hour. As expected, the positioning accuracy was significantly improved by the combination of GPS, BeiDou and Galileo as a result of the larger number of satellites used and the more uniform geometric distribution (DOP) of the satellites.

The evaluation of the coordinates from a GNSS survey (in Network Real Time Kinematic, Precise Point Positioning, or static mode) has been analyzed in several scientific and technical applications, and many have been carried out to compare Precise Point Positioning (PPP), Network Real Time Kinematic (NRTK), and static modes' solutions, using the latter as the true, or the most plausible solution. Another study has been developed using the Italian GNSS CORS of Sicily (Figure 12) to compare the GNSS survey methods mentioned above, using some benchmark points. The tests were carried out by comparing the survey methods in pairs to check their solution congruence. The NRTK and the static solutions were referred to a local GNSS CORS network's analysis. The NRTK positioning was obtained with different methods, such as VRS, Flächen-Korrektur-Parameter (FKP), Nearest (NEA) and the PPP solution, and calculated with two different software (RTKLIB and Canadian Spatial Reference System CSRS-PPP). A statistical approach was performed to check if the distribution frequencies of the coordinate's residual belonged to the normal distribution for all pairs. The results showed that the hypothesis of a normal distribution was confirmed in most of the pairs and, specifically, the static vs. NRTK pair seemed to achieve the best congruence. Involving the PPP approach, the pairs obtained with CSRS software achieved better congruence than those involving RTKLIB software [88].

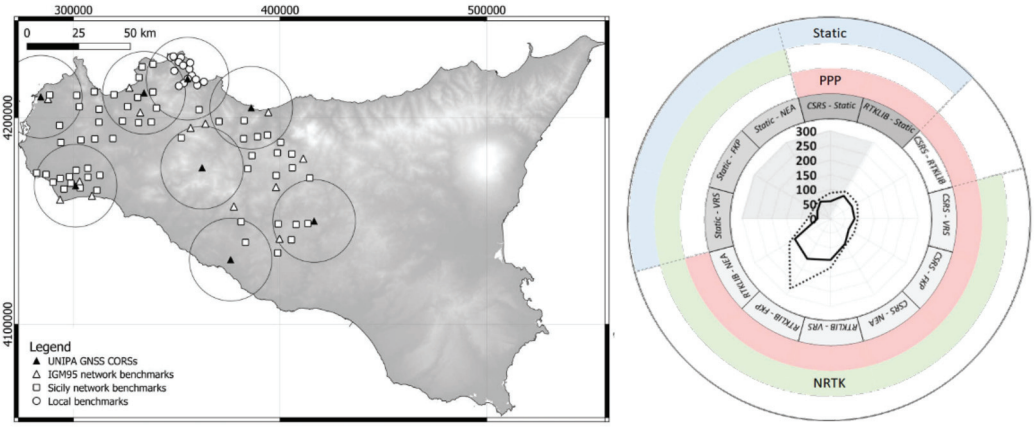

Figure 12. Different solutions for GNSS NRTK, PPP or static positioning. Left: UNIPA GNSS CORSs (black triangles) and GNSS reference benchmarks (IGM95 network benchmarks with white triangles; Sicily network benchmarks with white squares; and local benchmarks with white circles). 20 km buffer circles from the GNSS CORS are shown. Reference system UTM-WGS84 33N (ETRF2000-RDN2008)-EPSG6708. Right: Δh differences, pre- and post-outliers' removal (dashed and continuous lines, respectively) [88].

4. Discussion and Conclusions

A detailed review on multi-GNSS for Earth Observation and the progress of its emerging applications has been presented in this paper. One of the main findings from this study is that, nowadays, the GNSS technique is involved not only in traditional positioning applications, but more widely for remote sensing applications, which represents one of the most used techniques in the field of Earth observations. As it has been deeply discussed in the paper, with continuous improvements and developments, in terms of performance, availability, modernization and hybridizing, multi-GNSS could become a milestone in the future applications. So, what scenarios could we be looking at in the coming years? The answer to this question is quite difficult, but, obviously, there are various fields of multi-GNSS applications to be explored and analyzed. One of these is the use of *GNSS for Autonomous Space Navigation*, since the use of GNSS for this purpose is crucial for space missions. In fact, it can be performed directly on-board and in real time to enable autonomous guidance with reducing or avoiding the delays in Earth-to-space communications and lack of signal coverage. For this purpose, different technologies (GNSS and IMU) and algorithms can be used with enabling, e.g., the precise spacecraft formation flights and landings required in these operational areas.

Another investigation concerns *GNSS atmospheric modeling*. It is widely known that multi-GNSS are influenced by the Earth's atmosphere, including the ionosphere (electrically charged), and the troposphere (neutral atmosphere), modeled with complex mathematical equations [89–91]. Although atmospheric effects on GNSS signals are annoying parameters for positioning and navigation applications, they can provide valuable information for many applications, such as natural hazard monitoring or weather forecasting. Therefore, the modeling of atmospheric effects on multi-GNSS positioning applications (GPS, GLONASS, Galileo, BDS, QZSS and IRNSS) on the ground and in space needs to be deeply analyzed so as to improve ZTD and TEC modeling at regional and global scales, as well as scintillation and forecast models, ionosphere models and tropospheric gradient models.

Further interesting applications of satellite navigation are focused on *GNSS-R* emerging applications, such as methods and measurements techniques for *Remote Sensing of Soil Moisture Content (SMC)*. As it is known, SMC plays an important environmental role in the assessment of climate change and environmental monitoring of areas prone to flooding,

drought and evapotranspiration. SMC also allows the monitoring of water runoff and surface erosion. By correlating other environmental variables, such as land surface temperatures, land cover or precipitations, SMC is commonly used as an input parameter for many climate models. In agriculture, SMC is a crucial indicator of plant growth and crop yield. In recent decades, satellites closer to Earth equipped with GNSS-R receiver, active microwave (ALOS-2, Sentinel-1, TerraSar-X) or passive microwave (AMSR2 and SMOS), have provided an opportunity to detect SMC from space using a wide range of techniques and sensors. A scientific treatment of the issues related to SMC (e.g., GNSS-R Techniques, Methods, and Applications) has already recently developed with wide potential applications [92,93]. Another interesting investigation could be *GNSS-R Earth Remote Sensing from SmallSats* and substantial economic development investments were carried out in so-called small satellites in recent years, such as BuFeng-1 [94], CYGNSS [95], Fengyun-3 series [96], FSSCat [97], HydroGNSS [98], PRETTY [99], and Spire CubeSats series [100]. Small satellites are changing the Earth remote sensing parameters by exploiting innovative payloads. Thus, the spatiotemporal sampling properties of GNSS-R could create new scenarios for studying, specifically devoted to wind speed determination, SMC determination, vegetation water content monitoring, and supporting sustainable soils developments. Additionally, GNSS-R can be used for *ocean monitoring*, as presented in the work of [101–104].

In addition, GNSS can provide meaningful support to *Precision Farming* (PF). PF has been widely implemented in almost all agricultural production systems over the past 20 years. Obviously, PF developments differ in the world according to technological, agronomic, economic and cultural differences existing between countries. PF has been widely used in developed agricultural countries. Considering benefits and limits of increasing PF adoption all around the world, GNSS could provide innovative methods and applications to optimize operating modes, particularly in developing agricultural economies [105–108].

The use of *GNSS* for *forest and wetland hydrology* is also developing. According to other geomatics techniques (Remote Sensing, UAV/UAS and LiDAR), it can be considered a resource for the assessing of climate-related environmental risks, such as fires, landslides, epidemics of forest diseases, rapid deterioration of the quality of watercourses, and conversion of forest wetlands to montane forests, due to the deposition of eroded soil [109–111]. Newer ECOSTRESS [112] and SMAP [113] satellite types, specifically designed to obtain soil moisture information with dense forest cover, may be an important improvement in this emerging study.

The use of ground-based GNSS and/or radio occultation techniques can also be useful in the field of *natural hazards*, such as those related to the emission of hazardous gases and ash into the atmosphere from *volcanic clouds*. Analysis of Signal Noise Ratio (SNR) data can demonstrate daily repeatability and seasonal trends indicating the strong dependence of multipath error on changes in the antenna environment, but can also be an indicator of sudden changes in volcanic cloud composition and height [114–117]. *GNSS interference* detection and spoofing provide an important area of exploration, since multipath and Non-Line-Of-Signals (NLOS) are the main errors occurring in different GNSS applications, e.g., civil (urban transport applications) and military uses [118–122].

Last, but not least, the massive deployment of multi-frequency *GNSS CORS* at global, regional, and national scales has allowed the continuous use of time series data that is mostly free of charge. Moreover, regarding the upcoming CORS upgrades to quadric stellation (BDS, Galileo, GLONASS, GPS), these infrastructures can provide unlimited potential for both technical and scientific applications, e.g., the evaluation of a global reference system and its inconstancy, geodynamic analysis, PF, mining, SHM, surveying and land cadastral management, soil moisture mapping, drought, snow depth, airborne UAV, road and rail transport and logistics, maritime navigation and aviation [123–126].

Author Contributions: Conceptualization of the Manuscript Idea: S.J. and G.D.; Methodology and Software: Q.W. and S.J.; Supervision and Funding Acquisition: S.J. and G.D.; G.D., Q.W. and S.J. wrote the original draft preparation; S.J. and G.D. reviewed and edited this paper. All authors have read and agreed to the published version of the manuscript.

Funding: This research was funded by the National Natural Science Foundation of China (NSFC) Project (Grant No. 12073012), Shanghai Leading Talent Project (Grant No. E056061) and Jiangsu Natural Resources Development Special Project (Grant No. JSZRHYKJ202002).

Data Availability Statement: The BDS observation data from IGS MGEX networks can be obtained https://cddis.nasa.gov/archive/gps/data/daily, last accessed on 31 July 2022.

Acknowledgments: The authors thank IGS for providing the BDS observation data of MGEX networks. The authors would like to express their sincere thanks to Claudia Pipitone for her valuable work in revising the English throughout the text.

Conflicts of Interest: The authors declare no conflict of interest.

References

1. BDS. Available online: http://www.csno-tarc.cn/en/system/constellation (accessed on 7 July 2022).
2. Galileo. Available online: https://www.gsc-europa.eu/system-service-status/constellation-information (accessed on 7 July 2022).
3. GLONASS. Available online: https://www.glonass-iac.ru/en/sostavOG (accessed on 7 July 2022).
4. GPS. Available online: https://www.gps.gov/systems/gps/space (accessed on 7 July 2022).
5. Jin, S.; Jin, R.; Liu, X. *GNSS Atmospheric Seismology: Theory, Observations and Modeling*; Springer: Berlin, Germany, 2019.
6. Su, K.; Jin, S. Real-time seismic waveforms estimation of the 2019 Mw = 6.4 and Mw = 7.1 California earthquakes with high-rate multi-GNSS observations. *IEEE Access* **2020**, *8*, 85411–85420. [CrossRef]
7. Jin, S.; Su, K. Co-seismic displacement and waveforms of the 2018 Alaska earthquake from high-rate GPS PPP velocity estimation. *J Geod.* **2019**, *93*, 1559–1569. [CrossRef]
8. Jin, S.; Cardellach, E.; Xie, F. *GNSS Remote Sensing: Theory, Methods and Applications*; Springer: Dordrecht, The Netherlands, 2014; p. 276.
9. Najibi, N.; Jin, S. Physical reflectivity and polarization characteristics for snow and ice-covered surfaces interacting with GPS signals. *Remote Sens.* **2013**, *5*, 4006–4030. [CrossRef]
10. Kruger, G.; Springer, R.; Lechner, W. Global Navigation Satellite Systems (GNSS). *Comput. Electron. Agric.* **2007**, *11*, 3–21. [CrossRef]
11. Su, K.; Jin, S. Analytical performance and validations of the Galileo five-frequency precise point positioning models. *Measurement* **2021**, *172*, 108890. [CrossRef]
12. Su, K.; Jin, S. Triple-frequency carrier phase precise time and frequency transfer models for BDS-3. *GPS Solut.* **2019**, *23*, 86. [CrossRef]
13. Yang, Y.; Li, J.; Xu, J.; Tang, J.; Guo, H.; He, H. Contribution of the Compass satellite navigation system to global PNT users. *Chin. Sci. Bull.* **2011**, *56*, 2813–2819. [CrossRef]
14. RINEX 4.00. Available online: https://files.igs.org/pub/data/format/rinex_4.00 (accessed on 7 July 2022).
15. Leick, A.; Rapoport, L.; Tatarnikov, D. *GPS Satellite Surveying*, 4th ed.; John Wiley & Sons: Hoboken, NJ, USA, 2015.
16. Zhang, B.; Hou, P.; Liu, T.; Yuan, Y. A single-receiver geometry-free approach to stochastic modeling of multi-frequency GNSS observables. *J Geod.* **2020**, *94*, 37. [CrossRef]
17. Xu, Y.; Ji, S.; Chen, W.; Weng, D. A new ionosphere-free ambiguity resolution method for long-range baseline with GNSS triple-frequency signals. *Adv. Space Res.* **2015**, *56*, 1600–1612. [CrossRef]
18. Duong, V.; Harima, K.; Choy, S.; Laurichesse, D.; Rizos, C. An assessment of wide-lane ambiguity resolution methods for multi-frequency multi-GNSS precise point positioning. *Surv. Rev.* **2019**, *52*, 442–453. [CrossRef]
19. Hofmann-Wellenhof, B.; Lichtenegger, H.; Wasle, E. *GNSS—Global Navigation Satellite Systems*; Springer: Berlin, Germany, 2008; ISBN 978-3-211-73017-1. [CrossRef]
20. Jin, S.G. *Global Navigation Satellite Systems: Signal, Theory and Applications*; InTech-Publisher: Rijeka, Croatia, 2012; p. 426. ISBN 978-953-307-843-4.
21. Kouba, J.; Héroux, P. Precise Point Positioning Using IGS Orbit and Clock Products. *GPS Solut.* **2001**, *5*, 12–28. [CrossRef]
22. Jin, S.; Su, K. PPP models and performances from single- to quad-frequency BDS observations. *Satell. Navig.* **2020**, *1*, 13. [CrossRef]
23. Zumberge, J.F.; Heflin, M.B.; Jefferson, D.C.; Watkins, M.M.; Webb, F.H. Precise point positioning for the efficient and robust analysis of GPS data from large networks. *J. Geophys. Res. Solid Earth* **1997**, *102*, 5005–5017. [CrossRef]
24. Liu, S.; Yuan, Y. Generating GPS decoupled clock products for precise point positioning with ambiguity resolution. *J. Geod.* **2022**, *96*, 6. [CrossRef]
25. An, X.; Meng, X.; Jiang, W. Multi-constellation GNSS precise point positioning with multi-frequency raw observations and dual-frequency observations of ionospheric-free linear combination. *Satell. Navig.* **2020**, *1*, 7. [CrossRef]
26. Tu, R.; Zhang, P.; Zhang, R.; Liu, J.; Lu, X. Modeling and performance analysis of precise time transfer based on BDS triple-frequency un-combined observations. *J. Geod.* **2019**, *93*, 837–847. [CrossRef]
27. Zhou, F.; Cao, X.; Ge, Y.; Li, W. Assessment of the positioning performance and tropospheric delay retrieval with precise point positioning using products from different analysis centers. *GPS Solut.* **2020**, *24*, 12. [CrossRef]

28. Jin, S.; Feng, G.P.; Gleason, S. Remote sensing using GNSS signals: Current status and future directions. *Adv. Space Res.* **2011**, *47*, 1645–1653. [CrossRef]
29. Su, K.; Jin, S.; Jiao, G. Assessment of multi-frequency GNSS PPP models using GPS, Beidou, GLONASS, Galileo and QZSS. *Meas. Sci. Technol.* **2020**, *31*, 064008. [CrossRef]
30. Su, K.; Jin, S. Analysis and comparisons of the BDS/Galileo quad-frequency PPP models performances. *Acta Geod. Cartogr. Sin.* **2020**, *49*, 1189–1201.
31. Su, K.; Jin, S. Improvement of Multi-GNSS Precise Point Positioning Performances with Real Meteorological Data. *J. Navig.* **2018**, *71*, 1363–1380. [CrossRef]
32. Su, K.; Jin, S.; Hoque, M. Evaluation of Ionospheric Delay Effects on Multi-GNSS Positioning Performance. *Remote Sens.* **2019**, *11*, 171. [CrossRef]
33. Montenbruck, O.; Steigenberger, P.; Prange, L.; Deng, Z.; Zhao, Q.; Perosanz, F.; Romero, I.; Noll, C.; Stuerze, A.; Weber, G. The Multi-GNSS Experiment (MGEX) of the International GNSS Service (IGS)—Achievements, prospects and challenges. *Adv. Space Res.* **2017**, *59*, 1671–1697. [CrossRef]
34. Rizos, C.; Montenbruck, O.; Weber, R.; Weber, G.; Neilan, R.; Hugentobler, U. The IGS MGEX experiment as a milestone for a comprehensive multi-GNSS service. In Proceedings of the ION 2013 Pacific PNT Meeting, Honolulu, Hawaii, 23–25 April 2013; Institute of Navigation: Manassas, WV, USA, 2013; pp. 289–295.
35. Montenbruck, O.; Steigenberger, P.; Khachikyan, R.; Weber, G.; Langley, R.; Mervart, L.; Hugentobler, U. IGS-MGEX: Preparing the ground for multi-constellation GNSS science. *Inside GNSS* **2014**, *9*, 42–49.
36. Wang, Y.; Li, M.; Jiang, K.; Li, W.; Qin, G.; Zhao, Q.; Peng, H.; Lin, M. Reduced-dynamic precise orbit determination of haiyang-2b altimetry satellite using a refined empirical acceleration model. *Remote Sens.* **2021**, *13*, 3702. [CrossRef]
37. Jin, B.; Li, Y.; Jiang, K.; Li, Z.; Chen, S. Grace-fo antenna phase center modeling and precise orbit determination with single receiver ambiguity resolution. *Remote Sens.* **2021**, *13*, 4204. [CrossRef]
38. Bevis, M.; Businger, S.; Herring, T.A.; Rocken, C.; Anthes, R.A.; Ware, R.H. GPS meteorology: Remote sensing of atmospheric water vapor using the Global Positioning System. *J. Geophys. Res. Atmos.* **1992**, *97*, 15787–15801. [CrossRef]
39. Wu, M.; Jin, S.; Li, Z.; Cao, Y.; Ping, F.; Tang, X. High-precision GNSS PWV and its variation characteristics in china based on individual station meteorological data. *Remote Sens.* **2021**, *13*, 1296. [CrossRef]
40. Zhu, G.; Huang, L.; Liu, L.; Li, C.; Li, J.; Huang, L.; Zhou, L.; He, H. A new approach for the development of grid models calculating tropospheric key parameters over china. *Remote Sens.* **2021**, *13*, 3546. [CrossRef]
41. Klobuchar, J.A. Ionospheric Time-Delay Algorithm for Single-Frequency GPS Users. *IEEE Trans. Aerosp. Electron. Syst.* **1987**, *AES-23*, 325–331. [CrossRef]
42. Aragon-Angel, A.; Zürn, M.; Rovira-Garcia, A. Galileo Ionospheric Correction Algorithm: An Optimization Study of NeQuick-G. *Radio Sci.* **2019**, *54*, 1156–1169. [CrossRef]
43. Zhang, H.; Yuan, Y.; Li, W.; Zhang, B. A real-time precipitable water vapor monitoring system using the national GNSS network of China: Method and preliminary results. *IEEE J. Sel. Top. Appl. Earth Obs. Remote Sens.* **2019**, *12*, 1587–1598. [CrossRef]
44. Yuan, Y.; Wang, N.; Li, Z.; Huo, X. The BeiDou Global Broadcast Ionospheric Delay Correction Model (BDGIM) and Its Preliminary Performance Evaluation Results. *Navigation* **2019**, *66*, 55–69. [CrossRef]
45. Schaer, S. *Mapping and Predicting the Earth's Ionosphere Using the Global Positioning System*; Astronomical Institute, University of Berne: Dhaka, Bangladesh, 1999.
46. Jin, S.G.; Jin, R.; Li, D. Assessment of BeiDou differential code bias variations from multi-GNSS network observations. *Ann. Geophys.* **2016**, *34*, 259–269. [CrossRef]
47. Jin, R.; Jin, S.G.; Feng, G.P. M_DCB: Matlab code for estimating GNSS satellite and receiver differential code biases. *GPS Solut.* **2012**, *16*, 541–548. [CrossRef]
48. Zhang, B.; Teunissen, P.J.G.; Yuan, Y.; Zhang, X.; Li, M. A modified carrier-to-code leveling method for retrieving ionospheric observables and detecting short-term temporal variability of receiver differential code biases. *J. Geod.* **2019**, *93*, 19–28. [CrossRef]
49. Li, M.; Yuan, Y.; Zhang, X.; Zha, J. A multi-frequency and multi-GNSS method for the retrieval of the ionospheric TEC and intraday variability of receiver DCBs. *J. Geod.* **2020**, *94*, 102. [CrossRef]
50. Zha, J.; Zhang, B.; Yuan, Y.; Zhang, X.; Li, M. Use of modified carrier-to-code leveling to analyze temperature dependence of multi-GNSS receiver DCB and to retrieve ionospheric TEC. *GPS Solut.* **2019**, *23*, 103. [CrossRef]
51. Shi, C.; Fan, L.; Li, M.; Liu, Z.; Gu, S.; Zhong, S.; Song, W. An enhanced algorithm to estimate BDS satellite's differential code biases. *J. Geod.* **2015**, *90*, 161–177. [CrossRef]
52. Gu, S.; Wang, Y.; Zhao, Q.; Zheng, F.; Gong, X. BDS-3 differential code bias estimation with undifferenced uncombined model based on triple-frequency observation. *J. Geod.* **2020**, *94*, 45. [CrossRef]
53. Fan, L.; Li, M.; Wang, C.; Shi, C. BeiDou satellite's differential code biases estimation based on uncombined precise point positioning with triple-frequency observable. *Adv. Space Res.* **2017**, *59*, 804–814. [CrossRef]
54. Su, K.; Jin, S. Three Dual-Frequency Precise Point Positioning Models for the Ionospheric Modeling and Satellite Pseudorange Observable-Specific Signal Bias Estimation. *Remote Sens.* **2021**, *13*, 5093. [CrossRef]
55. Wang, J.; Huang, G.; Zhou, P.; Yang, Y.; Gao, Y. Advantages of Uncombined Precise Point Positioning with Fixed Ambiguity Resolution for Slant Total Electron Content (STEC) and Differential Code Bias (DCB) Estimation. *Remote Sens.* **2020**, *12*, 304. [CrossRef]

56. Ren, X.; Chen, J.; Li, X.; Zhang, X. Ionospheric Total Electron Content Estimation Using GNSS Carrier Phase Observations Based on Zero-Difference Integer Ambiguity: Methodology and Assessment. *IEEE Trans. Geosci. Remote Sens.* **2020**, *59*, 817–830. [CrossRef]
57. Yan, X.; Yang, G. An Enhanced Mapping Function with Ionospheric Varying Height. *Remote Sens.* **2019**, *11*, 1497.
58. Hoque, M.M.; Jakowski, N. Mitigation of Ionospheric Mapping Function Error. In Proceedings of the 26th International Technical Meeting of the Satellite Division of The Institute of Navigation (ION GNSS+ 2013), Nashville, TN, USA, 16–20 September 2013.
59. Su, K.; Jin, S.; Jiang, J.; Hoque, M.; Yuan, L. Ionospheric VTEC and satellite DCB estimated from single-frequency BDS observations with multi-layer mapping function. *GPS Solut.* **2021**, *25*, 68. [CrossRef]
60. Abdelazeem, M.; Çelik, R.N.; El-Rabbany, A. MGR-DCB: A Precise Model for Multi-Constellation GNSS Receiver Differential Code Bias. *J. Navig.* **2015**, *69*, 698–708. [CrossRef]
61. Li, Z.; Yuan, Y.; Li, H.; Ou, J.; Huo, X. Two-step method for the determination of the differential code biases of COMPASS satellites. *J. Geod.* **2012**, *86*, 1059–1076. [CrossRef]
62. Jin, S.G.; Wang, J.; Zhang, H.; Zhu, W. Real-time monitoring and prediction of the total ionospheric electron content by means of GPS observations. *Chin. Astron. Astrophys.* **2004**, *28*, 331–337. [CrossRef]
63. Yuan, Y.; Tscherning, C.C.; Knudsen, P.; Xu, G.; Ou, J. The ionospheric eclipse factor method (IEFM) and its application to determining the ionospheric delay for GPS. *J. Geod.* **2008**, *82*, 1–8. [CrossRef]
64. Li, M.; Yuan, Y. Estimation and Analysis of the Observable-Specific Code Biases Estimated Using Multi-GNSS Observations and Global Ionospheric Maps. *Remote Sens.* **2021**, *13*, 3096. [CrossRef]
65. Liu, T.; Zhang, B. Estimation of code observation-specific biases (OSBs) for the modernized multi-frequency and multi-GNSS signals: An undifferenced and uncombined approach. *J. Geod.* **2021**, *95*, 97. [CrossRef]
66. Su, K.; Jin, S. A Novel GNSS Single-Frequency PPP Approach to Estimate the Ionospheric TEC and Satellite Pseudorange Observable-Specific Signal Bias. *IEEE Trans. Geosci. Remote Sens.* **2022**, *60*, 5801712. [CrossRef]
67. Jin, S.; Gao, C.; Yuan, L.; Guo, P.; Calabia, A.; Ruan, H.; Luo, P. Long-term variations of plasmaspheric total electron content from topside GPS observations on LEO satellites. *Remote Sens.* **2021**, *13*, 545. [CrossRef]
68. Su, Y.-C.; Sha, J. A Study of Possible Correlations between Seismo-Ionospheric Anomalies of GNSS Total Electron Content and Earthquake Energy. *Remote Sens.* **2022**, *14*, 1155. [CrossRef]
69. Jiang, H.; Jin, S.; Hernández-Pajares, M.; Xi, H.; An, J.; Wang, Z.; Xu, X.; Yan, H. A new method to determine the optimal thin layer ionospheric height and its application in the polar regions. *Remote Sens.* **2021**, *13*, 2458. [CrossRef]
70. Wang, Q.; Jin, S.; Ye, X. A Novel Method to Estimate Multi-GNSS Differential Code Bias without Using Ionospheric Function Model and Global Ionosphere Map. *Remote Sens.* **2022**, *14*, 2002. [CrossRef]
71. Lan, X.; Wang, L.; Li, J.; Jiang, W.; Zhang, M. Maritime Multiple Moving Target Detection Using Multiple-BDS-Based Radar: Doppler Phase Compensation and Resolution Improvement. *Remote Sens.* **2021**, *13*, 4963. [CrossRef]
72. Shi, Q.; Jin, S. Variation Characteristics of Multi-Channel Differential Code Biases from New BDS-3 Signal Observations. *Remote Sens.* **2022**, *14*, 594. [CrossRef]
73. Qian, X.; Jin, S. Estimation of snow depth from GLONASS SNR and phase-based multipath reflectometry. *IEEE J. Sel. Top. Appl. Earth Obs. Remote Sens.* **2016**, *9*, 4817–4823. [CrossRef]
74. Su, K. Models and Applications of the BDS/GNSS Precise Point Positioning. Ph.D. Thesis, Shanghai Astronomical Observatory, CAS, Shanghai, China, 2021.
75. Fortunato, M.; Ravanelli, M.; Mazzoni, A. Real-time geophysical applications with Android GNSS raw measurements. *Remote Sens.* **2019**, *11*, 2113. [CrossRef]
76. Lăpădat, A.M.; Tiberius, C.C.J.M.; Teunissen, P.J.G. Experimental evaluation of smartphone accelerometer and low-cost dual frequency gnss sensors for deformation monitoring. *Sensors* **2021**, *21*, 7946. [CrossRef] [PubMed]
77. Sousa, J.J.; Hlaváčová, I.; Bakoň, M.; Lazecký, M.; Patrício, G.; Guimarães, P.; Ruiz, A.M.; Bastos, L.; Sousa, A.; Bento, R. Potential of Multi-Temporal InSAR Techniques for Bridges and Dams Monitoring. *Procedia Technol.* **2014**, *16*, 834–841. [CrossRef]
78. Pipitone, C.; Maltese, A.; Dardanelli, G.; Lo Brutto, M.; La Loggia, G. Monitoring Water Surface and Level of a Reservoir Using Different Remote Sensing Approaches and Comparison with Dam Displacements Evaluated via GNSS. *Remote Sens.* **2018**, *10*, 71. [CrossRef]
79. Maltese, A.; Pipitone, C.; Dardanelli, G.; Capodici, F.; Muller, J.-P. Toward a Comprehensive Dam Monitoring: On-Site and Remote-Retrieved Forcing Factors and Resulting Displacements (GNSS and PS–InSAR). *Remote Sens.* **2021**, *13*, 1543. [CrossRef]
80. Yigit, C.O.; Gurlek, E. Experimental testing of high-rate GNSS precise point positioning (PPP) method for detecting dynamic vertical displacement response of engineering structures. *Geomat. Nat. Hazards Risk* **2017**, *8*, 893–904. [CrossRef]
81. Xi, R.; Jiang, W.; Meng, X.; Chen, H.; Chen, Q. Bridge monitoring using BDS-RTK and GPS-RTK techniques. *Meas. J. Int. Meas. Confed.* **2018**, *120*, 128–139. [CrossRef]
82. Meng, X.; Nguyen, D.T.; Xie, Y.; Owen, J.S.; Psimoulis, P.; Ince, S.; Chen, Q.; Ye, J.; Bhatia, P. Design and implementation of a new system for large bridge monitoring—Geoshm. *Sensors* **2018**, *18*, 775. [CrossRef]
83. Xi, R.; He, Q.; Meng, X. Bridge monitoring using multi-GNSS observations with high cutoff elevations: A case study. *Meas. J. Int. Meas. Confed.* **2021**, *168*, 108303. [CrossRef]
84. Manzini, N.; Orcesi, A.; Thom, C.; Brossault, M.-A.; Botton, S.; Ortiz, M.; Dumoulin, J. Performance analysis of low-cost GNSS stations for structural health monitoring of civil engineering structures. *Struct. Infrastruct. Eng.* **2022**, *18*, 595–611. [CrossRef]

85. Shen, N.; Chen, L.; Liu, J.; Wang, L.; Tao, T.; Wu, D.; Chen, R. A Review of Global Navigation Satellite System (GNSS)-Based Dynamic Monitoring Technologies for Structural Health Monitoring. *Remote Sens.* **2019**, *11*, 1001. [CrossRef]
86. Baybura, T.; Tiryakioğlu, I.; Uğur, M.A.; Solak, H.I.; Şafak, S. Examining the Accuracy of Network RTK and Long Base RTK Methods with Repetitive Measurements. *J. Sens.* **2019**, *2019*, 3572605. [CrossRef]
87. Lu, Y.; Ji, S.; Tu, R.; Weng, D.; Lu, X.; Chen, W. An improved long-period precise time-relative positioning method based on rts data. *Sensors* **2020**, *21*, 53. [CrossRef] [PubMed]
88. Dardanelli, G.; Maltese, A.; Pipitone, C.; Pisciotta, A.; Lo Brutto, M. Nrtk, ppp or static, that is the question. Testing different positioning solutions for gnss survey. *Remote Sens.* **2021**, *13*, 1406. [CrossRef]
89. Jin, S.; Park, J.-U.; Cho, J.-H.; Park, P.-H. Seasonal variability of GPS-derived zenith tropospheric delay (1994–2006) and climate implications. *J. Geophys. Res. Atmos.* **2007**, *112*, D09110. [CrossRef]
90. Jin, S.; Han, L.; Cho, J. Lower atmospheric anomalies following the 2008 Wenchuan Earthquake observed by GPS measurements, *J. Atmos. Sol.-Terr. Phys.* **2011**, *73*, 810–814. [CrossRef]
91. Boehm, J.; Werl, B.; Schuh, H. Troposphere mapping functions for GPS and very long baseline interferometry from European Centre for Medium-Range Weather Forecasts operational analysis data. *J. Geophys. Res. Solid Earth* **2006**, *111*, B02406. [CrossRef]
92. Edokossi, K.; Calabia, A.; Jin, S.; Molina, I. GNSS-Reflectometry and Remote Sensing of Soil Moisture: A Review of measurement Techniques, Methods, and Applications. *Remote Sens.* **2020**, *12*, 614. [CrossRef]
93. Wu, X.; Ma, W.; Xia, J.; Bai, W.; Jin, S.; Calabia, A. Spaceborne GNSS-R Soil Moisture Retrieval: Status, Development Opportunities, and Challenges. *Remote Sens.* **2021**, *13*, 45. [CrossRef]
94. BuFeng-1. Available online: https://space.skyrocket.de/doc_sdat/bufeng-1.htm (accessed on 7 July 2022).
95. CYGNSS. Available online: https://www.nasa.gov/cygnss (accessed on 7 July 2022).
96. Fengyun-3 Series. Available online: https://directory.eoportal.org/web/eoportal/satellite-missions/content/-/article/fy-3 (accessed on 7 July 2022).
97. FSSCat. Available online: https://www.esa.int/Applications/Observing_the_Earth/Ph-sat/FSSCat_F-sat-1_ready_for_launch (accessed on 7 July 2022).
98. HydroGNSS. Available online: https://www.esa.int/ESA_Multimedia/Images/2021/03/HydroGNSS (accessed on 7 July 2022).
99. PRETTY. Available online: https://www.esa.int/ESA_Multimedia/Images/2021/09/PRETTY_CubeSat (accessed on 7 July 2022).
100. Spire CubeSats Series. Available online: https://spire.com/spirepedia/cubesat/ (accessed on 7 July 2022).
101. Gleason, S.; Hodgart, S.; Sun, Y.; Gommenginger, C.; Mackin, S.; Adjrad, M.; Unwin, M. Detection and processing of bistatically reflected GPS signals from low earth orbit for the purpose of ocean remote sensing. *IEEE Trans. Geosci. Remote Sens.* **2005**, *43*, 1229–1241. [CrossRef]
102. Clarizia, M.P.; Gommenginger, C.P.; Gleason, S.T.; Srokosz, M.A.; Galdi, C.; Di Bisceglie, M. Analysis of GNSS-R delay-Doppler maps from the UK-DMC satellite over the ocean. *Geophys. Res. Lett.* **2009**, *36*, L02608. [CrossRef]
103. Soulat, F.; Caparrini, M.; Germain, O.; Lopez-Dekker, P.; Taani, M.; Ruffini, G. Sea state monitoring using coastal GNSS-R. *Geophys. Res. Lett.* **2004**, *31*, L21303. [CrossRef]
104. Jin, S.; Komjathy, A. GNSS reflectometry and remote sensing: New objectives and results. *Adv. Space Res.* **2010**, *46*, 111–117. [CrossRef]
105. Griffin, T.W.; Miller, N.J.; Bergtold, J.; Shanoyan, A.; Sharda, A.; Ciampitti, I.A. Farm's sequence of adoption of information-intensive precision agricultural technology. *Appl. Eng. Agric.* **2017**, *33*, 521–527. [CrossRef]
106. Marucci, A.; Colantoni, A.; Zambon, I.; Egidi, G. Precision farming in hilly areas: The use of network RTK in GNSS technology. *Agriculture* **2017**, *7*, 60. [CrossRef]
107. Kunz, C.; Weber, J.F.; Gerhards, R. Benefits of precision farming technologies for mechanical weed control in soybean and sugar beet—Comparison of precision hoeing with conventional mechanical weed control. *Agronomy* **2015**, *5*, 130–142. [CrossRef]
108. Pini, M.; Marucco, G.; Falco, G.; Nicola, M.; De Wilde, W. Experimental Testbed and Methodology for the Assessment of RTK GNSS Receivers Used in Precision Agriculture. *IEEE Access* **2020**, *8*, 14690–14703. [CrossRef]
109. Sferlazza, S.; Maltese, A.; Dardanelli, G.; La Mela Veca, D.S. Optimizing the Sampling Area across an Old-Growth Forest via UAV-Borne Laser Scanning, GNSS, and Radial Surveying. *ISPRS Int. J. Geo-Inf.* **2022**, *11*, 168. [CrossRef]
110. Sferlazza, S.; Maltese, A.; Ciraolo, G.; Dardanelli, G.; Maetzke, F.G.; La Mela Veca, D.S. Forest accessibility, Madonie mountains (northern Sicily, Italy): Implementing a GIS decision support system. *J. Maps* **2021**, *17*, 464–473. [CrossRef]
111. Petropoulos, G.P.; Maltese, A.; Carlson, T.N.; Provenzano, G.; Pavlides, A.; Ciraolo, G.; Hristopulos, D.; Capodici, F.; Chalkias, C.; Dardanelli, G.; et al. Exploring the use of Unmanned Aerial Vehicles (UAVs) with the simplified 'triangle' technique for soil water content and evaporative fraction retrievals in a Mediterranean setting. *Int. J. Remote Sens.* **2021**, *42*, 1623–1642. [CrossRef]
112. ECOSTRESS. Available online: https://ecostress.jpl.nasa.gov/ (accessed on 7 July 2022).
113. SMAP. Available online: https://www.jpl.nasa.gov/missions/soil-moisture-active-passive-smap (accessed on 7 July 2022).
114. Bekaert, D.P.S.; Walters, R.J.; Wright, T.J.; Hooper, A.J.; Parker, D.J. Statistical comparison of InSAR tropospheric correction techniques. *Remote Sens. Environ.* **2015**, *170*, 40–47. [CrossRef]
115. Biondi, R.; Steiner, A.K.; Kirchengast, G.; Brenot, H.; Rieckh, T. Supporting the detection and monitoring of volcanic clouds: A promising new application of Global Navigation Satellite System radio occultation. *Adv. Space Res.* **2017**, *60*, 2707–2722. [CrossRef]
116. Iguchi, M.; Nakamichi, H.; Tanaka, H.; Ohta, Y.; Shimizu, A.; Miki, D. Integrated monitoring of volcanic ash and forecasting at sakurajima volcano, Japan. *J. Disaster Res.* **2019**, *14*, 798–809. [CrossRef]

117. Cigala, V.; Biondi, R.; Prata, A.J.; Steiner, A.K.; Kirchengast, G.; Brenot, H. GNSS radio occultation advances the monitoring of volcanic clouds: The case of the 2008 Kasatochi eruption. *Remote Sens.* **2019**, *11*, 2199. [CrossRef]
118. Akos, D.M. Who's afraid of the spoofer? GPS/GNSS spoofing detection via automatic gain control (agc). *Navig. J. Inst. Navig.* **2012**, *59*, 281–290. [CrossRef]
119. Groves, P.D.; Jiang, Z.; Rudi, M.; Strode, P. A portfolio approach to NLOS and multipath mitigation in dense urban areas. In Proceedings of the 26th International Technical Meeting of the Satellite Division of the Institute of Navigation, ION GNSS 2013, Nashville, TN, USA, 16–19 September 2013; pp. 3231–3247.
120. Jiang, Z.; Groves, P.D. NLOS GPS signal detection using a dual-polarisation antenna. *GPS Solut.* **2014**, *18*, 15–26. [CrossRef]
121. Broumandan, A.; Jafarnia-Jahromi, A.; Lachapelle, G. Spoofing detection, classification and cancelation (SDCC) receiver architecture for a moving GNSS receiver. *GPS Solut.* **2015**, *19*, 475–487. [CrossRef]
122. Borio, D. GNSS acquisition in the presence of continuous wave interference. *IEEE Trans. Aerosp. Electron. Syst.* **2010**, *46*, 47–60. [CrossRef]
123. Teunissen, P.J.G.; Odijk, D.; Zhang, B. PPP-RTK: Results of CORS network-based PPP with integer ambiguity resolution. *J. Aeronaut. Astronaut. Aviat.* **2010**, *42*, 223–230.
124. Forlani, G.; Dall'Asta, E.; Diotri, F.; di Cella, U.M.; Roncella, R.; Santise, M. Quality assessment of DSMs produced from UAV flights georeferenced with on-board RTK positioning. *Remote Sens.* **2018**, *10*, 311. [CrossRef]
125. Li, B.; Verhagen, S.; Teunissen, P.J.G. Robustness of GNSS integer ambiguity resolution in the presence of atmospheric biases. *GPS Solut.* **2014**, *18*, 283–296. [CrossRef]
126. Jin, S.; Zhang, T. Terrestrial water storage anomalies associated with drought in Southwestern USA derived from GPS observations. *Surv. Geophys.* **2016**, *37*, 1139–1156. [CrossRef]

MDPI
St. Alban-Anlage 66
4052 Basel
Switzerland
www.mdpi.com

Remote Sensing Editorial Office
E-mail: remotesensing@mdpi.com
www.mdpi.com/journal/remotesensing

Academic Open
Access Publishing

mdpi.com

ISBN 978-3-0365-8997-8